DEVELOPMENT OF RAPID ASSESSMENT TOOLS FOR GROUNDWATER VULNERABILITY MAPPING USING INTEGRATED GEOSCIENTIFIC DATASETS AND ARTIFICIAL INTELLIGENCE ALGORITHMS: CASE STUDY FROM WITBANK AND ERMELO COALFIELDS, SOUTH AFRICA

Emmanuel Sakala

Submitted in fulfilment of the requirements for the degree

Philosophiae Doctor

in the

Faculty of Natural and Agricultural Sciences

(Institute for Groundwater Studies)

at the

University of the Free State

Supervisor: Dr Francois Fourie

2017

Our intelligence is what makes us human, and artificial intelligence is an extension of that quality.

YANN LECUN

DECLARATION

I, Emmanuel SAKALA, hereby declare that the thesis hereby submitted by me to the Institute for Groundwater Studies in the Faculty of Natural and Agricultural Sciences at the University of the Free State, in fulfilment of the degree of Doctor Philosophiae, is my own independent work. It has not previously been submitted by me to any other institution of higher education. In addition, I declare that all sources cited have been acknowledged by means of a list of references.

I furthermore cede copyright of the thesis and its contents in favour of the University of the Free State and the Council for Geoscience.

Emmanuel SAKALA

18 April 2018

ACKNOWLEDGEMENTS

First, I want to thank Almighty God for having given me strength through this period.

A special thank you to my supervisor Dr Francois Fourie for assistance, guidance and patience during this research period. Your inputs through advice, data analysis and eventually right through the final write up of the dissertation are highly appreciated.

Another special thank you goes to Dr Modreck Gomo for help with the geochemical and hydrogeological interpretation of the data.

The thesis emanated from the Mine Water Management Project, funded under the Medium Term Expenditure Framework by the Department of Mineral Resources (DMR) of South Africa. I wish to extend a sincere thank you to the DMR and the Council for Geoscience for allowing me to do the research that I am positive will have a valuable impact on the entire nation. Thank you to Dr Henk Coetzee, the project manager of the Mine Water Management project for allowing me to be part of the project team.

Editorial assistance by Dr Vunganai Midzi, Ms Zahn Nel, Dr Godfrey Madzivire and Mr Emmanuel Chirenje is greatly appreciated.

My gratitude for help with Python programming goes to Mr Patrick Cole and the Stock Overflow online community.

I would like to thank my family for your support during many late nights and when I was away from home on field trips during the course of the research. Thank you also to my friends for your support and encouragement.

My sincere thanks goes to the Council for Geoscience geophysics and remote sensing team for invaluable assistance with fieldwork and to the laboratory unit for making their facilities available.

Finally, I would like to extend my sincerest gratitude to everyone with whom I did not mention by name but who contributed to the fulfilment of this dissertation.

To my beloved wife Joyce and my son Tinashe

TABLE OF CONTENTS

List of Acronyms i
Measurement Units iv
Outcomes of the Research v

CHAPTER 1 : INTRODUCTION 1

1.1 Background 1
1.2 Aims and Objectives 4
1.3 Outline of Research Methodology 5
1.4 Limitations of the Research 6
1.5 Structure of the Thesis 7

CHAPTER 2 : GROUNDWATER VULNERABILITY ASSESSMENT METHODS 9

2.1 Introduction 9
2.2 General Concept of Groundwater Vulnerability 9
2.2.1 Laws of Groundwater Vulnerability 10
2.3 Review of Groundwater Vulnerability Assessment Approaches 11
2.3.1 Overlay and Index Approach 11
2.3.1.1 DRASTIC 11
2.3.1.2 GOD 14
2.3.1.3 SINTACS 15
2.3.1.4 AVI 16
2.3.2 Process-Based Simulation Modelling 17
2.3.3 Statistical Approaches 18
2.4 Acid Mine Drainage Formation Processes 18
2.5 Shortcomings of Groundwater Vulnerability Assessment Methods 20
2.6 Overview of Artificial Intelligence Systems 21
2.7 Applications of Artificial Intelligence in Groundwater Vulnerability Assessments 23
2.8 Globally Accepted Regional Assessment Approaches 25
2.8.1 Mineral Systems Approach 26
2.8.2 Petroleum Systems 27
2.8.3 Source-Transport-Attenuation Approach 28
2.9 Summary 28

CHAPTER 3 : DEVELOPMENT OF GIS-BASED GROUNDWATER VULNERABILITY ASSESSMENT FOR ACID MINE DRAINAGE 30

3.1 Introduction 30
3.2 Overview of the SPT Approach 30
3.3 The SPT Input Map Layers 32
3.3.1 Sources 32
3.3.1.1 Sources of energy 33
3.3.1.2 Sources of ligands (water) 35
3.3.1.3 Mappable sources of AMD pollution 36
3.3.1.4 Subsurface sources of pollution 36
3.3.2 Transportation Pathway 36
3.3.2.1 Transportation pathway in soils 36
3.3.2.2 Transport in the vadose zone 37
3.3.2.2.1 Preferential pathways 37
3.3.2.2.2 Rock permeability 37
3.3.2.3 Transport in the aquifer system 37
3.3.3 AMD Pollution Traps 38
3.3.3.1 Chemical traps of acid mine drainage in soils 38
3.3.3.2 Pollution traps in the vadose zone and aquifer media 39

3.3.3.2.1 Depth to water table ... *39*
3.3.3.2.2 Rock-AMD reactivity ... *39*
3.3.4 SPT Groundwater Vulnerability Modelling ... 39
3.4 Generation of SPT Input Map Layers for the Witbank, Ermelo and Highveld Coalfields ... 40
3.4.1 Location of the Witbank, Ermelo and Highveld Coalfields ... 40
3.4.1.1 Location of the Witbank coalfield ... 40
3.4.1.2 Location of the Highveld coalfield ... 41
3.4.1.3 Location of the Ermelo coalfield ... 41
3.4.2 Physiography ... 42
3.4.3 Geological and Hydrogeological Setting ... 43
3.4.3.1 Regional geology ... 43
3.4.3.2 Local geological setting ... 45
3.4.3.2.1 The Basement Complex ... *46*
3.4.3.2.2 The Witwatersrand Supergroup ... *47*
3.4.3.2.3 The Transvaal Supergroup ... *47*
3.4.3.2.4 Bushveld Igneous Complex ... *48*
3.4.3.2.5 Waterberg Group ... *49*
3.4.3.2.6 Karoo Supergroup ... *49*
3.4.3.2.7 Quaternary deposits ... *50*
3.4.3.3 Hydrogeological setting ... 51
3.4.3.3.1 Aquifer types ... *51*
3.4.3.3.2 Hydrochemistry ... *55*
3.4.4 Mining Activities and their Contribution to AMD Pollution ... 58
3.4.4.1 Coal mining history of the Witbank, Ermelo and Highveld coalfields ... 58
3.4.4.2 Coal geology ... 59
3.4.4.2.1 Witbank coalfield ... *59*
3.4.4.2.2 Highveld coalfield ... *59*
3.4.4.2.3 Ermelo coalfield ... *59*
3.4.4.3 Coal mining activities and their impacts to the environment ... 60
3.4.5 SPT Inputs for the Witbank, Ermelo and Highveld Coalfields ... 61
3.4.5.1 Sources of energy (topographic slope) ... 61
3.4.5.2 Sources of ligands (water) ... 62
3.4.5.3 Surface sources of AMD pollution ... 65
3.4.5.3.1 Methodology for identification of AMD surface sources ... *65*
3.4.5.3.2 Results and discussions ... *71*
3.4.5.4 Subsurface sources ... 76
3.4.5.5 Transport and attenuation in the soils ... 76
3.4.5.5.1 Materials and methods ... *80*
3.4.5.5.2 Experimental results and discussion ... *83*
3.4.5.6 Preferential pathways ... 88
3.4.5.7 Rock permeability ... 92
3.4.5.8 Hydraulic conductivity ... 93
3.4.5.9 Depth to water table ... 94
3.4.5.10 Rock-AMD reactivity ... 95
3.4.5.10.1 Materials and methods ... *96*
3.4.5.10.2 Sample mineralogy results and discussions ... *98*
3.4.5.10.3 Experimental results and discussion ... *103*
3.4.5.10.4 Summary ... *113*
3.5 Summary ... 116

CHAPTER 4 : KNOWLEDGE-DRIVEN FUZZY EXPERT SYSTEM ... 118

4.1 Introduction ... 118
4.2 Knowledge-Driven Artificial Intelligence Systems ... 118
4.3 Overview of Fuzzy Expert Systems ... 118
4.3.1 Fuzzification ... 119
4.3.2 Fuzzy Inference Engine ... 120
4.3.2.1 Fuzzy (AND) operation ... 120

4.3.2.2 Fuzzy (OR) operation 120
4.3.2.3 Fuzzy (SUM) operator 121
4.3.2.4 Fuzzy (PRODUCT) operator 121
4.3.2.5 Fuzzy (GAMMA) operator 122
4.3.3 Defuzzification 122
4.4 Application of the Fuzzy Expert System to Groundwater Vulnerability Assessment 122
4.4.1 Cognitive Reasoning 123
4.4.1.1 Sources factor 123
4.4.1.1.1 Energy sources 123
4.4.1.1.2 Ligand (water) sources 123
4.4.1.1.3 Pollutant sources 123
4.4.1.2 Transportation pathway factor 124
4.4.1.3 Traps 124
4.5 Fuzzy Expert System: Application to the Witbank, Ermelo and Highveld Coalfields 124
4.5.1 Fuzzification 124
4.5.1.1 Assigning map weights, class weights and confidence factors for the sources factor 126
4.5.1.2 Assigning map weights, class weights and confidence factors for the transportation pathway factor 127
4.5.1.3 Assigning map weights, class weights and confidence factors for the traps factor 128
4.5.2 Fuzzy Inference Engine 128
4.5.2.1 Sources factor input (S) 129
4.5.2.2 Transportation pathway factor input (P) 134
4.5.2.3 Traps factor input (T) 139
4.5.2.4 Resultant fuzzy output model 142
4.5.3 Defuzzification 143
4.5.4 Model Validation of the Fuzzy Expert System 145
4.5.4.1 Model validation using hydrochemistry data 145
4.5.4.1.1 Correlation coefficient approach 145
4.5.4.1.2 Cross-section method of validation 146
4.5.4.2 Validation using geophysical techniques 148
4.5.4.2.1 Materials and methods 148
4.5.4.2.2 Results and discussion 151
4.5.4.2.3 Summary 157
4.6 Discussion 158
4.7 Summary 159

CHAPTER 5 : DATA PREPARATION AND AUTOMATION FOR DATA-DRIVEN ARTIFICIAL INTELLIGENCE MODELLING 160

5.1 Introduction 160
5.2 Selection of Training Sites 160
5.3 Model Selection 160
5.3.1 Spatial Association Testing of Input Map Layers 161
5.3.1.1 Ligand water sources (rainfall) layer 162
5.3.1.2 Energy sources (slope) layer 164
5.3.1.3 Surface sources of AMD layer 165
5.3.1.4 Subsurface sources of AMD layer 166
5.3.1.5 Soil clay content layer 168
5.3.1.6 Preferential pathway layer 169
5.3.1.7 Aquifer hydraulic conductivity layer 171
5.3.1.8 Rock permeability layer 172
5.3.1.9 Rock-AMD reactivity layer 173
5.3.1.10 Depth to water table layer 174
5.3.2 Determination of Optimal Data-Driven Model Parameters 177
5.3.2.1 Epoch determination algorithm for data-driven approaches 177
5.3.2.2 Hidden layer neuron number determination algorithm for data-driven approaches 177
5.3.2.3 Data splitting algorithms 177
5.4 Discussion 178
5.5 Summary 179

CHAPTER 6 : DATA-DRIVEN ARTIFICIAL NEURAL NETWORK SYSTEM.....180

6.1 Introduction 180
6.2 Overview of Data-Driven Artificial Neural Network systems 180
6.2.1 Biological Neural Network Background 180
6.2.2 Artificial Neural Network Background 181
6.2.3 History of ANNs 184
6.2.4 Architecture of ANNs 185
6.2.5 Learning by ANNs 187
6.2.5.1 Supervised training 187
6.2.5.2 Unsupervised training 187
6.2.5.3 Hybrid training 188
6.2.6 Learning Algorithms – Backpropagation using a Sigmoid Activation Function 188
6.2.6.1 Feed-forward computation 188
6.2.6.2 Back propagation to the output layer 188
6.2.6.3 Back propagation to the hidden layer 190
6.2.7 Types of Artificial Neural Networks 190
6.2.7.1 Feed-forward ANNs 190
6.2.7.2 Recurrent ANNs 191
6.3 Data-Driven Artificial Neural Network: Application to the Witbank, Ermelo and Highveld Coalfields 191
6.3.1 ANN Training 192
6.3.1.1 Selection of training sites 192
6.3.1.2 Binary map creation 192
6.3.1.3 Establishing the optimum number of epochs and neurons in the hidden layer 193
6.3.1.4 Selection of cross-validation method 194
6.3.1.5 Artificial neural network modelling 194
6.3.2 Data-Driven ANN Model Results 196
6.3.3 Validation of the ANN Model 198
6.3.3.1 Model validation using hydrochemistry data 198
6.3.3.1.1 Correlation coefficient approach 198
6.3.3.1.2 Cross-section method of validation 199
6.3.3.2 Validation using geophysical techniques 200
6.4 Discussion 201
6.5 Summary 202

CHAPTER 7 : HYBRID ARTIFICIAL INTELLIGENCE SYSTEM 203

7.1 Introduction 203
7.2 Overview of the Hybrid System 203
7.2.1 Types of Neuro-Fuzzy Systems 203
7.2.1.1 Neural-fuzzy systems 204
7.2.1.2 Fuzzy-neural systems 204
7.2.1.3 Hybrid neuro-fuzzy systems 205
7.2.1.3.1 ANFIS system operation 206
7.2.1.3.2 Learning algorithm of the ANFIS 208
7.3 The ANFIS System for Groundwater Vulnerability Assessments: Application to the Witbank, Ermelo and Highveld Coalfields 212
7.3.1 Design Step of the ANFIS for Groundwater Vulnerability 212
7.3.1.1 Selection of system inputs and outputs 212
7.3.1.2 ANFIS system training 213
7.3.2 Hybrid System Model Results 214
7.3.3 Validation of the ANFIS Model 216
7.3.3.1 Model validation using hydrochemistry data 216
7.3.3.1.1 Correlation coefficient approach 216
7.3.3.1.2 Validation using the cross-section method 217
7.3.3.2 Validation using geophysical techniques 218
7.4 Discussion 219
7.5 Summary 220

CHAPTER 8 : TOOLBOX FOR RAPID ASSESSMENT OF GROUNDWATER VULNERABILITY 221

8.1 Introduction 221
8.2 Overview of the Toolbox 221
8.2.1 Main Menu Module 223
8.2.2 Data Input Module 223
8.2.3 Fuzzy Expert System Module 224
8.2.4 Data Pre-Processing Module for Data-Driven AI Systems 226
8.2.5 ANN Module 227
8.2.6 ANFIS Module 229
8.2.7 Model Validation Module 231
8.3 Discussion and Summary 232

CHAPTER 9 : CONCLUSIONS AND RECOMMENDATIONS 234

9.1 Concluding Remarks 234
9.1.1 Development of AMD Specific Groundwater Vulnerability Approach 234
9.1.2 Laboratory and Field Experiments for Groundwater Vulnerability Input Selection and Model Validation 235
9.1.3 Application of AI to the Assessment of Groundwater Vulnerability Specific for Coalfields 235
9.1.4 Groundwater Vulnerability Graphic User Interface Toolbox 236
9.2 Recommendations 237
9.2.1 General Recommendations 237
9.2.2 Limitations of the Developed Data-Driven Approaches 237
9.2.3 Recommendations for Future Work 238

REFERENCES 240

APPENDICES

Appendix 1: Soil Batch Leach Experiment 254
Appendix 1.1 Results of leachate analysis after the soil batch leach with AMD 254
Appendix 1.2 Results of leachate analysis after the soil batch leach with de-ionised water 254
Appendix 1.3 Results of major elements of soil samples analysed by XRF 254
Appendix 2: Rock-AMD Column Leach Experiment 255
Appendix 2.1 Results of chemical analysis of leachate under saturated conditions 255
Appendix 2.2 Results of chemical analysis of leachate under unsaturated conditions 256
Appendix 2.3 Results of the mineralogical analysis of rock samples by XRD 257
Appendix 2.4 Results of the XRF analysis of the major elements of rock samples 257
Appendix 3: Determination of Optimal Data-Driven Model Parameters 258
Appendix 3.1: Epoch determination algorithm for data-driven approaches 258
Appendix 3.2: Hidden layer neuron number determination algorithm for data-driven approaches 259
Appendix 3.3: Data splitting algorithms 260
Appendix 4: Example of how the Backpropagation Algorithm Works 267
Appendix 5: Example of Hybrid Learning of the ANFIS System 269
Appendix 6: GVAI Software Operating Manual 272

ABSTRACT 286

LIST OF FIGURES

Figure 2.1: Branches of the AI field 23

Figure 2.2: Mineral systems approach flow diagram 26

Figure 2.3 : Petroleum systems approach flow diagram 28

Figure 3.1: Developed groundwater vulnerability approach flow diagram 31

Figure 3.2: Schematic illustration of the parameters which make up the proposed groundwater vulnerability approach 32

Figure 3.3: Decreasing mean measured and least-squares mean final infiltration rates with increasing slope angle (error bars are ± 1 standard error) 34

Figure 3.4: Relationship between percentage slope and slope angle 34

Figure 3.5: Overland flow velocity increases with slope angle (error bars are ± 1 standard error) 34

Figure 3.6: Schematic illustration of the parameters used to calculate topographic slope 35

Figure 3.7: Location of the study area in relation to provincial and international boundaries 41

Figure 3.8: Climatic data for the Ermelo station showing temperature and rainfall distribution throughout the year 43

Figure 3.9: Extent of the Karoo basin in South Africa, with coalfields. The blue line indicates the location of the cross-section AB shown in Figure 3.10 44

Figure 3.10: Schematic north–south section across the main Karoo basin 45

Figure 3.11: Local geology of the study area mapped at a 1:250 000 scale showing borehole locations 46

Figure 3.12: Rock exposure of the granites found in the study area 47

Figure 3.13: Malmani Subgroup dolomite rock exposed in the study area displaying an elephant skin texture ... 48

Figure 3.14: Pretoria Group mudrock outcrop showing heavy fracturing and bedding planes 48

Figure 3.15: Weathered sandstone outcrop in the Witbank coalfield 49

Figure 3.16: Hydrogeological setting of the study area 53

Figure 3.17: Conceptual model of a karst aquifer 54

Figure 3.18: Locations of groundwater samples used in this study 56

Figure 3.19: Piper diagram showing the major water classifications in relation to the TDS concentration 57

Figure 3.20: Scatter plot of TDS against sulphate concentration 58

Figure 3.21: AMD surface flow from a coal mining operation south of Carolina in the Ermelo coalfield. The brownish-orange colour is attributed to iron hydroxyl precipitation 60

Figure 3.22: Elevation image of the study area showing the drainage pattern and rivers 61

Figure 3.23: Topographic slope image of the study area 62

Figure 3.24: Average long-term rainfall of the study area **63**

Figure 3.25: Recharge image of the study area **64**

Figure 3.26: Relationship between average long-term rainfall and net recharge **65**

Figure 3.27: Spectral signatures of iron-bearing minerals extracted from the USGS spectral library **68**

Figure 3.28: Secondary iron minerals spectrum resampled to Landsat 8 bandwidths **68**

Figure 3.29: Secondary iron minerals spectrum resampled to Sentinel 2 bandwidths **69**

Figure 3.30: Decision tree used to identify secondary Fe minerals from Landsat 8 data **70**

Figure 3.31: Decision tree used to identify secondary Fe minerals from Sentinel 2 data **70**

Figure 3.32: AMD surface sources as interpreted from Landsat 8 remote sensing data **72**

Figure 3.33: AMD surface sources as interpreted from Sentinel 2 remote sensing data **73**

Figure 3.34: Combined results from Landsat 8 and Sentinel 2 results plotted as a function of distance from interpreted AMD surface sources. The areas within the two black polygons are selected for detailed analysis **74**

Figure 3.35: Zoomed-in results (a) Iron-bearing minerals: (b) Landsat 8 band combination 764 for a detailed analysis of interpreted secondary Fe minerals **75**

Figure 3.36: Zoomed-in results for Arnot North discard mine dump **76**

Figure 3.37: Subsurface AMD sources as interpreted from geology data **77**

Figure 3.38: Soil types found in the study area **78**

Figure 3.39: Distribution of soil clay content within the study area showing the locations of soil samples collected for the chemical traps experiment **79**

Figure 3.40: Experimental setup for determining the attenuation effect of soils on AMD pollution **81**

Figure 3.41: Soil CEC map of the study area **82**

Figure 3.42: Scatter plot between soil CEC and soil clay content **83**

Figure 3.43: XRF Mineralogical composition of the soil samples **83**

Figure 3.44: Plot of soil clay content against iron (Fe) leachate concentration. The red line marks the initial Fe concentration of the AMD. The blue and black points are leachate concentration values resulting from the effect of adding de-ionised water and AMD to soils respectively **84**

Figure 3.45: Plot of soil clay content against Aluminium (Al) leachate concentration. The red line marks the initial Fe concentration of the AMD and the blue and black points are leachate concentration values resulting from the effect of adding de-ionised water and AMD to soils respectively **85**

Figure 3.46: Plot of soil clay content against Sulphate (SO_4^{-2}) leachate concentration **86**

Figure 3.47: Plot of soil clay content against leachate Calcium (Ca) concentration **86**

Figure 3.48: Plot of soil clay content against leachate Magnesium (Mg) concentration **87**

Figure 3.49: Plot of soil clay content against leachate Sodium (Na) concentration **87**

Figure 3.50: Residual magnetic field with lineaments and interpretations of the faults 89

Figure 3.51: Magnetic analytical signal showing the interpretation of the sills 90

Figure 3.52: Magnetic interpretation of the possible preferential pathways..... 91

Figure 3.53: Possible regional preferential pathways for AMD represented as a distance map 92

Figure 3.54: Rock permeability map generated from the literature, reflecting the values of the rocks found in the study area. Values in brackets are in cm^2 93

Figure 3.55: Aquifer hydraulic conductivity map of the study area 94

Figure 3.56: Depth to water level map derived from monitoring borehole information from the Department of Water and Sanitation..... 95

Figure 3.57: Schematic laboratory setup for (a) saturated and (b) unsaturated column tests 97

Figure 3.58: Experimental setup for determining the attenuation effect of vadose zone and in the aquifer system. The yellow section was replaced by AMD collected from the field..... 98

Figure 3.59: Mineral composition of various rocks as measured by XRD, showing the five selected samples for the column leach experiment..... 99

Figure 3.60: XRF minerals composition of various rocks showing the five selected for the column leach experiment 99

Figure 3.61: Microscopic view of the medium to coarse-grained diabase showing elongated crystals of plagioclase feldspar (Sample WITS1)..... 100

Figure 3.62: Quartzitic sandstone with lithic fragments as seen under the microscope for sample WITS7 101

Figure 3.63: Very fine grains of quartz and feldspar as seen under the microscope for sample WITS8..... 101

Figure 3.64: Plagioclase laths ophitically to sub-ophitically enclosed in clinopyroxene, as seen under the microscope for sample WITS9..... 102

Figure 3.65: Very fine-grained calcite and dolomite predominate in sample WITS14, as seen under the microscope 102

Figure 3.66: Graphic plot of leachate pH against time for various rocks under saturated conditions 103

Figure 3.67: Graphic plot of leachate pH with time for various rocks under unsaturated conditions 104

Figure 3.68: Graphic plot of leachate EC with time for various rocks under saturated conditions..... 105

Figure 3.69: Graphic plots of leachate EC with time for various rocks under unsaturated conditions..... 105

Figure 3.70: Graphic plot of leachate sulphate concentrations over time for various rocks under saturated conditions..... 106

Figure 3.71: Graphic plot of leachate sulphate concentration over time for various rocks under unsaturated conditions..... 106

Figure 3.72: Graphic plot of leachate iron concentrations over time for various rocks under saturated conditions 107

Figure 3.73: Graphic plot of leachate iron concentration over time for various samples under unsaturated conditions 107

Figure 3.74: Graphic plot of leachate aluminium concentrations over time under saturated conditions 107

Figure 3.75: Graphic plot of leachate aluminium concentration over time for various samples under unsaturated conditions 108

Figure 3.76: Graphic plot of leachate manganese concentrations over time for various samples under saturated conditions 108

Figure 3.77: Graphic plot of leachate manganese concentrations over time for various samples under unsaturated conditions 109

Figure 3.78: Graphic plot of leachate magnesium concentrations over time for various samples under saturated conditions 109

Figure 3.79: Graphic plot of leachate magnesium concentrations over time for various samples under unsaturated conditions 110

Figure 3.80: Graphic plot of leachate sodium concentrations over time for various samples under saturated conditions 110

Figure 3.81: Graphic plot of leachate sodium concentrations over time for various samples under unsaturated conditions 111

Figure 3.82: Graphic plot of leachate calcium concentrations over time for various samples under saturated conditions 111

Figure 3.83: Graphic plot of leachate calcium concentrations over time for various samples under unsaturated conditions 111

Figure 3.84: Graphic plot of leachate chloride concentrations over time for various samples under saturated conditions 112

Figure 3.85: Graphic plot of leachate chloride concentrations over time for various samples under unsaturated conditions 112

Figure 3.86: Rock-AMD reactivity map of the study area showing the relative classification in terms of extraction of AMD pollutants 116

Figure 4.1: Structure of the fuzzy expert system 119

Figure 4.2: Crisp to fuzzy translation for (a) sources factor, (b) transportation pathway factor, (c) traps 126

Figure 4.3: Sources of energy in fuzzy space 129

Figure 4.4: Sources of ligand (water) in fuzzy space 130

Figure 4.5: Surface sources of AMD pollution in fuzzy space 131

Figure 4.6: Subsurface sources of AMD pollution in fuzzy space 132

Figure 4.7: All sources of AMD pollution in fuzzy space constituted by combining surface and subsurface sources 133

Figure 4.8: Sources factor produced by integration energy, ligand (water) and pollution sources..... 134

Figure 4.9: Transportation pathways in soils (clay content) expressed in fuzzy values 135

Figure 4.10: Preferential pathways expressed in fuzzy values..... 136

Figure 4.11: Rock permeability expressed in fuzzy values..... 137

Figure 4.12: Aquifer hydraulic conductivity expressed in fuzzy values..... 138

Figure 4.13: Transportation pathways factor generated by combining AMD transport parameters in the soil, vadose zone and the aquifer system..... 139

Figure 4.14: Rock-AMD reactivity expressed in fuzzy values 140

Figure 4.15: Depth to water table expressed in fuzzy values 141

Figure 4.16: Traps factor generated by combining natural AMD trapping parameters in the soil, vadose zone and the aquifer system 142

Figure 4.17: Multistage fuzzy inference network used for combining input layers to produce the groundwater vulnerability model 143

Figure 4.18: Resultant groundwater vulnerability model of the Witbank, Ermelo and Highveld coalfields 144

Figure 4.19: Aerial size distribution of various groundwater vulnerability classes..... 145

Figure 4.20: Correlation scatter plots for sulphate against groundwater vulnerability model values..... 146

Figure 4.21: Sulphate concentration map generated from the NGA database..... 147

Figure 4.22: Profile along cross-section A–B showing the DWS borehole sulphate concentrations and the fuzzy vulnerability model profile..... 148

Figure 4.23: Simple layout of conventional four-electrode array used to measure the subsurface resistivity..... 149

Figure 4.24: Simple layout of conventional seismic refraction survey 151

Figure 4.25: 2D resistivity survey results for site 1 showing (a) the modelled apparent resistivity-elevation, (b) the derived porosity-elevation and (c) seismic velocity plot..... 152

Figure 4.26: 2D resistivity survey results for site 2 showing (a) the modelled apparent resistivity-elevation plot, (b) the derived porosity-elevation plot and (c) the seismic velocity plot 153

Figure 4.27: 2D resistivity survey results for site 3 showing (a) the modelled apparent resistivity-elevation plot, (b) the derived porosity-elevation plot and (c) the seismic velocity plot 155

Figure 4.28: Black clay layer observed overlying the weathered sandstone at an excavated trench next to the surveyed site 3 155

Figure 4.29: 2D resistivity survey results for site 4 showing (a) the modelled apparent resistivity-elevation, (b) the derived porosity-elevation and (c) the seismic plots..... 157

Figure 5.1: Spatial association test results for the rainfall parameter 163

Figure 5.2: Rainfall map layer in binary format..... 164

Figure 5.3: Spatial association test results for the slope parameter 165

Figure 5.4: Slope map layer in binary format 165

Figure 5.5: Spatial association test results for surface sources parameter 166

Figure 5.6: Surface sources map layer in binary format 167

Figure 5.7: Spatial association test results for the subsurface sources parameter 167

Figure 5.8: Subsurface sources map layer in binary format 168

Figure 5.9: Spatial association test results for the soil clay parameter 169

Figure 5.10: Soil clay map layer in binary format 169

Figure 5.11: Spatial association test results for the pathway parameter 170

Figure 5.12: Pathway map layer in binary format 170

Figure 5.13: Spatial association test results for the relative aquifer hydraulic conductivity 171

Figure 5.14: Relative aquifer hydraulic conductivity map layer in binary format 171

Figure 5.15: Spatial association test results for the relative rock permeability parameter 172

Figure 5.16: Relative rock permeability map layer in binary format 173

Figure 5.17: Spatial association test results for the rock-AMD reactivity parameter 174

Figure 5.18: Rock-AMD reactivity map layer in binary format 174

Figure 5.19: Spatial association test results for the depth to water table parameter 175

Figure 5.20: Depth to water table map layer in binary format 175

Figure 6.1: Simplified illustration of a biological neuron 181

Figure 6.2: Working principle of an artificial neuron 182

Figure 6.3: Activation functions commonly used in artificial neural networks: (a) binary (b) sigmoid and (c) hyperbolic tangent 184

Figure 6.4: Artificial neural network architecture defined by the way in which neurons (yellow, green and blue blobs) are connected by synapses (lines) 186

Figure 6.5: Testing errors at various training epochs 193

Figure 6.6: Testing errors at various number of neurons in the hidden layer 194

Figure 6.7: ANN architecture used for training 195

Figure 6.8: Graph for determining the best fold with the lowest validation error 196

Figure 6.9: Groundwater vulnerability model of the Witbank, Ermelo and Highveld coalfields generated by using ANNs 197

Figure 6.10: Aerial size distribution of various groundwater vulnerability classes 198

Figure 6.11: Correlation scatter plots for sulphate against groundwater vulnerability model values 199

Figure 6.12: Profile along cross-section A–B showing the DWS borehole sulphate concentration and the ANN vulnerability model profile 200

Figure 7.1: Neural-fuzzy system 204

Figure 7.2: Fuzzy neural system 205

Figure 7.3: First-order Sugeno ANFIS architecture 207

Figure 7.4: Membership functions used for the ANFIS system for a groundwater vulnerability assessment 213

Figure 7.5: Determining the cut-off epoch value for training the ANFIS system 214

Figure 7.6: ANFIS groundwater vulnerability model of the Witbank, Ermelo and Highveld coalfields 215

Figure 7.7: Aerial size distribution of the various groundwater vulnerability classes 216

Figure 7.8: Correlation scatter plots for sulphate against the ANFIS groundwater vulnerability model 217

Figure 7.9: Profile along cross-section A–B showing the DWS borehole sulphate concentrations and the ANFIS vulnerability model profile 218

Figure 8.1: Systems design flowchart of the groundwater vulnerability (GVAI) toolbox 222

Figure 8.2: Main menu module window 223

Figure 8.3: Input module window 224

Figure 8.4: The "about" window, showing the software details 224

Figure 8.5: Fuzzy expert system flow chart 225

Figure 8.6: Fuzzy expert system module window 226

Figure 8.7: Data-driven artificial intelligence data pre-processing module window 227

Figure 8.8: ANN system flow chart showing the relationships of various algorithms 228

Figure 8.9: ANN module window 229

Figure 8.10: ANFIS expert system flow chart 230

Figure 8.11: ANFIS module window 231

Figure 8.12: Model validation module 232

Figure A1: Determining the optimum number of epochs with minimum testing MSE 256

Figure A2: Determining the optimum number of neurons in hidden layer with minimum testing MSE 257

Figure A3: Illustration of three way data splitting 258

Figure A4: Holdout method splitting the dataset into training, validation and testing sets 259

Figure A5: Random subsampling and splitting of the dataset into training, validation and testing sets 260

Figure A6: K-fold cross-validation splitting of the dataset into training, validation and testing 261

Figure A7: Leave-one-out cross-validation splitting of the dataset into training, validation and testing 262

Figure A8: Leave-one-out cross-validation graph 263

Figure A9: Example of how the back propagation algorithm works 264

Figure A10: Plot of fuzzy membership function for each of the rules 267

Figure A11: Example of calculations and layer connections for layers 1, 2 and 3 267

Figure A12: Example of calculations and layer connections for layers 4 and 5 268

Figure A13: GVAI launch module 270

Figure A14: Input module window 272

Figure A15: About window 273

Figure A16: Input module window 273

Figure A17: Input module window 274

Figure A18: Fuzzy expert system module window 275

Figure A19: Source output in fuzzy values 276

Figure A20: Map output after combining all the inputs from the sources 276

Figure A21: Fuzzy expert system output map 277

Figure A22: Data-driven artificial intelligence data pre-processing module window 278

Figure A23: Spatial association test result 278

Figure A24: ANN module window 279

Figure A25: Display of ANN results 279

Figure A26: Adaptive Neural-Fuzzy Inference System module window 280

Figure A27: Adaptive Neural-Fuzzy Inference module 281

Figure A28: Model comparison module 282

Figure A29: Validation graph of the fuzzy model 282

LIST OF TABLES

Table 2.1: Original DRASTIC parameters (Aller *et al.*, 1987) 13

Table 2.2: Original GOD parameters (Gogu and Dassargues, 2000) 15

Table 2.3: Vulnerability classes of the AVI method (Fraga *et al.*, 2013) 17

Table 2.4: Brief history of Artificial Intelligence 22

Table 2.5: Interpretation of the R value (Arikunto, 2002) 25

Table 3.1: Summary of the geology of the Witbank, Ermelo and Highveld coalfields 50

Table 3.2: Properties of Landsat 8 data (Cole *et al.*, 2015) 67

Table 3.3: Properties of Sentinel 2 (Satellite Imaging Corporation., 2017) 67

Table 3.4: Soil types found in the study area and their associated estimated clay content 79

Table 3.5: Chemical composition of AMD used for the soil batch leach experiment 81

Table 3.6: CEC, pH and clay content of the soil samples used in the batch leach experiment 82

Table 3.7: Groups of samples according to their mineral speciation as interpreted from XRF results 100

Table 3.8: Summary of rock–AMD reactivity expressed in terms of AMD removal by rocks 114

Table 3.9: Summary of the rock-AMD reactivity for the Witbank, Ermelo and Highveld coalfields 115

Table 4.1: Assigning map weights, class weights and confidence factors for various layers 125

Table 4.2: Aerial coverage of various vulnerability classes 145

Table 4.3: Comparison of derived porosity values and groundwater vulnerability model values for each of the survey sites 158

Table 5.1: Relationships of parameters used for the calculation of spatial association 162

Table 5.2: Assignment of binary classes 176

Table 6.1: Aerial coverage of various vulnerability classes 197

Table 6.2: Comparison of derived porosity values and the ANN groundwater vulnerability model values for each of the survey sites 201

Table 7.1: Passes in the hybrid learning algorithm (Jang and Sun, 1995) 209

Table 7.2: Aerial coverage of various vulnerability classes of the ANFIS model 216

Table 7.3: Comparison of derived porosity values and ANFIS groundwater vulnerability model values for each of the survey sites 219

Table 9.1: Recommendations for the management of the water resources of the Witbank, Ermelo and Highveld coalfields 238

Table A2: Example of a dataset with four points for running the leave-one-out cross-validation technique 263

Table A3: Data splitting of a four points example using the leave-one-out algorithm 263

LIST OF ACRONYMS

KZN	–	KwaZulu-Natal
MKB	–	Main Karoo Basin
RBCT	–	Richards Bay Coal Terminal
AI	–	Artificial Intelligence
AMD	–	Acid Mine Drainage
ANFIS	–	Adaptive Neural-Fuzzy Inference System
ANN	–	Artificial Neural Network
ARC- ISCW	–	Agricultural Research Council Institute of Soil, Climate and Water
ASI	–	Italian Space Agency
AVI	–	Aquifer Vulnerability Index
CEC	–	Cation Exchange Capacity
CMB	–	Chloride Mass Balance
DLR	–	German Aerospace Centre
DN	–	Digital Number
DRASTIC	–	Depth to water table, net Recharge, Aquifer media, Soil media, Topographic slope, Impact of vadose zone, hydraulic Conductivity
DWS	–	Department of Water and Sanitation
EC	–	Electrical Conductivity
ERT	–	Electrical Resistivity Tomography
ESKOM	–	Electricity Supply Commission
FMF	–	Fuzzy Membership Function
FMV	–	Fuzzy Membership Value
GARIC	–	Generalised Approximate Reasoning-based Intelligent Control
GIS	–	Geographic Information System
GOD	–	Groundwater occurrence, Overall lithology, Depth to water table
GPS	–	Global Positioning System

GUI	–	Graphic User Interface
GVAI	–	Groundwater Vulnerability Artificial Intelligence
IC	–	Ion Chromatography
ICP-MS	–	Inductively Coupled Plasma Mass Spectrometry
LISP	–	Locator/Identifier Separation Protocol
LSM	–	Least Squares Method
MSE	–	Mean Square of Errors
MTEF	–	Medium Term Expenditure Framework
NASA	–	National Aeronautics and Space Administration
NGA	–	National Groundwater Archive
NGIA	–	National Geospatial Intelligence Agency
NIR	–	Near-Infra-Red
NNDFR	–	Neural Network Driven Fuzzy Reasoning
NP	–	Non-Polluted
P	–	Polluted
pH	–	potential Hydrogen
SACS	–	South African Committee for Stratigraphy
SAWS	–	South African Weather Services
SCMAI	–	Supervised Committee Machine Artificial Intelligence
SIINTACS	–	Soggiacenza, Infiltrazione efficace, Non saturo, Tipologia della copertura, Acquifero, Conducibilita idraulica, Supeficia topografica
SPT	–	Sources, transportation Pathway, Traps
SRTM	–	Shuttle Radar Topographic Mission
STA	–	Source, Transport, Attenuation
SWIR	–	Short-Wave Infra-Red
T and DB	–	Transvaal and Delagoa Bay
TDS	–	Total Dissolved Solids
TIR	–	Thermal Infra-Red

USEPA	–	United States Environmental Potential Agency
USGS	–	United States Geological Survey
VNIR	–	Visible and Near-Infra-Red
WSI	–	Weighted Sum of Inputs
XRD	–	X-Ray Diffraction
XRF	–	X-Ray Fluorescence

MEASUREMENT UNITS

%	-	percentage
km	-	kilometre
km^2	-	square kilometre
mm	-	millimetre
m	-	metre
ha	-	hectare
Mt	-	million tonnes
Bt	-	billion tonnes
p.a.	-	per annum
m/s	-	metre per second
m/d	-	metre per day
yr	-	year
mg/L	-	milligram per litre
^{o}	-	degree
mm/h	-	millimetre per hour
cm/s	-	centimetre per second
mm/a	-	millimetre per annum
µm	-	micro metre
nT	-	nanoTesla
nT/m	-	nanoTesla per metre
mS/m	-	milliSiemens per metre
cmol/kg	-	centimoles per kilogram
gpd/ft^2	-	gallons per day per square foot

OUTCOMES OF THE RESEARCH

Sakala, E., Fourie, F., Gomo, M. and Coetzee, H. 2018. GIS-based groundwater vulnerability modelling: a case study of the Witbank, Ermelo and Highveld coalfields in South Africa, *Journal of African Earth Sciences*, 137, 46–60. doi: 10.1016/j.jafrearsci.2017.09.012.

Sakala, E., Fourie, F., Gomo, M. and Coetzee, H. 2017a. Hydrogeological investigation of the Witbank , Ermelo and Highveld coalfields : implications for the subsurface transport and attenuation of acid mine drainage, in Wolkersdorfer, C., Sartz, L., Sillanpää, M., and Häkkinen, A. (eds) *13th International Mine Water Association Congress – Mine Water & Circular Economy*. Lappeenranta, Finland: IMWA, 564–571.

Sakala, E., Fourie, F., Gomo, M. and Coetzee, H. 2017b. Mapping surface sources of acid mine drainage using remote sensing: case study of the Witbank , Ermelo and Highveld coalfields, in Wolkersdorfer, C., Sartz, L., Sillanpää, M., and Häkkinen, A. (eds) *13th International Mine Water Association Congress – Mine Water & Circular Economy*. Lappeenranta, Finland: IMWA, 1246–1253.

Sakala, E., Fourie, F., Gomo, M., Coetzee, H. and Magadaza, L. 2016. Specific groundwater vulnerability mapping: case study of acid mine drainage in the Witbank coalfield, South Africa, in *6th IASTED International Conference on Environment and Water Resource Management*, 93–100. doi: 10.2316/P.2016.836-010.

CHAPTER 1: INTRODUCTION

1.1 BACKGROUND

Globally, groundwater is an important and most valuable source of water for various purposes (consumption, irrigation, industry and mining, etc.) owing to its relatively low susceptibility to pollution and relative abundance. However, the resource is under serious threat by human activities that introduce pollutants or group of pollutants on surface or in the subsurface (e.g. mining, industrial, agricultural and waste disposal). Once a groundwater system is polluted it is often costly and technically challenging to restore, and can be practically impossible to remediate in some instances (Thirumalaivasan *et al.*, 2003; Kaur and Rosin, 2009). Thus, it is important to identify the groundwater systems and geo-environmental settings which are most vulnerable to pollution. This necessity has prompted researchers, government agencies and environmentalists to devise ways of addressing groundwater pollution issues.

Several methodologies have been developed since the 1980s to predict the consequences of a pollutant or group of pollutants entering the groundwater from the surface or near surface through human activities (Aller *et al.*, 1987; Van Stempvoort *et al.*, 1993; Civita, 1994). That is, investigations are conducted to identify areas that are more likely than others to become polluted, leading to the usage of the phrase "*groundwater vulnerability to pollution*" (NRC, 1993).

Groundwater vulnerability assessments are undertaken with the overall goal of assessing the relative impact with which a given hydrogeology, geology or subsurface can inhibit pollutants from reaching the groundwater system. Assessments of groundwater vulnerability are divided in two major types, namely the "*intrinsic vulnerability assessment"* and the "*specific vulnerability assessment"* (NRC, 1993). The intrinsic type defines only the ease with which a pollutant or a group of pollutants migrates from the surface to the groundwater (Aller *et al.*, 1987). The specific type, in turn, takes into consideration the properties of the pollutant and its interaction with the subsurface (Vrba and Zoporozec, 1994; Huan *et al.*, 2012). According to Huan *et al.* (2012), nowadays, the impact of intrinsic vulnerability is negligible when compared to specific vulnerability because factors that affect intrinsic vulnerability, such as depth to the water table, soil and recharge are constantly subject to the influences of human intervention. Hence, most assessments are formulated for a specific pollutant or group of pollutants or certain human activities which have an impact on the groundwater environment. Groundwater vulnerability results are a very useful tool for advising policy and decision makers on the vulnerability of groundwater systems which may be incorporated into groundwater management programmes and are thus instrumental in the protection of groundwater.

It should be noted that groundwater vulnerability assessments are a general planning and decision-making tool rather than a scientifically precise protocol for predicting future pollution. They are used to assess the general likelihood of pollution occurring in groundwater. According to the NRC (1993), a specific limitation of groundwater vulnerability assessments is that all groundwater is vulnerable to some degree. Furthermore, uncertainty and subjectivity are inherent in most vulnerability assessments as these assessments rely on expert opinions. These limitations have to be taken into consideration when formulating groundwater vulnerability assessments, especially if the results are intended to be used for critical applications such as policy and decision-making.

In order to reduce the subjective nature of assessment approaches and to reduce the uncertainty in groundwater vulnerability data processing, Artificial Intelligence (AI) systems, which have been successfully used in fields such as robotics, science and engineering, can be utilised (PWC, 2017). Artificial intelligence is the study of how to make computers do things, which at the moment are better accomplished by people, such as perception, learning, reasoning and action (Rich and Knight, 1991; Russell and Norvig, 1995; Negnevitsky, 2005). The benefits of using AI for data processing and the automation of some processes is that while human minds can only consider a limited number of variables at a time and are prone to subjective bias, AI programmed computers can process much larger amounts of information at much faster speeds with great accuracy. Therefore, groundwater vulnerability assessments can be greatly improved in terms of speed, reliability and consistency while reducing human induced uncertainties by incorporating AI systems that can imitate human cognitive and learning processes (Fijani *et al.*, 2013; Porwal and Carranza, 2015).

Groundwater vulnerability assessments were originally formulated and widely used for pollution from agricultural pesticides (Aller *et al.*, 1987; Secunda *et al.*, 1998; Huan *et al.*, 2012; Sorichetta *et al.*, 2012; Boufekane and Saighi, 2013; Jang and Chen, 2015; Kazakis and Voudouris, 2015; Pisciotta *et al.*, 2015) and to investigate municipality pollutant sources (Somaratne *et al.*, 2013). In the literature, there are a few groundwater vulnerability assessment case studies on mining activities as a source of pollution, specifically coal mining (Atanacković *et al.*, 2016; Ewusi *et al.*, 2017; Haque *et al.*, 2018). Yet, coal is one of the cornerstones of economic development and is a vital contributor to the industrial development of many developed and developing countries, such as China, the United States of America, India, South Africa, Zimbabwe and Mozambique (World Coal Association, 2012; Statistics South Africa, 2016).

Globally, coal is currently the most widely used primary fuel, accounting for approximately 40% of the world's electricity production (World Coal Association, 2012; Eskom, 2016). The call to decrease the world’s dependence on coal as an energy source is purposeful where lowering its use reduces

greenhouse gas emissions and lowers the environmental impacts associated with coal mining (World Coal Association, 2012; Statistics South Africa, 2016). However, for countries that are heavily dependent on coal, a migration to more environmentally friendly sources of energy would take a long time owing to a number of social and economic factors such as the significant infrastructural investment that has already been made in the coal industry and a lack of suitable alternative sources. Moreover, coal can currently be exploited at an extremely favourable cost and the industry has offered significant employment opportunities (World Coal Association, 2012; Jeffrey *et al.*, 2014; Department of Energy, 2016). Considering the benefits of coal coupled with recent global research mainly focussed on the mitigation of environmental problems associated with coal mining and its utilisation, carbon capture, clean coal technologies and best practice environmental management options for coal mining and coal waste disposal, coal may still be fully utilised with minimum or no harm to the environment.

The environmental problems associated with coal mining and coal waste disposal include dust fallouts, land subsidence at undermined areas, the appearance of tension cracks at the surface and crown-hole development, deterioration of surface and groundwater quality and spoil heaps (Bell *et al.*, 2001). The most significant of these is the deterioration of surface and groundwater quality owing to mine drainage, particularly Acid Mine Drainage (AMD) (Zaporozec, 1981). AMD occurs when sulphide minerals (pyrite and marcasite) associated with the ore and host rock are exposed to atmospheric conditions during coal mining operations and are oxidised in the presence of oxygen and water. The process is catalysed by iron and sulphur-oxidising bacteria producing an acidic solution characterised by low pH values, high concentrations of sulphate and total dissolved solids (TDS). In this acidic environment heavy metals such as iron, aluminium and manganese may be remobilised resulting in elevated concentrations in the groundwater (U.S Environmental Protection Agency, 1977; Bell *et al.*, 2001; Pinetown *et al.*, 2007). Elevated concentrations of these elements in water resources (ground and surface water) cause the water quality to deteriorate which may affect aquatic life and may pose serious health concerns to humans and animals dependent on the water resource (U.S Environmental Protection Agency, 1977).

In ensuring that coal mining and coal waste disposal can be done without harming the environment, policy and decision makers play a vital role. In order to assist policy and decision makers to formulate strategies which help in the prevention and remediation of environmental problems, policy and decision making processes need to incorporate groundwater vulnerability assessments that support land-use planning and regulate mining activities. Groundwater vulnerability assessment methodologies range from simple, qualitative and relatively inexpensive approaches to rigorous, quantitative, and costly assessments, where trade-offs must be carefully considered among the

competing influences of cost, scientific defensibility and the amount of acceptable uncertainty in meeting the decision making objectives (Focazio *et al.*, 2002).

This research involves the development of cost-effective groundwater vulnerability assessment tools driven by the power of AI to overcome current challenges faced by many groundwater vulnerability techniques. At the same time, the research fills a gap in groundwater vulnerability assessments for AMD pollution on a typical coalfield scale. The tools to be developed are anticipated to provide scientifically defensible information which can easily be incorporated into a typical water-resource management decision-making process for policy and decision-makers, ultimately guiding environmental management options for coal mining and coal waste disposal.

The Witbank, Ermelo and Highveld coalfields in Mpumalanga Province of South Africa are the country's current largest producers of coal. Their coal is of good quality and is suitable for electricity generation. The coalfields have vast coal deposits, which are relatively economical to mine (Banks *et al.*, 2011). These coalfields have been exploited for over a century and have contributed to the economic development of the country by supplying energy to developing industries and to the growing urban population of South Africa (McCarthy and Pretorius, 2009). These coalfields supply more than 50% of South Africa's saleable coal and feed the country's major coal-fired power stations, including the Kendal, Duvha, Komati and Arnot Power Stations (Hancox and Götz, 2014).

However, the coal mining operations in the Highveld, Ermelo and Witbank coalfields have caused water quality deterioration of both surface and groundwater resources as a result of AMD and heavy metals pollution (Bell *et al.*, 2002; McCarthy and Pretorius, 2009) and pose a serious concern for local communities, as well as environmental, mining and water regulatory authorities. Several areas have been mined out and some areas are still to be mined. Thus, appropriate tools to avoid and mitigate impacts of mining on the groundwater need to be developed. These coalfields will be used in the current study to develop and test the rapid groundwater vulnerability assessment tools for policy and decision makers, specifically dealing with AMD pollution at a coalfield scale.

When the title of the PhD thesis was registered, the research aimed at using only Witbank and Ermelo coalfields as units of study but the scope was increased to cover Highveld coalfield as a bonus as it is located adjacent to these coalfields.

1.2 AIMS AND OBJECTIVES

This research is part of a broader Mine Water Management Project undertaken by the Council for Geoscience, funded under the Medium Term Expenditure Framework (MTEF) by the Department of Mineral Resources (DMR) of South Africa. The overall goal of the Mine Water Management Project

is to generate proactive environmental management strategies dealing specifically with the management of mine water in the coalfields and goldfields of South Africa. The main aim of this research is to develop scientifically defensible groundwater vulnerability assessment tools for use by policy and decision makers in controlling coal mining and coal waste disposal in a typical coalfield using the Witbank, Ermelo and Highveld coalfields of South Africa as case studies.

The objectives for the research are:

- To critically analyse available groundwater vulnerability approaches and AMD pollution to develop a specific approach applicable to a typical coalfield.
- To incorporate AI in the form of expert systems and machine learning (adaptive learning) algorithms in order to enhance the human capabilities in the assessment of groundwater vulnerability, specifically to coalfields.
- To perform laboratory and field experiments and to analyse results in view of selecting appropriate groundwater vulnerability input map layers and validating vulnerability models.
- To develop a simple-to-use graphic user interface toolbox from where the rapid assessment tools for groundwater vulnerability of a typical coalfield can be used.

1.3 OUTLINE OF RESEARCH METHODOLOGY

To achieve the research aim and objectives, the following research methodology was applied:

1. A review of relevant publications (journals, books, theses and websites) dealing with AMD, groundwater vulnerability assessments, coal mining and waste disposal, AI and regional assessment tools was undertaken.
2. Globally accepted and well-structured frameworks for regional spatial data assessments (mineral systems and petroleum approaches) were translated into a standardised holistic approach for the assessment of groundwater vulnerability to AMD pollution.
3. The developed approach was applied to the largest coal producing coalfields of South Africa, in particular the Witbank, Ermelo and Highveld coalfields.
4. A knowledge-driven, data-driven and hybrid AI system was developed and tested to assess its applicability in obviating shortcomings inherent to currently used approaches to evaluating groundwater vulnerability.
5. Using the Witbank, Ermelo and Highveld coalfields as the unit of study, the following experiments and studies were carried out:

- Laboratory column leachate experiments (both for saturated and unsaturated conditions) were carried out to observe and rank various rocks in terms of their neutralising potential and to determine which rock formations are able to extract pollutants from AMD.
- Mineralogical studies of rocks using x-ray florescence (XRF), x-ray diffraction (XRD) and petrography were undertaken to aid in the interpretation of the rock-AMD reactivity experiment.
- A soil batch leach experiment was used to study AMD pollution in the soils.
- Hydrogeological studies were conducted to understand the transport of AMD in the vadose zone and the aquifer system.
- The results of the above studies were combined with other datasets to produce groundwater vulnerability models for the three coalfields. The results were validated by statistical and hydro-geochemical methods.

1.4 LIMITATIONS OF THE RESEARCH

Groundwater vulnerability assessments are inherently scale dependent, ranging from local to large — that is, from a point location to a catchment or coalfield scale. The present research mainly focussed on developing groundwater vulnerability assessment tools intended for general land-use planning and water resource management and mining regulatory purposes at a large scale such as over a coalfield or catchment area. The results allowed for comparison between areas concerning the likelihood of AMD infiltrating the groundwater system when released from the earth's surface. The results may provide general guidelines from which site-specific studies can be done for local scale modelling.

Drainage emanating from mining activities may be classified according to the drainage pH: acid, neutral or alkaline mine drainage types. The present research only focusses on AMD which has been identified as a major problem affecting a typical coalfield and which can hinder the full utilisation of the coal resources. The acidity remobilises heavy toxic metals in solution, resulting in the deterioration of the quality of surface and groundwater resources.

The approach developed in this research only takes into consideration the vertical movement of pollutants which are soluble and move together with the water. Although pollution can diffuse laterally, this aspect was not considered in the present research.

Within a given coalfield, there are a large number of types of AMD point sources, such as opencast mines, waste rock dumps, tailings dumps and loading bays. Owing to their distribution over a large regional area, they will be considered as a regional nonpoint problem and a regional assessment methodology used.

1.5 STRUCTURE OF THE THESIS

The thesis is structured as follows:

- **Chapter 1** is an introductory chapter which provides background information leading to the formulation of the research. It highlights the general outline of the research and the envisaged benefits from such a research to the global drive towards the sustainable utilisation of coal resources while ensuring minimum damage to the environment.
- **Chapter 2** discusses the various groundwater vulnerability approaches, their strengths and shortcomings with reference to their usage for AMD specific groundwater vulnerability assessment and how they can be improved by usage of AI. Globally accepted and well-structured frameworks (mineral systems, petroleum and source-pathway-receptor approaches) are also discussed.
- **Chapter 3** outlines the formulation of a standardised holistic approach SPT for the assessment of groundwater vulnerability with regard to AMD. SPT represents the following groundwater vulnerability factors: source, transportation pathways and traps.
- **Chapter 4** gives an outline of knowledge-driven artificial intelligence methodologies, in particular the fuzzy expert system. The chapter provides a formulation of the fuzzy expert system, together with its results and a validation and discussion of the system, as applied to a groundwater vulnerability assessment of the Witbank, Ermelo and Highveld coalfields using SPT input parameters.
- **Chapter 5** deals with the data preparation steps followed in converting the raw data into a format that is accepted by data-driven approaches. A description of the algorithms that are used for the autonomous processing of data-driven approaches are given in this chapter.
- **Chapter 6** describes the data-driven artificial intelligence methodology, in particular artificial neural networks (ANN). This chapter includes a formulation of the methodology, the results, validation and a discussion of the application of the methodology to a groundwater vulnerability assessment of the Witbank, Ermelo and Highveld coalfields of South Africa using the SPT input parameters.
- **Chapter 7** gives an outline of the hybrid artificial intelligence methodology, in particular of the adaptive neuro-fuzzy inference system (ANFIS). A discussion of its formulation, results and validation as applied in the context of a groundwater vulnerability assessment of the Witbank, Ermelo and Highveld coalfields of South Africa using SPT input parameters is given in this chapter.

- **Chapter 8** deals with a formulation of a software platform (toolbox) for the rapid assessment of the AMD-specific groundwater vulnerability of a typical coalfield and a discussion of how the platform can be applied in policy and decision-making processes.
- **Chapter 9** provides overall concluding remarks and recommendations based on the findings of this research and highlights possible further research areas.
- The **Appendices** contain all the data gathered during the course of the research, developed algorithms and the software platform manual.

CHAPTER 2: GROUNDWATER VULNERABILITY ASSESSMENT METHODS

2.1 INTRODUCTION

This chapter discusses various conventional groundwater vulnerability approaches, their merits and shortfalls with regard to their application in modelling groundwater vulnerability specific to AMD pollution at a regional coalfield scale. A literature review of AMD formation, transport and attenuation will be done in view of informing the modelling of AMD-specific groundwater vulnerability. An overview of the concept of AI and its current utilisation for groundwater vulnerability will also be discussed in this chapter. Finally, a review of the globally accepted regional assessment approaches from various fields such as mineral prospectivity mapping, petroleum exploration and environmental regulations will be given in a bid to formulate an approach for groundwater vulnerability which is specific to AMD pollution at a regional coalfield scale.

2.2 GENERAL CONCEPT OF GROUNDWATER VULNERABILITY

Groundwater vulnerability, related to groundwater protection, is intended to evaluate the likelihood of pollution reaching the groundwater system after its introduction on the ground surface. General aims of understanding groundwater vulnerability at a regional scale range from (NRC, 1993):

- Policy analysis and development, where the potential for groundwater pollution is assessed and policy refined accordingly to protect groundwater resources from possible impacting factors which can be brought about by governing policies.
- Informing land-use decisions, where land-use practice is altered to reflect the potential for groundwater pollution.
- Improving the general education of and awareness among all groundwater users and authorities in charge of managing the water resources.

Similar to other fields of science, groundwater vulnerability is governed by a set of laws from which assessment methodologies are formulated.

2.2.1 Laws of Groundwater Vulnerability

The three laws of groundwater vulnerability formulated by the NRC (1993) are given as follows:

First law - The first law of groundwater vulnerability states that all groundwater is to a certain extent vulnerable to pollution. Thus, assessments of groundwater vulnerability are meant to give a relative likelihood of pollution occurring in the groundwater system after its introduction on the ground surface. From the first law, the issue of time-travel of pollution to reach the groundwater should not be used as a measure of vulnerability because a longer travel time does not guarantee that the aquifer has a low vulnerability. The best approach, in line with the first law, is to consider the extent to which processes such dispersion, sorption, dilution, ionic exchanges, and biochemical would contribute to the reduction of pollution concentration or to the transformation of pollution to other less environmentally damaging products.

Second law - The second law of groundwater vulnerability states that uncertainty is inherent in all vulnerability assessments. Thus, the fundamental problem with an assessment of how pollution will behave at the subsurface is limited. Moreover, for any assessment, spatial data are used and these data are often derived by interpolation methods which themselves introduce uncertainties. Precise knowledge concerning the behaviour of any pollution in the subsurface is limited to the current level of understanding of the processes, based on laboratory or field site investigations used to interpolate the results to cover the whole assessment area. Thus, owing to the inherent uncertainties, assessment should be expressed in probabilistic terms such as "*likelihood*" or "*tendency*" so that the inherent uncertainty of the assessment is apparent. The most common causes of uncertainty in groundwater vulnerability assessments include (NRC, 1993):

- errors in obtaining input data;
- errors due to natural spatial and temporal variability;
- errors in computerisation and storage of data;
- data processing errors;
- modelling and conceptual errors; and
- output and visualisation errors.

Third law - The third law of groundwater vulnerability states that groundwater vulnerability results often obscure obvious differences or make it difficult to discern subtle differences. Thus, while it may be easy to identify areas where groundwater is very likely to be polluted it is difficult to delineate areas where groundwater is indeed unlikely to be affected by pollution. It is important that groundwater classes consider these aspects.

In summary, a formulation of groundwater vulnerability assessment methods should adhere to the fundamental laws: thus, groundwater is expressed in terms of pollution concentration loads (first law). An assessment is done and expressed in probabilistic terms as opposed to providing a precise definition of pollution migration mechanisms (second law). Ultimately, the assessment should show groundwater vulnerability as high, moderate, low and avoid class names such as “impossible” or “difficult” (third law).

2.3 REVIEW OF GROUNDWATER VULNERABILITY ASSESSMENT APPROACHES

Groundwater vulnerability is a relative dimensionless parameter of the natural attenuation of pollutants by the surface and/or subsurface which cannot be measured directly in the field. Assessments are often done to understand the natural conditions of the geology, hydrogeology and/or can be expanded to include the nature of pollutants and their migration into and interaction with the subsurface. This is achieved by geological mapping, pump testing and column leach tests among other methods.

Groundwater vulnerability assessments may be divided into three general categories:

- overlay and index;
- process-based simulation model; and
- statistical approaches.

2.3.1 Overlay and Index Approach

This assessment approach is based on combining various geological, hydrogeological and other physical attributes deemed to be major factors controlling groundwater pollution. Weights are assigned to each attribute by comparing the relative importance of each attribute with groundwater vulnerability and its spatial resolution. The attributes are then combined manually or a in GIS environment to produce a groundwater vulnerability model (NRC, 1993). This approach is preferred because of its relative simplicity. Although data can be obtained easily, the approach includes all the important factors of groundwater vulnerability. The most commonly used approaches such as the DRASTIC, GOD, SINTACS and AVI will be discussed in this section.

2.3.1.1 DRASTIC

The methodology allows for a systematic evaluation of the pollution potential of an area using readily available hydrogeological, geological and morphological data which can be obtained and meaningfully mapped in minimal time and at minimal cost. The DRASTIC method was developed

by the United States Environmental Protection Agency (USEPA) as a proactive tool for the assessment of groundwater vulnerability to pollution, and has the following overall goals (Aller *et al.*, 1987):

- function as a management tool;
- simplicity and ease of use;
- ability to use available information; and
- ability to be used by individuals with diverse backgrounds and levels of expertise.

The method consists of two major elements: the designation of mappable units, termed hydrogeological settings and the assignation of relative rankings of hydrogeological parameters. The name "DRASTIC" comes from the acronym of the seven parameters which make up the methodology: Depth to water table (D), net Recharge (R), Aquifer media (A), Soil media (S), Topography (T), Impact of the vadose zone (I) and hydraulic Conductivity (C) of the aquifer. The DRASTIC parameters are combined to form one result, termed the "*DRASTIC Index*" which is determined by multiplying each hydrogeological factor weight by its point rating and summing the total, as given by Equation 2.1 (Neshat *et al.*, 2014).

$$V = \sum_{i=1}^{7} (W_i * R_i) \qquad 2.1$$

Where V is the DRASTIC index value and W_i is the weighted coefficient (importance weight) for parameter i, with an associated rating (class rating) value of R_i.

Each parameter is divided into classes, each with a rating value weighted based on its relative importance in respect to groundwater vulnerability. Each of these hydrogeological factors is given a rating from 1 to 10, and the DRASTIC parameters are weighted from 1 to 5 according to their relative contributions to the potential pollution. The resulting index is a relative measure of vulnerability to pollution where areas with higher index values are more vulnerable than those with lower indices.

Table 2.1 shows the ranges, ratings and weights for each of the seven parameters making up the original DRASTIC methodology as proposed by Aller *et al* (1987) in the 1980s. These values only serve as a guide to which modifications may be made by changing the weights, ratings and by adding or removing parameters to suit a particular hydrogeological condition. This would be referred to as the modified DRASTIC. The DRASTIC method has two versions; one for intrinsic vulnerability (DRASTIC-typical) and one for the specific vulnerability of a particular pollution manifestation (DRASTIC-Pollution). The difference between these versions resides in the redefinition of their parameter weights and the addition of the pollution scores (Kazakis and Voudouris, 2015). Since the

development of the DRASTIC model for groundwater vulnerability assessments by USEPA in the late 1980s, this type of indexing method has become popular and generally used worldwide (Al-Adamat *et al.*, 2003; El-Naqa, 2004; Musekiwa and Majola, 2013; Saida *et al.*, 2017). The advantage of the DRASTIC approach includes the usage of many parameters, which ensures that most hydrogeological processes are included (Babiker *et al.*, 2005). The method also allows pollution of any hydrogeological setting to be systematically evaluated from relatively accessible and available data at a reasonable cost (Aller *et al.*, 1987; Metni *et al.*, 2004).

Table 2.1: Original DRASTIC parameters (Aller *et al.*, 1987)

Layer	Range	Rating	Weight
Depth to water table (feet)	0 - 5	10	5
	5 – 15	9	
	15 – 30	7	
	30 – 50	5	
	50 – 75	3	
	75 – 100	2	
	100 +	1	
Net recharge (inches)	0 – 2	9	4
	2 – 4	8	
	4 – 7	6	
	7 – 10	3	
	10 +	1	
Aquifer media	Karst limestone	10	3
	Basalt	9	
	Sand and gravel	8	
	Massive limestone, sandstone, shale sequences	6	
	Weathered metamorphic / igneous	4	
	Metamorphic / igneous	3	
	Missive shale	2	
Soil media	Thin or Absent, Gravel	10	2
	Sand	9	
	Peat	8	
	Shrinking or aggregated clay	7	
	Sandy loam	6	
	Loam	5	
	Silty loam	4	
	Clay loam	3	
	Muck	2	
	Non(Shrinking or aggregated) clay	1	

Table 2.1 (continued): Original DRASTIC parameters (Aller *et al.*, 1987)

Topographic slope (%)	0-2	10	1
	2-6	9	
	6-12	5	
	12-18	3	
	18+	1	
Impact of the vadose zone	Karts limestone	10	5
	Basalt	9	
	Sand and gravel	8	
	Metamorphic/ Igneous	4	
	Sand, sandstone, gravel/silt, shale, limestone	6	
	Shale	3	
	Silt, clay	1	
Aquifer hydraulic conductivity (gpd/ft^2)	1 – 100	10	3
	100 – 300	8	
	300 – 700	6	
	700 – 1000	4	

Moreover, the DRASTIC approach is independent of the aquifer type and the weights and ratings can be adjusted to suit a particular given hydrogeological setting or climatic condition (Voss and Tesoriero, 1997; Al-Hanbali and Kondoh, 2008). However, this method also has several drawbacks which have caused many researchers to question the index and overlay methods.

2.3.1.2 GOD

The GOD approach is a vulnerability assessment methodology developed in Great Britain, where most groundwater resources are in hard rock aquifers, primarily consisting of sandstone and limestone covered by unconsolidated overburden or soil layers (Foster, 1998; Harter, 2008). Like DRASTIC, GOD is an index-and-overlay method designed for a quick assessment of groundwater vulnerability over large regions based on a few important parameters: groundwater occurrence (G), overall lithology of the unsaturated zone (O) (overlying aquitard) and depth to the groundwater table (D). Scores are assigned to each of the three categories and then multiplied to yield a final score according to Equation 2.2 (Draoui *et al.*, 2008).

$$I_{GOD} = I_G * I_o * I_D \qquad 2.2$$

The value of the index varies from 0 to 1 (Table 2.2) and five vulnerability classes, also ranging from 0 to 1, are differentiated by the method. Because the parameters can only take values from 0 to 1, when multiplied together, the overall result is usually a value lower than the score assigned to each parameter (Gogu and Dassargues, 2000).

Table 2.2: Original GOD parameters (Gogu and Dassargues, 2000)

Layer	Range	Rating
Groundwater occurrence (G)	Unconfined	1
	Confined	0.6
Overall lithology of the unsaturated zone (O)	Gravels, pebbles	0.8
	Sands	0.7
	Loam sands	0.6
	Marls and loams	0.5
	Clays	0.4
Depth to groundwater table (D)	0-2	1
	2-5	0.9
	5-10	0.8
	10-20	0.7

The advantage of this method is that very few parameters are used and can easily be obtained at a very low cost and the method takes into consideration the likelihood of fractures or fracture systems developing in the soils, overburden, or overlying geological units of the aquifer. However, owing to the use of so few parameters, the model produced is over-simplified in respect of the prevailing conditions contributing to groundwater vulnerability. In addition, parameter scores are subjectively assigned, making the approach very biased and dependent on the expert's opinions and level of understanding of the hydrogeological processes in the particular area.

2.3.1.3 SINTACS

The SINTACS (Civita, 1994, 2010), method was derived from the DRASTIC model and is another example of an index and overlay method. SINTACS was developed for vulnerability assessment and mapping requirements (medium and large-scale maps) by Italian hydrogeologists, and hydrogeological, climatic, and impact settings typical of the Mediterranean countries were chosen. The method uses the same seven parameters as DRASTIC, but the rating and weighting procedure is more flexible. There are four weight classifications, with the possibility of creating new ones. The acronym "SINTACS" represents the seven parameters included in the method: *Soggiacenza* (depth to water, S), *Infiltrazione efficace* (recharge, I), *Non saturo* (vadose zone, N), *Tipologia della copertura* (soil cover, T), *Acquifero* (aquifer, A), *Conducibilità idraulica* (hydraulic conductivity, C), *Supeficie topografica* (slope, S) (Civita, 2010).

The assignment of weights and ratings is similar to that of the DRASTIC method. The user encodes the input data as functions of the local conditions in each area, and has the possibility of using different classifications depending on the circumstances. The SINTACS vulnerability index is computed using Equation 2.3:

$$I_{SINTACS} = \sum_{i=1}^{7} (P_i * W_i) \quad 2.3$$

Where $I_{SINTACS}$ is the SINTACS index and P_i is the rating of each of the seven parameters used and W_i is the corresponding weight in each class. The final results outline vulnerability classes, where higher values represent high groundwater vulnerability and low values represent low groundwater vulnerability.

The SINTACS method is able to distinguish degrees of vulnerability at regional scales where there are different lithologies, but it is much less effective at assessing the vulnerability of carbonate aquifers, as it does not take into account the peculiarities of karst (Vías *et al.*, 2005). With particular reference to an AMD assessment at a regional scale, even though this approach is an intrinsic type, it does not factor in regional pathways which would have been useful in understanding how pollutants might reach the aquifer system.

2.3.1.4 AVI

Stempvoort *et al.* (1993) developed the aquifer vulnerability index (AVI) method for the assessment of groundwater vulnerability by quantifying the vulnerability by hydraulic resistance in respect of the vertical flow of water through the protective layers. Hydraulic resistance C is defined by Equation 2.4:

$$C = \sum_{i} \frac{d_i}{K_i} \quad 2.4$$

Where d_i is the layer thickness and K_i is the hydraulic conductivity of each protective layer.

As K_i has the unit length/time (m/s or m/d), the dimension of C is time. Thus, the resultant can be used as a rough estimate of the vertical travel time of water through the unsaturated layers, although important parameters controlling travel time such as hydraulic gradient and diffusion are not considered (Van Stempvoort *et al.*, 1993). The resultant hydraulic resistance may be reclassified into five groundwater vulnerability classes, as shown in Table 2.3.

Table 2.3: Vulnerability classes of the AVI method (Fraga *et al.*, 2013)

Hydraulic resistance (years)	Vulnerability Class
0 – 10	Extremely High
10 – 100	High
100 – 1000	Moderate
1000 – 10000	Low
10000 +	Extremely Low

While the index system is based on an assumption that the vulnerability is a linear superposition of artificially specified parameters, studies have shown a nonlinear relationship between vulnerability and specific parameters (Neukum and Azzam, 2009). In addition, the ratings and weights are all specified artificially by an expert according to subjective judgments which can introduce some bias into the overall results (Gogu *et al.*, 2003; Frind *et al.*, 2006; Yu *et al.*, 2010). Finally, otherwise continuously varying parameters are discretised (Yu *et al.*, 2010).

Therefore, the general assumptions for the index and overlay methods include the following (Kazakis and Voudouris, 2015):

- the pollution is introduced at the ground surface;
- the pollution reaches the groundwater table by precipitation/infiltration;
- the pollution has the same mobility (velocity) as water; and
- the approach is best suited to large areas.

2.3.2 Process-Based Simulation Modelling

This approach involves solving mathematical equations that govern pollution transport by simulating models. Thus, an attempt is made to predict pollution transport in space and time which could include a one, two or three dimensional model of the unsaturated and saturated conditions (Brindha and Elango, 2015). The modelling is mainly specific to a certain hydrogeological condition and type of pollution. Examples of such modelling include: the LEACHM model which was formulated to simulate the behaviour of pesticides in the unsaturated zone and include: water flow, runoff, solute transport, solute dispersion, sorption, degradation and evapotranspiration, the GLEAMS and the PRZM which were designed to assist in management decisions (NRC, 1993). The limitations of the process-based simulation include a failure to account for flow and transport processes at spatial scales regionally. The approach often requires a large amount of data which are sometimes very difficult or very costly to acquire over a large area.

2.3.3 Statistical Approaches

Statistical approaches involve the calculation of the probability distribution of groundwater pollution based on the frequency of the pollution, pollution concentrations or pollution probability over an aerial extent e.g. logistical regression, principal component analysis, fuzzy logic, analytical hierarchical process and kriging (NRC, 1993; Dixon, 2005b; Pathak *et al.*, 2014). While statistical methods, similar to other approaches, rely heavy on the quality of data, for statistical methods the model is derived from the data. Thus, the higher the data quality the better the model is able to represent the actual conditions. In modelling using statistical approaches, some modelling may be complex and may require experts in that statistical method to help in the model development. Advantages of the statistical approach are that they deal more effectively with differences in scale than other approaches and there is a myriad of statistical methods from which to choose to suit a given dataset and the current knowledge of the system to be modelled. Thus, the approach is more flexible than many others are.

Considering the benefits of the three approaches (index and overlay, process-based and statistical), a hybrid system which takes the benefits from these approaches may be useful. These benefits include the simplicity and easily available dataset from the index and overlay approaches, expression vulnerability in terms of processes specific to pollution being discussed (from the process-based simulation approach) and the availability of statistical methods to combine input maps into one vulnerability map (from the statistical approach).

In this research, the groundwater vulnerability assessments are meant specifically for AMD; hence, an understanding of how AMD is formed, transported and attenuated in the subsurface is vital.

2.4 ACID MINE DRAINAGE FORMATION PROCESSES

Iron sulphide oxidation produces acidic drainage water, often referred to as AMD. Prediction of AMD generation and its properties are key to understanding how dissolved metals from active and past mining operations are released into the environment, particularly into the groundwater system (Moncur *et al.*, 2009). The prerequisite for AMD is the generation of protons at a faster rate than they can be neutralised by any alkaline materials (e.g. carbonates) in the orebody or waste disposal facility, access to oxygen and water, and a rate of precipitation higher than evaporation.

The most common mineral causing AMD is pyrite, but other metal sulphides may also contribute. The oxidation of pyrite, preceding iron hydrolysis, occurs in three steps. The first step (Equation 2.5) occurs slowly at a pH above 4.3, with high sulphate and low iron concentrations, with little or no

acidity (Molson and Aubertin, 2006; Pinetown *et al.*, 2007). The reaction can proceed both abiotically and by direct bacterial oxidation:

$$FeS_2(s) + 7/2O_2(g) + H_2O(l) \rightarrow Fe^{2+}(s) + 2SO_4^{2-}(aq) + 2H^+(aq) \quad 2.5$$

The second step (Equation 2.6) occurs with a pH range between 2.5 and 4.15 representing high acid levels, and where the total iron increases. The Fe^{3+} /Fe^{2+} ratio is still low (Pinetown *et al.*, 2007):

$$Fe^{2+}(s) + H^+(aq) + 1/4O_2(g) \rightarrow Fe^{3+}(s) + H_2O(l) \quad 2.6$$

This stage proceeds predominantly by direct bacterial oxidation determined by the activity of microorganisms of the genus Acidithiobacillus (Hedrich and Johnson, 2013).

The third step (Equation 2.7) occurs at pH values below 2.5, characterised by high sulphate and iron levels. The ratio of Fe^{3+}/Fe^{2+} is high. The reaction is totally determined by bacterial oxidation, that enhances the solubility of metal sulphides, catalysed by chemolithoautotrophic acidophile microorganisms (e.g. Thiobacillus Ferrooxidans) (Hedrich and Johnson, 2013):

$$FeS_2(s) + 15/4O_2(g) + 1/2H_2O(l) \rightarrow Fe^{3+}(s) + 2SO_4^{2-}(aq) + H^+(aq) \quad 2.7$$

These three stages are the primary factors, directly involved in the acid production process (Ferguson and Erickson, 1988). The intensity of acid generation by these primary factors is determined (Salomons, 1995) by environmental (e.g. grain size, pH, temperature, oxygen concentration, metal activity) and biological parameters (population density of the bacteria, rate of bacterial growth, supply of nutrients).

AMD is also generated naturally when rocks containing AMD generating material such as pyrite are weathered to form an acid solution. The process occurs very slowly, so slowly in fact that the natural neutralisation processes readily remove the acidity. However, during mining and mineral extraction, the rock mass is extensively fragmented into very small particles, a process which increases the surface area and thus increases the rate of acid generation considerably (McCarthy, 2011). Geomorphology and the extraction and distribution of AMD generation material are other parameters affecting the overall impact of AMD on the surrounding environment.

It follows that when designing a groundwater vulnerability assessment which is specific to AMD, it is important that areas with acid generation material be identified and the availability of water for the AMD formation reactions to occur be mapped out. In addition, when AMD is released into the environment, owing to the lowering of pH and with high sulphate ad iron concentrations the fate of the AMD should be investigated as it passes through the soils, the unsaturated zone below the soils and in the aquifer.

2.5 SHORTCOMINGS OF GROUNDWATER VULNERABILITY ASSESSMENT METHODS

Based on the understanding of the formation of AMD and considering at the conventional approaches discussed in section 2.3, it can be seen that assessment approaches suffer the following pitfalls when used for specific groundwater vulnerability assessments at a regional scale:

- Approaches such as DRASTIC and SINTACS use recharge parameters calculated from soils and topography parameters where all these parameters are used to generate the groundwater vulnerability model. This means that the output model will increasingly mimic these parameters and mask out the effects of other parameters. This is called parameter dependence. Thus, parameters need to be redistributed and some removed to reduce the parameter dependence problem.
- The approach mentioned here does not specifically consider fracturing and preferential pathways in the modelling, yet when dealing with pollutants such as AMD these would be particularly important where some lithological units of a typical coalfield may be fractured.
- The allocation of rates and weights is subjective and varies from one expert to another. Hence, the generated groundwater vulnerability models are often variable and highly debated by many experts.

Thus, the groundwater vulnerability assessment methods need to be able to simulate or take into account the effects of fracturing and preferential flows. The review of characteristics and processes occurring in the unsaturated zone and the review of models indicated the following knowledge gaps need to be addressed in order to produce improved approaches for groundwater vulnerability assessment:

- determination of hydraulic properties in the unsaturated zone (permeability, porosity and water retention);
- inclusion of a proxy which would involve the presence of possible preferential flow, in particular short-circuiting (fractures and rocks);
- inclusion of chemical properties (pollutant – rock reactivity, solubility, volatilisation, sorption and degradation) of specific pollutants and groups of pollutants; and
- inclusion of data mining approaches such AI to reduce the subjective nature of many of the groundwater vulnerability assessment approaches.

2.6 OVERVIEW OF ARTIFICIAL INTELLIGENCE SYSTEMS

Artificial Intelligence (AI) is the study and creation of computer systems that can perceive reason and act with the primary aim of producing intelligent machines or programs. The intelligence should be exhibited by thinking, making decisions, solving problems and, importantly, by learning. AI is an interdisciplinary field that requires knowledge of computer science, linguistics, psychology, biology and philosophy.

The question of whether a machine is able to exhibit human-like intelligence has been a subject of debate for a number of years. Many have opposed this idea, claiming that highly sophisticated behaviour such as love, creative discovery and moral choice will always be beyond the scope of machines. Others have accepted that machines can indeed exhibit aspects of human-like intelligence. This disagreement remains unresolved. In order to understand AI, it is important to define the concept of "intelligence". Intelligence may be defined in two ways (Negnevitsky, 2005):

- intelligence is the ability to understand and learn things; and
- intelligence is the ability to think and understand instead of doing things by instinct or automatically.

The first definition does not include machines, whereas the second definition is more flexible to accommodate machines exhibiting intelligence. Thus, for a machine or someone to exhibit intelligence, it or he/she should be able to think, learn and/or understand. Thinking may be defined as "the activity of using the brain to consider a problem or to create an idea". Thus, intelligence may be defined as "the ability to think, learn and/or understand to solve problems and to make decisions" (Negnevitsky, 2005). Humans, animals and machines are capable of this. Fundamentally, AI seeks to answer the question as to whether a machine is able to do things which at present are done by humans. The field of AI is relatively new, having been formulated in 1943, and having developed steadily until the present day.

Table 2.4 shows the brief history of AI from 1943 to the present day. The table reflects the many vagaries that the field has undergone in its ±74 year history.

Table 2.4: Brief history of Artificial Intelligence

Era	Year	Activities/description of events
Birth of AI (1943–1956)	1943	McCulloch and Pitts develop the Boolean circuit model of the brain
	1950	Alan Turing introduces the Turing Test for the evaluation of intelligence and published '*Computing Machinery and Intelligence*'.
	1956	John McCarthy organised the Dartmouth conference where the name (AI) was formally used. This event is considered the birth of AI.
Golden years (1956–1974)	1958	John McCarthy invents the Locator/Identifier Separation Protocol (LISP) programming language of AI.
	1969–1973	Many successful programs were written and a new direction was set in the fields of natural language and neural networks.
	1969	A scientist at the Stanford Research Institute develops an intelligent agent equipped with locomotion, perception and problem solving capabilities.
	1973	A robot capable of using vision to locate and assemble models is built.
First AI winter	1974–1980	AI falls into disuse owing to a lack of funding because of high expectations and the failure of AI to produce the promised results. Criticism of the idea shut down the neural network field for the next ten years.
Boom	1980–1987	The concept of "expert systems" is adopted by many corporations around the world and knowledge becomes the focus of mainstream AI research. The Japanese government funds the 5th generation computer. Rebirth of the neural network by John Hopfield with the introduction of the Hopfield Net. Redevelopment and popularisation of the back-propagation learning algorithm.
Second AI winter	1987–1993	AI suffers another series of financial setbacks, but still continues to make progress. The focus of AI shifts to intelligent agents (robots) to show the world the power of intelligence. This leads to the development of fields such as cybernetics and control theory.
Success	1993–2001	The field finally achieves most of its goals. Successfully used throughout the technology industry owing to improved computing power.
	1997	Deep Blue becomes the first chess computer to beat a (human) world chess champion in 1997. Adverse development of the intelligent agent (robots). An increase in collaborative research with fields such as mathematics, economics, operation research and programming. Uses of AI now include data mining, industrial robots, logistics, speech recognition, banking, medical diagnosis and Web search engines.
Deep learning, big data, artificial general intelligence	2000-present	Owing to access to large datasets, faster computing power and advanced machine learning, AI is now being used in virtually all spheres of life. The deep learning algorithm is developed to overcome the shortcomings of the conventional neural networks such as overfitting. Towards the development of machines capable of general intelligent action such as the AlphaGo program that beats the human world champion in the ancient Chinese game '*GO*' in 2016. Development of smart computing aimed at automating many human functions such as self-driving cars.

The field of AI has many branches, all of which are connected and share commonalities. The most widely used today include: machine learning, expert systems, natural language processing, robotics, speech, planning and vision which can be further broken down into various other applications

(Logica, 2015). Figure 2.1 shows branches of AI among which, in terms of the present research, only the machine learning and expert system are applicable to groundwater vulnerability assessments.

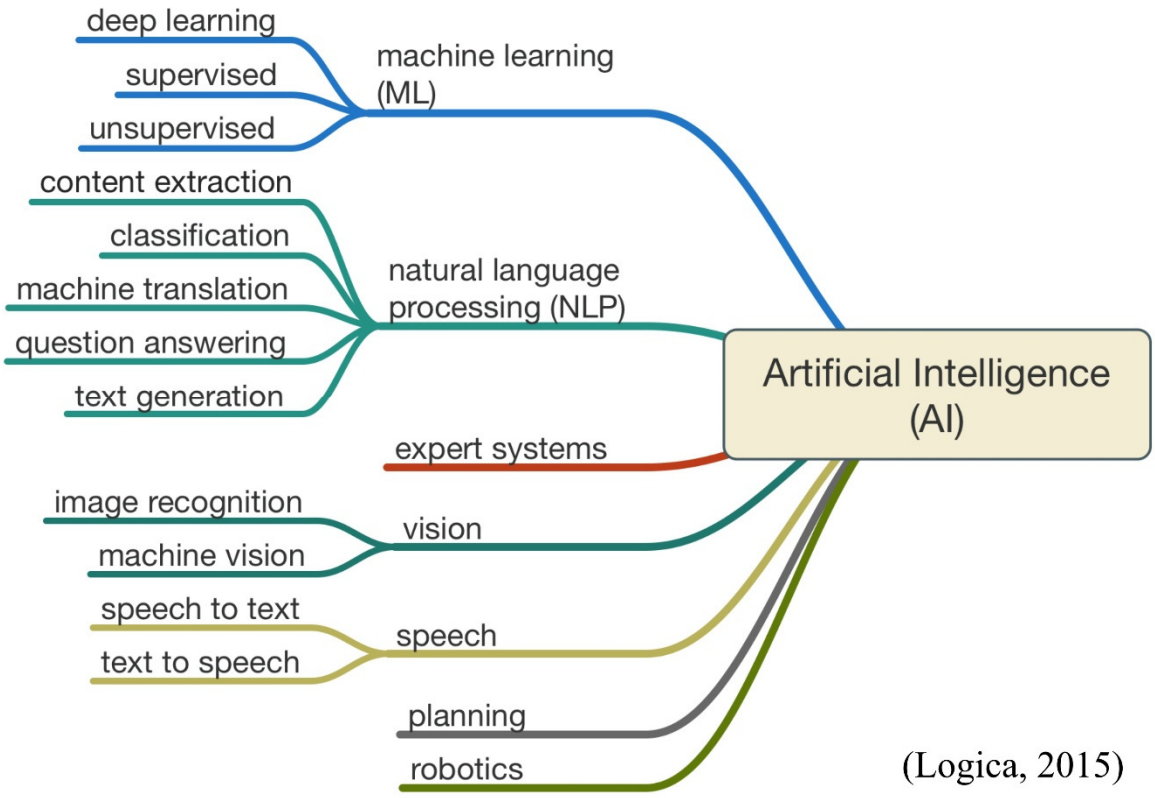

Figure 2.1: Branches of the AI field

2.7 APPLICATIONS OF ARTIFICIAL INTELLIGENCE IN GROUNDWATER VULNERABILITY ASSESSMENTS

Several authors have applied AI to groundwater vulnerability assessments (Dixon, 2005b; Fijani *et al.*, 2013; Nadiri *et al.*, 2015; Baghapour *et al.*, 2016). Fijani *et al.* (2013) used an integrated approach which combines four AI systems (Sugeno fuzzy logic, Mamdani fuzzy logic, Artificial Neural Networks (ANN) and neuro-fuzzy) to optimise the DRASTIC method for groundwater vulnerability assessments. The four AI models were produced separately and then combined by using the outputs as inputs to another ANN to produce one output. The authors termed the approach "Supervised Committee Machine Artificial Intelligence" (SCMAI). They applied the approach to estimate groundwater vulnerability to nitrate (NO_3-N) pollution of Maragheh–Bonab Plain aquifer in Iran. The seven parameters of the DRASTIC method were used as training inputs and the NO_3-N concentration in the borehole as the training output. The results of the Maragheh–Bonab Plain aquifer showed a better correlation between the results from the SCMAI with the nitrate concentration testing boreholes than from the individual AI models.

In another case study, Baghapour *et al.* (2016) used AI to assess groundwater vulnerability in an unconfined aquifer of the Shiraz Plain in Iran. Artificial neural networks were used to estimate the groundwater vulnerability of the aquifer using the several parameters of the DRASTIC method as the training input and nitrate concentration as the training output.

Dixon (2005b) used the Fuzzy Expert system to model the groundwater vulnerability of Woodruff County of the Mississippi Delta region of Arkansas in the USA. Detailed land-use/pesticide and soil structure in conjunction with selected parameters of the DRASTIC method were used. Results significantly coincided with field data.

The neuro-fuzzy technique, which is one of the branches of AI, combines artificial neural networks and the fuzzy expert system. This technique was used to assess groundwater vulnerability to nitrate pollution in a subbasin of the Illinois River watershed located east of the Arkansas–Oklahoma border in the USA (Dixon, 2005a). Four plausible parameters, which are critical in transporting pollutants through the soil profile to the groundwater were identified, namely soil hydrological group, depth of soil profile, soil structure and land use.

From the case studies, it was clear that the AI system could be used to produce groundwater vulnerability models which correlated well with field measurements when used for nitrate pollution. No application of AI in groundwater vulnerability dealing specifically with the AMD pollution of a typical coalfield in a geological setting similar to that of the South African Karoo environment could be found. However, the success of AI in other geological contexts is promising for its use in the development of a groundwater vulnerability assessment specific to AMD at a regional coalfield scale in South Africa.

To validate the groundwater vulnerability models generated from the application of AI, the models are compared with a measureable parameter which could be either a pollution tracer or pollution already in groundwater (e.g. nitrate is commonly used as a main pollutant indicator of the human induced pollution of groundwater) (Gheisari, 2017). The correlation coefficient (R) which is sometimes referred to as the *Pearson product moment correlation coefficient* is used to measure the strength and direction of the linear relationship between two variables (Roberts and Roberts, 2000) such as the groundwater vulnerability model value and the value of the measured parameter in the groundwater vulnerability assessment.

The mathematical formula used to calculate the correlation coefficient (R) between two variables (x, y) is given by equation (2.8) (Roberts and Roberts, 2000):

$$R = \frac{n\sum xy - (\sum x)(\sum y)}{\sqrt{n(\sum x^2) - (\sum x)^2}\sqrt{n(\sum y^2) - (\sum y)^2}} \quad 2.8$$

Where n is the number of data points and R varies between -1 and +1.

The interpretation of the R is given in Table 2.5.

Table 2.5: Interpretation of the R value (Arikunto, 2002)

R value	Interpretation
-1 to -0.8	Very strong negative relationship
-0.8 to - 0.6	High negative relationship
-0.6 to - 0.4	Fair negative relationship
-0.4 to - 0.2	Low negative relationship
-0.2 to 0	Very low negative relationship
0 to 0.2	Very low positive relationship
0.2 to 0.4	Low positive relationship
0.4 to 0.6	Fair positive relationship
0.6 to 0.8	High positive relationship
0.8 to 1	Very strong positive relationship

When the correlation coefficient value is squared, the result is called the coefficient of determination (R^2) which may be considered an approximate measure of the strength of the linear relationship between the variables (Zar, 1999).

For example, if A and B are related and have a correlation coefficient value (R) of 0.85, then R^2 would be 0.7225, which means that for the equation relating A and B, B explains 72.5% of the variability in A.

2.8 GLOBALLY ACCEPTED REGIONAL ASSESSMENT APPROACHES

Having understood the fundamentals of groundwater vulnerability and approaches to improve them in order to produce a groundwater assessment approach which can be used for AMD assessment, various globally accepted regional assessment approaches were examined. These include the well-known mineral systems approach used for mineral exploration, the petroleum system used for oil and gas exploration and the source-pathway-receptor approach which is utilised for environmental regulatory purposes.

2.8.1 Mineral Systems Approach

The mineral systems approach was first proposed by Fyfe and Kerrich in 1976 (Wyman *et al.*, 2016) and reintroduced to mineral exploration by Wyborn *et al.* (1994). The mineral systems approach for mineral exploration involves an understanding of all geological factors that are required to form and preserve a mineral deposit. The approach defines mineral deposits as focal points of much larger earth processes operating on a variety of scales to focus mass and energy flux in the formation of mineral deposits (Porwal and Kreuzer, 2010; Porwal and Carranza, 2015). The approach emphasises those processes that are critical to the formation of a mineral deposit. These processes, among others, involve the energy that drives the mineralising fluids (i.e. a source of heat), ligands (fluid) that will aid in carrying the metals in solution, fluid migration pathways and trapping sites where the metals are precipitated and preserved, ultimately forming mineral deposits (Figure 2.2) (Wyborn *et al.*, 1994; Knox-Robinson and Wyborn, 1997). The approach offers a process-based workflow for mineral prospectivity analysis and is neither restricted to a particular geological setting or specific mineral deposit type. For these reasons, it is widely used in mineral exploration programmes (Porwal *et al.*, 2015; Chudasama *et al.*, 2016). Figure 2.2 shows the scale dependence of the approach, where all the parameters (energy source, fluid-metal source, migration factor and traps factor) are used for a regional systems scale with a radius between 5 and 500 km and only the trap factor is used for camp and deposit scales with a radius between 0.5 and 10 km and less than 5 km respectively.

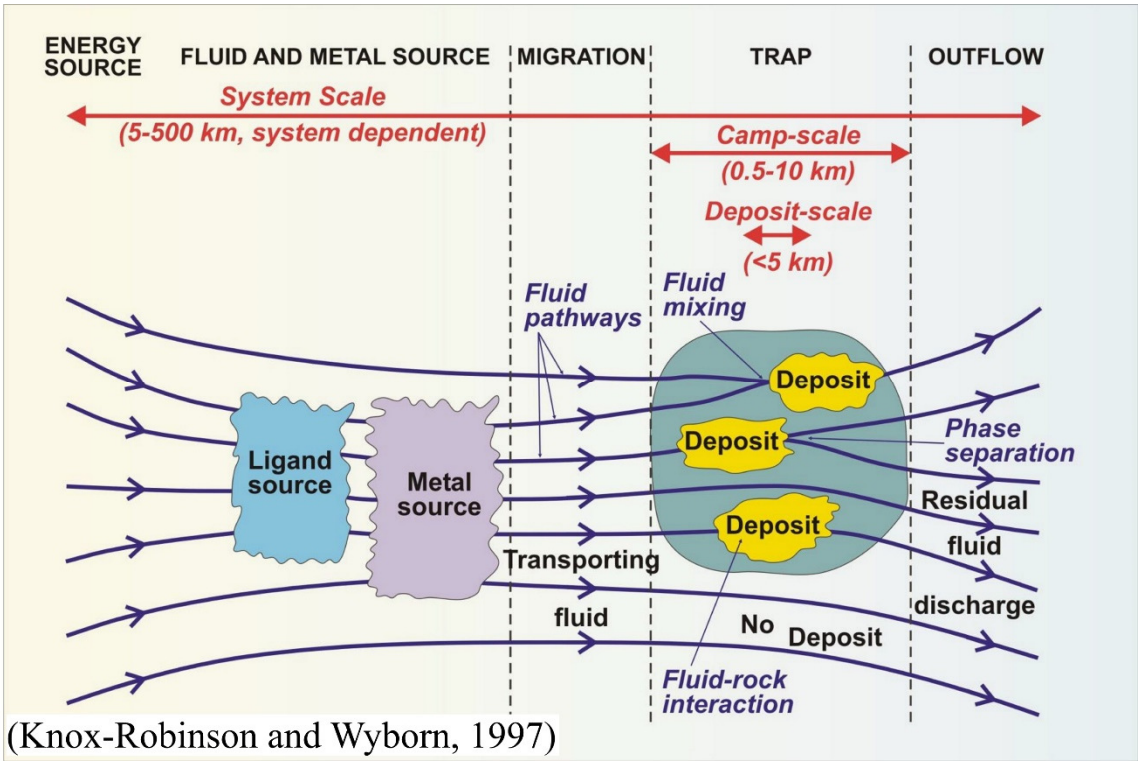

Figure 2.2: Mineral systems approach flow diagram

2.8.2 Petroleum Systems

The "oil system" concept (Dow, 1974) has an ideology parallel to that of the mineral systems approach which is based on the identification of oil-source rocks which have led to the development of "petroleum systems" (a concept first used by Perrodon in 1980).

Petroleum systems represent an amalgamating concept incorporating unrelated elements and processes in petroleum geology, favouring the accumulation of hydrocarbons in the subsurface (Magoon and Beaumont, 1999). The term "*petroleum"* in petroleum systems describes any compound that includes high concentrations of any of the following substances (Magoon and Beaumont, 1999):

- thermal and biological hydrocarbons and gas found in conventional reservoirs as well as in gas hydrates, tight reservoirs, fractured shale and coal;
- condensates;
- crude oils; and
- natural bitumen in reservoirs, generally in siliciclastic and carbonate rocks.

The term "*systems*" in petroleum systems describes the interdependent elements and processes that form the functional unit that creates hydrocarbon accumulations (Magoon and Beaumont, 1999). The critical elements include: a petroleum source rock, reservoir rock, seal rock, and overburden rock and the processes of trap formation and the generation-migration-accumulation of petroleum (Magoon and Dow, 1994; Railsback, 2017) (Figure 2.3). These essential elements and processes must occur in time and space so that organic matter found in the source rock can be expelled from a source rock through a migration pathway to a reservoir enclosed by a seal in a trapping configuration where petroleum accumulates to form a petroleum deposit (Magoon and Dow, 1994; Magoon and Beaumont, 1999). The application of petroleum systems in exploration has led to a significant improvement in petroleum discovery (Al-Hajeri *et al.*, 2009). Thus, the petroleum systems approach also forms a process based workflow for petroleum exploration and is neither restricted to a particular geological setting nor limited to a particular petroleum commodity. No literature on the scale dependence of this approach could be found at the time of writing of this thesis.

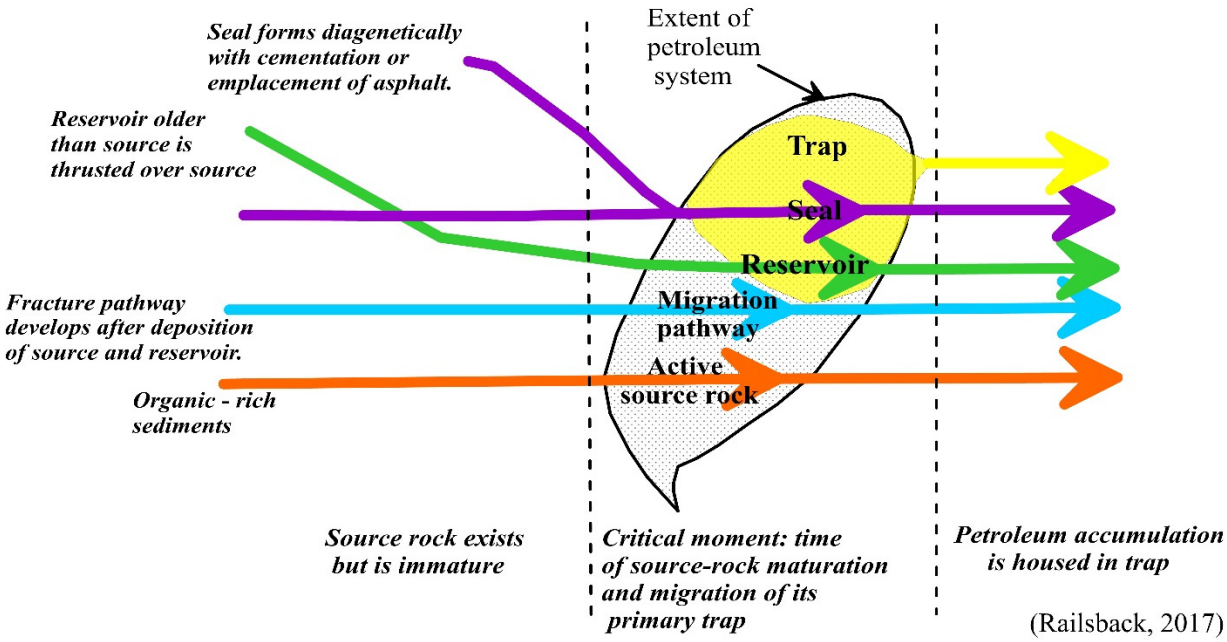

Figure 2.3 : Petroleum systems approach flow diagram

2.8.3 Source-Transport-Attenuation Approach

In groundwater vulnerability assessments, the approach which is most similar to the mineral systems and petroleum systems approaches is the Source-Transport-Attenuation (STA) system described by Gurdak and Qi (2012). However, when Gurdak and Qi (2012) applied the STA approach to nitrate pollution they were unable to establish a clear correlation with field measurements. Thus, Gurdak *et al.* (2015) modified the approach in order to improve the correlation. The shortfall of the modified STA approach in solving the regional assessment of AMD pollution is that it does not clearly define the sources of energy driving pollutant migration. Moreover, the approach is also affected by parameter dependency. Parameter dependency occurs when one or more parameters used in modelling occur more than once or their combined effect affects the resultant modelling output such that the output results resemble these parameters only, greatly masking out the effect of other parameters (Rahmati *et al.*, 2016). The approach being developed in this research redistributes the sources of energy and other parameters to obviate dependence amongst them.

2.9 SUMMARY

In the chapter, various approaches used for groundwater vulnerability assessment were described. Their strengths and shortcomings with respect to addressing groundwater vulnerability to AMD at a regional scale were identified. For the generation of a regional assessment methodology specific to AMD, a holistic approach would have to be considered by learning from the successful and globally

accepted regional assessment approaches in the field of mineral prospectivity mapping, oil-gas exploration and environmental regulatory.

The findings in this chapter need to be considered in the development of a groundwater vulnerability assessment approach which incorporates the nature of the AMD pollution, its production, transport and attenuation on the surface and in the subsurface. AI will be used to assist the generation of groundwater vulnerability models by incorporating the knowledge and learning patterns from the data.

CHAPTER 3: DEVELOPMENT OF GIS-BASED GROUNDWATER VULNERABILITY ASSESSMENT FOR ACID MINE DRAINAGE

3.1 INTRODUCTION

A literature review of the various groundwater vulnerability methods was presented in Chapter 2. Research gaps and the shortcomings which prevent the methods from fully addressing an assessment of groundwater vulnerability to AMD at a regional coalfield scale were identified.

In this chapter, an approach to assess groundwater vulnerability is developed and discussed. Input map layers used for the developed approach are formulated through a series of field and laboratory experiments coupled with a consideration of the availability of other relevant datasets. The developed approach for a groundwater vulnerability assessment at a regional coalfield scale is parallel and analogous to globally accepted regional assessment approaches in the field of mineral prospectivity mapping, oil-gas exploration and environmental regulations. Next, the approach will be discussed and the input layers formulated. The approach is termed SPT for reference purposes. The acronym is derived from elements which make up the assessment (S – Sources, P – Transportation pathways and T – Traps). Input map layers for the Witbank, Ermelo and Highveld coalfields will be generated.

Some parts of this chapter were extracted from Sakala *et al.* (2018), a publication written as part of this research.

3.2 OVERVIEW OF THE SPT APPROACH

An approach analogous to the mineral systems, petroleum systems and STA approaches was devised for the assessment of groundwater vulnerability to AMD at a coalfield scale following the shortfall of the current approaches to groundwater vulnerability assessments. Figure 3.1 shows the process-based connectivity of the various processes and parameters. According to this approach, the topographic gradient is regarded as the energy factor driving the pollution migration processes and rainfall as a source of ligands. Pollutant sources are regarded as analogous to metal sources, while the transport properties of soil, the vadose zone and the aquifer are correlated with the transport component and the subsurface (physical and chemical) trapping properties are correlated with the trapping component referred to in the mineral systems approach.

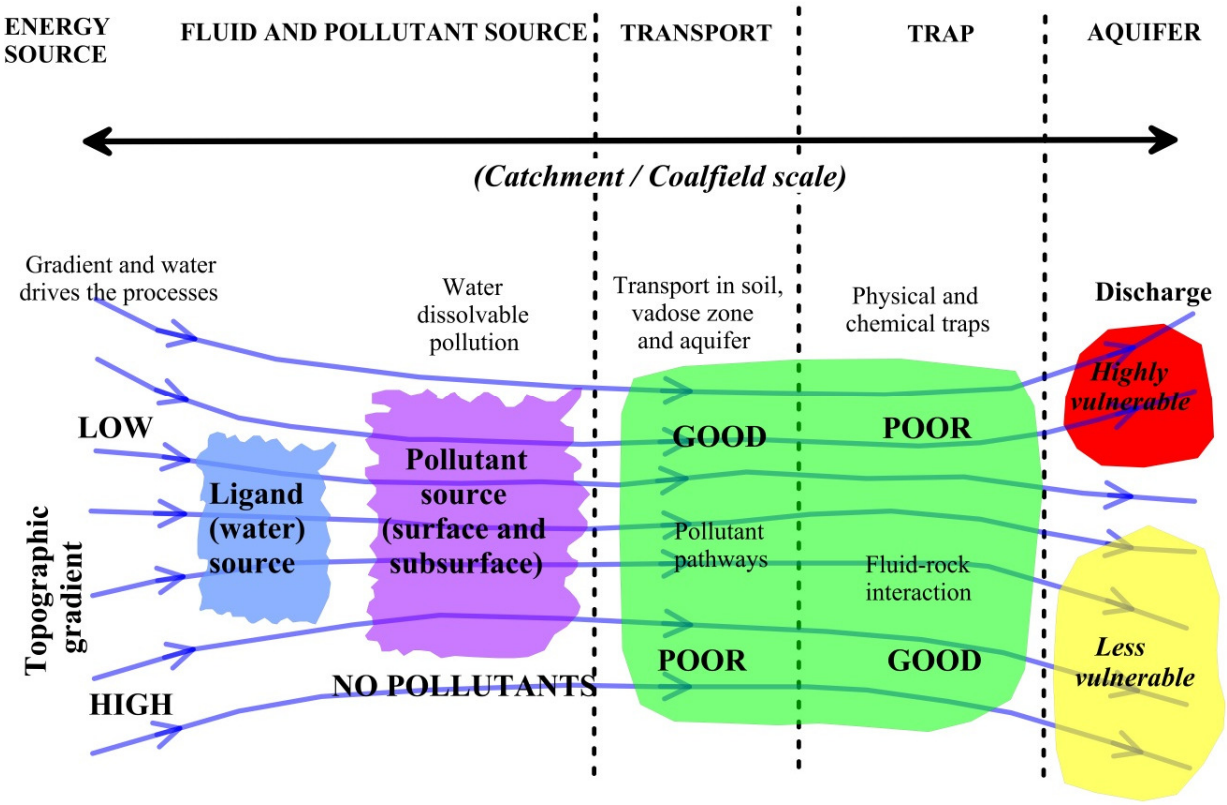

Figure 3.1: Developed groundwater vulnerability approach flow diagram

The energy flow through various components of the vulnerability approach is summarised as follows (Figure 3.1):

- The topographic gradient (slope), in particular gravity, acts as the source (S) of energy to drive the migration of water from the surface to the groundwater.
- Rainfall acts as a ligand source (S) of water which carries pollutants to the groundwater and is also an input to the formation of AMD formation.
- Presence and proximity of pollutant sources (S) to the groundwater also play a role in the vulnerability of the groundwater system to those particular pollutants.
- Soil properties, preferential pathways and aquifer media control the vertical and lateral movement and transportation pathways (P) of the pollutants or group of pollutants.
- Pollutants are trapped (T) in the subsurface by physical and chemical processes such as sorption, neutralisation, filtration, chemical reactions and dispersion.

In general, the groundwater vulnerability approach involves the mapping of three broad factors (sources, transportation pathway and traps) which are critical to the vulnerability of groundwater in respect of pollution. Figure 3.2 illustrates how the selected groundwater vulnerability assessment parameters can be related in space.

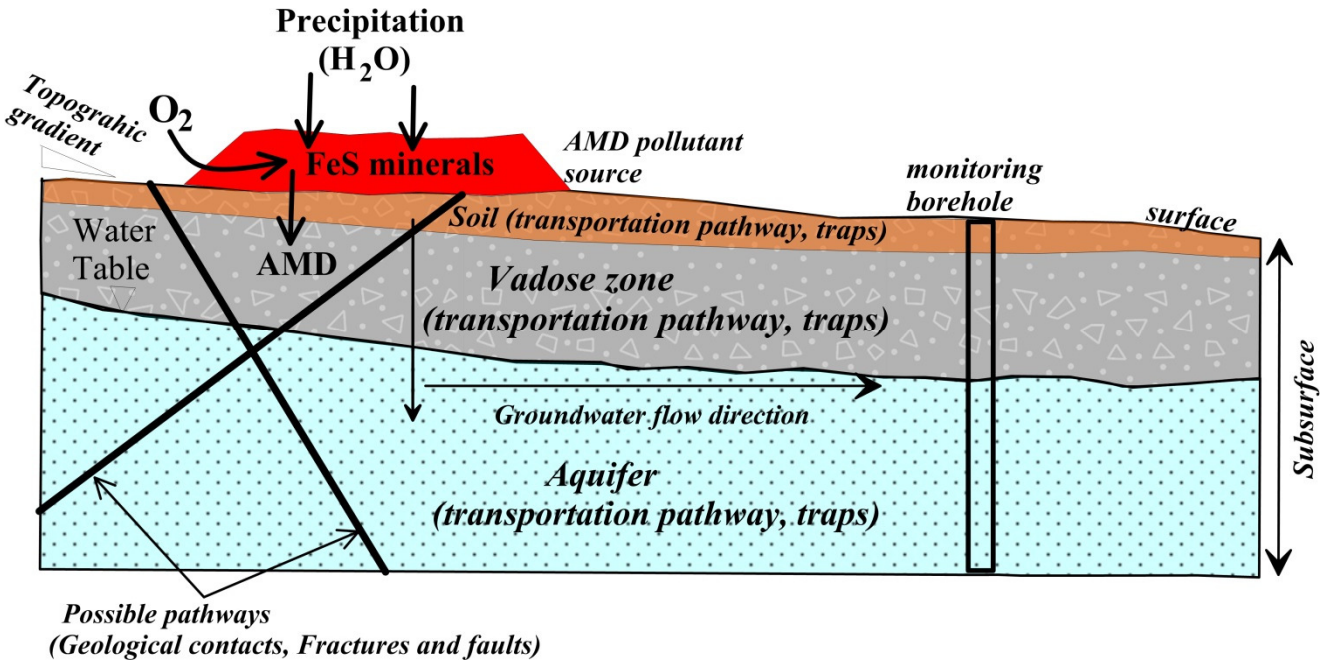

Figure 3.2: Schematic illustration of the parameters which make up the proposed groundwater vulnerability approach

The approach is also scale dependent, where all the parameters (energy sources, fluid and pollutant sources, transport and traps) are used at catchment/coalfield scale whereas, at a small scale such as a mining area, only transport and traps are considered. At a small scale, changes in parameters such as the ligands are considered to be insignificant, and are thus not used in the modelling of groundwater vulnerability.

3.3 THE SPT INPUT MAP LAYERS

This section describes the input parameters which make up the SPT approach and shows how they were formulated. The description is given according to the three broad components (sources, transportation pathway and traps).

3.3.1 Sources

The Oxford English Dictionary (Oxford, 2017) defines "source" as "a place, person, or thing from which something originates or can be obtained". In the SPT groundwater vulnerability approach, "sources" thus define the origins of AMD pollution: its formation and the surface morphology which controls its initial migration. The developed groundwater vulnerability approach includes three components which make up the sources factor whose proxies can be extracted from readily available datasets and literature.

These parameters are:

- sources of energy;
- sources of ligands (water); and
- sources of AMD pollution.

3.3.1.1 Sources of energy

In mineral systems, the hydrothermal fluid drives the movement of ligands and metals to a deposition location where a deposit is formed. In the mineral systems approach, the hydrothermal fluid drives the movement of ligands and metals to a deposition location where a deposit is formed. In the groundwater vulnerability approach, the energy driving the pollution migration process is determined by the topographic gradient. The topographic gradient plays an important role as it controls the likelihood that pollutants will run off or remain on the surface where they will ultimately infiltrate the subsurface (Aller *et al.*, 1987; Goderniaux *et al.*, 2013).

Several field and laboratory studies have been done in different parts of the world with the overall goal of determining the effect of topographic gradient, in particular soil slope angle, on the infiltration rate (Nassif and Wilson, 1975; Djorovic, 1980; Sharma *et al.*, 1983; Luk *et al.*, 1993; Fox *et al.*, 1997). All these studies have observed a decrease in infiltration rates with increasing slope angle regardless of soil type. Luk *et al.* (1993), however, observed that for storms of short duration, the infiltration rate increased with increasing slope angle, while for longer storms, the reverse occurred, with the infiltration rate decreasing with increasing slope angle. Results from laboratory experiments by Fox *et al.* (1997) show that the relationship between infiltration rate and slope angle is negative and non-linear where the infiltration rate decreased with increasing slope angle until 11.5° where the infiltration rate remained unchanged at steeper slope angles (Figure 3.3). Slope angles can be converted to the topographic slope, a proxy of the topographic gradient, using the relationship by Menashe (2004). Thus, a 11.5° slope angle translates to topographic slope of 20.1% as the cut off in topographic slope at which point there is no change in infiltration rate (Figure 3.4). With results from the same experiment, Fox *et al.* (1997) also plotted rainwater surface velocity against slope angle and established that, as the slope angle increases, so does the overland flow velocity (Figure 3.5). This phenomenon can be accounted for by the fact that the lower infiltration rates on steeper slopes observed in these experiments were attributable to shorter detention times since flow velocities are much greater on steeper slopes than on flat or gentle slopes.

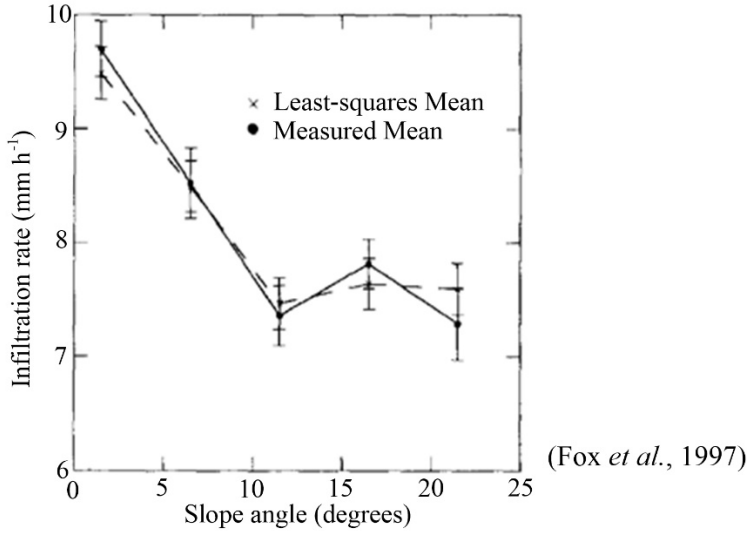

Figure 3.3: Decreasing mean measured and least-squares mean final infiltration rates with increasing slope angle (error bars are ± 1 standard error)

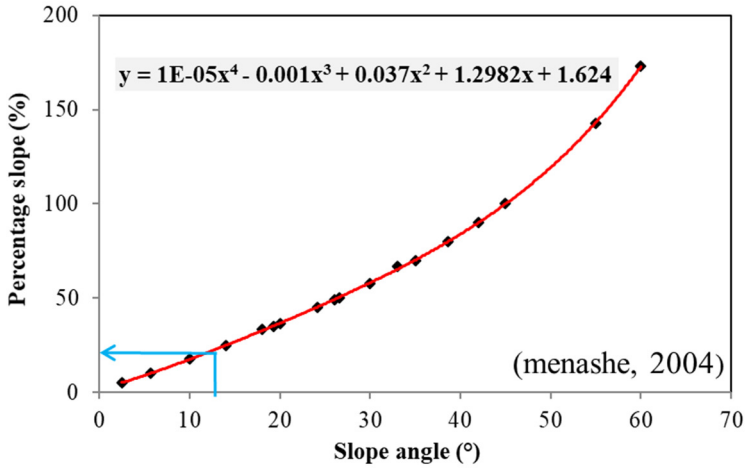

Figure 3.4: Relationship between percentage slope and slope angle

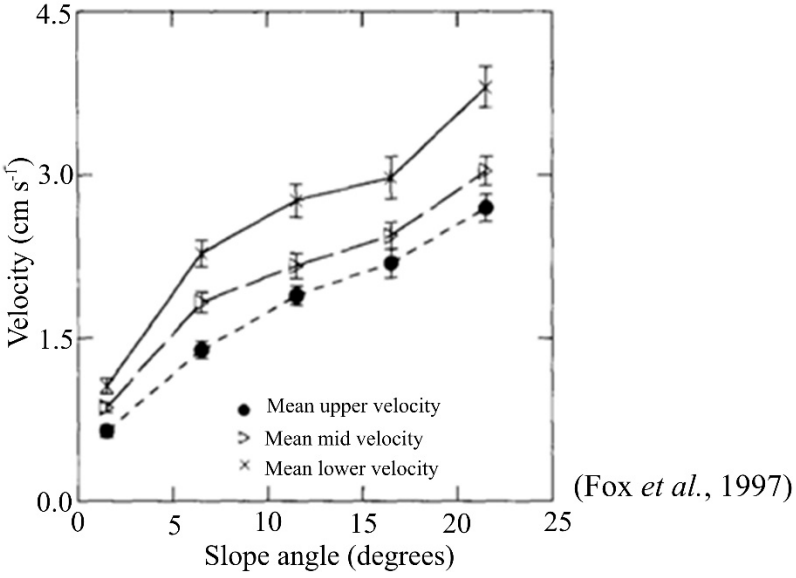

Figure 3.5: Overland flow velocity increases with slope angle (error bars are ± 1 standard error)

Topographic slope is the measure of steepness or the degree of inclination of a terrain feature relative to the horizontal plane and can be easily calculated from contour lines on a topographic elevation map. To find the topographic slope of a terrain feature, the horizontal distance (run) and the vertical distance (rise) between two points on a line parallel to the terrain feature are determined (Figure 3.6). The topographic slope can be obtained using Equation 3.1:

$$Topographic\ slope\ (\%) = \frac{Rise}{Run} * 100 \qquad 3.1$$

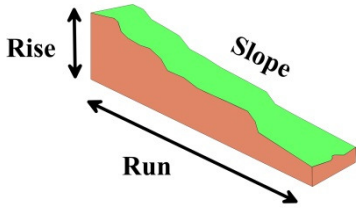

Figure 3.6: Schematic illustration of the parameters used to calculate topographic slope

Thus, the smaller the slope values, the flatter the surface and, conversely, the higher the slope values, the steeper the terrain. Flat-lying and gentle slope areas are more likely to allow infiltration than runoff, making such areas favourable for the infiltration of water and dissolved pollutants.

Shuttle Radar Topography Mission (SRTM) elevation data with 30 m resolution (USGS, 2016) which is freely available to download can be used to calculate the topographic slope in percentage. SRTM was an international project spearheaded by the National Geospatial-Intelligence Agency (NGIA), National Aeronautics and Space Administration (NASA), the Italian Space Agency (ASI) and the German Aerospace Centre (DLR). The project was carried out during an eleven-day mission in February 2000 using a specially modified radar system that was flown on-board the space shuttle Endeavour. The main objective of the mission was to obtain elevation data on a near-global scale and to make the information publically available.

3.3.1.2 Sources of ligands (water)

The rate of pyrite oxidation in the mining waste, tailings or subsurface is mainly controlled by the availability of oxygen and water at the mineral grain surface (Anawar, 2013). Mining operations expose the pyritic material to the atmosphere, making them prone to water and oxygen. Rainfall is often a major factor which supplies water for AMD reactions and which acts as a ligand for the transportation of products of the AMD reactions as surface runoff or as infiltration. According to Chemicool (2017), a ligand is "an ion or molecule that binds to a central metal atom to form a complex (alternatively known as a coordination entity)". In the groundwater vulnerability assessment rainfall data can be an event, monthly, annual or average long term and can easily be obtained from a local

weather company. Data may take the form of gridded data or rainfall values at several stations where the kriging method can be used to interpolate data between stations with gridded rainfall produced.

3.3.1.3 Mappable sources of AMD pollution

Sources of AMD pollution range from settling ponds, tailings-cast dumps, opencast pits, waste rock dumps, washing plants and loading bays. These sources of AMD pollution can be mapped manually by taking global position system (GPS) coordinates of possible sources and taking samples for analysis for acid generation potential testing. Another approach for mapping possible AMD sources is the use of freely available orbital remote sensing data where the spectral uniqueness of AMD generated secondary iron bearing minerals is used to build a decision tree for differentiating these from other minerals.

3.3.1.4 Subsurface sources of pollution

Subsurface sources of AMD pollution refer to those rock formations under the surface which are capable of generating AMD under natural conditions or when exposed to oxygen and water by coal mining activities. These include opencast mining, underground workings and coal seams in the unsaturated zone, where oxygen and water may be in contact with pyrite rich coal seams and AMD can be formed. Information on subsurface sources can be extracted from geology maps where rock formations known to contain pyrite are outlined and used as a proxy of the subsurface sources.

3.3.2 Transportation Pathway

In the mineral systems approach, hydrothermal fluids transport ligands and metals through discontinuous structures (faults, bedding planes, joints, etc.) within the earth's subsurface and/or at the surface. The ligands and metals are concentrated at some preservation location to form mineral deposits. In the petroleum system approach, petroleum migrates from organic-rich sediments (source rocks) to a reservoir by migrating along fracture pathways. Therefore, the transport mechanism is vital to the formation of mineral and petroleum deposits. Similarly, the developed groundwater vulnerability approach also incorporates studies of AMD transport in the soil, the vadose zone and the aquifer system.

3.3.2.1 Transportation pathway in soils

Soils are an independent, dynamic body and occupy the outermost part of the earth's crust. Soils possess distinct morphological, mineralogical, chemical and physical properties inherited because of their unique location in space and time and other environmental factors that exist at that location (Bear, 1964). Thus, soils are a natural phenomenon controlling the initial transport and attenuation of

pollution into the subsurface. Aquifers under soils with physical, chemical and biological properties that promote or increase the sorption of pollutants are considered less vulnerable to pollution than aquifers without these properties (Mongwe and Fey, 2004). According to Mongwe and Fey (2004), an understanding of the various sorption and adsorption mechanisms involved in pollution retention is crucial in assessing groundwater vulnerability, as these mechanisms determine the initial rate and transport of most pollutants. Soil structure largely governs the size of the soil pores through which the pollutants pass. Thus, soils with a high clay content have small pore spaces that reduce infiltration and permeability rates (Huddleston, 1994; Mongwe and Fey, 2004) and which, in turn, increase the residence time for the chemical removal of pollution by processes such as sorption and adsorption. These chemical processes will be dealt with under the attenuation section.

3.3.2.2 Transport in the vadose zone

This factor involves those parameters of the vadose zone which are involved in the transport of pollution and can be incorporated at a regional scale. In this regard, the parameters chosen include the pathways and rock permeability.

3.3.2.2.1 Preferential pathways

Possible preferential pathways for AMD and water in the vadose zone may include: contacts of dykes and sills with other rocks, faults, fractures and joints (Woodford and Chevallier, 2002). These geological features are possible indicators of zones of weakness within the subsurface which may act as preferential conduits for the migration of pollutants from the surface to the groundwater. Such information can be obtained from published geology and geophysical maps covering the area of interest.

3.3.2.2.2 Rock permeability

Rock permeability affecting the transport of water and pollutants is measurable. Alternatively, the information can be extracted from the geological literature. Rock permeability values of rocks can be determined by laboratory tests or fieldwork but this would be very costly. Another option is to produce a relative comparison map of rock permeability using published values since groundwater vulnerability assessment results present relative comparisons between various areas in terms of the likelihood of groundwater pollution.

3.3.2.3 Transport in the aquifer system

Aquifer hydraulic conductivity defines the ability of the aquifer material to transmit water (Heath, 1983; Aller *et al.*, 1987). This also controls the movement of dissolved pollutants.

3.3.3 AMD Pollution Traps

In the mineral systems approach, metalliferous fluids migrate until they reach zones where physical, chemical and/or biological processes modify the metalliferous fluid composition, leading to the deposition of the metals and the formation of a deposit (Wyborn *et al.*, 1994). Within a groundwater vulnerability assessment, subsurface properties seen to inhibit or delay the movement of pollutants are regarded as the trapping mechanisms. That is, aquifers overlain by subsurface conditions lacking properties that inhibit or delay the movement of pollutants will be vulnerable to pollution. The vadose trapping mechanisms considered in this study include physical (soil clay content, depth to water table) and chemical (soil clay content, rock-AMD reactivity) traps.

When AMD is released on the ground surface, the natural attenuation processes of the earth will attempt to minimise the effect. The processes of the natural attenuation in soils, the vadose and the aquifer play a major role in the attenuation of AMD and are therefore included in the SPT approach.

3.3.3.1 Chemical traps of acid mine drainage in soils

The processes promoting pollution attenuation in the subsurface are not quite as obvious and depend on many factors, including soil, rock types and the nature of pollution involved. The soils form the first part of the unsaturated zone where processes such as sorption, ion exchange, filtration and precipitation are some of the processes which contribute to the natural attenuation of major pollution. Of these many processes, the ion exchange and precipitation processes will be considered, as they are dependent on the nature of the pollutant well as the nature of the unsaturated zone medium. A single value describing the potential for the medium to attract cations, the cation exchange capacity (CEC), is the most useful parameter in assigning the soil attenuation potential. Thus, CEC can be used as a meaningful surrogate for the overall attenuation processes that are likely to occur in the vadose zone. Soil CEC is the total of the exchangeable cations that a soil can hold at a specified pH and is known to be contributed by clay and organic matter content (Martel *et al.*, 1978; Manrique *et al.*, 1991). However, CEC values are not commonly available for the vadose zone or for the soil zone. It is useful, therefore, to use the clay mineral content of the vadose zone as a proxy for CEC (Robins, 1998; Griffiths *et al.*, 2008). A second part of the attenuation process is controlled by the availability of carbon as a catalyst for adsorption and precipitation in the soil medium. Thus, the two key indicators used to derive the attenuation potential of the soil and unsaturated zone of the aquifer are clay minerals and organic contents. Published soil maps containing this information may be obtained from custodial institutes where the soil database of a state or country is held.

3.3.3.2 Pollution traps in the vadose zone and aquifer media

3.3.3.2.1 Depth to water table

Depth to water table refers to the distance between the ground level and the water table, including pore spaces which are partially filled with air and water (Aller *et al.*, 1987; Snyder, 2008). This parameter determines the depth of material through which a pollutant or group of pollutants must travel before reaching the groundwater system. This distance is important in that it defines the amount of time available for various natural attenuation processes which can degrade the pollution. In a groundwater vulnerability assessment, depth to water table data can easily be obtained from a custodial institute where the groundwater database of a state or country is held. Data can be in the form of a gridded contour map or boreholes with water level values where the kriging method may be used to interpolate between the boreholes and a gridded depth to water table map produced and used for the assessment of groundwater vulnerability.

3.3.3.2.2 Rock-AMD reactivity

In order to understand how AMD interacts chemically with various rocks found in a typical coalfield, laboratory experiments must be conducted. The overall goal of the experiments is to study how AMD interacts with various rocks under typical saturated and unsaturated conditions in the subsurface. Using an understanding of the interactions between various rocks and AMD, rocks are then ranked according to their abilities to extract AMD pollutants and neutralise capacity. The results from the ranking of various rocks in terms of their ability to extract AMD pollutants will be used as one of the inputs to the SPT approach.

3.3.4 SPT Groundwater Vulnerability Modelling

The SPT approach is a hybrid groundwater vulnerability approach which combines the index and overlay, process-based simulation and statistical approaches. Parameters which were extracted from popular approaches such as DRASTIC include: depth to water table, aquifer hydraulic conductivity, rainfall which replaced recharge, soils and topographic slope. Other parameters which were incorporated in the assessment include those which are specific to AMD pollution such as surface and subsurface sources of pollution, rock-AMD reactivity, pathways and rock permeability. The input map layers can be joined together by an appropriate statistical method: multivariate methods (logistical regression, principal component analysis, weight of evidence) or AI.

3.4 GENERATION OF SPT INPUT MAP LAYERS FOR THE WITBANK, ERMELO AND HIGHVELD COALFIELDS

The SPT approach involves mapping those properties of the earth's surface and subsurface which can play a role in transport, and trapping of AMD if released onto the surface. To illustrate how the inputs for the SPT approach are devised, the Witbank, Ermelo and Highveld coalfields were used as unit of study. The massive deterioration of groundwater quality by AMD in these coalfields is a growing concern for local authorities; hence such an approach would help in the understanding of AMD at a regional coalfield scale.

3.4.1 Location of the Witbank, Ermelo and Highveld Coalfields

The Witbank, Highveld and Ermelo coalfields are located between latitude 25°30" to 27°45" South and longitude 28°30" and 30°30" East, covering a total area of approximately 27 500 km^2 (Figure 3.7).

3.4.1.1 Location of the Witbank coalfield

The Witbank coalfield is situated in the northern part of the main Karoo basin, extending from roughly 25°30′S to 26°30′S by 28°30′E to 30°00′E, and covering an area of over 568 000 ha. The coalfield extends from the town of Springs in the west to Belfast in the east, and from the town of Middelburg in the north of the Smithfield ridge (Figure 3.7). The northern boundary of the coalfield is formed by pre-Karoo basement rocks, whilst the southern boundary in the central portion of the basin is widely considered to be a sub-outcrop against a basement paleo-high known as the Smithfield ridge, a broadly east–west trending, crescent shaped ridge of pre-Karoo felsite, granite and diabase of the Bushveld Igneous Complex. The Highveld coalfield is located to the west and the Ermelo coalfield to the east on the southern side of the Smithfield ridge. The western and eastern edges of the coalfields are arbitrarily defined by the sub-outcrop of the coal-bearing sedimentary succession against the pre-Karoo basement.

For over a century, this coalfield has been the most important in South Africa, supplying more than 50% of South Africa's saleable coal. The area produces both metallurgical coal and thermal coal for the export and local markets, and hosts many of the major coal-fired power stations in South Africa including Kendal, Duvha, Komati and Arnot. The coalfield is named after the city formerly known as Witbank, which was renamed to eMalahleni in 2006 (Hancox and Götz, 2014).

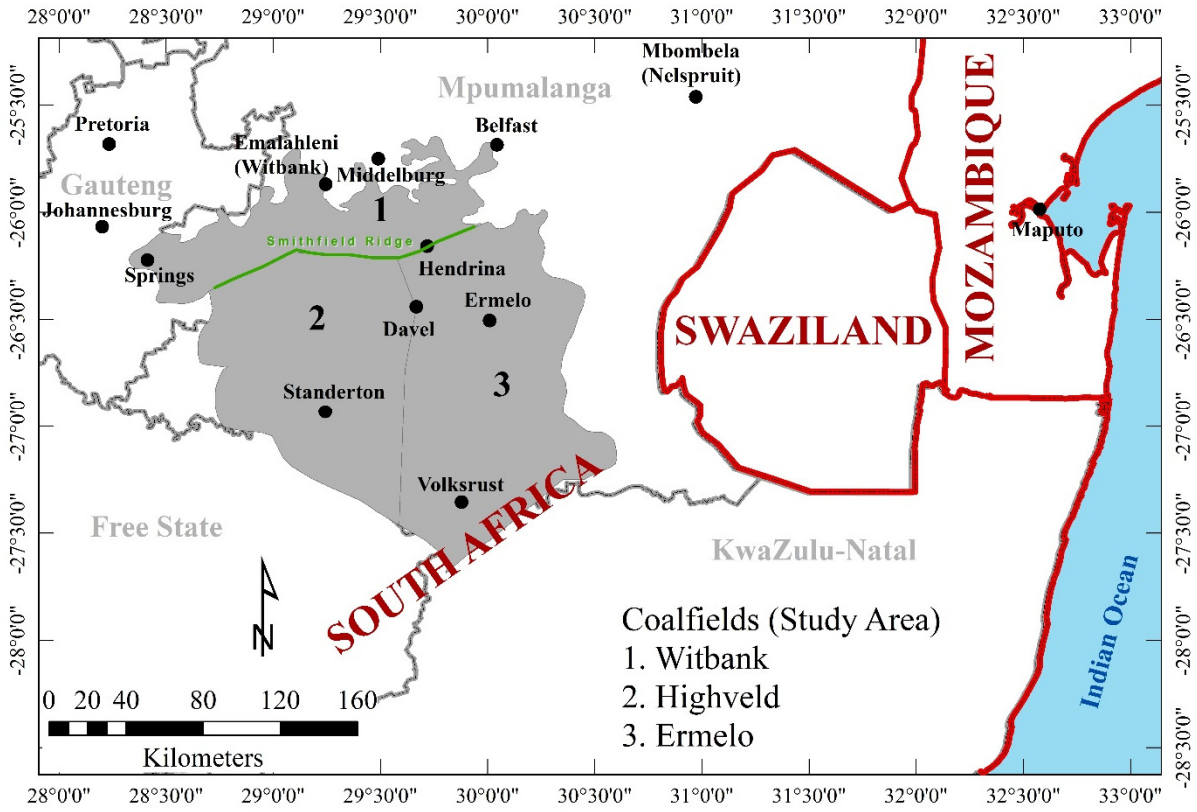

Figure 3.7: Location of the study area in relation to provincial and international boundaries

3.4.1.2 Location of the Highveld coalfield

The Highveld coalfield is situated in southeastern Gauteng and Mpumalanga Provinces and covers an area of approximately 700 000 ha. The coalfield is separated from the Ermelo coalfield by an arbitrarily line extending from Hendrina in the northeast, through Davel to the Klip River coalfield in the south. The coalfield is bound to the north by Smithfield ridge which separates it from the Witbank coalfield. On the western side, the coalfield is bordered by outcrops of granite and rocks of the Witwatersrand Supergroup. The southern boundary is located south of Standerton along the Klip River to its confluence with the Vaal River, and from there along the Vaal River. Economically, the coal resources within the Highveld coalfield are important to the long-term life of Sasol's Synthetic Fuels and Sasol Chemical Industries, which require some 50 million tonnes a year (Hancox and Götz, 2014).

3.4.1.3 Location of the Ermelo coalfield

The Ermelo coalfield is a fair producer of coal, but over the past two decades production has declined because of the thinner coal seams (Snyman, 1998; Jeffrey, 2005). However, since 2004, this coalfield has seen an increase in exploration and mining activities owing to the higher quality of its coal as compared to the Witbank and Highveld coalfields, and its proximity to the Richards Bay Coal Terminal from where coal is exported overseas. The Ermelo coalfield is located in the districts of

Carolina, Dirkiesdorp, Hendrina, Breyten, Davel, Ermelo and Morgenzon in the southeastern part of Mpumalanga Province. The coalfield extends approximately 75 km east–west, and 150 km north–south, covering an area of about 1 125 000 ha (Hancox and Götz, 2014). The northern and eastern boundaries of the Ermelo coalfield are defined by the sub-outcrop of the coal-bearing strata against the pre-Karoo basement. In the west, the Ermelo coalfield shares a boundary with the Witbank and Highveld coalfields and, to the south, with the Klip River and Utrecht coalfields of KwaZulu-Natal (Greenshields, 1986).

3.4.2 Physiography

The area receives average long-term rainfall of between 600 to 1 100 mm (ARC-ISCW, 2014). The winters are typically dry and cold with occasional frost, while the summers, between October and March, are hot (Barnard, 2000). The altitude ranges from 1 225 m to 2 237 m metres above sea level (m.a.s.l) with the Olifants River and its tributaries being the main drainage system.

With reference to climatic data collected between 1982 and 2012 recorded at the eMalahleni, Ermelo, Sanderton and Volkrust stations, the study area receives monthly rainfall of between 2 mm in June and 150 mm in December (Climate-data.org, 2017). The monthly distribution of average daily maximum temperatures shows that the average midday temperatures for the study area range from 2 °C in July to 26 °C in January with July as the coldest month (SAWS, 2016).

According to the Köppen climate classification, the study area falls in the Cwb class. Areas in the Cwb class are characterised by a subtropical highland climate with dry winters. Temperatures in the coldest month average above 0 °C, and all months have average temperatures below 22 °C. In at least four months, temperatures average above 10 °C, with at least ten times more rain in the wettest month of summer than in the driest month of winter (Geiger, 1954). Figure 3.8 shows the typical temperature and rainfall distribution throughout the year.

Understanding the climatic conditions of the study area is particularly important in view of the fact that AMD generation is controlled by the climate and one of the key reactants (water) directly depends on climatic conditions. In general, South Africa has a very pronounced east–west climatic gradient with rainfall decreasing from over 1 000 mm/a in the east to less than 100 mm/a in the west. Potential evapotranspiration increases from about 1 500 mm/a in the east to 3 000 mm/a in the west, causing most of the country (including the study area) to experience a negative water balance (i.e. evapotranspiration <rainfall) (McCarthy, 2011). When rain falls on exposed pyrite/sulphide minerals in a strongly evaporative environment, it is less likely that the acidity or toxicity of produced products will be diluted. Thus, any rainfall event affecting exposed pyrite/sulphide minerals would contribute significantly to AMD reactions and the concomitant transport of the products.

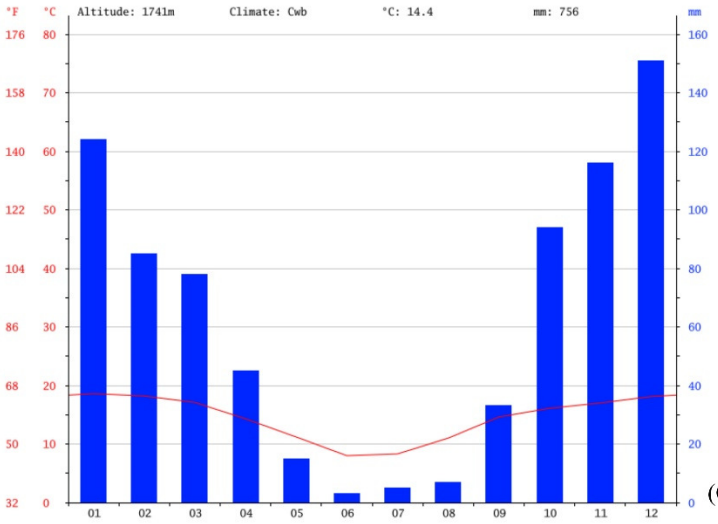

(Climate-data.org, 2017)

Figure 3.8: Climatic data for the Ermelo station showing temperature and rainfall distribution throughout the year

3.4.3 Geological and Hydrogeological Setting

An understanding of the geological and hydrogeological setting is particularly important as the natural attenuation properties of the subsurface are derived from this information.

3.4.3.1 Regional geology

The Witbank, Ermelo and Highveld coalfield are found in rocks of the main Karoo basin (MKB). This basin outcrops over more than half of South Africa (Figure 3.9) and forms part of a major series of Gondwana basins that developed through subduction, compression, collision, and terrane accretion along the southern margin of Gondwana. This series includes the Paraná basin in South America, the Beacon basin in Antarctica and the Bowen basin in Australia (Hancox and Götz, 2014). The sedimentary filling of these basins is particularly important from a geological and palaeontological perspective in that they contain an almost unbroken record of 120 million years the history of the earth, at a period when the Pangaean supercontinent had reached its maximum extent, and during which major evolutionary changes were taking place (Hancox and Götz, 2014). The economic significance in terms of energy resources of these sedimentation events is that they brought about important energy resources (coal, coal bed methane, shale gas and uranium) which are vital to the economic development of the country.

The sedimentary part of the main Karoo basin Supergroup is subdivided into four main lithostratigraphic units: the Dwyka, Ecca, Beaufort and Stormberg Groups (Molteno, Elliot and Clarens Formations) (SACS, 1980; Johnson *et al.*, 1996). The lithostratigraphic units which host coal

deposits in South Africa include the Ecca Group (Vryheid Formation), Beaufort Group (Emakwezeni Formation) and the Molteno Formation.

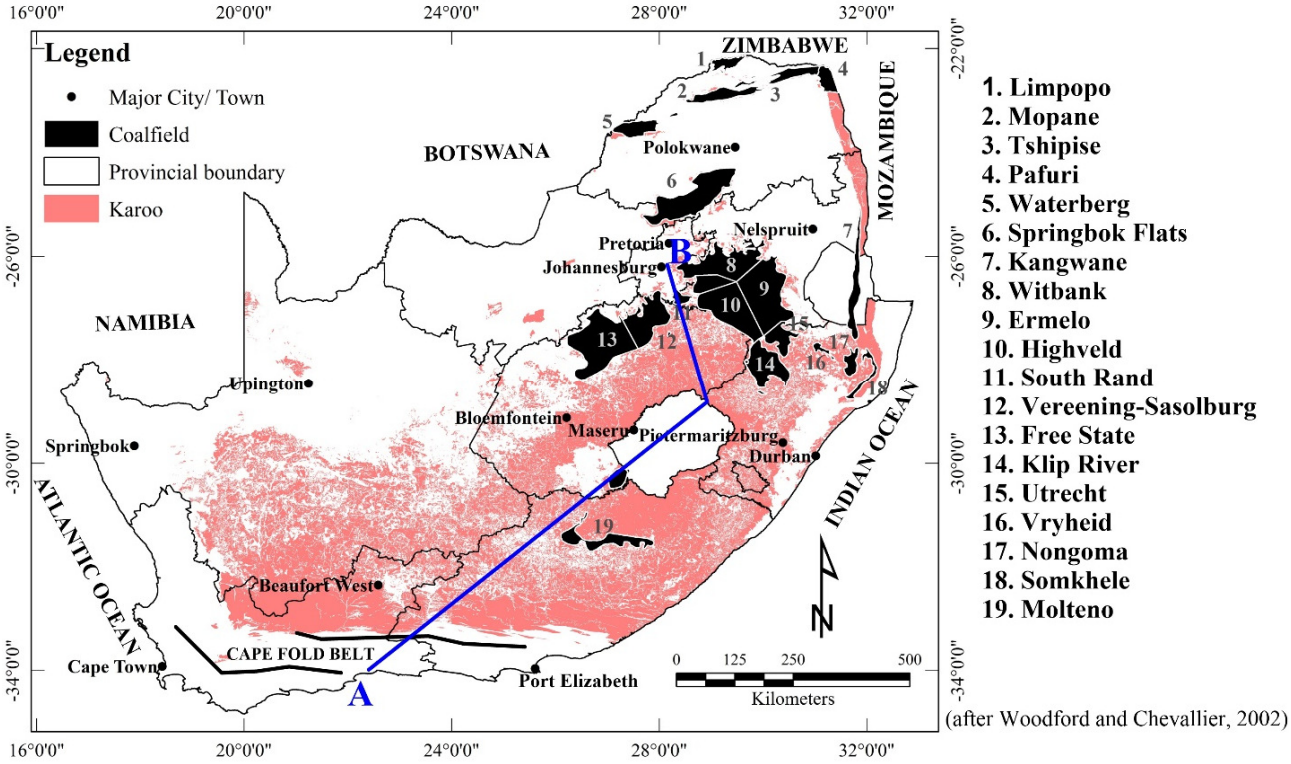

Figure 3.9: Extent of the Karoo basin in South Africa, with coalfields. The blue line indicates the location of the cross-section AB shown in Figure 3.10

During the Permian–Carboniferous, a period of glacial sedimentation marked the start of various sedimentation events which gave rise to the Karoo Supergroup (Lindeque *et al.*, 2011). In the glacial sedimentation period, the diamictites and associated fluvio-glacial sediments (Dwyka Group) were deposited. A shallow sea remained after the glaciation event which led to the deposition of the black clays and muds which form the lower Ecca Group. The prevailing cold climatic conditions and submerged environments favoured this deposition event and deltas progressed towards the sea which later combined to form broad alluvial plains that make up the upper Ecca Group. As the glacial ice sheet retreated northwards, the glacial valleys were filled by fluvioglacial sediments such that shallow postglacial lakes were formed, which were transformed into swamps resulting in the formation of the lower coal seams directly overlying the sediments of the Dwyka Group in the Witbank, Highveld, Free State and Vereeniging–Sasolburg coalfields. After the deposition of the Ecca Group, the prevailing semi-arid environment possibly led to the deposition of the Beaufort Group in the alluvial plains of the basin. This occurred towards the end of the Triassic.

Economic deposits of coal are restricted to the northeastern section of the basin in the Ecca Group. The lower coal seams found in the Ecca Group reflect the pre-Karoo valleys and mountains and the upper coal seams mark the basinward extent of the delta as it progresses towards the basin margin.

The main Karoo basin is largely underlain by a stable floor, comprising the Kaapvaal Craton in the north and the Namaqua-Natal Metamorphic Belt in the south, and is bounded along its southern margin by a fold-thrust belt known as the Cape Fold Belt. The basin is thick in the south and thins towards the north as shown on the regional S–N geological cross-section (Figure 3.10).

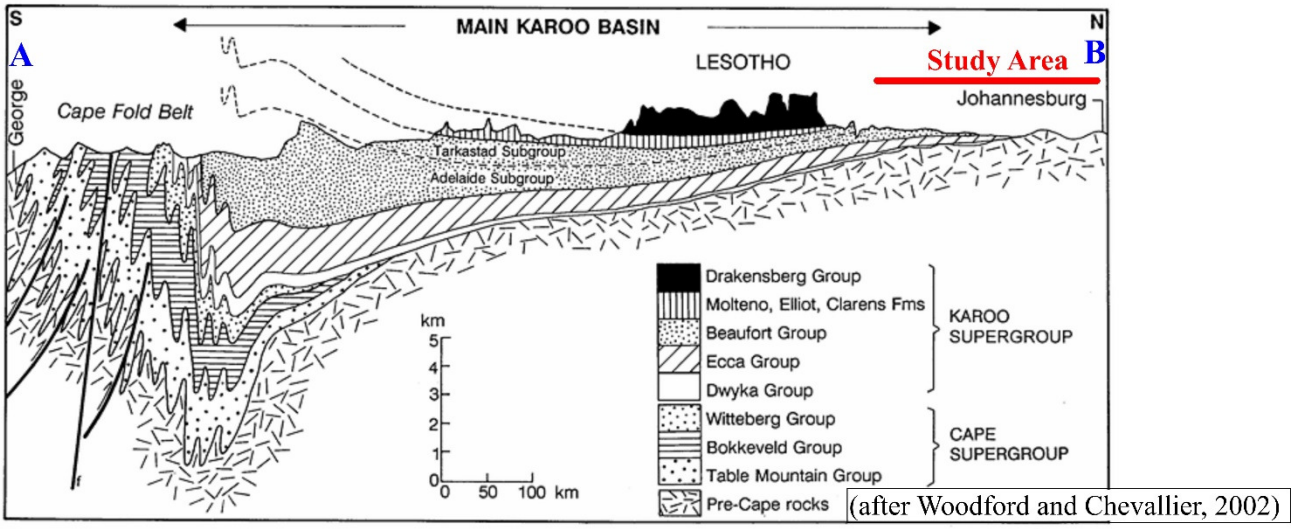

Figure 3.10: Schematic north–south section across the main Karoo basin

There are nineteen coalfields in South Africa (Figure 3.9), with current mining activities largely taking place in the Witbank, Ermelo and Highveld coalfields of Mpumalanga Province (Banks *et al.*, 2011).

3.4.3.2 Local geological setting

The local geological information used in this study was drawn from 1:250 000-scale geological maps (Pretoria 2528 and East Rand 2628) published by the Council for Geoscience (Figure 3.11). The study area comprises eight major lithological domains, namely:

- Basement Complex;
- Witwatersrand Supergroup;
- Transvaal Supergroup;
- Bushveld Complex;
- Dwarsfontein Complex;
- Waterberg Group;
- Karoo Supergroup; and
- Tertiary–Quaternary alluvial deposits.

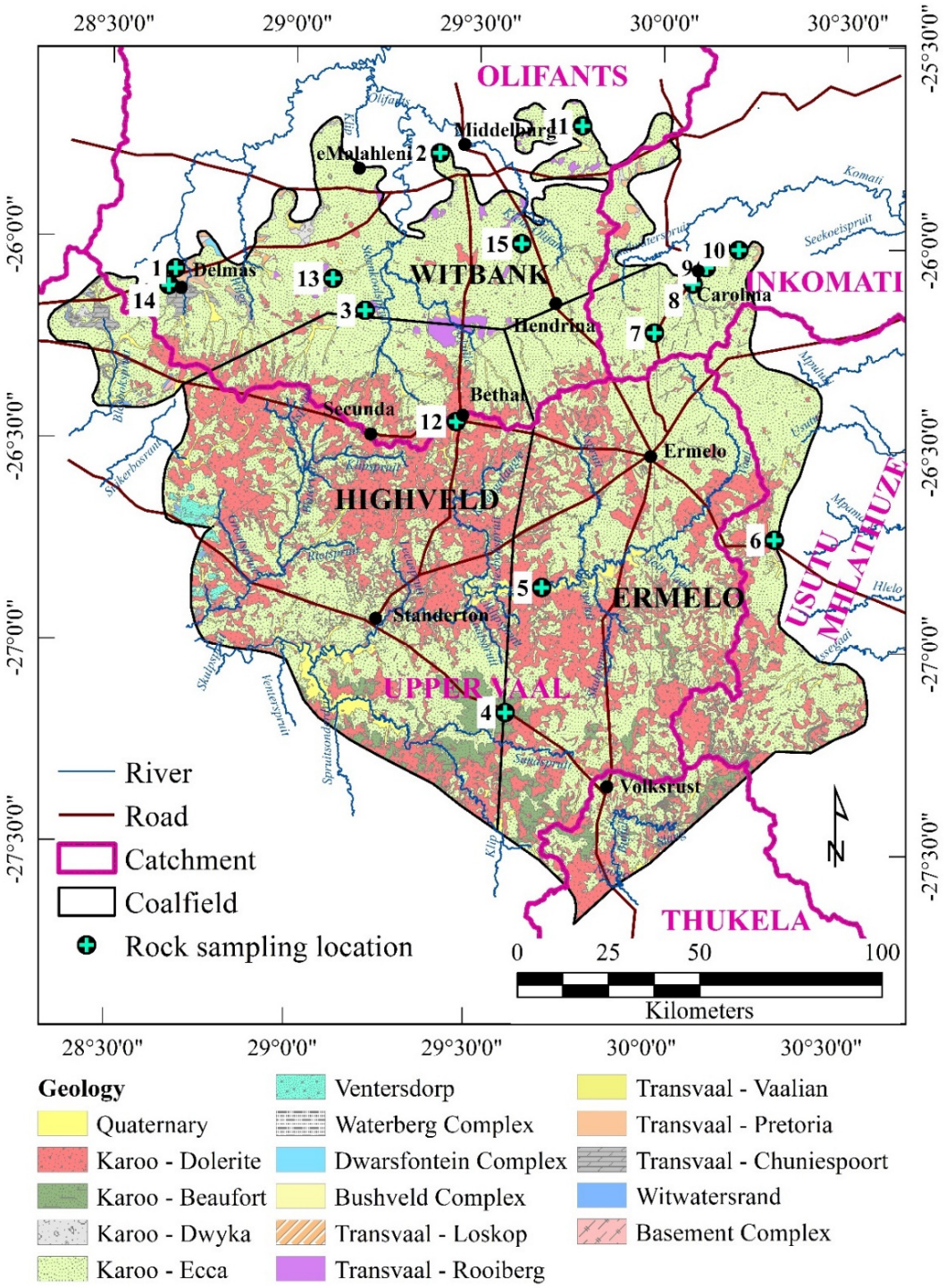

Figure 3.11: Local geology of the study area mapped at a 1:250 000 scale showing borehole locations

3.4.3.2.1 The Basement Complex

In the study area, the oldest rocks are leucocratic biotite granite of the Swazian Era with a small exposure in the south-eastern part of the study area. Figure 3.12 shows the rock exposure of the granite displaying signs of exfoliation.

Figure 3.12: Rock exposure of the granites found in the study area

3.4.3.2.2 The Witwatersrand Supergroup

The Hospital Hill Formation is the only member of the Witwatersrand Supergroup found in the study area, with its outcrops being exposed near Delmas. The outcrops consist primarily of shallow-marine orthoquartzites, siltstone, outer-shelf shales and iron formation (McCarthy, 2006).

3.4.3.2.3 The Transvaal Supergroup

The sedimentary and volcanic rocks of the Transvaal Supergroup are found in the northern part of the study area and lie north of the Karoo Supergroup outcrops. According to SACS (1980), the rocks of the Transvaal Supergroup represent a tectono-sedimentary phase of clastic, volcanic and chemical sedimentation within a large sedimentary basin resting unconformably on Swazian basement rock. The Transvaal Supergroup in the study area is represented by the Chuniespoort, Pretoria and Rooiberg Groups and the Loskop Formation. The Malmani Subgroup of the Chuniespoort Group comprises chert and dolomite with only minor clastic sediments (Button, 1973). In the study area, dolomites of the Malmani Subgroup are found around Delmas and exposed rocks are greyish in colour with an elephant skin-like texture (Figure 3.13). The Pretoria Group is the uppermost group of the Transvaal Supergroup and is unconformably overlain by the Rooiberg Group. The Pretoria Group mainly comprises mudrock alternating with quartzitic sandstone, subordinate conglomerate, diamictite, interbedded basaltic-andesite lavas and carbonate rocks (Eriksson *et al.*, 2006).

Figure 3.13: Malmani Subgroup dolomite rock exposed in the study area displaying an elephant skin texture

Exposed mudrocks of the Pretoria Group within the study area clearly show bedding planes and fractures (Figure 3.14). The Rooiberg Group consists of rhyolite and felsite forming the roof of the intrusive Bushveld Complex and represents the first igneous activity associated with the complex (Buchanan and Reimold, 1998). In the northern extremity of the study area, the Rooiberg Group grades conformably into the Loskop Formation, with the latter consisting of 1 100 m of red shale intercalated with conglomerate in the lower part and mainly impure quartzite in the upper part (Clubley-Armstrong, 1977; Martini, 1999).

Figure 3.14: Pretoria Group mudrock outcrop showing heavy fracturing and bedding planes

3.4.3.2.4 Bushveld Igneous Complex

The Bushveld Igneous Complex occurs in the northeastern part of the study area. The complex is mainly represented in the mapped area by the Rustenburg Suite, a succession of mafic and ultramafic layered rocks including gabbros, norites, diorites, anorthosites and gabbronorites (Barnard, 2000). The Lebowa Suite, representing a younger felsic phase occurs as a single granite pluton is named the Nebo granite and is found in the north-eastern part of the study area.

3.4.3.2.5 Waterberg Group

The Waterberg Group is a sedimentary suite of rocks consisting of medium- to coarse-grained sandstone with interbedded conglomerate and shale (Barnard, 2000). In the study area, the Waterberg Group is represented by the Wilge River Formation.

3.4.3.2.6 Karoo Supergroup

The Karoo Supergroup was deposited in a vast intracratonic basin reaching its maximum depth in the south and in a few satellite basins to the north (Du Toit and Sonnekus, 2014). The Karoo Supergroup consists of a variety of sediments that reflect the environmental changes during the migration of the Gondwana continent over a period of 200 million years from polar to lower latitudes (Du Toit and Sonnekus, 2014). These sediments, covering over 80% of the study area, represent the northern tip of the main Karoo basin in South Africa (Figure 3.10). Three main groups are found in this part of the Karoo basin. These are the Ecca and Dwyka Groups and the dolerite intrusive rocks. The Dwyka Group sediments consist mainly of diamictite (tillite) which are generally massive with little jointing, but may be stratified in some places (Woodford and Chevallier, 2002). The Ecca Group (Vryheid Formation) consists of undifferentiated grit, sandstone (Figure 3.15), shale and coal seams with interlayered siltstone and mudstone comprising up to five mineable coal seams (Hancox and Götz, 2014).

Figure 3.15: Weathered sandstone outcrop in the Witbank coalfield

Several dolerite intrusions are found within the study area. The intrusions represent the roots of a volcanic system. The Karoo dolerite system consists of an interconnected network of dykes and sills and it is therefore nearly impossible to single out any particular intrusive or tectonic system. It is likely that a very large number of features were intruded simultaneously by magma and that the dolerite intrusive network acted as a shallow stockwork-like reservoir. The emplacement of dykes in

the study area appear to be lithologically controlled, as seen by a sharp decrease in intrusion density at the boundary between the Ecca and Beaufort Groups. The bulk of the dykes are stratabound and concentrated in the Beaufort Group in the southern part of the study area. In general, dolerite dykes develop by rapid hydraulic fracturing via the propagation of a fluid-filled open fissure, resulting in a transgressive contact with the country rock. They develop vertically upwards or laterally along strike over very long distances.

3.4.3.2.7 Quaternary deposits

According to Woodford and Chevallier (2002), Quaternary deposits are a common characteristic along the major rivers in the Karoo basin. Deposits on the beds of braided streams consist mainly of coarse sediments, conglomerates and patches of finer material on their banks while meandering streams deposit mainly fine-grained sand, mudstone and siltstone (Gomo and Van Tonder, 2013).

The geology of the study area is summarised in Table 3.1 with the spatial arrangement of the geological features shown in Figure 3.11.

Table 3.1: Summary of the geology of the Witbank, Ermelo and Highveld coalfields

Lithology group (youngest to oldest)	Description
Quaternary	
Alluvial	Unconsolidated sediments along rivers
The Karoo Supergroup	
Dwyka Group	Diamictite (Tillite)
Ecca Group	Sandstone, shale and coal
Beaufort Group	Mudrock, sandstone
Intrusive rocks	Dolerite (dykes and sills)
Waterberg Complex	Sandstone with interbedded conglomerate and shale
The Bushveld Complex	
Rustenburg Suite	Gabbro, norite, anorthosite
Lebowa Suite	Felsic granite
Transvaal Supergroup	
Chuniespoort Group	Dolomite, Chert
Pretoria Group	Shale, Quartzite
Intrusive rocks	Diabase
Rooiberg Group	Rhyolite and felsite
Loskop Formation	Sandstone, conglomerate
Witwatersrand Supergroup	
Hospital Hill Formation	Shale and Quartzite
Basement Complex	Granite and Gneiss

3.4.3.3 Hydrogeological setting

The hydrogeological setting of the Witbank, Ermelo and Highveld coalfield also contributes to defining pollution migration mechanisms. Thus, the contribution of the hydrogeological setting (aquifer types and hydrochemistry) of these coalfields to groundwater vulnerability will be discussed.

3.4.3.3.1 Aquifer types

The study area falls within the Johannesburg 2526 and the Nelspruit 2530 1:500 000-scale hydrogeology maps. Therefore, the hydrogeology background for the study is based on the explanations of these two hydrogeology maps (Barnard, 2000; Du Toit and Sonnekus, 2014). The aquifers for the study area are divided into four classes:

- Intergranular – Mainly alluvial deposits of limited lateral extent and thickness along many river terraces;
- Fractured – Represented by the Witwatersrand Supergroup, Pretoria Group quartzites, the Waterberg and Dwyka Groups;
- Fractured and intergranular – Represented by the Rooiberg Group, the Loskop Formation, the Bushveld Complex, the Ecca Group, the Karoo dolerite dykes and sills, the Pretoria Group; and
- Karst – Limestone and dolomites of the Chuniespoort Group.

In the Witbank, Ermelo and Highveld coalfields, the most dominant aquifer system is the fractured and intergranular type found in the weathered sediments at the interface between the soil and the bedrock and occurs at depths of between 5 to 12 m below the surface (Pinetown and Boer, 2006). The shallow depth of this aquifer system makes it highly susceptible to pollutants as a result of the reduced distance that these have to cover in order to reach the aquifer system.

The Ecca Group rocks of the Karoo aquifers occupy extensive parts of the study area and comprise sandstones, shales and coal layers with the sandstones and coal usually forming reasonable aquifers, while the shale serves as an aquitard (Burger, 2012). Layered aquifers are commonly perched on the relatively impermeable shale. The groundwater is generally associated with fractures and joints which develop along the bedding planes, lithology contact zones and in proximity to structural geological features such as shear zones, faults and dykes (Barnard, 2000). The quality of the groundwater in the Ecca Group rocks is generally considered to be excellent in areas where no mining operations have been carried out, but in the vicinity of mining operations and downstream of these operations the quality deteriorates, displaying the characteristic AMD footprint of elevated concentrations of sulphates and heavy metals and a low pH.

The Dwyka Group which comprises consolidated products of glaciation (with high amounts of clay) is normally considered to be an aquiclude owing to low permeability values associated with the rocks of this group. However, where the Dwyka Group is highly weathered, permeability increases and when a borehole is drilled in such areas the rocks may supply a reasonable yield for a household (Barnard, 2000). The chemistry of the groundwater in the Dwyka Group is generally considered suitable for domestic and irrigation uses. Background sulphate values range between 1 and 93 mg/L based on 46 samples extracted from boreholes drilled in the Dwyka Group in South Africa, but not necessarily within the study area. These values may vary owing to other factors such as variability in the mineral composition of the Dwyka Group rocks depending on their depositional location.

Abundant Karoo dolerite intrusions outcropping mostly in the south (Figure 3.16) comprise sills, which vary from being concordant to transgressive and feeder dykes. In terms of hydrogeology, the dykes are vertical to sub-vertical discontinuities that in general represent thin, linear zones of relatively higher permeability which act as conduits for groundwater flow within the aquifer. They may also act as semi to impermeable barriers to the movement of groundwater. The high permeability of the dyke contact zone is a result of shrinkage joints that developed during cooling of the intrusion. Intrusion of dolerite results in localised metamorphism of the country rock which increases the porosity within the localised zone. Thus, in Karoo sediments found in the study area, high yielding aquifers are localised in proximity to dykes and sills. Although these structures serve as aquitards they tend to compartmentalise the groundwater regime and their contact zones with the pre-existing geological formations also serving as groundwater conduits (Burger, 2012). These zones also may form preferential pathways for pollutants to reach the groundwater system. The special alteration of the hydrogeology brought about by dykes and sills needs to be considered when formulating groundwater vulnerability approaches. The preferential pathway parameter will accommodate the special condition played by the dykes and sills.

Karst aquifers are also found in the northwestern part of the study area at the town of Delmas. These aquifers belong to the dolomites of the Malmani Subgroup of the Chuniespoort Group and are considered to be very important aquifer systems in South Africa owing to their high yield which is in excess of 5 L/s. This aquifer system is formed when weakly acidic rainwater dissolves carbonate minerals found in the dolomite along planes of weakness such as faults, fractures and joints.

The process of dolomite dissolution may be summarised by Equation 3.2 given by Barnard (2000):

$$CaCO_3.2MgCO_3 + 5H_2CO_3 \rightarrow 3Ca(HCO_3)_2 + 2Mg(HCO_3)_2 \quad 3.2$$

$$Dolomite + carbonic\ acid \rightarrow calcium - bicarbonate + magnesium - bicarbonate$$

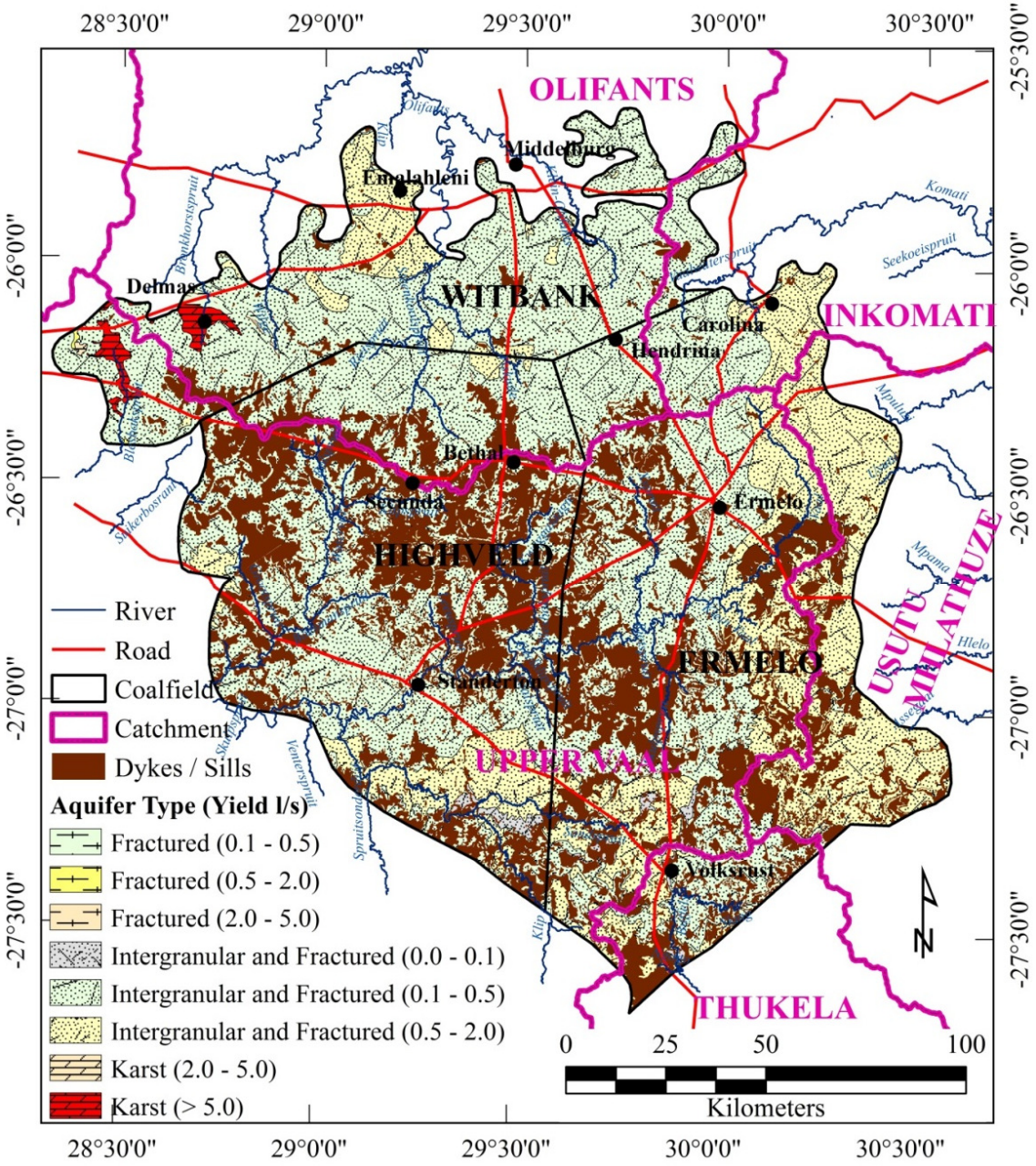

Figure 3.16: Hydrogeological setting of the study area

The resultant soluble bicarbonate is easily washed away in solution, leaving behind openings which can be filled with water, making up the aquifer system. The openings may be interconnected to form large groundwater storage reserves.

In terms of karst specific groundwater vulnerability mapping, no standardised approach has been developed specific to South African karst terrains. The only comprehensive available study focussing on groundwater vulnerability in karst terrains is the COST action 620 (Zwahlen, 2003). Groundwater is stored in karstic voids that develop around the conduits and are connected by high water head loss zones (Leyland *et al.*, 2008). The large magnitude strong permeability contrast between the matrix and conduits renders the storage in the matrix negligible. Recharge of karst aquifers can occur in

various ways, as stated by Gunn (1986). Figure 3.17 illustrates the various ways in which karst aquifers can be recharged:

- directly from an infiltration zone from closed points breakings such as sinkholes and shallow holes;
- diffuse through epikarst;
- stream-sink; or
- through permeable cap rocks.

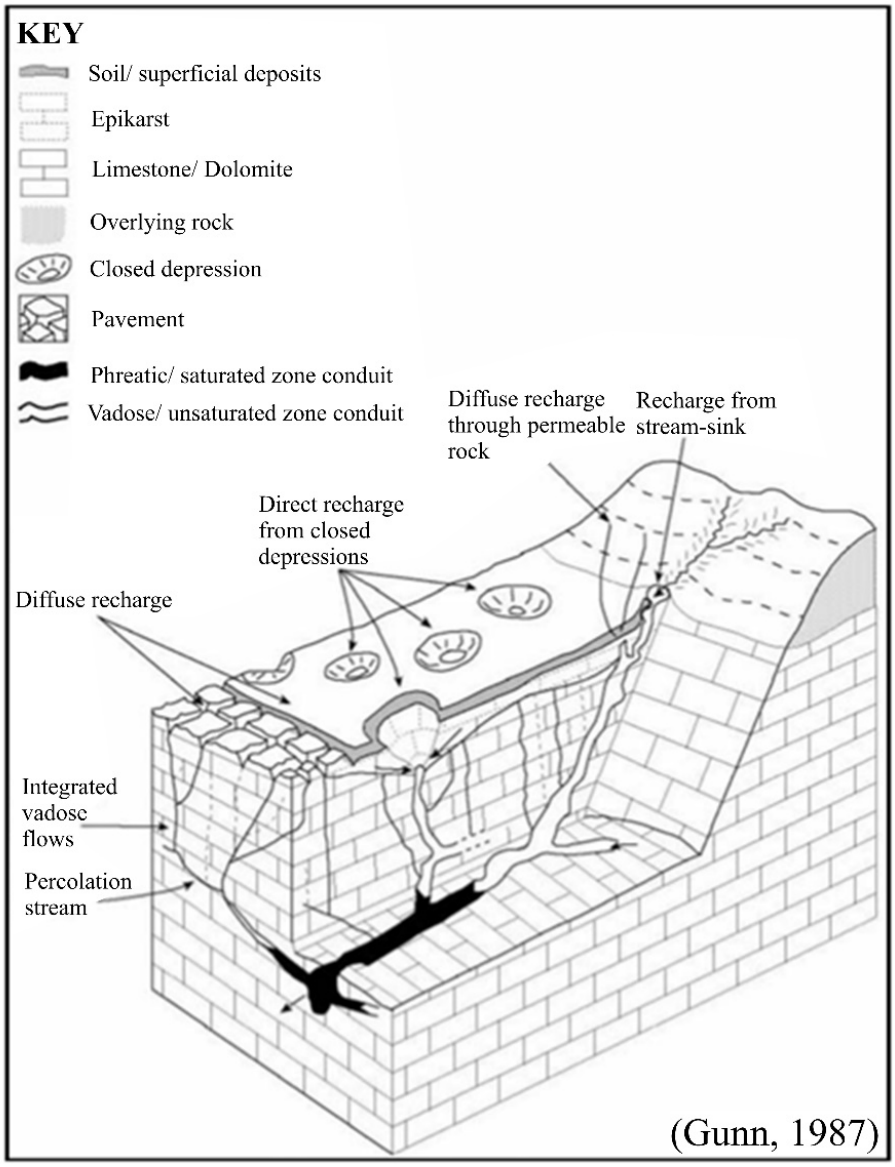

Figure 3.17: Conceptual model of a karst aquifer

Karst aquifers are often characterised by a dual or triple porosity comprising solution voids, fractures and the rock matrix (Leyland *et al.*, 2008). The fractures and the rock matrix provide the groundwater storage and the conduits act as transportation pathways. Thus, transport of dissolved pollutants in

karst aquifers is a fast advective transport similar to fractured aquifers, where pollutants migrate mostly along the voids as compared to through the matrix. Thus, karst aquifers have unique properties which should be taken into account during a vulnerability assessment. Karst aquifer vulnerability assessment methods are usually either methods especially dedicated to karst or methods that, although applicable to all aquifer types, contain special methods to be used when being applied to karst areas. Since karst aquifers are only localised at a small area within the study area, the special properties of karst will be generalised in the development of a groundwater vulnerability approach for a coalfield.

Owing to the shallowness of the groundwater systems in the study areas, there is an urgent need for a groundwater vulnerability assessment to be conducted to highlight sensitive areas to study the ease with which pollutants can migrate and enter the groundwater system. As has been mentioned, the study area represents over 100 years of coal mining activities and there are new areas that are still to be mined. Therefore, it is important that areas identified for possible mining first be subjected to a groundwater vulnerability assessment.

3.4.3.3.2 Hydrochemistry

Hydrochemistry data used in this research were collected from several boreholes during the dry season of July 2013 using conventional best practice groundwater sampling guidelines, as described by Weaver *et al.* (2007). The uses of boreholes in the study area range from domestic, monitoring, industrial and irrigation, where groundwater is extracted from shallow phreatic aquifers.

Sampling was accompanied by recordings of physical parameters (pH, electrical conductivity and total dissolved solids) using Aquaread GPS multi-parameter aquameters. Fifty-two (52) groundwater samples were collected within the study area (Figure 3.18) in sets of three, filtered, preserved and transported in a temperature-controlled environment to the Council for Geoscience laboratory in Pretoria where they were analysed for cations, anions and alkalinity using inductively coupled plasma mass spectrometry (ICP-MS), ion chromatography (IC) and spectrophotometry respectively.

Sample duplicates and blanks (deionised water) were used to evaluate analytical consistency and errors. The results showed relative percentage differences lower than 10% for duplicate samples and below detection limit for the blank samples. Data quality was assessed using the anion-cation balance electroneutrality method (Hounslow, 1995), where all the water samples were below the acceptable ±5% error.

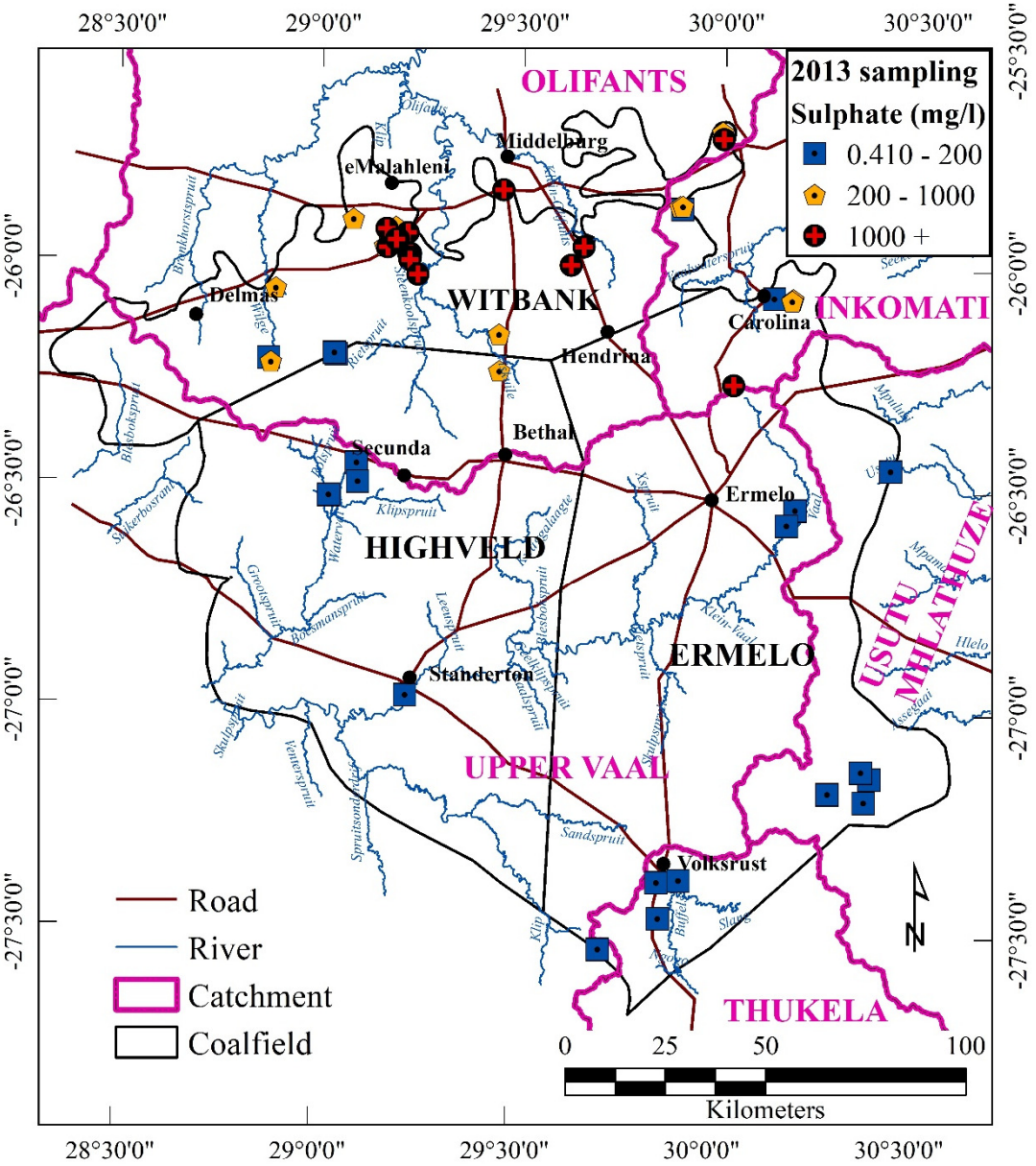

Figure 3.18: Locations of groundwater samples used in this study

The variability in groundwater chemistry may be attributed to the natural chemical evolution of the groundwater chemistry resulting from water-rock interaction and anthropogenic influences (Hounslow, 1995). Groundwater samples were classified on the basis of the composition of the major ions composition and results presented in a Piper diagram (Figure 3.19). The diagram shows the presence of at least two main water types: Ca-HCO_3 and the Ca-Mg-SO_4 named groups I and II respectively with few samples belonging to the Na-HCO_3 types.

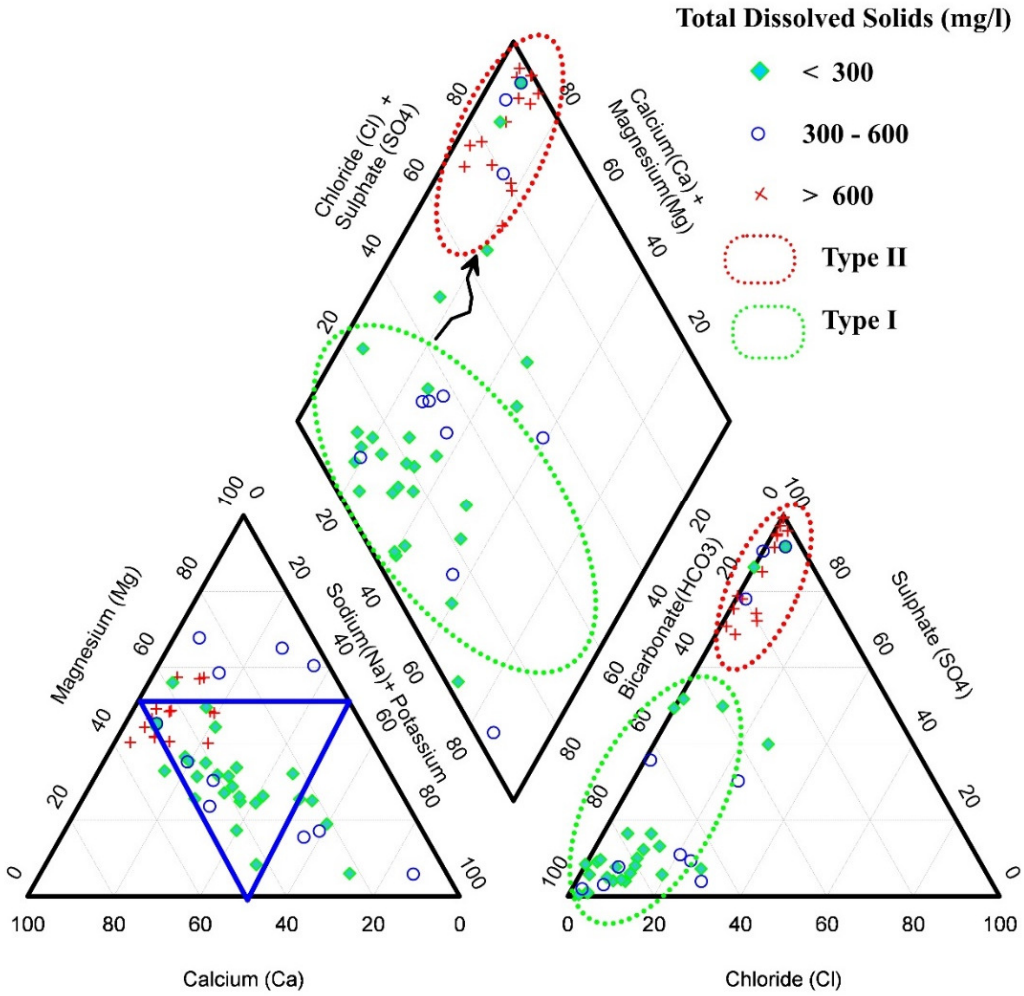

Figure 3.19: Piper diagram showing the major water classifications in relation to the TDS concentration

Group I samples reveal a chemical composition resulting from weathering processes affecting the regional rocks. According to Bartolino and Cole (2002), the Ca-HCO_3 type shows early stages of water-rock interaction which often takes place at a shallow depth where the rock mineralogy does not significantly influence the composition of groundwater.

On the other hand, Group II water samples are characterised by high TDS values greater than 600 mg/L and high SO_4^{2-} greater than 200 mg/L. The TDS-sulphate scatter plot (Figure 3.20) shows a very high coefficient of determination value of 0.924 which means that the hydrogeochemical reactions enriching sulphates into the groundwater are contribute about 92% to TDS values.

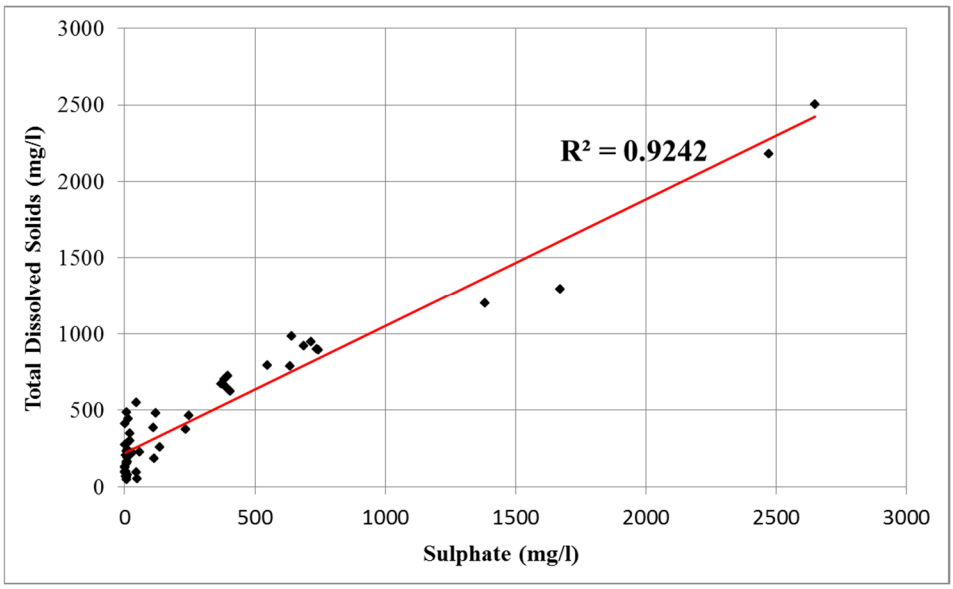

Figure 3.20: Scatter plot of TDS against sulphate concentration

Considering the location of the study area, the most likely processes which add sulphate into the groundwater are AMD reactions. The orebodies, waste rock and tailings dumps in the mining areas are rich in sulphate minerals which react with water and oxygen to form SO_4^{2-}, Fe compounds and H^+ ions (Wild, 1996). The AMD generation reaction produces H^+ ions which are responsible for the low pH values of samples of group II. As the AMD generation reaction produces more SO_4^{2-} ions into the system, this changes the anion chemistry from juvenile HCO_3^{2-} dominance to SO_4^{2-} dominance. The black arrow in Figure 3.19 shows the possible evolution route of the groundwater system from HCO_3^{2-} to the SO_4^{2-} water type. The majority of the sampled boreholes fall within the blue inverted triangle of the Piper diagram which does not show the most dominant cation, possibly due to groundwater mixing. The red points in Figure 3.19 are characterised by very high sulphate, high TDS and very low bicarbonate, indicating an origin from mine water where the bicarbonates have been depleted by acidity.

3.4.4 Mining Activities and their Contribution to AMD Pollution

3.4.4.1 Coal mining history of the Witbank, Ermelo and Highveld coalfields

In South Africa, the first recorded discovery of coal was in 1699 at Franschhoek in the Western Cape, but there are claims supported by scant evidence that the indigenous inhabitants of South Africa may have exploited some of the easily accessible coal reserves before the arrival of European settlers. The opening of the T and DB Mine located in what is now known as the Witbank coalfield in the 1890s caused the coalfield to become the principal energy source of power generation for the country's industries, mines and rail systems. Since the 1890s, the coalfield has been mined to fuel power stations.

3.4.4.2 Coal geology

In general, the coal-bearing horizons in the Karoo coalfields are the result of peat accumulations at a broad subsidence and in-filled geosynclinal basin at discrete intervals during the evolution of the Karoo sequence leading to many coal seams found in the coalfields (Hancox and Götz, 2014).

3.4.4.2.1 Witbank coalfield

The Witbank coalfield is a multiple seam deposit type with five major seam horizons having developed there. The primarily economic coal seams have been the no. 2 and 4 seams, the 4 lower seam and, in some places, the no. 5 seam. Structurally, the coal horizons are undeformed with each layer displaying a very slight dip to the southeast of less than a degree and minor discrete faulting events that have a southwest to northeast trend of graben features and other minor faulting events. The most distinctive post-depositional feature is the intrusion of dolerites related to the Lesotho basalts that has resulted in a variety of sills and dykes of various ages.

3.4.4.2.2 Highveld coalfield

The coalfield is host to up to five coal seams contained within the middle Ecca Group sediments of the Karoo Supergroup. The five identified coal seams contained in the Vryheid Formation are named, from the base up, as follows: no. 1, 2, 3, 4, and 5. The coalfield is characterised by the fact that in the northern regions, all the coal seams, with the exception of the no. 3 seam, attain mineable thicknesses with economic potential while, in the southern regions, only the no. 4 seam and, in very localised areas, the no. 2 seam, attain mineable dimensions of economic importance. These intrusive dolerite sills and dykes are related to the Drakensberg Formation flood basalts and adversely affect the coal seams in the vicinity of the intrusions in terms of coal quality by devolatilising and burning the coal. The bulk of the coal produced is consumed in power stations and syn-fuel production (Exxaro, 2006).

3.4.4.2.3 Ermelo coalfield

There are five major coal seams which are developed in the Ermelo coalfield, named from the base up: E, D, C, B and A seams. The seams are relatively unaffected by folding although faulting and associated dolerite (igneous) intrusions are common throughout the coalfield. Dolerite intrusions take the form of vertical to near-vertical dykes, often intruding existing faults and sills, which are parallel to the bedding planes. Sills are also often transgressive, resulting in the relative displacement of the strata. The number of sills increases to the south and up to eight major sills has been identified. An additional effect of the dolerite intrusions is the burning or devolatilisation of coal in close proximity to the dolerites (Exxaro, 2006).

3.4.4.3 Coal mining activities and their impacts to the environment

Within the Witbank, Ermelo and Highveld coalfields, coal mining started over a century ago with both opencast and underground mining, each having its own impact on the environment and health in general. Some mining operations have since been abandoned, and some established at new locations. The environmental effects caused by coal mining in the Witbank, Ermelo and Highveld coalfields include collapsed ground over areas where underground mining was done, with coal fires and drainage (acid, neutral or alkaline) emanating from the mining activities. Ultimately, the drainage enters the groundwater and surface local river systems such as the Olifants River, if not controlled. Figure 3.21 shows surface flow of AMD from an operational mine being discarded to a local stream connected to a major river.

Figure 3.21: AMD surface flow from a coal mining operation south of Carolina in the Ermelo coalfield. The brownish-orange colour is attributed to iron hydroxyl precipitation

The AMD which enters the surface river network ends up in major reservoirs such as the Middelburg and Witbank dams. Although the AMD is neutralised, the concentration of salts and sulphates remains high in solution. For example, the sulphate concentration of the Witbank dam is now over 200 mg/L, which exceeds the maximum recommended domestic use such that ESKOM, the leading electricity generating company located within the study area imports water from the eastern escarpment for use in its power stations (McCarthy, 2011). This prompts the need for a groundwater vulnerability assessment to be done with a specific focus on the AMD pollution of the coalfields.

This research, based on a holistic approach, mainly focusses on differentiating between sensitive and non-sensitive areas in a typical coalfield affected by AMD pollution as an environmental issue. The resultant models generated would go a long way in advising policy and decision makers on how to handle different geological, hydrogeological settings and appropriate mitigation measures suggested which would minimise groundwater pollution from coal mining activities.

3.4.5 SPT Inputs for the Witbank, Ermelo and Highveld Coalfields

3.4.5.1 Sources of energy (topographic slope)

In the study area, the elevation data at spatial resolution of a 30 x 30 m grid cell size was extracted from the USGS (2017). The elevation ranges between 1 225 and 2 237 m.a.s.l, with the highest areas located in the Upper Vaal catchment area within the Ermelo coalfield (Figure 3.22). The Usutu-Mhlathuze catchment is at the lowest elevation compared to other catchments. Most of the Witbank coalfield lies in the Olifants catchment, with the Olifants River being the main drainage system. Several catchments that drain the Ermelo coalfield, such as the Olifants, Upper Vaal, Inkomati, Thukela and Usutu-Mhlathuze, with the largest area located in the Upper Vaal catchment. The Highveld coalfield covers parts of the Olifants and Upper Vaal catchments.

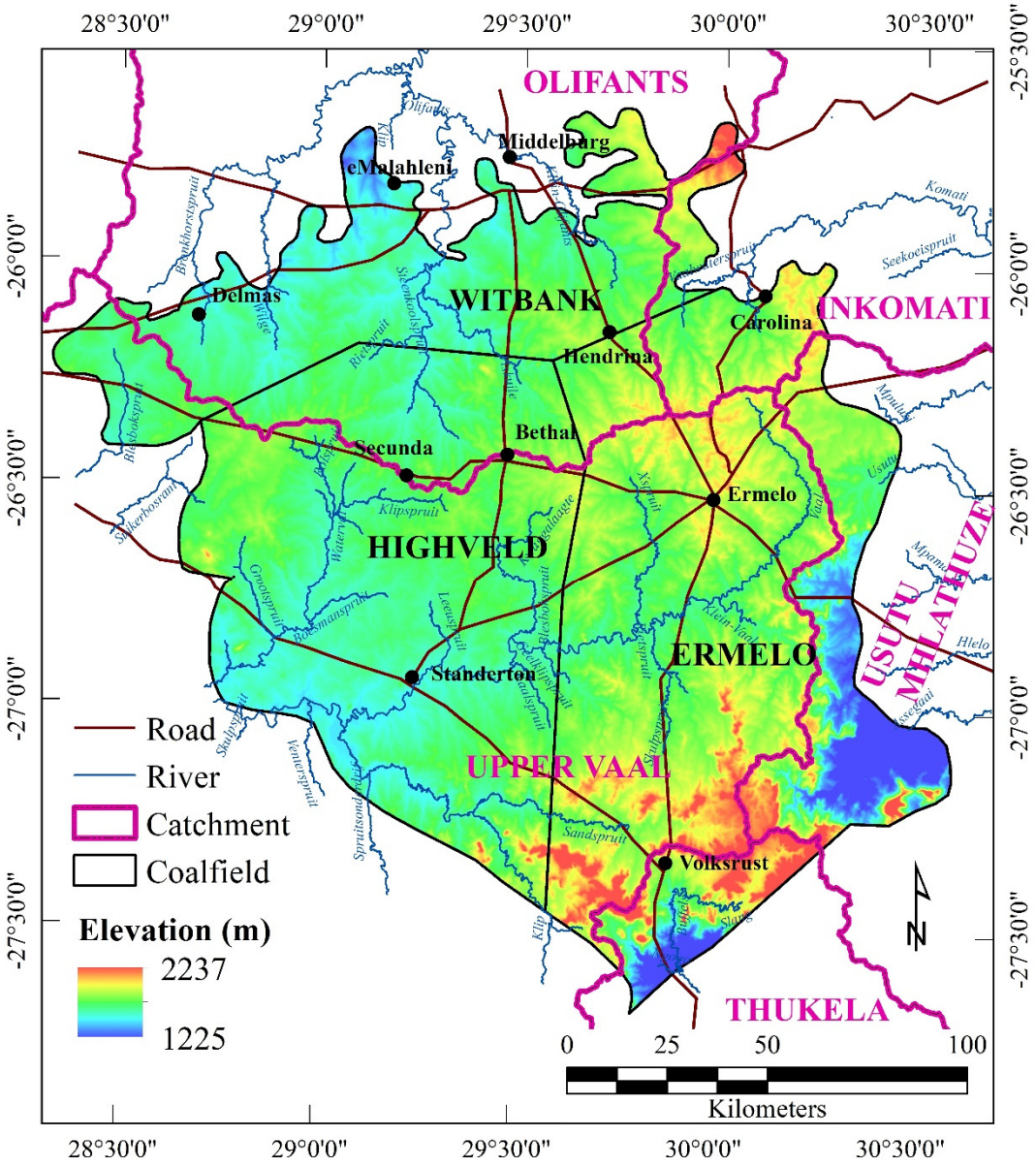

Figure 3.22: Elevation image of the study area showing the drainage pattern and rivers

The topographic slope for the study area varies between 0 and 121% (Figure 3.23) with the largest part of the area being flat, characterised by slopes below 5%. The southern portion, corresponding to the Majuba Mountains around the Volksrust area, is marked by very steep terrain.

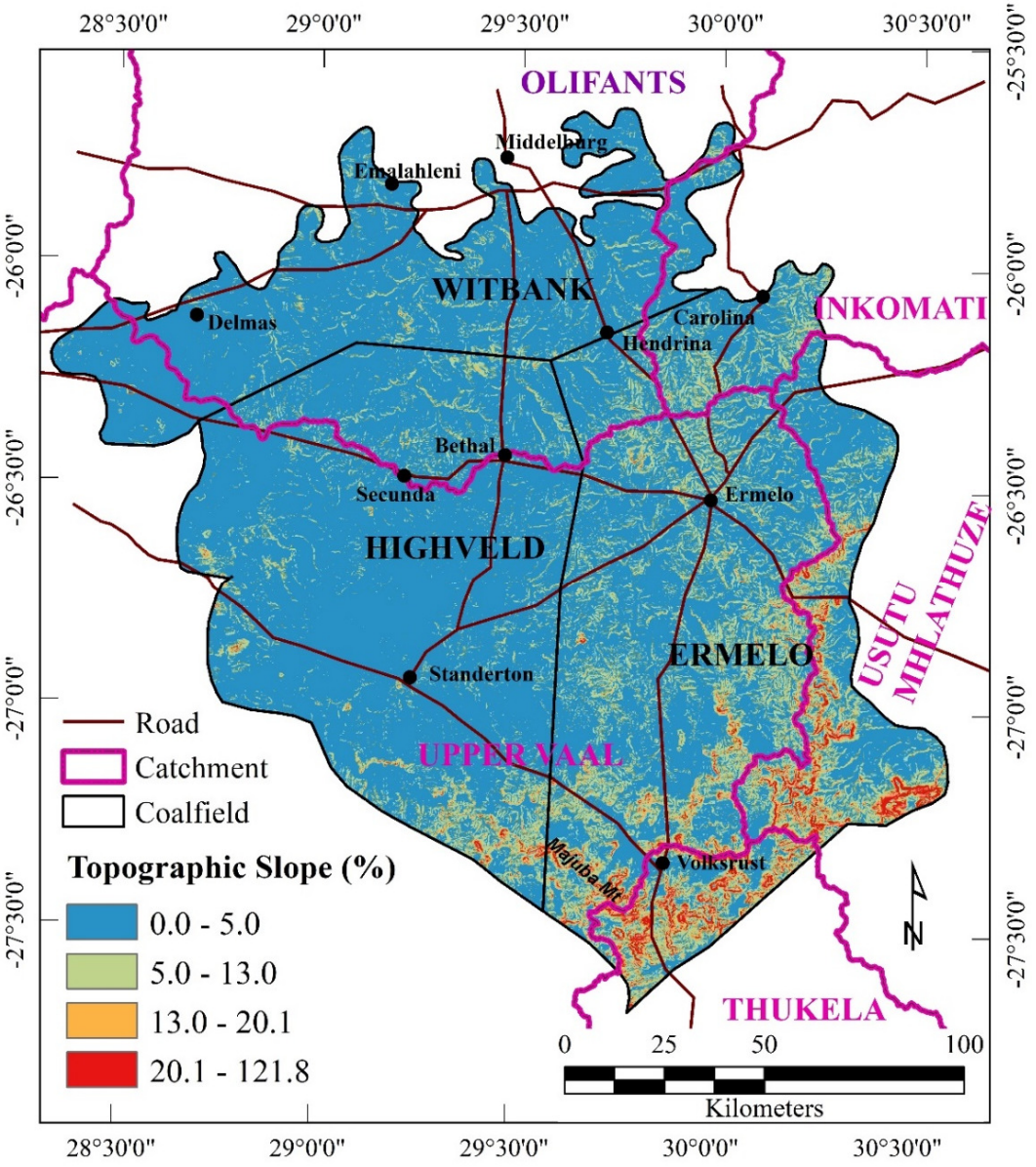

Figure 3.23: Topographic slope image of the study area

3.4.5.2 Sources of ligands (water)

In the study area, the sources of ligands used was the average long-term rainfall which was obtained from historical data published by the South African Weather Services (SAWS, 2016). Figure 3.24 shows the average long-term rainfall which ranges between 634 and 1 045 mm and increases in a southeasterly direction. Most popular groundwater vulnerability assessment approaches (e.g. the DRASTIC method) use recharge values as a parameter that represents the transportation of pollutants. In this research where a specific groundwater vulnerability approach is being developed, average

long-term rainfall will be used as it captures both the availability of water for AMD reactions and availability of water (ligands) for the transportation of pollution from the surface to the groundwater.

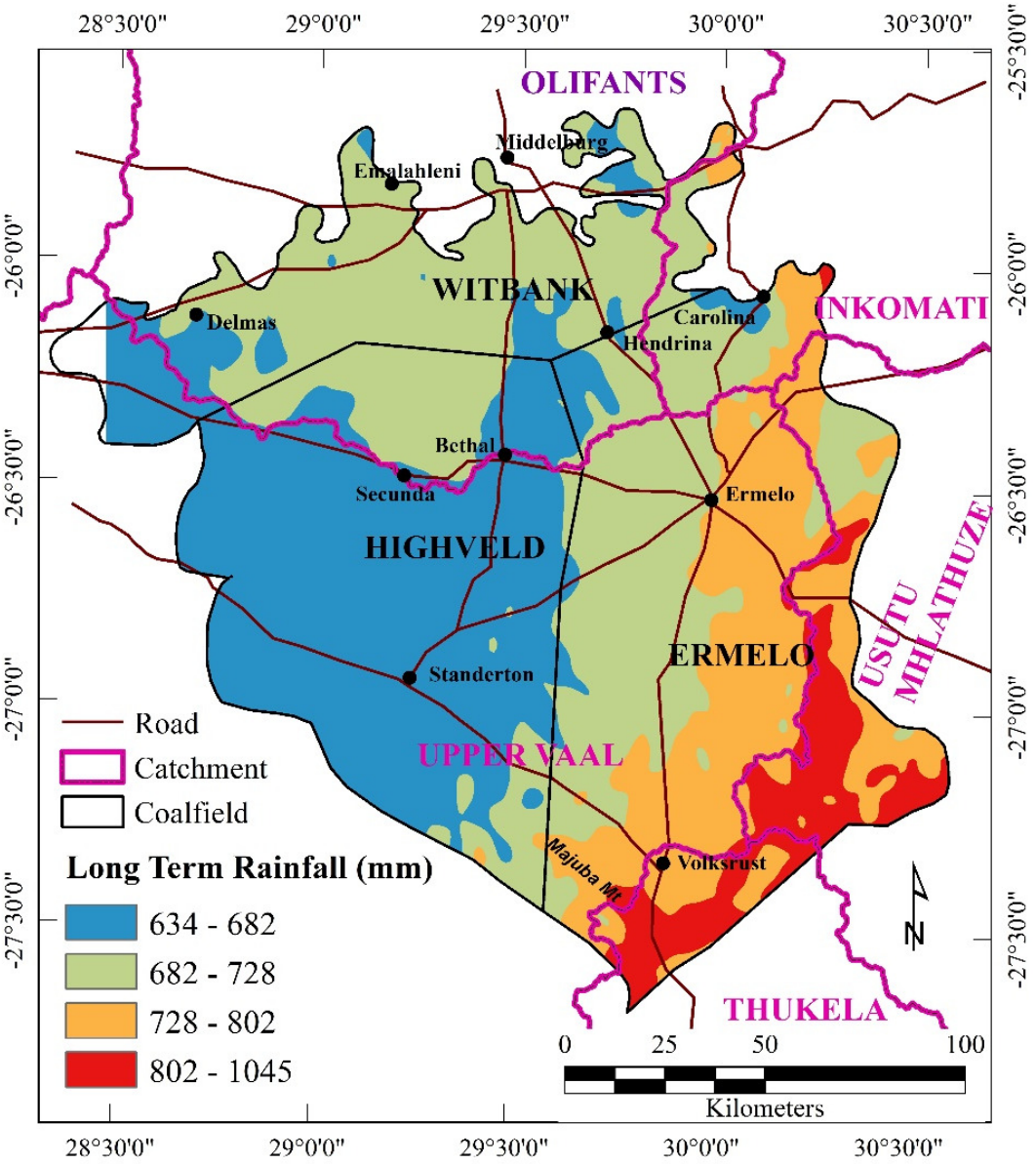

Figure 3.24: Average long-term rainfall of the study area

In order to verify whether if the average rainfall is correlated with recharge data, regional recharge data from Department of Water and Sanitation (DWS) were used.

The DWS conducted a study to generate a groundwater recharge map for South Africa at 1 km by 1 km grid cell size (DWS, 2006). The method used to produce the recharge map is GIS-based and Quaternary catchments were used as the unit of measure. The recharge method essentially comprises four main components:

- the Chloride Mass Balance (CMB) approach;
- empirical rainfall/recharge relationships;

- layer model (GIS based) approach; and then
- cross calibration of the results with field measurements and detailed catchment studies.

The results obtained from the recharge study by the DWS were in agreement with results obtained from earlier recharge studies (DWS, 2006). Though the approach did not differentiate between preferred path and matrix diffusion recharge, it is GIS-based, making it sufficiently flexible to include updates and new datasets. Figure 3.25 shows the recharge map of the study area as extracted from the countrywide recharge map of South Africa. In the study area, high recharge areas (over 77 mm) are found in the eastern and south-eastern parts of the study area. The central and western parts of the study area are marked by lower recharge values (below 37 mm).

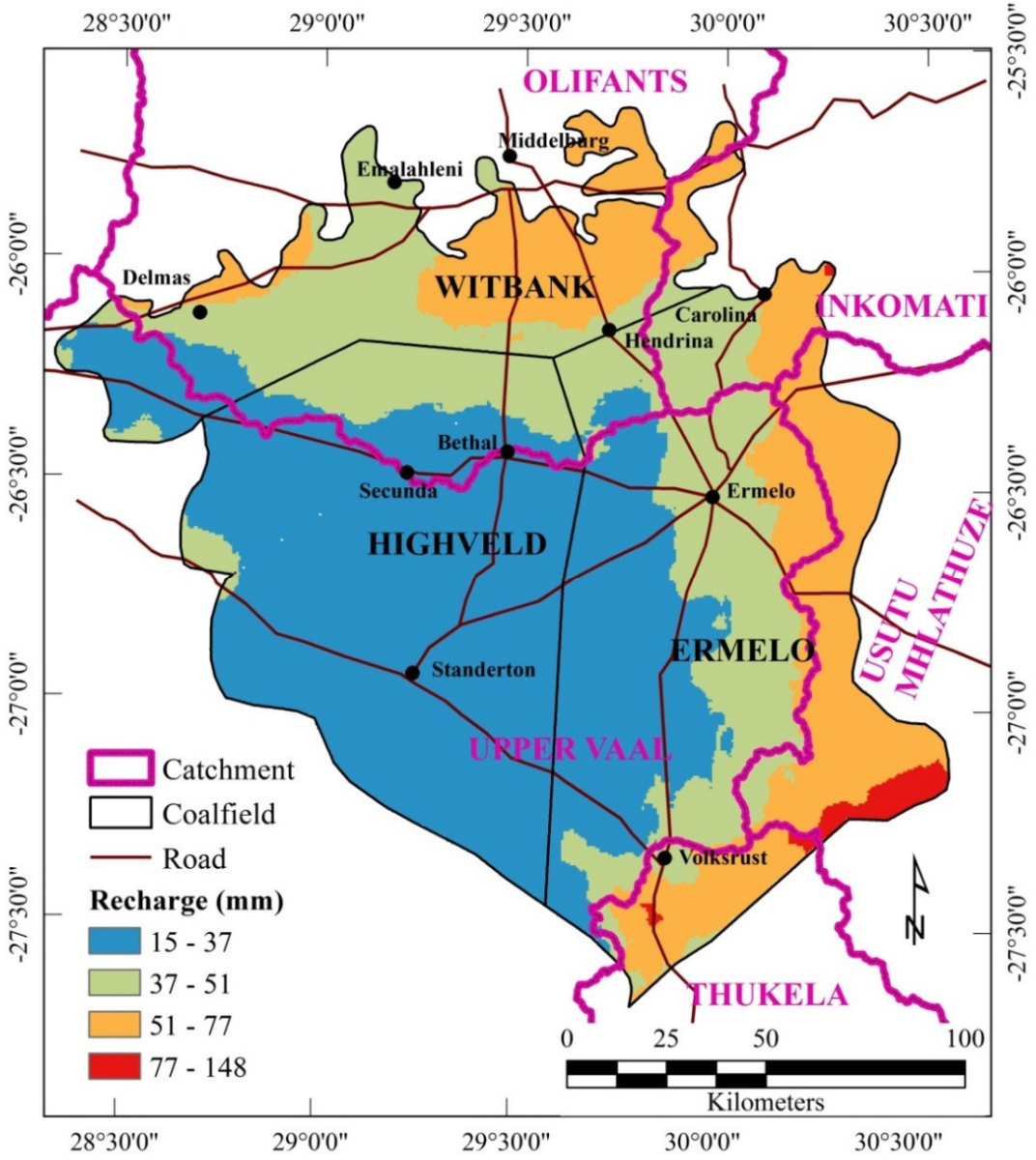

Figure 3.25: Recharge image of the study area

The net recharge data covering the study area was plotted against average long-term rainfall and the results presented as a scatter plot, shown in Figure 3.26. A correlation coefficient value (R) of 0.821 was obtained showing a strong positive correlation between net recharge values and average long-term rainfall. The coefficient of determination (R^2) of 0.6741 shows that ~ 67% of the rainfall parameter contributes to the recharge (Figure 3.26).

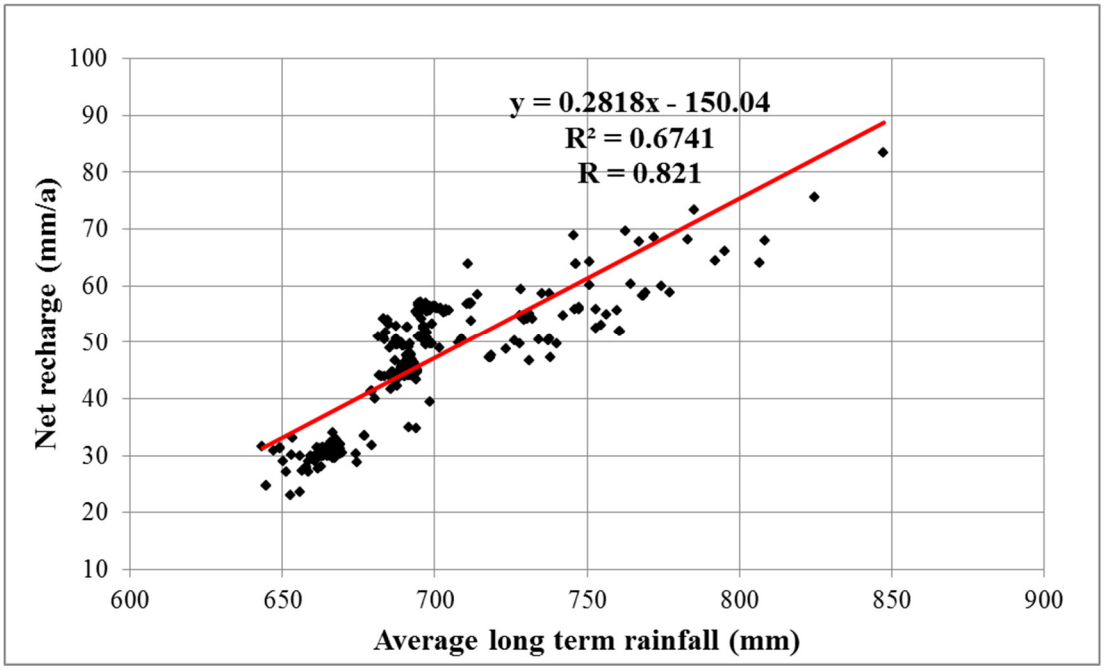

Figure 3.26: Relationship between average long-term rainfall and net recharge

The usage of rainfall data which is highly correlated with recharge would ensure that the vital transport mechanisms are captured in the modelling. Using rainfall as a parameter would also reduce parameter dependencies which affect methodologies such as the DRASTIC methods.

3.4.5.3 Surface sources of AMD pollution

For the Witbank, Ermelo and Highveld coalfields, remote sensing (Landsat 8 and Sentinel 2) was used to identify secondary iron-bearing minerals which are produced by AMD formation reactions. The advantage of using orbital remote sensing data is that very large areas can be mapped at a relatively low cost and that most sources are mapped at the spatial resolution of the remote sensing data.

3.4.5.3.1 Methodology for identification of AMD surface sources

This section, based on a peer-reviewed conference publication (Sakala *et al.*, 2017b) written as part of this research, was presented at the 13th International Mine Water Association Congress in Lappeenranta, Finland.

The methodology for the identification of AMD sources from Landsat 8 remote sensing data involves the following process flow:

- Identification of the spectral signature of iron-bearing minerals in mine discard dumps within the study area. Identification can be done by taking several spectral readings of the mine discard dumps using a handheld spectroradiometer or extracting spectral data from publications from, for example, the USGS mineral spectral library (Swayze *et al.*, 2000). The iron-bearing minerals are often indicators of the geochemical environment in which they were formed. The commonly known Fe-bearing minerals which are sensitive indicators of pH, Eh, relative humidity, degree of oxidation and other environmental conditions are copiapite ($Fe^{+2}Fe_4^{+3}(SO_4)_6(OH)_2{\cdot}20(H_2O)$), jarosite ($KFe_3^{+3}(SO_4)_2(OH)_6$), schwertnannite ($Fe_{16}^{+3}O_{16}(SO_4)_2\ (OH)_{12}{\cdot}nH_2O$(n~10 to 12)), ferrihydrite ($5Fe_2O_3{\cdot}9H_2O$), goethite ($Fe^{+3}O(OH)$) and haematite (Fe_2O_3) (Swayze *et al.*, 2000; Crowley *et al.*, 2003). Within the study area, the Fe-bearing minerals which form in abundance are haematite and jarosite, according to a study by Cole *et al.* (2015). The spectral uniqueness of these Fe-bearing minerals makes it possible to identify them from orbital and airborne imaging data.
- Resampling of the mineral spectral data to remote sensing data, i.e. Landsat 8 and Sentinel 2 bandwidth sizes in this study.
- Comparison of various bands and identification of the reflectance value differences to be used in order to differentiate between the AMD indicator minerals and the other minerals present.
- Developing a decision tree for differentiating various minerals using their reflectance responses at various bandwidths. The decision tree is then applied to the Landsat 8 and Sentinel 2 data to produce maps showing the distribution of the AMD indicator minerals.
- Verification of the results by follow-up ground investigations over the identified AMD sources or onscreen verification on Google Earth images.

In this study, free Landsat 8 and Sentinel 2 data downloaded from the USGS and Copernicus websites respectively were used to identify secondary iron-bearing minerals. Landsat 8 data comprise nine bands in the visible and near-infrared (VNIR) and short-wave infrared (SWIR) ranges (Band 8 is the panchromatic band and Band 9 is a cloud detection band) and two bands in the thermal infrared (TIR) range (Table 3.2).

Table 3.2: Properties of Landsat 8 data (Cole *et al.*, 2015)

Range	Band	Wavelength range (µm)	Spatial resolution (m)
VNIR	1	0.433 – 0.453	30
	2	0.450 – 0.515	30
	3	0.525 – 0.600	30
	4	0.630 – 0.680	30
	5	0.845 – 0.885	30
	8	0.500 – 0.680	15
SWIR	6	1.560 – 1.660	30
	7	2.100 – 2.300	30
	9	1 360–1 390	30
TIR	10	10.600 – 11.200	100
	11	11.500 – 12.500	100

Sentinel 2 data comprise 13 spectral bands in the VNIR and SWIR spectral range as shown in Table 3.3.

Table 3.3: Properties of Sentinel 2 (Satellite Imaging Corporation., 2017)

Range	Band	Central wavelength (µm)	Spatial resolution (m)
Coastal aerosol	1	0.443	60
Blue	2	0.490	10
Green	3	0.560	10
Red	4	0.665	10
Vegetation Red Edge	5	0.705	20
Vegetation Red Edge	6	0.740	20
Vegetation Red Edge	7	0.783	20
NIR	8	0.842	10
Vegetation Red Edge	8A	0.865	20
Water vapour	9	0.945	60
SWIR - Cirrus	10	1.375	60
SWIR	11	1.610	20
SWIR	12	2.190	20

The data are pre-processed by doing atmospheric correction and converting the Digital Number (DN) into reflectance values using QGIS automatic pre-processing modules. Clouds, cloud shadows and vegetation are masked out of the reflectance data to obviate the creation of false classification when running the minerals mapping process. The spectral signatures of all the secondary iron-bearing minerals can be extracted from the USGS spectral library (Clark *et al.*, 2007).

The spectral signatures of copiapite, goethite, hematite, jarosite, ferrihydrite and schwertmannite from the USGS spectral library reveal that these six minerals show unique reflectance signatures which can be used to distinguish them from other minerals (Figure 3.27).

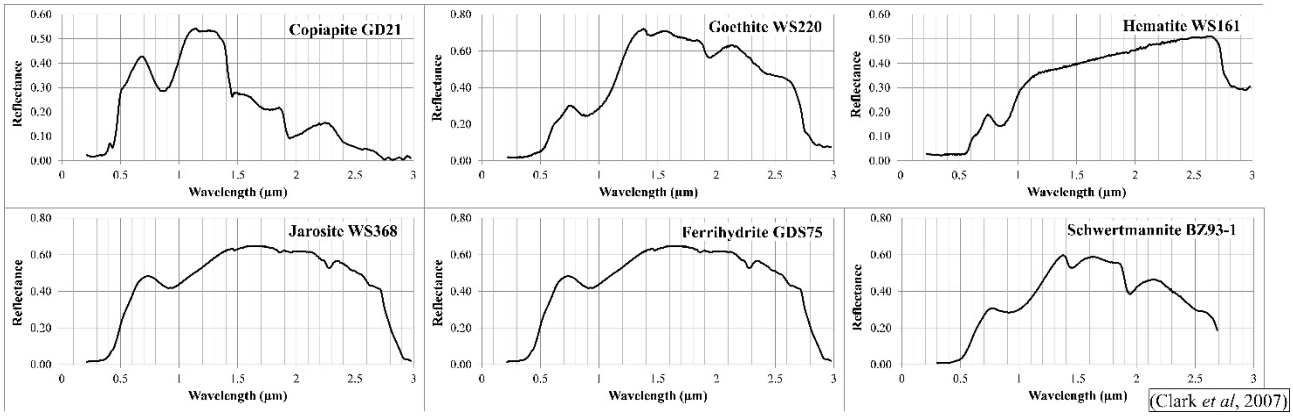

Figure 3.27: Spectral signatures of iron-bearing minerals extracted from the USGS spectral library

The spectral signatures of all the Fe-bearing minerals were resampled to the detection ranges of Landsat 8 and Sentinel 2 bands. The resampled spectral signatures of the six minerals (copiapite, goethite, hematite, jarosite, ferrihydrite and schwertmannite) still show their distinct spectral signatures on Landsat 8 and Sentinel 2 spectrum, as is evident from Figure 3.28 and Figure 3.29 respectively. The spectral uniqueness of these Fe-bearing minerals makes it possible to identify them from orbital and airborne imaging data. Hence, only these minerals will be identifiable from the remote sensing data.

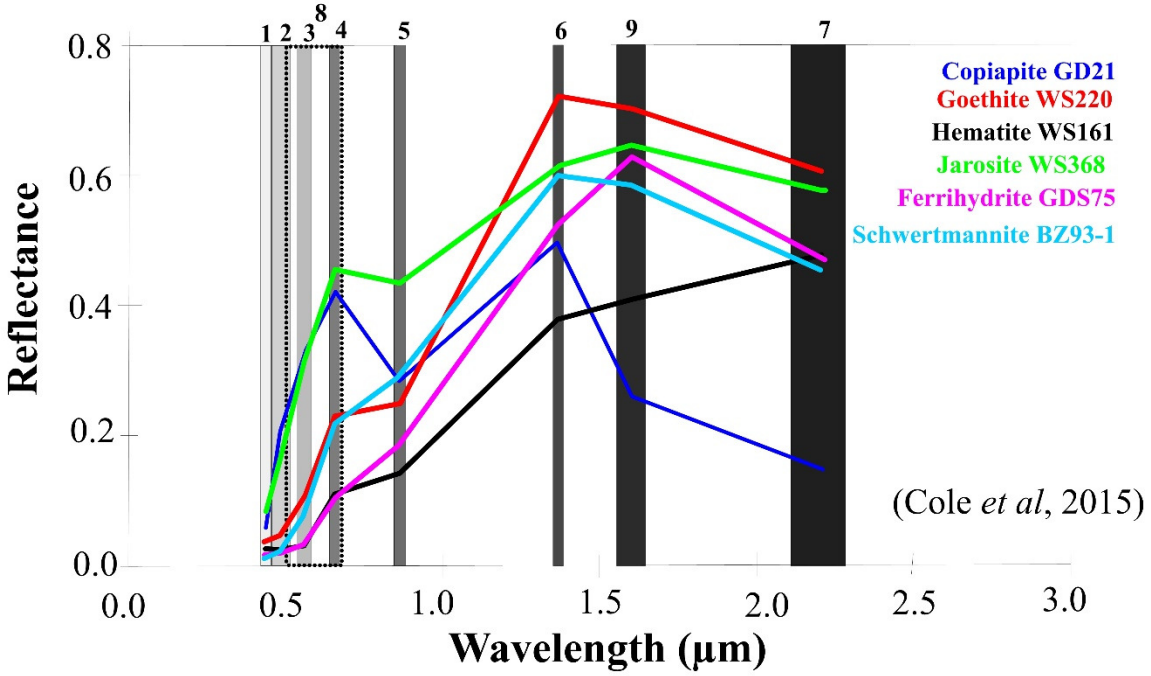

Figure 3.28: Secondary iron minerals spectrum resampled to Landsat 8 bandwidths

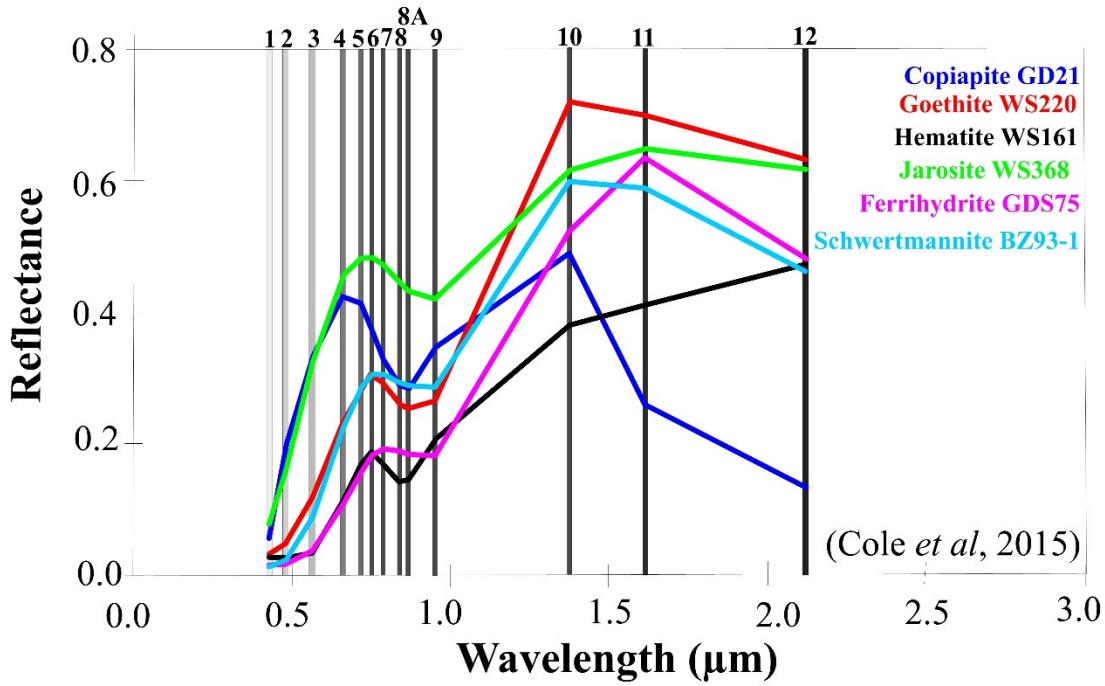

Figure 3.29: Secondary iron minerals spectrum resampled to Sentinel 2 bandwidths

An examination of the mineral spectrum which has been resampled to Landsat 8 (Figure 3.28) bandwidth, shows that the reflectance value for band 4 is greater than that of band 5 and that the reflectance value band 9 is greater than that of band 6. This is the spectral uniqueness of jarosite when compared with other secondary iron minerals which may be found in an acid environment. For haematite, the spectral uniqueness on Landsat 8 data is such that the reflectance value for band 5 is greater than that of band 4; the reflectance value for band 7 is greater than that of band 6 and the reflectance value of band 9 is greater than the reflectance value for band 6 (Figure 3.28). This spectral uniqueness of these minerals was used to create a decision tree to identify these minerals using Landsat 8 reflectance data.

Sentinel 2 data has many bands which makes it easy to differentiate the minerals within a 10 m pixel sized grid cell. For jarosite, the spectral uniqueness on Sentinel 2 data is such that the reflectance value for band 11 is greater than that of band 12, the reflectance value for band 5 is greater than that of band 4, the reflectance value for band 8 is greater than that of band 9 and the reflectance value for band 10 is greater than that of band 11 (Figure 3.29). For hematite, the spectral uniqueness on Sentinel 2 data is such that the reflectance value for band 12 is greater than that of band 11, band 11 is greater than the reflectance value for band 10, the reflectance value for band 9 is greater than that of band 8, the reflectance value for band 7 is greater than that of band 7 and the reflectance value for band 6 is greater than that of band 5 (Figure 3.29).

Using the observed spectral uniqueness of the two minerals, decision trees for Landsat 8 and Sentinel 2 were produced and are presented in Figure 3.30 and Figure 3.31 respectively. The decision tree was implemented in ArcGIS and the AMD-related secondary iron-bearing zones were identified.

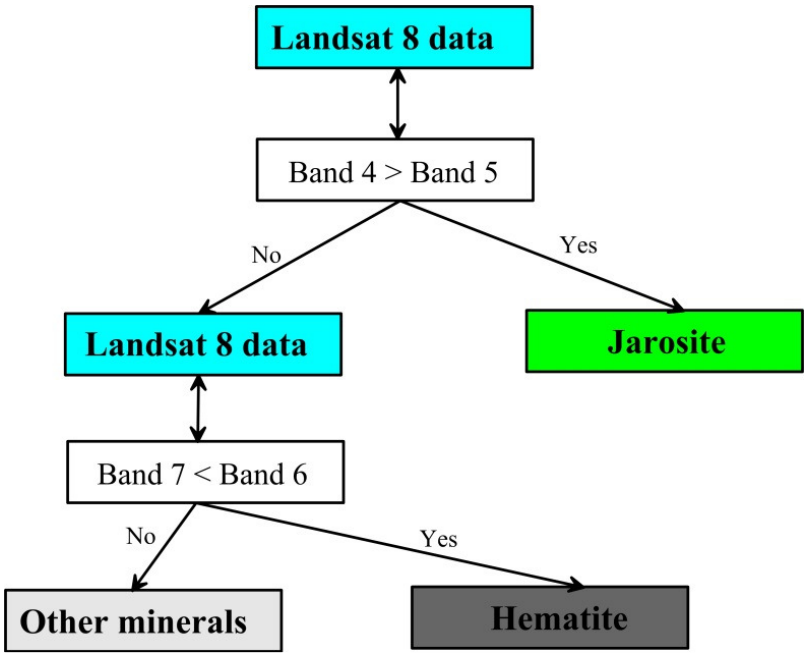

Figure 3.30: Decision tree used to identify secondary Fe minerals from Landsat 8 data

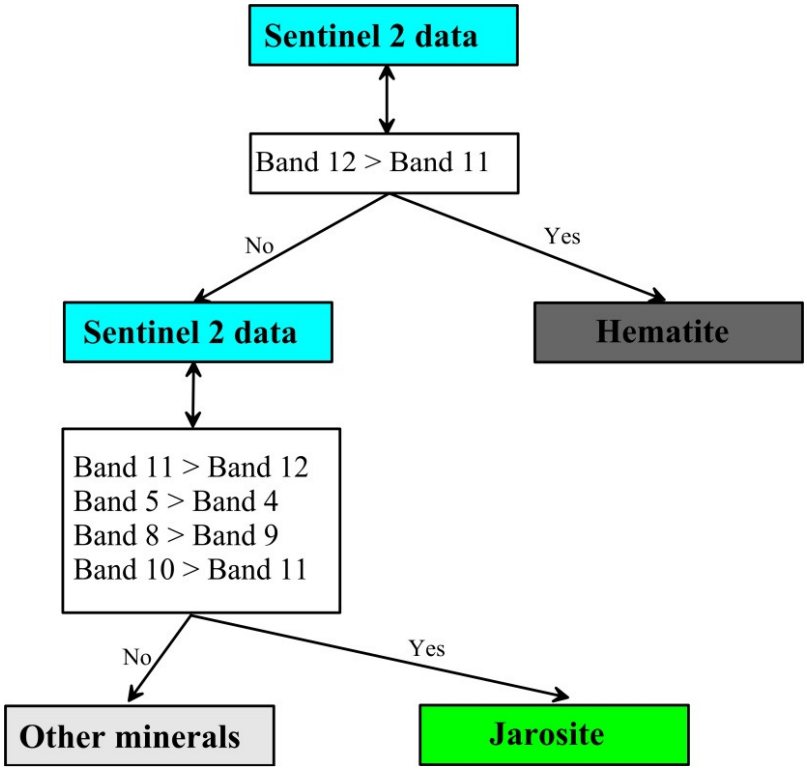

Figure 3.31: Decision tree used to identify secondary Fe minerals from Sentinel 2 data

3.4.5.3.2 Results and discussions

Not all mine residue dumps or coal discard faculties are acid generating. Only those that are indeed acid generating will precipitate the secondary iron minerals and thus be identifiable using this approach. After implementing the decision tree in a GIS environment: Landsat 8 and Sentinel 2 data covering the whole study area were used to produce maps showing only the interpreted Fe-bearing minerals which can be used as potential AMD surface sources.

Figure 3.32 shows the interpreted Fe-bearing minerals (jarosite, hematite) extracted from Landsat 8 data and the results are presented as a function of distance (Euclidean distance) from the pixel that is interpreted to contain these minerals. The Euclidean distance which is an "*ordinary*" straight-line distance between two points in the Euclidean space (Michel and Elena, 2009) was implemented in ArcGIS software using the Spatial Analysist tool.

The Euclidean distance ($\overline{pq}$) between points p and q on a map is the length of the line segment between them. In the Cartesian coordinates, if $p = p_1, p_2, \ldots, p_n)$ and $q = (q_1, q_2, \ldots, q_n)$ are two points in Euclidean n-space, then the distance (d) from p to q, or from q to p, is given by the Pythagorean formula (Equation 3.3).

$$d(p,q) = d(q,p) = \sqrt{\sum_{i=1}^{n}(q_i - p_i)^2} \qquad 3.3$$

The Witbank coalfields are marked by the highest density of the interpreted Fe-bearing minerals while the Ermelo and Highveld coalfields are marked by low densities where the minerals are only patchily located throughout the coalfields.

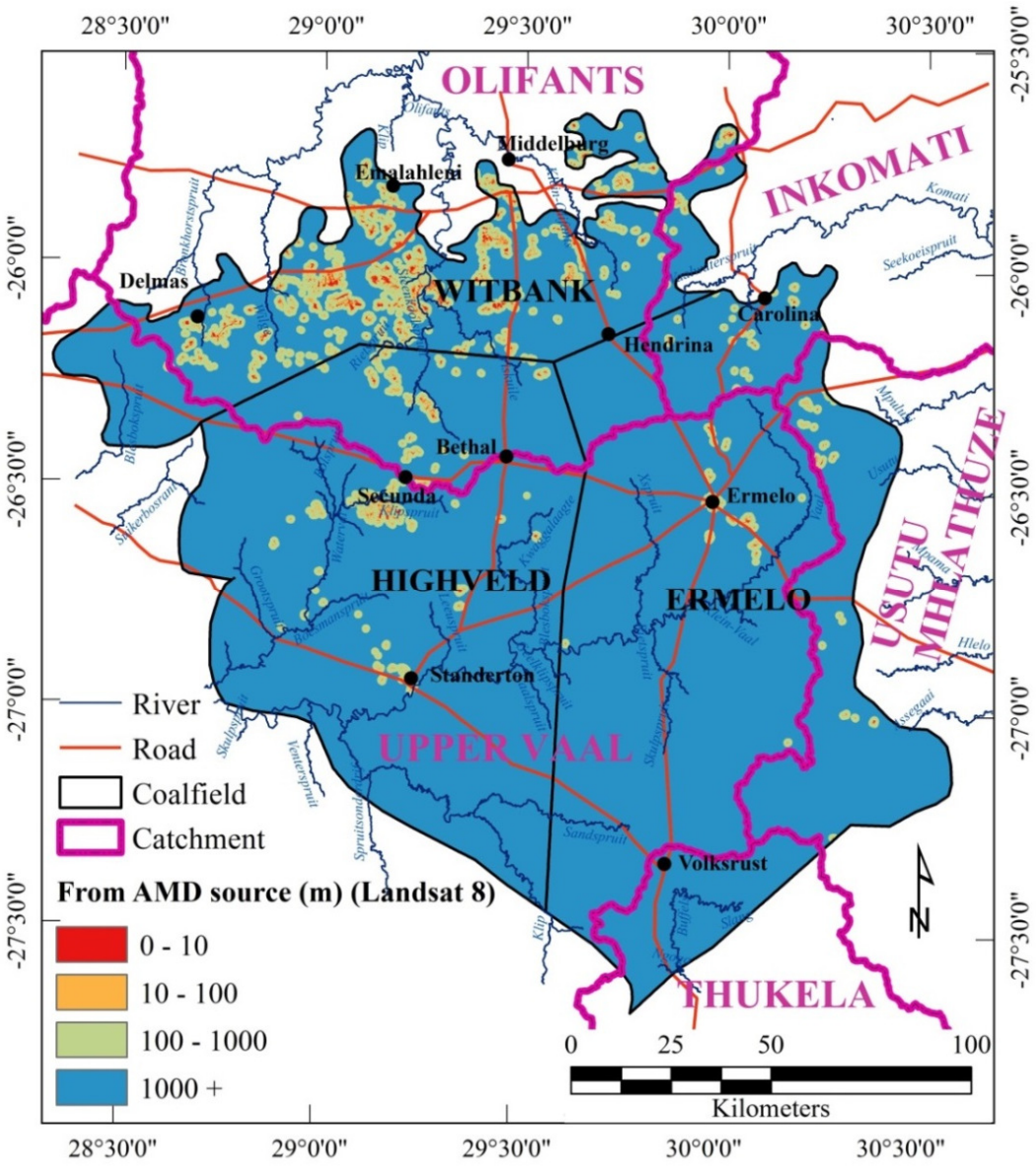

Figure 3.32: AMD surface sources as interpreted from Landsat 8 remote sensing data

Figure 3.33 shows the interpreted Fe-bearing minerals (jarosite, hematite) extracted from Sentinel 2 data respectively and results presented as a function of distance from the pixel that is interpreted to be having these minerals. Similarly, to the Landsat data, the Euclidean distance was implemented in ArcGIS software. The results from interpretation of Fe-bearing minerals on Sentinel 2 data show more pixels with these minerals compared to the Landsat 8 results. This could be because the Sentinel 2 data have more bands which define the absorption features of jarosite and hematite, hence the resolution of detection of these minerals is greatly improved. Also, the grid cell size of Sentinel 2 data is smaller than that of Landsat 8 data which means that more pixels can be classified better without spectral mixing which is attributable to the classification of a larger grid cell size.

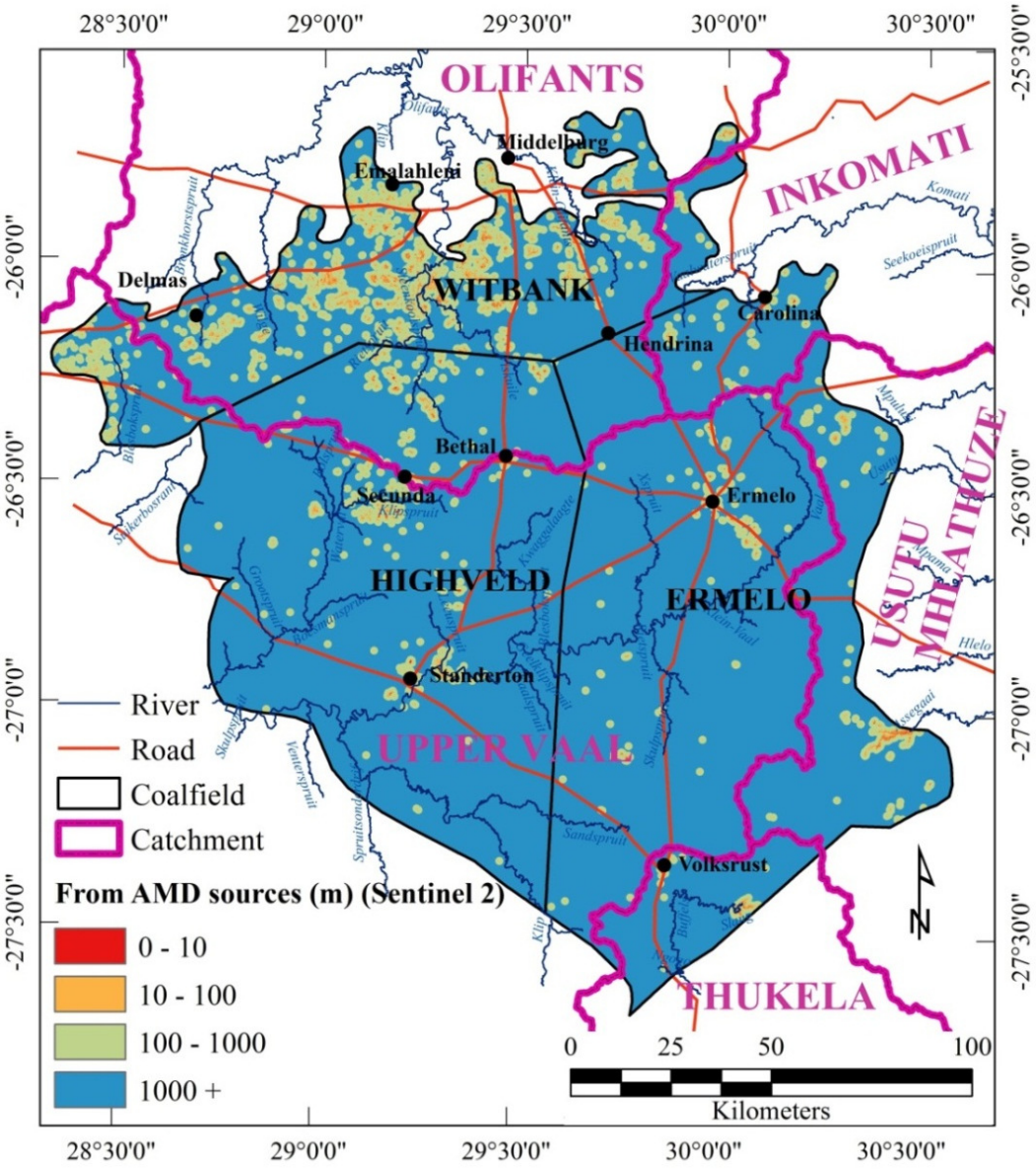

Figure 3.33: AMD surface sources as interpreted from Sentinel 2 remote sensing data

The results from Landsat 8 and Sentinel 2 were combined using the logical "AND" operator to generate one combined interpretation map (Figure 3.34). The logical "AND" operator was chosen because minerals should appear on pixels of both the Landsat 8 and Sentinel 2 datasets. The logical "AND" output results which fuse the two datasets show that the Witbank coalfield is marked by the highest density of the secondary iron-bearing minerals while the Ermelo coalfield has the lowest density. A small section (black polygon in Figure 3.34) of the Witbank coalfield, where the density of pixels is highest was selected for a detailed analysis of the results. Another area (light blue polygon in Figure 3.34) where previous sampling had been done was also selected for comparison with the results of remote sensing interpreting.

Using the area within the black polygon in Figure 3.34, the interpreted jarosite and hematite minerals are shown in red in Figure 3.35a. The area lies south of eMalahleni (black polygon in Figure 3.34)

and covers the Kendal, Ogies, Minnaar and Coalville areas (Figure 3.35a). When the interpreted results are overlain onto the Landsat 8 band 764 combination, it is clear that the mapped jarosite and hematite minerals coincide with some mine discard areas and coal loading terminals (Figure 3.35b).

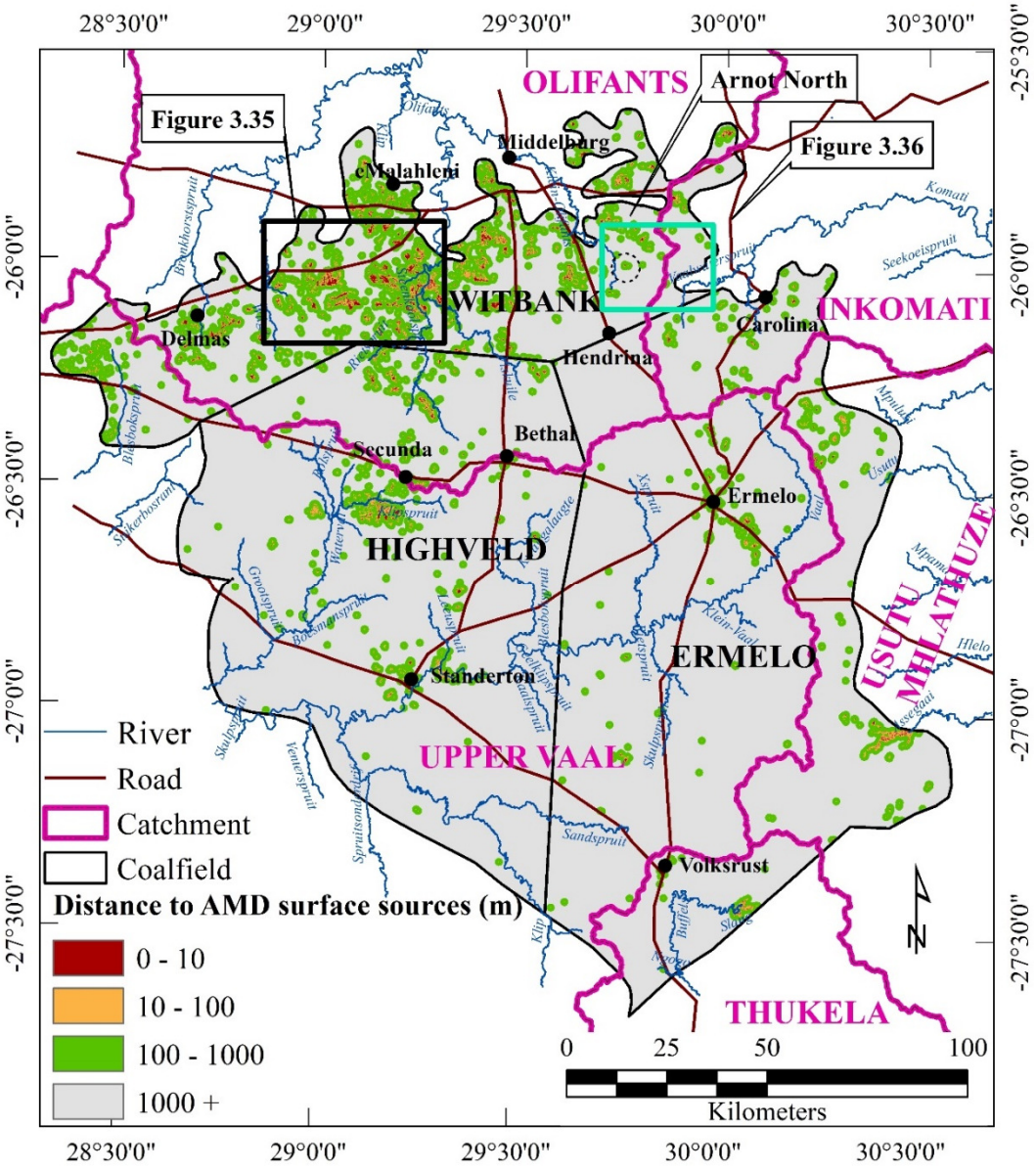

Figure 3.34: Combined results from Landsat 8 and Sentinel 2 results plotted as a function of distance from interpreted AMD surface sources. The areas within the two black polygons are selected for detailed analysis

The interpretation of the hyperspectral survey results covering the active coal mining areas of the Witbank coalfield (Cole *et al.*, 2015) identified most mine discard dumps as potentially acid generating. The approach used in this research are in agreement with these findings and with the finding that several mine discard dumps around Ogies, Minnaar, Coalville and Kendal consisting of secondary iron-bearing minerals (represented in red in Figure 3.35) can be used as proxy as potentially acid generating phenomena.

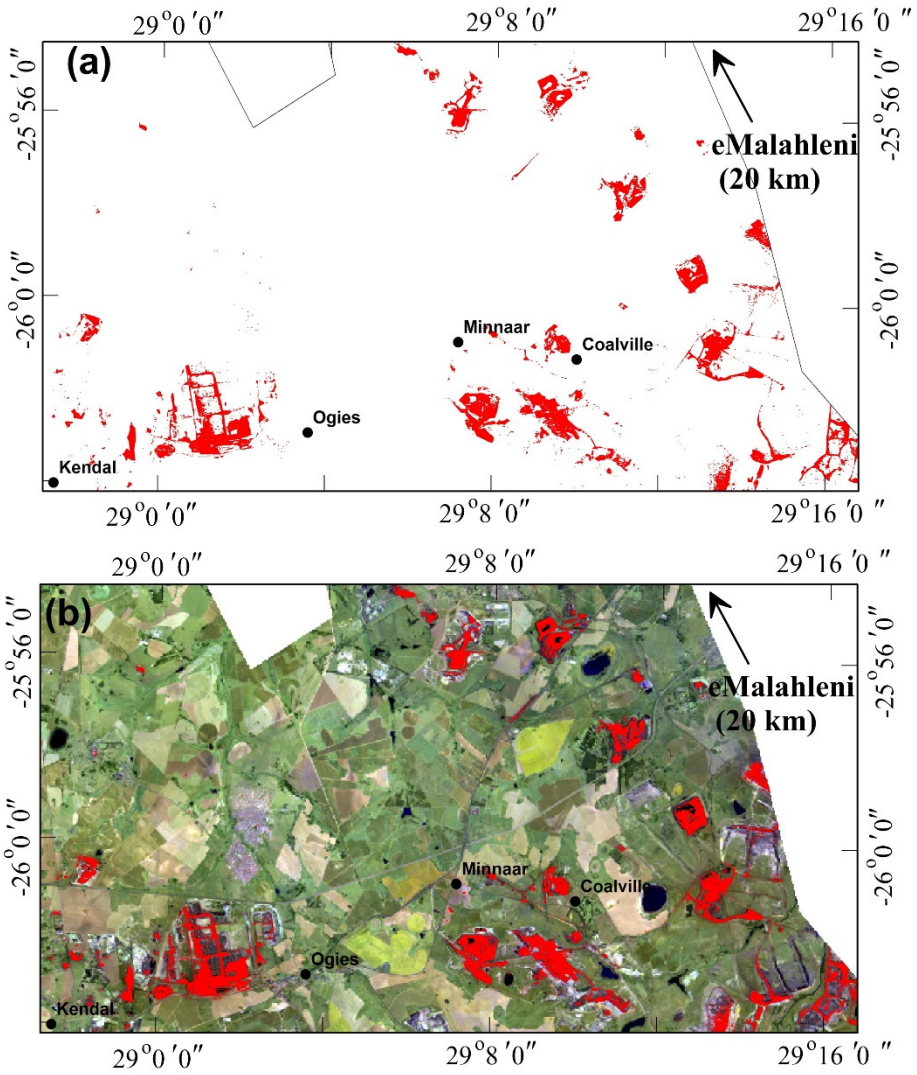

Figure 3.35: Zoomed-in results (a) Iron-bearing minerals: (b) Landsat 8 band combination 764 for a detailed analysis of interpreted secondary Fe minerals

Several mine discard dumps in the Witbank coalfield which were identified as acid generating in a study conducted by Novhe *et al.* (2013) correspond to the mapped jarosite and hematite minerals. This finding is in agreement with the literature which states that the Witbank coalfield currently is the highest producer of coal while the Ermelo coalfield is the lowest (Bell *et al.*, 2001; Hobbs *et al.*, 2009).

To test the validity of the identified AMD sources, Novhe *et al.* (2013) compared the mine discard dumps classified as AMD sources with the dumps identified as acid generating by. Novhe *et al.* (2013) used static tests including paste pH, a neutralisation analysis, acid potential determination and kinetic tests (column leach tests) to identify AMD generating mine discard dumps in the Witbank coalfield. Consequently, the Arnot North Mine discard dump was identified as acid generating. The dump is characterised by high secondary Fe-bearing minerals (Figure 3.36). The results from the remote sensing technique are in agreement with these laboratory tests, thus increasing confidence in the usage of remote sensing data.

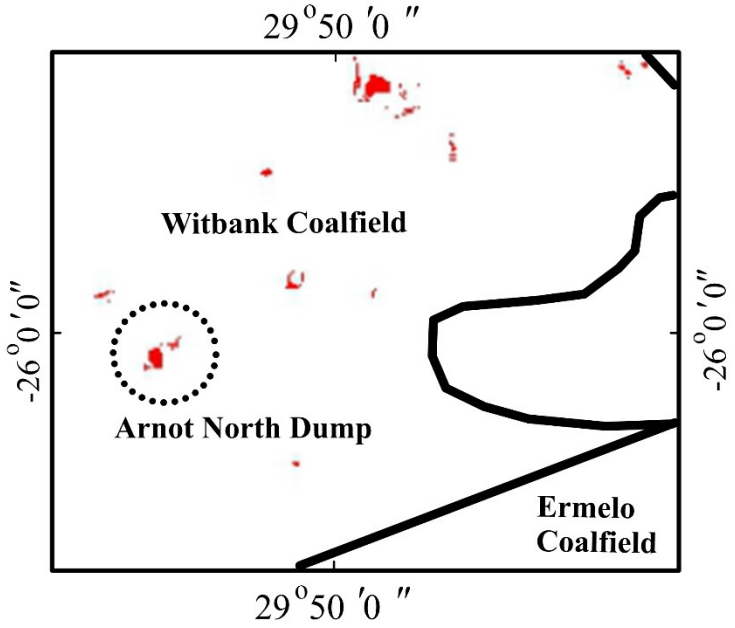

Figure 3.36: Zoomed-in results for Arnot North discard mine dump

A selection of secondary Fe-bearing minerals based on aerial remote sensing data ensured that most of these minerals occurring in waste rocks and mine dumps and those that have been transported and deposited on roads, railway lines, loading bays, wetlands and river banks are all mapped at 30 m resolution. The mapped AMD pollutant sources can be used as an input to an AMD specific groundwater vulnerability assessment.

3.4.5.4 Subsurface sources

In the study area, the Ecca Group is known to generate AMD. The rock formation consists of sandstone, shale and pyrite-rich coal seams covering over 50% of the Witbank, Ermelo and Highveld coalfields. In this research, the Ecca Group rocks extracted from the 1:250 000-scale geology were considered as proxy for potential subsurface sources of AMD pollution (Figure 3.37).

The subsurface sources are mainly found between the central and the northern part of the study area covering the northern parts of Highveld and Ermelo coalfields and the entire Witbank coalfield.

3.4.5.5 Transport and attenuation in the soils

The study areas is found in the main Karoo basin where the amount of soil clay content is considered to be of the important geological/hydrogeological factors which should be used for a groundwater vulnerability assessment (Woodford and Chevallier, 2002).

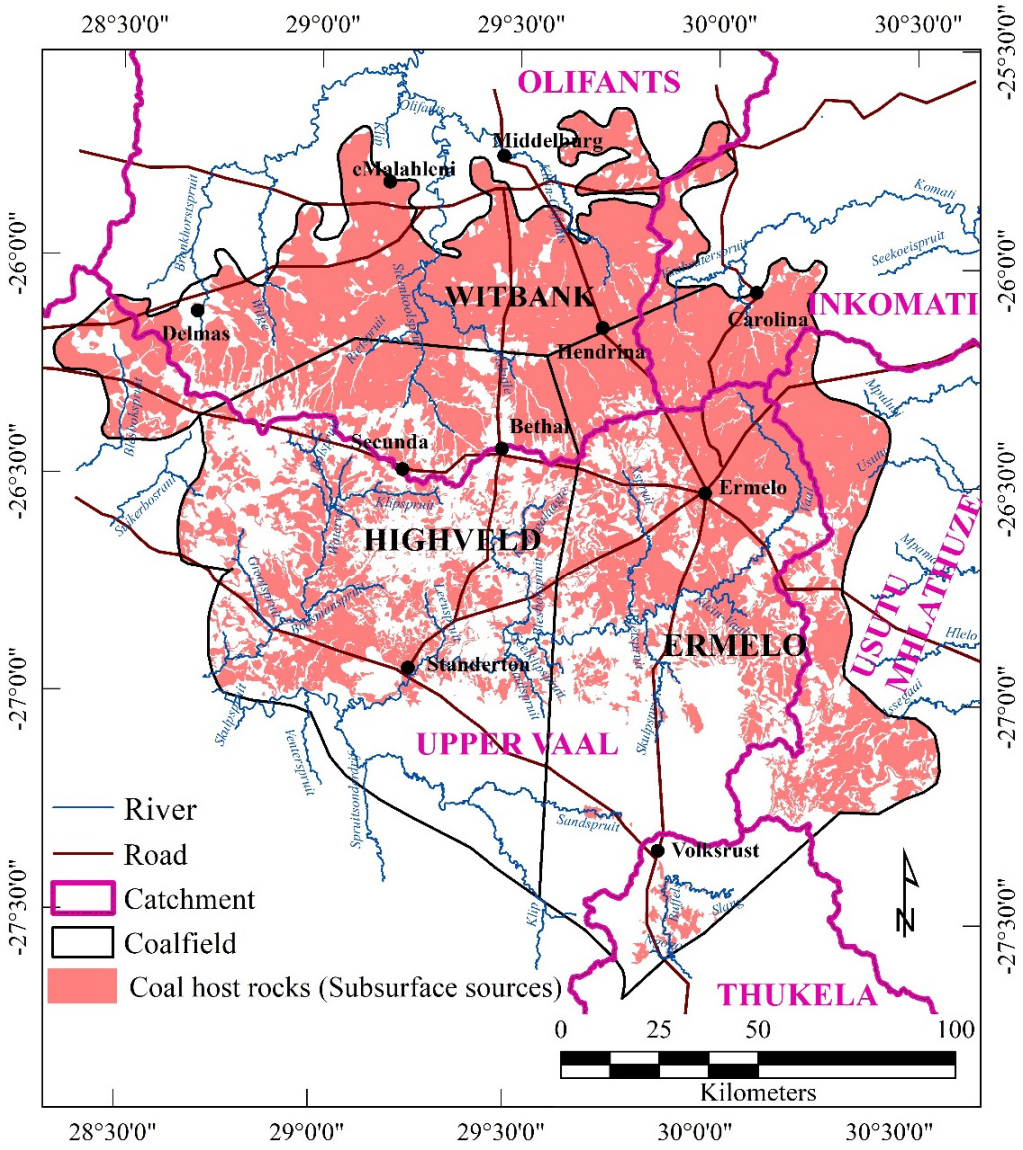

Figure 3.37: Subsurface AMD sources as interpreted from geology data

In this study, only the soil clay content was used as a proxy for the transportation pathway and chemical traps in the soils. Soil data covering the study area at a scale of 1:250 000 were obtained from the Agricultural Research Council Institute for Soil, Climate and Water (ARC-ISCW). The soil types found in the study area range from freely drained apedal, plinthic catena, duplex, Glenrosa and Mispah (Figure 3.38).

The Witbank coalfield is mainly covered by plinthic catena red soils, with small patches of Duplex and freely drained apedal soils. Almost the entire Highveld coalfield is covered by undifferentiated Duplex soils. Red plinthic catena, freely drained soils are also found in the northern part of the Highveld coalfield and small exposures of undifferentiated plinthic catena, Glenrosa and Mispah are found in the south. The Ermelo coalfield is covered by many soil types, ranging from red plinthic catena in the north to Duplex, plinthic, freely drained soils in the centre and small patches of Glenrosa and Mispah soils in the southern to eastern parts of the coalfield.

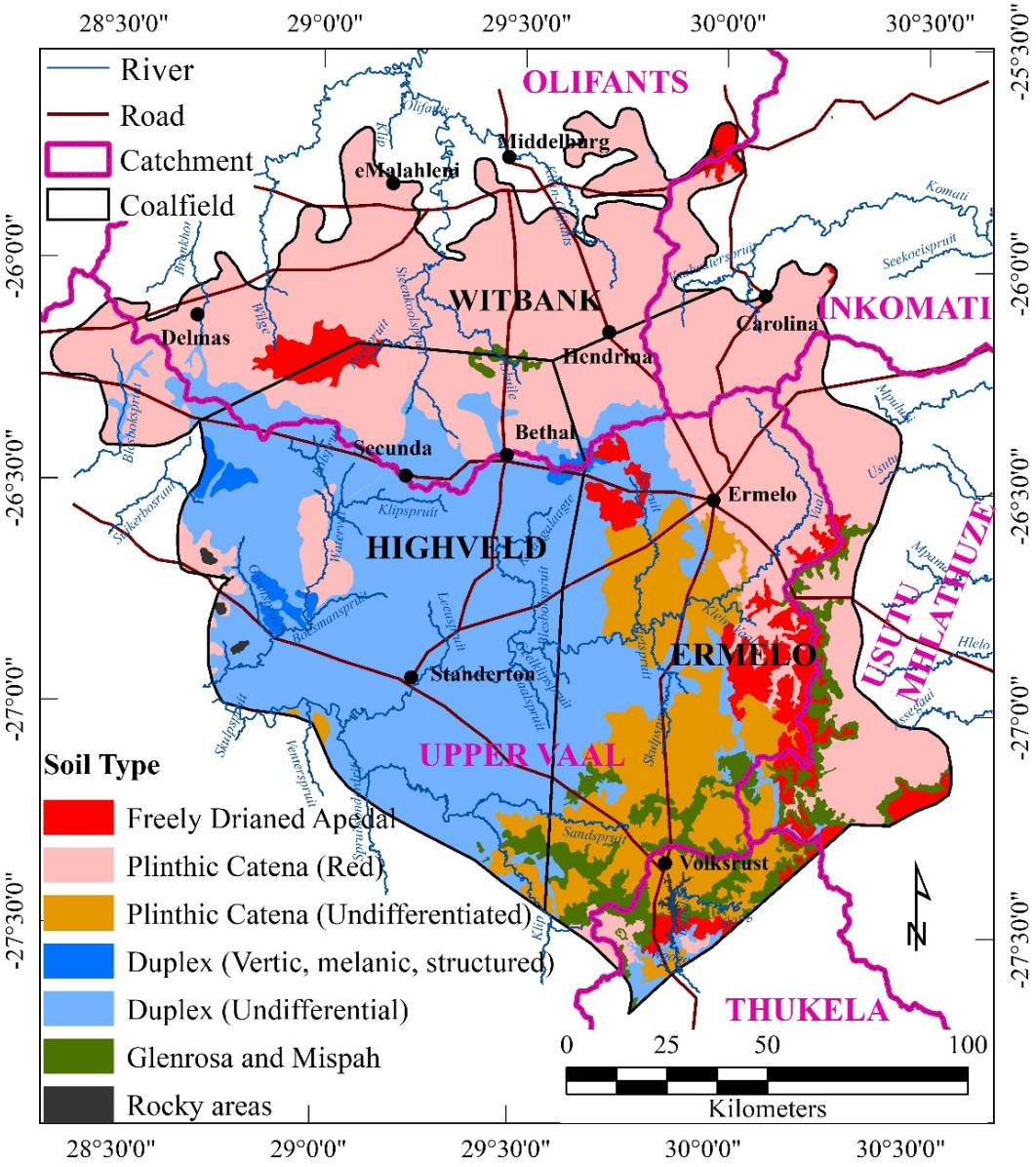

Figure 3.38: Soil types found in the study area

These different soil types are characterised by varied clay content. Table 3.4 shows the various soil types found in the study area with their associated clay content.

In the study area, the soil clay content varies between 9.9 and 51.2% (Figure 3.39). The Witbank coalfield is characterised by soils with a low clay content and thick soil cover. Conversely, the central part of Highveld and Ermelo coalfields is marked by high clay content.

The soil CEC values which can be used as a meaningful surrogate for the overall attenuation processes in soils are a function of clay content and organic content. For the Witbank, Ermelo and Highveld coalfields, no high-resolution organic matter in soil data could be found, hence only the soil clay content will be used.

In order to establish whether various soils with different clay contents have an influence on attenuation (traps) on AMD pollution, laboratory batch leach experiments were conducted.

Table 3.4: Soil types found in the study area and their associated estimated clay content

Soil Type	Soil clay content (%)
Freely Drained Apedal (Red / Yellow)	21 – 51
Plinthic Catena (Red)	12 – 30
Plinthic Catena (Undifferentiated)	12 – 30
Duplex (Vertic, Melanic, Structured)	21 – 30
Duplex (Undifferentiated)	30 – 51
Glenrosa and Mispah	12 – 30
Rocky areas	30 – 43

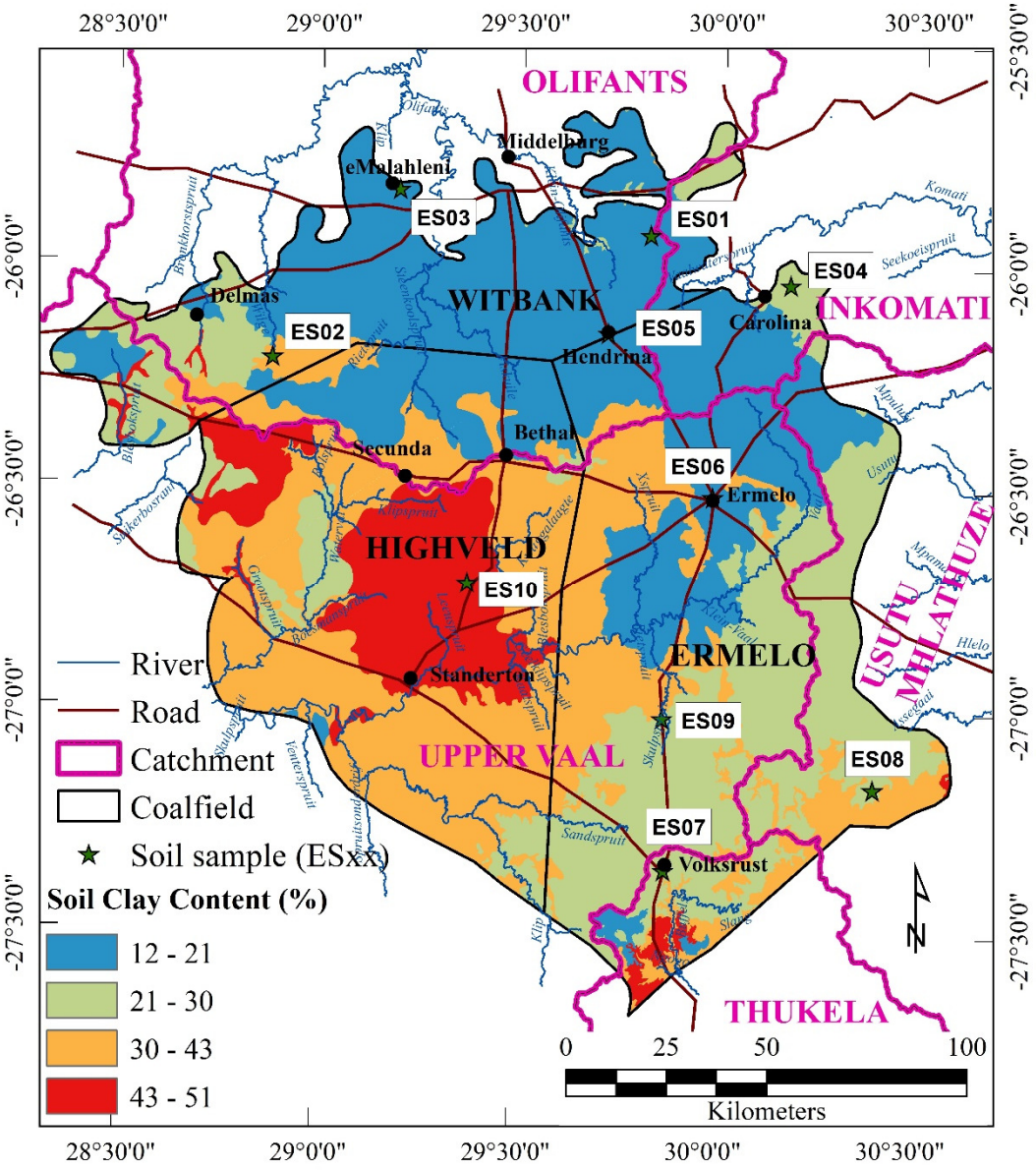

Figure 3.39: Distribution of soil clay content within the study area showing the locations of soil samples collected for the chemical traps experiment

3.4.5.5.1 Materials and methods

The experimental procedure for the batch leach experiment to study the chemical effects of soils on AMD pollution involved the following steps:

1. Ten soil samples with distinct soil parameter values (soil clay content, soil CEC, soil organic matter, soil pH), based on the regional soil map (ARC-ISCW, 2015) of South Africa, were collected from various locations within the study area. The locations of the sampling points on the soil clay content map of the study area are shown as dark green stars in Figure 3.39. Mine water from an abandoned collapsed underground mine which is now decanting AMD was used. The chemistry of the mine water is shown in Table 3.5.

2. The soils were air dried, crushed and sieved down to below the 2 mm particle size. Twenty grams (20 g) of the soil samples was weighed and transferred into 20 high-density polyethylene (HDPE) plastic bottles. Then 400 ml of AMD solution was transferred into ten of the bottles containing the soil samples. In view of control purposes and to provide the background values of the leachate unaffected by AMD, 400 ml of de-ionised water was transferred into the other ten bottles of soil samples. The 20 bottles were then loaded onto an automatic shaker and run for 48 hours as shown in Figure 3.40.

3. After 48 hours, the leachate was collected and tested for pH and electrical conductivity (EC) and filtered prior to chemical analysis using the ICP-MS/DA and discrete analyser techniques. Full analyses can be found in Appendix 1.1 and 1.2.

4. An XRF elemental composition analysis of the samples was done with the overall objective of understanding the mineral composition of each sample in support of the interpretation of the resulting leachate chemistry. A water chemistry analysis was done by checking the effect of soils on various AMD parameters such as pH, Fe, Al, SO_4, Ca, Mg, Cl and Na.

The actual laboratory setup is shown in Figure 3.40 and the properties of the soils used for the experiment are presented in Table 3.6.

Table 3.5: Chemical composition of AMD used for the soil batch leach experiment

	Concentration (mg/l)
pH	2.2
Electrical Conductivity	3 600 mS/m
Fe	118 mg/l
Al	600 mg/l
Mn	35 mg/l
Zn	11.2 mg/l
Cu	1.4 mg/l
Co	3.4 mg/l
Ni	4.6 mg/l
As	0.1 mg/l
Ag	0.00 mg/l
Pb	0.00 mg/l
SO_4	2 865 mg/l
Mg	117 mg/l
Na	3.2 mg/l
Ca	232 mg/l
Cl	0.1 mg/l

Figure 3.40: Experimental setup for determining the attenuation effect of soils on AMD pollution

A scatter plot between soil clay content and regional CEC data (Figure 3.41) was generated for the ten sample locations and the results are displayed in Figure 3.42. The scatter plot shows a very strong positive correlation (R) value of 0.856 between soil clay content and regional CEC values. The fitted regression line (red line) (R^2 = 0.7326) shows that the clay parameter accounts for ~73% of the CEC value. This is in agreement with findings by Lambooy (1984) who also observed a strong positive correlation between the clay content and the CEC for many South African soils. Thus, the soil clay content can be used as a proxy for traps in the soils.

Table 3.6: CEC, pH and clay content of the soil samples used in the batch leach experiment

Soil Sample	Soil CEC (cmol/kg)	Paste pH	Soil clay content (%)
ES01	10.1	4.91	17.6
ES02	10	6.58	31.6
ES03	6	4.88	13.1
ES04	10	4.92	23.7
ES05	12.55	5.93	19
ES06	10.1	6.08	14
ES07	12.55	6.68	27.3
ES08	12.55	5.29	28.5
ES09	15	7.16	40.9
ES10	25	6.65	51.2

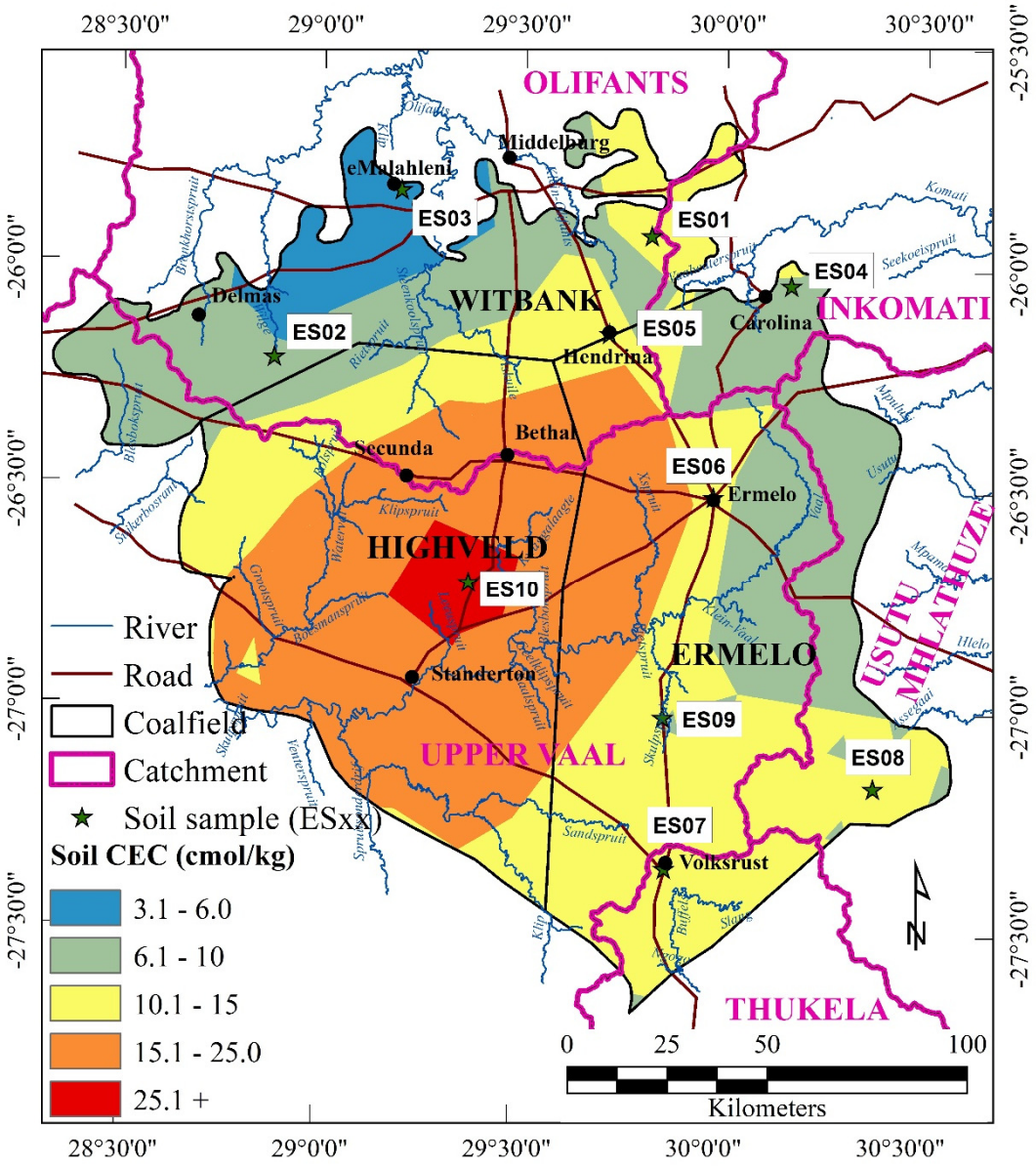

Figure 3.41: Soil CEC map of the study area

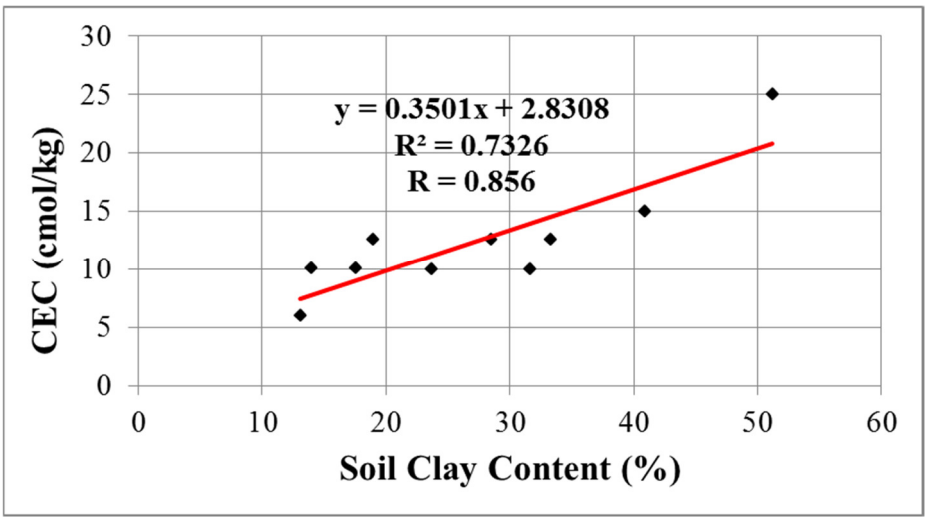

Figure 3.42: Scatter plot between soil CEC and soil clay content

3.4.5.5.2 Experimental results and discussion

After completing the batch experiment, the resulting chemistry of the leachate was analysed to establish whether clay content can be used as parameter for the chemical attenuation of AMD pollutants in the soils found in the Witbank, Ermelo and Highveld coalfields.

Figure 3.43 shows the XRF elemental oxide analysis of the ten soil samples collected within the Witbank, Ermelo and Highveld coalfields. The order has been rearranged according to clay content to facilitate visualisation. It is evident that soils with a higher clay content are associated with the presence of elemental oxide of MgO and CaO and low SiO_2. Full analysis can be found in Appendix 1.3.

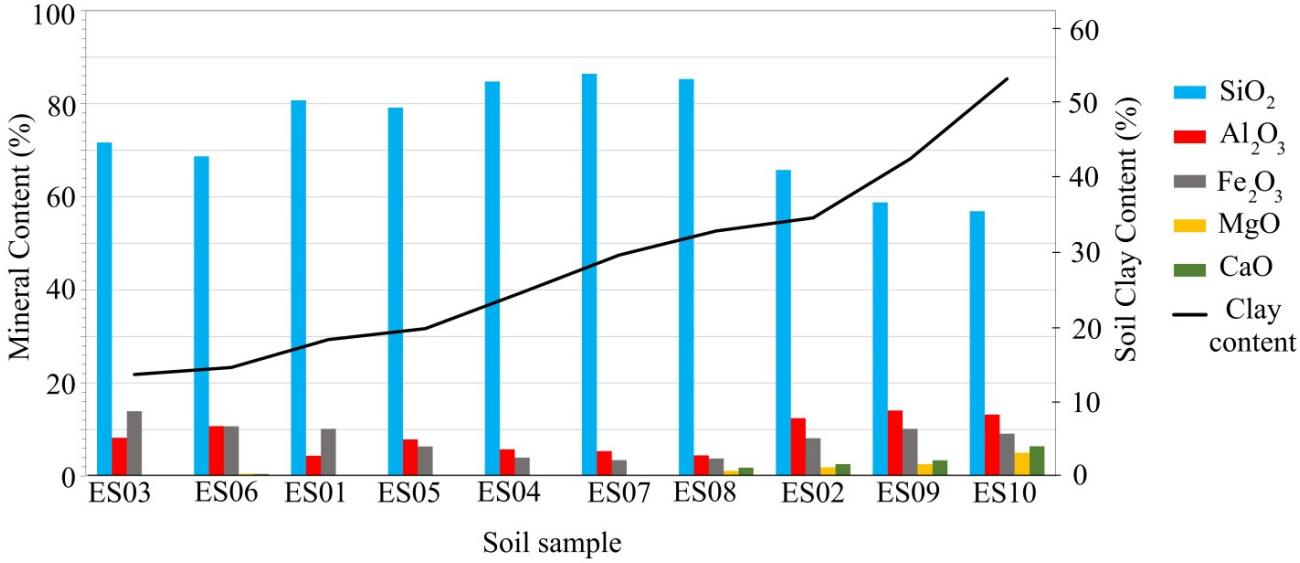

Figure 3.43: XRF Mineralogical composition of the soil samples

Iron

Figure 3.44 shows the effect of introducing AMD to soils under laboratory conditions with reference to the original iron (Fe) concentration of AMD water and de-ionised water which was used as a control from which background leachate values can be compared.

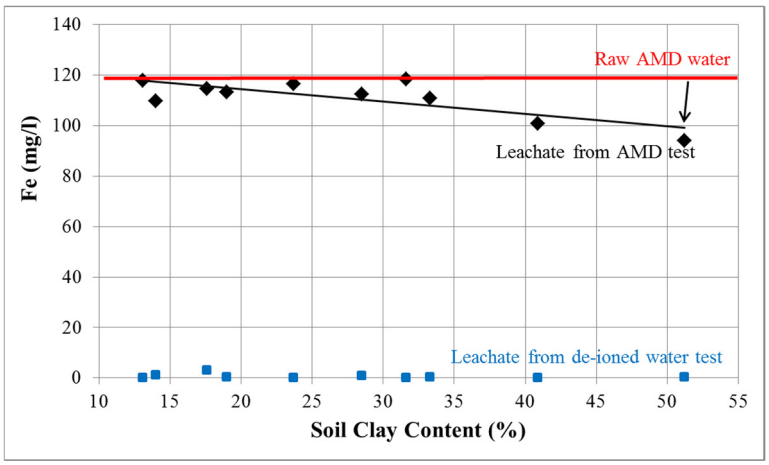

Figure 3.44: Plot of soil clay content against iron (Fe) leachate concentration. The red line marks the initial Fe concentration of the AMD. The blue and black points are leachate concentration values resulting from the effect of adding de-ionised water and AMD to soils respectively

If soils have no influence on the Fe concentration of AMD after being its addition, then the Fe concentration in the resulting leachate would remain almost unchanged. However, from the fitted regression line (black line in Figure 3.44) a change in Fe concentration is noticeable where soils with high clay content show a slight reduction in the Fe concentration by over 20 mg/L in the 24 hour experimental period. However, no significant change in Fe concentration was observed for soils with a lower clay content. A possible explanation for the effect of the clay content on Fe concentration can be deduced by comparing the elemental oxide of soils with a high clay content and those with a lower content. The XRF results show that soils with high clay content (ES07, ES02, ES09 and ES10) also contain a slightly higher amount of exchangeable bases (calcium as CaO and magnesium as MgO) which could be displaced by Fe. Soils with a high clay content have more cation exchange sites which are initially occupied by MgO and CaO, but after addition of AMD, the pH lowers and Fe, which is very soluble at low pH, probably displaces the Mg^{+2} and Ca^{+2} from the exchange sites. The Fe concentration remained unchanged in soils with a lower clay content, meaning that no Fe is removed at a lower clay content as there will be fewer cation exchange sites available to extract the Fe ions from the AMD solution.

Aluminium

No significant change in the Al concentration was observed as can be seen by the fitted regressing line which almost plots on the raw AMD water line (Figure 3.45). This probably shows that at low pH, Al is the main preferred ion that holds strongly on the soil exchangeable sites and is not easily replaced by any ion, accounting for the lack of change in the observed Al concentration.

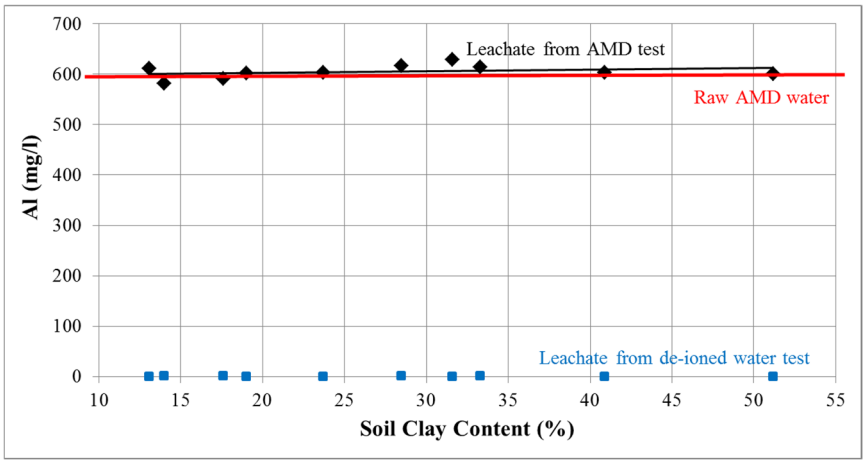

Figure 3.45: Plot of soil clay content against Aluminium (Al) leachate concentration. The red line marks the initial Fe concentration of the AMD and the blue and black points are leachate concentration values resulting from the effect of adding de-ionised water and AMD to soils respectively

Sulphate

The blue points in Figure 3.46 show that the sulphate (SO_4^{-2}) concentration of leachate after batch reaction with de-ionised water is very low (<10 mg/L) compared to the leachate SO_4^{-2} concentration produced after adding AMD to soils of varied clay contents. When AMD is added to the soils, the SO_4^{-2} concentration decreases slightly with increasing clay content but is in the same order of magnitude. This may mean that the effect on SO_4^{-2} concentration is not too pronounced across soils of varied clay content. This can also be seen by the regression line (black line in Figure 3.46) plotting very close to the raw AMD line. The decrease in SO_4^{-2} concentration in the leachate with increasing clay content could be explained by the fact that soils with a high clay content have a strong ionic bond which prevents the mobilisation of SO_4^{-2} into solution. At a low clay content, the ionic bonds are weaker and results in the desorption of SO_4^{-2} ions into solution, resulting in an increase in the SO_4^{-2} concentration. This relationship between SO_4^{-2} concentration and clay content was also observed by Tabatabai (1987).

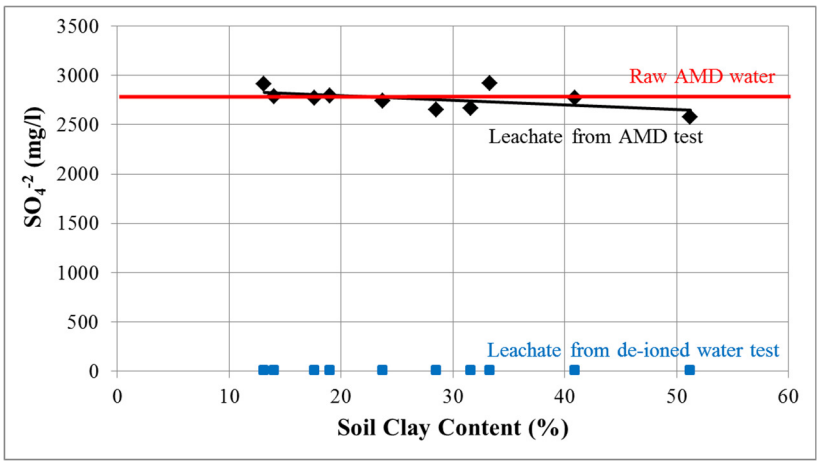

Figure 3.46: Plot of soil clay content against Sulphate (SO_4^{-2}) leachate concentration

Thus, the soils were unable to attenuate SO_4^{-2} significantly in AMD conditions to which they had been subjected. In addition, the SO_4^{-2} concentration remained almost constant across all clay content values within the ranges of the ten samples. This may mean that SO_4^{-2} is slightly conservative across soils of varied clay content. Translating these findings to groundwater vulnerability, it appears that, irrespective of the clay content value of the soil, sulphates will pass through the soils with very little chemical attenuation. Thus, this property of SO_4^{-2} makes it a possible natural tracer of AMD pollution.

Magnesium and calcium

For soils with a clay content greater than 31%, magnesium (Mg) and calcium (Ca) ions are released in solution when AMD is added to soil in the batch leach experiment. This is reflected by an increase in Mg (Figure 3.47) and Ca (Figure 3.48) concentrations above the original concentration of AMD. This could be because these exchangeable bases were involved in ion exchange processes which liberated them into solution as observed by the increase in their concentration in the leachate. Below 31% clay content, Mg and Ca concentrations remain unchanged after the batch leach experiment, as shown in Figure 3.47 and Figure 3.48 respectively.

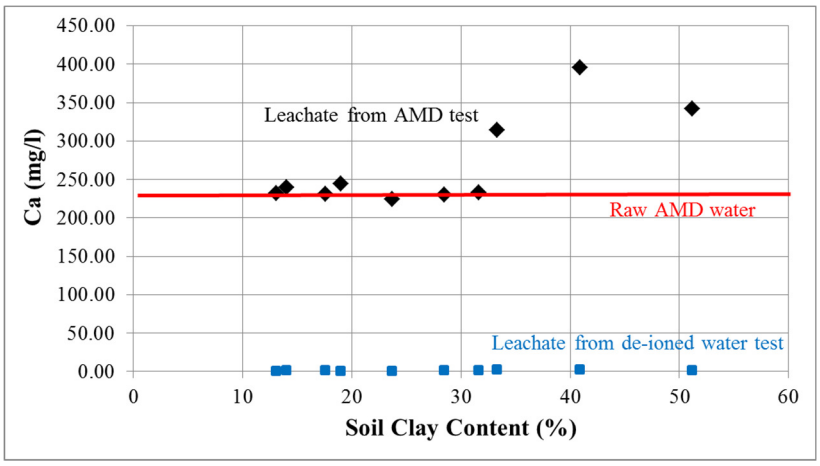

Figure 3.47: Plot of soil clay content against leachate Calcium (Ca) concentration

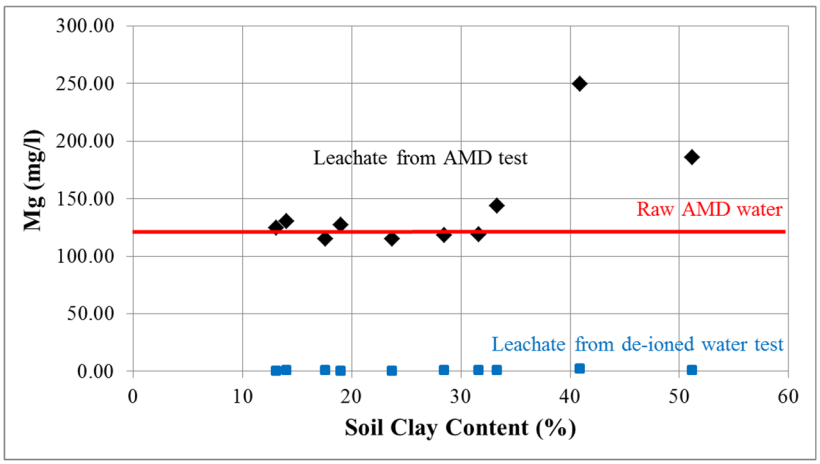

Figure 3.48: Plot of soil clay content against leachate Magnesium (Mg) concentration

Sodium

No change in the response of various soils in terms of sodium (Na^+) concentration was observed, as reflected by the similarity in the response curves when soils are subjected to AMD and de-ionised water (Figure 3.49). The addition of AMD only increased the Na^+ concentration by a factor which was preserved across all soil samples regardless of clay content. A possible explanation could be that Na^+ ions did not partake in any exchange reactions during the time frame of the batch leach experiment. By considering the exchange affinity of Na^+ ions (on Equation 3.4) in strongly acidic conditions such as that found in the batch experiment, Na^+ is found at the edge of the list where the exchange sites are weakly held (Mani, 2014).

$$H^+ \geq Al^{3+} > Ca^{+2} > Mg^{+2} > NH_4^+ = K^+ > Na^+ \qquad 3.4$$

Held more strongly Held more weakly

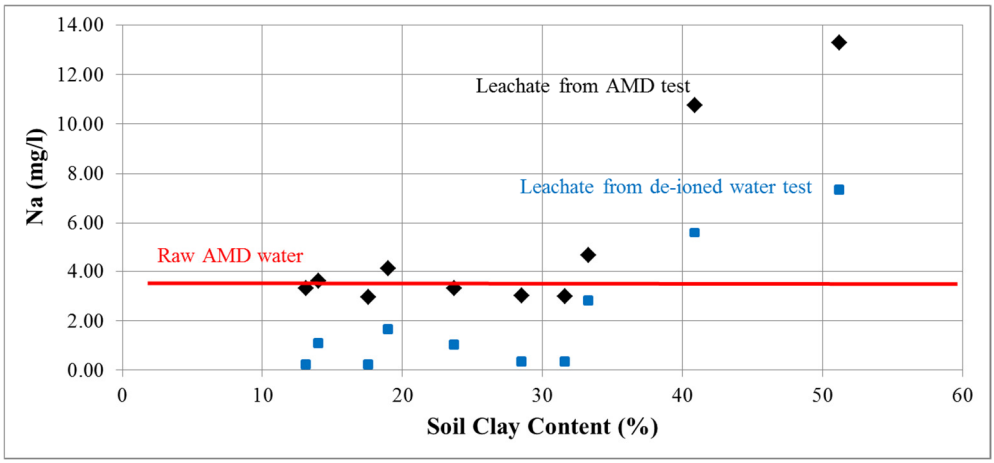

Figure 3.49: Plot of soil clay content against leachate Sodium (Na) concentration

Summary

In summary, the batch leach experiment revealed that soil clay content plays a role in attenuating of some of the pollutants found in AMD. Soils with a high clay content (greater than 31%) were able to reduce the concentration of iron and sulphates from the AMD as the leachate concentrations of magnesium and calcium increase. This could be explained by an exchange reaction where iron displaced magnesium and calcium from soil exchange sites. In the development of groundwater vulnerability specific to AMD at a coalfield, these experimental findings will be incorporated, where clay content will be used as proxy of the chemical attenuation of AMD by soils.

3.4.5.6 Preferential pathways

The information on regional faults was extracted from the 1:250 000-scale geology maps published by the Council for Geoscience and the lineaments (fractures, dyke) were interpreted from the regional airborne magnetic data and used as proxy for preferential pathways at a regional scale. Regional airborne magnetic data acquired at a height of 150 ± 15 metres above the ground with 1 km line spacing along an E–W direction was accessed from the Council for Geoscience geophysics database. Figure 3.50 shows the residual magnetic field intensity map with an interpretation of the lineaments and possible faults.

Different processing techniques were applied to the magnetic data in order to achieve the objectives of mapping possible preferential pathways within the Witbank, Ermelo and Highveld coalfields. These techniques included the vertical derivative and analytic signal derived from the total magnetic intensity map of the area. The first vertical derivative and the analytic signal are high-pass filters which enhance lineaments and geological contacts at a shallow depth. The airborne magnetic data were interpreted to identify dykes, lineaments and magnetic source bodies that exercise some form of control over the migration of AMD pollutants in the subsurface. The magnetic anomalies range from dipolar (low–high) positive magnetic types to subdued and high linear anomalies. The subdued to high linear anomalies were interpreted as dolerite dykes and magnetic mineral-filled fracture zones (blue lines in Figure 3.50).

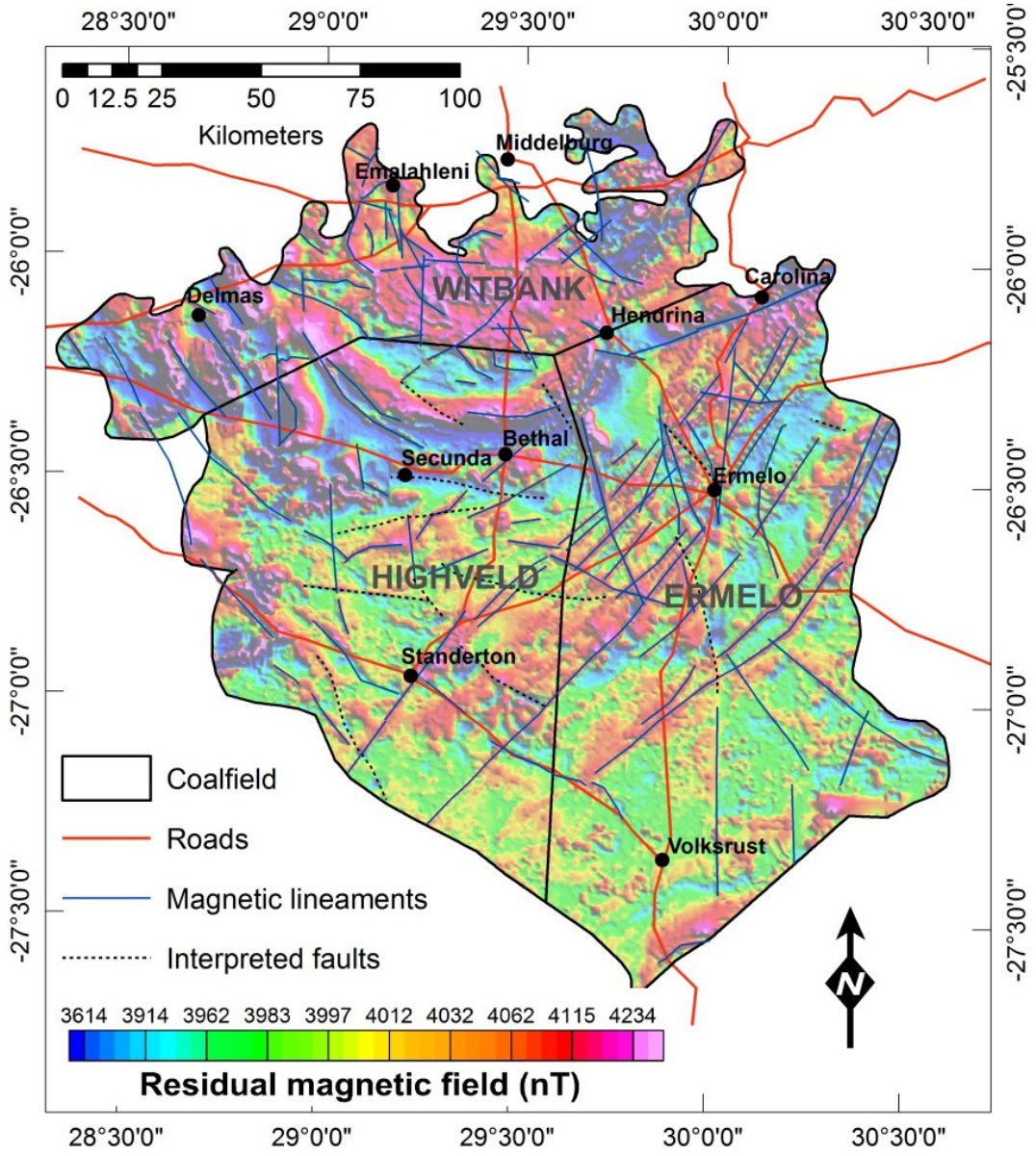

Figure 3.50: Residual magnetic field with lineaments and interpretations of the faults

The dipolar (low–high) magnetic anomalies in the northern part of Highveld coalfield extending into the Witbank coalfield could be attributable to dolerite sills which are generally characterised by a high content of magnetic minerals compared to the surrounding sandstones and shales found in these coalfields (Figure 3.51). The analytical signal image clearly shows these sills to be very high-amplitude anomalies. Faults were also interpreted as these features appear on magnetic maps as an abrupt break or the displacement of an otherwise continuous geological feature. Some appear as sudden truncation of geological features. No in-depth study to discern whether the linear anomalies are attributable to dykes or fractures was done because the effects of these geological features on groundwater pollution migration is the same, in that they both act as conduits that transport pollution from the surface to the groundwater.

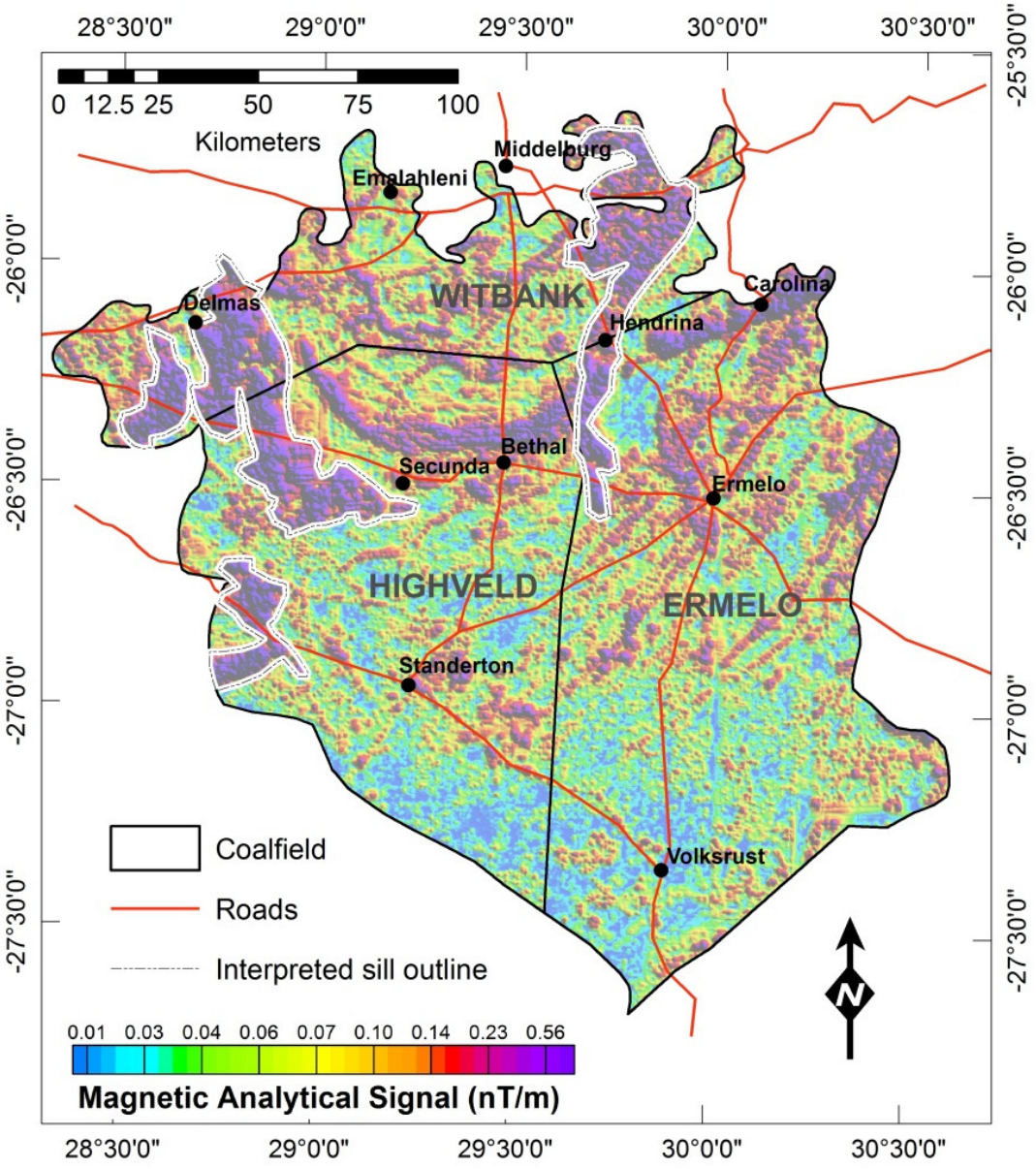

Figure 3.51: Magnetic analytical signal showing the interpretation of the sills

Figure 3.52 shows the combined interpretation of possible preferential conduits as mapped from regional magnetic data for the three coalfields. The interpreted sills are shown in gold and lineaments are represented by long lines blue lines. Faults, as interpreted from magnetic data, are represented by black dotted lines.

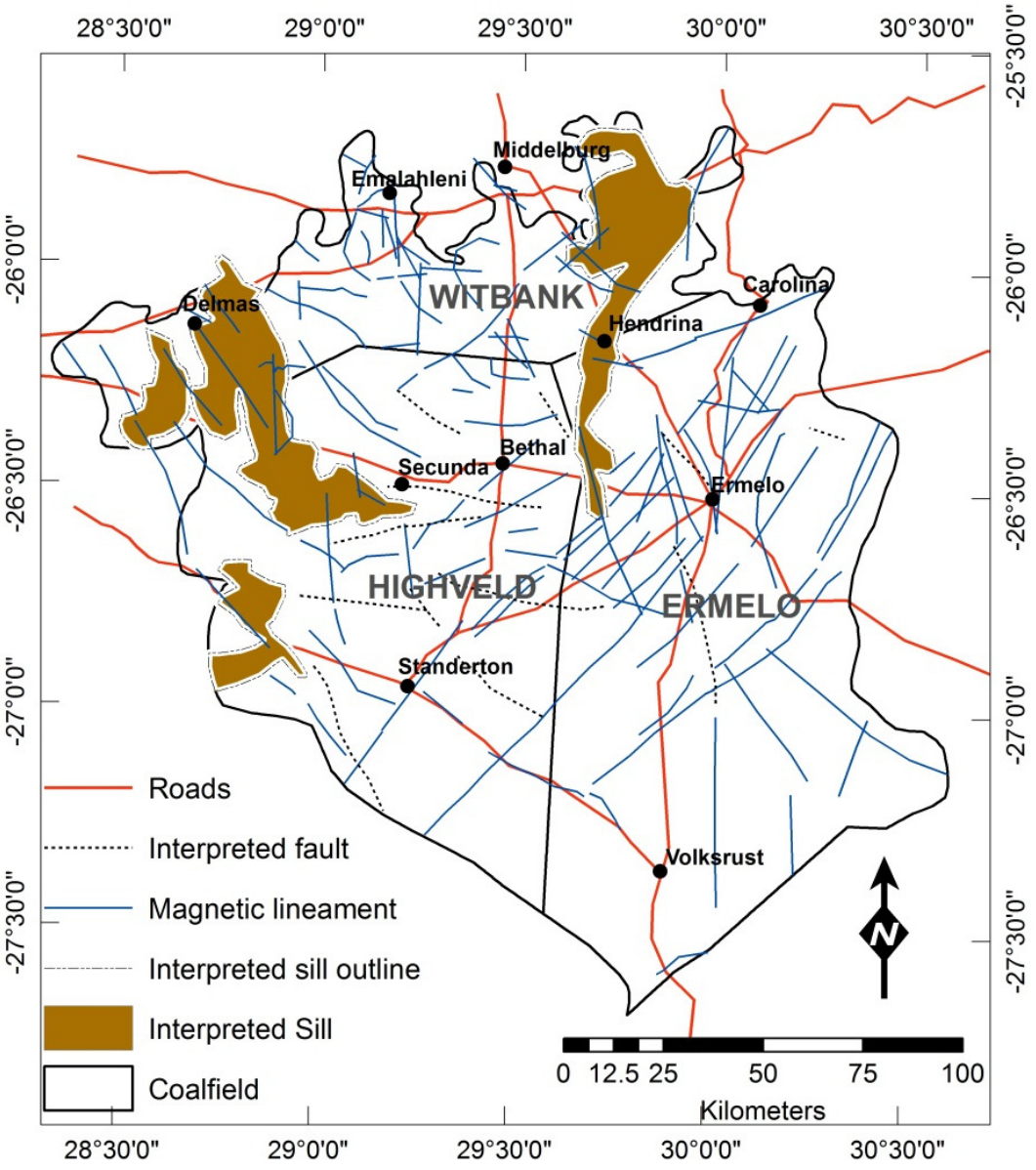

Figure 3.52: Magnetic interpretation of the possible preferential pathways

These pathways interpretations were converted into a Euclidean distance, shown in Figure 3.53. The ArcGIS spatial analysist tool was used to generate the Euclidean distance which shows distance from the interpreted lineaments and sill boundaries. A high density of lineaments is found around the town of Ermelo and very few lineaments were interpreted in the southern part of the study area.

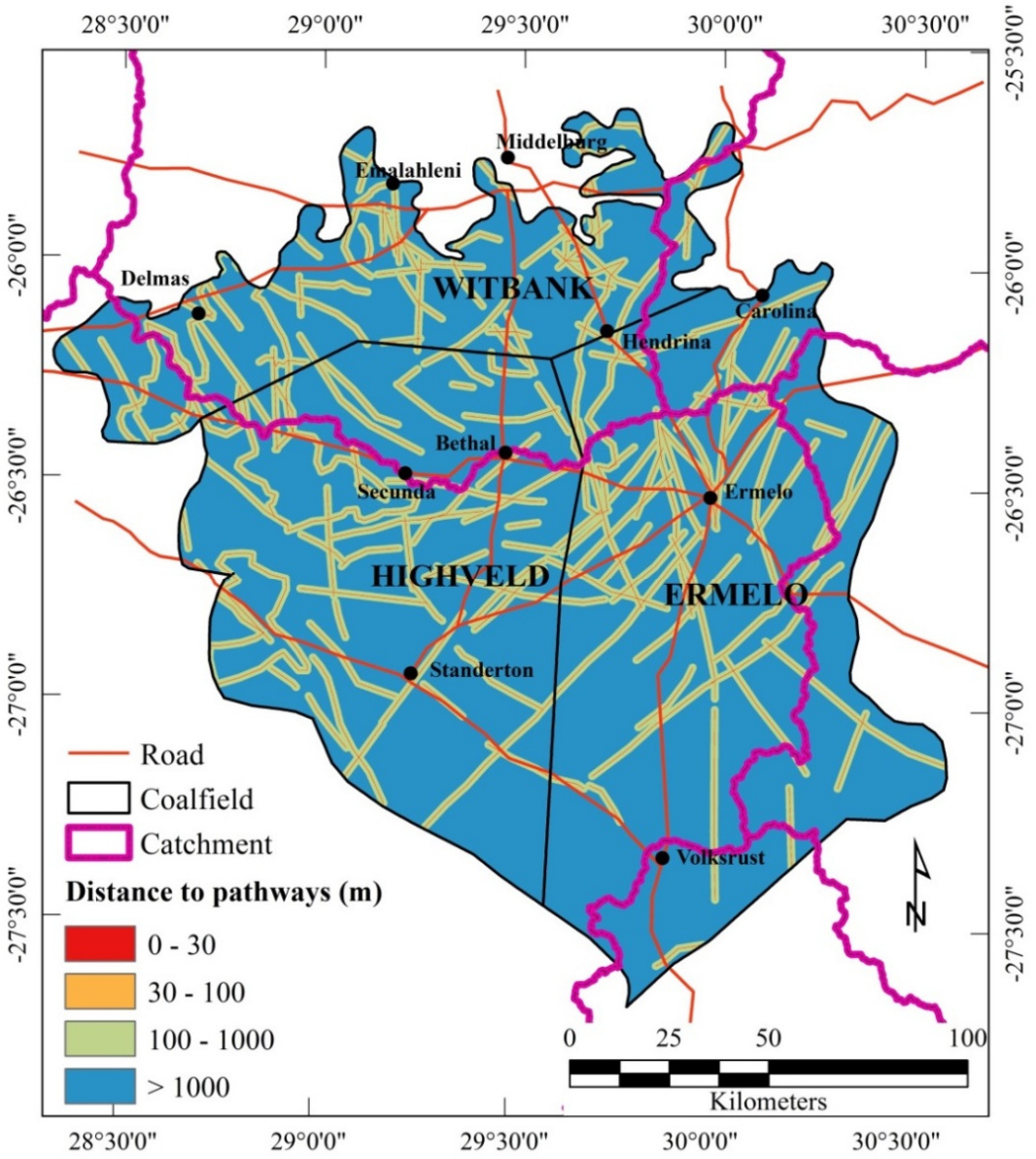

Figure 3.53: Possible regional preferential pathways for AMD represented as a distance map

3.4.5.7 Rock permeability

For this study, rock permeability values were obtained from Wolff (1982) for all the different rock types found in the study area and used to produce a relative permeability distribution map (Figure 3.54). The rock permeability of various rocks in the study area varies between 10^{-11} to 10^{-2} cm^2 were expressed as relative values between 1 and 10, where 10 represents the rocks with the highest values and 1 represents those with the lowest values.

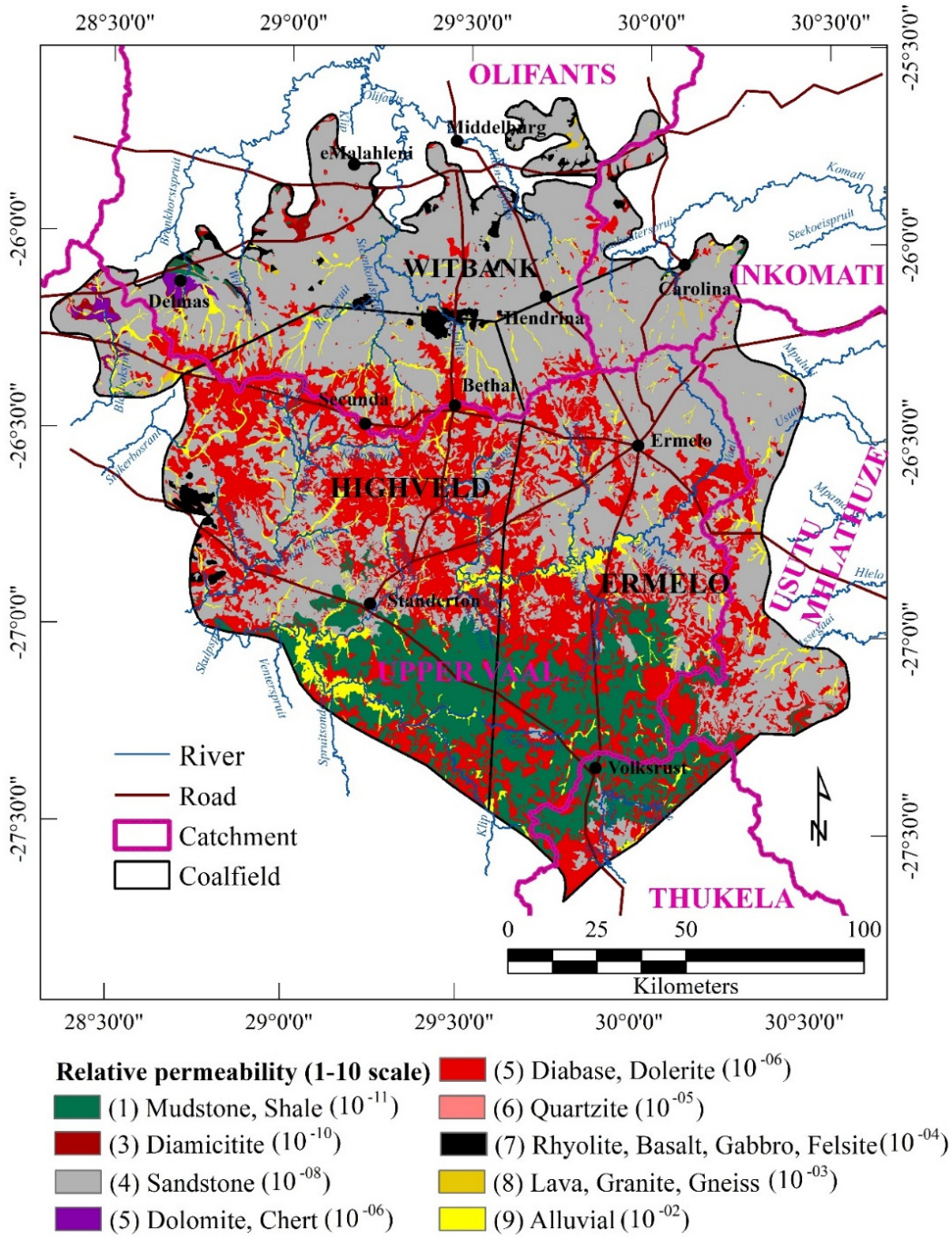

Figure 3.54: Rock permeability map generated from the literature, reflecting the values of the rocks found in the study area. Values in brackets are in cm^2

3.4.5.8 Hydraulic conductivity

No pump testing was done in this research with the hydraulic conductivity values having been extracted from literature (Freeze and Cherry, 1979; Domenico and Schwartz, 1990; Barnard, 2000) for various rocks within the study area and assigned to each rock formation. The values for aquifer hydraulic conductivity ranges between 10^{-11} and 10^{-2} m/s and were expressed as relative values between 1 and 10, where 10 represents the rocks with the highest values and 1 represents those with the lowest values. Figure 3.55 shows the relative aquifer hydraulic conductivity values for various rocks.

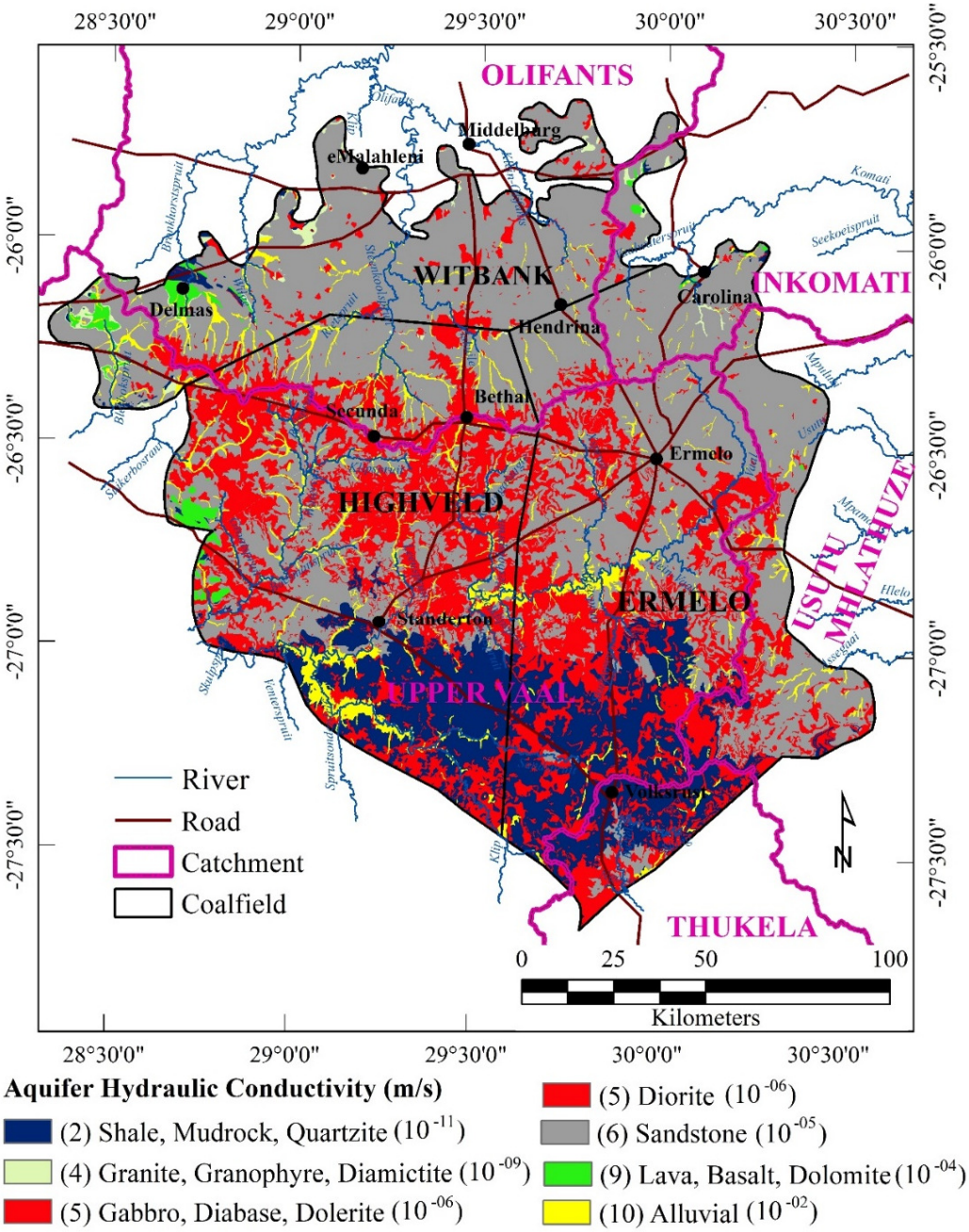

Figure 3.55: Aquifer hydraulic conductivity map of the study area

3.4.5.9 Depth to water table

The water level data covering the study area was obtained from the South African Department of Water and Sanitation (DWS) National Groundwater Archive database where 4 927 boreholes with depth to water table values are recorded within the study area. The ArcGIS spatial analyst kriging technique was used to produce a depth to water table gridded map (Figure 3.56). The central part of the study areas covering both the Highveld and the Ermelo coalfields is characterised by a very shallow depth to water table. A depth to water table below 15 m is found in the northwestern part of the Witbank coalfield around Delmas.

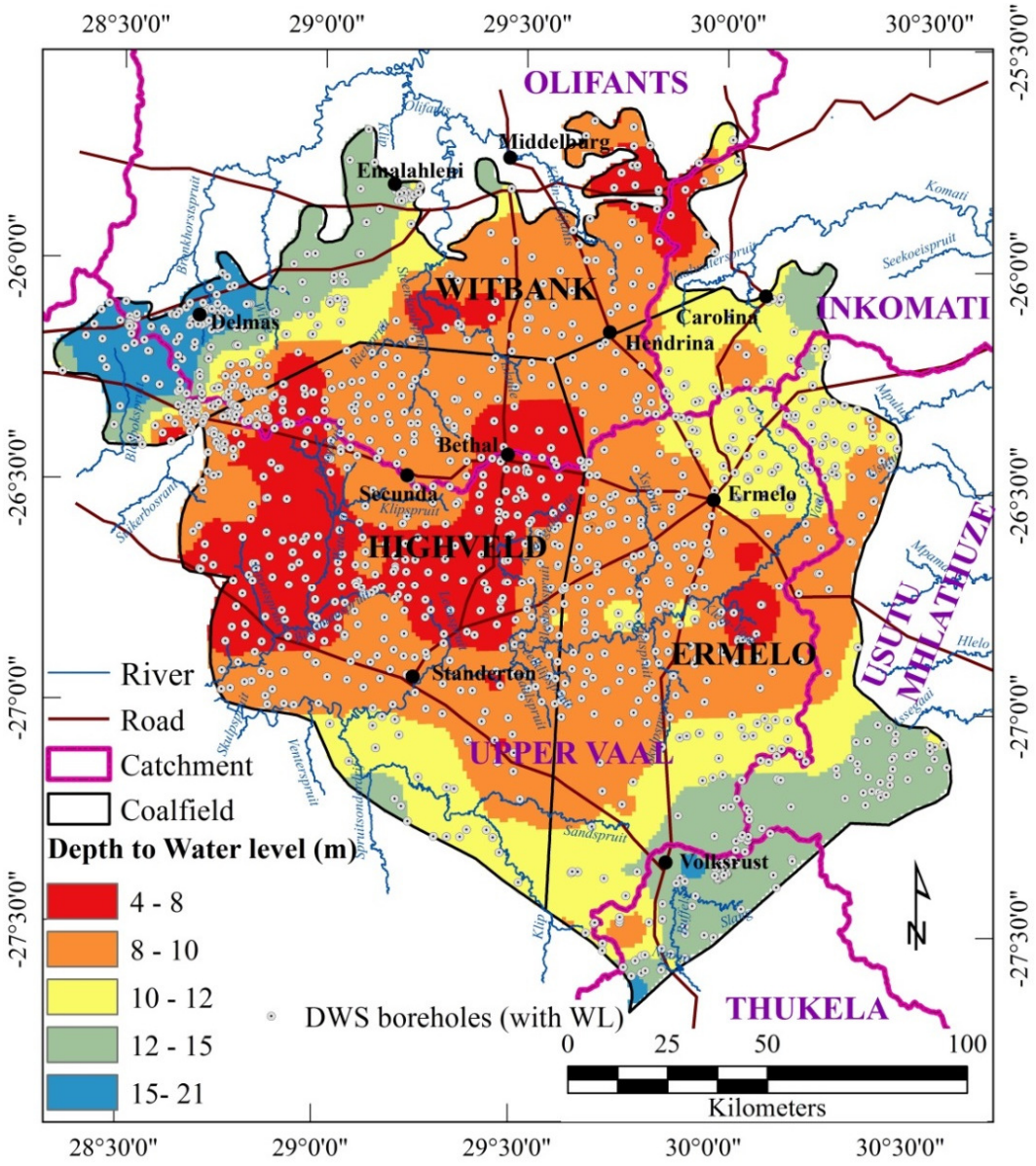

Figure 3.56: Depth to water level map derived from monitoring borehole information from the Department of Water and Sanitation

3.4.5.10 Rock-AMD reactivity

In order to understand how AMD interacts chemically with various rocks found in the Witbank, Ermelo and Highveld coalfields, various laboratory experiments were conducted. The overall goal of the experiments was to study how AMD interacts with various rocks under the saturated and unsaturated conditions which typically prevail in the subsurface. Moreover, the tests focussed on clarifying the interactions between various rocks and the AMD ranking reflecting their ability to extract AMD pollutants and their buffering capacities. The results from the ranking of various rocks in terms of their ability to extract AMD pollutants would be used as an input to the SPT approach being developed in this research. The experiment attempted to mimic the natural attenuation of the subsurface with reference to rock-AMD interaction. Two column leach experiments for saturated and unsaturated conditions were set up for this study.

3.4.5.10.1 Materials and methods

The experimental procedure for the rock-AMD interaction study involved the following steps:

1. Fifteen representative fresh rock samples weighing 5–8 kg per sample were collected from various outcropping major lithologies and one sample was collected at a coal mining waste rock dumping site within the Witbank, Ermelo and Highveld coalfields. The rock samples were milled and sieved to below 2 mm particle size. A full mineralogical analysis of the samples was done with the overall objective of understanding the mineral composition of each sample and selecting five classes representing the general mineral distribution of the whole coalfield area. Although reducing the sample sizes statistically would increase the error when dealing with spatial distribution over a large area, financial constraints dictated the restriction of the number of samples to five.
2. Mineral and elemental analyses using XRF, XRD and petrographic examination were carried out on the 15 samples. The results will be discussed and a justification of selection of the five samples given.
3. After selecting five samples for the column leach test, each sample was split into two for two experiments (saturated and unsaturated). Then, the samples were fed into separate columns, thus amounting to a total of five columns for the saturated and five columns for the unsaturated conditions. Figure 3.57 presents a schematic diagram of the setup of the columns for the saturated and unsaturated experiments.
4. The saturated column test was set up as shown in Figure 3.57a, where AMD was introduced from the bottom and passed through the rock sample to ensure its complete submersion in AMD and the resultant leachate was analysed weekly until an appreciable comparison could be made between the various rocks samples.
5. The unsaturated column test was set up as shown in Figure 3.57b, where AMD occasionally fed from the open top and passed through the rock sample react with the AMD in the presence of atmospheric air to mimic unsaturated conditions. The resultant leachate was analysed weekly until such time as an appreciable comparison could be made between the various rocks samples.
6. Mine water used in the soil batch leach experiment was also used for the rock-AMD reactivity experiment.

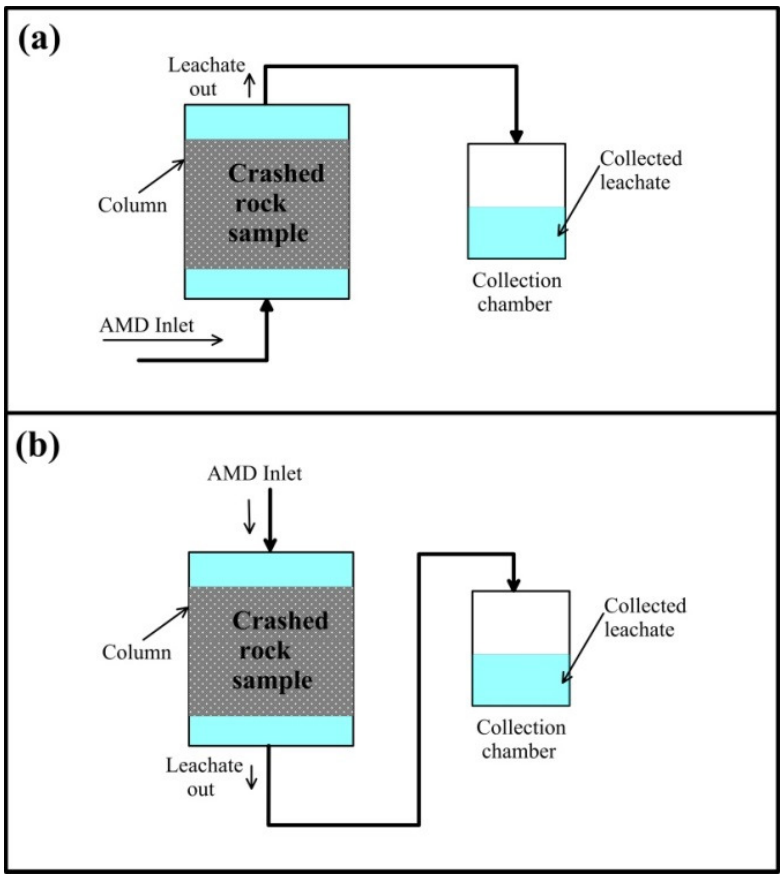

Figure 3.57: Schematic laboratory setup for (a) saturated and (b) unsaturated column tests

7. Originally, the experiment was designed to extract the mine waste material from a mine in the study area containing pyrite and to use it to generate AMD in the laboratory to be fed into each column. This plan was abandoned after realising that the output from the AMD generating column was variable for each of the AMD generating columns, a result that would complicate the subsequent interpretation of the reactions. The laboratory setup before modifications was made is shown in Figure 3.58. The section of the experiment highlighted by a yellow dotted line was replaced by a container of AMD which had been collected from a decanting abandoned underground mine in the Witbank coalfield. The chemical analysis of the AMD is shown in Table 3.5.

8. The parameters for the actual experiment are as follows: column height – 45 cm, column diameter – 11 cm, crushed rock sample weight – 1.38 kg. The experiments were run for 90 days. The flow rate for the saturated experiment was maintained at 0.01 ml/min to ensure that the column was completely saturated while at the same time allowing enough time for the reactions to occur.

9. The analyses of the leachate from the collection include: pH, TDS, EC, alkalinity, Al, Mn, SO_4^{2}, Ca, Mg, Na, K, N, Cl and others using ICP-MS and IC analytical techniques. A full chemical

analysis can be found in Appendix 2.1 and 2.2 for saturated and unsaturated conditions respectively.

10. The actual laboratory setup is shown in Figure 3.58.

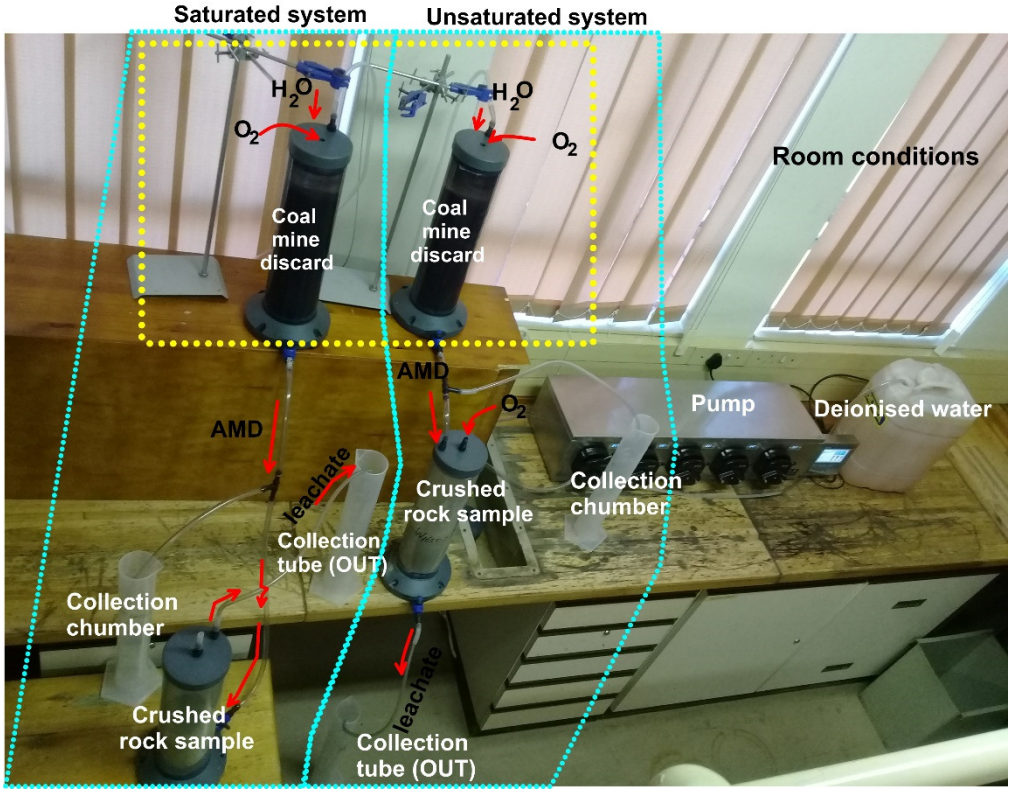

Figure 3.58: Experimental setup for determining the attenuation effect of vadose zone and in the aquifer system. The yellow section was replaced by AMD collected from the field

3.4.5.10.2 Sample mineralogy results and discussions

In the X-ray diffraction machine the samples were scanned from 2 to 70° 2θ $Cu_{k\alpha}$ radiation and phase concentrations were determined as semi-quantitative estimates using relative peak height/area proportions. The results for the 15 samples were plotted on a bar graph in order to compare and classify the mineral compositions of the various rock samples. Sample WITS01 uniquely contained almost equal proportions of silicates, plagioclase, quartz and chlorite; thus, this sample was selected. A full XRD analysis can be found in Appendix 2.3.

Samples WITS07 and WITS14 were composed almost entirely of quartz and dolomite respectively (Figure 3.59). These rocks are known to have almost opposite responses (Eary and Williamson, 2006) in an AMD environment. The 15 samples were also analysed for their elememtal composition using XRF. The results from the XRF analysis (Appendix 2.4) were plotted on a bar graph to facilitate visualisation and comparison. Figure 3.60 shows that the most dominant elemental oxide for all the samples (except sample WITS14) is SiO_2 followed by Al_2O_3. Other elemental oxides which showed

up prominently were MgO and CaO. These elemental oxides which accounted for 10% or more of the composition of the samples, were found in samples WITS01, WITS09, WITS10, WITS11 and WITS14. The 15 samples were grouped into five groups according to their elememtal composition, as shown in Table 3.7.

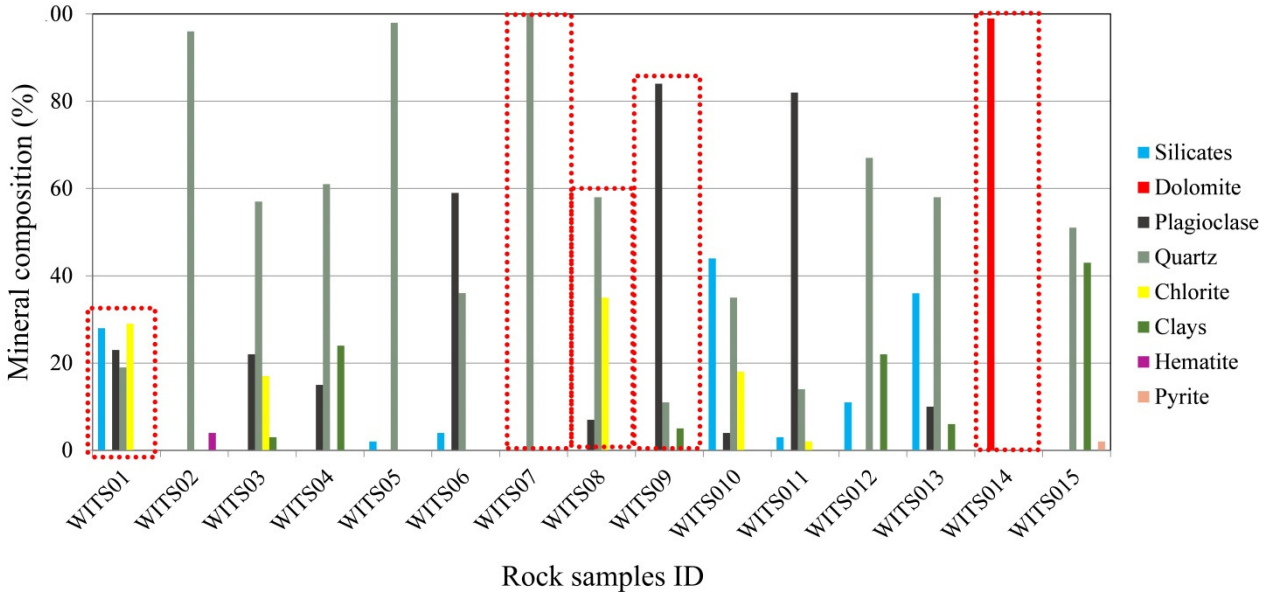

Figure 3.59: Mineral composition of various rocks as measured by XRD, showing the five selected samples for the column leach experiment

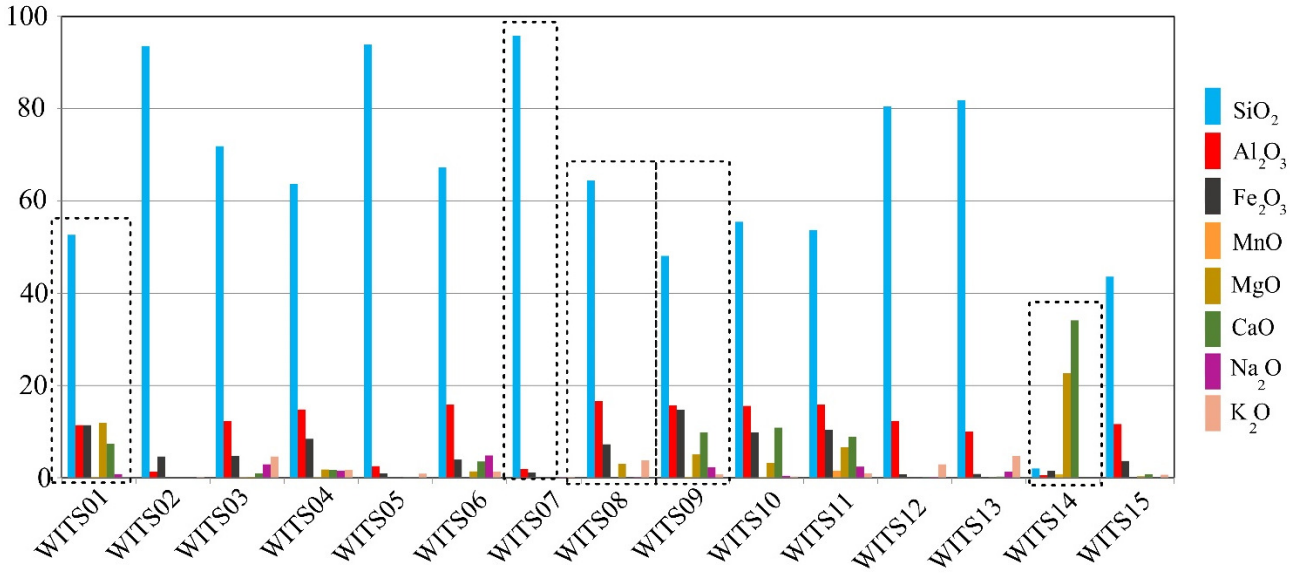

Figure 3.60: XRF minerals composition of various rocks showing the five selected for the column leach experiment

Table 3.7: Groups of samples according to their mineral speciation as interpreted from XRF results

Sample name (WITSxx)	Major mineral species	Group and representative sample
01	SiO_2, Al_2O_3= Fe_2O_3= MgO, CaO	I, WITS01
02, 05, 07	SiO_2	II, WITS07
03, 04, 06, 08, 12, 13	SiO_2, Al_2O_3, Fe_2O_3	III, WITS08
09, 10, 11	SiO_2, Al_2O_3, Fe_2O_3, MgO, CaO	IV, WITS09
14	MgO, CaO	V, WITS14

The selected five representative samples (Table 3.7) were further analysed under a microscope to establish the spatial arrangement of their minerals in detail.

Diabase (WITS1) sample: under the microscope, the sample section is dominated by medium to coarse-grained elongate crystals of plagioclase feldspar, with some wrapped around by strongly coloured varieties of augitic pyroxenes (clinopyroxene characteristic) crystals (Figure 3.61). Observation under the microscope identified the grain size of plagioclase to be in the order of 1.8 mm.

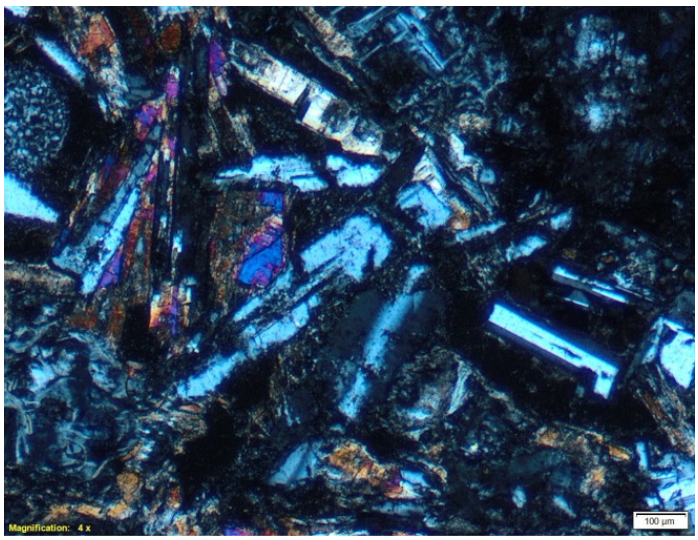

Figure 3.61: Microscopic view of the medium to coarse-grained diabase showing elongated crystals of plagioclase feldspar (Sample WITS1)

Sandstone (WITS7) sample: under the microscope, the sample section is dominated by medium to fine-grained quartz with some grains occurring as angular to sub-angular crystals while others are euhedral (Figure 3.62). Both kaolinite and mica appear as fairly fine-grained colourful crystals and develop as rims surrounding the quartz crystal boundaries. Under the microscope, the grain size of quartz is just under 0.68 mm.

Pillow lava (WITS8) sample: under the microscope, the sample shows very fine-grained quartz minerals and feldspar crystals forming a clay-rich matrix around them (Figure 3.63). Feldspar occurs

as fine-grained crystals which make it difficult to precisely distinguish whether the section comprises plagioclase or sanidine or both. Alteration phases observed in the section include chlorite which occurs with clay minerals such as kaolinite. Lamination was also observed.

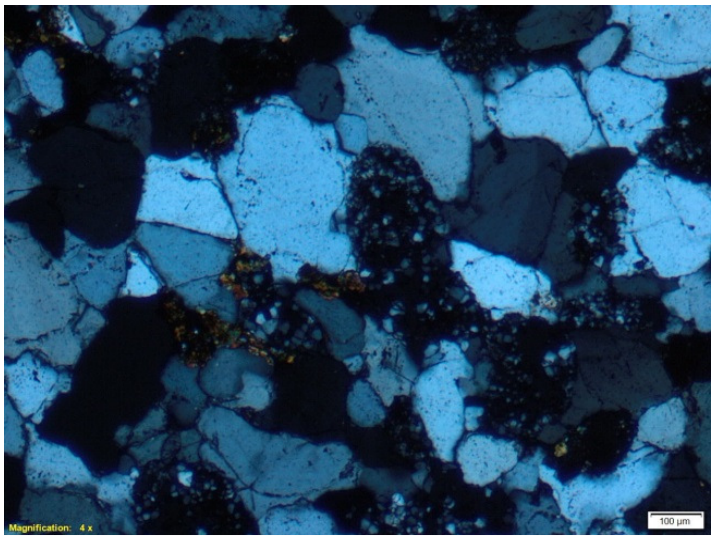

Figure 3.62: Quartzitic sandstone with lithic fragments as seen under the microscope for sample WITS7

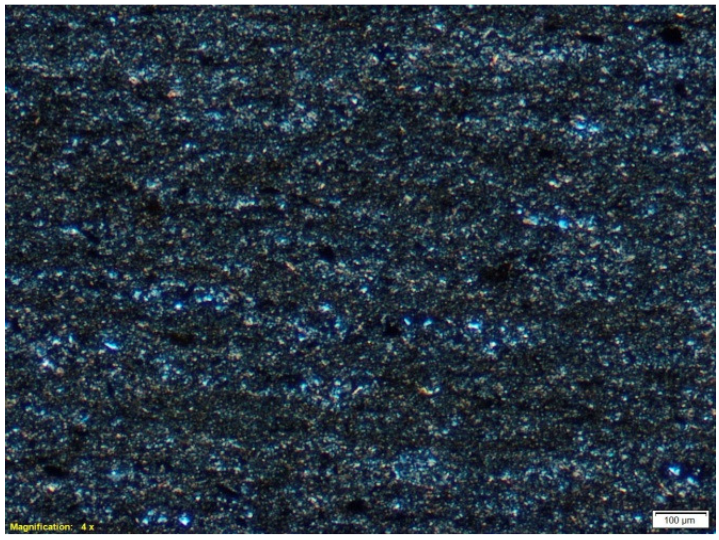

Figure 3.63: Very fine grains of quartz and feldspar as seen under the microscope for sample WITS8

Hornfeld (WITS 9) sample: the microscopic section of this rock sample is dominated by fine- to coarse-grained randomly oriented laths of plagioclase which generally exhibit lamella twinning (Figure 3.64). The plagioclase laths generally occur in localised clusters with interlocking grain-to-grain boundaries. A fine- to medium-grained patch of pyroxene, which appears to be predominantly clinopyroxene, occurs interstitially with the plagioclase laths. Clinopyroxene patches locally enclose laths of plagioclase subophitically. Large patches of plagioclase that appear to have been altered to sericite were also recorded scattered throughout the section. Patches of smectite, which appear to

have been derived from the alteration of clinopyroxene, are also present. Under the microscope, the grain size of plagioclase is just under 3.15 mm.

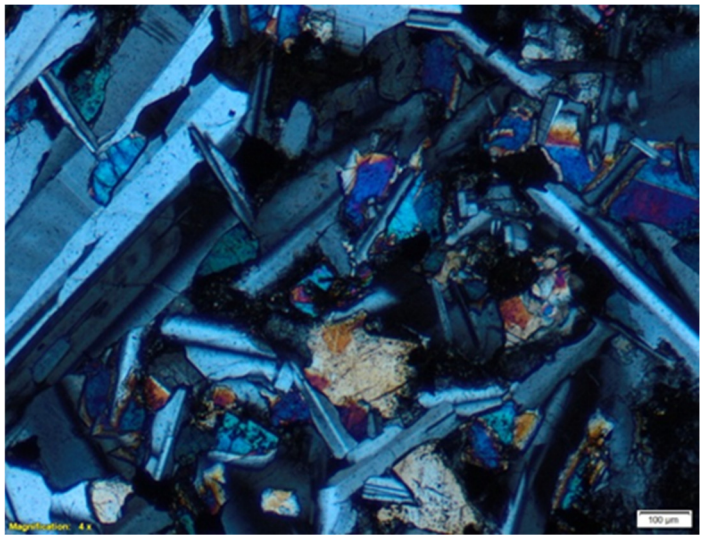

Figure 3.64: Plagioclase laths ophitically to sub-ophitically enclosed in clinopyroxene, as seen under the microscope for sample WITS9

Dolomite (WITS 14) sample: the microscopic section of this rock sample is dominated by fine-grained tightly packed anhedral crystals of calcite and dolomite (Figure 3.65). The dolomite crystals appear transparent, cloudy to dark in colour. Calcite has high birefringence; its colour with crossed polars shows distinctive rainbow colours of pink and green flashes. This section reveals dolomite and calcite presenting a mosaic of fine-grained crystals with poorly defined, non-planar boundaries. The section also shows clinopyroxene crystals occurring with dolomite and calcite.

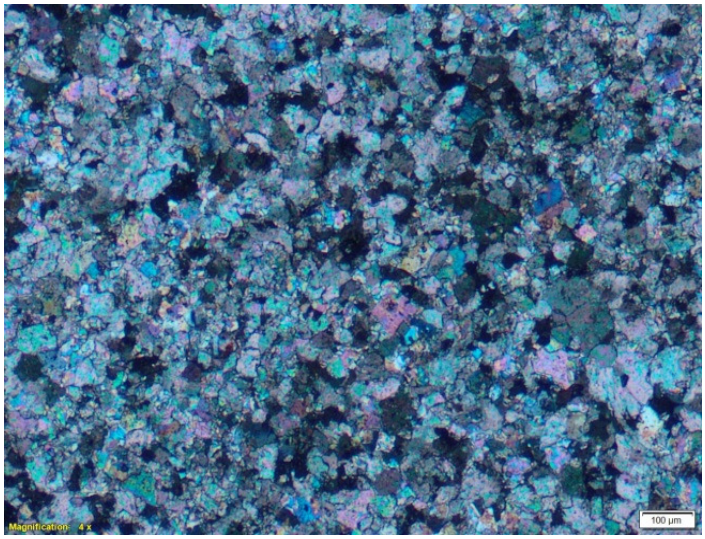

Figure 3.65: Very fine-grained calcite and dolomite predominate in sample WITS14, as seen under the microscope

3.4.5.10.3 Experimental results and discussion

Leachate samples were collected on a weekly basis and analysed for major, minor and trace elements, but only results for pH, iron (Fe), sulphate (SO_4), aluminium (Al), manganese (Mn), calcium (Ca), sodium (Na) and magnesium (Mg) against time in days were presented as graphs. The graph (Figure 3.66) shows the neutralising capacity of various rocks in an AMD environment under saturated conditions at room temperature in the laboratory.

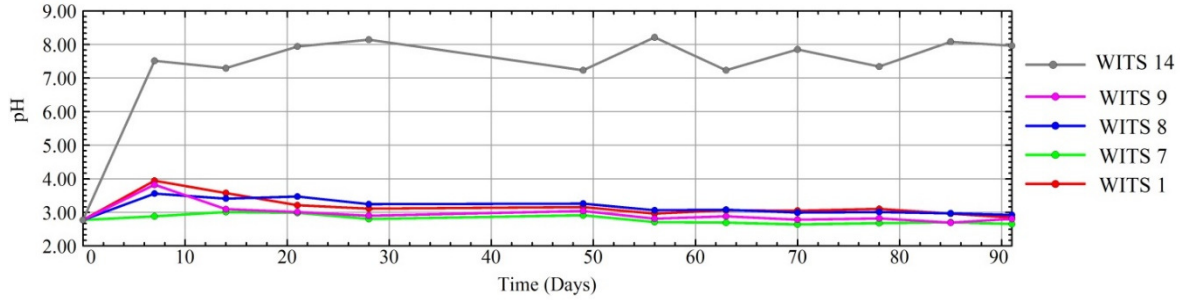

Figure 3.66: Graphic plot of leachate pH against time for various rocks under saturated conditions

pH

When AMD was reacted with different rock samples containing different minerals, different pH changes were observed, as shown in Figure 3.66. Sample WITS14 raised the pH from an initial 2.8 to near-neural (around 7 to 8) from the seventh day until the end of the sampling period. The sample is made up of dolomitic carbonate minerals which react and change the pH to a neutral condition. Then other rock samples (WITS1, WITS7, WITS8 and WITS9) showed a minor change in the pH of the AMD.

A small increase in pH was recorded for the other rock samples (WITS1, WITS7, WITS8 and WITS9) after the first week before the pH returned back to around 2.8. Sample WITS7 showed the least neutralisation capacity as it is composed of over 90% quartz and therefore lacked the ability to neutralise pH within the time frame of the experiment. Despite the little change in pH for the other rock samples, a buffering order (from high to low) can be deduced in term of neutralisation capacity under saturated conditions in the laboratory as follows:

WITS14 > WITS1 > WITS9 > WITS8 > WITS7

Figure 3.67 shows the neutralisation capacity of various rocks under unsaturated conditions at room temperature and pressure. The graph clearly shows that WITS14 buffered the pH from 2.8 to a pH of around 8 from the seventh day until the end of the experiment. The carbonate minerals found in the dolomite accounted for the neutralisation. An increase in neutralisation of the other rocks was recorded when the rock and AMD reacted under unsaturated conditions, probably as a result of the effect of the presence of oxygen on the kinetics of reactions. Sample WITS 1 raised the pH from 2.8

to neutral from the seventh day until the 29th day, when neutralising capacity was lost and the leachate pH returned to acidic conditions of around pH 4. Sample WITS 9 also neutralised the pH but the effect was short lived lasting only eight days, after which the pH returned to an acidic condition of around 3.5. Little change in pH was observed for WITS8, with the pH remaining acidic at a value of below 5. No pH buffering was recorded for sample WITS7. The pH neutralisation in unsaturated conditions is similar to that observed for saturated conditions and follows the order:

WITS14 > WITS1 > WITS9 > WITS8 > WITS7

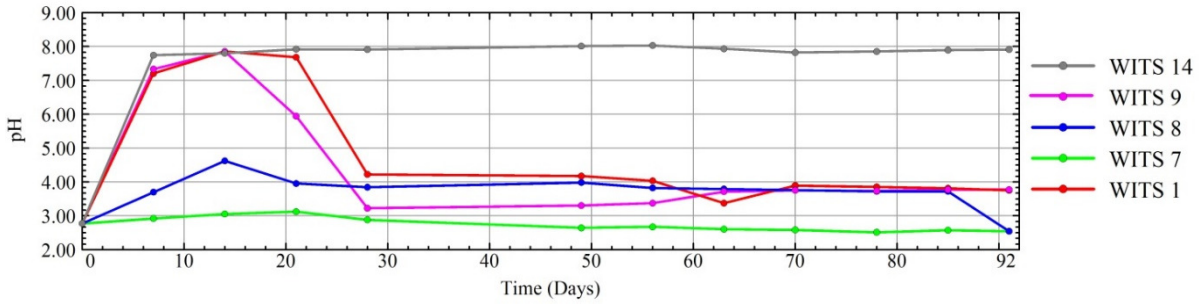

Figure 3.67: Graphic plot of leachate pH with time for various rocks under unsaturated conditions

The difference between the neutralisation capacity of various saturated and unsaturated rocks is very pronounced. This probably shows the role played by the presence of oxygen which caused the reactivity of some of the minerals to be increased. More research can be done by reactive modelling to establish why the kinetics are faster in reactions with oxygen than in those where oxygen is not present.

Electrical Conductivity

Figure 3.68 shows plots of the EC of leachate against time in days for various rock samples under saturated conditions. All the plots show a similar trend with regard to changes in EC with time where the EC values decrease until day 63 when a gradual increase in EC is observed until the end of the experiment. This trend can be attributed to the removal of minerals which make up the EC from solution by the rock mass. This removal is sustainable only for the first 63 days, after which the minerals are released back into solution. This accounts for the gradual increase in EC after 63 days. No clear order in terms of the reduction of EC could be established from the saturated conditions.

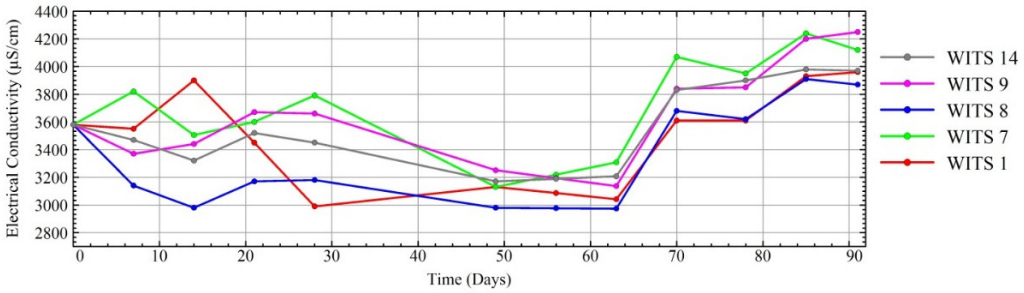

Figure 3.68: Graphic plot of leachate EC with time for various rocks under saturated conditions

In unsaturated conditions, EC plots show a general decrease in EC values for the first 63 days of the experiment, after which a notable increase is observed (Figure 3.69). The order in which various rocks reduce EC is not very clear, but using results from day 21 to 78, the order of reduction is as follows: WITS1 > WITS8 > WITS9 > WITS14 > WITS7. The diabase sample, WITS 1, which consists of over 40% plagioclase feldspar, and the pillow lava sample (WITS 8) which consists of quartz, feldspar and chlorite were able to reduce the EC to below 3 000 µS/cm even though this result did not last longer than 63 days, after which the EC values started to increase.

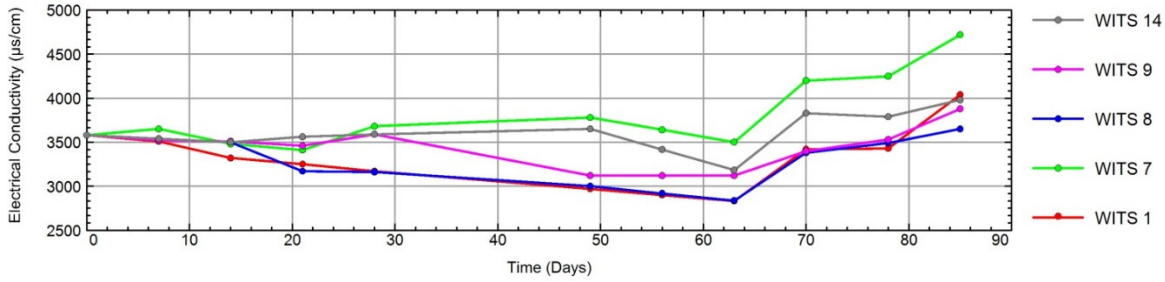

Figure 3.69: Graphic plots of leachate EC with time for various rocks under unsaturated conditions

The sandstone sample (WITS7) consisting almost entirely of quartz showed the least decrease in EC. No noticeable effect with regards to EC was recorded for the dolomite (WITS14) and quartz (WITS7) in terms of decreasing the EC values. A slight decrease was observed for the hornfels (WITS9) samples.

Sulphate

Under saturated conditions, a noticeable decrease in sulphate concentration from 2 865 mg/L to below 2 400 mg/L was observed for all the rock samples (Figure 3.70). This may be attributed to the initial removal of sulphate ions from the solution by the process of absorption of the negative ions onto the rock mass surfaces. This effect only lasted for 50 days when the sulphate ions were gradually released back into solution, thus increasing the concentration, as observed. The order of removal of the sulphate ions is not very clear for the saturated conditions.

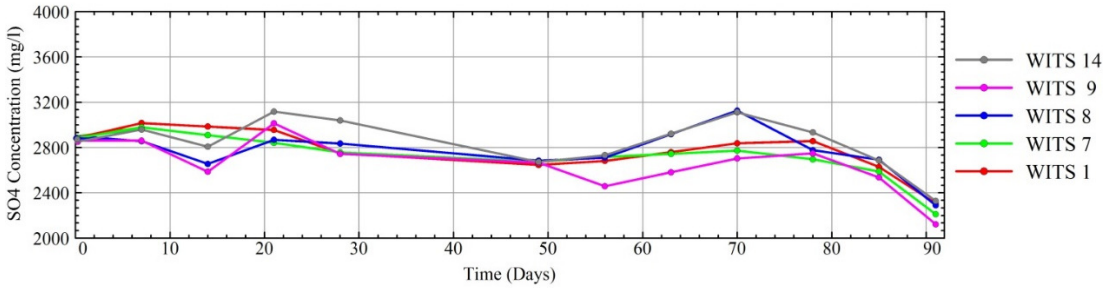

Figure 3.70: Graphic plot of leachate sulphate concentrations over time for various rocks under saturated conditions

A significant reduction in sulphate concentration from 2 865 mg/L to 2 400 mg/L was recorded in the first 20 days of the experiment (Figure 3.71) under unsaturated conditions. All the rock samples showed a similar change in leachate sulphate concentration over time. In terms of the reduction of sulphate concentration, samples WITS9, WITS7, WITS1 and WITS8 followed a similar trend and registered similar sulphate concentration values.

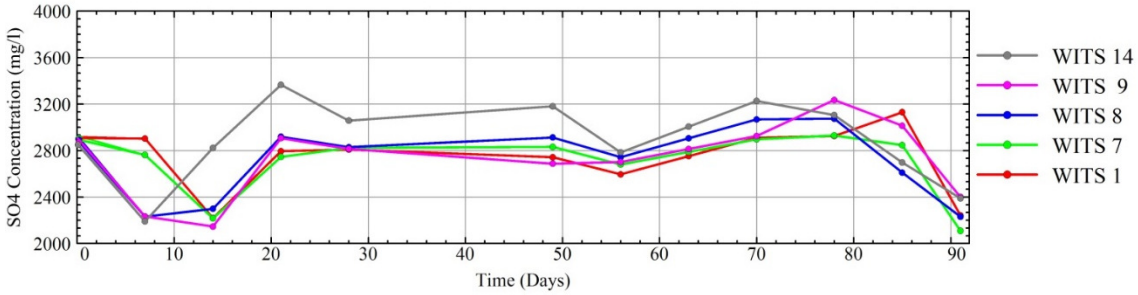

Figure 3.71: Graphic plot of leachate sulphate concentration over time for various rocks under unsaturated conditions

Dolomite sample WITS14 showed the least reduction of sulphate concentration. The order of sulphate reduction in the various rocks is not very clear but can be approximated as follows: WITS1 = WITS7 = WITS8 = WITS9 > WITS14. The sulphate plots for the various rocks are similar, showing that the geology does not affect sulphate removal or addition. Thus, sulphate movement is fairly conservative over various rocks within the time frame over which the experiment was conducted.

Iron

In terms of iron removal by various rocks, the order is not clear for saturated conditions. Nevertheless, it is noticeable that dolomite (WITS14) and pillow lava (WITS8) were able to reduce the Fe concentration to values below 40 mg/L for WITS 8 and below 1 mg/L for WITS14 (Figure 3.72). For unsaturated conditions, samples WITS1, WITS8, WITS9, WITS14 followed a similar trend where the iron concentration was decreased from 140 mg/L to very low values below 20 mg/L (Figure 3.73). A decrease in Fe concentration was recorded for sample WITS7, although the decrease was

significant and resulted in the lowest value recorded for all the rock samples. The order of iron reduction from solution can be approximated as follows: WITS14 > WITS1 = WITS8 > WITS9 > WITS7.

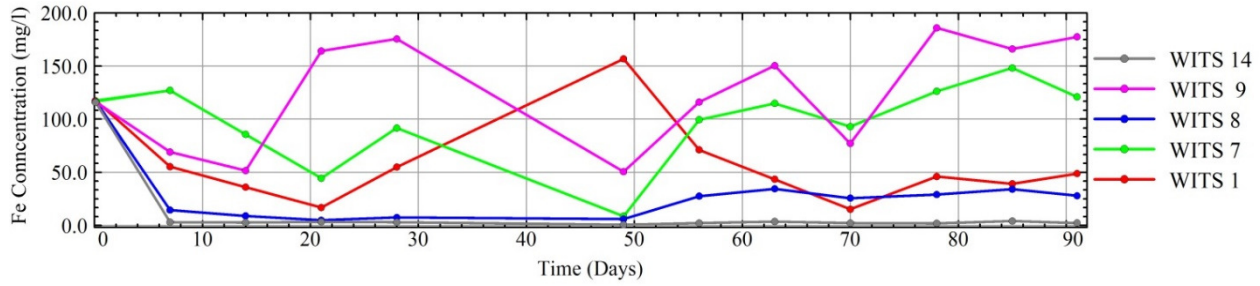

Figure 3.72: Graphic plot of leachate iron concentrations over time for various rocks under saturated conditions

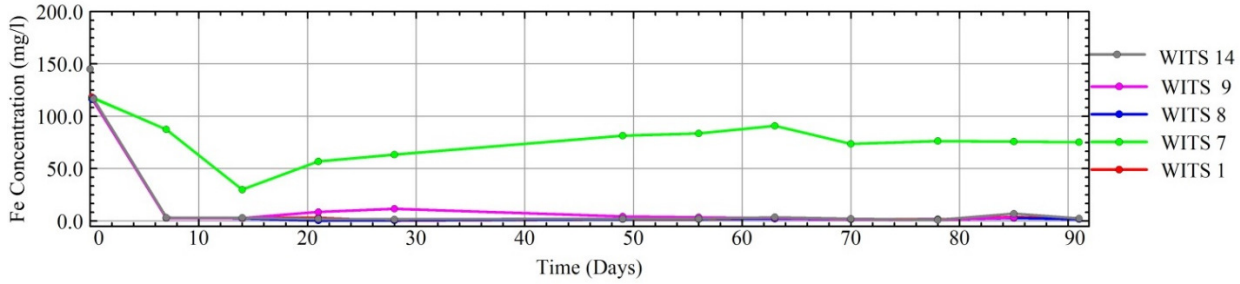

Figure 3.73: Graphic plot of leachate iron concentration over time for various samples under unsaturated conditions

Aluminium

In the first seven days, WITS14 was able to reduce the concentration of aluminium (Al) to a very low value ~ 1 mg/L (Figure 3.74). For samples, WITS8 and WITS7, an increase in the Al concentration was observed. Under unsaturated conditions, dolomite (WITS14) was again observed to be able to reduce the Al concentration to below 1 mg/L (Figure 3.75). For the first 21 days, the Al concentration was reduced to very low values for samples WITS9 and WITS1.

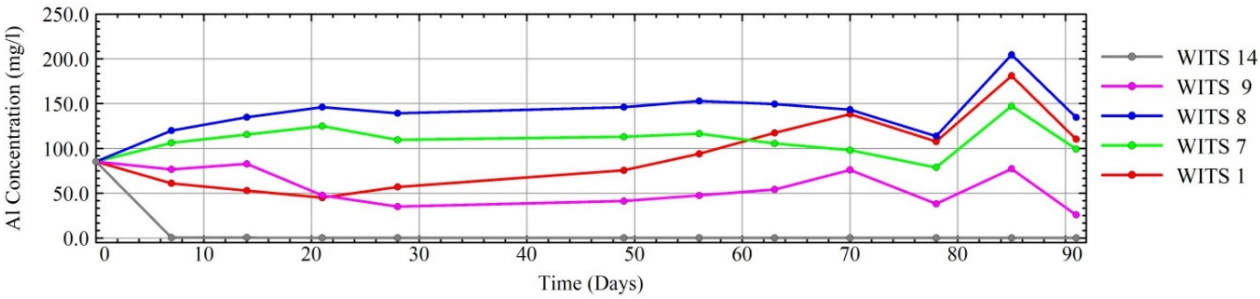

Figure 3.74: Graphic plot of leachate aluminium concentrations over time under saturated conditions

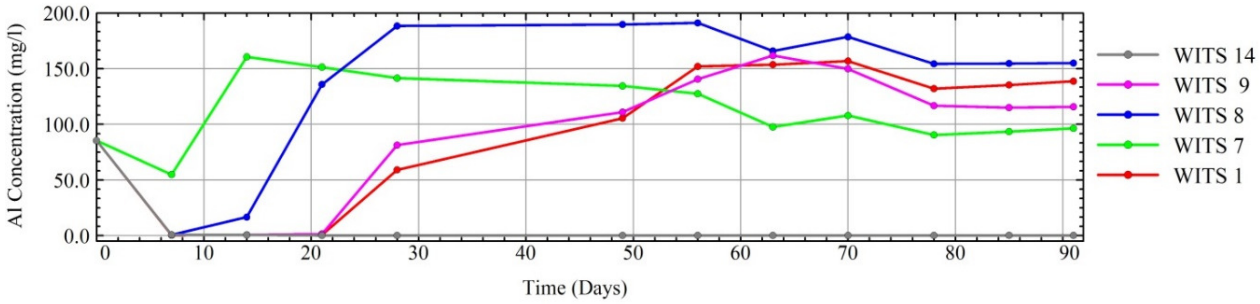

Figure 3.75: Graphic plot of leachate aluminium concentration over time for various samples under unsaturated conditions

Sample WITS8 also showed a slight decrease in Al concentrations but the effect was short lived, lasting only a few days. The order in which each of the five samples reduced Al concentrations from the leachate may be summarised as follows: WITS14 > WITS1 > WITS9 > WITS8 > WITS7.

Manganese

A similar trend in the change over time in regard to manganese (Mn) concentrations in the leachate was observed for samples (WITS7, WITS8, WITS1 and WITS9) under saturated conditions. Sample WITS14 showed a reduction in Mn concentrations instead of a slight increase as was the case for the other samples (Figure 3.76).

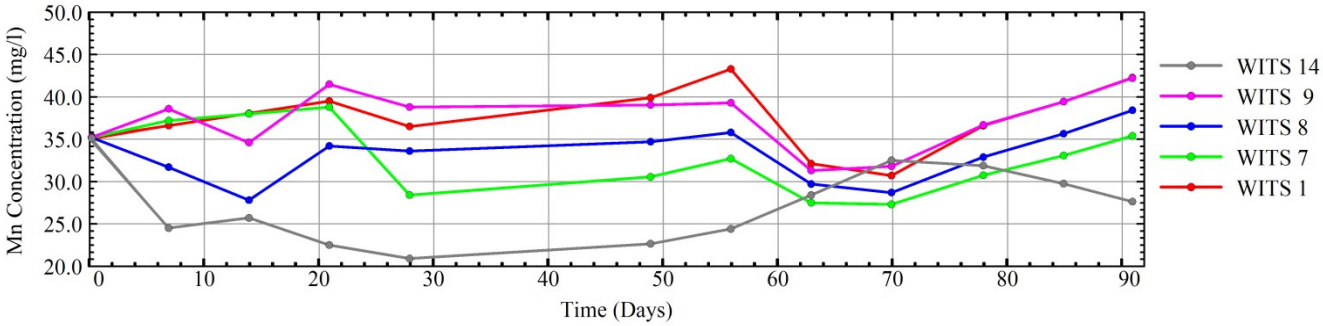

Figure 3.76: Graphic plot of leachate manganese concentrations over time for various samples under saturated conditions

Figure 3.77 shows plots of Mn concentrations against time for the five samples subjected to AMD under unsaturated conditions. The plots show that the dolomite in sample WITS14 reduced the Mn concentration from solution in the first 47 days after which the Mn started to increase gradually until the end of the experiment. For sample WITS1, the Mn concentration only decreased to less than 10 mg/L in the first 7 days after which it increased to over 50 mg/L before returning to the background value of around 30 mg/L. The order of reduction in Mn for the various rocks may be summarised as follows: WITS14 > WITS1 > WITS9 > WITS8 > WITS7.

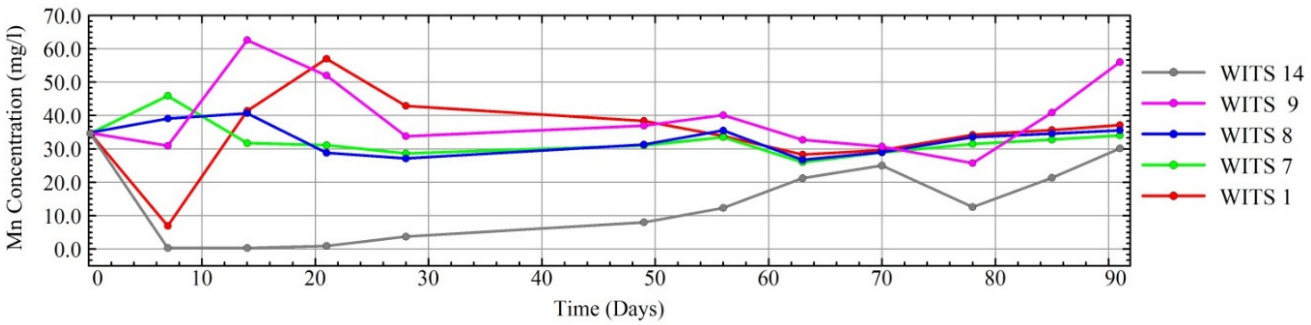

Figure 3.77: Graphic plot of leachate manganese concentrations over time for various samples under unsaturated conditions

Magnesium

Figure 3.78 shows the change in magnesium (Mg) concentration in the leachate over the time period of the experiment under saturated conditions. In all the columns, there is a slight increase in Mg concentration in the first 7 days. The trend then flattens over the next 63 days, after which a sharp decrease to 40 mg/L is observed in all the columns. The greatest increase in Mg was recorded in the column with dolomitic material (WITS14) while the least change was observed for WITS07.

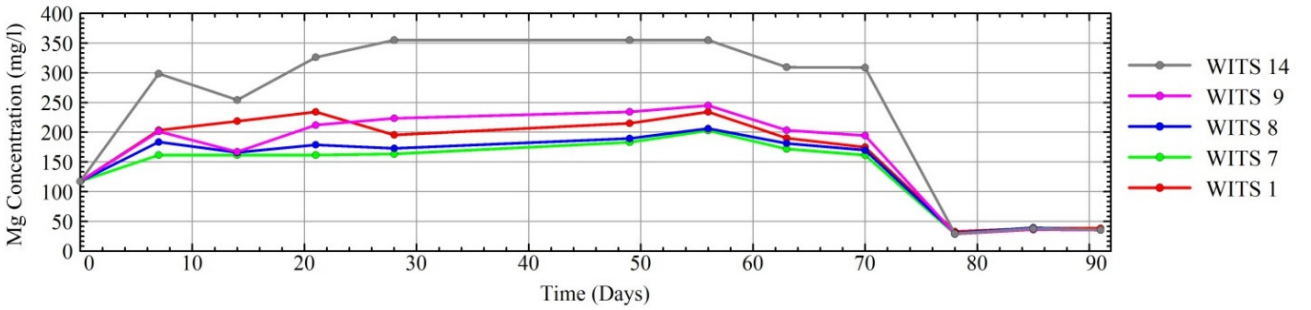

Figure 3.78: Graphic plot of leachate magnesium concentrations over time for various samples under saturated conditions

Figure 3.79 shows plots of Mg concentration versus time for the five samples subjected with AMD under unsaturated conditions. The plots show a similar trend as for the saturated conditions, probably implying that the availability of oxygen does not play a major role in the effect of AMD on various rocks in terms of magnesium concentration.

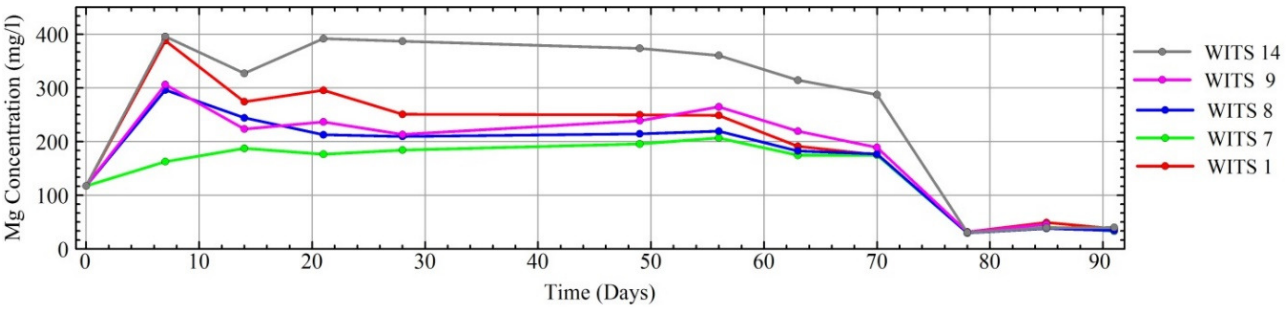

Figure 3.79: Graphic plot of leachate magnesium concentrations over time for various samples under unsaturated conditions

Sodium

Figure 3.80 shows the change in sodium (Na) concentrations in leachate over the time period of the experiment under saturated conditions. In all the columns, there was no change in Na concentration over the first 70 days of the experiment, after which a significant increase was observed in all the columns, with dolomitic sample (WITS14) showing the greatest change. The change occurred when the Mg concentration started to decrease from the leachate, probably reflecting an exchange reaction between Mg and Na, where Mg displaced Na into solution, causing its concentration increase in the leachate from the columns.

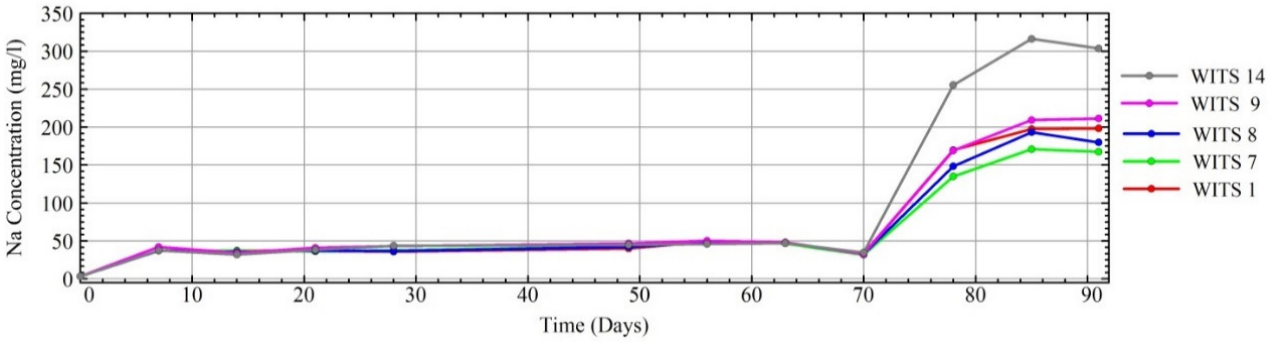

Figure 3.80: Graphic plot of leachate sodium concentrations over time for various samples under saturated conditions

Figure 3.81 shows plots of Na concentrations over time for various rocks which mimic unsaturated conditions. The results for Na concentrations show a similar trend as for saturated conditions, probably implying that the availability of oxygen does not play a major role in Na concentration in rocks subjected to AMD.

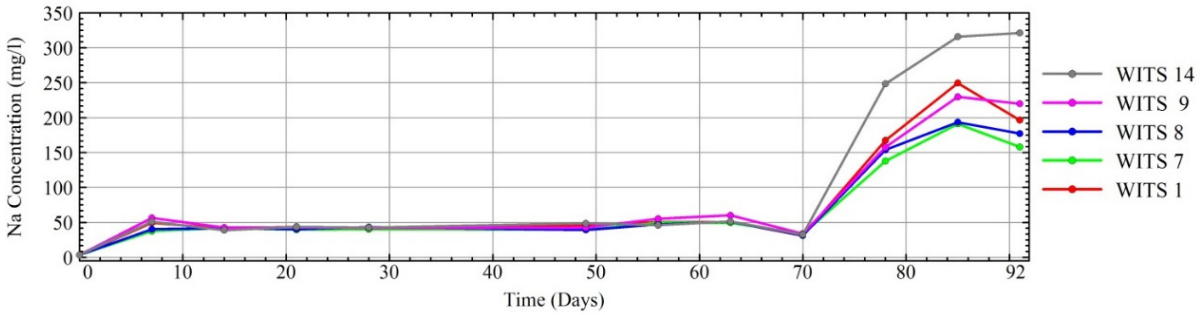

Figure 3.81: Graphic plot of leachate sodium concentrations over time for various samples under unsaturated conditions

Calcium

A plot of calcium concentrations obtained in the leachate from various columns plotted against time showed almost no change in Ca concentrations in all the samples, with the exception of WITS14. Leachate from column with WITS14 dolomitic samples showed an increase in Ca concentrations over the first seven days in response to the change in pH which had been observed over the same period. From the seventh day until the end of the experiment, the pH remained almost constant at near neutral ~7.5 and the leachate Ca concentration remained high as well, probably showing the effect of pH on the leaching of Ca in solution. Similar trends in Ca concentration were observed for the unsaturated condition, as shown in Figure 3.83.

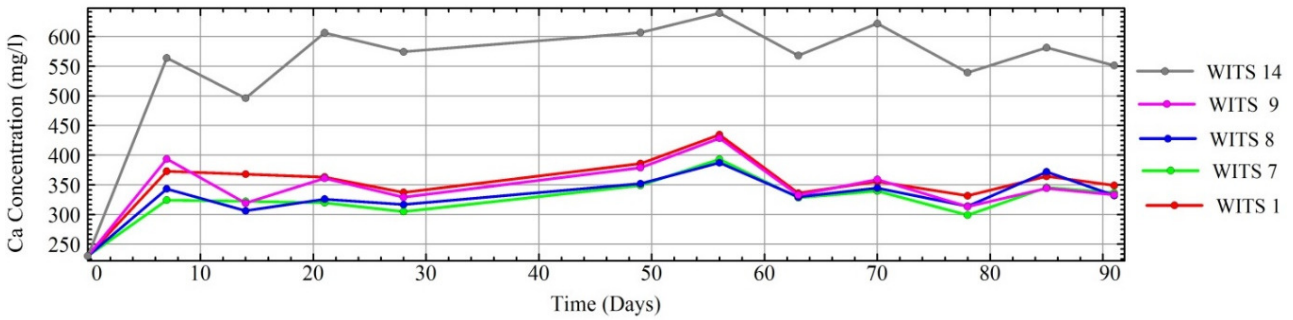

Figure 3.82: Graphic plot of leachate calcium concentrations over time for various samples under saturated conditions

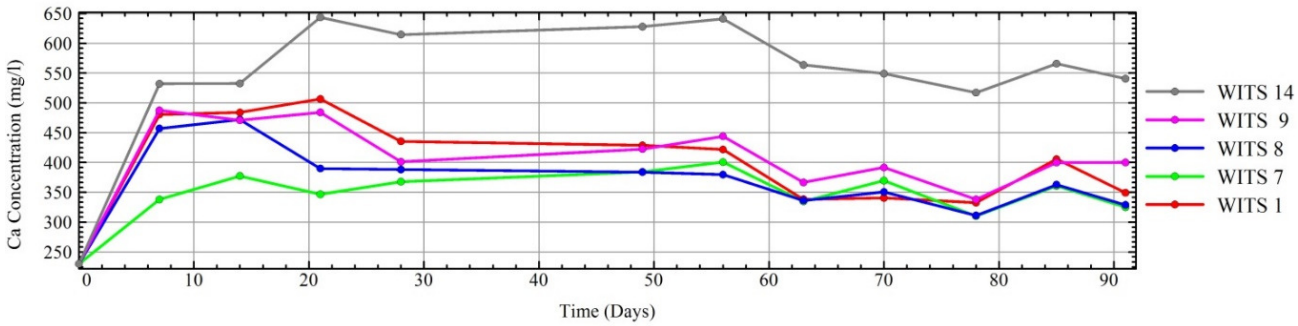

Figure 3.83: Graphic plot of leachate calcium concentrations over time for various samples under unsaturated conditions

Chloride

Rocks in the column tubes were subjected to AMD under saturated and unsaturated conditions and the chloride (Cl) concentrations of the resultant leachate were measured (Figure 3.84 and Figure 3.85). It was discovered that the concentration of chloride remained almost unchanged over the time period of the experiment, probably reflecting the lack of effect in regard to Cl for all the reactions when rocks are subjected to AMD in either saturated or unsaturated conditions. Thus, Cl is conservative as it remains unchanged for the various rocks, maintaining the same concentrations over time regardless of pH conditions.

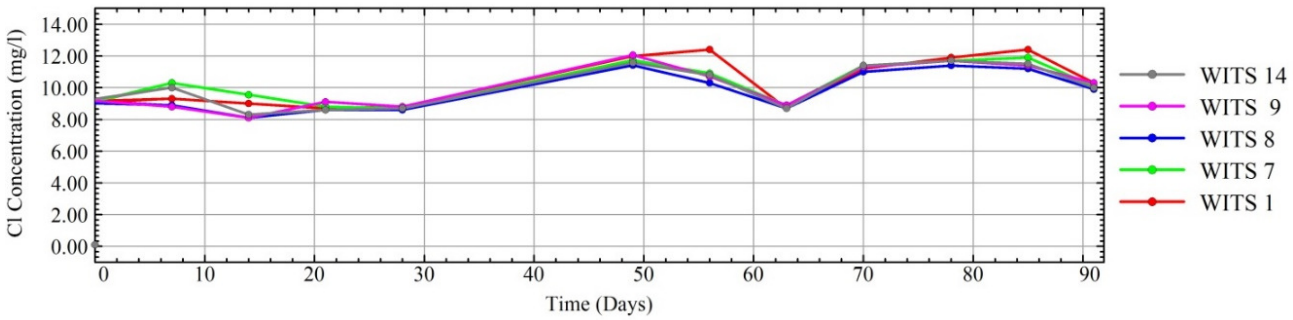

Figure 3.84: Graphic plot of leachate chloride concentrations over time for various samples under saturated conditions

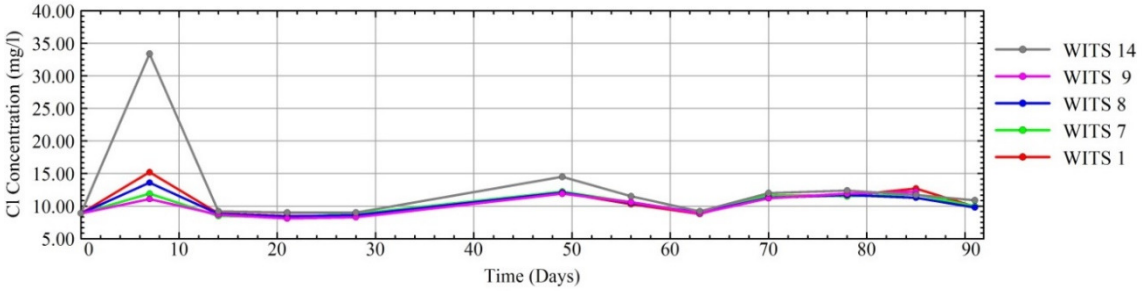

Figure 3.85: Graphic plot of leachate chloride concentrations over time for various samples under unsaturated conditions

Dissolution of Dolomite, Plagioclase, Quartz

Research conducted in order to explain the results of the various columns in terms of the processes responsible for the nature of the leachate produced, showed that the dissolution of the various major minerals constituting each sample could be used.

Dissolution of dolomite in the column with sample WITS14: when dolomite is the only available carbonate (as shown by the XRD results in the presence of oxygen and water-saturated conditions) neutralisation reactions occur according to Equation 3.5 as stated by Stumm and Morgan (1996) and Gomo and Masemola (2016):

$$FeS_2 + CaMg(CO_3)_2 + 3.75O_2 + 1.5H_2O \leftrightarrow Fe(OH)_3 + 2SO_4^{-2} + Ca^{+2} + Mg^{+2} + 2CO_2 \qquad 3.5$$

The dolomite AMD buffering reaction Equation 3.5 conceptually shows that when FeS_2 from the AMD reacts with dolomite ($CaMg(CO_3)_2$) in the presence of oxygen (O_2) and water (H_2O), a hydroxyl complex of iron (III) ($Fe(OH)_3$) is produced together with sulphates (SO_4^{-2}), calcium (Ca^{+2}), magnesium (Mg^{+2}) and carbon dioxide (CO_2). Based on this conceptual model, when such reactions occur, calcium and magnesium concentrations are likely to increase as was seen in the Ca and Mg plots for WITS14 under unsaturated conditions where both oxygen and water were present.

At the same time, Fe concentrations decreased as free Fe ions form complexes which adhere to the mineral grains of the rock sample, thus accounting for the observed decrease in Fe concentration. The solubility of aluminium and manganese is pH dependent (Wright *et al.*, 2001) when pH is neutral they precipitate and when pH is low they are in solution, as was reflected by the change in the leachate concentrations of these elements as pH changed from low to neutral (Figure 3.66 and Figure 3.67).

Dissolution of plagioclase in column with sample WITS09: based on the XRF results (Figure 3.60), the most elemental oxides in the WITS09 sample are SiO_2, Al_2O_3, Fe_2O_3 CaO; thus the chemistry of this sample was controlled by the dissolution of anorthite ($CaAl_2Si_2O_8$) minerals. The dissolution of anorthite is a well-studied phenomenon and may be represented by Equation 3.6 given by Oelkers and Schott (1995):

$$CaAl_2Si_2O_8 + 8H^+ \leftrightarrow Ca^{+2} + 2Al^{+3} + 2SiO_2 + 4H_2O \qquad 3.6$$

Based on this conceptual understanding of Equation 3.6 representing the dissolution of anorthite which makes up sample WITS09, it can be seen that the dissolution reactions produce Ca^{+2} and Al^{+3} ions in solution. This was particularly noted when the dissolution reactions took place, as evidenced by the change in pH from acidic to near neutral accompanied by an increase in calcium concentrations found in the leachate. However, the aluminium concentration did not increase in solution because the Al^{+3} ions formed complexes of hydroxyl which adhered to the grains of the rock material and were not found in solution, as may be seen by the low concentrations of the resultant leachate.

Dissolution of quartz in the column with sample WITS07: sample WITS07 is made up of over 95% SiO_2, thus, the dissolution of silicate minerals can be used to explain the results of the leachate collected. The dissolution of silicate is a very slow process, even in an acidic environment (Kamiya *et al.*, 1974). This explains why no significant change was observed for pH, sulphate, iron, aluminium and the manganese concentrations for the column with sample WITS07.

3.4.5.10.4 Summary

Based on the interpretation of the leachate concentration in relationship to the rock mineral composition for various rocks in the AMD environment, an approximate order of rock-AMD

reactivity can be deduced for the Witbank, Ermelo and Highveld coalfields. Table 3.8 shows a summary of the findings of the experiment.

From the experiment it can be deduced that dolomite, which contains of 90% dolomitic carbonate minerals, was able to buffer the pH to neutral conditions which, in turn removed the heavy metals (Fe, Al and Mn) from the AMD solution. Diabase with medium- to coarse-grained elongate crystals of plagioclase feldspar which are aluminium complexes was also able to buffer the acidic conditions, but given that the buffering minerals are easily exhausted, buffering only lasted a few weeks. In terms of AMD extraction by rocks, hornfels follows diabase where the fine- to coarse-grained randomly oriented laths of plagioclase are responsive in buffering the acidic conditions and removing heavy minerals. The process is kinetically fast and only lasts a few weeks. Pillow lava, which is dominated by very fine-grained quartz and feldspar crystals, are also able to buffer the acidity to a lesser extent, but the process lasts a few days. Sandstones are the least effective in terms of buffering acidity and removing heavy metals (Fe, Al, Mn) from AMD solution. The sandstones are made up almost entirely of quartz minerals which lack the ability to buffer acidity or remove heavy metals in the time frame of the experiment.

Table 3.8: Summary of rock–AMD reactivity expressed in terms of AMD removal by rocks

Parameter	Order of AMD reduction by rocks	Dedications
pH	WITS 14 ➤ WITS 1 ➤ WITS 9 ➤ WITS 8 ➤ WITS 7	Dolomite buffers acidity better than other rocks and sandstone being the least.
EC	WITS 1 ➤ WITS 8 ➤ WITS 9 ➤ WITS 14 ➤ WITS 7	Diabase/ dolerite rocks reduce the EC better than most rock with sandstone being the least in this regards.
SO_4	WITS 1 = WITS 7 = WITS 8 = WITS 9 ➤ WITS 14	Sulphate generally remains unaffected by interaction with various rocks.
Fe	WITS 14 ➤ WITS 1 = WITS 8 ➤ WITS 9 ➤ WITS 7	Dolomite removes Fe better than other rocks and sandstone being the least.
Al	WITS 14 ➤ WITS 1 ➤ WITS 9 ➤ WITS 8 ➤ WITS 7	Dolomite removes Al better than other rocks and sandstone being the least.
Mn	WITS 14 ➤ WITS 1 ➤ WITS 9 ➤ WITS 8 ➤ WITS 7	Dolomite removes Mn better than other rocks and sandstone being the least.

Where WITS 14 – Dolomite, WITS 1 – Diabase, WITS 9 – Hornfels, WITS 8 – Pillow lava and WITS 7 - Sandstone

Of particular interest is that hardly any rocks tested were able to remove sulphates under saturated and/or unsaturated conditions. Moreover, all the rock leachates were shown to follow an almost

similar pattern over time. Thus, sulphate may be considered conservative in both saturated and unsaturated conditions and can be used as a possible tracer for AMD pollution. Another interesting observation from the experiment is that pH buffering and metal removals were more pronounced in the unsaturated zone than in the saturated zone, probably as a result of the presence of oxygen.

The results from the rock-AMD reactivity experiment were used as a guide to the classification of the rocks in the coalfields based on the mineralogical similarities between those rocks and the rock samples of the experiment. Table 3.9 shows the classification of various rocks found in Witbank, Ermelo and Highveld coalfields in terms of their reactivity in the AMD environment.

Table 3.9: Summary of the rock-AMD reactivity for the Witbank, Ermelo and Highveld coalfields

Lithology group	Description	Sample representative	Relative AMD extraction (1-10)
Quaternary			
Alluvial	Unconsolidated sediments along rivers	WITS 7	1
The Karoo Supergroup			
Dwyka Group	Diamictite (Tillite)	WITS 7	1
Ecca Group	Sandstone, shale and coal	WITS 7	1
Beaufort Group	Mudrock, sandstone	WITS 1	7
Intrusive rocks	Dolerite (dykes and sills)	WITS 1	7
Waterberg Complex	Sandstone with interbedded conglomerate and shale	WITS 7	1
The Bushveld Complex			
Rustenburg Suite	Gabbro, norite, anorthosite	WITS 9	5
Lebowa Suite	Felsic granite	WITS 9	5
Transvaal Supergroup			
Chuniespoort Group	Dolomite, Chert	WITS 14	9
Pretoria Group	Shale, Quartzite	WITS 1	7
Intrusive rocks	Diabase	WITS 1	7
Rooiberg Group	Rhyolite and felsite	WITS 8	3
Loskop Formation	Sandstone, conglomerate	WITS 7	1
Witwatersrand Supergroup Hospital Hill Formation	Shale and Quartzite	WITS 1	7
Basement Complex	Granite and Gneiss	WITS 9	5

The rocks were assigned relative values from 1 to 10 according to their ability to buffer acidity and heavy metal pollutants typically associated with AMD pollution in the Witbank, Ermelo and Highveld

coalfields. Figure 3.86 shows the spatial distribution classes of rock-AMD reactivity within these coalfields as resampled from the geology dataset, using the results of the experiment.

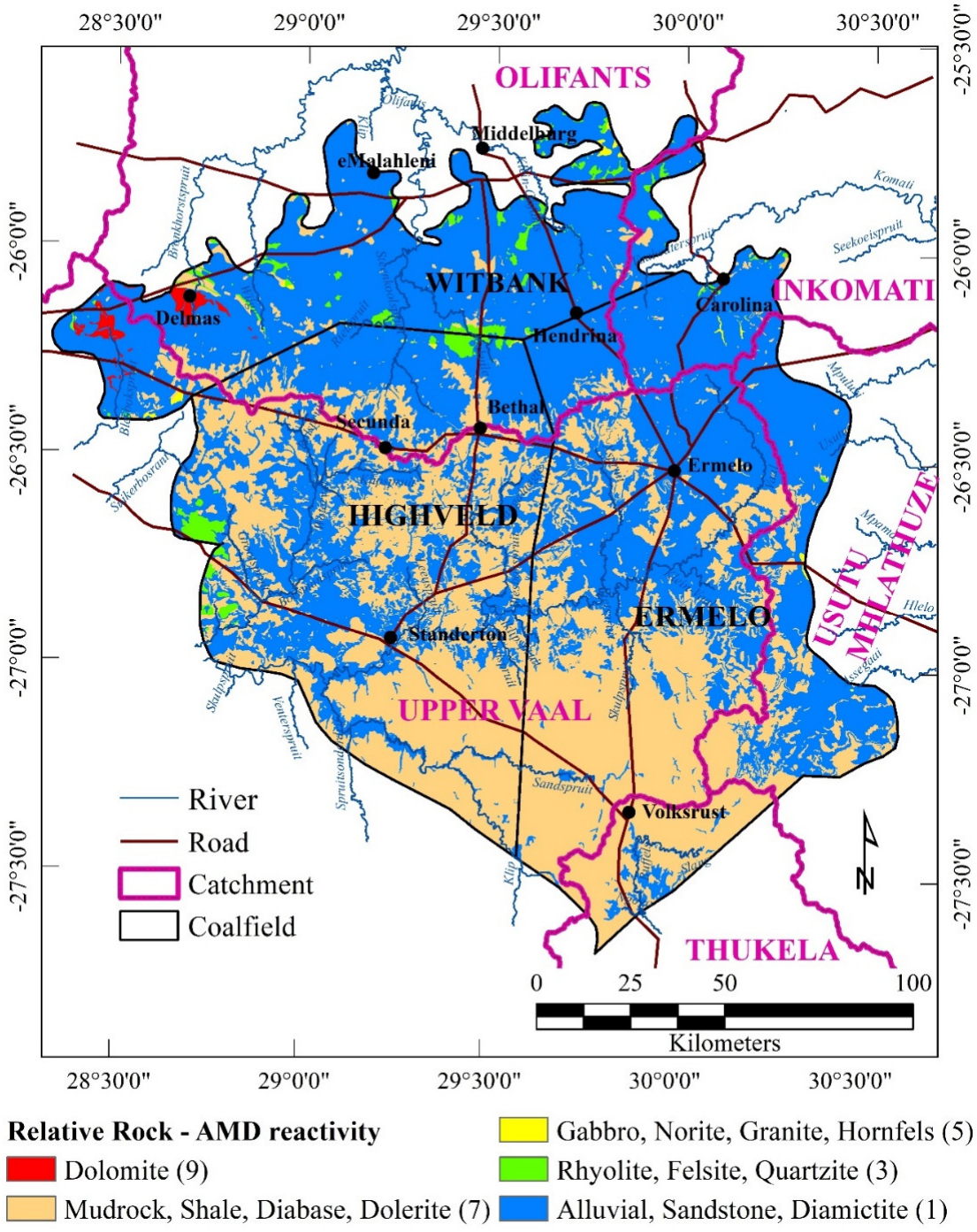

Figure 3.86: Rock-AMD reactivity map of the study area showing the relative classification in terms of extraction of AMD pollutants

3.5 SUMMARY

Chapter 3 reported the full details of how the SPT approach for the assessment of groundwater vulnerability of a typical coalfield with particular reference to AMD pollution and the input datasets used for the approach were derived. The approach is based on three broad factors, namely sources,

transportation pathways and traps, which were derived from the mineral systems, petroleum and source-transport-attenuation approaches. A total of ten parameters, namely rainfall, topography, slope, surface and subsurface sources of AMD pollution, soil clay content, rock permeability, preferential pathways, aquifer hydraulic conductivity, rock-AMD reactivity and depth to water table were used in the approach.

Other groundwater vulnerability approaches use groundwater recharge as one of the input parameters. This parameter is generally a combination of various parameters such as topography, soils and rainfall. Using the recharge parameter together with topography, soils and rainfall in the same model will result in parameter dependence, where the resultant model would mimic these parameters only and mask out the effects of other parameters. In the SPT approach developed in this study, recharge information was redistributed to its components and was not used directly in order to minimise parameter dependence. Nevertheless, all the necessary parameters affecting groundwater recharge were included in the assessment.

Rainfall was used as a proxy for the availability of water for AMD reactions and as a transport medium through which AMD can flow with as it migrates towards the groundwater system. Remote sensing was used to extract possible AMD sources on the surface which were combined with the coal host rocks to form the AMD sources. The clay content parameter was identified as an appropriate parameter with reasonable resolution to address the transport and traps of AMD within the soil layer. Laboratory experiment in the research which involves AMD reactions with various soils of varied CEC, clay content and types showed that the clay content is a reasonable proxy parameter which addresses both the transport of pollution (size of pore spaces) and the number of exchangeable sites controlling the traps of AMD as it passes through the soil.

The possible preferential pathways parameter is very difficult to obtain for an area as extensive as a coalfield. Hence, a proxy of the pathways was interpreted from airborne magnetic data which are ready available at a reasonable scale covering the entire coalfield area.

The experiment of neutralising acidity and removal heavy metals from five samples which represent the variability of the rock mineralogies found in the study area produced exciting results. The dolomite sample was able to extract most of the heavy metal pollutants from the AMD solution and was also able to buffer the acidity to a neutral pH. Sandstone was the least effective in terms of buffering the acidity and removal of heavy metals from the AMD solution. Sulphate and chloride were conservative, as none of the five rock samples was able to significantly reduce the sulphate and chloride concentration. Hence, sulphate may be used as a proxy tracer for AMD where its presence in the groundwater can be used as an indicator of pollution.

CHAPTER 4: KNOWLEDGE-DRIVEN FUZZY EXPERT SYSTEM

4.1 INTRODUCTION

In the previous chapter, an approach for the assessment of groundwater vulnerability to AMD pollution at a typical coalfield scale was discussed. A total of ten parameters were identified as being appropriate for the assessment of groundwater vulnerability to AMD at a regional scale. The next significant challenge is to find ways of combining these parameters to generate groundwater vulnerability models. There are several approaches, ranging from simple index-weight, knowledge-driven systems, data-driven systems and hybrid systems. This chapter describes a knowledge-based GIS fuzzy expert system which was built to aggregate the ten input map layers using the current understanding of AMD pollution migration mechanisms converted into four vulnerability factors (sources, transportation pathways and traps) and used to generate a groundwater vulnerability model of the coalfields.

A review of the knowledge-driven system fuzzy expert system will be done, followed by application of the system to generate a groundwater vulnerability model of the Witbank, Ermelo and Highveld coalfields. The model will be validated, followed by a discussion of the results.

This chapter is based on Sakala *et al.* (2018) which was published as part of this research.

4.2 KNOWLEDGE-DRIVEN ARTIFICIAL INTELLIGENCE SYSTEMS

The implementation of knowledge-driven AI systems involves an understanding, the design and implementation of ways of representing information by means of computers so that programs (agents) are able to use this information (Shapiro, 1995):

- to derive information and relationships amongst inputs;
- to aid people in natural languages;
- to support decision taking and future planning; and
- to solve problems in areas that normally require human expertise.

4.3 OVERVIEW OF FUZZY EXPERT SYSTEMS

The fuzzy expert system is centred on the fuzzy logic theory which was developed by Zadeh (1965). The theory expresses logic as a continuum of truth or falsehood, as opposed to the classic (crisp) tradition where logic is presented as either true or false. The fuzzy expert system is a knowledge-driven AI technique that involves formulating computer-based systems that are able to extract and

copy cognitive reasoning in drawing conclusions. Thus, the computer emulates human thought processes (Porwal *et al.*, 2003, 2015).

The fuzzy expert system may be considered a fuzzy set which consists of fuzzy membership functions (FMF) comprising fuzzy membership values (FMV). According to Joly *et al.* (2012), a generalised fuzzy set $\tilde{Z}_i$ is given such that: if Y is a set of n input layers Y_i $(i = 1\ to\ n)$ with r classes denoted generically by y_{ij} $(j = 1\ to\ r)$, then n fuzzy sets $\tilde{Z}_i$ in Y, containing "vulnerable factors" may be defined by Equation 4.1 (Joly *et al.*, 2012):

$$\tilde{Z}_i = \left(y_{ij}, \mu_z\right) \left| y_{ij} \in Y_i \right. \quad 4.1$$

Where μ_z is the fuzzy membership function for estimating the fuzzy membership value (weight assigned by the hydrogeologist) of y_{ij} in the fuzzy set $\tilde{Z}_i$.

The fuzzy expert system can be implemented to a real application using a three-stage process which involves fuzzification, fuzzy engine and defuzzification (Figure 4.1) (Hellmann, 2002).

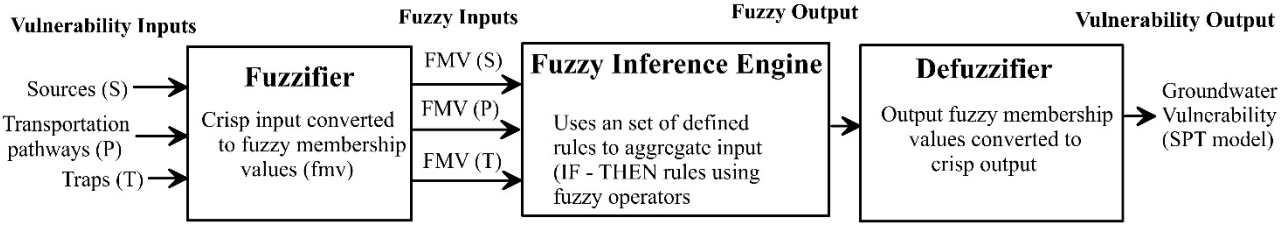

(After Fijani *et al*, 2013)

Figure 4.1: Structure of the fuzzy expert system

4.3.1 Fuzzification

In this approach, a fuzzifier converts the crisp input variables into FMV making up a FMF (Figure 4.1). The FMF as an appropriate function which best describes the relationship of the inputs to the output and should be well defined. The fuzzy membership function may be linear, Gaussian or of any other type. For the study area, a linear function, given by Equation 4.2 was used (Joly *et al.*, 2012):

$$\mu_{\tilde{Z}_i} = \frac{m_i * w_j * cf_i}{1\ 000} \quad 4.2$$

where m_i is the map weight, w_j is the class weight and cf_i is the confidence factor.

The map weight m_i for each map is subjectively assigned an integer value between 1 and 10 based on expert knowledge of the importance of the parameter with respect to groundwater vulnerability and whether it is directly or indirectly related to groundwater vulnerability. The confidence factor cf_i of a vulnerability input layer is also subjectively assigned an integer value between 1 and 10 based

on the data resolution and level of uncertainty in the data sources (Porwal *et al.*, 2003). Values of class weights w_j are assigned values between 1 and 10. Classes with a vulnerability input layer which has a high contribution are assigned a high class weight and those with little or no contribution to vulnerability are assigned very low class weights approaching zero but never actually reaching zero. According to Joly *et al.* (2012), zero values should not be assigned as they will be transmitted through the fuzzy expert system and render the output to be zero even though other layers may show high values owing to multiplication with zero in the fuzzy expert system.

For example, according to Equation 4.2, if a point on the depth to water table map with map weight value of 9, a confidence factor of 6 and lying in a class with value of 10 is taken, the fuzzy membership value will be given by (9 x 6 x 10)/1 000 = 0.54.

4.3.2 Fuzzy Inference Engine

The fuzzy inference engine aggregates the FMF for all the input layers with fuzzy rules to derive the fuzzy output (Figure 4.1). The five fuzzy operators (AND, OR, PRODUCT, SUM and GAMMA) commonly used for aggregation are discussed in detail by Kanungo *et al.* (2009) but a summary of those used in this thesis will be given in this section.

4.3.2.1 Fuzzy (AND) operation

This operator compares the FMVs at each corresponding location on various layer maps and takes the minimum values as the output fuzzy value (μ_{AND}) for that particular location. It is appropriate where two or more pieces of evidence from layer maps must be present together for a hypothesis to be true. The Fuzzy (AND) operator may be expressed by Equation 4.3 (Bonham-Carter, 1994):

$$\mu_{AND} = MIN(\mu_A, \mu_B, \mu_C, \dots\dots\dots) \quad 4.3$$

Where μ_A is the fuzzy value of map A and μ_B is the fuzzy value of map B, and so on.

For example, at some location, when the membership value for map A is 0.5 and for map B, the value is 0.25, then the membership for the combination using fuzzy (AND) takes the smallest value of 0.25.

4.3.2.2 Fuzzy (OR) operation

This operator compares the FMVs at each corresponding location on various layer maps and takes the maximum values as the output fuzzy value (μ_{OR}) for that particular location. It is appropriate for any one of the two or more pieces of evidence from the layer maps to be present for a hypothesis to be true. The fuzzy (OR) operator may be expressed by Equation 4.4 (Bonham-Carter, 1994):

$$\mu_{OR} = MAX(\mu_A, \mu_B, \mu_C, \dots\dots\dots) \quad 4.4$$

Where μ_A is the fuzzy value of map A and μ_B is the fuzzy value of map B and so on.

For example, if at some location the membership value for map A is 0.5 and for map B the value is 0.25, then the membership for the combination using fuzzy (OR) takes the largest value of 0.5.

4.3.2.3 Fuzzy (SUM) operator

This operator combines the FMVs at each corresponding location on various layer maps in such a way that the output result (μ_{SUM}) is always larger (or equal to) the largest contributing FMV. Therefore, the fuzzy (SUM) behaves as an "increasive" function. This is appropriate where two pieces of evidence both favour a hypothesis reinforcing one another and the combined evidence is more supportive than either piece of evidence taken individually. The expression for the fuzzy SUM is given by Equation 4.5 (Bonham-Carter, 1994):

$$\mu_{SUM} = 1 - \prod_{i=1}^{n}(1 - \mu_i) \quad 4.5$$

Where μ_i is the fuzzy membership function for the ith map, and i= 1, 2 ... n maps are to be combined. For example, where at some location the membership value for map A is 0.5 and for map B the value is 0.25, then the membership for the combination using fuzzy (SUM) would be 1-(1-0. 5)×(1-0.25) = 0.625.

4.3.2.4 Fuzzy (PRODUCT) operator

This operator combines the FMVs in such a way that the output result tends to be very small owing to the effect of multiplying several numbers <1 (Bonham-Carter, 1994). The output is always smaller than, or equal to, the smallest contributing membership value, and is therefore a "decreasive" function. This is appropriate where two pieces of evidence contribute to a hypothesis with the result being smaller than either pieces of the evidence. The expression for fuzzy (PRODUCT) is given by Equation 4.6 (Bonham-Carter, 1994):

$$\mu_{PRODUCT} = \prod_{i=1}^{n}\mu_i \quad 4.6$$

Where μ_i is the FMF for the i-th map, and i = 1,2,... n maps are to be combined.

For example, assuming at some location, the membership value for map A is 0.5 and for map B the value is 0.25, then the membership for the combination using fuzzy (PRODUCT) would be 0.5 * 0.25 = 0.125.

4.3.2.5 Fuzzy (GAMMA) operator

This operator may be expressed in terms of the fuzzy (SUM) and fuzzy (PRODUCT) operators by Equation 4.7 (Bonham-Carter, 1994):

$$\mu_{GAMMA} = (\mu_{SUM})^{\gamma} * (\mu_{PRODUCT})^{1-\gamma} \quad 4.7$$

Where γ is a gamma value chosen between 0 and 1.

The result produced with $\gamma = 1$ is the same as the fuzzy (SUM) result and result for $\gamma = 0$ is same as for the fuzzy (PRODUCT). Therefore, the fuzzy (GAMMA) operator creates a flexible compromise between the "increasive" tendencies of the fuzzy (SUM) and the "decreasive" effects of the fuzzy (PRODUCT). The choice of the gamma value should be such that the resultant output (μ_{GAMMA}) reflects the likely subjective decision making of a typical expert. For example, assuming at some location the membership value for map A is 0.5 and for map B the value is 0.25, and $\gamma = 0.5$ is chosen. The resultant output after applying the fuzzy (GAMMA) operator would be given by Equation 4.8:

$$\mu_{GAMMA} = (0.625)^{0.5}(0.125)^{1-0.5} = 0.2795 \quad 4.8$$

4.3.3 Defuzzification

In this step, a defuzzifier converts the fuzzy output membership values in the crisp output variable (Figure 4.1). The crisp output variables express the results of the modelling process, which may be a mathematical function or subjectively or objectively defined (Porwal *et al.*, 2003). Several methods are available for defuzzification, but the most important criterion to consider when selecting a method is that the small change in inputs of a fuzzy model should not cause a significant change in the output result (Hellendoorn and Thomas, 1993). In this study, the natural break (ESRI, 2006) was used for the defuzzification process.

4.4 APPLICATION OF THE FUZZY EXPERT SYSTEM TO GROUNDWATER VULNERABILITY ASSESSMENT

The application of knowledge-driven fuzzy expert system approaches to groundwater vulnerability assessment is not new and has been successfully used in nitrate pollution studies (Zhou *et al.*, 1999;

Dixon, 2005b; Nobre *et al.*, 2007; Pathak and Hiratsuka, 2011). However, the knowledge-driven fuzzy expert system has not been used for the assessment of groundwater vulnerability to AMD at a regional scale, prompting more research in this area, hence this research was formulated to fill in this research gap. Knowledge-based fuzzy expert systems for groundwater vulnerability mapping are achieved by extracting the spatial relationships between groundwater vulnerability inputs layers in a GIS environment on the basis of the pollution migration, and quantifying and integrating these spatial relationships using mathematical logical operators (Dixon, 2005a). Cognitive reasoning is used for the formulation of these relationships and the assumptions made are defined.

4.4.1 Cognitive Reasoning

In order to apply the fuzzy expert system for assessment purposes, cognitive reasoning for each parameter affecting groundwater vulnerability is used in the formulation of fuzzy rules and to assign the correct map and class weights.

4.4.1.1 Sources factor

4.4.1.1.1 Energy sources

The cognitive reasoning for the energy source layer is such that groundwater systems under topographically flat areas are likely to receive more recharge than those overlain by sloped surfaces. The reasoning behind this assertion is that the availability of water in flat areas increases infiltration which is responsible for the transportation of AMD reaction products to the groundwater system. The effect of evapotranspiration and dilution processes on AMD pollution concentration at a regional scale is seldom known, and therefore was not used in this research.

4.4.1.1.2 Ligand (water) sources

The availability of water for AMD formation and the transportation of the AMD products also contributes to the fate of the groundwater with regards to AMD pollution where water acts as both the reactant for the formation of AMD and as a transport medium through which AMD pollution can reach the groundwater system. Thus, the likelihood of AMD being formed and transported linked to the availability of water constitutes the cognitive reasoning for the ligand sources parameter.

4.4.1.1.3 Pollutant sources

The closer the groundwater system is to a potential AMD pollutant source, the higher the likelihood of the groundwater system being polluted. This assertion underlies the cognitive reasoning behind the pollution sources layer. That is, the further away a groundwater system is from pollutant sources, the more the natural attenuation processes filter out the pollutants from reaching the groundwater system.

The closer the groundwater system is to potential AMD pollutant sources, the higher the chances of the groundwater system being polluted (Ellis *et al.*, 2014).

4.4.1.2 Transportation pathway factor

The cognitive reasoning behind the transportation factor assumes that those properties of the soils, unsaturated and saturated zones which favour the easy transportation of AMD reaction products also contribute to the vulnerability of the groundwater to AMD pollution. That is, soils with a low clay content coupled with the presence of preferential vadose pathways, high rock permeability and high aquifer hydraulic conductivity tend to facilitate the easy movement of dissolved pollutants, thereby increasing groundwater vulnerability.

4.4.1.3 Traps

The cognitive reasoning assumptions behind the trap parameter hold that the physical and chemical properties (rock-AMD in the unsaturated and saturated conditions, and depth to water table) contribute to the natural attenuation of AMD and prevent it from reaching the groundwater system. That is, groundwater systems in areas with rocks which lack the ability to extract the AMD pollutant coupled with a shallow water table are more vulnerable to pollution owing to their decreased ability to attenuate the pollution.

4.5 FUZZY EXPERT SYSTEM: APPLICATION TO THE WITBANK, ERMELO AND HIGHVELD COALFIELDS

Using the SPT approach developed in this research and cognitive reasoning, a GIS-based fuzzy expert system was built and applied to generate a groundwater vulnerability model of the Witbank, Ermelo and Highveld coalfield. A three-stage fuzzy expert system involving fuzzification, fuzzy engine and defuzzification was used.

4.5.1 Fuzzification

Existing knowledge about AMD migration in soils, the vadose zone and aquifers combined with cognitive reasoning was used to assign map weights and class weights to various map layers. Confidence factors were assigned to an input layer based on the data resolution and level of uncertainty, as explained previously. The FMV for each vulnerability layer was estimated from the map and class weights and the confidence factor using the linear membership function given by Equation 4.2. Table 4.1 shows the map and class weights, the confidence factors and the fuzzy membership values for each of the ten crisp layer maps used in this research. In order to visualise the

translation of the cognitive reasoning, graphs of fuzzy functions versus crisp variables were plotted in Figure 4.2a, b and c to depict the sources, transportation pathway and trap factors respectively.

Table 4.1: Assigning map weights, class weights and confidence factors for various layers

Vulnerability factor	Crisp layer	Map weight	Confidence factor	Class	Class weight	Fuzzy values
Sources (S)	Ligand (water) sources	9	5	802–1 045 mm	9	0.405
				728–802 mm	7	0.315
				682–728 mm	5	0.225
				634–682 mm	3	0.135
	Energy sources	5	8	Linear between 0 and 5 %	10-1	0.40-0.04
				>5 %	1	0.04
	Surface pollution sources	9	8	0–400 m	10	0.720
				400–800 m	10 and 1	0.720–0.072
				>800 m	1	0.072
	Subsurface sources	8	6	0–200 m	5	0.240
				Distance >200 m	1	0.048
Transportation pathway (P)	Soil clay content	6	6	31% clay content in soil	1	0.036
				Linear between clay content 9%–31%	1-10	0.036–0.36
				9% clay content in soil	10	0.36
	Preferential pathways	4	6	At the geological contact or lineament	10	0.240
				Linear between distances of 0 m to 300 m	10–1	0.024–0.240
				Distance >300 m	1	0.024
	Relative vadose zone (rock) permeability	4	4	Mudstone, Shales (10^{-11} cm^2)	1	0.016
				Diamictite (10^{-10} cm^2)	3	0.048
				Sandstone (10^{-8} cm^2)	4	0.064
				Dolomite, Chert (10^{-6} cm^2)	5	0.080
				Diabase, Dolerite (10^{-6} cm^2)	5	0.080
				Quartzite (10^{-5} cm^2)	6	0.096
				Basalt, Gabbro, Felsite, Diorite (10^{-4} cm^2)	7	0.112
				Lava, Granite, Gneiss (10^{-3} cm^2)	8	0.128
				Alluvial (10^{-2} cm^2)	9	0.144
	Aquifer hydraulic conductivity	4	4	Alluvial (10^{-2} m/s)	10	0.160
				Andesitic lava, dolomite, chert (10^{-4} m/s)	9	0.144
				Sandstone (10^{-5} m/s)	6	0.096
				Gabbro, diabase, dolerite (10^{-6} m/s)	5	0.080
				Pyroclasts, diorite (10^{-6} m/s)	5	0.080
				Granite, granophyre, diamictite (10^{-9} m/s)	4	0.064
				Shales, mudrock, quartzite (10^{-11} m/s)	2	0.032
Traps (T)	Rock-AMD reactivity	7	9	Alluvial	1	0.063
				Diamictite, sandstone, quartzite	1	0.063
				Rhyolite, felsite	3	0.189
				Gabbro, diorite, norite, anorthosite	5	0.315
				Andesitic lava, pyroclasts	5	0.315
				Granite, gneiss, granophyre	5	0.315
				Diabase, dolerite	7	0.441
				Mudrock, shales	7	0.441
				Dolomite with chert	9	0.567
	Depth to water table	7	5	Depth of 4.8 m	10	0.350
				Linear between depths of 4.8– 21.8 m	10 and 1	0.035–0.35
				Depth of 21.8 m	1	0.035

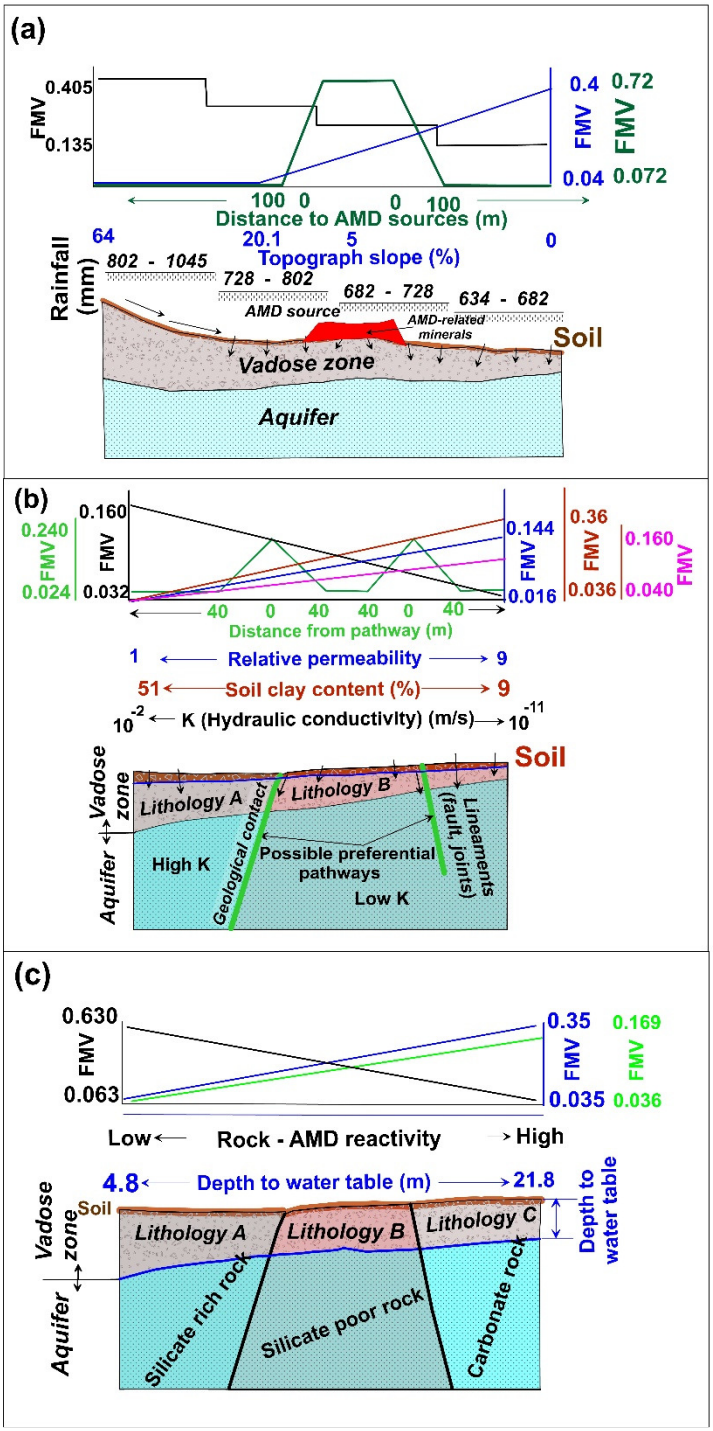

Figure 4.2: Crisp to fuzzy translation for (a) sources factor, (b) transportation pathway factor, (c) traps

4.5.1.1 Assigning map weights, class weights and confidence factors for the sources factor

The ligand (water) source layer was assigned a map weight value of 9, as water is one of the main inputs into AMD reactions and is responsible for the transportation of the reaction products. Surface sources of the AMD pollution map layer were also assigned a map weight value of 9 because the pyritic minerals found in these sources are exposed to atmospheric conditions where all the elements needed for the formation of AMD are present. Hence, surface sources are a very important parameter as the groundwater vulnerability assessment is specific to AMD pollution and this parameter relates

directly to AMD pollution. Subsurface sources of the AMD pollution layer were assigned a map weight value lower than that of the surface sources of the AMD sources layer because, even though they contain pyritic minerals, these are partially starved of oxygen (a key ingredient in AMD generation) and therefore their effect as an AMD source is diminished. The energy factor was assigned the lowest map weight of the parameters used as this parameter is not directly related to AMD generation but rather indirectly affects the residence time of reactions and the initial migration of the products of AMD reactions.

The ligand (water) source was assigned the lowest confidence factor of 5, as the dataset was extracted from countrywide data available at a relatively low resolution of 1 km. The confidence factors for the energy and surface sources of pollution are very high as these parameters were extracted from high-resolution datasets with a spatial resolution of less than 30 m. The subsurface sources of pollution were assigned a confidence factor of 6 as the information was extracted from lower-resolution geology data mapped at a scale of 1:250 000.

The classes for ligand (water) sources were calculated using the natural breaks method (ESRI, 2006). Class weight values were then assigned to each class according to the cognitive reasoning and a linear increasing relationship assumed between ligand (water) sources and groundwater vulnerability. The classes for the energy sources were derived from work by Fox *et al.* (1997) who established that the relationship between infiltration rates and slope angle is linear between 0 and 20% and flattens afterwards. The class weights for pollutant sources were assigned using the cognitive reasoning that, as the distance from the source increases, the effect of the pollution decreases owing to natural attenuation by various earth processes.

4.5.1.2 Assigning map weights, class weights and confidence factors for the transportation pathway factor

The map weight values of transportation pathway are relatively lower that those assigned for the sources factor because they only affect the transportation passage for pollution and not the AMD generation or attenuation directly. For the four crisp layers which make up the transportation pathway, the soil clay content was assigned a relatively higher map weight value of 6 as the clay content parameter affects the initial movement of AMD and contributes to the sorption processes which retard the AMD pollution from moving further into the subsurface. Preferential pathways, vadose zone permeability and aquifer hydraulic conductivity only affect the transport and thus were assigned a map weight value of 4.

The soil clay content and the preferential pathways were assigned confidence factor of 6 as they were derived from data mapped at a scale of 1:250 000. Relative rock permeability values and aquifer

hydraulic conductivity values were extracted from literature and a relative comparison of the values undertaken to generate the map layers. Since the information was derived from literature and no field or laboratory work had been done to generate these parameters a lower confidence factor of 4 was assigned to these map layers.

A linear increasing relationship for soil clay content was used for the classes and class weight values. The geological contacts, fractures, joints can act as preferential pathways through which pollution can migrate and transportation is restricted around these regions. A conservative buffer zone of 30 m was assigned around these geological structures. A higher class weight values of 10 was assigned to these geological structures and the buffer zone and values of 1 assigned at distances greater than 30 m where the preferential pathways were assumed to be negligible. The class and class weight for rock permeability and aquifer hydraulic conductivity were assigned according to the cognitive reasoning that the higher the permeability and hydraulic conductivity the more easily the pollution will migrate.

4.5.1.3 Assigning map weights, class weights and confidence factors for the traps factor

The depth to the water table layer was assigned a map weight value of 7 as this layer is one of the main controls of natural attenuation. In this layer, distance directly affects the travel time of the pollution, affecting the degradation and/or retardation processes impacting on the flux of the pollution. The rock-AMD reactivity map layer was assigned a map weight value of 7 as this parameter plays an important role in controlling the chemical retardation of AMD pollution.

The confidence factor of rock-AMD was assigned a very high value of 9 because laboratory simulation experiments were done in this regard, thereby increasing confidence in the usage of this parameter. The confidence factor for depth to water table layer was assigned a value of 5, as the data had been derived from spatially located boreholes whose depth to water table data had been interpolated between the boreholes to generate the map layer.

The classes and class weight for the rock-AMD reactivity layer were assigned for various rocks according to their reactivity with AMD at room temperature, as suggested by the results from the laboratory experiment and their mineral compositions. An increasing linear relationship for depth to water table was used to assign the class and class weight.

4.5.2 Fuzzy Inference Engine

In order to produce a holistic result which accommodates all three critical factors, a multistage fuzzy expert system was used (Figure 4.17). First, the ten input maps were grouped according to their respective relevant factors according to the SPT approach, as outlined in Chapter 3.

4.5.2.1 Sources factor input (S)

Energy sources: the topographic slope data were converted into fuzzy values as shown in Figure 4.2 and Table 4.1. Generally, the study area is marked by a high energy source because over 90% of the study is flat with slope values below 5% (Figure 4.3). This means that the residence time over which AMD reactions occur and the conditions favouring the infiltration of water are higher for most of the study area.

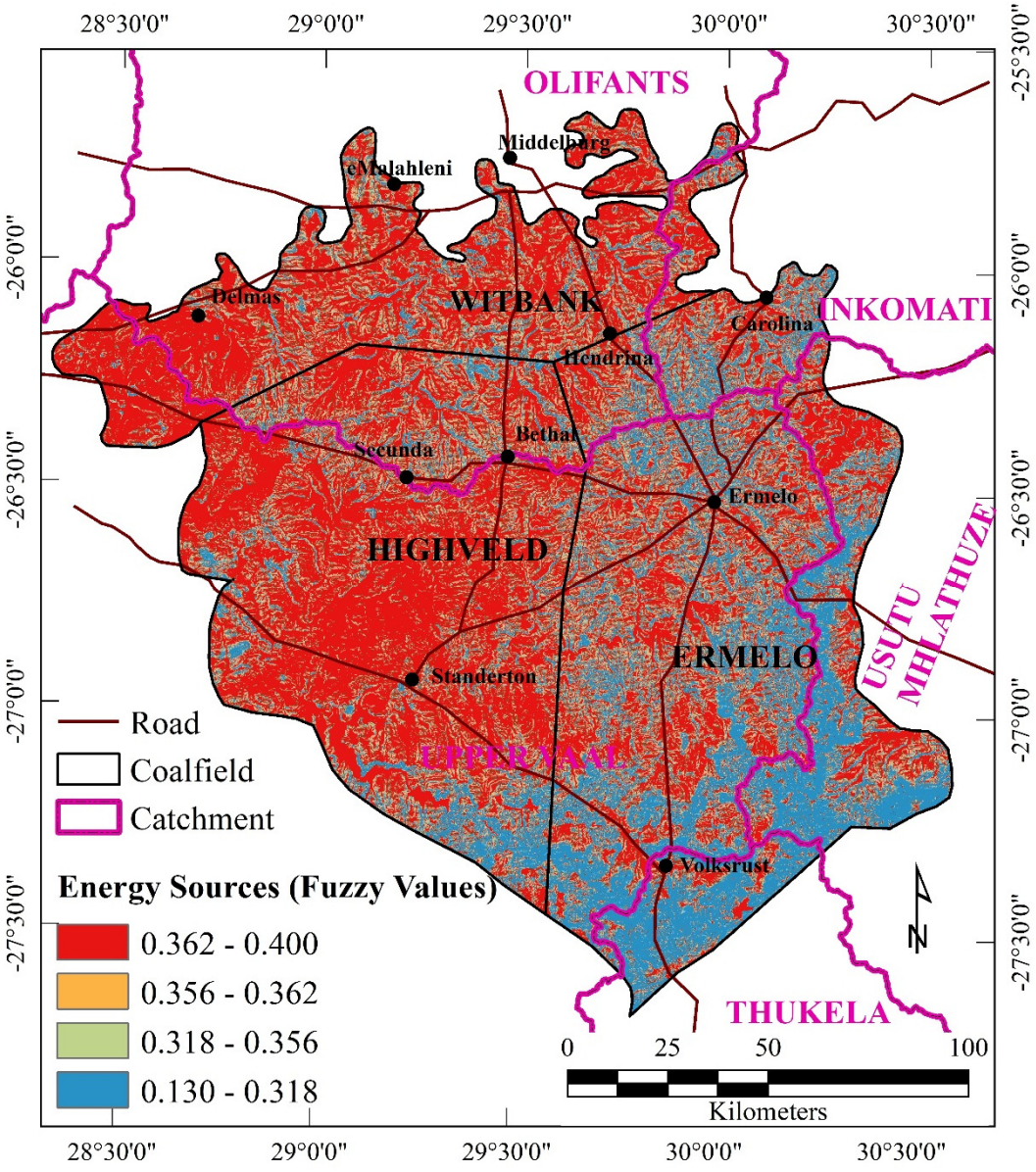

Figure 4.3: Sources of energy in fuzzy space

Ligand (water) sources: the average long-term rainfall was converted into fuzzy values using the translation shown in Figure 4.2. The highest ligand sources values were found in the southeastern part of the study area (Figure 4.4) along the foot of the Majuba Mountains (Figure 3.22) where the prevalence of relief rainfall is possibly attributable to elevation and such amounts of ligand sources

are able to drive pollution migration processes more than in the other parts of the study area with low to moderate ligand source values.

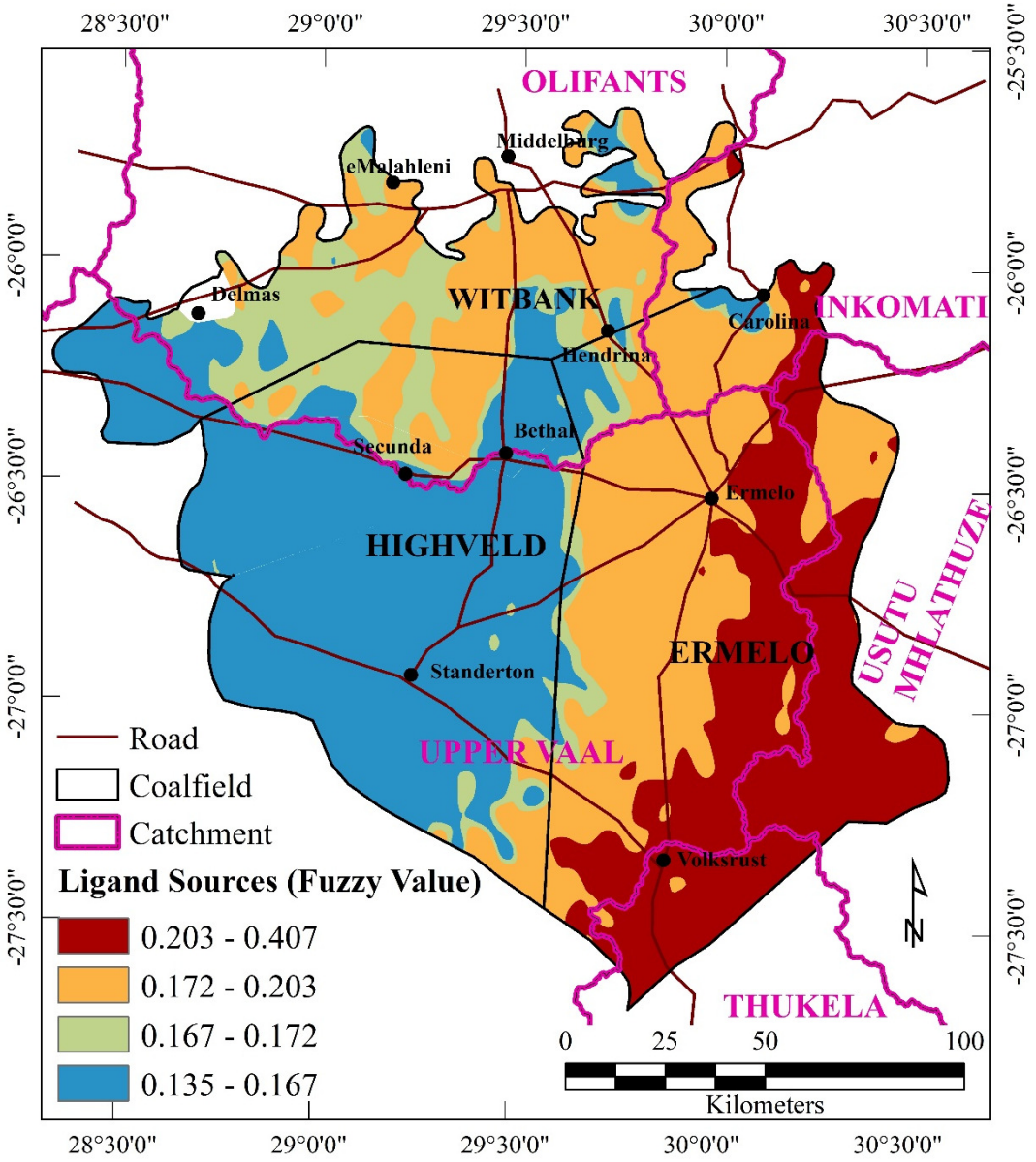

Figure 4.4: Sources of ligand (water) in fuzzy space

Pollution sources: the interpretation of Fe-bearing minerals on Landsat 8 and Sentinel 2 remote sensing data was converted to fuzzy values using the translation shown in Figure 4.2a. The spatial presentation of the translation is shown in Figure 4.5. Blue represents fuzzy values <0.234 corresponding to pixels (grid cells) located at distances greater than 174 m from the interpreted Fe-bearing minerals. Red represents the grid cells close to the interpreted Fe-bearing minerals within the 84 m zone which were translated to fuzzy values >0.558.

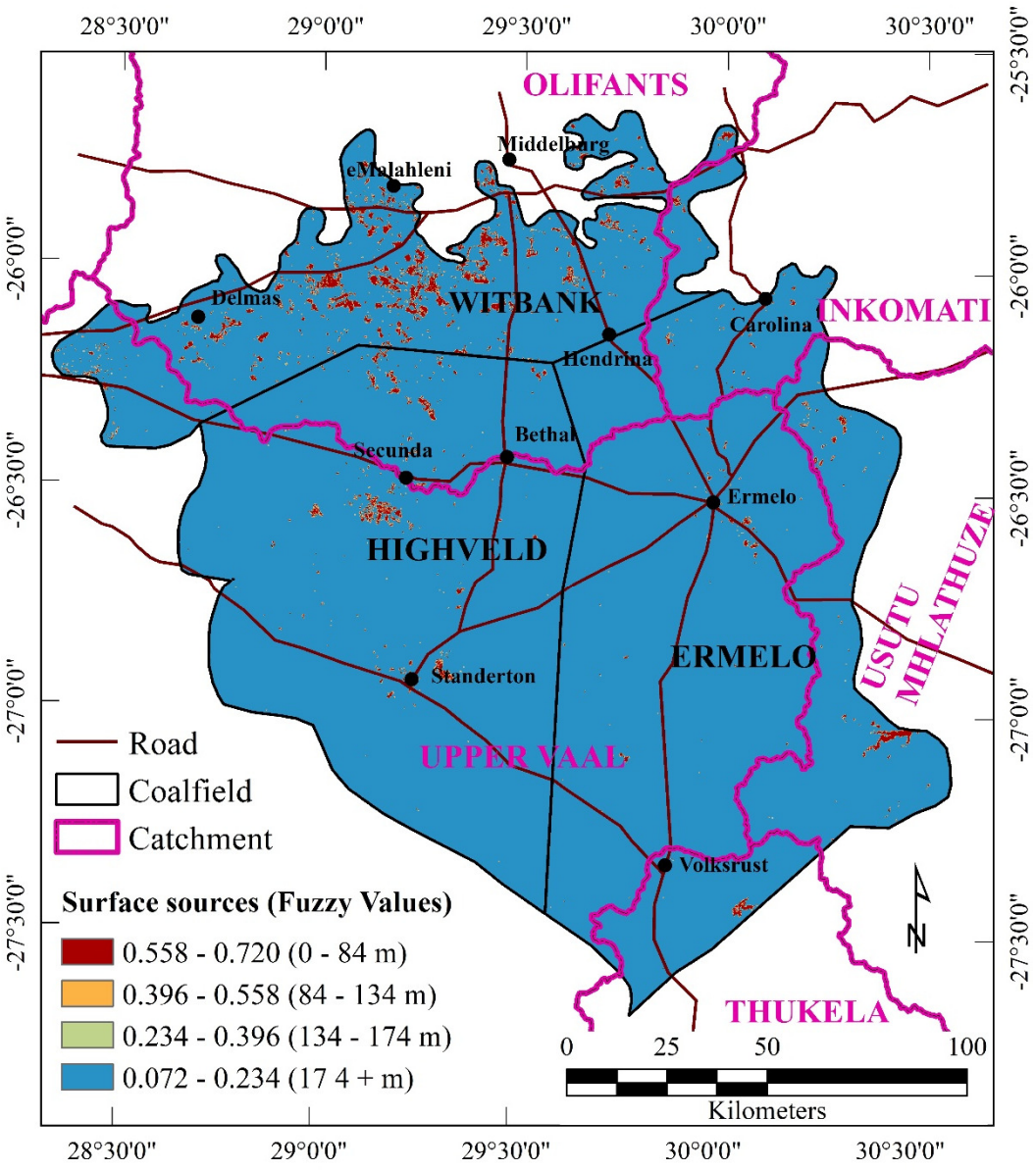

Figure 4.5: Surface sources of AMD pollution in fuzzy space

The subsurface sources were converted to fuzzy values with two distinct zones being presented (0 – 30 m and > 30 m). The red zone (0-30 m) corresponds to fuzzy value 0.240 and the grid cells located at distances greater than 30 m correspond to fuzzy value (0.048) and are marked in blue in Figure 4.6. Areas with high fuzzy values are located from the centre to the north where coal-bearing rocks (Ecca Group) are found and the southern part, without these rocks, is marked by low values.

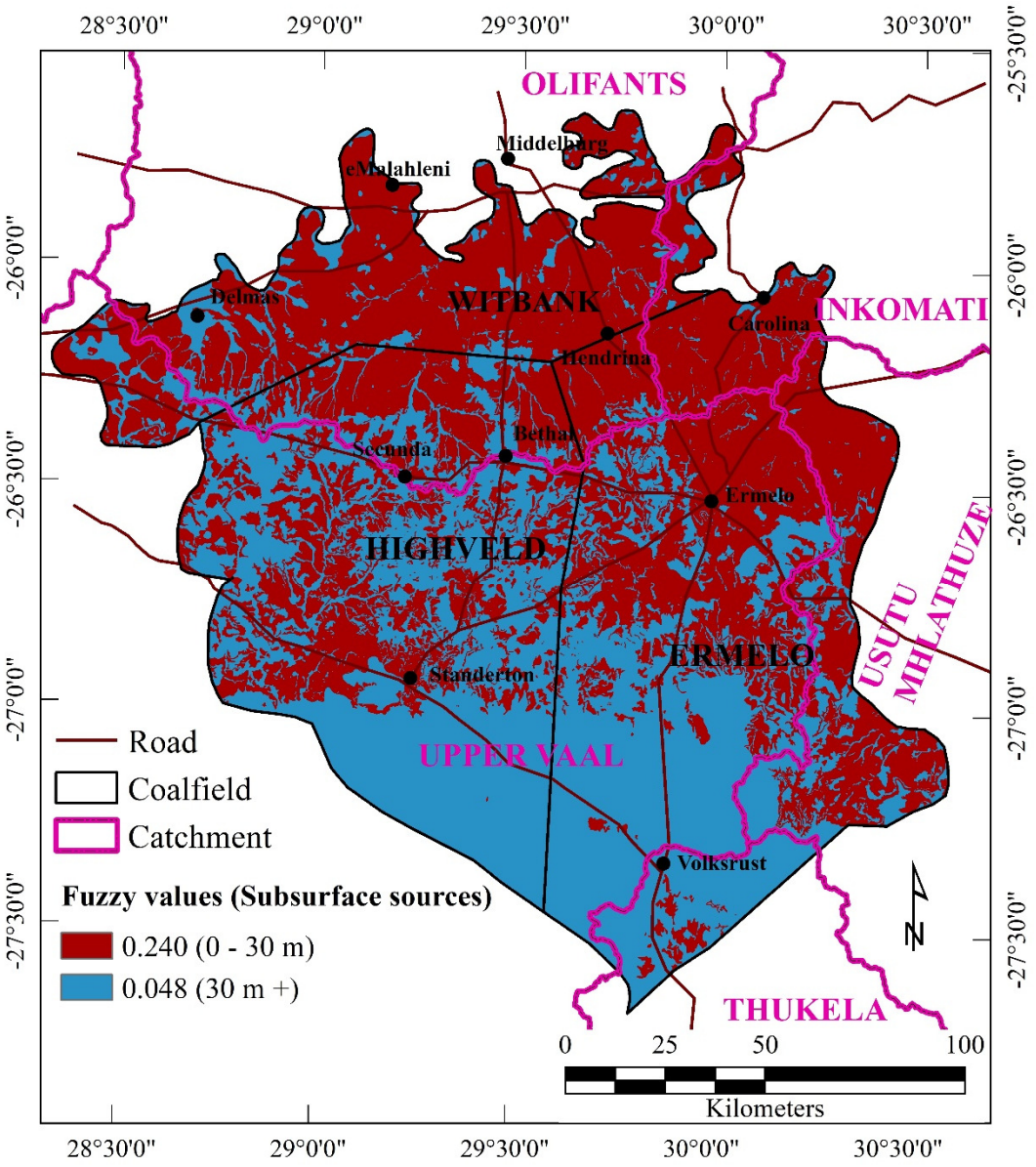

Figure 4.6: Subsurface sources of AMD pollution in fuzzy space

The fuzzy functions for AMD surface sources and the subsurface (Ecca Group rocks) sources were aggregated using a fuzzy (OR) operator to produce the pollutant sources layer (Figure 4.7). The fuzzy (OR) operator was used as any one of two sources can act as a source of AMD pollution which can affect the groundwater system. The result was divided into four classes (at the source, closer to the source, further away and furthest away from the source) using the geometric interval method (ESRI, 2006) (Figure 4.7). Most of the study area lies within the (further away) class which is represented in green in Figure 4.7. The colour blue in Figure 4.7 represents areas where coal seams were not mapped and current mining operations fall within the orange to red areas.

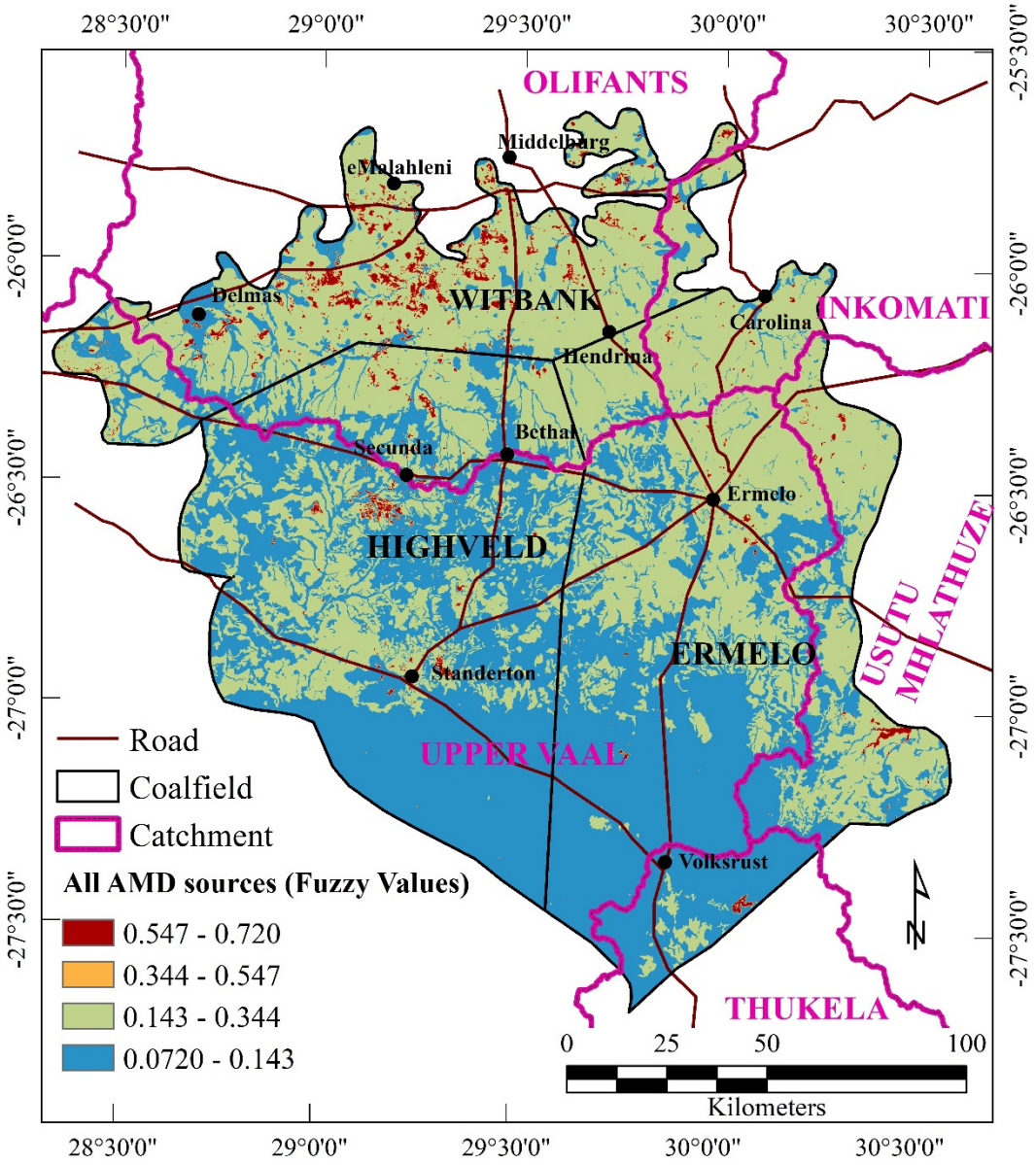

Figure 4.7: All sources of AMD pollution in fuzzy space constituted by combining surface and subsurface sources

The areas in red (Figure 4.7) mostly denote coal mining waste rock, tailings facilities and loading bays. These areas which are rich in pyritic minerals when exposed to oxygen and rain have a higher potential to form AMD. If proper waste management of these facilities is not practiced, any leakage can trigger the migration of AMD pollution into the subsurface and ultimately the groundwater system.

The three sources (energy, ligands and pollutants) were combined using the fuzzy (SUM) operator to produce the sources factor (MFs) in fuzzy values. The fuzzy (SUM) operator was chosen as it takes into consideration small changes in each of the input map layers. Thus, the generated source factors map is a good reflection of all the input map layers used to generate it. Figure 4.8 shows the resultant sources map in fuzzy values.

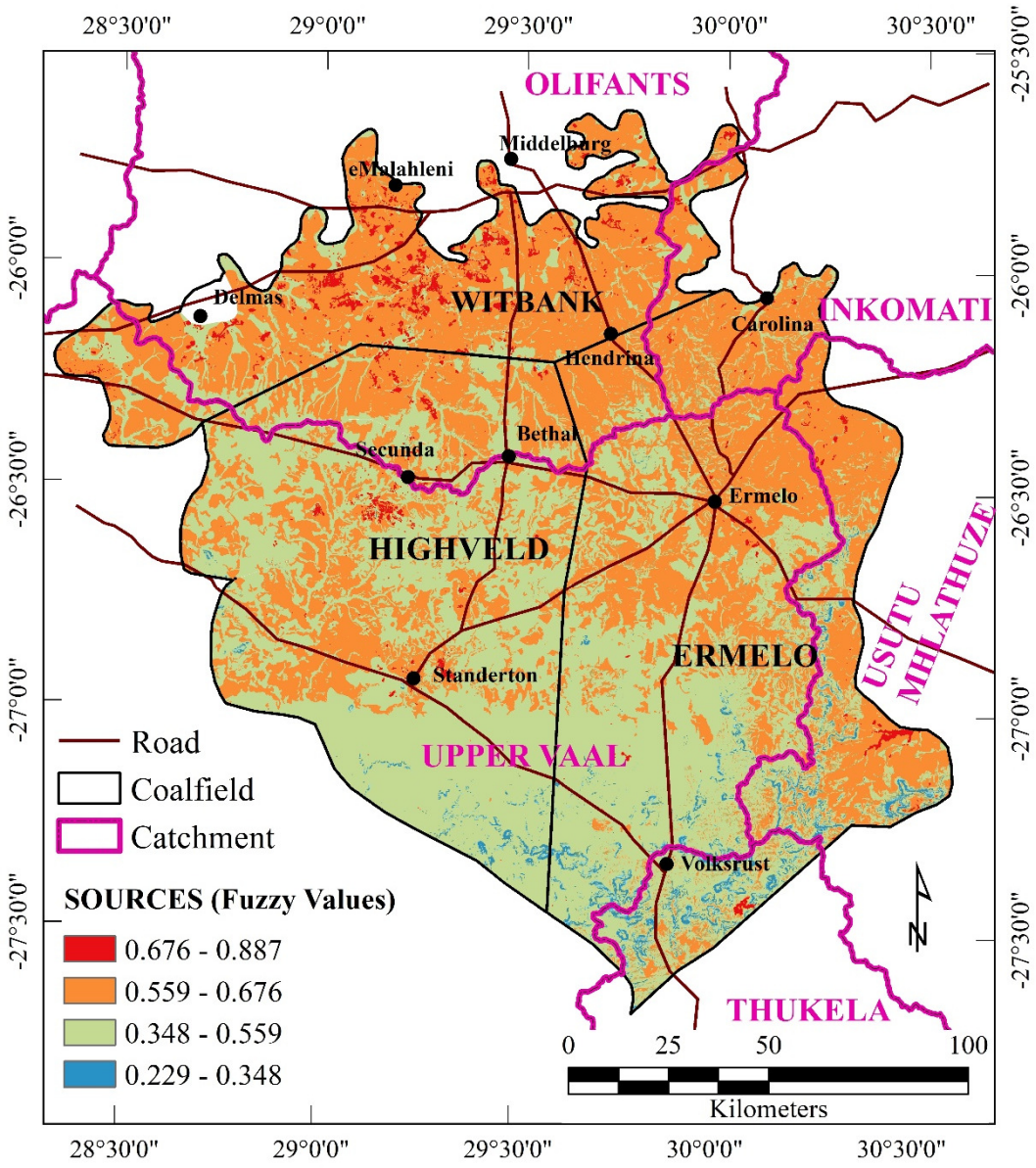

Figure 4.8: Sources factor produced by integration energy, ligand (water) and pollution sources

4.5.2.2 Transportation pathway factor input (P)

Soil clay content: the soil clay content layer was converted to fuzzy values using translation, as shown in Figure 4.2. The central part to the eastern end of the Witbank coalfield and the northern edge of the Ermelo and Highveld coalfields is marked by high fuzzy values because of high clay content. The Highveld coalfield and the southern part of the Ermelo coalfields are marked by relatively low fuzzy values owing to soils with a higher clay content there (Figure 4.9).

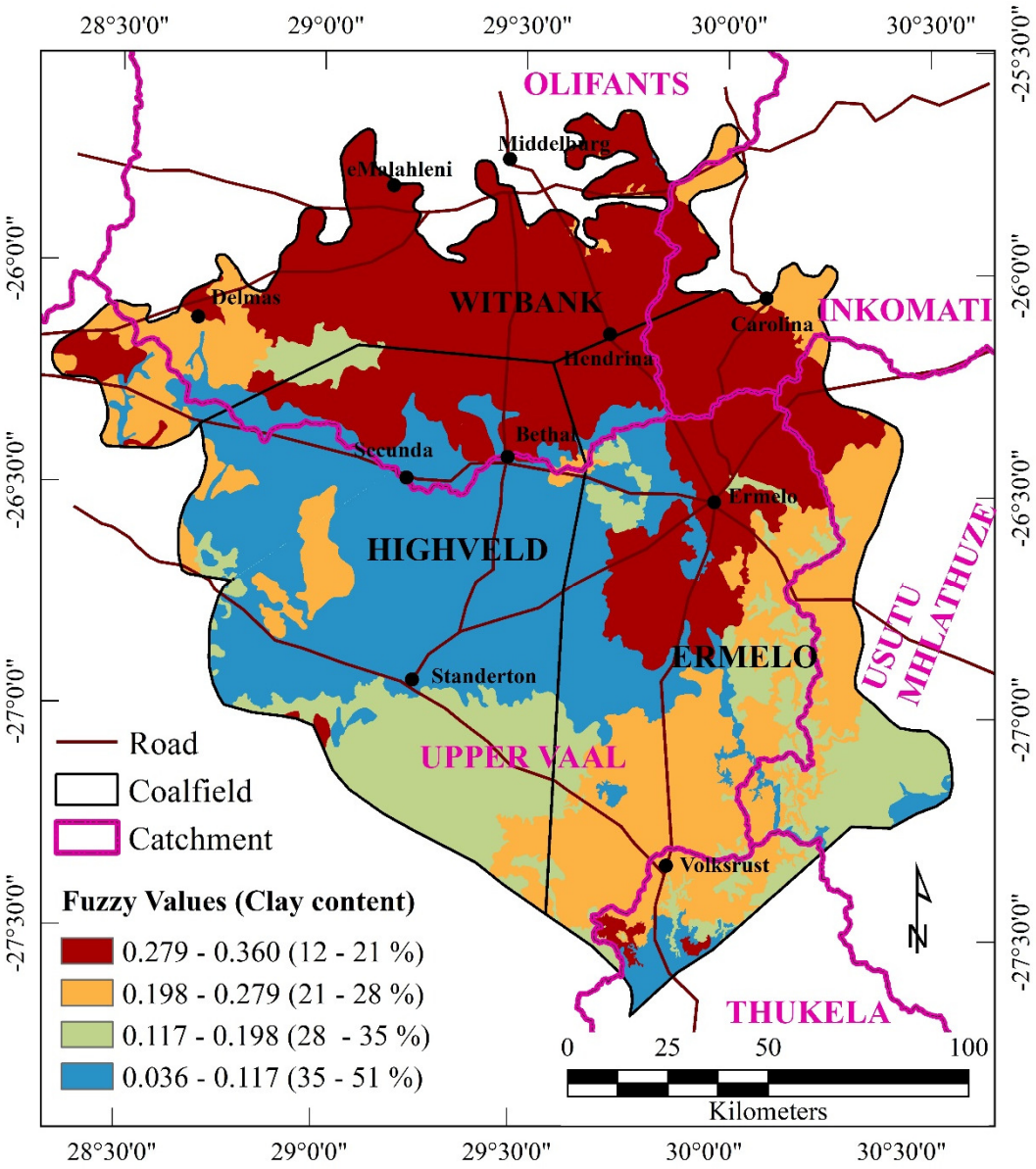

Figure 4.9: Transportation pathways in soils (clay content) expressed in fuzzy values

Preferential pathways: Figure 4.10 shows the preferential pathways which were interpreted from geological maps and airborne magnetic data expressed in fuzzy values according to translation, as shown in Figure 4.2. These pathways are more prominent in the area between Standerton, Ermelo and eMalahleni where an extensive network of Karoo dolerite dykes and sills was mapped. The presence of this extensive network of dykes may be an indication of the weakness within the subsurface as the emplacement of dykes normally occurs at weak zones of the crust.

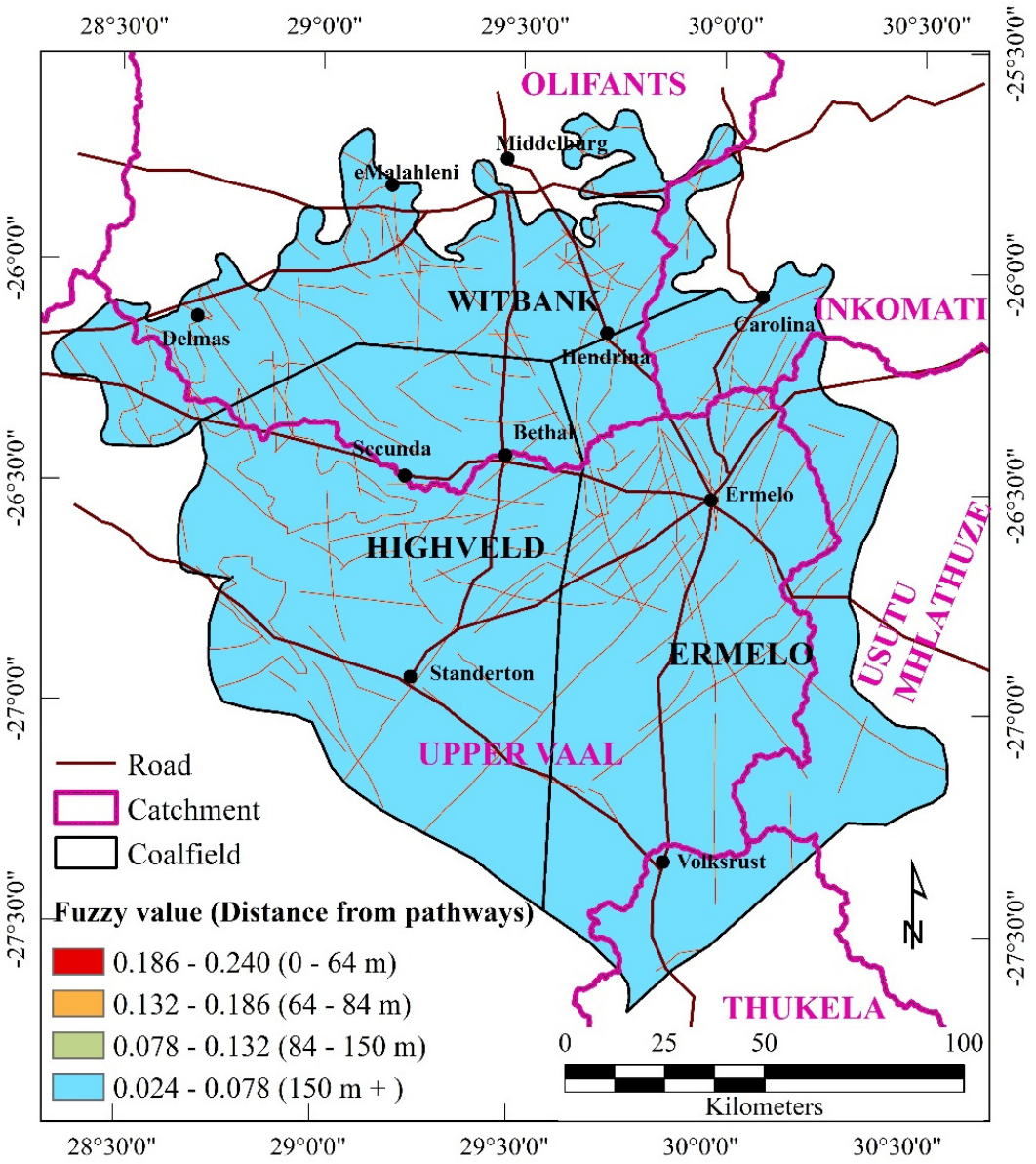

Figure 4.10: Preferential pathways expressed in fuzzy values

Rock permeability: the rock permeability layer extracted from the literature values was translated into relative fuzzy values. The results of the translation are shown in Figure 4.11. The high values are found along major rivers with well-developed alluvial systems where the permeability values are relatively higher than for most rocks in the study area. Areas where sandstones were mapped are marked by relatively higher permeability values than for most rocks but lower than for those of the alluvial systems. The other rocks were assigned accordingly with diabase and dolerite ranked at the bottom of the list as these are characterised by very low permeability values and thus the lowest fuzzy values.

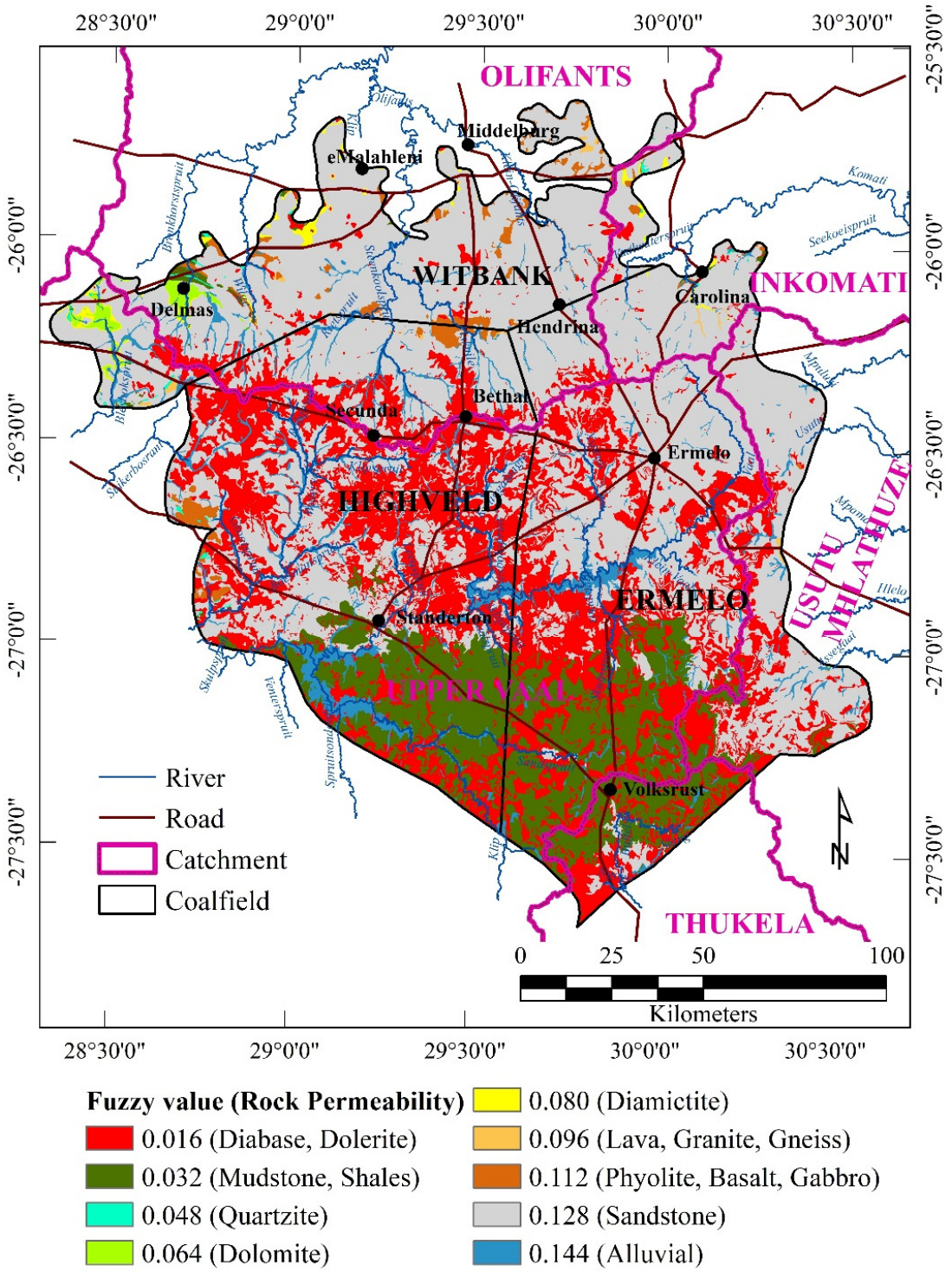

Figure 4.11: Rock permeability expressed in fuzzy values

Aquifer hydraulic conductivity: the high fuzzy values are found along rivers with well-developed alluvial systems, making up the intergranular aquifer system characterised by high hydraulic conductivity values. Conversely, low values are found in areas where shales, mudrocks were mapped owing to the low hydraulic conductivity values of these rock formations (Figure 4.12).

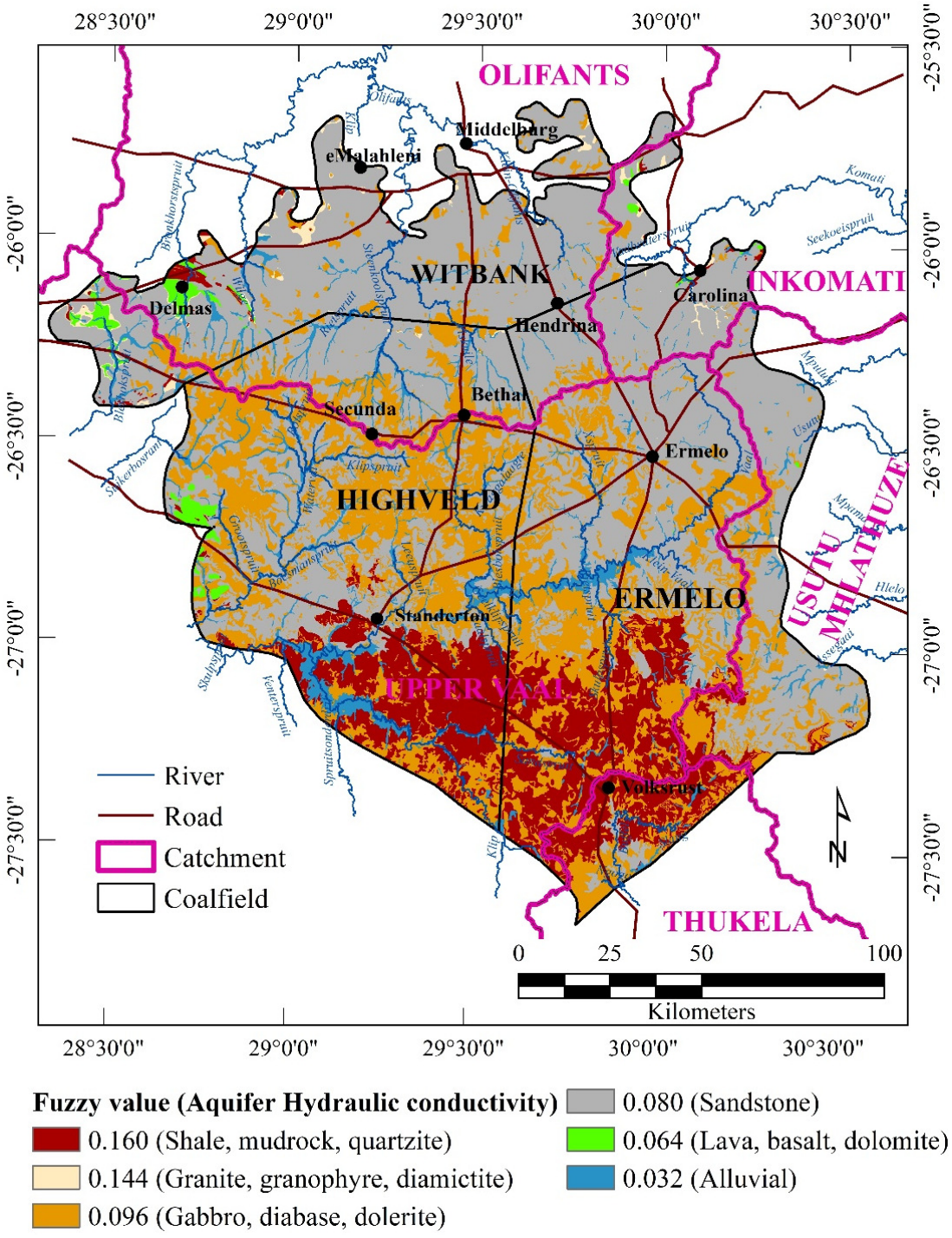

Figure 4.12: Aquifer hydraulic conductivity expressed in fuzzy values

The transportation pathway factor is made up of soil clay content, preferential pathways, vadose zone permeability and aquifer transport (hydraulic conductivity). These parameters with their respective fuzzy functions were combined using the fuzzy (SUM) operator to produce the transportation pathway factor (MF_T). Figure 4.13 shows the resultant transportation pathway factor map depicting variations in the AMD transport properties of the study area. Good transport properties were identified in the Witbank coalfield and in the eastern part of the Ermelo coalfield as a result primarily of the presence of soils with low clay content (<17.6%) coupled with the presence of subsurface rocks with

high permeability and hydraulic conductivity. Areas surrounding the major rivers in the Witbank coalfield also have good AMD transport properties, making the underlying aquifer vulnerable to pollution.

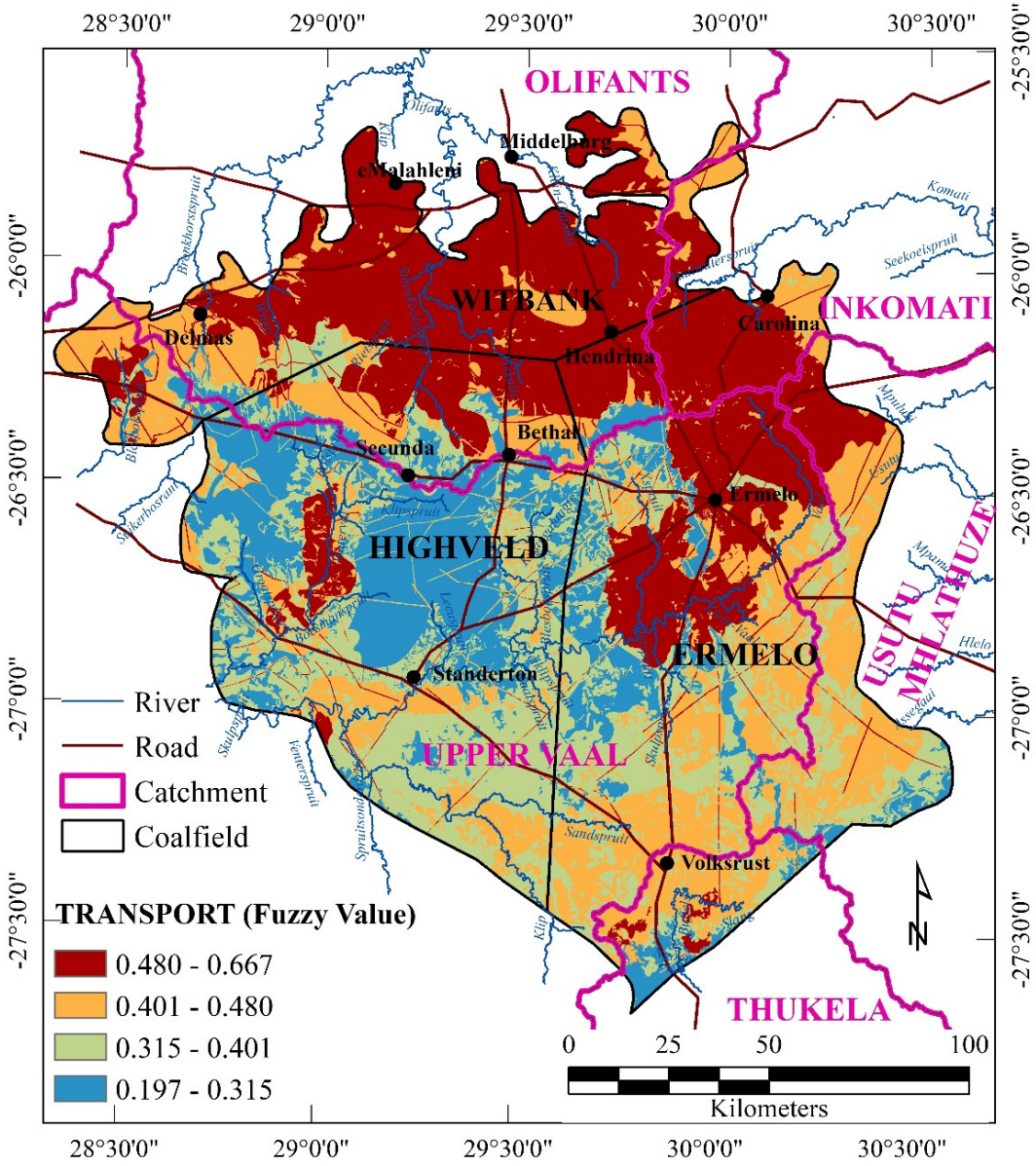

Figure 4.13: Transportation pathways factor generated by combining AMD transport parameters in the soil, vadose zone and the aquifer system

4.5.2.3 Traps factor input (T)

Rock-AMD reactivity: the results of the laboratory experiments carried out in Chapter 3 on the effects of various rocks on the chemical attenuation of AMD were converted into fuzzy values using translation, as shown in Figure 4.2. The results displayed in Figure 4.14 show that the biggest portion of the study area is marked by high fuzzy values for rock-AMD reactivity. This may be ascribed to the sandstones which constitute the majority of the coalfields. These rocks comprise quartz minerals which are chemically non-reactive in the AMD environment over a short period of time. In the

western part of the study area around Delmas, low fuzzy values are the result of the presence of dolomites with high neutralising capacity as discussed in the rock-AMD reactivity experiment in Chapter 3 section 3.4.5.10.

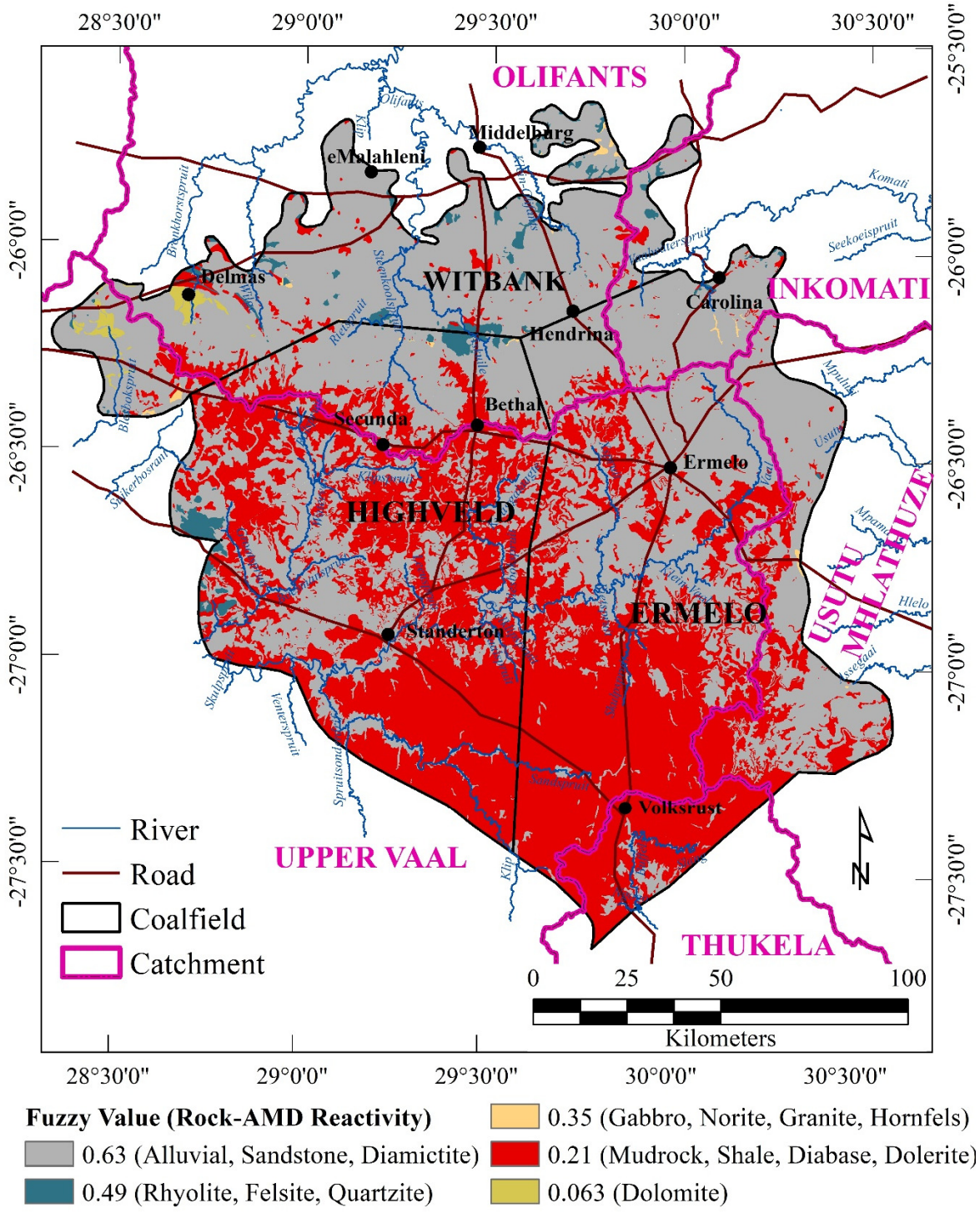

Figure 4.14: Rock-AMD reactivity expressed in fuzzy values

Depth to water table: the depth to water table map layer was converted into fuzzy values using translation as shown in Figure 4.2 and Table 4.1. The results are displayed in Figure 4.15. The area

in the centre of the study area is marked by a very shallow depth to water table, hence the high fuzzy values.

The rock-AMD reactivity and the depth to water table maps were combined using the fuzzy (SUM) operator to produce the traps factor (MF_T). The results are displayed in Figure 4.16 which depicts high fuzzy values in the central part of the study area characterised by sandstone, granite and alluvium with very low acid-neutralising capacity and a shallow depth to the water table. The north-western and south-eastern areas are characterised by average to good trapping properties because of the presence of rocks with the ability to attenuate AMD chemically and a deeper water table where pollution is likely to be attenuated before reaching the groundwater.

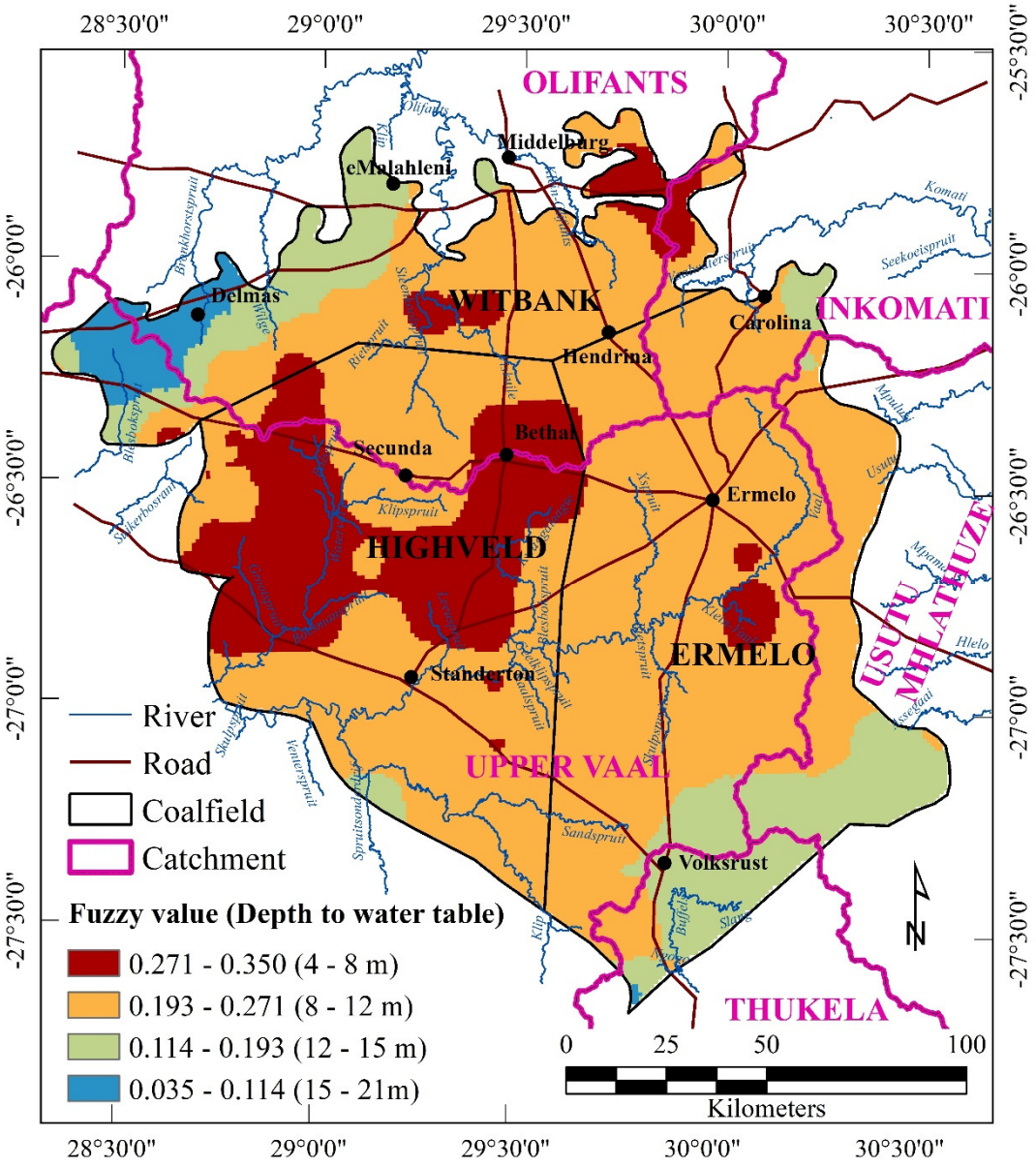

Figure 4.15: Depth to water table expressed in fuzzy values

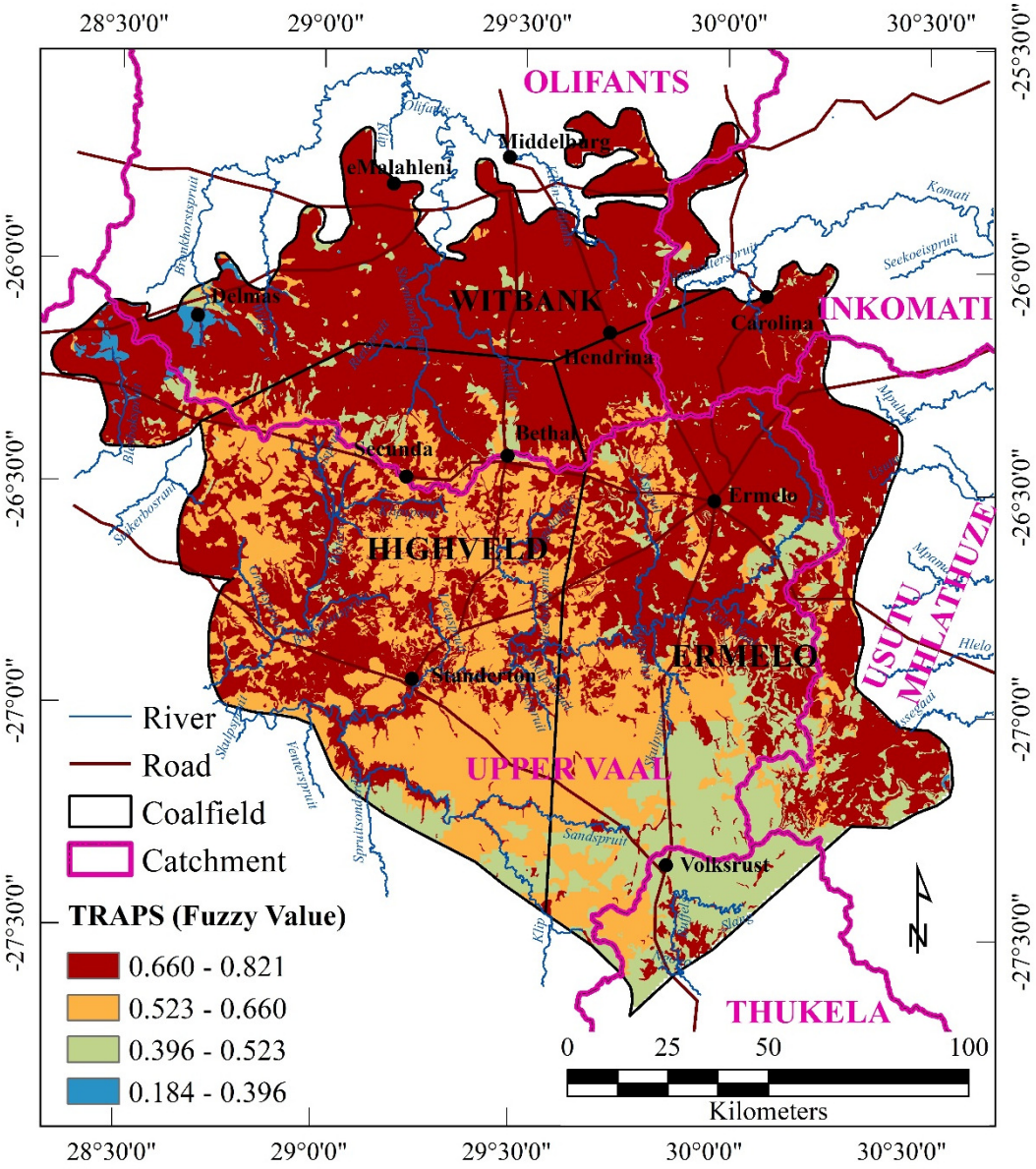

Figure 4.16: Traps factor generated by combining natural AMD trapping parameters in the soil, vadose zone and the aquifer system

4.5.2.4 Resultant fuzzy output model

The resultant three factors (sources, transportation pathways and traps) were then aggregated using the fuzzy rule given by Equation 4.9. Figure 4.17 illustrates the multistage fuzzy inference network which shows the relationship between the various input parameters and the fuzzy operators used for fuzzy modelling. The fuzzy (AND) operator was used in the fuzzy rule because all three factors must all be true and combine together in making the groundwater vulnerable to pollution.

$$IF\ (Sources\ (S)\ belong\ to\ MF_S)\ AND\ (Transport\ (P)\ belong\ to\ MF_T)\ AND\ (Traps\ (T)\ belong\ to\ MF_T)\ THEN\ (Vul\ belong\ to\ MF_{vul}) \quad 4.9$$

Where S – source factor, MF_S – input FMF for the source factor, P – transportation pathway factor, MF_T – input FMF for the transportation pathway factor, T – traps factor, MF_A – input FMF for the traps factor and Vul – groundwater vulnerability, MF_{vul} – output FMF for the groundwater vulnerability output.

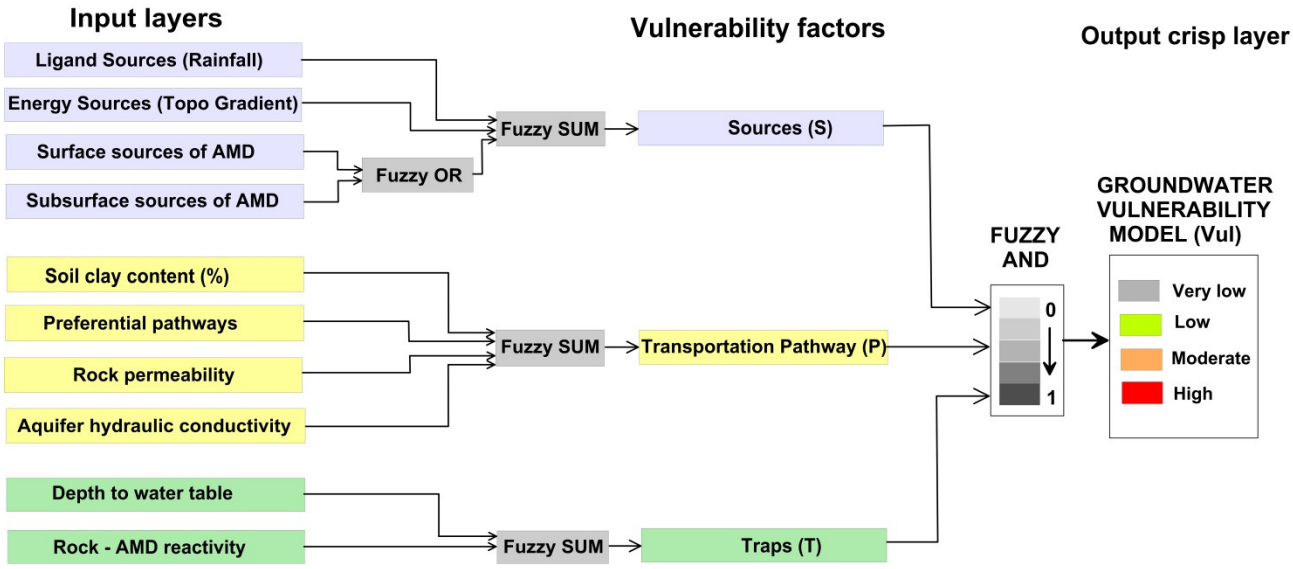

Figure 4.17: Multistage fuzzy inference network used for combining input layers to produce the groundwater vulnerability model

In this study, the fuzzy (AND) operator was used, as has been done by other authors, to combine various layers to produce groundwater vulnerability maps (Dixon, 2005b; Pathak and Hiratsuka, 2011; Fijani *et al.*, 2013).

4.5.3 Defuzzification

Defuzzification, which is a process of translating fuzzy outputs of a function back to crisp variables was done in ArcGIS using the natural breaks method (ESRI, 2006). The defuzzification results (Figure 4.18) show four groundwater vulnerability crisp variables (high, moderate, low and very low) making up the groundwater vulnerability model of the Witbank, Ermelo and Highveld coalfields. The study area falls in the main Karoo basin where the hydrogeological conditions warrant the usage of the Irish model given by Daly and Warren (1998). The Irish model describes groundwater vulnerability in terms of four classes (high, moderate, low and very low).

The results show that the western, central and the southern areas have moderate to low vulnerability owing to a combination of interconnected factors which enhance the natural attenuation and/or extraction of AMD pollutants thereby preventing it from reaching the groundwater system. The central to eastern part of the Witbank coalfield and the northern part of the Ermelo coalfield are marked by moderate to high groundwater vulnerability values. The distribution of classes in terms of

aerial coverage is shown in Table 4.2. The distribution of the groundwater vulnerability classes follows a skewed normal distribution curve, with the largest population being the moderate class and the high class being the smallest in terms of aerial extent (Figure 4.19).

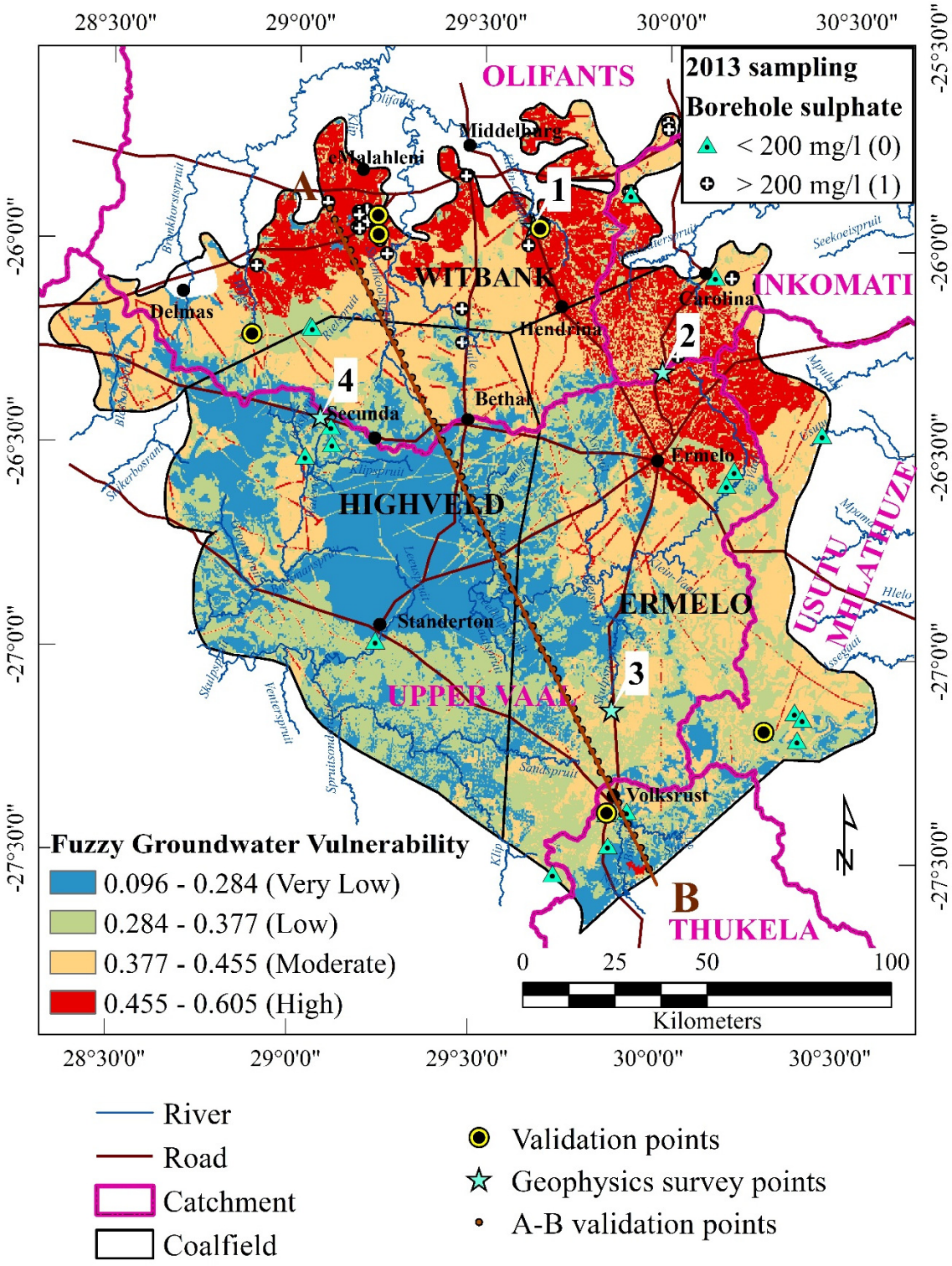

Figure 4.18: Resultant groundwater vulnerability model of the Witbank, Ermelo and Highveld coalfields

Table 4.2: Aerial coverage of various vulnerability classes

Vulnerability classification	Size (km^2)
Very Low	7 019.6 (25.4 %)
Low	7 731.9 (28.1 %)
Moderate	8 867 (32.2 %)
High	3 951 (14.3 %)

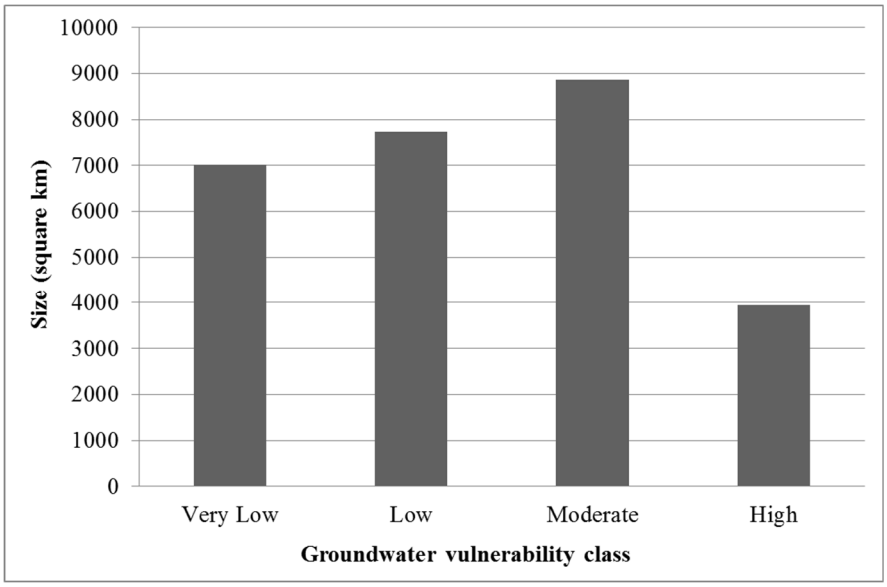

Figure 4.19: Aerial size distribution of various groundwater vulnerability classes

4.5.4 Model Validation of the Fuzzy Expert System

Groundwater vulnerability results are a relative comparison of various areas in terms of which area is more likely to be polluted than the others are. Therefore, there are no universally accepted validation procedures, as vulnerability results are relative and vary from place to place. Validation of groundwater vulnerability results is often done by a comparison of the results using measurable parameters which may be considered as a pollution tracer (e.g. nitrate) (Nobre *et al.*, 2007; Saidi *et al.*, 2010; Fijani *et al.*, 2013).

4.5.4.1 Model validation using hydrochemistry data

4.5.4.1.1 Correlation coefficient approach

In the study area, AMD is associated with high sulphate concentrations above the South African guidelines (SANS, 2011) for drinking water (Bell *et al.*, 2001). From Chapter 3, it was shown that sulphate is relatively conservative and may be considered as a tracer for AMD pollution. Based on these findings, sulphate concentration in boreholes from the 2013 sampling programme was used to validate the produced groundwater vulnerability model, where it was assumed that the sulphate values

in the groundwater are attributable to one or more of the vulnerability factors (energy, pollutant sources, transport and traps).

The spatial variation of sulphate concentrations in groundwater samples within the study area is shown in Figure 4.18, where samples with less than 200 mg/L are represented by green triangles and those greater than 200 mg/L are represented by a circle with a white star. It is interesting to note that groundwater samples with a high sulphate concentration coincide with moderate to high groundwater vulnerability zones while samples with low sulphate concentrations lie in low to very low groundwater vulnerability zones.

A correlation analysis between model values and AMD indicators (sulphate) was done and a scatter plot produced, as shown in Figure 4.20. Correlation scatter plots between model values and measured parameters show high correlation coefficient value (R) values of 0.809 which show a strong positive correlation between the fuzzy model and sulphate concentration in the groundwater.

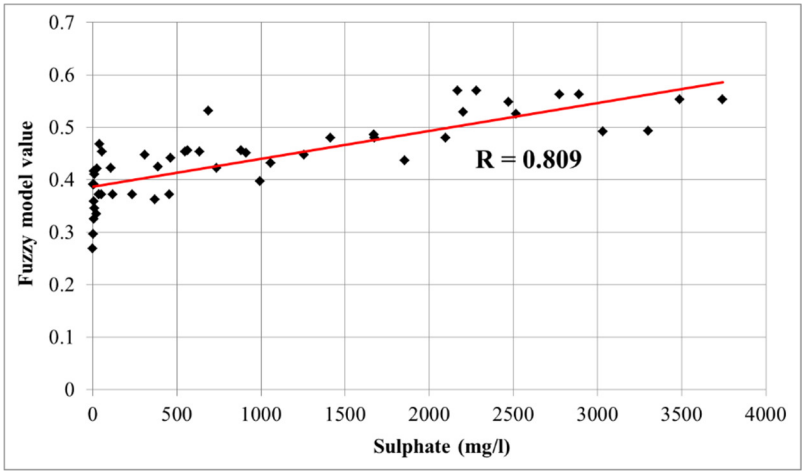

Figure 4.20: Correlation scatter plots for sulphate against groundwater vulnerability model values

4.5.4.1.2 Cross-section method of validation

To test the validity of the fuzzy groundwater vulnerability assessment using SPT inputs, sulphate data from a different source to the one used for the correlation coefficient approach was selected as a pollution indicator. Borehole hydrochemistry data from the National Groundwater Archive (NGA) with verified locations were tested for ionic balance and only those with an ionic balance of less than ± 5% were selected for model validation. Sulphate data from 60 boreholes within the study area were used to compare relative SO_4^- concentration to vulnerability values. The kriging interpolation method was used to generate the sulphate concentration map of the study area, as shown in Figure 4.21. The map shows high sulphate concentrations in the Olifants catchment covering the area south of eMalahleni and Middelburg. To illustrate this validation test, a cross-section, A–B, was created on

the vulnerability and the sulphate maps and values extracted to make profiles (Figure 4.22). The comparison of these cross-sections enabled an evaluation of the validity of the vulnerability map.

The comparison between the map of sulphate concentrations and the vulnerability maps shows that areas with high sulphate concentrations in the groundwater correspond to the highest vulnerability values whereas those with low sulphate concentrations are correlated with the lowest vulnerability values. This coincidence is very clear in the northern section of the cross-section between distances 10 to 140 km.

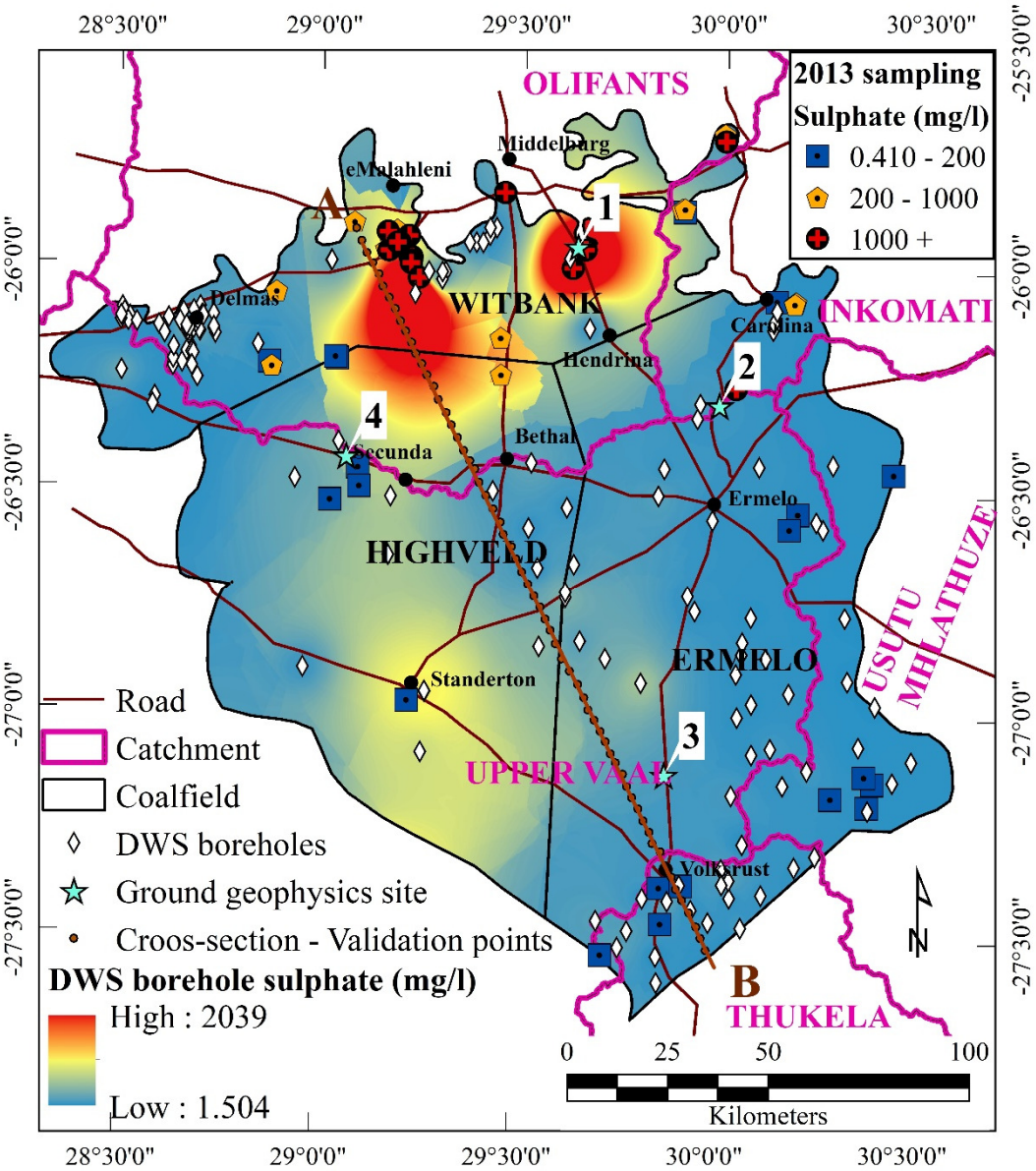

Figure 4.21: Sulphate concentration map generated from the NGA database

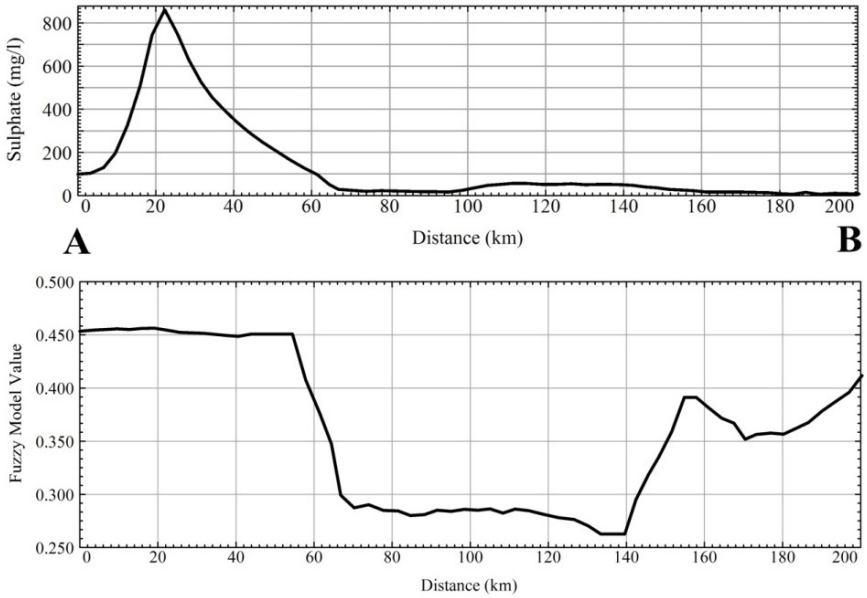

Figure 4.22: Profile along cross-section A–B showing the DWS borehole sulphate concentrations and the fuzzy vulnerability model profile

The profile (Figure 4.22) differs slightly towards the southern end of the section where the fuzzy model values increase slightly although the sulphate concentration remains constant. This could be attributable to gridding artefacts as there are no gridding points in this area which is at the edge of the gridded areas.

4.5.4.2 Validation using geophysical techniques

Geophysical techniques can be used to estimate *in situ* hydrogeological parameters (porosity, permeability, particle size) which, in turn, can be used to validate a groundwater vulnerability model. Electrical resistivity tomography (ERT) and seismic refraction techniques were done at four sites (1 to 4) which fall into very low, low, moderate and high groundwater vulnerability classes respectively. The aim of the surveys was to determine whether various modelled groundwater vulnerability classes are able to produce measurable geophysical responses which can, in turn, be used as a model validation tool.

4.5.4.2.1 Materials and methods

Resistivity method

The concept behind the electrical survey is based on the current flow through a subsurface medium consisting of various layers of material with different resistances to current flowing through them where resistivity ρ_o of a material is a measure of how well the material resists the flow of electrical current. Resistivity surveys are done on the ground, where an electrical current (I) is injected into the ground using a set of electrodes (A) and (B) and the earth's response is measured as a voltage

difference (V) at potential electrode (M) and (N), as shown in Figure 4.23. The apparent resistivity can be calculated using Equation 4.10 (Loke, 2000):

$$\rho_o = K \frac{V}{I} \tag{4.10}$$

Where V, the voltage, is the difference of the potential electrodes and I is the current injected by the current electrode. K is the geometric factor which depends on the configuration of the electrodes — for example Wenner, Schlumberger, dipole-dipole, pole-dipole and other hybrid configurations.

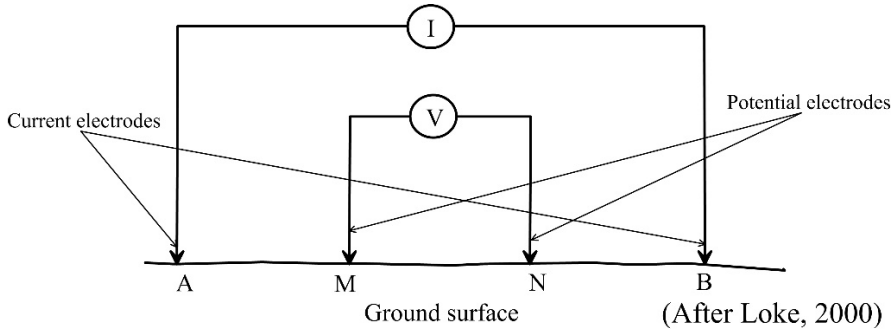

Figure 4.23: Simple layout of conventional four-electrode array used to measure the subsurface resistivity

The choice of the configuration depends on the purpose of the survey and is controlled by factors such as survey costs, available manpower, target feature configuration and geology. In this research, the hybrid Wenner-Schlumberger configuration was used as it offers good depth and lateral resolution in a sedimentary setting such as that found in the study area. A multi-electrode configuration of the Wenner-Schlumberger array with an electrode spacing of 5 m was used. The resistivity values obtained from the field survey were inverted to apparent resistivity values using the RES2DINV program. The program calculates apparent resistivity and displays them as a pseudo-2D resistivity section using the finite difference method with a robust inversion constraint. To produce the pseudo 2D resistivity section of the subsurface, the program first subdivides the subsurface into a number of small blocks and then uses a least-squares inversion scheme to determine the appropriate resistivity value for each block. The resistivity values for each block are then combined to produce a 2D pseudo resistivity section.

To convert resistivity values into porosity, Archie's Law (Archie, 1942) can be used. For the sandstone and to cater for both saturated and unsaturated conditions, Archie's Law was modified by Everett (2013) and is given by Equation 4.11:

$$\sigma_o = a\sigma_w S_w^n \theta^m \tag{4.11}$$

where σ_o is the conductivity of the rock, a is a constant that depends on the pore cementation tortuosity, grain size and shape, fluid wettability and clay content and ranges between 0.4 and 2, σ_w represent the conductivity of water which ranges between 0.3 and 1 where 0.3 represents very high salinity and 1 represents fresh water, S_w^n is a constant that specifies the level of saturation, i.e. $S_w^n = 1$ for fully saturated conditions. θ presents the porosity and m is the cementation exponent which depends on grain shape and lies within the range 1.2–2.2 for sandstone.

Rewriting Equation 4.11, the porosity can be estimated by Equation 4.12:

$$\theta = \left(\frac{\sigma_o}{a\sigma_w S_w^n}\right)^{1/m} \tag{4.12}$$

Using values, $a = 2$, $\sigma_w = 1$, $S_w^n = 1$ for saturated conditions and $S_w^n = 0.5$ for unsaturated conditions, $m = 2$, resistivity values were converted to porosity as in Equation 4.13:

$$\theta = \left(\frac{\sigma_o}{2 * 1 * 1}\right)^{\frac{1}{2}} = \left(\frac{\sigma_o}{2}\right)^{\frac{1}{2}} \; for\ saturated\ conditions$$

$$\theta = \left(\frac{\sigma_o}{2 * 1 * 0.5}\right)^{\frac{1}{2}} = (\sigma_o)^{\frac{1}{2}} \; for\ unsaturated\ conditions \tag{4.13}$$

Seismic refraction method

The seismic method is a geophysical technique which involves measuring the acoustic impedance of the subsurface and deducting the velocities which are related to the density. This is done by hitting the surface to generate a seismic signal which travels underground. The generated seismic waves are either reflected or refracted upon reaching an interface between two rock layers. The time of arrival of the seismic signal is extracted from the seismic trace and used to calculate the velocities and depths of different geological boundaries (Geosphere, 2007). The velocity information carries information about the nature of the rocks. Important hydrogeological parameters can be deduced from the seismic data. In this particular case, seismic information was collected with the overall goal of testing whether areas with different groundwater vulnerabilities would produce a measurable velocity contrast and for verifying whether these results could be used as a model validation tool. A detailed description of the seismic refraction method can be found in any standard geophysics textbook such by as Telford *et al.* (1990).

In this study, geophones which measure the arrival of the seismic wave were set up at 5 m spacing intervals and a hammer was used to produce the seismic waves by hitting a metal plate placed on the ground (Figure 4.24). A geode 72 channel seismic system was used for the data acquisition.

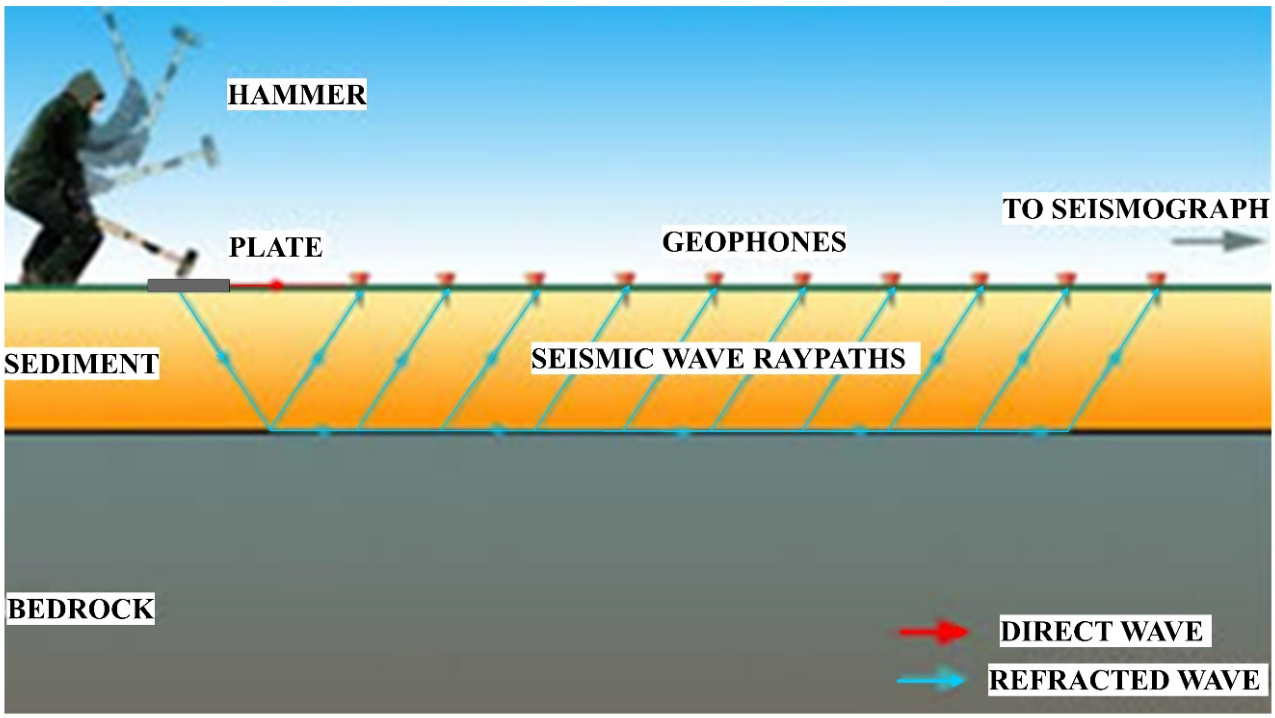

(After geosphere, 2007)

Figure 4.24: Simple layout of conventional seismic refraction survey

4.5.4.2.2 Results and discussion

Survey site 1

A resistivity survey was carried out at survey site 1 along a south–north-oriented 250 m line and the measured resistivity values inverted with the results displayed as pseudo 2D resistivity-depth section (Figure 4.25a). The resistivity section showed low resistivity values in the top layer probably due to wet soils observed on the surface. Figure 4.25b shows the porosity distribution along survey site 1. Generally, porosity increases with depth where the estimated porosity for weathered sandstone ranges between 9 and 25%. The low porosity values down to 8% are associated with fresh sandstone with less porosity owing to compactness and less weathering. High porosity values of the weathered sandstone and soils may be an indication of large matrix void spaces which are typically associated with weathered rock masses. With reference to groundwater vulnerability this could be a possible justification for why this area falls in the high groundwater vulnerability class.

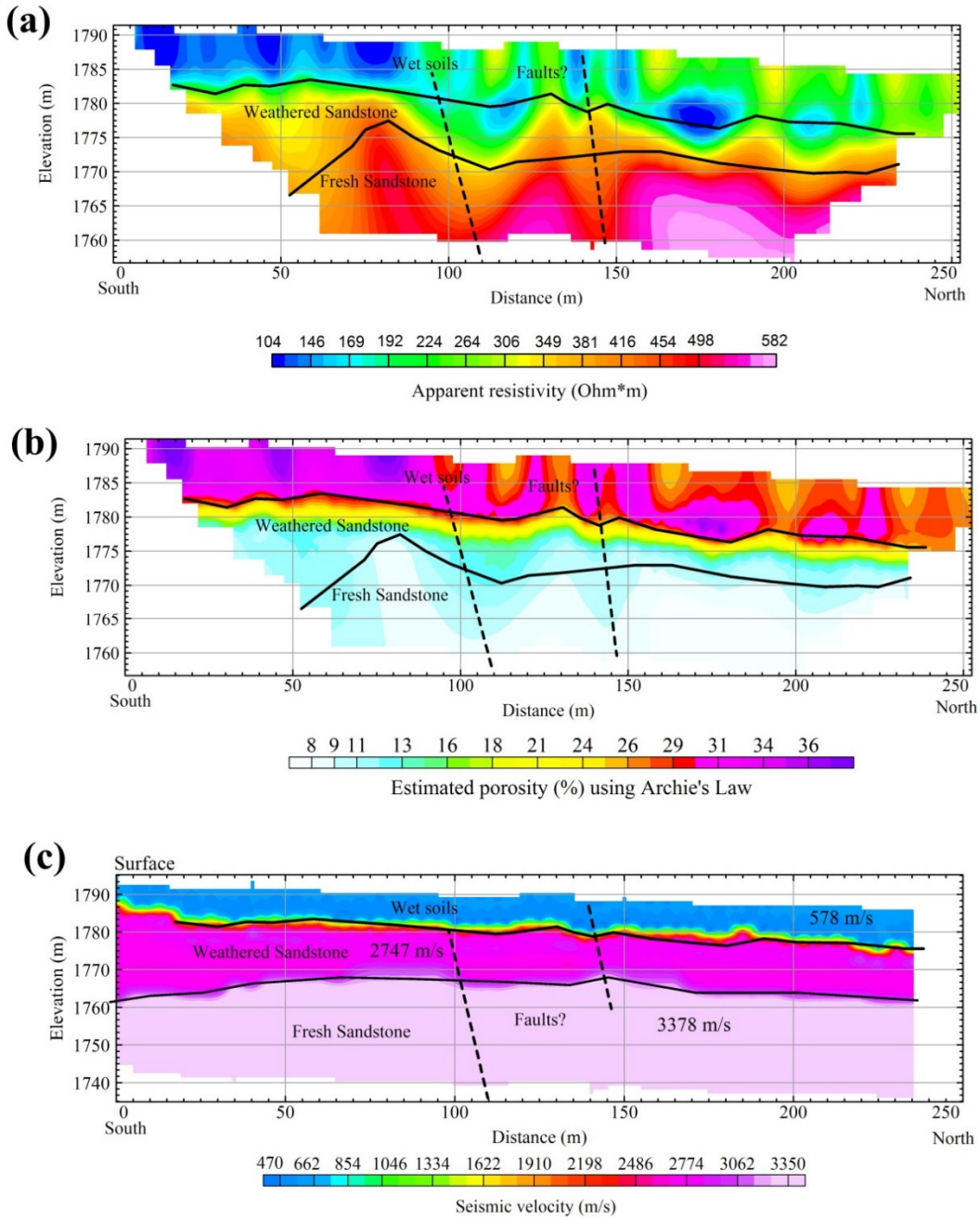

Figure 4.25: 2D resistivity survey results for site 1 showing (a) the modelled apparent resistivity-elevation, (b) the derived porosity-elevation and (c) seismic velocity plot

Figure 4.25c shows the seismic velocity distribution along survey site 1. Generally, velocity increases with depth where the estimated velocity of the soil, weathered sandstone and fresh sandstone are 578, 2 747 and 3 378 m/s respectively, as shown in Figure 4.25c. Possible faults were also interpreted at the site which could act as conduits through which pollution migrates. This complements the resistivity results and offers a possible reason why the site is classified as highly vulnerable.

Survey site 2

A resistivity survey was carried out along a south–north-oriented 250 m line. The resistivity values were inverted with the results displayed as pseudo 2D resistivity-depth section (Figure 4.26a). The

resistivity section showed high resistivity values in the saturated zone below the water table corresponding to the location where coarse-grained sandstone had been mapped. The survey line passed through several ponds, as highlighted in Figure 4.26. This was responsible for the low resistivity values recorded near the surface and below the locations of the ponds.

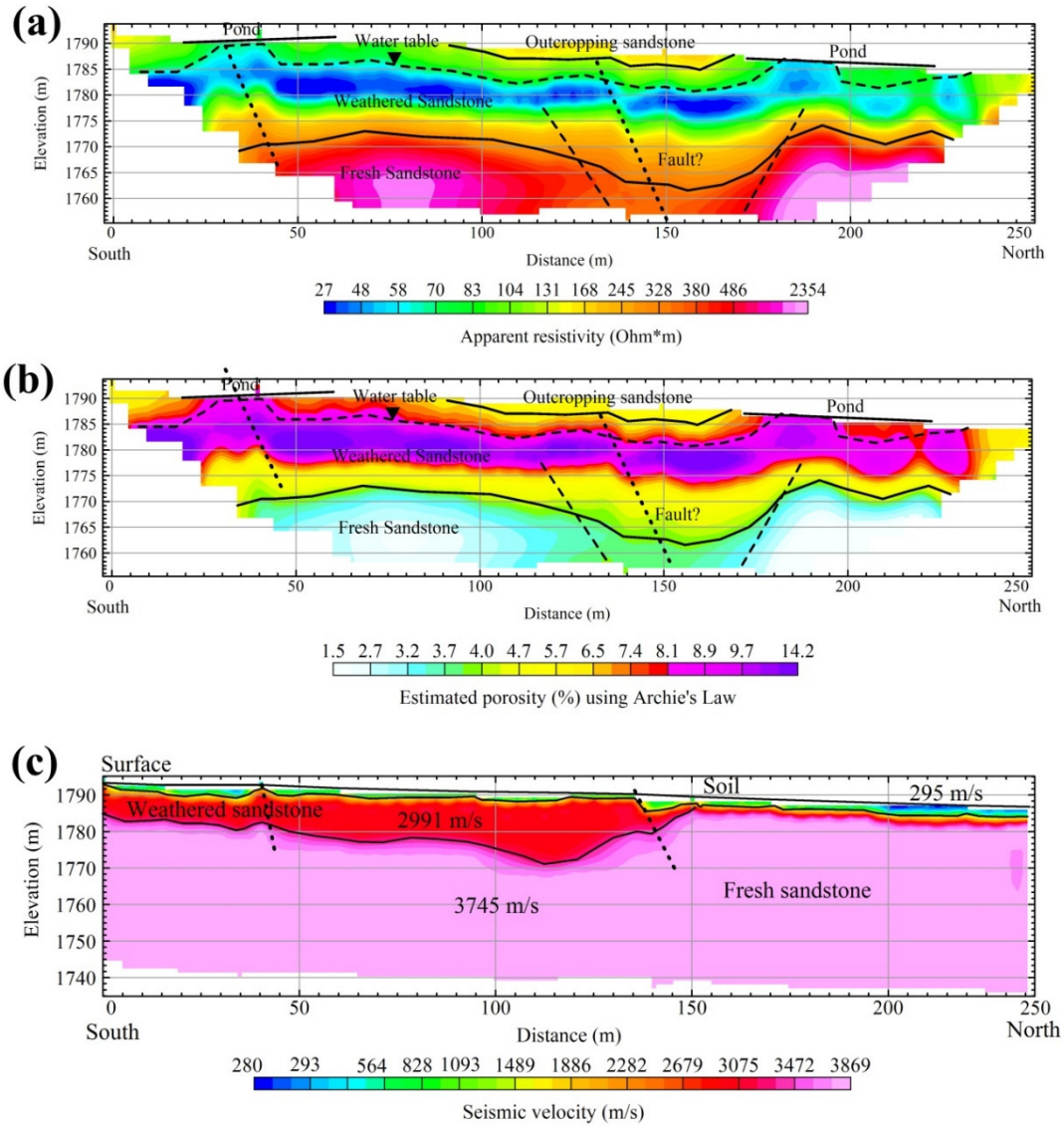

Figure 4.26: 2D resistivity survey results for site 2 showing (a) the modelled apparent resistivity-elevation plot, (b) the derived porosity-elevation plot and (c) the seismic velocity plot

The resistivity parameter which is the inverse of conductivity, was converted to porosity, using Equation 4.13. The resultant porosity distribution along the survey line at site 2 is shown in Figure 4.26b. The porosity distribution at site 2 ranges between 1.5 and 14.2%, where the fresh sandstone was characterised by very low porosity values.

The high values corresponded to weathered sandstone and soils. This is in agreement with findings by several authors (Tuğrul, 2004; Navarre-Sitchler *et al.*, 2015) who carried out experiments and

found that, as sandstones weathers, the porosity increases owing to the dissolution of cementing material surrounding the sandstone matrix, thereby creating openings which increase the porosity.

Above the water table in the unsaturated zone, the porosity values range from 6.8 to 26.2% slightly less than those obtained at survey site 1. Below the water table, the porosity values vary widely, ranging between 4.1 and 34.2%. Apart from a possible fault which was interpreted at distance 150 m, the resistivity layers were continuous. The inferred fault is also visible on the seismic plot, as shown in Figure 4.26c. The seismic plot (Figure 4.26c) shows three layers with average seismic velocities 295, 2 991 and 3 745 m/s which were interpreted as corresponding to soils, weathered sandstone (aquifer) and fresh sandstone respectively.

The survey site falls in the high to moderate groundwater vulnerability class and the porosity values of the weathered sandstone which constitutes the aquifer range between 5 and 14 % with the high values below the estimated water table line.

Survey site 3

A resistivity survey was carried out at site 3 along a south–north-oriented line of length 250 m with the aim of establishing the hydrogeology parameters which can be used to validate the groundwater vulnerability model. The resistivity values from field observations were inverted and the results displayed as a pseudo 2D resistivity-depth section (Figure 4.27a) for site 3. The resistivity section shows an increase in resistivity values with depth, probably reflecting a change in the weathering profile of the sandstone. Resistivity values at site 3 range from 15 to 1425 Ohm*m and, although the water table line could not be interpreted from this site, according to the regional depth to water table, it is located at around 9 m below the ground surface.

Using equation (4.13), the resistivity parameter, which is an inverse of the conductivity, was converted to porosity and the resultant porosity distribution for site 3 is shown in Figure 4.27b. The porosity distribution decreases with increasing depth as the degree of weathering decreases. The top layer is marked by a high porosity value of over 24% and resistivity values of below 20 Ohm*m could be attributed to clay material. A black clay layer was observed in an excavated trench, as shown in Figure 4.28. These observations are correlated with the location of the site on the regional clay content map (Figure 3.39) where the site falls in the 21–30% clay content region. This layer can act as a protective barrier, preventing pollution from reaching the underlying aquifers in the area.

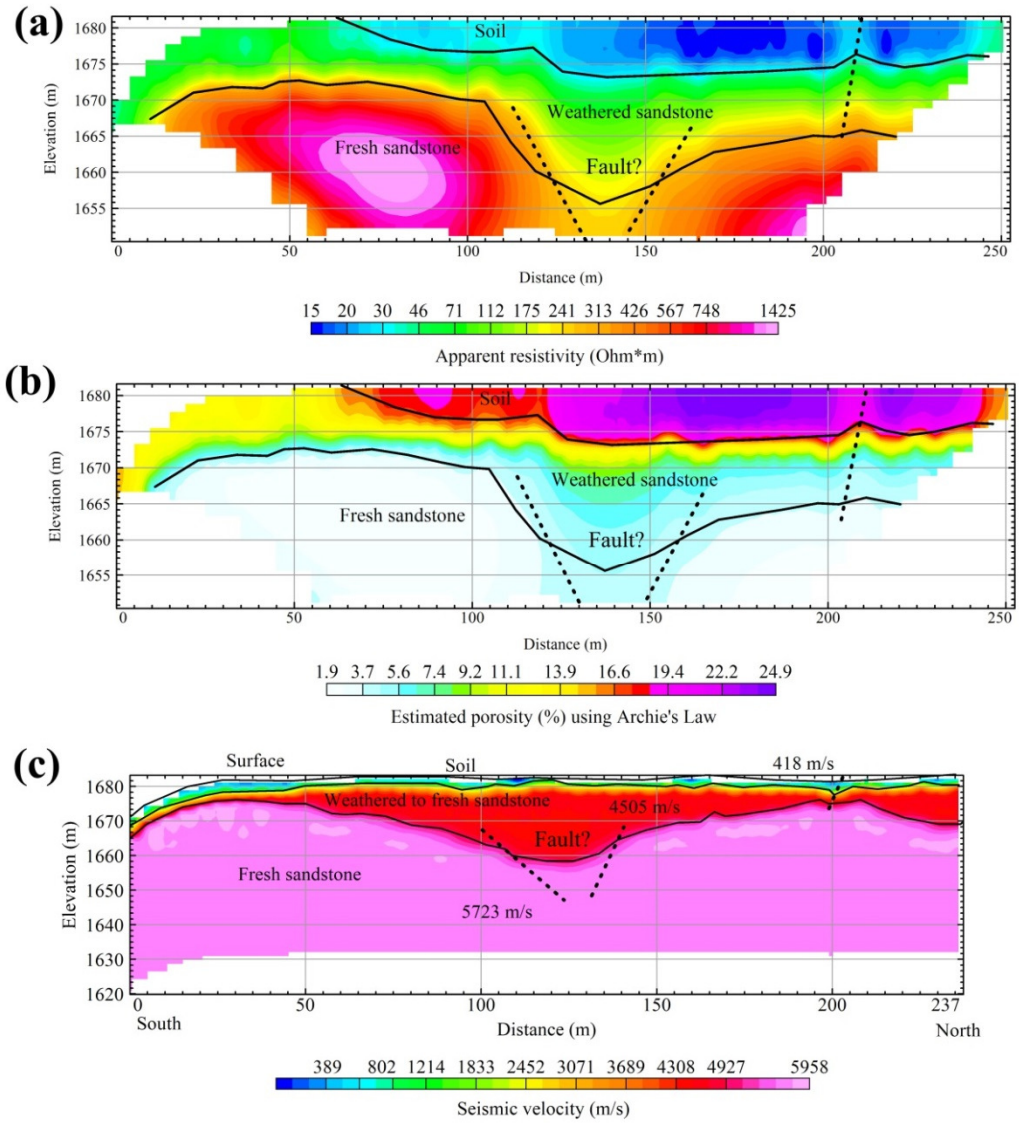

Figure 4.27: 2D resistivity survey results for site 3 showing (a) the modelled apparent resistivity-elevation plot, (b) the derived porosity-elevation plot and (c) the seismic velocity plot

Figure 4.28: Black clay layer observed overlying the weathered sandstone at an excavated trench next to the surveyed site 3

The seismic plot at site 3 (Figure 4.27c), as anticipated, shows an increase in seismic velocity with depth as the density of the rocks and the compaction increases. The top low velocity layer was interpreted as soil underlain by higher-velocity layers. The seismic velocity of the weathered sandstone which forms the aquifer system has an average seismic velocity of 4 505 m/s which is slightly higher than that observed at site 2. The fresh sandstone at site 3 is marked by an average seismic velocity value of 5 723 m/s.

A possible fault zone was interpreted at distance 140 m where there is a depression zone visible on both the resistivity and seismic velocity plots. This fault zone may act as a possible preferential transport zone for pollution from the surface to the aquifer system.

Considering the location of site 3 in Figure 4.18, it can be seen that this site falls within the moderate fuzzy groundwater vulnerability class. Thus, the presence of the protective clay layer, despite the interpreted fault zone, may account for why the fuzzy expert system model predicted a moderate groundwater vulnerability class.

Survey site 4

A resistivity survey was carried out at site 4 along a west–east-oriented line of length 250 m with the aim of establishing the hydrogeology parameters which can be used to validate the groundwater vulnerability model. The site falls within the groundwater vulnerability low class. The resistivity values from field were inverted and the results displayed as a pseudo 2D resistivity-depth section (Figure 4.29a) for site 4. The resistivity section shows an increase in resistivity values with depth probably reflecting a change in the weathering profile of the sandstone, similar to the observation at the other sites. Resistivity values at site 4 range from 16 to 1 681 Ohm*m. Using Equation 4.13, the resistivity parameter, which is an inverse of conductivity, was converted to porosity and the resultant porosity distribution for site 4 is shown in Figure 4.29b.

The porosity distribution decreases with depth as the degree of weathering decreases, similar to what was observed at site 3. The top layer is marked by a high porosity value of over 19% and resistivity values of below 28 Ohm*m which may be accounted for by the clayish material as observed during fieldwork. The field observations are correlated with the location of the site on the regional clay content map (Figure 3.39) where the site falls in the 30–43% clay content region. Thus, the site is marked by higher clay content than that observed at the other surveyed sites. This layer may also act as a protective barrier preventing pollution from reaching the underlying aquifers in that area.

The seismic plot at site 4 (Figure 4.29c), as anticipated, also shows an increase in seismic velocity with depth and a fault zone was interpreted at this site. The layers were interpreted on the basis of their average seismic velocities where 356, 5 406 and 5 887 m/s correspond to soil, weathered

sandstone and fresh sandstone respectively. The seismic velocities of the weathered sandstone, which forms the aquifer system, has an average seismic velocity of 5 406 m/s which is slightly higher than that observed at all the other sites. This may be attributed to the high degree of compaction of the sandstone, as the sandstone found in the Highveld coalfield comprises fine-grained and well-cemented quartz minerals.

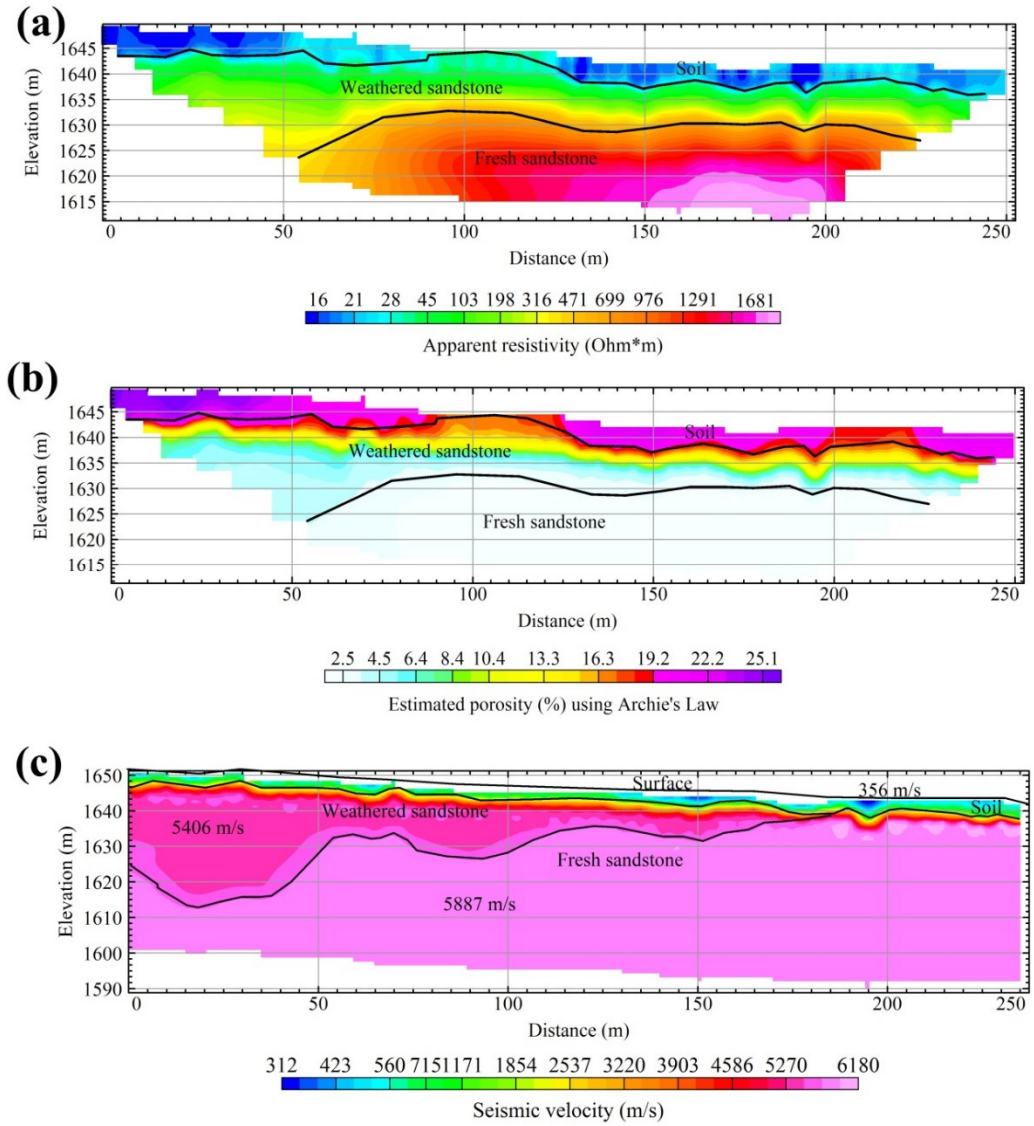

Figure 4.29: 2D resistivity survey results for site 4 showing (a) the modelled apparent resistivity-elevation, (b) the derived porosity-elevation and (c) the seismic plots

The presence of a protective clay layer at site 4 may provide a possible explanation as to why the fuzzy expert system model predicted low groundwater vulnerability in this area.

4.5.4.2.3 Summary

A comparison of the porosity and seismic velocities at the four sites was done to establish if there is any correlation between the measured earth's properties (geophysical responses) and groundwater

vulnerability. Table 4.3 summaries the geophysical responses compared to fuzzy model values for each of the surveyed sites. It can be seen that high seismic velocities and low porosities values are associated with areas with low fuzzy model values and the opposite is true for low seismic velocities and high porosities. Thus, even though only a few sites were surveyed, a relationship between geophysical responses (porosity and seismic velocity) and groundwater vulnerability can be drawn but if a statistical validation is to be done then a large number of sites need to be surveyed to obtain a statistical valid result such as a correlation coefficient value.

Table 4.3: Comparison of derived porosity values and groundwater vulnerability model values for each of the survey sites

Survey site	Porosity ranges of weathered zone (%)	Seismic velocity (m/s)	Fuzzy model value
1	9.0–25 (average = 17)	2 747	0.565 (High)
2	5.7–14 (average = 9.85)	2 991	0.383 (Moderate)
3	5.6–11 (average = 8.3)	4 505	0.329 (Low)
4	4.5–8.4 (average = 6.45)	5 406	0.262 (Very Low)

4.6 DISCUSSION

The fuzzy expert system used in this chapter belongs to the knowledge-based branch of AI where the parameter weighting factors were subjectively assigned but due diligence was done to ensure that most of the information with regard to AMD generation, transport and attenuation processes which can be obtained on a regional coalfield scale was used sparingly in the assessment. This may account for the strong correlation between the groundwater vulnerability model and the field measurements. The strong correlation may be explained as follows:

- The choice of parameters (S, P and T) and the allocation of appropriate weight allocations together with the selection of appropriate fuzzy operators made it possible to model AMD migration processes at a regional scale and was key to the production of a groundwater vulnerability model which is fairly consistent with field realities (water chemistry – sulphate concentration and geophysical responses).
- The knowledge-based fuzzy expert system used to produce the vulnerability model was able to mimic the thought processes of a human. For example, from a human perspective, areas with high sulphate concentrations are indicative of AMD and the AI model also shows high groundwater vulnerability model values in these areas.

A comparison of the resultant groundwater vulnerability model with the locations where surface AMD pollutants are known to occur shows that some areas marked as highly vulnerable are located

at or close to the interpreted AMD sources, with AMD signatures also appearing near monitoring boreholes. One possible explanation may be that these areas lack natural pollution attenuation properties, with AMD pollution easily travel and reach the groundwater system; hence it can be detected by the sampled boreholes. This may also indicate movement of AMD pollution from the surface or near-subsurface to the groundwater in these areas. Moreover, the groundwater vulnerability model shows low vulnerability in areas such as Delmas even though AMD sources are present. This may be attributable to the strong natural attenuation of AMD as the area is located in dolomitic terrain which is known to have better AMD buffering capabilities coupled with poor subsurface and soil transport properties. This is also evidenced the absence of an AMD signature in the monitoring boreholes within these areas.

The limitation of the methodology is that it does not account for the horizontal travel of pollutants, pollution travel time and residence (exposure) time. Where a highly invulnerable area is exposed to pollutants over a long period of time, an AMD signature may become evident, whereas a very vulnerable area exposed to pollutants for only a short period of time may not show an AMD signature.

4.7 SUMMARY

The SPT input vulnerability factors (sources, transportation pathway and traps) were integrated in a GIS environment using a knowledge-based fuzzy expert system to rank areas in terms of groundwater vulnerability to AMD pollution. Readily available data used to produce the four vulnerability factors were sourced from various governmental agencies. The high correlation between groundwater vulnerability model values and measured parameters (sulphate) and estimated porosity and seismic velocities proves the scientific defensibility of the approach in its use for policy and decision makers in the context of land use planning and water management research. Thus, the methodology provides a cost-effective approach to evaluating regional-scale areas whose results can provide useful spatial information.

The fuzzy expert approach used to combine the input maps for the SPT approach is based on a computer-based system which is solely dependent on the expert's cognitive reasoning which is translated into rules which are aggregated to generate a knowledge-driven groundwater vulnerability model. Other AIs which can deduce the relationships between the inputs and measurable parameters (known as data-driven approaches) may also be used for combining the SPT inputs and will be discussed in Chapter 6 and 7. However, first the pre-requisite data pre-processing and automation steps for data-driven approaches are discussed in Chapter 5.

CHAPTER 5: DATA PREPARATION AND AUTOMATION FOR DATA-DRIVEN ARTIFICIAL INTELLIGENCE MODELLING

5.1 INTRODUCTION

The previous chapters discussed the preparation of a methodology to assess groundwater vulnerability specific to a coalfield setting. A knowledge-driven model was formulated and validated in Chapter 4. The other AIs which can be used are data-driven approaches where the relationships between input map layers and measureable parameters are used in the development of data-driven groundwater vulnerability models. In order to utilise the data-driven algorithms, the input maps need to be tested for spatial associations with known polluted sites and binary maps created and pre-processed as outlined in this chapter. Some of the work in this chapter was extracted from a peer-reviewed publication (Sakala *et al.*, 2017a) written as part of this research. The research was presented at the 13th International Mine Water Association Congress in Lappeenranta, Finland in 2017.

5.2 SELECTION OF TRAINING SITES

In generating the training data, sulphate in groundwater was used to extract proxies for polluted (P) and non-polluted (NP) sites. The general assumption is based on the rock-AMD experimental results discussed in Chapter 3 where it was established that sulphate was preserved across various geological formations and can be used as possible tracer. The conservative value of 200 mg/L of the South African guidelines on potable water was used to partition sulphate in the groundwater where values lower than 200 mg/L were considered as NP sites and those above 200 mg/L as P sites. Of the 53 boreholes, 33 have values above 200 mg/L and were assigned a binary value of one (1) while the rest below 200 mg/L were assigned value zero (0).

5.3 MODEL SELECTION

After representative borehole locations were selected both with and without pollution, the next step was to use them for data-driven approaches. Before data-driven approaches are applied, the following question needs to be answered first:

- How is the best model going to be selected?
- How do we measure the performance of the model?

To answer these questions in the present study, various techniques were used including the generation of algorithms to determine the optimum parameters. These parameters are spatially associated with

known polluted groundwater and only the sections of the map layer showing a spatial association with high sulphate in groundwater were used. Thus, the following will be discussed in addressing these questions, with particular reference to the Witbank, Ermelo and Highveld coalfields:

- spatial association testing of input map layers;
- creation of binary map layers;
- determination of optimum parameters for the generation of the best model; and
- model input data splitting algorithms.

5.3.1 Spatial Association Testing of Input Map Layers

In selecting the parameters to be used for modelling by means of data-driven approaches, a spatial association between the available map layers and boreholes with sulphate concentration (> 200 mg/L) is made based on the assumption that only that region of the parameter which is spatially associated with high sulphate boreholes is somewhat related to AMD pollution in groundwater. The spatial association test involves measuring the degree to which elements are similarly arranged in space (Carranza, 2002). The distance distribution method by Bonham-Carter (1994) was modified and used to identify which section of a map layer is spatially associated with known polluted sites. In the method, the cumulative frequency distribution curve for each input layer (rainfall, slope, surface sources, subsurface sources, soil clay content, distance to preferential pathways, rock permeability, aquifer hydraulic conductivity, depth to water table and AMD-rock reactivity relative values) and cumulative frequency at every high sulphate borehole are plotted against the layer values. The graph will show the range of map layer values where boreholes with high sulphate concentrations are found.

Carranza (2002) modified this approach for mineral prospectivity modelling by including calculations of theoretical (expected) values which are compared with the cumulative frequency plot for deposit locations and a difference curve plot generated. The map layer or map section with positive difference values is spatially associated with the location of the deposit. This approach works well for mineral exploration data where the predictor map layers are mostly a function of distance from a geological feature (fault, contact, shear zone, dyke, etc.) but the approach does not work well for groundwater vulnerability datasets such as rainfall or depth to water table. The approach was tested and it was realised that a negative spatial association was obtained in the region of the map, while the cumulative frequency plot for known polluted sites shows that a large number of boreholes lie within that region. Based on this, only the cumulative frequency distribution curve was used to extract the range of values of the map layer where over 50% of the polluted sites are found.

For every borehole location with layer value x with a_o counts and the total number of boreholes with high sulphate concentration t_o, the frequency f_o is given by Equation 5.1:

$$f_o = \frac{a_o}{t_o} \quad 5.1$$

For the first layer value, x_1, the frequency f_{o1} is given by Equation 5.2:

$$f_{o1} = \frac{a_{o1}}{t_o} \quad 5.2$$

For the second layer value, x_2, the frequency f_{e2} is given by Equation 5.3:

$$f_{o2} = \frac{a_{e1} + a_{e2}}{t_o} \quad 5.3$$

And so on, until the last layer value, x_n, where the frequency f_{on} is given by Equation 5.4:

$$f_{on} = \frac{a_{o(n-1)} + a_{on}}{t_o} \quad 5.4$$

The calculations for the cumulative frequency for each borehole with high sulphate values were done for all the maps and graphs drawn for each. The relationships between the parameters used for the calculations are shown in Table 5.1.

Table 5.1: Relationships of parameters used for the calculation of spatial association

Map layer value	Cumulative frequency
x_1	f_{o1}
x_2	f_{o2}
x_3	f_{o3}
.	.
.	.
.	.
x_n	f_{on}

5.3.1.1 Ligand water sources (rainfall) layer

Figure 5.1 shows the cumulative frequency plot results of the rainfall map layer. The plot shows that from the lowest rainfall value to 662 mm no boreholes with high sulphate were found. Between 662 and 714 mm the number of boreholes with high sulphate values increased to just over 80% at 714 mm and reached 100% at 776 mm. Based on the spatial location of boreholes with high sulphate concentrations when compared to rainfall data, the range 662 to 714 mm is the region where most of the boreholes are located which may mean that this amount of rainfall may be correlated with the

availability of water for AMD reactions and also drives the AMD pollution from the surface to the groundwater. The classification into two binary classes (1 and 0), as shown in Figure 5.2 was based on a spatial association test carried out on the rainfall map. The map shows that the central part of the study area falls within the binary class (1) where all the boreholes with sulphate concentrations >200 mg/L are found. Other boreholes with low sulphate concentrations also fall within the areas classified as class (1) possibly because rainfall is not a direct parameter which determines sulphate concentration in the groundwater. Hence, other parameters are also considered in the following sections.

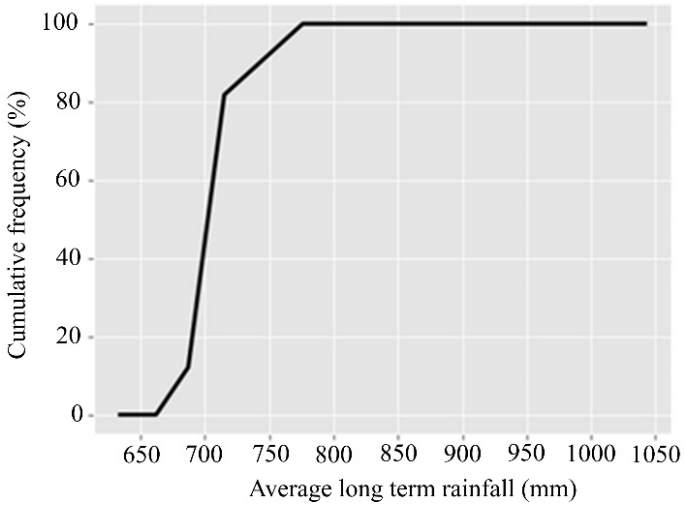

Figure 5.1: Spatial association test results for the rainfall parameter

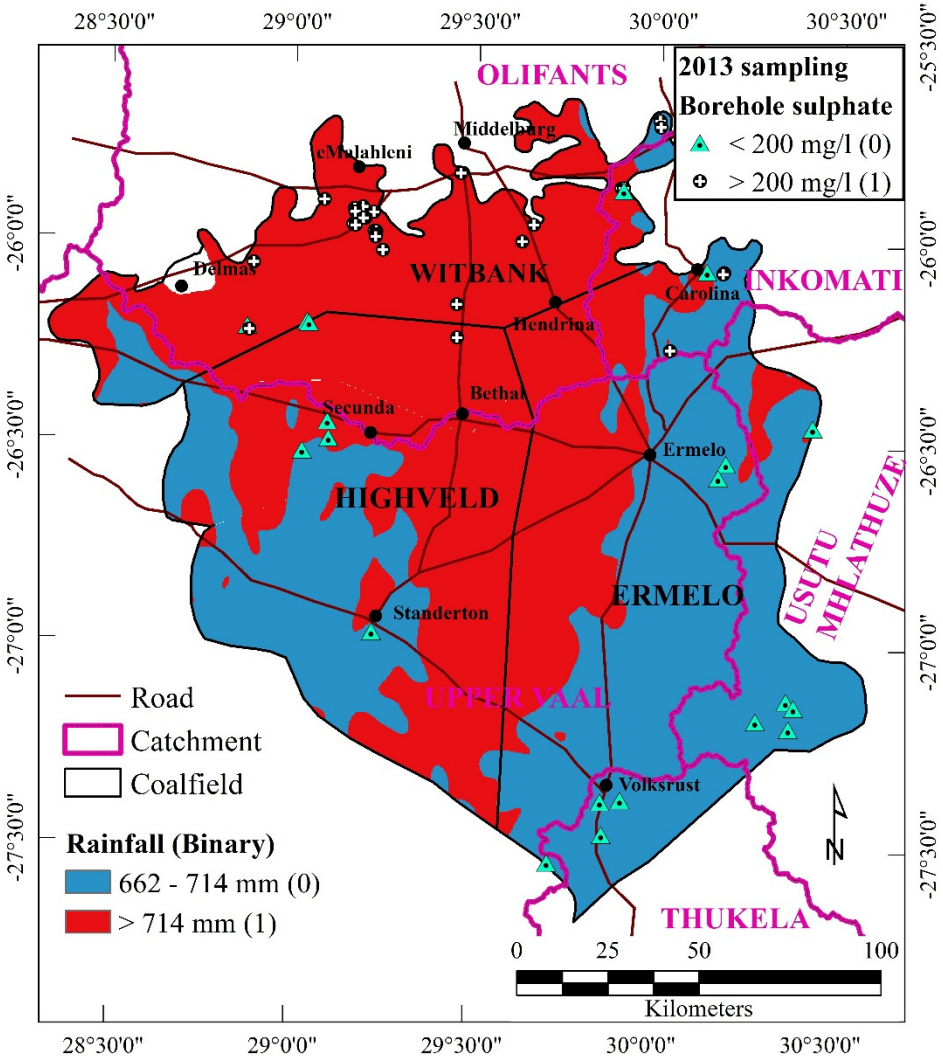

Figure 5.2: Rainfall map layer in binary format

5.3.1.2 Energy sources (slope) layer

The cumulative frequency plot for the slope parameter shows that 100% of boreholes with high sulphate concentrations are found in the slope range 1 to 5% (Figure 5.3). Thus, according to these results, sulphate in the groundwater may be associated with flat areas where infiltration is higher than runoff, giving enough time for AMD to infiltrate together with the water into the subsurface. This is in agreement with the general assumption made in the current research and the infiltration-slope relationship by Fox *et al.* (1997) that states that areas with flat surfaces favour vertical infiltration of water more than runoff. A cut-off value of 5% was used to generate the binary map of the study area (Figure 5.4).

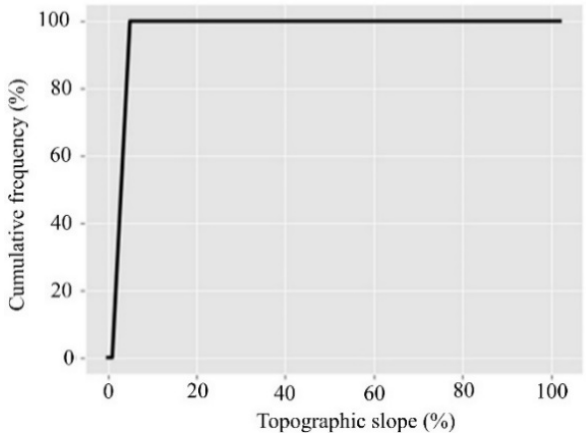

Figure 5.3: Spatial association test results for the slope parameter

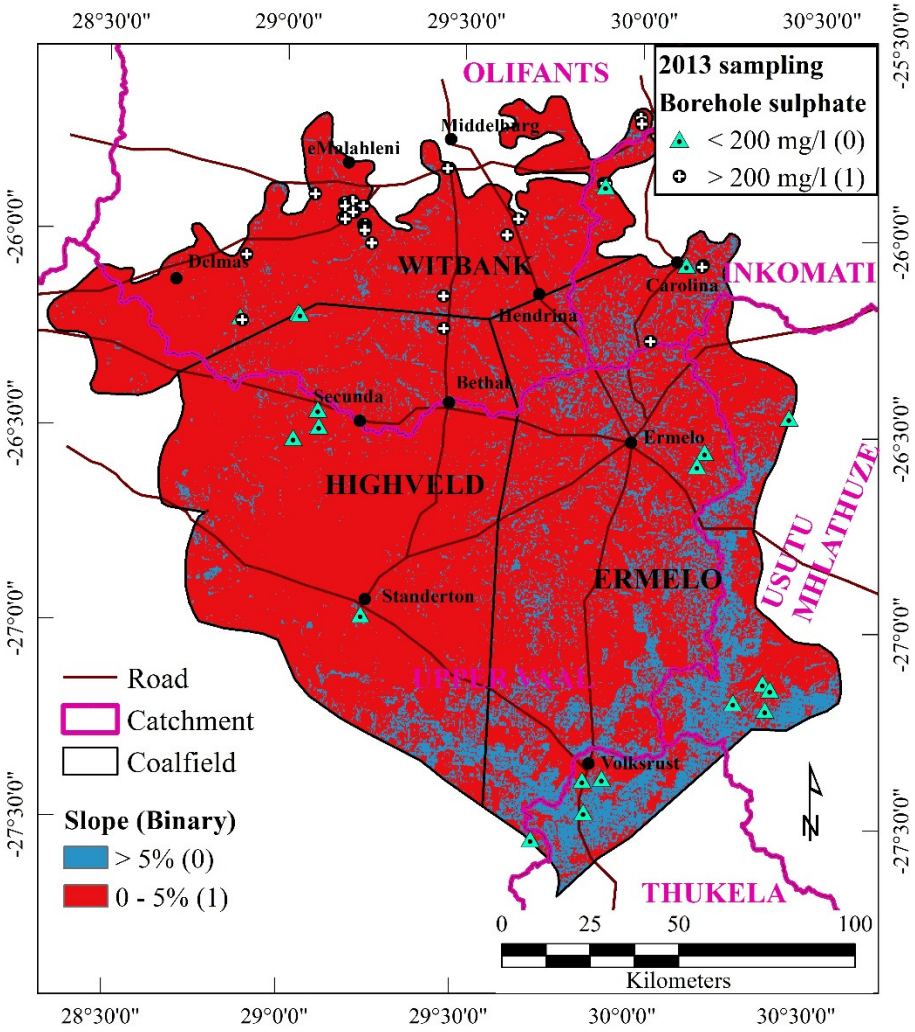

Figure 5.4: Slope map layer in binary format

5.3.1.3 Surface sources of AMD layer

Figure 5.5 shows the cumulative frequency plot for the surface sources of the AMD pollution layer. The plot increases sharply from 0 to 80% within the range 0 to 871 m up to 97% after which the gradient flattens at 100% at a distance of 2 384 m. The results clearly show that between 0 to 871 m away from the remote sensing interpreted AMD sources, over 80% of the boreholes with high

sulphate values are located within this region. The possible explanation is that the closer the groundwater system is to surface sources within the 871 m horizontal distance, the higher the possibility of AMD entering the groundwater system. Thus, proximity to the mapped sources may playing an important role in making the groundwater vulnerable to AMD as can be deduced from this plot. Hence the distance 0 to 871 m was assigned a binary class value (1) and those areas further away than 871 m were assigned a binary value (0), as shown in Figure 5.6. The areas assigned a value (1) are found near the major towns and the Witbank coalfield has the largest area with interpreted AMD surface sources.

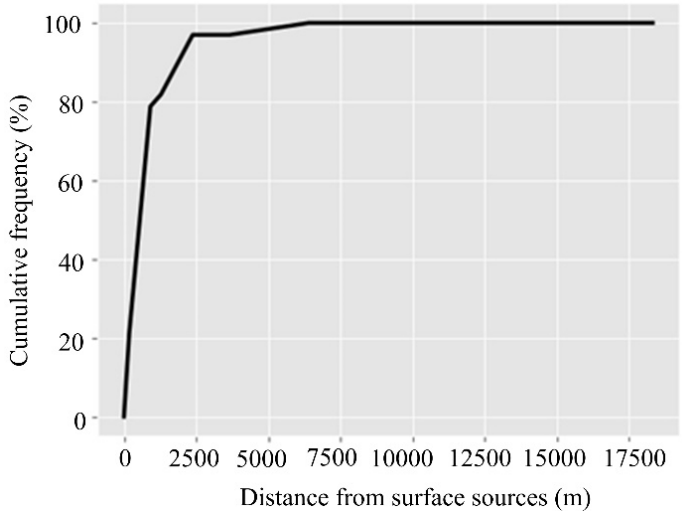

Figure 5.5: Spatial association test results for surface sources parameter

5.3.1.4 Subsurface sources of AMD layer

The plot of cumulative frequency for subsurface sources is almost a straight line from 0 to 100% within a very short distance from the location of the subsurface sources (Figure 5.7). This shows that almost all the boreholes with high sulphate values are located within or very close (within 248 m) to the subsurface sources. Thus, the high sulphate in boreholes is found within a distance of 248 m from the coal host rocks.

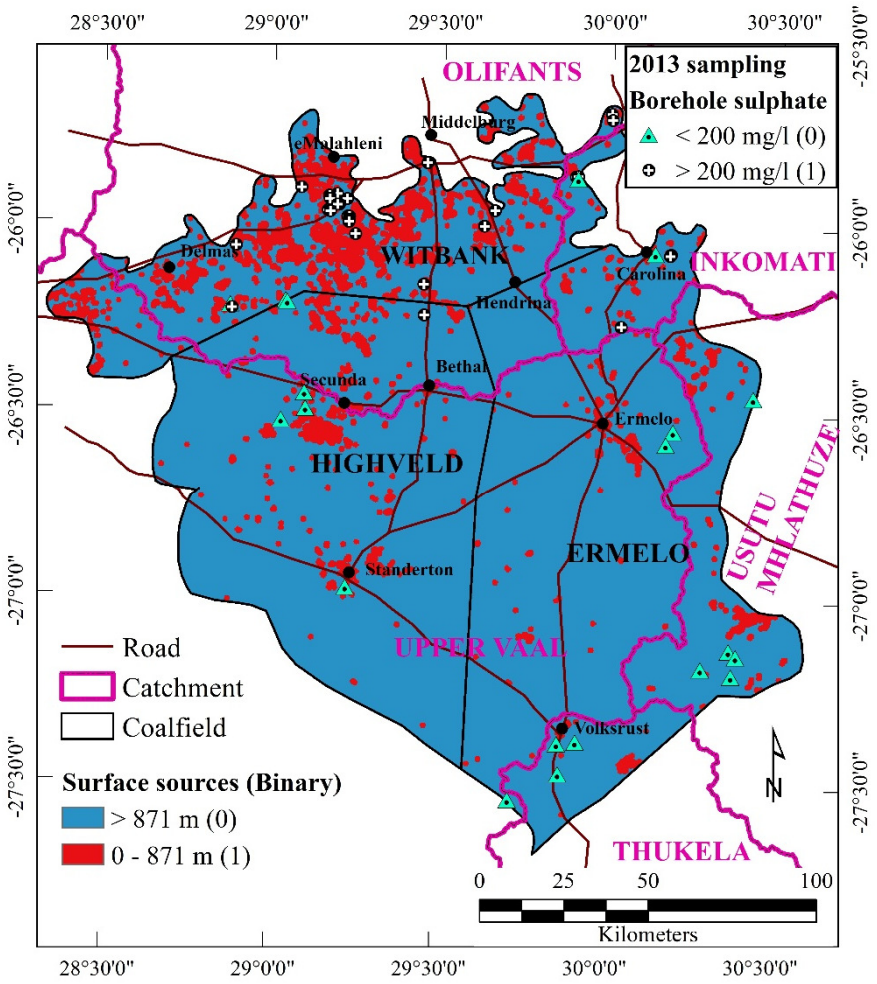

Figure 5.6: Surface sources map layer in binary format

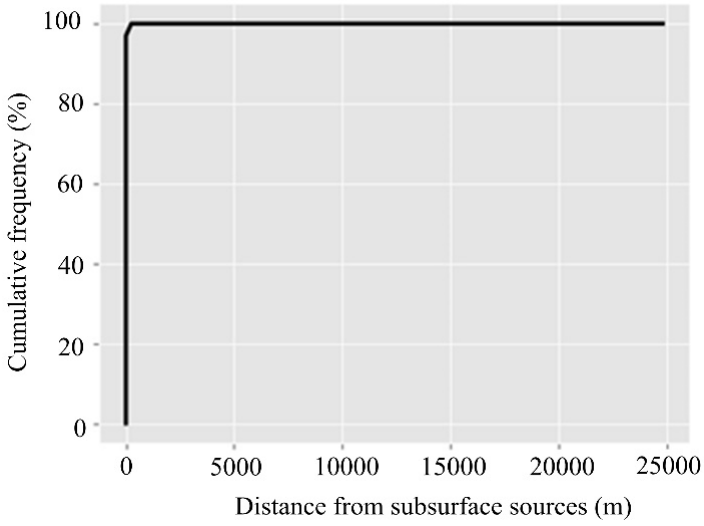

Figure 5.7: Spatial association test results for the subsurface sources parameter

The spatial association test results of the subsurface sources show that those boreholes with high sulphate concentrations are located within 248 m of the coal-hosting geological formations. Hence, the distance 0– 248 m was assigned a binary class value (1) and those areas found further away than

248 m assigned binary value (0), as shown in Figure 5.8. The areas assigned a value (1) are found in the northern parts of the Ermelo and Highveld coalfields and over almost the entire Witbank coalfield.

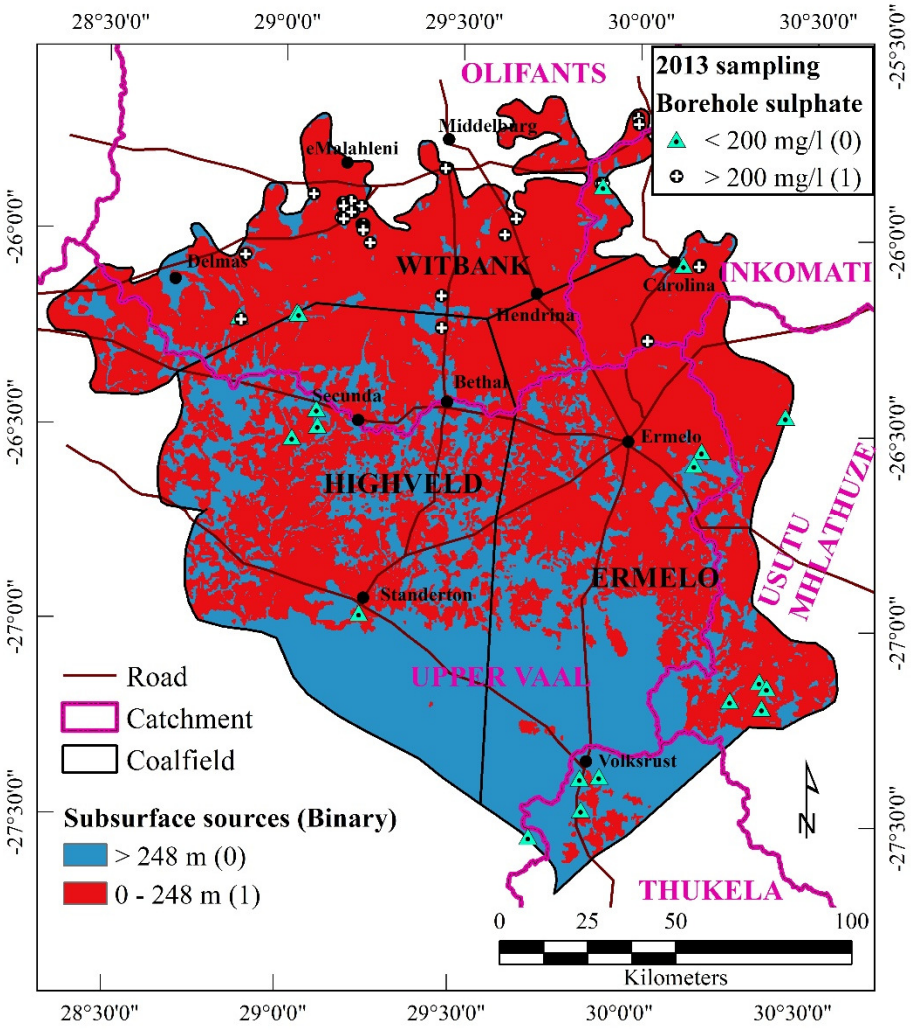

Figure 5.8: Subsurface sources map layer in binary format

5.3.1.5 Soil clay content layer

The cumulative frequency plot for soil clay content shows an increase in the frequency of boreholes with high sulphate concentrations from 0 to 91% within the 12 to 25% clay content zone (Figure 5.9). This may mean that boreholes with high sulphate concentrations are found in areas with less soil clay content which is in agreement with the general assumption used for formulating the fuzzy expert system. Areas with between 12 and 25% soil clay content are spatially associated with high sulphate in the groundwater while areas with a soil clay content above 25% are not. Hence, a binary class value (1) was assigned to areas with 12 to 25% soil clay content, as shown in Figure 5.10. Almost the entire Witbank coalfield and the area between Carolina and Ermelo are characterised by a low clay content, as represented in red in Figure 5.10.

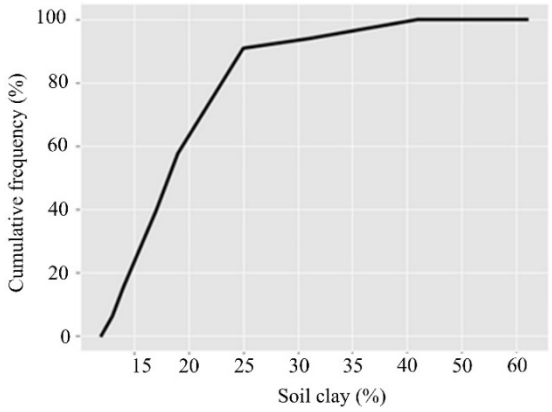

Figure 5.9: Spatial association test results for the soil clay parameter

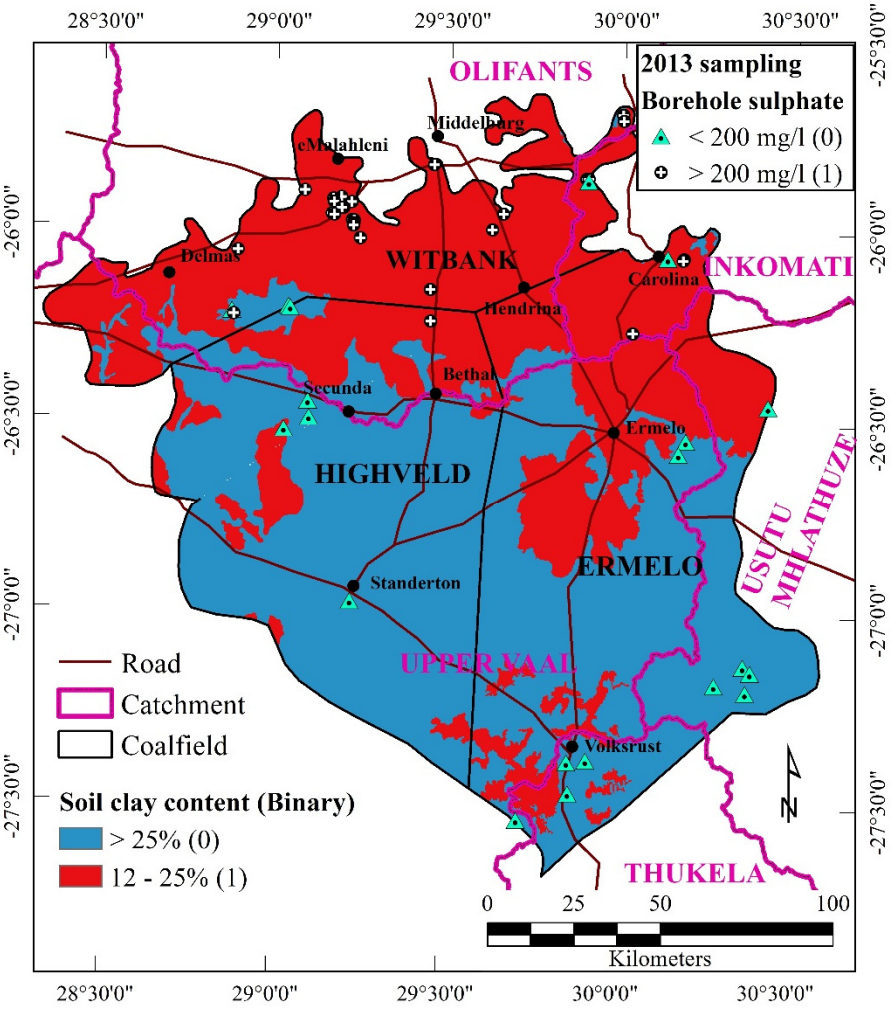

Figure 5.10: Soil clay map layer in binary format

5.3.1.6 Preferential pathway layer

Figure 5.11 shows the cumulative frequency plot for the pathways layer. The plot shows three breaks (305 m, 892 m and 3 851 m) where the gradient changes and the percentage of boreholes change from 50% to 84% to 100%. The extent to which a mapped pathway can contribute to groundwater vulnerability as a possible pathway for pollution is highly localised around the structure. Thus,

considering the breaks, the 305 m region surrounding the structure was selected as a zone in respect of which the preferential pathway can be effective and slightly over 50% of the boreholes are located in this zone. Thus, proximity to the geological features which could indicate possible zones of weakness within the subsurface plays an important role in determining the vulnerability of groundwater to AMD. Hence, the distance 0–305 m was assigned a binary class value (1) and those areas found further away than 305 m were assigned a binary value (0), as shown in Figure 5.12.

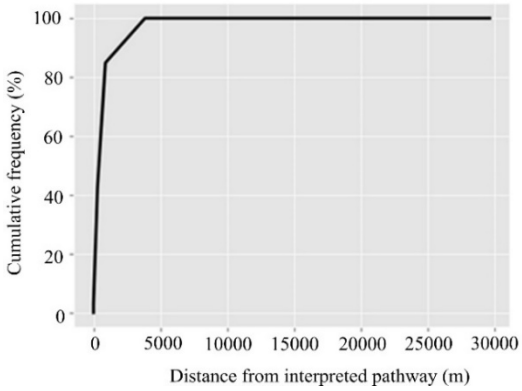

Figure 5.11: Spatial association test results for the pathway parameter

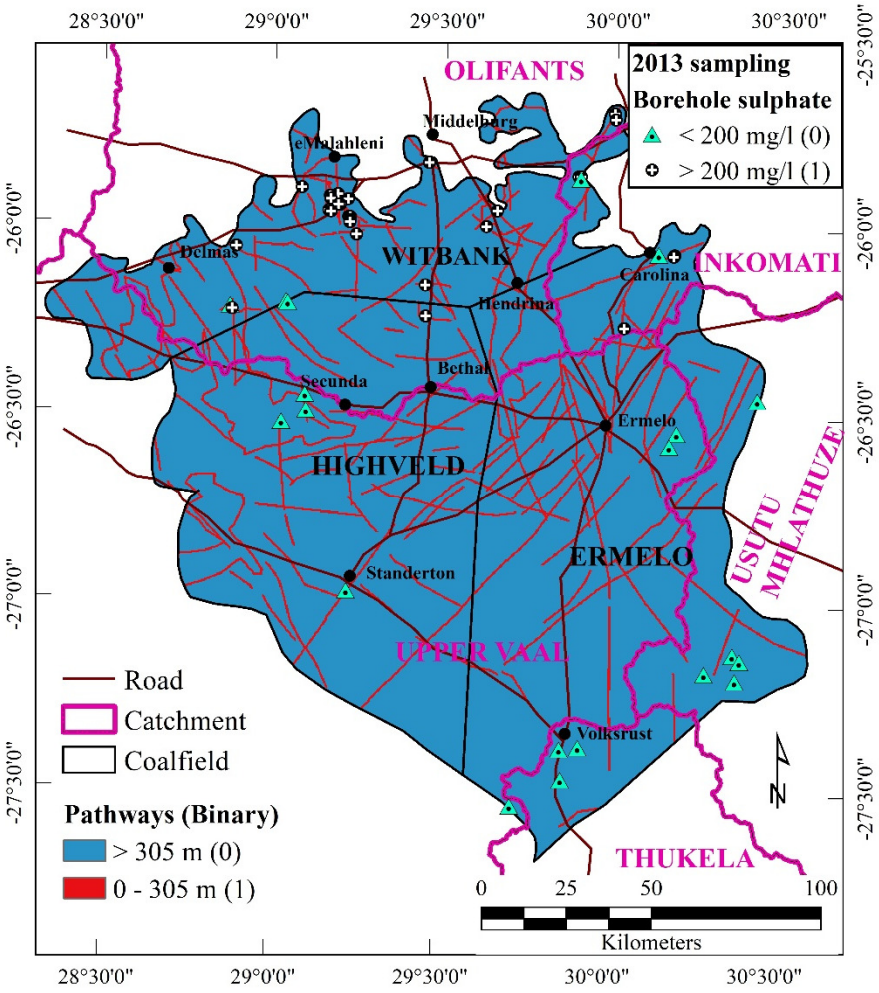

Figure 5.12: Pathway map layer in binary format

5.3.1.7 Aquifer hydraulic conductivity layer

The spatial association test for the aquifer hydraulic conductivity layer shows that below 4 no boreholes with high sulphate concentrations were found. The cumulative frequency plot (Figure 5.13) shows 0% cumulative frequency from relative hydraulic conductivity (2 to 4). From relative hydraulic conductivity values 4 to 6, the number of boreholes with high sulphate values increased to 100% at 6 which flattened out afterwards with no change in the number of borehole beyond this value. Thus, the range of values (4–6) is where all the boreholes with high sulphate were found. Figure 5.14 shows that a large section of the map falls in the binary class (1).

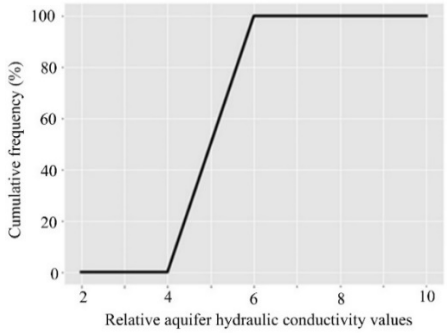

Figure 5.13: Spatial association test results for the relative aquifer hydraulic conductivity

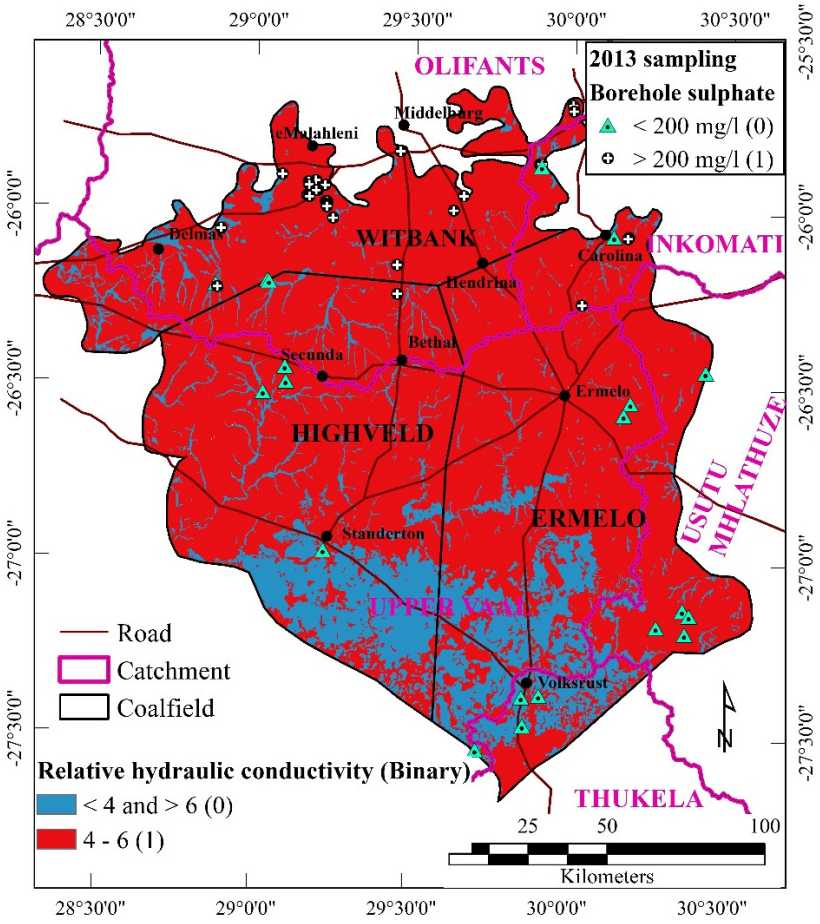

Figure 5.14: Relative aquifer hydraulic conductivity map layer in binary format

5.3.1.8 Rock permeability layer

The spatial association results for rock permeability show a straight line between 1 and 7 where fewer than 4% of boreholes were found. Within the 7– 8 range of rock permeability values, the frequency of boreholes with high sulphate increased from 4 to 100% and flattened afterwards (Figure 5.15). The 7 – 8 range is the region characterised by relative permeability values with the largest numbers of boreholes with high sulphate concentrations. Thus, the results show that rocks with relatively higher permeability values are spatially associated with locations of boreholes with high sulphate concentrations. The high rock permeability association with high sulphate in the groundwater may be an indication of the link between the increased interconnectivity of pores in the rocks with movement of AMD pollution through the rocks up to the groundwater system.

The spatial association results were used to produce the binary map (Figure 5.16) where binary value (1) was assigned to areas with rock permeability values between 7 and 8 and other areas with permeability values outside this range were assigned a value (0). Binary class (1) assigned to rocks with relative permeability values between 7 and 8 covers the central to eastern part of the Witbank coalfield and the area between Ermelo and Carolina. These areas correspond to areas with sandstone, rhyolite, basalts, gabbro and felsite rock types. These rocks have high permeability values indicating the ease with which water and pollution can flow.

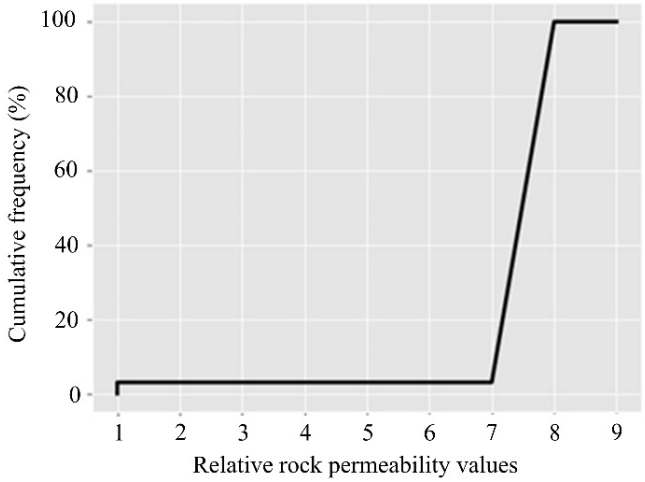

Figure 5.15: Spatial association test results for the relative rock permeability parameter

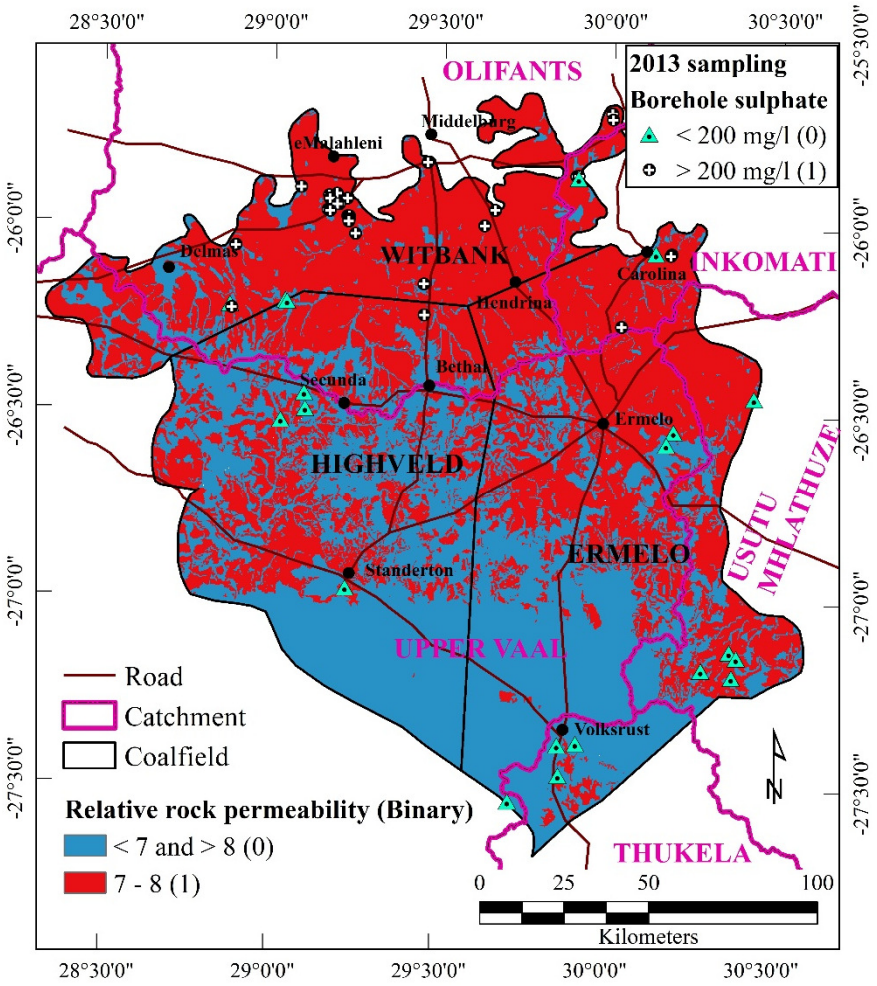

Figure 5.16: Relative rock permeability map layer in binary format

5.3.1.9 Rock-AMD reactivity layer

Figure 5.17 shows the cumulative frequency plot for the contribution of rock-AMD reactivity towards groundwater vulnerability. The contribution of rock-AMD reactivity is an inverse of the relative rock-AMD reactivity values given in Table 3.9. It must be noted that from relative values 1 to 9, fewer than 4% of the boreholes with high sulphate concentrations are found. The frequency increases sharply to 100% from relative values 9 to 10. Thus, areas with rocks which lack the capacity to extract the pollutants from AMD have high relative contribution to making the groundwater vulnerable to AMD; hence most of the boreholes with high sulphate are found in these areas, as seen by the high frequency of boreholes at high relative values. Rocks such as sandstone, alluvium and diamictite are found in this range of values. Figure 5.18 shows the spatial distribution of the binary classes (1 and 0) for the Witbank, Ermelo and Highveld coalfields. The contribution of rock-AMD reactivity values 9 and 10 which correspond to alluvial, sandstone and shales were assigned a binary class value (1) because of their spatial association with high sulphate in the groundwater. The other relative rock-AMD reactivity classes were assigned a binary class value (0) as they showed no association with high sulphate concentrations in the groundwater.

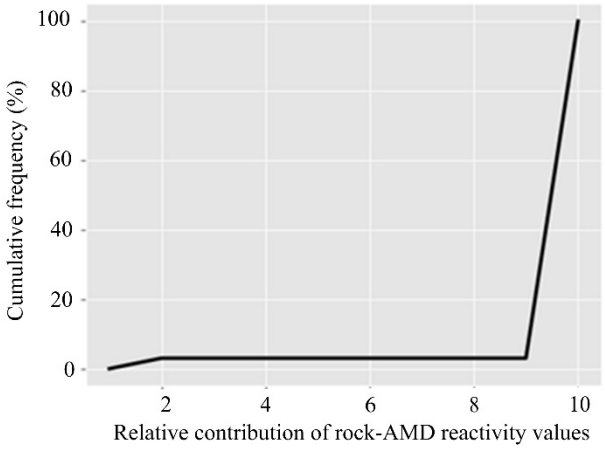

Figure 5.17: Spatial association test results for the rock-AMD reactivity parameter

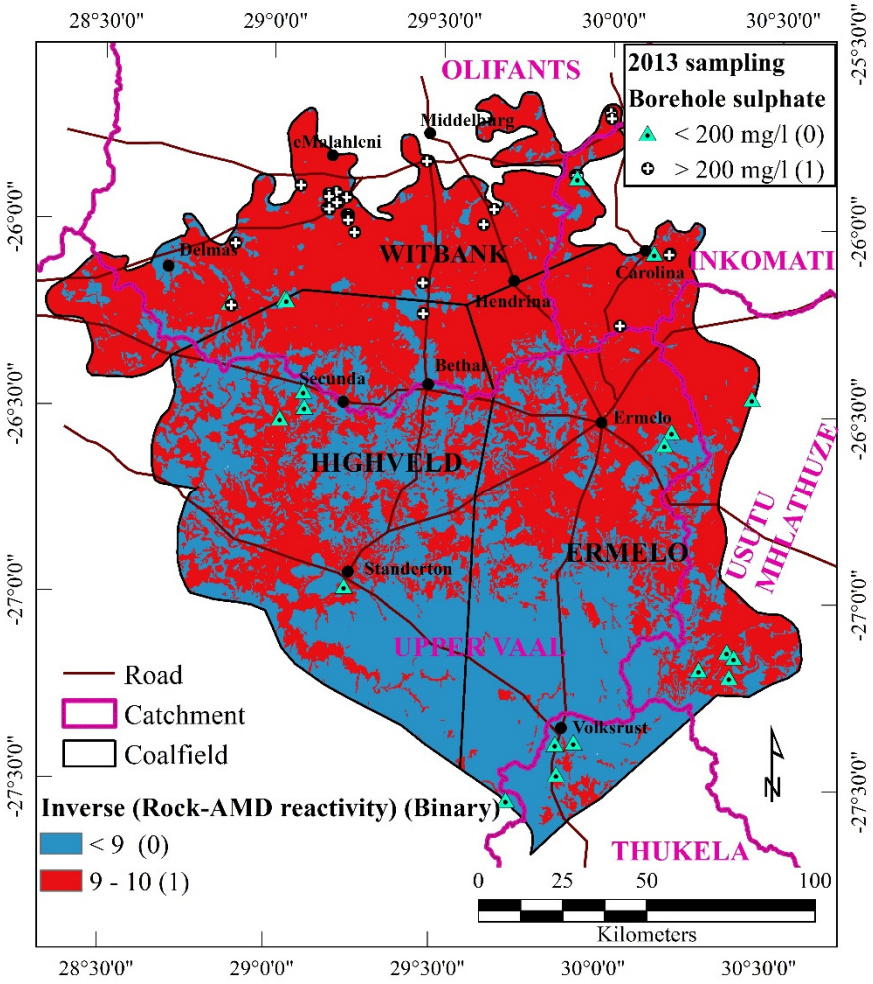

Figure 5.18: Rock-AMD reactivity map layer in binary format

5.3.1.10 Depth to water table layer

The depth to water table in the study area ranges between 4.8 and 21.8 m. The spatial association plot for depth to water table is a sigmoid shape with the frequency of boreholes increasing linearly from 4.8 to 12 m after which the gradient decreases from 12 m and flattens at 100% at depth values greater than 13.9 m (Figure 5.19). Thus, from 4.8 to 12 m, over 89% of the boreholes with high sulphate

concentrations are found in this region. Areas with depth to water table values of between 4.8 to 12 m were assigned a class value (1) and those with values above 12 m assigned a binary class value (0) (Figure 5.20).

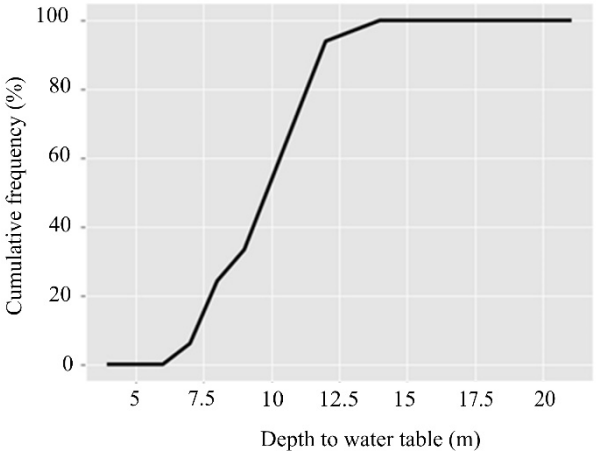

Figure 5.19: Spatial association test results for the depth to water table parameter

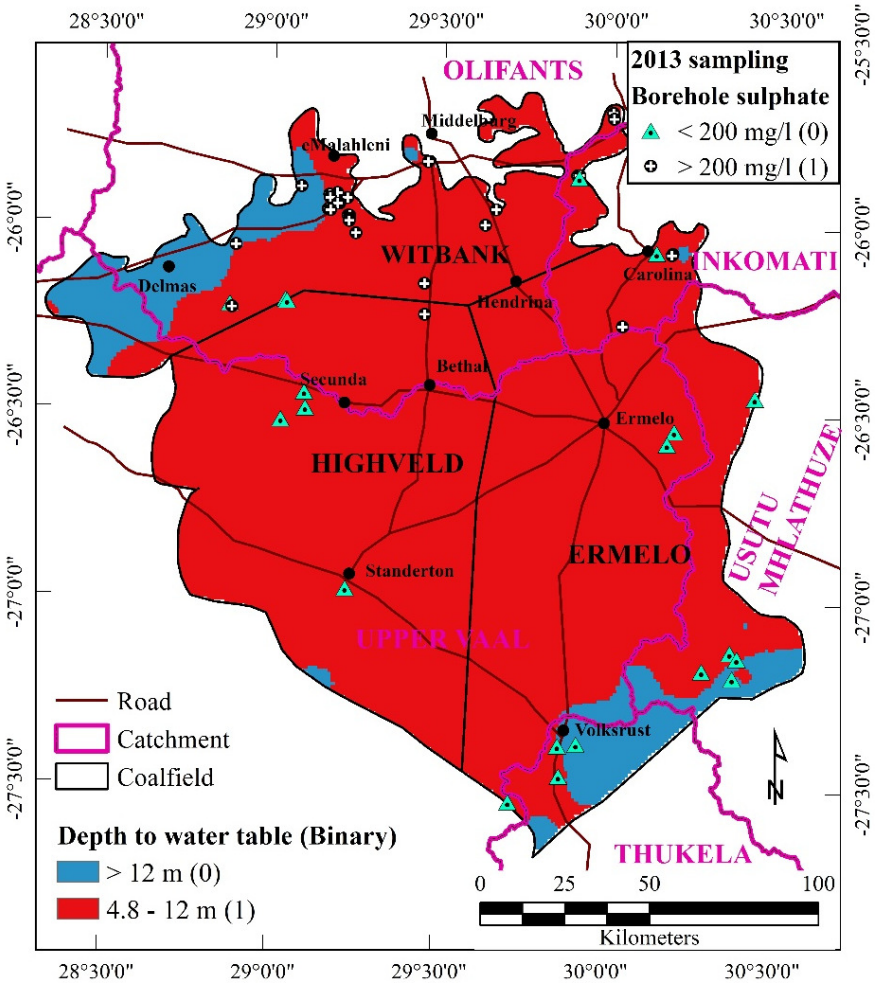

Figure 5.20: Depth to water table map layer in binary format

From the depth to water table graph (Figure 5.19) it can be said that the groundwater systems with water table values below 12 m from ground surface are potentially vulnerable to AMD pollution as seen by the large frequency of boreholes with high sulphate concentrations in this range of values.

Table 5.2 summarises the binary class allocations for all the map layers using the spatial locations of boreholes with high sulphate concentrations.

Table 5.2: Assignment of binary classes

Vulnerability factor	crisp layer	Class	Binary class
Sources (S)	Ligand (water) sources	Rainfall <662 mm and rainfall >714 m	0
		Rainfall between 662–714 m	1
	Energy sources	0–5%	1
		5–121%	0
	Surface pollution sources	Distance >871 m	0
		Distance 0–871 m	1
	Subsurface pollution sources	Distance >248 m	0
		Distance 0- 248 m	1
Transportation pathway (P)	Soil clay content	>25%	0
		12–25%	1
	Preferential pathways	Distance >305 m	0
		Distances 0–305 m	1
	Aquifer hydraulic conductivity	Alluvial (10^{-2} m/s) (10)	0
		Andesitic lava, dolomite, chert (10^{-4} m/s) (9)	0
		Sandstone (10^{-5} m/s) (6)	1
		Gabbro, diabase, dolerite (10^{-6} m/s) (5)	1
		Pyroclasts, diorite (10^{-6} m/s) (5)	1
		Granite, granophyre, diamictite (10^{-9} m/s) (4)	1
		Shales, mudrock, quartzite (10^{-11} m/s) (2)	0
	Relative vadose zone (rock) permeability	Mudstone, Shales (10^{-11} cm^2) (1)	0
		Diamictite (10^{-10} cm^2) (3)	0
		Sandstone (10^{-8} cm^2) (4)	0
		Dolomite, Chert (10^{-6} cm^2) (5)	0
		Diabase, Dolerite (10^{-6} cm^2) (5)	0
		Quartzite (10^{-5} cm^2) (6)	0
		Basalt, Gabbro, Felsite, Diorite (10^{-4} cm^2) (7)	1
		Lava, Granite, Gneiss (10^{-3} cm^2) (8)	1
		Alluvial (10^{-2} cm^2) (9)	0
Traps (T)	Rock-AMD reactivity (contribution values)	Alluvial (9)	1
		Diamictite, sandstone, quartzite (9)	1
		Rhyolite, felsite (7)	0
		Gabbro, diorite, norite, anorthosite (7)	0
		Andesitic lava, pyroclasts (5)	0
		Granite, gneiss, granophyre (5)	0
		Diabase, dolerite (3)	0
		Mudrock, shales (3)	0
		Dolomite with chert (1)	0
	Depth to water table	Depth <4 m and depth >12 m	0
		Depth between 4–12 m	1

Given that the input map layers of the SPT approach needed to be reclassified into binary format using cumulative frequency graphs, a selection of zones within each map where over 50% of the boreholes are located was completed. The next task was the selection of data-driven approaches for combining the ten maps into one map. Various approaches exist but in this research only two machine

learning AI systems were used namely the Artificial Neural Networks (ANN) and the Adaptive Neuro-Fuzzy Inference System (ANFIS). But before these approaches could be applied, it was necessary to formulate algorithms to determine the general optimal parameters. In the following sections algorithms are discussed which were used to automate some of the processes for using AI to generate groundwater vulnerability models.

5.3.2 Determination of Optimal Data-Driven Model Parameters

In the design of data-driven approaches for rapid groundwater vulnerability assessments, the determination of optimal parameters is required to enhance the performance of the AI system. The parameters to be determined include the number of training iterations, termed "epochs", for all machine learning (data-driven); these include both the ANN and the ANFIS approaches and a number of neurons in the hidden layer of the ANN approach. A full description of ANN and ANFIS are given in Chapter 6 and Chapter 7 respectively.

5.3.2.1 Epoch determination algorithm for data-driven approaches

Binary map data are feed into a data-driven AI algorithm where training is carried out at various training iterations (epochs) with a fixed initial number of neurons in the hidden layer for training. The initial number of neurons in the hidden layer may be determined randomly or by using calculations by Shigidi and Garcia (2005).The trained model at each epoch is used to classify/predict test datasets (with known output values) which had not been used in the training. The training epoch (M) with the least error between the predicted and the known value is selected as the optimum number of epochs. The step by step procedure for the epoch determination algorithm is given in Appendix 3.1.

5.3.2.2 Hidden layer neurons determination algorithm for data-driven approaches

Using the optimum number of epochs (M) as fixed, the machine learning algorithm is run with varying numbers of neurons in the hidden layer. For each neuron in hidden layer training step, the learnt system is used to determine the output values of a validation dataset. The predicted value is compared with the actual values and the error is returned for each training point. The number of neurons in the hidden layer with the least error between the predicted values and the actual is the optimum number of neurons in the hidden layer (H). The procedure for this algorithm is found in Appendix 3.2.

5.3.2.3 Data splitting algorithms

Using the optimum number of neurons in the hidden layer (H) and epochs (M) the next task is to determine the best data split for the data-driven algorithm modelling. This can be done using a data

splitting algorithm (holdout, random, k-fold and leave-one-out). Choice depends on the data size, randomness, speed, etc. By considering the nature of the dataset used for groundwater vulnerability assessment and the comparison of the various data splitting algorithms, the k-fold and the leave-one-out will be used in this research.

In summary, the leave-one-out algorithm splits the data into three datasets: training, validation and testing. During training, the algorithm excludes one point from training and uses it for validation before repeating the same process with the next point until all the points have been used as validation. The algorithm works best for small datasets and is very slow for bigger datasets. Details of the leave-one-out algorithm can be found in Appendix 3.3.

The other data-splitting algorithm is the k-fold cross-validation approach, which involves splitting the data into folds (partitions). During training, the algorithm excludes one fold from training and uses it for validation before repeating the same process with the next fold until all the folds have been used as validation. The algorithm works best for larger datasets and cannot be used for small datasets where splitting into folds is not possible. Details of the leave-one-out algorithm can be found in Appendix 3.3. A special case of the k-fold, called the stratified k-fold, will be used. The stratified k-fold ensures that each generated fold contains ones and zeros in almost the same representation as the original dataset before splitting (Kohavi, 1995). The advantages of using the stratified k-fold cross-validation is that the original dataset structure is preserved. Thus, the model produced is validated using datasets with a similar structure, resulting in a more representative validated model than the model generated without the stratification. This is particularly important when the generated models are intended for critical application such as informing policy and decision makers (as is the focus of this research).

5.4 DISCUSSION

Determination of the region of a map layer which is spatially associated with high sulphate in groundwater is particularly important as this will highlight only the region of the map layer which is associated with AMD pollution, given the assumption that high sulphate in groundwater can be used as a proxy of polluted sites.

Conversion of map layers to binary form reduces the dimensions of the data but is necessary in view of computer memory constraints. Binary maps are used for data-driven modelling as this will reduce the number of permutations for the ten map layers to accommodate the current limits of the virtual memory of a personal computer. This is done because if the full data spectrum datasets were to be used, an excessively large number of permutations would be generated which cannot be processed by a personal computer at this time.

In the development of rapid groundwater vulnerability assessment tools, using data-driven approaches, the stratified tenfold and leave-one-out cross-validation approaches are selected owing their advantages over other techniques such as the random subsampling and holdout techniques. For a large dataset, the stratified tenfold approach is preferred and for a small dataset the leave-one-out method is used. An algorithm which verifies the size of the dataset and decides which of these two approaches to used needs to be designed and incorporated into the assessment tools. This inter-link between algorithms will ensure that the results are generated fast and very accurately.

5.5 SUMMARY

The spatial association test was thus successful in extracting only those sections of the input map layers and map layers which are spatially associated with high sulphate in groundwater. Next, the results are used to generate binary maps for each selected parameter. Algorithms to be used to automate some of the processes for data-driven approaches such as establishing the number of epochs and number of neurons in the hidden layer and the selection of the best model are also given. A detailed explanation of artificial neural networks and the neuro-fuzzy system will be presented in Chapters 6 and 7.

CHAPTER 6: DATA-DRIVEN ARTIFICIAL NEURAL NETWORK SYSTEMS

6.1 INTRODUCTION

The SPT approach was developed and successfully used to generate a knowledge-driven groundwater vulnerability model for the Witbank, Ermelo and Highveld coalfields. Another approach that can be used to generate groundwater vulnerability models is a data-driven approach where the system learns from given known input-output data pairs and where it deduces meaningful relationships which can be used to determine output values when only input values are given.

In the Chapter 5, data preparation techniques and algorithms for the automation of some processes were discussed. In this chapter, a data-driven artificial neural network system will be formulated and used to generate a groundwater vulnerability model for the Witbank, Ermelo and Highveld coalfields. The generated model will also be validated and discussed.

6.2 OVERVIEW OF DATA-DRIVEN ARTIFICIAL NEURAL NETWORK SYSTEM

6.2.1 Biological Neural Network Background

Artificial neural networks are inspired by the biological nervous system, also known as the natural neural network or biological neural network. Therefore, it is of paramount importance to understand the basic functioning of biological neural networks. Most highly developed animals and humans who have the ability to adapt to a changing environment are equipped with a complex control system which is capable of learning. This is facilitated by a very complex network of highly specialised neurons ~ 10^{11} of them making up the building blocks of the central nervous system (Schmidt, 2000). A neuron contains all the structures of an animal cell and can be broken down into three main components, namely the soma (cell body for information processing), the dendrite (for receiving information) and axon (for sending information). Dendrites form a tree-like network of nerve fibres which are connected to the soma (Seyam, 2009) (Figure 6.1). The soma is the spherical compact area of the neuron that contains the nucleus and fluid material called the cytoplasm surrounding the nucleus. The axon is a long slender projection of the neuron that typically conducts electrical impulses away from the soma of the neuron. Axons are connected to one another by synapses. The transmission of signals from one neuron to another at synapses is a complex chemical process in which specific transmitter substances are released from the sending cell. The effect is to raise or lower the electrical potential inside the body of the receiving cell. If the potential reaches a threshold, a pulse is sent down

the axon and the cell is '*fired*' (Ajith, 2005). Together, the neurons form a complex system, with the brain as the control unit which operates as a highly sophisticated computer capable of processing vast amounts of information at relatively fast speeds and with great precision.

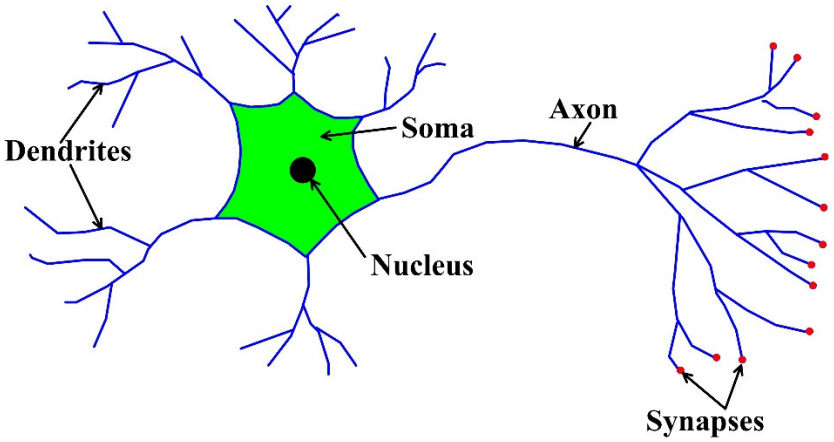

(Ajith, 2005)

Figure 6.1: Simplified illustration of a biological neuron

6.2.2 Artificial Neural Network Background

Artificial neural networks (ANNs) belong to the data-driven branch of AI which is inspired by the biological neural system in terms of which the computer is trained to do the functions which, at the moment, are best handled by humans, such as learning (Shigidi and Garcia, 2005). Artificial neural networks (ANN) form a class of non-linear parallel distributed information processing and adaptive systems originally based on studies of the brains of living species (McCulloch and Pitts, 1943).

The basic building blocks of artificial neural networks are artificial neurons which function similarly to their biological counterparts. These building blocks may be regarded as constituting a simple mathematical model or function on which complex networks are based. Such a model is made up of three simple sets of rules: multiplication, summation and activation (Figure 6.2) (Krenker *et al.*, 2011). Initially, inputs are weighted, meaning that every input value X_i is multiplied by an individual weight W_i. The weights represent the strengths of the interconnections between individual neurons inside the neural network and are used to solve a problem. In the centre of an artificial neuron is the sum function (Y_{WSI}) that sums all the weighted inputs and bias b, according to Equation 6.1. At the exit of an artificial neuron, the sum of previously weighted inputs and the bias are passed through the activation function, also known as a transfer function (Figure 6.2).

$$Y_{WSI} = \sum_{i=1}^{m} X_i * W_i + b \qquad 6.1$$

where Y_{WSI} is the weighted sum of inputs which constitute the input to the activation function,

X_i is the input value in discrete time, k, where i goes from 1 to m, and,

W_i is the weight value in discrete time k where i goes from 1 to m, b is the bias.

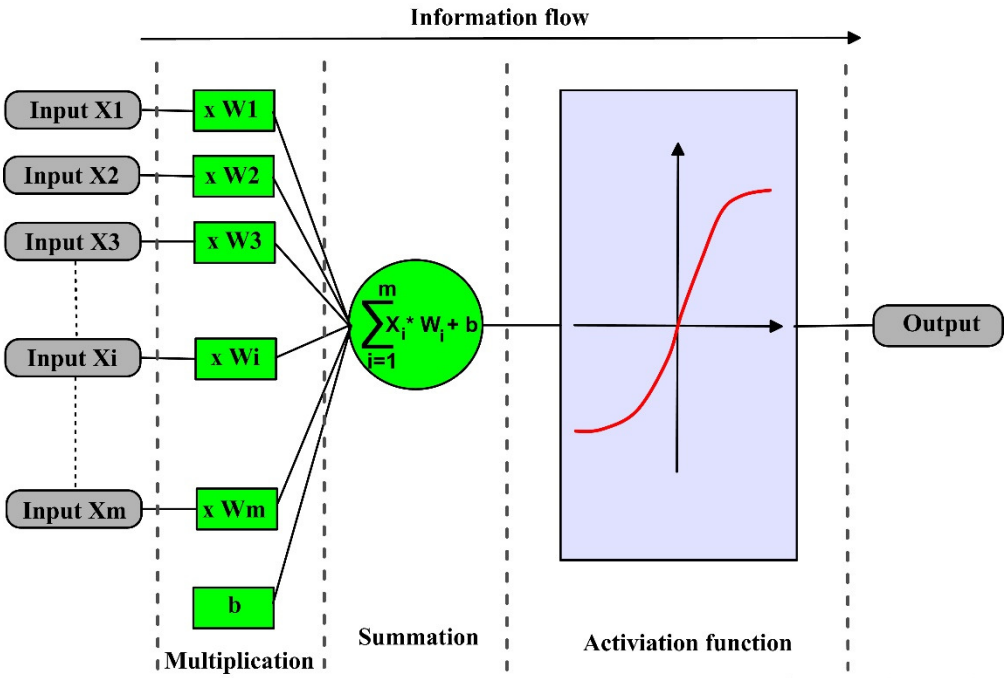

(Krenker *et al.*, 2011)

Figure 6.2: Working principle of an artificial neuron

In case the weighted sum from the weighted inputs is zero, a bias is added to make the output not-zero or to scale up the system response. The output from the summation function can be any numerical value from -infinity to +infinity. Thus, in order to limit the output response, a threshold value is set up. This is done by passing the output response (Y_{WSI}) through the activation function (f). The activation function is set as the transfer function used to obtain the desired output. Equation 6.2 represents the mathematical representation of the relationship between the activation function, inputs, weights and the bias:

$$y(k) = f\left(\sum_{i=1}^{m} X_i(k) * W_i(k) + b\right) \qquad 6.2$$

where $X_i(k)$ is input value in discrete time k where i goes from 1 to m,

$W_i(k)$ is the weight value in discrete time k where i goes from 1 to m,

b is the bias,

f is the transfer function,

$y(k)$ is the output value in discrete time k.

The activation functions which are commonly used are binary, sigmoid or hyperbolic tangent (Xenonstack., 2017). The binary function has only two possible output values (0 and 1) (Figure 6.3a). This means if the input value meets a specific threshold, the output value (1) is produced and if the specific threshold is not met, the output value (0) is produced. This can be described mathematically by Equation 6.3.

$$y = \begin{cases} 1 \; if \; Y_{WSI} \geq threshold \\ 0 \; if \; Y_{WSI} \; < threshold \end{cases} \tag{6.3}$$

The most commonly used activation function in most neural networks is the sigmoid function, which manifests as an "S" shaped curve (Figure 6.3b). The sigmoid resembles a Boolean model, as it is "off" until a given weighted sum of inputs (WSI) value is reached, then it quickly (but not instantly) switches to "on". This is similar to the step function but is continuous and used simply to calculate its derivative. This models the behaviour of a natural neuron, which is generally either "firing" or "inactive" (Dan., 2017). The sigmoid function may be expressed by Equation 6.4 which normalises the output to values in the range between 0 and 1:

$$y = \frac{1}{1 + \; e^{-\sigma Y_{WSI}}} \tag{6.4}$$

where y is the output value after the activation function operation,

σ is the steepness parameter that controls the steepness of the curve,

Y_{WSI} is the weighted sum of the inputs (Equation 6.1) which feeds into the activation function.

The hyperbolic tangent function may also be used as an activation function. This function normalises the output to values in the range between -1 to 1 (Figure 6.3c) and it may be described by Equation 6.5:

$$y = \; tanh\left(\sum_{i=1}^{m} X_i * W_i + b\right) \tag{6.5}$$

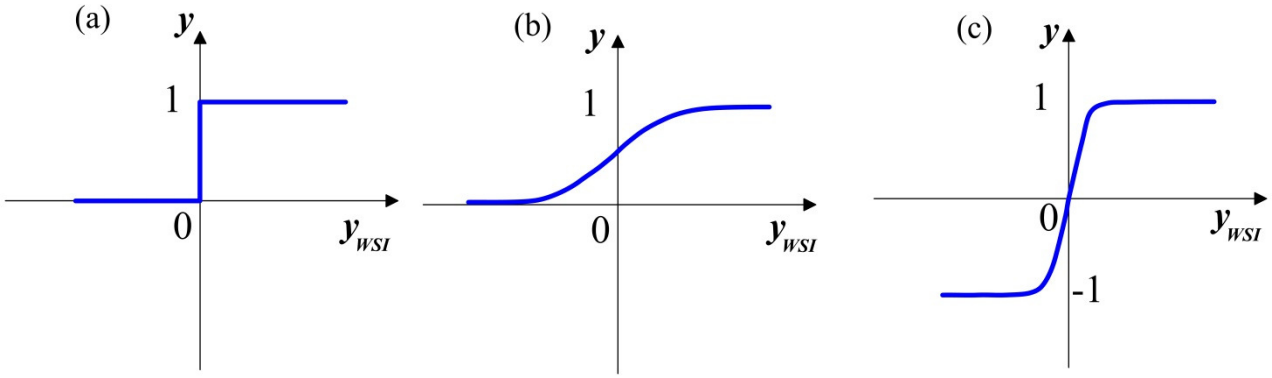

Figure 6.3: Activation functions commonly used in artificial neural networks: (a) binary (b) sigmoid and (c) hyperbolic tangent

For all these activation functions, if the input is lower than the weighted sum of inputs (WSI) the neuron is inactive, but as the input increases beyond the WSI, this causes the neuron to "fire". Altering the weights connecting neurons can change the relationships between the neurons, thus changing the behaviour of the network.

Artificial neurons are interconnected in an artificial neural network, where their working principles and simple set of rules are combined to solve various complex problems such as automated speech recognition, visual recognition, medical diagnosis and signature verification. Artificial neural networks have been found to have a sound theoretical basis from the perspective of machine learning and usually perform well when used for real-world data analysis (Bishop, 1995). In addition, ANNs have good generalisation capabilities and are usually robust against noisy or missing data (Idowu *et al.*, 2012). They include the ability to learn and generalise from examples to produce meaningful solutions to problems even when the input data contain errors or are incomplete, and to adapt solutions over time to compensate for changing circumstances and to process information rapidly (Jain *et al.*, 2004).

6.2.3 History of ANNs

The first information about artificial neural networks was recorded in 1943 when Warren McCulloch and Walter Pitts developed the first model of neural networks based on simple elements which were considered to be binary devices with fixed thresholds in what was called the "all-or-none" character of nervous activity (McCulloch and Pitts, 1943).

In 1944, Joseph Erlanger and Herbert Spencer Gasser identified several varieties of nerve fibre and established the relationship between action potential velocity and fibre diameter.

In 1949, Hebb introduced in his book "*The organisation of behaviour*" the concept that neural pathways are strengthened each time they are used. This principle is fundamental to the way humans learn (Hebb, 1949).

In 1958, Rosenblatt introduced the concept of a simple layer network called the perceptrons (Rosenblatt, 1958). Another system which used a different learning rule as the perceptron was developed in 1960. The system employed the least-mean-squares as a learning rule, expounded in the book "*Perceptrons: An introduction to computational geometry*" by Minsky and Papert (1969). In this book, the limitations of single layer perceptrons were demonstrated. The perceptron was defined as a two-layer machine that can handle only linear separable problems and cannot solve the exclusive "*OR*" problem. These limitations sent the field into hibernation for the next couple of years.

In 1972, Klopf developed a basis for learning in artificial neurons based on biological principles (Klopf, 1972).

In 1974, Paul Werbos developed the back propagation learning method.

Between 1980 and 1986, several events led to the rebirth of the field and several scientists, mathematicians and technologists joined the emerging field. In 1982, Hopefield presented a paper "Neural networks and physical systems with emergent collective computational abilities" which introduced the notion of the recurrent artificial neural network.

In 1986, the back propagation algorithm was rediscovered by Rumelhart and others, as described in the book "*Learning internal representation by error propagation*" (Rumelhart *et al.*, 1986). Since the conception of the back propagation algorithm, papers, books, workshops and conferences dealing with ANN have proliferated.

In 1987, the self-organising neural pattern recognition machine was developed by Carpenter and Grosberg (Carpenter and Grossberg, 1987).

Between the 2009 and 2012, the recurrent neural network and deep feedforward neural networks were developed in the research group of Schmidhuber (Schmidhuber, 2014).

6.2.4 Architecture of ANNs

Biological neural networks are made up of neurons which comprise connected cells which transmit electrical impulses. The electrical activity of a neuron is dependent on the electrical activity of the neurons to which it is connected. In the case of artificial neural networks, real numbers are used instead of electrical activity. Neurons output a value, which is passed to other neurons via synaptic connections and (together with values from any number of other neurons) determines the output of those neurons. Synaptic connections are one-way, so values generally propagate through the network in one direction.

Input data from outside the network are fed into the input layer neurons which are connected to other neurons in the network via synapses. Neurons in the network are generally arranged in layers or

groups of neurons which are linked only to similar groups to their left and right — the input neurons (the yellow "blobs" in Figure 6.4) form the first of such layers. Data from the input layer are fed from left to right through various hidden layers (the green "blobs" in Figure 6.4). The last layer of neurons in the network is known as the output layer (the blue "blobs" in Figure 6.4); the output values of neurons in the output layer are the outputs of the network. This layered architecture is inspired directly by the design of the brain, in which layers of neuron cells are arranged in an onion-skin pattern (Dan, 2017).

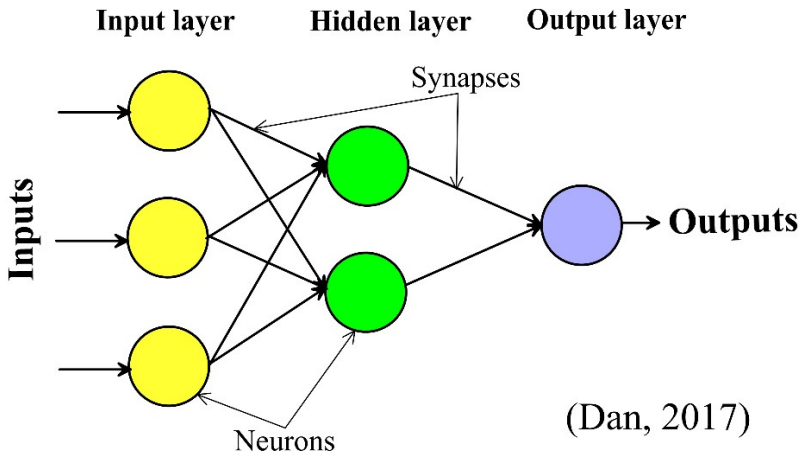

Figure 6.4: Artificial neural network architecture defined by the way in which neurons (yellow, green and blue blobs) are connected by synapses (lines)

In summary, there are various types of neurons in a neural network where each one generates its own output based on its function in the network. The functions of the various neurons may be summarised as follows (Dan, 2017):

- Input neurons: the function of the input neurons is to accept the input and output signal from the hidden layer neurons. The output data from the input neuron are the same as those that have been accepted from outside the network.
- Hidden (sigmoid) neurons: the function of the hidden neurons is to perform calculations on the data it has received from the input neurons. The output from the hidden neuron is the sum of its inputs multiplied by an activation function. The output data are then transmitted to the output neuron.
- Output neurons: output neurons provide a place from which network output values can be read from the network from the outside.

In the past, the ANN was thought to be akin to a "black box" system into which inputs are fed and results produced without any explanation of how the inputs are related to one another and how they

are combined generate the output. But with our current understanding of how they work from fundamental principles we can now obtain the weights relating each input to the output.

6.2.5 Learning by ANNs

The main property of a neural network is the ability to learn from its environment, and to improve its performance through a learning (training) process. During training, data are fed into the input layer which communicates with one or more "hidden layers" where the actual processing is done via a system of adjusting the weights "connections". The ANNs contain some form of "learning algorithm" which modifies the weights of the connections according to the input patterns with which it is presented (Shigidi and Garcia, 2005). In a sense, ANNs learn by example, in the same way a child learns to recognise dogs from examples of dogs.

Learning by neural networks may be viewed as a case whereby network weights are updated by neurons in view of producing the desired output, based on a set of examples. The most common types of network training are supervised, unsupervised or hybrid.

6.2.5.1 Supervised training

The networks are trained to extract the general relationships between the input layers and given outputs from a set of given examples and to store these relationships. After this, the trained ANN is given a set of input layers from which it produces an output based on the stored relationships.

The network learns by adjusting the weight values to reduce the differences between the example output (desired) and the training output (actual) until the error is below a certain acceptable value. The most commonly used supervised learning algorithm is the back propagation algorithm which means that learning is done by backward propagation of the error generated when the training output value is compared with the example output.

6.2.5.2 Unsupervised training

In this learning category, the network is only supplied with inputs from which it explores the underlying structure in the input data, or correlations between patterns in the input data, and organises the patterns into clusters. Thus, the neural network adjusts its own weights so that similar inputs result in similar outputs. After learning, when the network is given a new set of inputs it will be able to predict to which cluster the data belong using patterns and correlations learnt from the previous training data input. No external assistance or teacher is required for this category of learning. The Kohonen algorithm belongs into this category.

6.2.5.3 Hybrid training

This type of training combines supervised and unsupervised training. Parts of the weights are determined through supervised learning and the others are obtained through unsupervised learning.

6.2.6 Learning Algorithms – Back Propagation using a Sigmoid Activation Function

The back propagation algorithm considers the minimum of the error function in weight space using the method of gradient descent. The combination of weights which minimise the error function is considered to be a solution for the learning problem. The back propagation algorithm can best be categorised into four steps (Rojas, 2005):

- feed forward computation;
- back propagation to the output layer;
- back propagation to the hidden layer; and
- weight updates.

The algorithm is stopped when the value of the error function is sufficiently small.

6.2.6.1 Feed-forward computation

This step involves computing the output value by summing the weighted inputs and applying the activation function for each of the neuron connections in a forward direction. That is, calculations are done from the input layer neurons to the output layer neurons via the hidden layer neurons. This is achieved by multiplying the initial weight by the input values for each input layer neuron–hidden layer neuron connection. All the weighted inputs arriving at each hidden layer neuron are summed. The activation function is applied to the summed value to compute the output value for each hidden layer neuron. The results from an activation function operation at each of the hidden layer neurons become the input values to the output layer neurons. At the output layer neuron, the results from the hidden layer neuron activation function are multiplied by the initial weight of each hidden layer neuron–output layer neuron connection. Then all the weighted results arriving at the output layer neuron are summed and the activation function to generate the output value of the network is applied.

6.2.6.2 Back propagation to the output layer

The output value calculated from the previous step ($train_{output}$) is compared with the actual output value ($train_{target}$) for that given input value to compute the training error value. The training error is back propagated and used to adjust the weight such that the error is minimised. The equation for

calculating the error is the derivative of the activation function multiplied by the difference between the training output and the actual target value, given by Equation 6.6:

$$error_{h\_o} = derivative * (train_{target} - train_{output}) \quad 6.6$$

The sigmoid function for σ =1 is given by Equation 6.7:

$$y\,(x) = \frac{1}{1 + e^{-x}} \quad 6.7$$

The derivative of the sigmoid function can be expressed in terms of its original function, as shown by Equation 6.8:

$$y\frac{d}{dx}\,y(x) = \frac{e^{-x}}{(1 + e^{-x})^2} = y(x) * (1 - y(x)) \quad 6.8$$

Applying to the sigmoid function, the error is given by Equation 6.9:

$$error_{h\_o} = train_{output} * \left(1 - train_{output}\right) * (train_{target} - train_{output}) \quad 6.9$$

After the error has been calculated, it is first propagated from the output layer neurons to the hidden layer neurons. The hidden layer neuron-output layer neuron connections are first adjusted. The expression for adjusting the weight incorporates the learning rate (β) and the momentum (α).

The expression is given by Equation 6.10:

$$\Delta_{learn(h\_o)} = \beta * error * W_{old(h\_o)} \quad 6.10$$

where $\Delta_{learn(h\_o)}$ is the delta change in learning for the hidden layer-output layer connection,

β is the learning rate,

$error$ is the error calculated using Equation 6.9, and,

$W_{old(h\_o)}$ is the old weight for the hidden layer neuron-output layer neuron connection.

The new weight will be then be given by Equation 6.11:

$$W_{new(h\_o)} = W_{old(h\_o)} + \Delta_{learn(h\_o)} + \alpha * \Delta(t-1) \quad 6.11$$

where $\Delta(t-1)$ is the previous delta change of the weight. This is zero for the first iteration.

$W_{new(h\_o)}$ is the new weight for the hidden layer neuron–output layer neuron connection,

$W_{old(h\_o)}$ is the initial or previous iteration weight,

α is the momentum.

The new weights for all the hidden layer neuron–output layer neuron connections are calculated and stored for the next step.

6.2.6.3 Back propagation to the hidden layer

In this step, the error is propagated back to the input layer and the weights are adjusted accordingly. This is slightly more complicated than propagating the error from the output to the hidden layer that was calculated in the previous step using the known target output values. Here, the actual target values of the hidden layer neurons are unknown. To solve this problem, we use the new weights and error from the previous step. The new weight is multiplied by the error for the hidden layer neuron–output layer neuron connections. The equation for this calculation is given by Equation 6.12:

$$H_{error} = W_{new(h\_o)} * error_{h\_o} \quad 6.12$$

Once the error for the hidden layer nodes is known, weights between the input and hidden layer can be updated. First, the rate of change needs to be calculated for every weight, using Equation 6.13:

$$\Delta_{learn(i\_h)} = \beta * H_{error} * X_{input} \quad 6.13$$

Then the new weights between input and hidden layer are calculated using Equation 6.14:

$$W_{new(i\_h)} = W_{old(i-h)} + \Delta_{learn(i\_h)} + \alpha * \Delta(t-1) \quad 6.14$$

It is important not to update the weights until all the errors have been calculated. Using the new weights, the output error is calculated and the results compared with the previous error. This is done so as to evaluate the training as the training progresses. In the process, the error decreases until it is negligible. At this point, the network is termed to have been "trained" and will be ready for use to solve the problem it has been set.

6.2.7 Types of Artificial Neural Networks

6.2.7.1 Feed-forward ANNs

Artificial neural networks with a feed-forward topology are called feed-forward artificial neural networks and, as such, have only one condition namely that information must flow from input to output in only one direction with no back-loops. There are no limitations on the number of layers or type of transfer function used in the individual artificial neurons or the number of connections between the individual artificial neurons.

6.2.7.2 Recurrent ANNs

Artificial neural networks with a recurrent topology are called recurrent artificial neural networks. These are similar to feed-forward neural networks with no limitations regarding back-loops. In these cases, information is no longer transmitted only forwards but can also be fed backwards. This creates an internal state which allows the network to exhibit dynamic temporal behaviour.

The most basic topology of a recurrent artificial neural network is the fully recurrent artificial network where every basic building block (artificial neuron) is directly connected to every other basic building block in all directions. Recurrent artificial neural networks such as those by Hopefield, Elman, Jordan, and bi-directional networks are special cases of this type of neural network.

The aim of the technique is to train the network such that its response to a given set of inputs is as close as possible to a desired output. A number of algorithms are available for training neural networks. Back propagation is the most popular training algorithm (Werbos, 1990) and was used in this study. During feed-forward artificial neural network training, each hidden and output neuron processes inputs by multiplying each input by its weights. The products are summed and processed using an activation function. Here, a sigmoid function produces an output with reasonable discriminating power.

6.3 DATA-DRIVEN ARTIFICIAL NEURAL NETWORK: APPLICATION TO THE WITBANK, ERMELO AND HIGHVELD COALFIELDS

The application of artificial neural networks for the generation of a groundwater vulnerability model is a built up from the conference publication (Sakala *et al.*, 2016) where an ANN was built and used for assessment of groundwater vulnerability to AMD at a coalfield. In this publication, the training input parameters were DRIST parameters (Depth to water level, recharge, impact of the vadose zone, soils and topography) and hydrochemistry data (sulphates and total dissolved solids (TDS)) were used as the training output dataset. The SPT approach developed is an extended version of this methodology where other parameters such as recharge were replaced with rainfall to factor in the water availability for reactions while also capturing the role played by rainfall in the transportation of pollutants.

Using the input parameters as proposed by the SPT approach and an appropriately designed ANN system, a groundwater vulnerability model was generated for the Witbank, Ermelo and Highveld coalfields. An in-depth description and discussion of the formulation and validation of the model are given in this section.

6.3.1 ANN Training

The process followed in the preparation of the ANN groundwater vulnerability model comprises of six stages; some of the stages have been discussed in the Chapter 5. The stages involve:

1. Selection of training polluted and non-polluted sites, where local, national or international guideline threshold values for groundwater quality can be used (as discussed in Chapter 5, section 5.2);
2. Creation of the binary input maps based on spatial association test results for each of the input map layers (discussed in Chapter 5 section 5.3.1);
3. Establishing the optimum number of iterations (epochs) and number of neurons in the hidden layer which minimise over-fitting. This stage has already been discussed in Chapter 5, but results from ANN modelling will be given;
4. Selection of the cross-validation method involving an algorithm that checks the number of training points and decides on whether to use tenfold or leave-one-out cross-validation training;
5. Using the optimum number of epochs and number of neurons in the hidden layer obtained in stage 3 and the appropriate cross-validation training technique (stage 4), the ANN modelling algorithm is run to train the ANN network, after which it is then used to predict groundwater vulnerability values for all the grid cells within the entire study area; and
6. The final stage involves reclassifying the predicted ANN output into four groundwater vulnerability classes after which the model is validated with data that were not used to train the ANN.

6.3.1.1 Selection of training sites

As discussed in section 5.2, 53 boreholes within the Witbank, Ermelo and Highveld coalfields which were sampled and subjected to hydro-chemical analyses were reclassified into binary (0) and (1) values. Those with a sulphate concentration below 200 mg/L (non-polluted sites) were assigned binary class (0) and those above (polluted sites) this value were assigned class value (1).

6.3.1.2 Binary map creation

Binary maps generated in section 5.3.1 would be used as input map layers and borehole points (polluted and non-polluted), also in binary format, would be used as training outputs.

6.3.1.3 Establishing the optimum number of epochs and neurons in the hidden layer

In order to establish the optimum number of epochs in order to obviate the overfitting and inadequate training problems which are generally associated with ANN modelling, the epoch determination algorithm was used. Overfitting occurs when training the ANN network such that the predicted values precisely match the training data instead of producing generalised results as expected from a trained ANN. Inadequate training occurs when training is terminated before the network has gathered enough information about the relationship between the inputs and output pairs. The inputs to the ANN are the ten map layers and borehole sulphate concentrations in the groundwater as training outputs. When the epoch algorithm is run, the graph of testing the MSE against the epoch number is displayed. The results show that a number of training epochs produce low validation MSE values was obtained using 8 770 epochs with a validation MSE value of 0.0505 (Figure 6.5). This value was returned and passed on to the next algorithm which determined the optimum number of neurons in the hidden layer. Details of this algorithm can be found in Appendix 3.1.

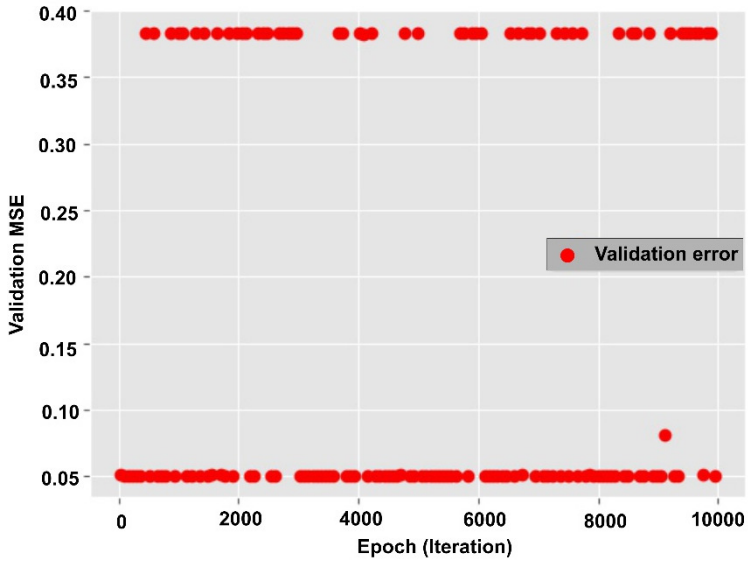

Figure 6.5: Validation errors at various training epochs

The hidden layer neuron number determination algorithm uses the optimum number of epochs to run several ANNs with varying number of neurons in the hidden layer and records the overall validation MSE for each neuron number. The output MSE values are plotted against the neurons in the hidden layer, as shown in Figure 6.6. The optimum number of neurons in the hidden layer with the least validation error was found to be nine layers with the lowest validation MSE value of 0.0525. Details of this algorithm can be found in Appendix 3.2.

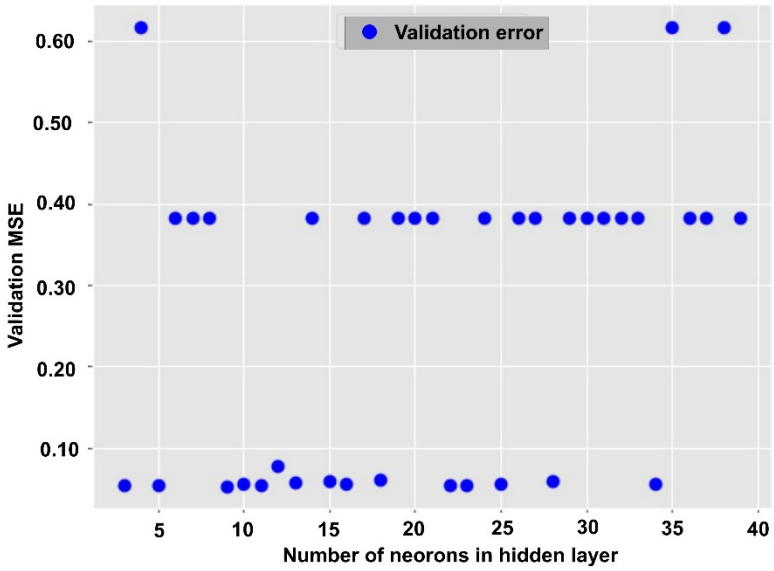

Figure 6.6: Validation errors at various number of neurons in hidden layer

6.3.1.4 Selection of cross-validation method

A simple algorithm was designed to verify the number of training data points and to choose between running the tenfold stratified or leave-one-out cross-validation method. The algorithm works as follows: given d number of training points, the decision to select a particular option is based on the structure of these two options. For the tenfold stratified method to work, the number of points for the polluted (p) and non-polluted (np) sites should be greater than ten for each, thus there should be a minimum of twenty points with at least ten points being polluted sites and ten points being non-polluted sites. When the leave-one-out method is used for a large number of training points, the computation time is greatly increased. Therefore, for large data points greater than twenty, the tenfold-stratified method is fastest as the number of training events is lower. At the same time, for fewer points below twenty or for data points which are fewer than ten for polluted and non-polluted points the leave-one-out approach is better. This can be summarised with the following expressions:

$if\ d > 20\ and\ p > 10\ and\ np > 10$, then use the tenfold stratified method otherwise

$if\ d < 20$ and / or $p < 10$ and / or $np < 10$ then use the leave-one-out method.

For the Witbank, Ermelo and Highveld coalfields with 53 boreholes of which 33 are polluted sites, the tenfold stratified method was selected.

6.3.1.5 Artificial neural network modelling

With the optimum number of training epochs and neurons in the hidden layer and the cross-validation method selected, the ANN algorithm is run. For the Witbank, Ermelo and Highveld coalfield study area, the topology (input-hidden-output) of the ANN model used was a (10-9-1) model, where 10 is the number of input map layers, 9 the optimum number of neurons in the hidden layer and finally 1

the number of outputs (sulphate concentration). Figure 6.7 shows the architectural layout of the ANN for the ten input map layers. The input layer is connected to the hidden layer by synapses with weights which are modified during the training process. The groundwater vulnerability model is the output layer.

The tenfold stratified cross-validation algorithm was run using the optimum values of epochs and neurons in the hidden layer which had been determined in the previous stages as 8 770 and 9 respectively. The results for validation for each training fold (experiment) are presented as a scatter plot of error values against the training fold value number (Figure 6.8). Thus, according to the results of the training, the lowest validation error is training fold number 4 with a validation error value of 0.001. This trained fold is therefore returned as the best-trained network for use in predicting groundwater vulnerability values for all the other map cell locations (pixel with a resolution of 30 x 30 m) within the Witbank, Ermelo and Highveld coalfields area.

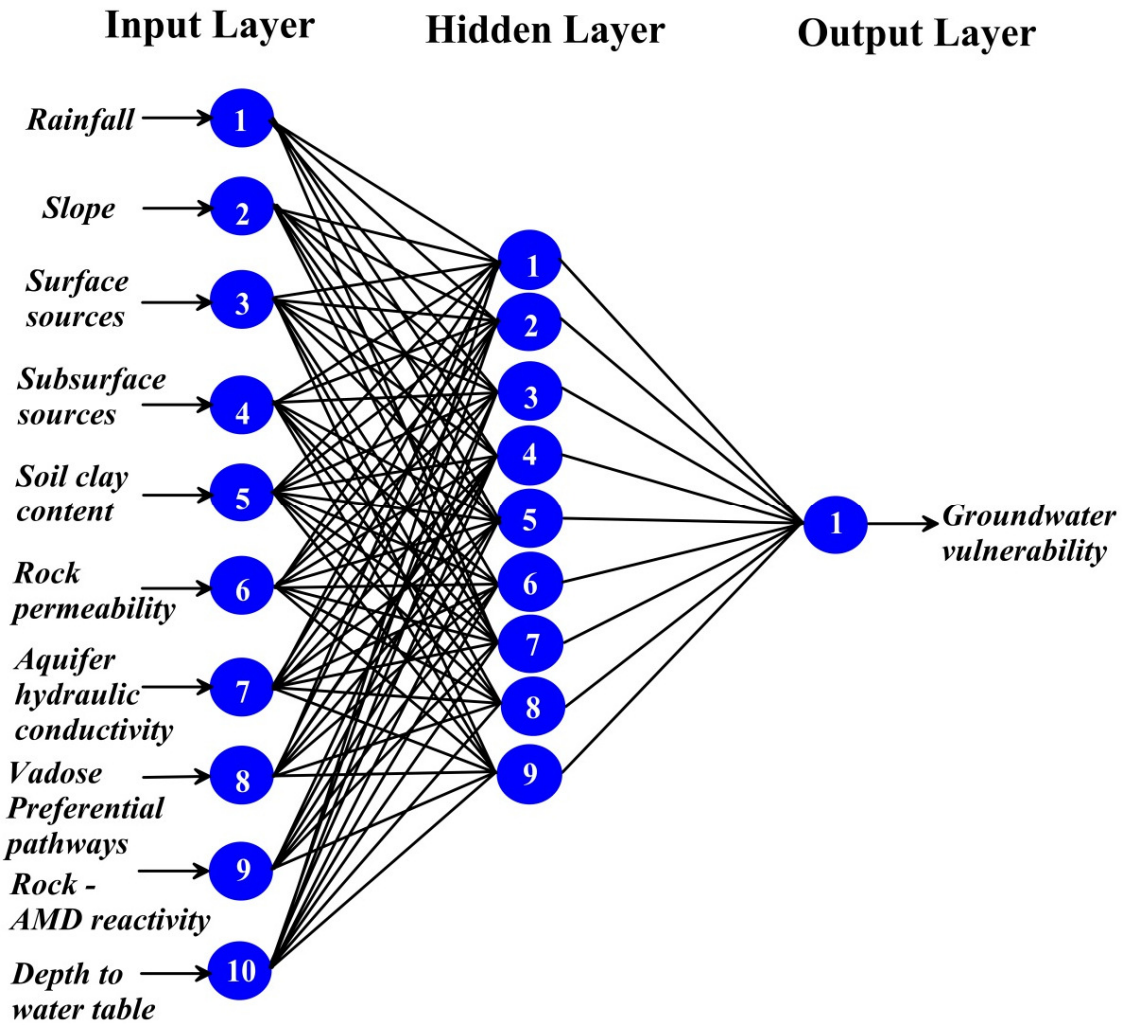

Figure 6.7: ANN architecture used for training

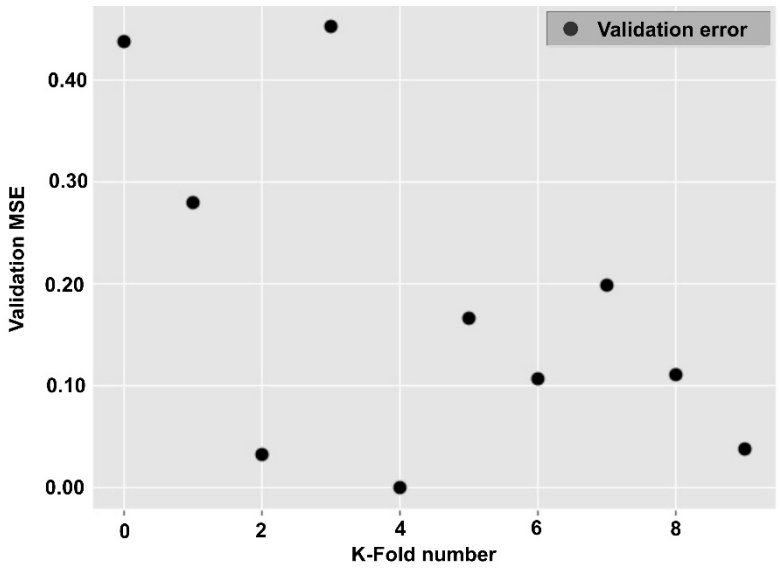

Figure 6.8: Graph for determining the best fold with the lowest validation error

6.3.2 Data-Driven ANN Model Results

The groundwater vulnerability model values were reclassified into four classes using the natural break method (ESRI., 2006) and the results presented in Figure 6.9. The model shows the groundwater vulnerability model generated using sulphate training where the areas in blue indicate the lowest vulnerability and the red coloured areas show the most vulnerable. The groundwater vulnerability model of the Witbank, Ermelo and Highveld coalfields produced using ANN systems shows that the largest portion of the area falls in the low groundwater vulnerability class.

The ANN model shows high groundwater vulnerability values in the area between Delmas, eMalahleni and Middelburg. The area to the south of Carolina towards Ermelo is also marked by relatively high values. The groundwater vulnerability model is derived from the relationship that the network established between the various map layers and the sulphate concentration. Thus, of the ten inputs maps, the highest values appear to fall in areas which are characterised by flat surfaces with moderate rainfall, close to AMD sources where the soil clay content is low, in the presence of rocks with high permeability values and very low rock-AMD reactivity.

The areas with low groundwater vulnerability may be attributed to a combination of earth properties which work together to inhibit AMD from to reaching the groundwater system. These properties include a lack of sources of AMD combined with soils and rocks which offer some resistance to the flow of pollution and good trapping properties.

Table 6.1 shows the aerial coverage sizes of the four groundwater classes where the low vulnerability class has the largest size and the size distribution decreases as the vulnerability class changes from low to high with the high class covering the smallest aerial extent.

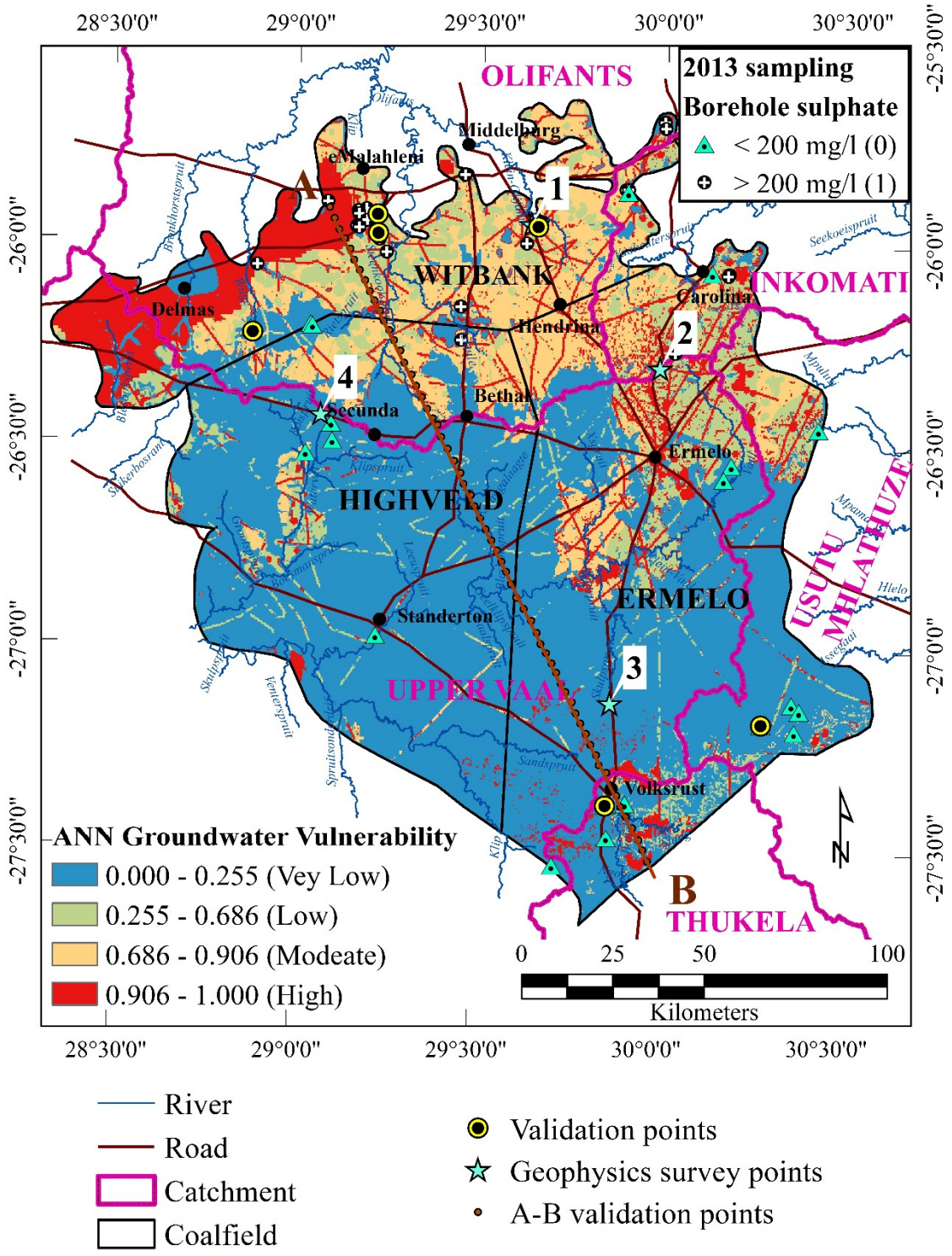

Figure 6.9: Groundwater vulnerability model of the Witbank, Ermelo and Highveld coalfields generated by using ANNs

Table 6.1: Aerial coverage of various vulnerability classes

Vulnerability classification	Size (km^2)
Very Low	16 361 (59.4%)
Low	3 756 (13.6%)
Moderate	3 955 (14.4%)
High	3 480 (12.6%)

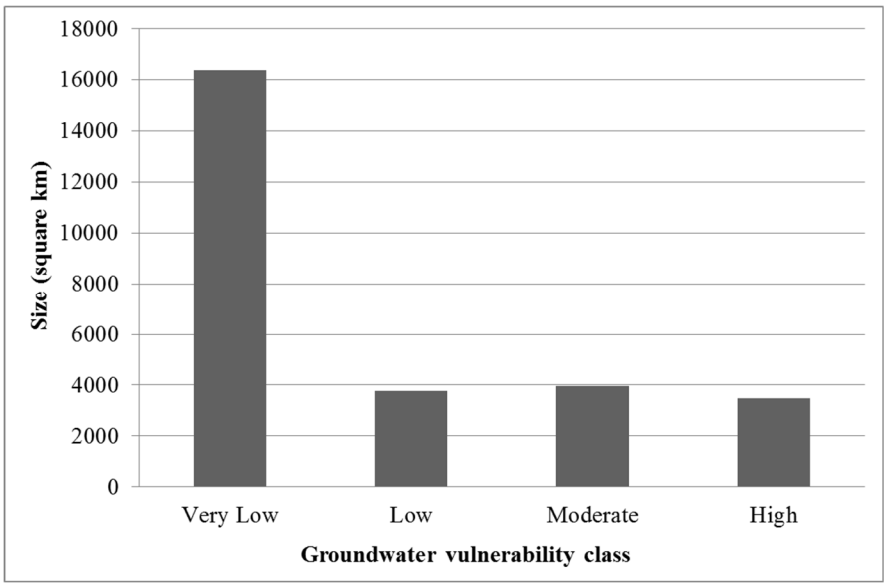

Figure 6.10: Aerial size distribution of various groundwater vulnerability classes

6.3.3 Validation of the ANN Model

Before the ANN groundwater vulnerability model can be used for critical applications such as policy and decision making in this research, the model needs to be validated by other datasets which were not used to generate the model. Three validation methods, namely correlation coefficient, cross-section and geophysical methods were used.

6.3.3.1 Model validation using hydrochemistry data

6.3.3.1.1 Correlation coefficient approach

The correlation coefficient method for model validation involves a comparison of the model values with a parameter which can be measured physically. Some of the boreholes with measured sulphate concentrations which were not used for model building were selected for validation purposes. The artificial neural network model values at each of these borehole locations were extracted. Sulphate was considered to be conservative in Chapter 3 and hence can be used as possible tracer for AMD pollution. The spatial locations of six points used for the validation of the ANN groundwater vulnerability model are shown in Figure 6.9 as yellow circles with a black dot in the centre. The sulphate concentrations in the groundwater at these points were used to validate the model. The groundwater samples with a high sulphate concentration coincide with moderate to high groundwater vulnerability zones, while samples with low sulphate concentrations lie in low to very low groundwater vulnerability zones. A few boreholes were used for validation so that most of the boreholes are used for model creation.

A correlation analysis between model values and AMD indicators (sulphate) was done and scatter plots produced as shown in Figure 6.11, where very a high correlation value of 0.909 was obtained

showing that the ANN was well trained and was able to predict with high accuracy the model values which it had not used for training. When generating the binary map layers, a range of map layer values was selected to cover between 50 and 100% of points instead of selecting the region of the map which completely covers 100% of the points. This was done so that the ANN can learn the general relationship between the various input layers and the spatial locations of the training points so that when new points are given to it after learning, it would be able to predict the output values better, as was borne out by the present scenario.

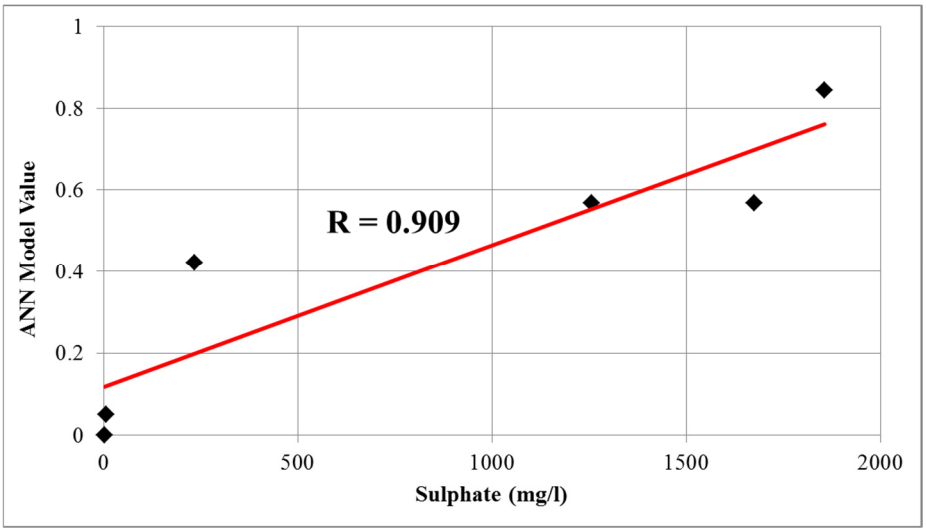

Figure 6.11: Correlation scatter plots for sulphate against groundwater vulnerability model values

6.3.3.1.2 Cross-section method of validation

In order to test the validity of the ANN groundwater vulnerability assessment using SPT inputs, sulphate data from a different source was selected as a pollution indicator. Borehole hydrochemistry data from the National Groundwater Archive (NGA) with verified locations was tested for ionic balance. Only those with an ionic balance of less than ± 5% were selected for the validation of the ANN model. The sulphate data from 60 boreholes within the study area were used to validate the ANN model by comparing the sulphate with vulnerability values. Again, the kriging interpolation method was used to generate a sulphate concentration map of the study area, as shown in Figure 4.21. To illustrate this validation test, a cross-section line A–B was created on the ANN vulnerability and the sulphate maps. A comparison of these cross-sections enabled an evaluation of the validity of the vulnerability map.

The comparison between the map of sulphate concentrations and the vulnerability maps shows that areas with high sulphate concentrations in the groundwater correspond to the highest vulnerability values. This coincidence is very clear in the northern section of the cross-section between distances 10 and 70 km (Figure 6.12). The graphs differ at the start of the section owing to a scarcity of

boreholes in this area when compared to the higher resolution of the ANN model. At the northern edge of the cross-section, the ANN model values increase yet the sulphate concentration drops. A close examination of the sulphate contour map shows that only one borehole with a low sulphate value is found in the area, and at the edge, thus the low interpolated values at the edge could be attributable to a gridding artefact which normally affects the edges of the gridded data.

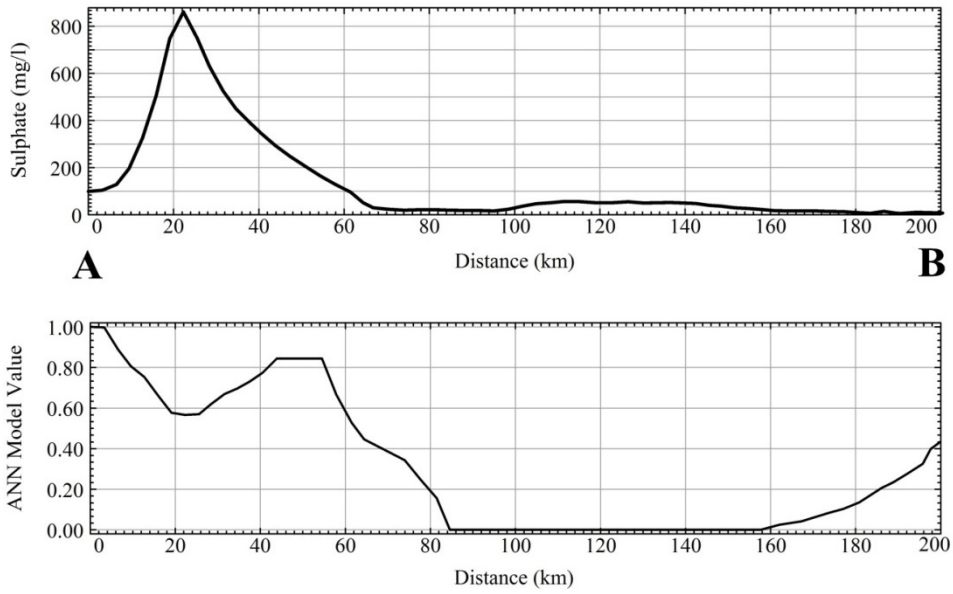

Figure 6.12: Profile along cross-section A–B showing the DWS borehole sulphate concentration and the ANN vulnerability model profile

6.3.3.2 Validation using geophysical techniques

Geophysical techniques (ERT and seismic refraction) were used to estimate *in situ* hydrogeological parameters (porosity and seismic velocity) which were used to validate the ANN groundwater vulnerability model. The survey results for the four survey sites are described in Chapter 4, section 4.5.4.2. The modified Archie's Law by Everett (2013) was used to convert the inverted apparent resistivity values to estimated porosity values.

From the comparison of the porosity ranges for the unsaturated zone of the four sites and their corresponding model values it can be seen that where the porosity values are high, the model values are high as well, with low model values being correlated with low porosity values (Table 6.2). According to these observations at the four sites, the higher the porosity, the higher the groundwater vulnerability values. A comparison of the porosity and seismic velocities at the four sites was done to establish whether there is any correlation between the measured earth properties and groundwater vulnerability. Table 6.2 summarises the geophysical results in comparison with the ANN model values for each site. The four sites surveyed fall in two classes, where the ANN model show values 1 and 0 for sites (1, 2) and (3, 4) respectively. Only four sites were surveyed to obtain geophysical

parameters and the sites with high porosity and low seismic velocities correspond to where the model predicts high groundwater vulnerability and where porosity is low and, for high seismic velocity, the model values are high. Thus, the model values are correlated with the physically measurable earth properties.

Table 6.2: Comparison of derived porosity values and the ANN groundwater vulnerability model values for each of the survey sites

Survey site	Porosity ranges of weathered zone (%)	Seismic velocity (m/s)	ANN model value
1	9.0 – 25 (average = 17)	2747	0.998 (High)
2	5.7 – 14 (average = 9.85)	2991	0.999 (High)
3	5.6 – 11 (average = 8.3)	4505	0.002 (Very Low)
4	4.5 – 8.4 (average = 6.45)	5406	0.0001 (Very Low)

6.4 DISCUSSION

Automation of some of the stages (i.e. determination of the termination number of iterations and number of neurons in the hidden layer) in the application of artificial intelligence for the generation of groundwater vulnerability model proves to be quite helpful in terms of processing speed as it obviates the trial and error approach which is normally used for these tasks. Automation gives the user of the developed tools for assessing groundwater vulnerability to AMD at a coalfield enough time to focus on preparing quality input map layers and interpreting the results as opposed to spending too much time on processing and modelling the data.

The ANN tool for the rapid assessment of groundwater vulnerability developed in the current research is very dynamic in the sense that upon modification of input training data, when more data of higher resolution becomes available, the model is modified accordingly. This is facilitated by the automatic algorithms developed during the current research. Owing to the automation of some of the processing in ANN modelling, the developed tool will produce results which are consistent even if used by different experts to run the modelling using the same input data. This proves to be particularly important when results are meant for critical decision making purposes such as mining regulatory and land use planning where results may need to be reproduced in the future.

6.5 SUMMARY

The ANN tool which belongs to the data-driven branch of AI was generated and applied in the creation of the groundwater vulnerability model for the Witbank, Ermelo and Highveld coalfields. The tenfold stratified cross-validation technique produced a groundwater vulnerability model which

is quiet consistent with field realities based on the validation methods used: correlation coefficient, cross-section and geophysics techniques (resistivity and seismics) methods.

Based on the ANN groundwater vulnerability model of the Witbank, Ermelo and Highveld coalfields, the Witbank coalfield has the largest area of highly vulnerable groundwater and the Highveld coalfield is the least vulnerable of three coalfields studied. These findings are also reflected by the number of mining activities both historic and current found in these coalfields, with most of the coal mining operations being concentrated in the Witbank coalfield. The SPT approach is a specific groundwater vulnerability assessment technique where sources of pollution are incorporated in the modelling; hence, areas where no AMD pollution has been mapped might appear to be of low vulnerability. Hence, the model needs to be updated over time as more mining takes place and new data are acquired.

CHAPTER 7: HYBRID ARTIFICIAL INTELLIGENCE SYSTEM

7.1 INTRODUCTION

The previous chapters presented the application of the fuzzy expert and neural network system to produce groundwater vulnerability models of the Witbank, Ermelo and Highveld coalfields of South Africa. In this chapter, the fuzzy expert system and the neural networks are combined to form a hybrid system which combines the benefits of these two powerful systems. An overview and theoretical background of the hybrid system will be given, after which a hybrid system model will be developed and validated for an assessment of the groundwater vulnerability of the Witbank, Ermelo and Highveld coalfields.

7.2 OVERVIEW OF THE HYBRID SYSTEM

Hybrid systems combining fuzzy logic, neural networks, genetic algorithms, and expert systems are proving their effectiveness in tackling a wide variety of real-world problems. Every intelligent technique has particular computational properties (e.g. ability to learn, explanation of decisions) that make it suited to particular problems and not to others. For example, while neural networks are good at recognising patterns, they are not useful for explaining how they reach these decisions. Fuzzy expert systems, which can reason using imprecise information, are good at explaining their decisions but they cannot automatically acquire the rules they use to make those decisions. These limitations have been a central driving force behind the creation of intelligent hybrid systems where two or more techniques are combined so as to overcome the limitations of individual techniques. While the fuzzy expert system provides an inference mechanism under cognitive uncertainty, computational neural networks offer exciting advantages, such as learning, adaptation, fault tolerance, parallelism and generalisation (Porwal *et al.*, 2003). To enable a system to deal with cognitive uncertainties in a manner approximating that used by humans, one may incorporate the concept of a fuzzy expert system into the neural networks.

7.2.1 Types of Neuro-Fuzzy Systems

There are several ways to combine neural networks and fuzzy expert systems. Efforts at merging these two technologies may be characterised by considering three main categories: neural-fuzzy systems, fuzzy-neural networks and fuzzy-neural hybrid systems (Fuller, 2000).

7.2.1.1 Neural-fuzzy systems

Neural-fuzzy systems are characterised by the use of neural networks to provide fuzzy systems with an automatic tuning method, but without altering their functionality. One example of this approach would be to use neural networks to formulate membership functions and to map relationships between fuzzy sets that are utilised as fuzzy rules (Fuller, 2000), as shown in Figure 7.1. In the training process, a neural network adjusts its weights in order to minimise the MSE between the output of the network and the desired output (Azar, 2010).

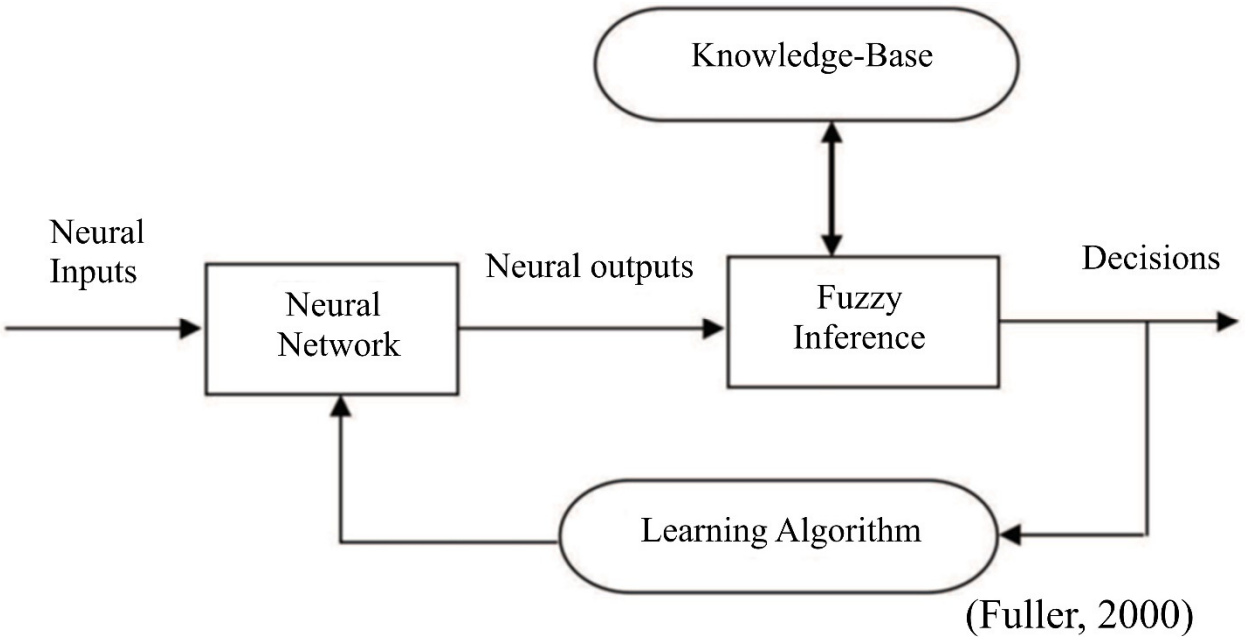

Figure 7.1: Neural-fuzzy system

The weights of the neural network represent the parameters of the fuzzification function, fuzzy membership function, fuzzy rule and defuzzification function. In this sense, the training of this neural network results in automatically adjusting the parameters of the fuzzy system and finding the optimal values. This kind of combination is mostly used in control systems applications in process automation in engineering (Azar, 2010).

7.2.1.2 Fuzzy-neural systems

In the fuzzy-neural system, the elements of the neural networks are fuzzified using fuzzy expert system theorems. Figure 7.2 shows the general flow diagram of a typical fuzzy-neural system. Crisp statements are fed into a fuzzy inference system whose outputs become inputs to an ANN which produces the output using a specified learning algorithm. In this case, a crisp neuron may be regarded as a fuzzy neuron. The inputs to the fuzzy neurons are crisp, but the weights are replaced by the fuzzy membership functions (Lin and Lee, 1996; Azar, 2010). The result of each weighting operation is the membership value of the corresponding input in the fuzzy set. Also, the aggregation operation used

in fuzzy operators (AND, OR, SUM etc.) can be used in the hybrid system. Since fuzzy neural networks are inherently neural networks, fuzzy-neural systems are mostly used in pattern recognition applications (Azar, 2010).

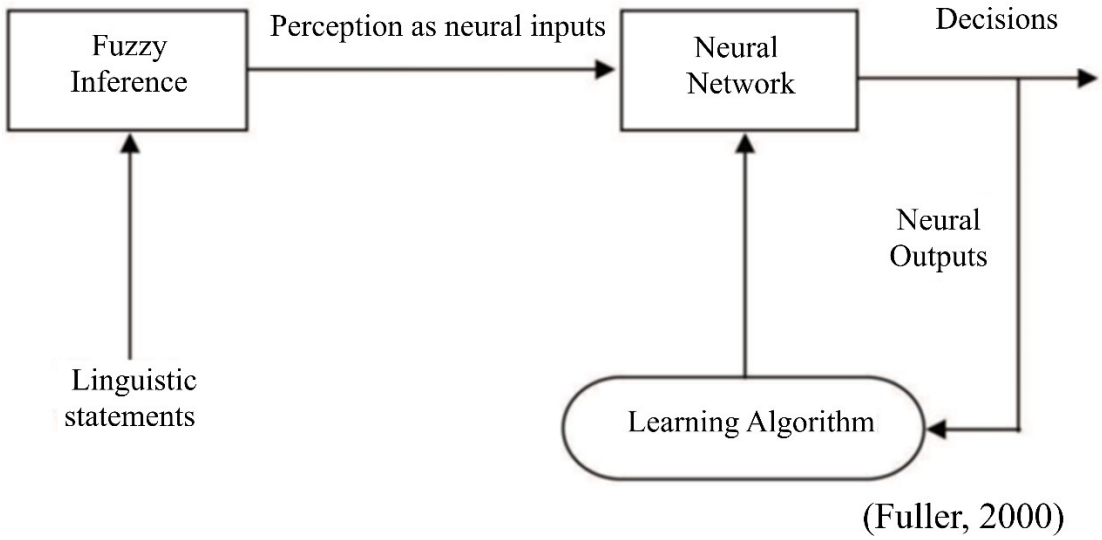

Figure 7.2: Fuzzy neural system

7.2.1.3 Hybrid neuro-fuzzy systems

In the hybrid neuro-fuzzy approach, both fuzzy and neural networks techniques are used independently, where each one serves a different function in the system. Each system incorporates and complements each other in order to achieve a common goal. This can be achieved by interpreting the fuzzy rule-base in terms of a neural network. The approach is versatile and has a wider range of uses than the fuzzy or the neural network systems when these are used individually. That is, the fuzzy sets can be interpreted as weights and the rules, and input variables and output variables can be represented as neurons. The learning algorithm, similar to that in neural networks, entails a change of the weights and/or creating or deleting connections. These changes may be interpreted both in terms of a neural net and in terms of a fuzzy controller, thus it is possible to avoid the "black box" behaviour of neural nets in this way.

Hybrid neuro-fuzzy come in various forms, for example, the ARIC (Berenji, 1992), the GARIC (Bersini *et al.*, 1993), the ANFIS (Jang, 1993) or the NNDFR model (Takagi and Hayashi, 1991). The Adaptive Neural-Fuzzy Inference System (ANFIS) is the most successfully used in combining the benefits of two powerful systems (neural network and fuzzy expert system) into a single capsule algorithm and will be used in this research.

The ANFIS applies neural learning rules to identify and adjust the parameters and structure of a fuzzy inference system. This approach has all the benefits of the two systems, including the following (Jang, 1993; Azar, 2010):

- easy implementation;
- fast processing;
- accurate learning;
- strong generalisation abilities, excellent explanation facilitated through fuzzy rules; and
- easy to incorporate both linguistic and numeric knowledge for problem solving.

The structure and parameter identification of the fuzzy rule base is done by the neural network by defining, adapting and optimising the topology and the parameters of the corresponding whole system based only on the available data. Thus, the ANFIS may be regarded as both as an adaptive fuzzy inference system with the capability of learning fuzzy rules from data and as a connectionist architecture provided with linguistic meaning. Fundamentally, ANFIS functions like a fuzzy inference system and the Sugeno Tsukamoto fuzzy model is commonly used.

7.2.1.3.1 ANFIS system operation

The ANFIS system is made up of five layers (1 to 5):

Layer 1 is the input module where the system obtains data from the outside world and generates output fuzzy values according to the fuzzy membership functions as suggested by the expert.

Layer 2 is the rule module which takes the output fuzzy values from layer 1 and applies the fuzzy rules to combine the inputs using the fuzzy rules as suggested by the expert.

Layer 3 is the average module. The output from the rule module is normalised according to the firing strength of the rules in layer 2.

Layer 4 is the consequent module which uses the normalised output from layer 3 as inputs to a machine learning algorithm. The machine learning algorithm adjust the weights of the nodes using the relationship it generates between the normalised outputs from layer 3 and the given output data.

Layer 5 is the output module which sums up all the incoming signals from layer 4 and generates one output value.

This process is done repeatedly until the system has been trained.

To illustrate the learning algorithm and for the purpose of simplicity, a network with two inputs, x and y, and one output, z, is considered. The first-order Sugeno fuzzy model with two rules may be used.

Rule 1: If x is A_1 and y is B_1, then $f_1 = p_1x + q_1y + r_1$

Rule 2: If x is A_2 and y is B_2, then $f_2 = p_2x + q_2y + r_2$

The system has five layers, as shown of Figure 7.3.

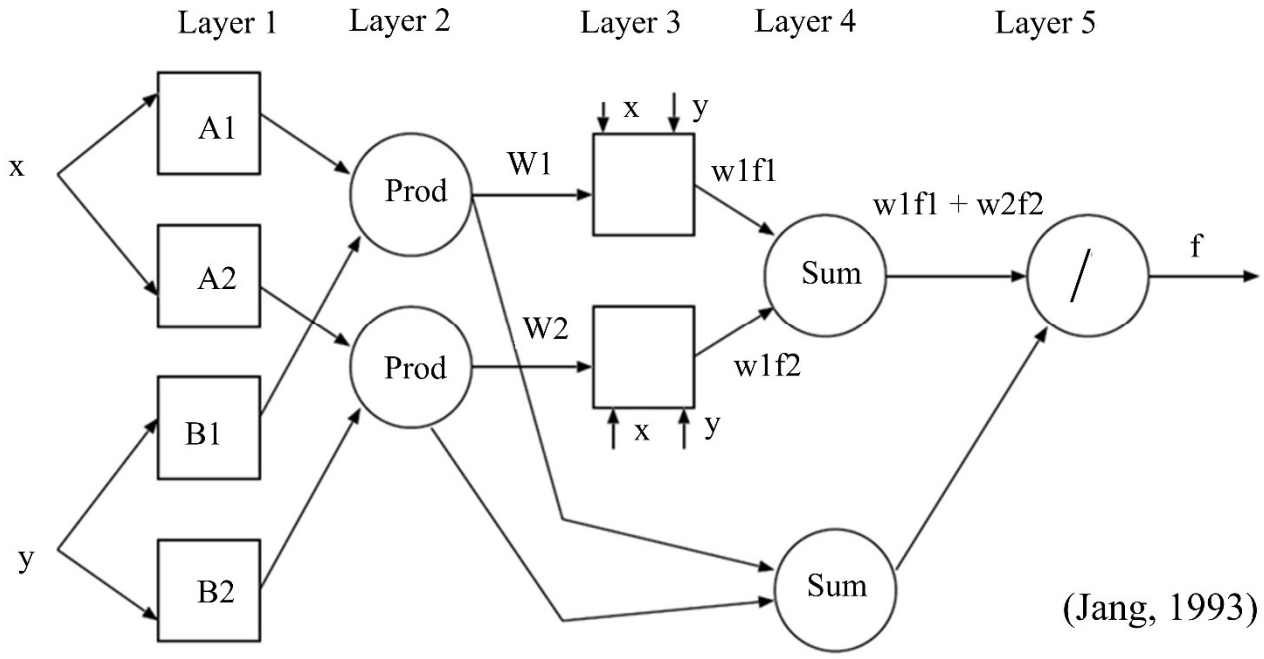

Figure 7.3: First-order Sugeno ANFIS architecture

Layer 1 (Input Module)

Every node, i, in this layer is an adaptive node with a node function. The output from each node $O_{l,i}$ will be given by Equation 7.1:

$$O_{1,i} = \mu A_i(x) \text{ for } i = 1, 2$$
$$O_{1,i} = \mu B_i(y) \text{ for } i = 1, 3 \qquad 7.1$$

where x and y are inputs to node i and A_i and B_i is a linguistic label associated with this node. Parameters in this layer are referred to as premise parameters.

$O_{l,i}$ is the membership function of A_i and B_i and specifies the degree to which the given x and y belong to the fuzzy set (A_i and B_i) respectively.

Layer 2 (Rule module)

Every node in this layer is a fixed node. The output is the product of all incoming signals. Thus, the output from this node is given by Equation 7.2:

$$O_{2,i} = \mu B_i(y) \ * \ \mu B_i(y) \ i = 1,3 \tag{7.2}$$

Each node represents the firing strength of the node.

Layer 3 (Average module)

Every node in this layer is a fixed node. The i^{th} node calculates the ratio of the firing strength of the i^{th} rule to the sum of the firing strengths of all rules, as represented by Equation 7.3:

$$O_{3,i} = \overline{\omega_i} = \frac{\omega_i}{\omega_1 + \omega_2} \ i = 1,2 \tag{7.3}$$

The outputs ($\overline{\omega_i}$) are called normalised firing strengths.

Layer 4 (Consequent module)

Every node in this layer is an adaptive node with a node function, given by Equation 7.4:

$$O_{3,i} = \overline{\omega_i} f_i = \ \overline{\omega_i}(p_i x + q_i y + \ r_i) \tag{7.4}$$

Where $\overline{\omega_i}$ is the normalised firing strength from the previous layer 3. p_i,, q_i and r_i are set of parameters of the nodes. Parameters in this layer are called consequent parameters.

Layer 5 (Output module)

The single node in this layer is a fixed node which computes the overall output ($O_{5,i}$) by summing all incoming signals. The node computation is given by Equation 7.5:

$$O_{5,i} = \sum_i \overline{\omega_i} f_i = \frac{\sum_i \omega_i f_i}{\sum_i \omega_i} \tag{7.5}$$

7.2.1.3.2 Learning algorithm of the ANFIS

The ANFIS can be trained using the hybrid learning algorithm presented by Jang (1993) where learning is done using two passes (forward and backward). In the forward pass, the algorithm uses the least squares method to identify the consequent parameters on layer 4. While in the backward pass, the errors are propagated backwards and the premise parameters are updated by gradient descent. Table 7.1 presents a summary of the activities in each of the two passes.

Table 7.1: Passes in the hybrid learning algorithm (Jang and Sun, 1995)

	Forward Pass	**Backward Pass**
Premise Parameters	Fixed	Gradient Descent
Consequent Parameters	Least squares estimator	Fixed
Signals	Node Outputs	Error Signals

Hybrid learning is used as it prevents learning from being trapped in local minima, which is a common problem of the gradient method of learning. This type of learning also increases learning speed, thus results can be obtained in a very short period of time compared to the neural network system.

To illustrate the learning processes of the ANFIS, let us consider a network with P entries with one output. This system can be summarised by Equation 7.6:

$$Output = F(I, S) \tag{7.6}$$

Where, I is the vector of input variables, S is the set of parameters and F is the function that implements the ANFIS.

If there exists a function H such that the composite function $H.F$ is linear in some elements of S then these elements can be identified by the least squares method (LSM). This method is about estimating parameters by minimising the squared difference between the observed data and the desired data (Jens *et al.*, 2012).

If the parameter set S can be decomposed into two sets $S = S_1 + S_2$ such that $H.F$ is linear in the elements of S_2, then, by applying function H to the $Output$, Equation 7.6 can be transformed to Equation 7.7:

$$H.Output = H.F(I, S) \tag{7.7}$$

Which is linear in the elements of S_2. If values of S_1 are given, then it is possible to plug P training data into Equation 7.7. Here we have a matrix equation of the form $A\theta = y$, where θ is the unknown vector whose elements S are parameters in S_2 and which can be easily be solved using LSM. For each of the iterations (epochs) during learning, both forward and backward passes are done.

Forward pass

In the forward pass, an input vector and output are presented and the equation $A\theta = y$ is solved for each training set. This is repeated for all the training datasets and parameters S_2 identified. After S_2 is identified, the errors for each pair are computed.

Backward pass

In the backward pass, the error signals propagate backwards and the premise parameters are updated using the gradient descendent. The derivative of the error measured with respect to each output is propagated from the output towards the input.

The hybrid learning approach converges much faster by reducing the search space dimensions of the original back propagation method. The overall output is given by Equations 7.8:

$$Hf = \frac{\omega_1}{\omega_1 + \omega_2} f_1 + \frac{\omega_2}{\omega_1 + \omega_2} f_2$$

$$f = \overline{\omega_\iota}(p_1 x + q_1 y + r_1) + \overline{\omega_\iota}(p_2 x + q_2 y + r_2) \qquad 7.8$$

$$f = \overline{(\omega_\iota} x) p_1 + \overline{(\omega_\iota} y) q_1 + \overline{(\omega_\iota)} r_1 + \overline{(\omega_\iota} x) p_2 + \overline{(\omega_\iota} y) q_2 + \overline{(\omega_\iota)} r_2$$

Where $p_1, q_1, r_1, p_2, q_2, r_2$ are linear consequent parameters.

The least squares method is used to identify the optimal values of these consequent parameters. The least squares method (forward pass) is used to optimise the consequent parameters. The gradient descent method (backward pass) is used to optimise the premise parameters. The output of the ANFIS is calculated by employing the consequent parameters found in the forward pass. The output error is used to adapt the premise parameters by means of a standard back propagation algorithm. It has been proven that this hybrid algorithm is highly efficient in training the ANFIS systems (Jang and Sun, 1997).

The most widely used activation functions are the generalised bell function and the Gaussian function. These two functions are used because of their generally smooth character across the entire spread of data. They also have parameters that can be adjusted to suit the most desired membership function.

The generalised bell function is given by Equation 7.9:

$$\mu_{Ai}(x) = \frac{1}{1 + \left|\frac{x - c_i}{a_i}\right|^{2b_i}} \qquad 7.9$$

The Gaussian function is given by Equation 7.10:

$$\mu_{Ai}(x) = exp\left[\left(\frac{x - c_i}{a_i}\right)^2\right] \qquad 7.10$$

Where a, b and c are parameters that represent the centre of the slope, and the centre and mean of the function respectively (Loganathan and Girija, 2014).

Learning with the back propagation neural network

Derivatives of error are used for the back propagation learning. Let us consider a training dataset with p entries. The error of the p^{th} entry can be calculated using Equation 7.11 which is given by:

$$E_p = \sum_{i=1}^{L} (T_{p,i} - O_{p,i}^{L})^2 \tag{7.11}$$

Where $T_{p,i}$ is the i^{th} component of the p^{th} target, $O_{p,i}^{L}$ is the i^{th} component of the actual output vector. The overall error will be given by Equation 7.12:

$$E = \sum_{i=1}^{P} E_p \tag{7.12}$$

To implement the gradient descent of the error, the derivative of the error is calculated for each node output O. The error rate of the output node will be given by Equation 7.13:

$$\frac{\partial E_p}{\partial O_{p,i}} = -2\left(T_{p,i} - O_{p,i}\right) \tag{7.13}$$

If α is a parameter of the i^{th} node at layer l. Thus, the derivative of the overall error measure E with respect to α will be given by Equation 7.14:

$$\frac{\partial E}{\partial \alpha} = \sum \frac{\partial E}{\partial \alpha} \tag{7.14}$$

The update formula for α will be given by Equation 7.15:

$$\Delta\alpha = -\eta \frac{\partial E}{\partial \alpha} \tag{7.15}$$

Where η is the learning rate. The new α value (α_{new}) will be calculated from the α_{old} of the previous epoch and is given by Equation 7.16:

$$\alpha_{new} = \alpha_{old} - \eta \frac{\partial E}{\partial \alpha} \tag{7.16}$$

For the hybrid learning algorithm, each epoch has two passes, the forward and the backward pass. Equation 7.11 is applied to obtain the derivative of the errors from the forward pass. In the backward pass, these errors propagate from the output end towards the input end. The gradient vector is found

for all training data pairs and parameter weights (parameter connections) updated by the steepest descent Equation 7.16.

An example to illustrate the hybrid learning of the ANFIS is given in Appendix 5.

7.3 THE ANFIS SYSTEM FOR GROUNDWATER VULNERABILITY ASSESSMENTS: APPLICATION TO THE WITBANK, ERMELO AND HIGHVELD COALFIELDS

Using the theoretical frame that has been discussed so far, an ANFIS hybrid system was developed in order to assess the groundwater vulnerability of the Witbank, Ermelo and Highveld coalfields. The hybrid system combines the fuzzy expert system and the artificial neural networks and tries to derive the best from these two powerful AI systems.

7.3.1 Design Step of the ANFIS for Groundwater Vulnerability

As mentioned before, the ANFIS is a hybrid system which combines artificial neural networks and the fuzzy expert system. The steps for using the ANFIS model for groundwater application includes:

- selection of system training inputs and output values;
- defining the fuzzy values for both inputs and outputs;
- defining the fuzzy rules and, finally; and
- creation and training of the artificial neural network.

To implement and test the ANFIS a development tool is required. The Python Adaptive Neuro-Fuzzy Inference System algorithm developed by Meggs (2015) was used. A graphic user interface and a fuzzy membership design section were added to the algorithm for easy design and visualisation of the membership functions and the output model.

7.3.1.1 Selection of system inputs and outputs

The training inputs for the ANFIS system were the ten map layers of the SPT approach which showed a positive association when tested with high sulphate in the groundwater. The training output was the sulphate concentration in the groundwater similar to the procedure applied in the ANN training. Both the inputs and outputs were in vector format. According to Al-Hmouz *et al.* (2012), when selecting inputs, one must remove irrelevant inputs, and avoid using inputs which depend on other inputs. The model should be transparent. Given that, for the groundwater vulnerability assessment, the ten inputs were selected based on extensive research of how AMD interacts with the subsurface and given that

the spatial association test showed the region of each input to be spatially associated, all ten inputs were used to build the ANFIS model.

7.3.1.2 ANFIS system training

The ANFIS is a combination of the least-squares method and the back propagation gradient descent method applied to optimise and adjust the membership function parameters which would be used to generate the ANFIS model. The training input and output datasets are used to find values of the premise values for the membership function, as illustrated by the example in Appendix 5. Next, the threshold value is determined used to compare the actual output produced and the desired output. The least squares method determines the consequent parameters, and if there is a difference between the actual and desired output, the premise values are adjusted using the gradient descent method. This happens until the difference between the actual and the desired is minimal. At this stage, the ANFIS has been trained and is ready to predict an output based only the inputs.

The membership functions for the ten input maps were designed using the same cognitive reasoning as that used for the fuzzy expert system. Figure 7.4 shows the membership functions of all ten input map layers. It is noteworthy that the membership functions for rainfall, clay content, hydraulic conductivity, depth to water table, rock-AMD reactivity and rock permeability constitute an increasingly positive function based on the conceptual model of groundwater vulnerability specific to AMD: the higher values of these parameters, the higher the vulnerability. For slope, surface sources, subsurface sources and pathways, the membership function is a steeper decreasing function which flattens after the threshold value in respect of the minimum value of the membership function has been reached. An increasing membership function was assigned to the clay and depth to water table parameters because low values of these parameters indicate where the groundwater vulnerability is highest.

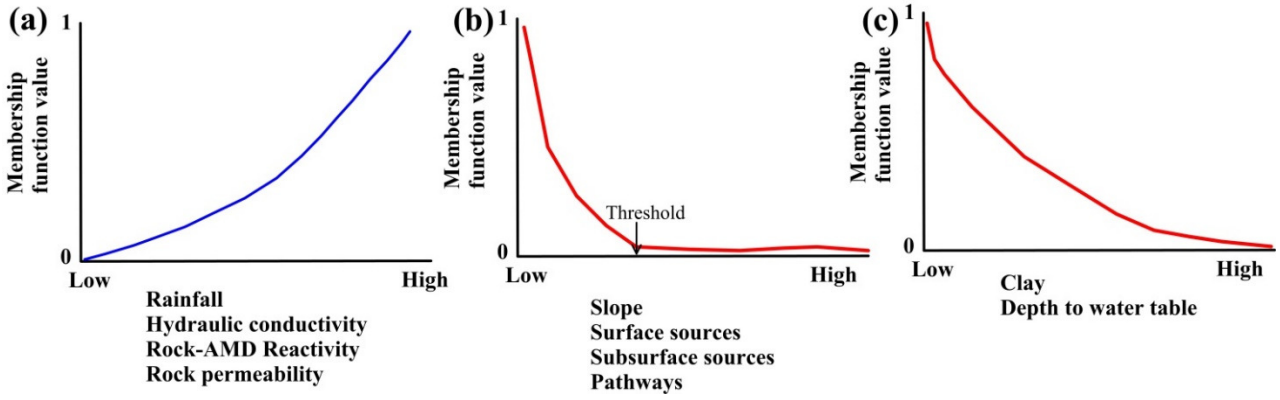

Figure 7.4: Membership functions used for the ANFIS system for a groundwater vulnerability assessment

After the membership function has been assigned to each of the ten map layers, the ANFIS algorithm is run for a given epoch value. Owing to the quick learning properties of the ANFIS there is no need to run an algorithm which determines the optimum number of epochs. One simply runs the ANFIS over 30 epochs and records the epoch value where the training error starts to increase. This value becomes the optimum number at which to terminate the training process. For the Witbank, Ermelo and Highveld coalfields, the ANFIS algorithm was run for 30 epochs and the results in Figure 7.5 show that the training error decreased up to 20 epochs when the MSE error was at its minimum value of 0.23. After this point, the error started to increase. Thus, the optimum number of epochs was set at 20 for this study area. The ANFIS algorithm was run again but this time with a cut off set at 20. This low number of epochs for which the system learns shows that the ANFIS could conceivably learn faster. Fast learning was achieved for the ANFIS as the selection of the ANN starting model from which it adjusts while running the iterations was obtained from the fuzzy membership functions which are also inputs to the ANFIS.

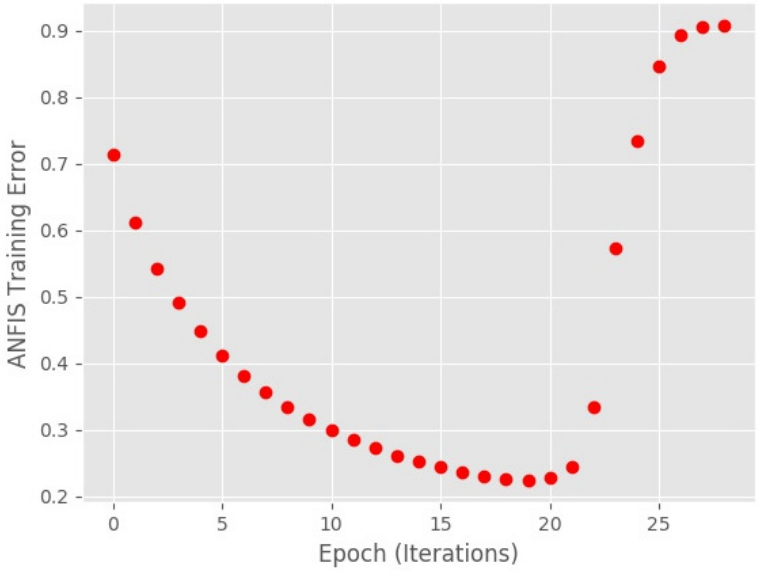

Figure 7.5: Determining the cut-off epoch value for training the ANFIS system

The minimum learning error obtained when the ANFIS was applied to generate a groundwater vulnerability model for the Witbank, Ermelo and Highveld coalfields was relatively higher because of the usage of the binary numbers which restricted learning to only ones and zeros.

7.3.2 Hybrid System Model Results

After training, the trained ANFIS system was used to determine the groundwater vulnerability values of the Witbank, Ermelo and Highveld coalfields at a spatial resolution of 30 x 30 m. The output from the ANFIS is a series of values at each of the map locations. In order to visualise these values, the data were interpolated using the kriging methods and the results reclassified into four classes (very

low, low, moderate and high) using the natural breaks method (ESRI, 2006). The results from the ANFIS are shown in Figure 7.6. The results show high groundwater vulnerability over the area between Ermelo and Carolina and the northwestern tip of the Witbank coalfield. Small areas south of Volksrust and Secunda are also marked by high values. The lowest values corresponded to the central part of the study area; otherwise, the rest of the study area was marked by low to moderate vulnerability.

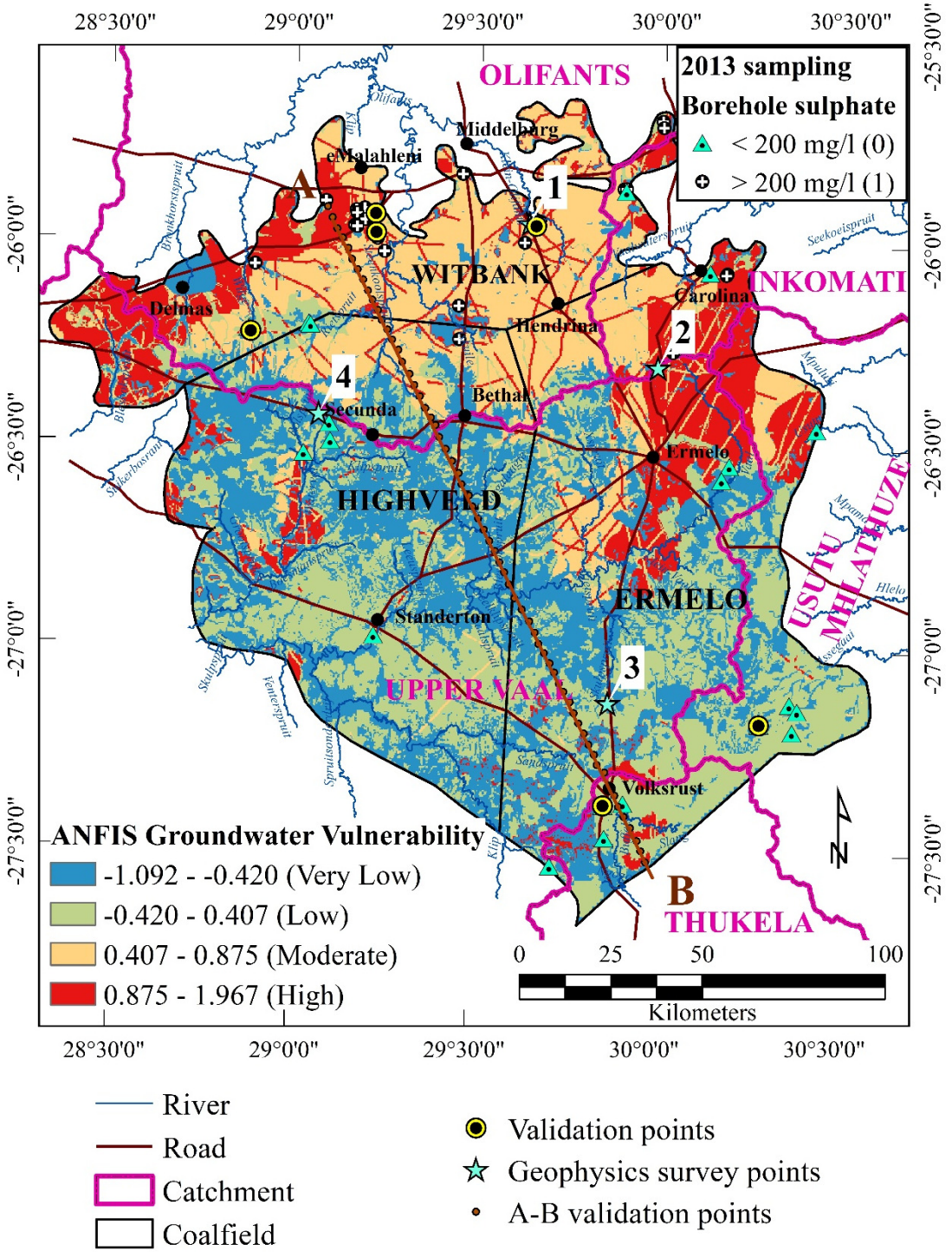

Figure 7.6: ANFIS groundwater vulnerability model of the Witbank, Ermelo and Highveld coalfields

Table 7.2 shows the aerial coverage sizes of the four groundwater classes, where the low vulnerability class has the largest size and the size distribution decreases as the vulnerability class changes from low to high with the high class covering the smallest aerial extent. Figure 7.7 shows a decreasing size of area with change in class from very low to low.

Table 7.2: Aerial coverage of various vulnerability classes of the ANFIS model

Vulnerability classification	Size (km^2)
Very Low	8 885 (32.2%)
Low	8 590 (31.2%)
Moderate	5 828 (21.1%)
High	4 248 (15.5%)

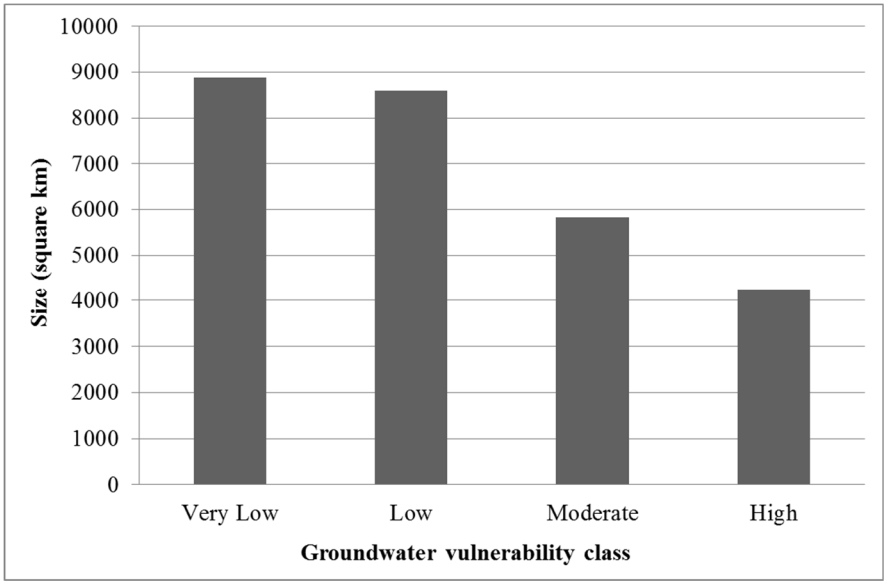

Figure 7.7: Aerial size distribution of the various groundwater vulnerability classes

7.3.3 Validation of the ANFIS Model

The ANFIS groundwater vulnerability model needed to be validated by another dataset which had not been used in the modelling. Three validation methods, namely correlation coefficient, cross-section and geophysical methods were used in a similar fashion to the fuzzy and ANN models.

7.3.3.1 Model validation using hydrochemistry data

7.3.3.1.1 Correlation coefficient approach

The correlation method for model validation involves a comparison of the model values with parameters which can be measured physically. This was done to determine the degree to which the model can accurately represent the real world. Some of the boreholes with measured sulphate concentrations which had not been used for model building were selected for validation purposes.

The ANFIS model values at each of these borehole locations were extracted. Sulphate was considered to be conservative in Chapter 3 and hence could be used as a possible tracer for AMD pollution. Figure 7.6 shows the spatial variation of sulphate concentration in the groundwater which was used for model validation (yellow circle with a black dot in its centre). The groundwater samples with a high sulphate concentration coincided with moderate to high groundwater vulnerability zones, while samples with low sulphate concentrations were located in low to very low groundwater vulnerability zones.

A scatter plot (Figure 7.8) shows the relationship between the ANFIS model and borehole sulphate concentrations. The R value of 0.8216 was obtained between the ANFIS model values and AMD indicators (sulphate). This shows that the generated model correlates with sulphate in the groundwater as measured in the boreholes.

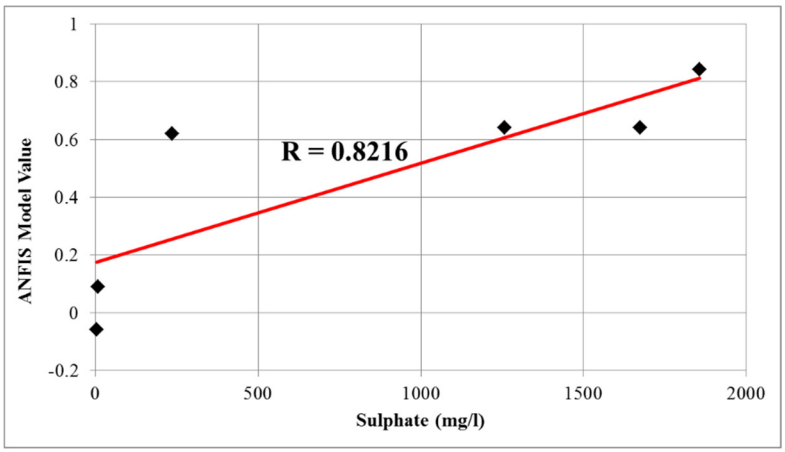

Figure 7.8: Correlation scatter plots for sulphate against the ANFIS groundwater vulnerability model

7.3.3.1.2 Validation using the cross-section method

Hydrochemistry data from the National Groundwater Archive (NGA) database maintained by the DWS were verified by a field reconnaissance survey and the ionic balance checked. Only the samples with an ionic balance below 5 were used for model validation. A sulphate map was generated and a cross-section across the coalfield was plotted with values extracted along the cross-section. This was done both for the sulphate map and the ANFIS model. The sulphate concentration map is shown in Figure 4.21.

The comparison between the map of sulphate concentrations and the vulnerability maps show that areas with high sulphate concentrations in the groundwater correspond to the highest vulnerability values whereas low concentrations indicate lower vulnerability areas (Figure 7.9). The differences at the start and end of the section (similar to the ANN model) were attributable to the scarcity of boreholes in this are causing gridding artefacts which normally affect the edges of the gridded data

as explained in ANN, Chapter 6. Excluding the edges of the profile line, the model values generally decrease from the Witbank coalfield towards the Ermelo coalfield corresponding to changes in the sulphate profile values.

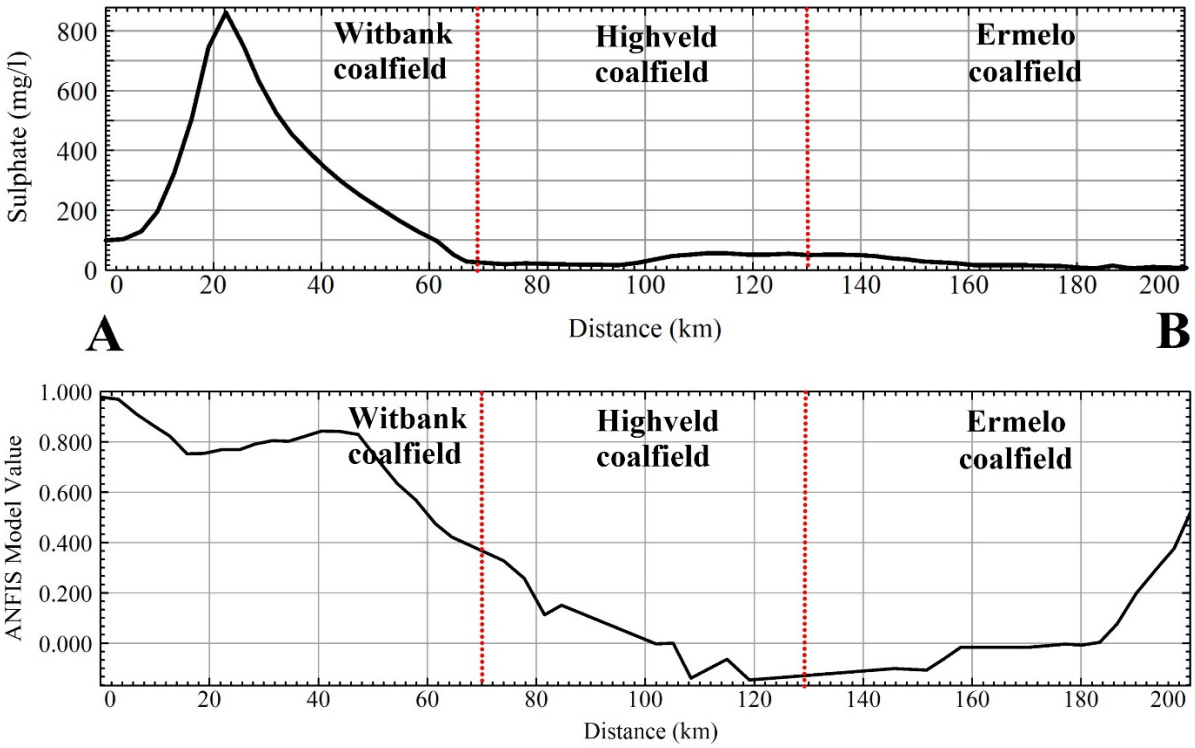

Figure 7.9: Profile along cross-section A–B showing the DWS borehole sulphate concentrations and the ANFIS vulnerability model profile

7.3.3.2 Validation using geophysical techniques

The geophysical survey results described in Chapter 4, section 4.5.4.2 were used to validate the ANFIS groundwater vulnerability model. From a comparison of the porosity ranges for the unsaturated zones of the four sites and their corresponding model values it can be seen that, where the porosity values are high, the model values are also high (Table 7.3). Using the observations at the four sites, the areas with high porosity values correspond to areas characterised by high groundwater vulnerability values. There is a clear leap in high porosity range values and the low porosity range coinciding with a leap in the model values owing to the usage of binary data to generate the ANFIS model. (Table 7.3). With regard to the seismic velocity, low seismic values correspond to high model values and high seismic values corresponds to low model values. A possible explanation for this relationship is given in section 4.5.4.2 discussing the validation of the fuzzy model using seismic survey data.

Table 7.3: Comparison of derived porosity values and ANFIS groundwater vulnerability model values for each of the survey sites

Survey site	Porosity ranges of weathered zone (%)	Seismic velocity (m/s)	ANFIS model value
1	9.0–25 (average = 17)	2747	0.998 (High)
2	5.7–14 (average = 9.85)	2991	1.000 (High)
3	5.6–11 (average = 8.3)	4 505	-0.407 (Very Low)
4	4.5–8.4 (average = 6.45)	5 406	-0.420 (Very Low)

7.4 DISCUSSION

The ANFIS used in this chapter belongs to the hybrid branch of AI which combines machine learning and a fuzzy inference system. When designing the ANFIS model, the fuzzy memberships were subjectively assigned but due diligence was done to ensure that most of the information with regard to AMD generation, transport and attenuation processes were used sparingly. This was done similarly to the fuzzy modelling in such a way that the models can be used at a regional coalfield scale. The ANFIS uses the fuzzy membership function and adjusts the input-output relationship by learning from the data in a similar fashion as the ANN. Thus, the ANFIS as a hybrid model produces an output groundwater vulnerability model that resembles both the fuzzy and ANN models.

The learning rate of the ANFIS was very fast, only requiring 20 epochs (compared to 8 770 epochs for the ANN). This was attributable to the hybrid learning algorithm used by the ANFIS which is a combination of the gradient descent learning of the ANN and the least squared method which increases the learning speed considerably.

The results for the ANFIS correlated very well with sulphate which may be explained as follows:

- The choice of parameters (S, P and T) and the allocation of appropriate fuzzy memberships for each input map layer were appropriate to the ANFIS for modelling AMD migration processes at a regional scale.
- The ANFIS was trained in such a way that the readjusted weights which connect the inputs to the output through a hybrid learning process was able to mimic the general human thought process with regard to groundwater vulnerability. For example, in Chapter 3, it was learnt that sulphate is conservative and that its concentration in the groundwater may be an indication of loading of sulphate from the surface or near surface. Thus, high sulphate would translate to high groundwater vulnerability. The ANFIS model values correlated with sulphate values which is a good indication that the ANFIS was well trained to possibly mimic human thought.

A limitation of the ANFIS (hybrid) system is that, unlike the ANN system, the membership functions needs to be defined for the ANFIS system to be implemented. This could be a problem if the system

to be modelled is not well known; hence, the ANNs are the more popular machine learning tools in AI applications.

7.5 SUMMARY

The ANFIS was developed and successfully used to generate a groundwater vulnerability model of the Witbank, Ermelo and Highveld coalfields where the model showed a strong correlation with borehole sulphate concentrations from two different datasets (DWS dataset and unused data from the 2013 sampling programme). Seismic velocities and porosity estimated from geophysical surveys also showed a linear relationship, where highly vulnerable areas were found to be associated with the subsurface with relatively higher seismic velocities and higher porosities derived from resistivity surveys.

Thus, knowledge-, data-driven and hybrid AI systems assessment tools were developed and successfully applied to the Witbank, Ermelo and Highveld coalfields. A toolbox in the form of a simple graphic user interface with all these AI tools will go a long way in assisting both AI and non-AI experts to successfully use these tools for groundwater vulnerability assessments of AMD at a coalfield scale.

CHAPTER 8: TOOLBOX FOR RAPID ASSESSMENT OF GROUNDWATER VULNERABILITY

8.1 INTRODUCTION

The previous chapters dealt with the development of the SPT groundwater vulnerability approach which was implemented using various artificial intelligence algorithms (fuzzy expert system, ANNs and ANFIS) in the generation of various groundwater vulnerability models. The models include knowledge-driven, data-driven and a hybrid system. In order to assist in the rapid generation of groundwater vulnerability AI models, a semi-automatic program "toolbox" was developed where all the tools developed in this research are found and will be described. All the AI models in this thesis were developed using the groundwater vulnerability tools from this toolbox. The user manual for the toolbox is found in Appendix 3.

8.2 OVERVIEW OF THE TOOLBOX

The toolbox was developed using Python open-source programming language and is entitled the "Groundwater Vulnerability Artificial Intelligence" (GVAI) toolbox. The toolbox is built using several Python built-in libraries: Tkinter, Numpy, Matplotlib, Osgeo and Pandas. Figure 8.1 presents an overall systems overview of the GVAI toolbox which summarises the tools developed in the current study.

The toolbox (program) accommodates the ten input raster data of the SPT groundwater vulnerability assessment and if data on polluted sites are available, three models (fuzzy expert system model, ANN model and the ANFIS mode) can be generated using the program. Conversely, if no polluted sites are known, only the fuzzy expert system model will be generated. The resultant models are georeferenced rasters which can be viewed or processed on any GIS program and print-ready jpeg images can also be produced.

The program starts by prompting the user to load the ten input map layers (rainfall, topographic slope, distance to surface sources, distance to subsurface sources, soil clay content, distance to pathways, rock permeability, aquifer hydraulic conductivity, depth to water table and rock-AMD reactivity) as defined by the SPT approach to groundwater vulnerability at a coalfield scale.

Once all the map layers have been loaded into the program, the user is able to view the map before proceeding to the other steps or modules. If it is possible to view the data, then the data are in the correct format for the programs otherwise the user has to correct the maps before proceeding.

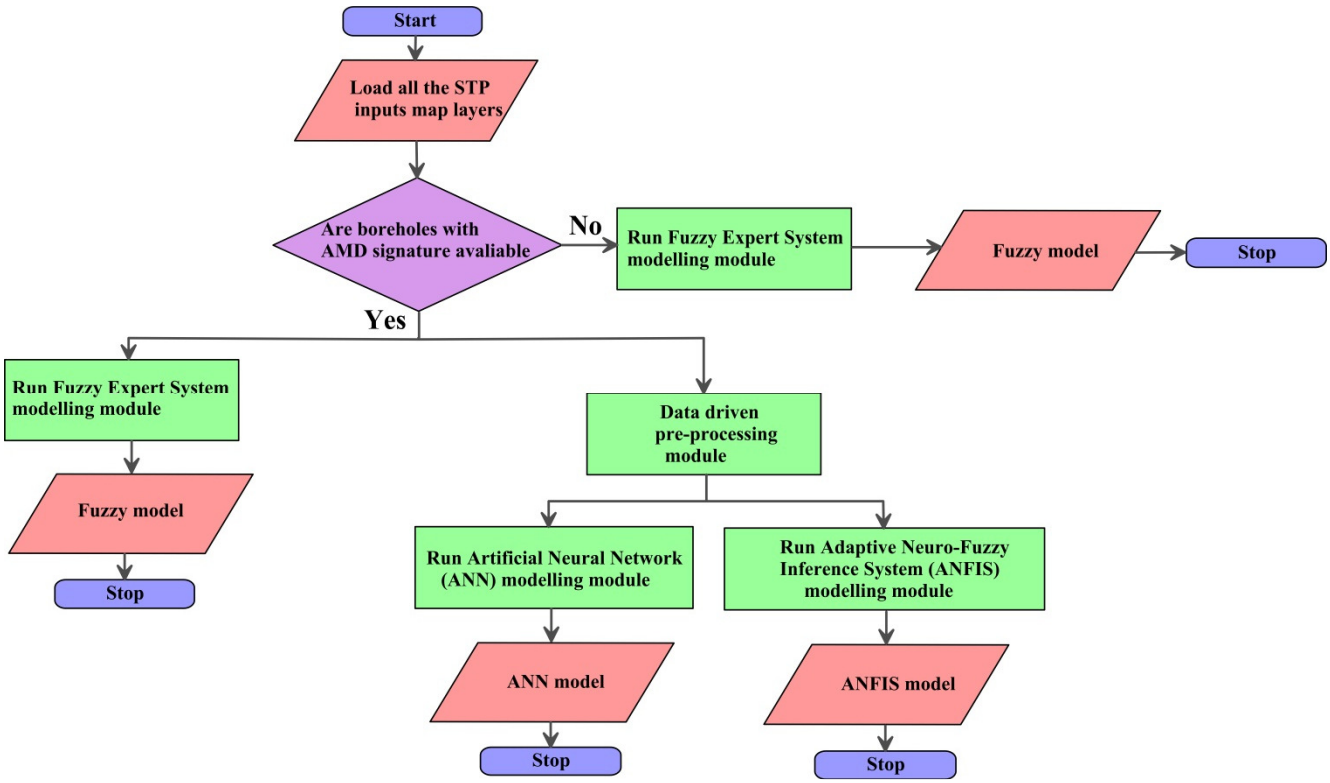

Figure 8.1: Systems design flowchart of the groundwater vulnerability (GVAI) toolbox

Once the map layers have been loaded, the program asks whether a polluted site dataset is available. If no such data are available only the knowledge-driven fuzzy expert system module is enabled. However, if the required data are available, two buttons representing the knowledge-driven approach (fuzzy expert system) and the data-driven approaches (ANN and ANFIS) are enabled. To run the knowledge-driven fuzzy expert system no polluted sites are required, but for the data-driven systems (ANN and ANFIS), polluted and non-polluted sites are required as training data points.

The GVAI software comprises seven modules:

1. main menu module which initialises the program;
2. data input module where data are loaded into the program;
3. fuzzy expert system module which executes the multistage fuzzy inference network;
4. data-driven data pre-processing module which executes spatial association tests and generates binary maps for data-driven AI modelling;
5. data-driven ANN module which executes the ANN algorithms to generate a groundwater vulnerability model;
6. data-driven ANFIS module which executes the ANN algorithms to generate a groundwater vulnerability model; and

7. the model comparison module which does a statistical comparison of the various models using a set of validation points.

8.2.1 Main Menu Module

This module is the main window which launches the program and from where the help files can be accessed (Figure 8.2).

8.2.2 Data Input Module

This module is where all the datasets that are required for modelling are fed into the program. First, the user loads each of the ten map layers rasters using the corresponding browse button and inspects the map by clicking the corresponding "plot" button (Figure 8.3). Once all the ten maps have been added to the program, the program asks whether groundwater pollution vector data are available. If the answer is "*YES*" then the borehole point "browse" and "plot" buttons are enabled prompting the user to load the data into the program. At the same time, the previously disabled knowledge-driven approach (fuzzy expert system) and data-driven approaches (ANN and ANFIS) buttons are enabled. Thus, with the ten maps and pollution data loaded, the user can execute both the knowledge and data-driven approaches. Alternatively, if the answer is "*NO*", then only the knowledge-driven approach (fuzzy expert system) can be performed.

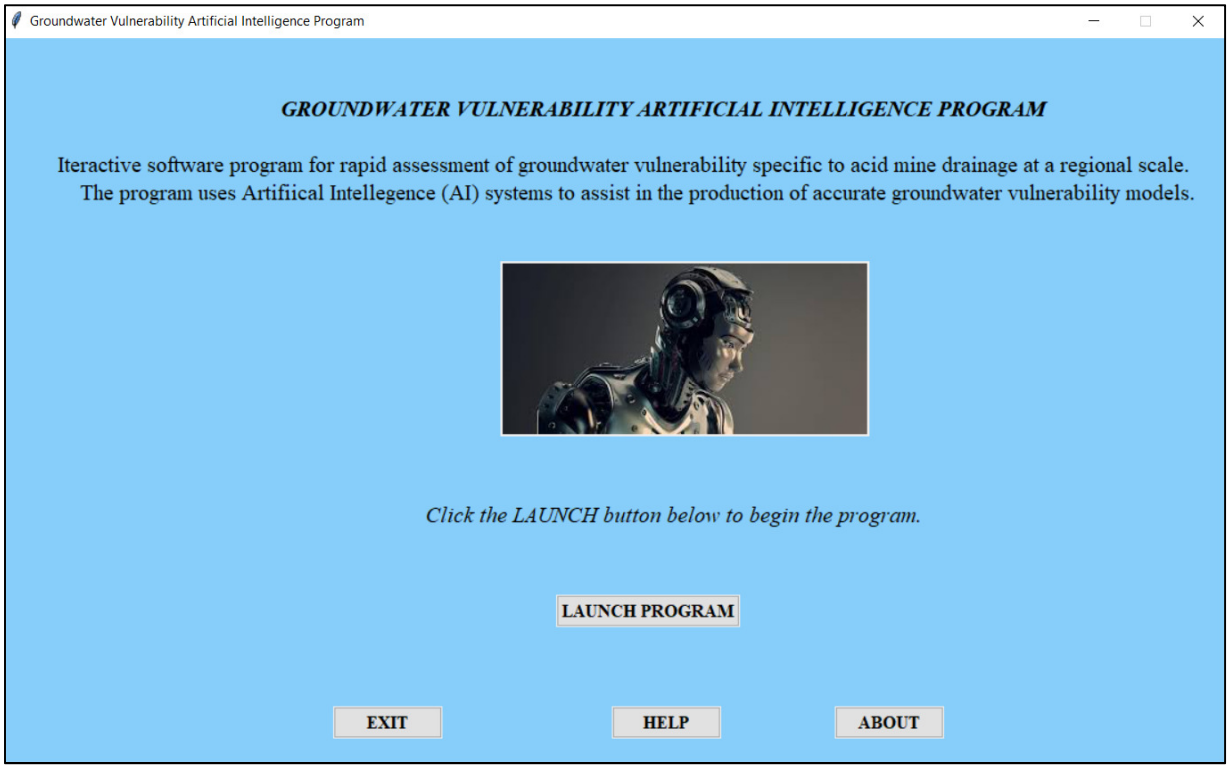

Figure 8.2: Main menu module window

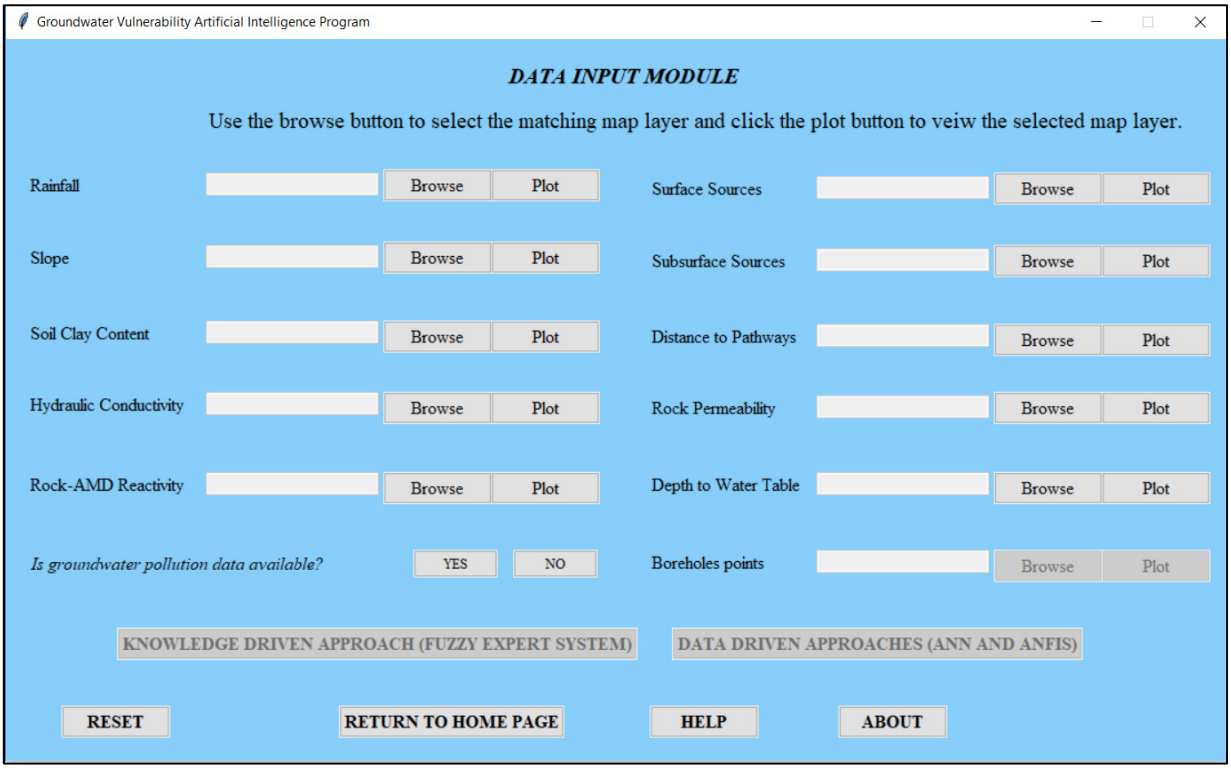

Figure 8.3: Input module window

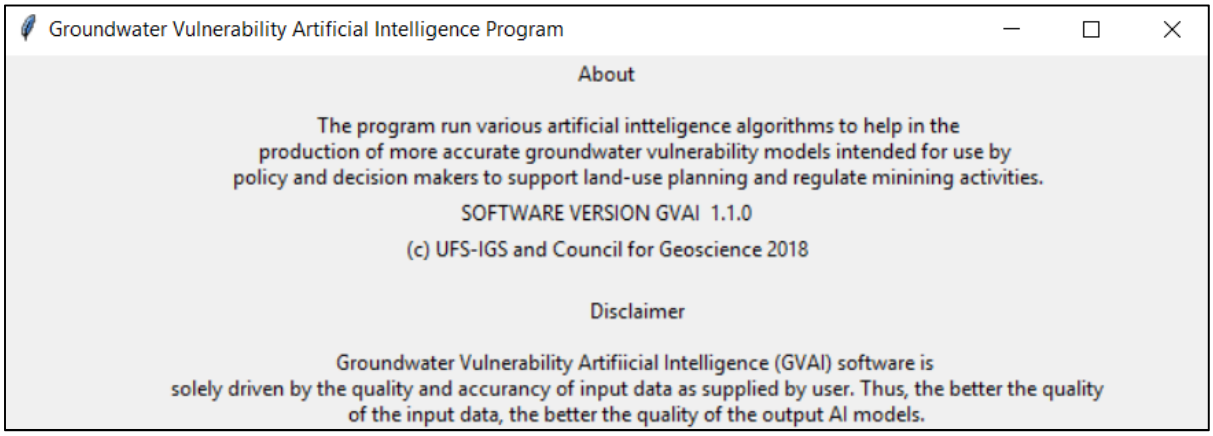

Figure 8.4: The "about" window, showing the software details

8.2.3 Fuzzy Expert System Module

The fuzzy expert system module accepts all ten map raster layers from the input data module. The module allows the user to design the fuzzy membership function for each map layer according to expert knowledge on AMD processes in the area under study. The user is also able to execute automatic processing which relies on parameters values as outlined in Sakala *et al.* (2018). When designing the fuzzy expert system, the drop-down buttons are used to select values for various map values (m_i), confidence (cf_i), c_max and c_min for each of the corresponding map layer. The c_max value specifies the maximum value of w_i and the c_min value specifies the minimum value of w_i according to Equation 4.2. The program then uses these values to generate the fuzzy values of each

map layer by executing Equation 4.2. The fuzzy membership functions for the slope, surface sources, subsurface sources and pathway are step functions where the user is required to specify a threshold value. Once all the design parameters have been adjusted, the program converts the raster inputs into fuzzy values and results can be viewed by clicking on the corresponding "plot" button. Figure 8.5 shows the process flow for the fuzzy expert system that starts with data input, after which the user defines the design parameters and operators and ultimately generates the output fuzzy model. This process flow is converted into a simple graphic user interface (GUI), as shown in Figure 8.6.

Once all the map layers have been converted to fuzzy values, the user then specifies the fuzzy operators (AND, OR, PRODUCT, GAMMA, SUM) accordingly. For example, any of the surface or subsurface sources of AMD pollution can contribute to groundwater vulnerability, hence the "OR" operator may be selected. Once all the user-defined parameters and operators have been specified, the program runs the fuzzy inference engine and produces output map layers for each operation. The user is then prompted to choose three map layers (sources, transportation pathways and traps) which will be combined to generate the final fuzzy groundwater vulnerability model.

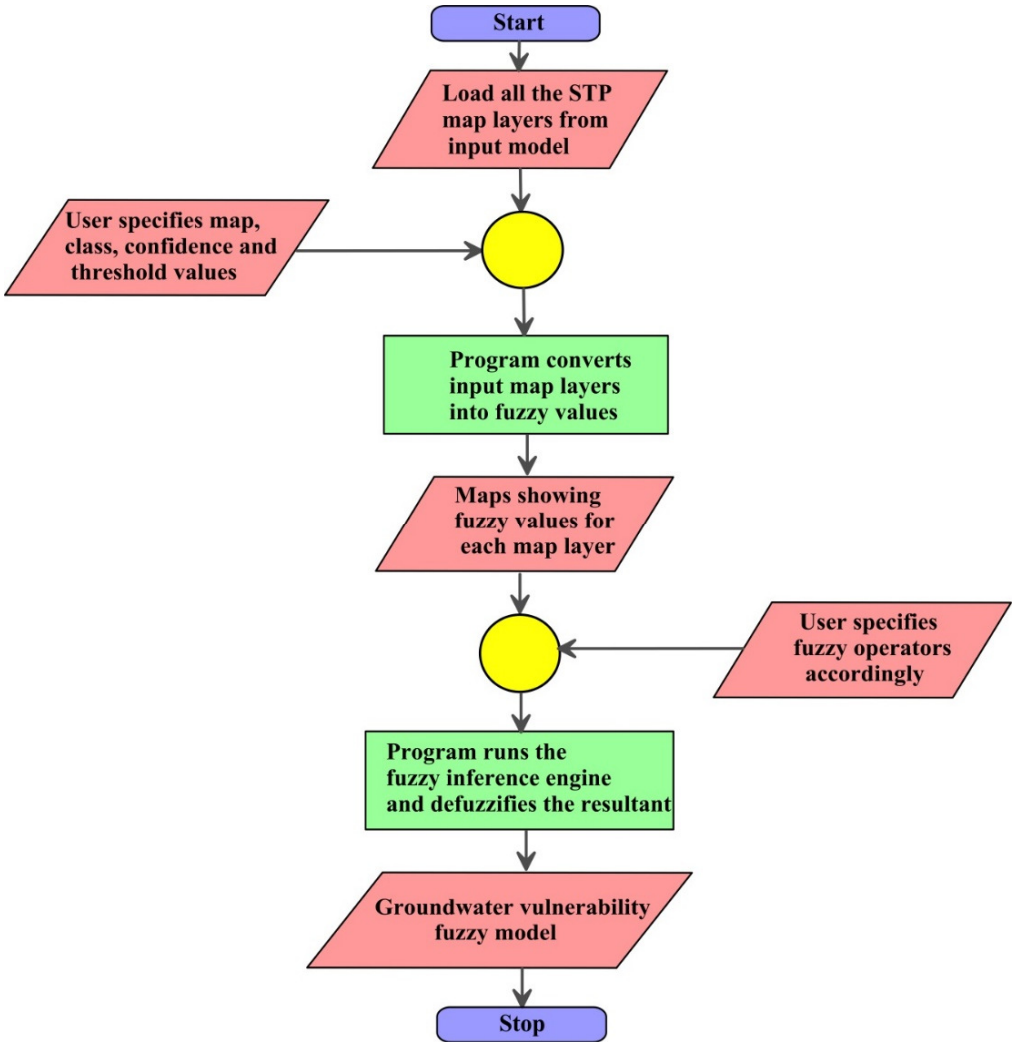

Figure 8.5: Fuzzy expert system flow chart

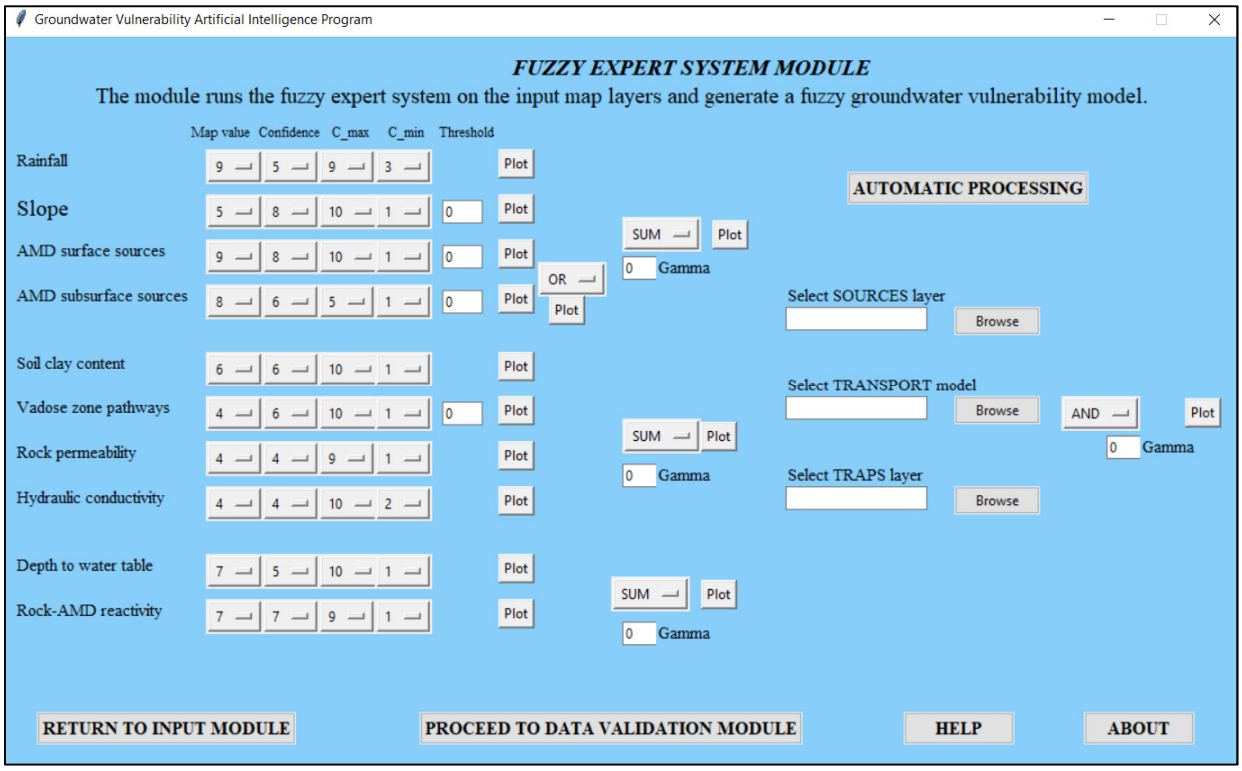

Figure 8.6: Fuzzy expert system module window

8.2.4 Data Pre-Processing Module for Data-Driven AI Systems

In order to execute the data-driven AI approaches, the datasets are first pre-processed in the pre-processing module (Figure 8.7). Two pre-processing steps are executed where each of the ten map layers are tested for spatial associations and regions that show over 50% of the high sulphate concentration in groundwater obtained. The steps are clearly outlined in section 5.3.1. When the test button is clicked, the program runs the spatial association test and outputs a graph showing the cumulative frequency curve compared to high sulphate borehole locations.

From the graph produced after clicking the "test" button, the user can identify the region range of each map layer where more than 50% of the boreholes with high sulphate concentrations are found.

After the spatial association test have been done for all ten of the map layers, the identified region ranges values are entered on the binary creation section. In the binary creation section, the user enters the low (A_{low}) and high (A_{high}) threshold values identified in the spatial association test section for each map layer. The program then reclassifies the map layer value (map_{value}) into binary format (y_b) according to Equation 8.1:

$$y_b = \begin{cases} 1 \; if \; A_{low} \leq map_{value} \leq A_{high} \\ 0 \; if \; map_{value} > A_{low} \; and \; map_{value} < A_{low} \end{cases} \quad 8.1$$

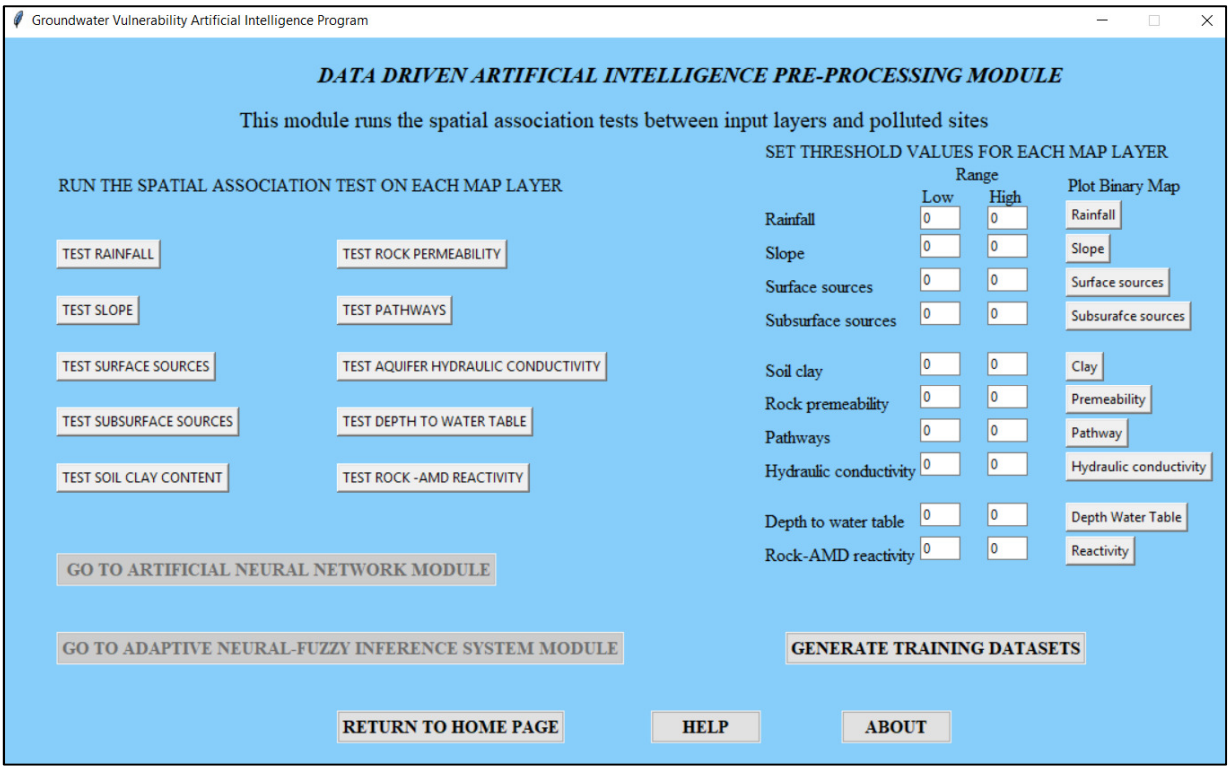

Figure 8.7: Data-driven artificial intelligence data pre-processing module window

The results may be viewed by clicking the corresponding plot binary map button on the extreme right-hand side of the module window. Once all binary maps have been created and viewed as correct, the "produce the training dataset" button is clicked and the program creates all the necessary files for running the ANN and the ANFIS algorithms. In order for this to be done, the program also needs to extract all the values for each of the cells covering the study area for each from the binary map layers generated in the pre-processing module. This is done by another algorithm designed to extract the unique combinations of the input map layer. The unique combination file with all the input data combinations is created.

Upon clicking the "produce the training dataset" button, the previously disabled "go to artificial neural networks module" and "go to adaptive neural-fuzzy inference system module" are enabled. The user can now click on either of these options to access these modules. The "return to home page", "help" and "about" buttons are discussed above.

8.2.5 ANN Module

The ANN module receives data from the pre-processing module and computes the groundwater vulnerability model using the ANN algorithm. Figure 8.8 shows the flow chart of the ANN processing module and its connection to the data input and the data pre-processing modules. The module has an algorithm which considers the input data distribution and number of points in determining whether to use the tenfold stratified or the leave-one-out cross-validation approach. The module allows the

user to run the ANN model in manual or automatic mode (Figure 8.9). When manual mode is selected, the user is prompted to specify the training parameters (number of neurons in the hidden layer, epochs (iterations) and activation function) and the ANN model is generated using these parameters. After training, the training error graph is produced, showing how the training has progressed.

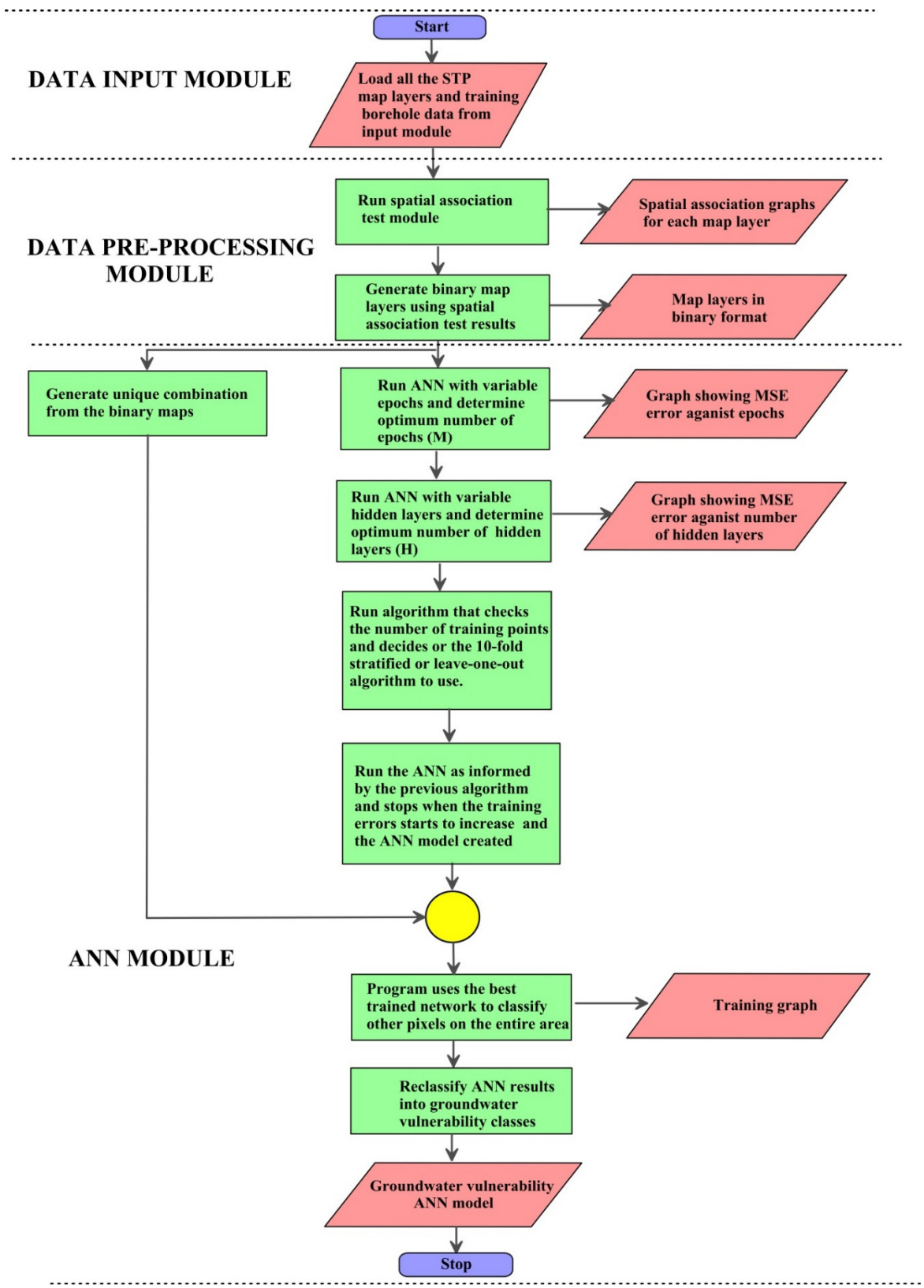

Figure 8.8: ANN system flow chart showing the relationships of various algorithms

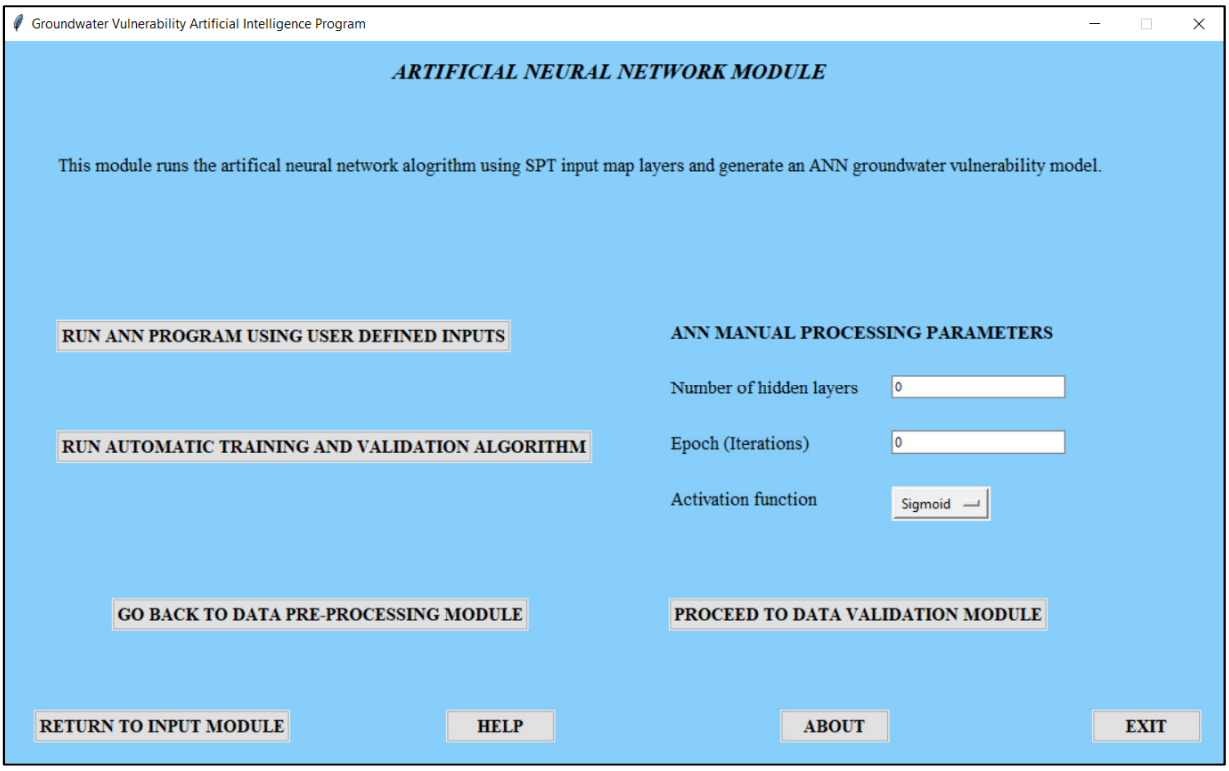

Figure 8.9: ANN module window

When the automatic mode is selected, data from the pre-processing module are fed into the epochs and hidden layer neurons determination algorithms. The algorithms are described in 5.3.2. Once the optimum number of epochs and number of neurons in the hidden layer has been determined, these parameters become the setting for the tenfold or leave-one-out training/validation algorithms which are explained in detail in 5.3.2. The best-trained network from either the tenfold or leave-one-out training/validation algorithms would be suitable for the prediction/classification of the entire study area. The trained network/system is then used to predict/classify the output values for each of the map cells. After the operation has been carried out, the training graph is produced and displayed.

The resultant from the prediction/classification is then reclassified into groundwater vulnerability classes using the natural break method (ESRI, 2006) and the module stops after the model has been generated.

8.2.6 ANFIS Module

The process flow (Figure 8.10) for the ANFIS system is almost similar to that of the ANN system described earlier. The only difference is that for the ANFIS system no hidden layers are determined as the ANFIS system replaces the hidden layers with membership functions. The ANFIS module allows the user to design the ANFIS membership functions for each of the map layers by specifying the Gaussian sigma and mean values and the resultant functions can be viewed. The program is only capable of executing the Gaussian function. Figure 8.11 shows the GUI for the ANFIS module.

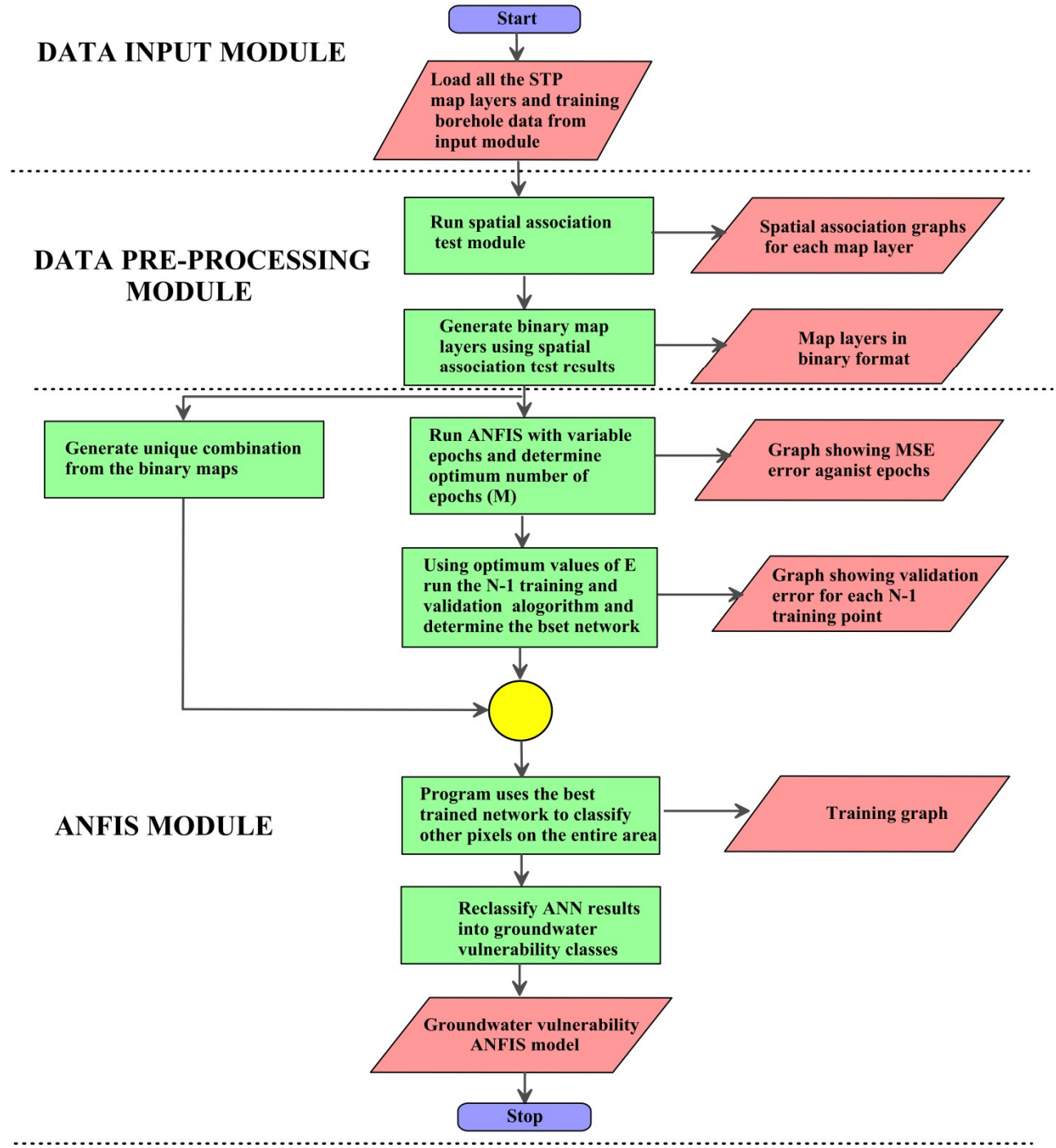

Figure 8.10: ANFIS expert system flow chart

When the button "run ANFIS using defined settings" is clicked, the ANFIS algorithm is run using these defined functions. The resultant model is produced and displayed together with the training error graph.

The module allows the user to run the ANFIS algorithm using the settings that the program would have calculated using the pre-set setting. In this mode, the user has no control over the membership functions as the program would use pre-defined values with consideration of the possible data ranges of each map.

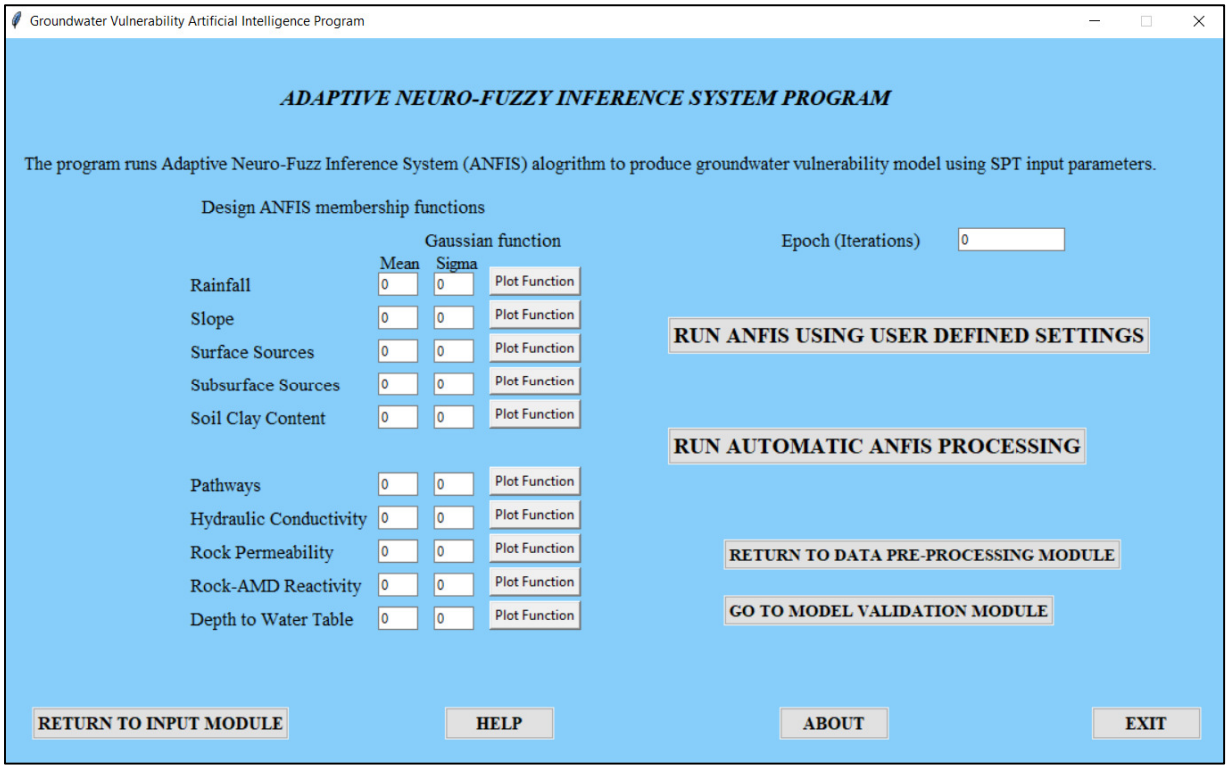

Figure 8.11: ANFIS module window

8.2.7 Model Validation Module

The model validation module (Figure 8.12) is a section when the AI models generated are statistically validated using a separate validation vector dataset. The module prompts the user to select the models using the "browser" button. The user can view the model by clicking the "plot" button for the corresponding model. The main aim of groundwater vulnerability mapping is to classify a large area into relative classes. Thus, the best model is one which is able to predict precisely polluted sites which were not used in the modelling process. Normally the worst-case location in respect of pollution is used in this module for validation. Pollution-area graphs are produced for each model and used to select the best model with the highest correlation value.

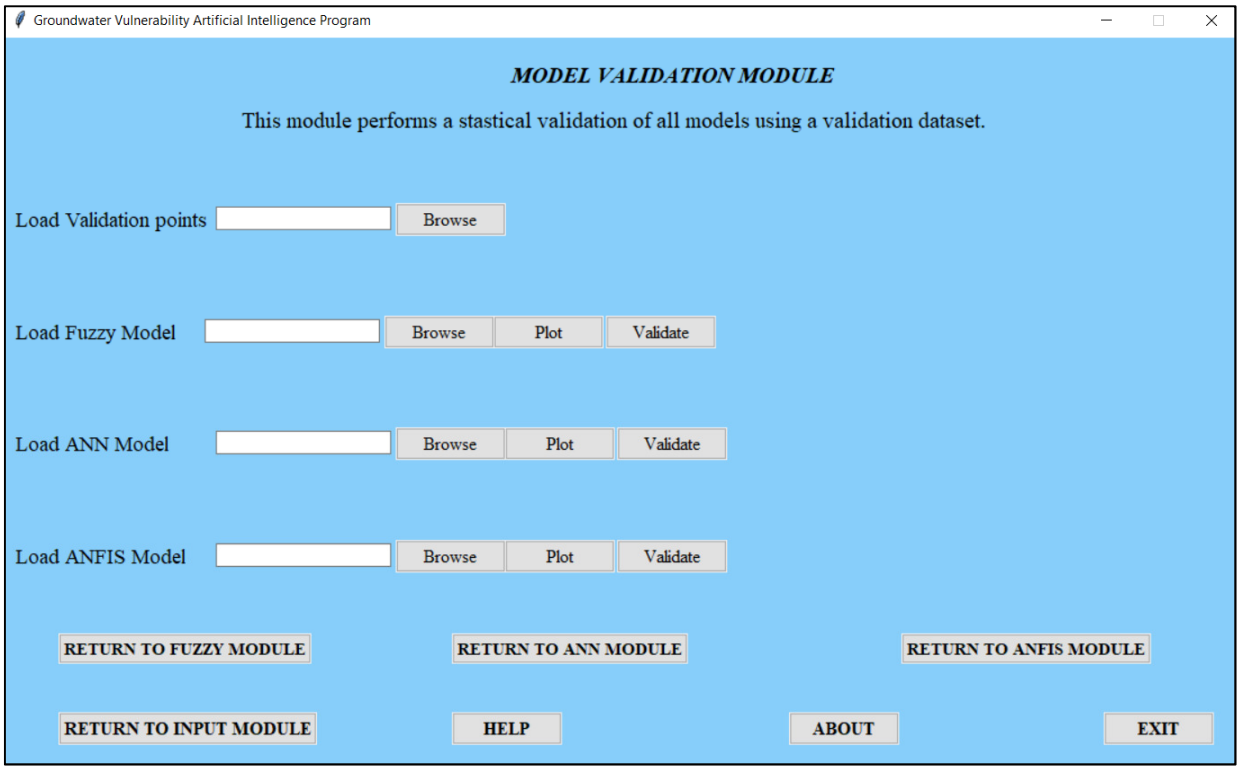

Figure 8.12: Model validation module

8.3 DISCUSSION AND SUMMARY

One of the research problems is the development of tools for a rapid assessment of groundwater vulnerability which does not significantly compromise the accuracy of the results. Hence, AI systems with proven success in solving similar problems were used in the development of the toolbox.

By doing several trials with machine learning (ANN, ANFIS) algorithms it was realised that if training is done using binary maps generated by assigning binary values (1) to cover 100% of the training points there is a large validation error. However, if between 50 and 100% of the training points are used, the validation error is lower. Thus, for machine learning to be effective for classification or prediction, noise in the data is important for the trained model to be generalised. This increases the system generalising capabilities for the classification or prediction of new data that were not used in the training process.

The Groundwater Vulnerability Artificial Intelligence toolbox developed is a simple to use program which runs complex algorithms in the background. The user interface proved to be quite easy to use for non-AI experts but it is recommended that the user must have at least some background of groundwater vulnerability and /or acid mine drainage systems.

The program, which is a stand-alone program dedicated to groundwater vulnerability assessments specific to AMD at a coalfield scale, accelerates the generation of models because only the necessary functions are included. The generated models can be redone as more information or higher-resolution

data become available. Future modification of the program includes an option to save the settings so that they can be accessed in future or at the next program start-up.

Using binary maps for machine learning reduces the amount of data to be constrained within the current limits of random access memory of a personal computer. However, this limits the classification or prediction to a binary output.

CHAPTER 9: CONCLUSIONS AND RECOMMENDATIONS

9.1 CONCLUDING REMARKS

The research involved critically analysing available groundwater vulnerability approaches and AMD pollution to develop a specific approach applicable to a typical coalfield by incorporating AI to enhance the human capabilities in the assessment of groundwater vulnerability. Laboratory and field experiments were done and results used in the selection of appropriate groundwater vulnerability input map layers and for validation of generated vulnerability models. To complement and summarise the research findings, a simple-to-use graphic user interface toolbox was developed which contains the rapid assessment tools for a groundwater vulnerability assessment of a typical coalfield. The Witbank, Ermelo and Highveld coalfields of South Africa which are Karoo sedimentary-hosted coal deposits was used as a case study from which the developed groundwater vulnerability approach and toolbox were tested.

9.1.1 Development of AMD Specific Groundwater Vulnerability Approach

An analysis of the three approaches of groundwater vulnerability (index and overlay, process-based modelling and statistical) identified that each has its own strengths and weaknesses. Using the analysis of these conventional approaches and inspiration gained from the globally accepted mineral systems process-based workflow for mineral prospectivity analysis, the petroleum systems and the source-transport-attenuation approaches, an approach (SPT) was developed which offers a holistic approach for the assessment of groundwater vulnerability to AMD at a coalfield scale. This was done by combining factors based on pollutant sources, energy that drives the pollution migration and ways in which AMD interacts physically and chemically with the subsurface. The approach is a hybrid approach built with the following characteristics from the three vulnerability approaches:

- built on readily available datasets to interpret an output groundwater vulnerability model that can be used by non-scientists or hydrogeologists (extracted from index and overlay approaches);
- incorporation of the processes in terms of which AMD interacts with the subsurface (extracted from process-based approaches); and
- inputs combined using appropriate statistical tools such as AI systems in this research (extracted from statistical approaches).

Parameters which were extracted from popular approaches such as DRASTIC include: depth to water table, aquifer hydraulic conductivity, rainfall which was replaced by recharge, soils and topographic

slope. Other parameters which were incorporated in the assessment included those which are specific to AMD pollution such as surface and subsurface sources of pollution, rock-AMD reactivity, pathways and rock permeability. The input map layers were joined together using AI. The SPT was successfully applied to the Witbank, Ermelo and Highveld coalfields.

9.1.2 Laboratory and Field Experiments for Groundwater Vulnerability Input Selection and Model Validation

Laboratory work done involved a simulated experiment where AMD from a typical coalfield was subjected to soils of varying clay content and it was found that soils with a high clay content, greater than 31%, were able to reduce iron concentrations and removed sulphates to an extent. The concentration of calcium and magnesium increased in the leachate. An ionic exchange reaction was identified as a possible cause, where the acidic environment causes iron to displace calcium and magnesium from soil particle exchange sites and occupies their position resulting in a decrease in iron and an increase in calcium and magnesium. Aluminium concentration remained unchanged in the leachate because their ions are tighly held on exchange sites owing to their high exchange affinity.

Other laboratory work done was a column leach experiment under saturated and unsaturated conditions with the aim of understanding how various rocks respond in an AMD environment. In this experiment, AMD from a typical coalfield was reacted with various rocks found in a typical Karoo coalfield over a period of 91 days and leachate was collected and analysed. An analysis of the leachate revealed interesting findings:

- Dolomite was able to neutralise the pH within the first seven days and maintained a neutral pH till the end of the experiment. At the time when the pH became neutral, AMD heavy metal pollutants (aluminium, iron and manganese) were removed from the AMD solution, whilst the concentration of calcium and magnesium in the leachate increased. Dolomite dissolution processes are responsible for these observations.
- Rocks with plagioclase such as diabase and dolerite were also able to neutralise pH and remove AMD heavy metal pollutants (aluminium, iron and manganese) but this effect only lasted for a few weeks.
- Other rocks dominated by quartz minerals were not able to significantly affect the pH and hence the AMD heavy metal pollutants were not removed.
- The order in which rocks attenuated AMD in a typical Karoo coalfield was found to be in the following order: dolomite, dolerite, mudrock, diamictite and sandstone, which can be expressed in terms of mineral composition as carbonate, plagioclase, chloride and quartz, where the

dissolution of minerals also follows this sequence. The sequence was used to rank rocks according to the removal of AMD heavy metal pollutants.

- The chemical parameters which can be used as possible natural tracers for an AMD-specific groundwater vulnerability assessment are sulphate and chloride concentrations. This was obtained from the column leach experiment where it was discovered that sulphate and chloride concentration remained unchanged for various typical coalfield geological formations and over a time period of 91 days when rocks had been subjected to AMD under saturated and unsaturated conditions.
- The column leach experiment showed that the reactions between AMD and rock masses are more pronounced in the unsaturated zone than the saturated zone, showing the role played by the presence of oxygen in the attenuation of AMD in the subsurface.

Fieldwork done involved the collection of water samples from boreholes within the Witbank, Ermelo and Highveld coalfields, which were analysed for hydrochemistry. The results revealed two water types, one due to natural weathering processes showing very early stages of water-rock interaction and another showing signs of enrichment of sulphate which was interpreted to be attributable to human activities such as coal mining.

In the research, ground geophysical surveys that were conducted found that resistivity and seismic refraction survey results in the form of porosity and seismic velocities correlated well with all the three AI generated groundwater vulnerability models for the Witbank, Ermelo and Highveld coalfields. Thus, these methods can be used to validate groundwater vulnerability models, but the surveys need to be done at many sites and on similar geological formations. This would reduce the ambiguities in geophysical interpretations and minimise the effect of geological variations which can affect the geophysical response. This would leave only the hydrogeology properties, which may be compared with interpreted geophysical responses at various groundwater vulnerability classes.

9.1.3 Application of AI to the Assessment of Groundwater Vulnerability Specific for Coalfields

Three groundwater vulnerability assessment tools were developed, the knowledge driven fuzzy expert system, data-driven artificial neural network and the hybrid adaptive neural-fuzzy inference system. The fuzzy expert system, a knowledge-based system, is solely dependent on the expert's cognitive reasoning on the AMD pollution transport and attenuation and was able to produce a groundwater vulnerability model which was highly correlated ($R = 0.809$) with sulphate concentration. The ANN which belongs to the data-driven AI with topology 10-9-1 was trained for 8 770 epochs and was able to generate a groundwater vulnerability model which was highly correlated ($R = 0.909$) with sulphate

concentrations. Lastly, the ANFIS, which is a hybrid system made by combining the fuzzy expert system and ANN, was trained using a hybrid training algorithm and also generated a groundwater vulnerability model which was closely correlated ($R = 0.8216$) with groundwater sulphate concentrations. While any of the models can be used, the ANN had the highest correlation with sulphate concentrations in groundwater.

This gives the users of the tools options in regard to which of the three tools to use. At the same time the validation results for each model can be used to assist in making the decision as to which model to select. The three groundwater vulnerability tools produced different models, but with remarkably similarities at a regional scale. All three models were fairly consistent with field realities in the form of geophysical responses and hydrochemistry datasets.

9.1.4 Groundwater Vulnerability Graphic User Interface Toolbox

The rapid groundwater vulnerability assessment tools generated by the research were packaged into a toolbox which contains all the tools needed for the AI modelling of groundwater vulnerability. The program is called the "Groundwater Vulnerability Artificial Intelligence (GVAI)" toolbox and works in both manual and semi-automatic mode, where on all the options, the user can contribute to the decisions taken in the modelling process. Tedious processes which are normally done by trial and error have been automated to assist the user in the production of groundwater vulnerability models at high speed and improved accuracy. The program is also flexible in the sense that if a map layer is changed the user can quickly update the model.

9.2 RECOMMENDATIONS

9.2.1 General Recommendations

The recommendations on the interpretation of the groundwater vulnerability models in a language understandable by policy and decision makers are summarised as shown in Table 9.1. This simplification goes a long way in the development of water resource management models and in facilitating their incorporation into a water-resource management decision-making process.

Table 9.1: Recommendations for the management of the water resources of the Witbank, Ermelo and Highveld coalfields

Vulnerability classification	Recommendations for water resource management
Very Low	Green flagged zone: Groundwater systems falling within this classification are at lowest chances for pollution by AMD owing to the presence of natural AMD attenuation properties of the subsurface and their location far enough from pollutant sources. However, this does not warrant that best practice guidelines for water resource management should be ignored as this can trigger other pollutant types other than AMD to reach the groundwater system which can be catastrophic to groundwater beneficiaries (humans, plants, aquatic animals, etc.).
Low	Green–amber flagged zone: For these low vulnerability areas, the chances for pollution is low to moderate because even though the natural attenuation of AMD is present, introduction of AMD can easily surpass the natural attenuation, leading to the possibility of polluting the groundwater system. Hence best practice guidelines for coal waste rock disposal, rehabilitation and water resource management should be adhered to.
Moderate	Amber–red flagged zone: For moderate vulnerability areas, the chance for pollution is moderate to high because of the relatively low natural attenuation of AMD. This means that AMD can easily pass through the subsurface and end up in the groundwater. Coal mining activities which exposed the pyrite to open air and water should be closely monitored. Mining and water management regulators should closely monitor current mining activities and control future mining in these areas. The regulatory authorities should enforce monitoring programmes, water protection designs and mining plans.
High	Red flagged zone: Groundwater systems falling within this classification are at the greatest chance of pollution by AMD and warrant an immediate remedial action plan to avoid further impact on the water quality. Strict management controls as outlined by the GARD (INAP, 2009) on the disposal of AMD generated waste should be adhered to. In addition, more work including a detailed desk study, site investigations, on-going monitoring programmes and a demonstrated remedial action plan for clean-up, which analyses the effectiveness of the remediation approach in achieving designated water quality criteria (Piscopo, 2001) should be carried out.

9.2.2 Limitations of the Developed Data-Driven Approaches

The vulnerability approaches developed make use of sulphate concentrations mainly because of their observed conservative nature in saturated and unsaturated conditions from the soils batch leach, rock-AMD reactivity column leach experiments and supported by findings by Li *et al.* (2006) and Bottrell *et al.* (2008). Sulphate concentrations in groundwater were used both for modelling and validation from data collected by sampling several boreholes. Analytical errors emanating from field water

sampling, water sample preparation and laboratory analytical analysis cannot be ruled out and are often difficult to quantify accurately. Hence, the produced models include these inherent uncertainties even though water quality tests were done and results showed an acceptable ± 5% ionic balance.

9.2.3 Recommendation for Future Work

The approach developed in this research opens up more avenues for its application in generating groundwater vulnerability models for other pollutant sources such as nitrates, landfill, domestic, industrial and mining areas. The developed approach was only tested for three coalfields in South Africa and more vigorous testing and validation of similar or different coalfields need to be done to determine the robustness of the methodology to different hydrogeological conditions. However, based on the conceptual model and the adaptive nature of the developed tools, it is anticipated that the correct groundwater vulnerability models will be generated for other coalfields as well.

Complex learning algorithms such as deep learning, currently used for data mining of very large datasets ranging from internet search engines, speech recognition and image processing, can be tested for their applicability to the generation of groundwater vulnerability models for very large areas at a high resolution.

Incorporation of groundwater flow information into the model design can be considered as the SPT approach developed in this research only focussed on the vertical migration of AMD and its interaction with the subsurface. In nature, pollution also migrates laterally in a three-dimensional space in a process which is quite complex where fractures also need to be mapped and incorporated into the model. Such an approach is likely to make the modelling expensive as fractures are small and mapping them over large area will require closely spaced borehole density data. Pump testing would need to be carried out. However, for an area as large as the present study area, it is believed that these measures are not necessary as the results are meant to produce a relative comparison of various areas in terms of groundwater vulnerability rather than a precise AMD migration modelling at a local scale.

REFERENCES

Ajith, A. 2005. Artificial Neural Networks, in Sydenham, P. H. and Thorn, R. (eds) *Handbook of Measuring System Design*. John Wiley and Sons, Ltd.

Al-Adamat, R. A. N., Foster, I. D. L. and Baban, S. M. J. 2003. Groundwater vulnerability and risk mapping for the Basaltic aquifer of the Azraq basin of Jordan using GIS, Remote sensing and DRASTIC, *Applied Geography*, 23(4), 303–324. doi: 10.1016/j.apgeog.2003.08.007.

Al-Hajeri, M. M., Al-Saeed, M., Derks., Fuchs, T., Hantschel, T., Kauerauf, A., Neumaier, M., … Peters, K. 2009. Basin and Petroleum Systemes Modelling, *Oilfield Rev*, 21(2), 14–29.

Al-Hanbali, A. and Kondoh, A. 2008. Aquifer vulnerability Assessment and Evaluation of Human Activities Impact (HAI) within the Dead Groundwater Basin, Jordan, *Hydrogeology Journal*, 16, 499–510.

Al-Hmouz, A., Shen, J. and Yan, J. 2012. Modelling and simulation of an Adaptive Neuro-Fuzzy Inference System (ANFIS) for Mobile Learning, *IEEE Transactions on Systems, Man and Cybernetics*, 3, 226–237. doi: 10.1109/TLT.2011.36.

Aller, L., Bennett, T., Lehr, J. H., Pretty, R. J. and Hackett, G. 1987. *DRASTIC: a standardized system for evaluating ground water pollution potential using hydrogeologic settings. US Environmental Protection Agency, Ada, Oklahoma*. Report No. EPA/600/ 2-87-036.

Anawar, H. M. 2013. Impact of climate change on acid mine drainage generation and contaminant transport in water ecosystems of semi-arid and arid mining areas, *Physics and Chemistry of the Earth*. Elsevier, Ltd, 58(60), 13–21. doi: 10.1016/j.pce.2013.04.002.

ARC-ISCW. 2014. *Climate Monitoring Services*. Available at: http://www.arc.agric.za/arc-iscw/Pages/Climate-Monitoring-Services.aspx (Accessed: 29 December 2017).

ARC-ISCW. 2015. Soils of South Africa 1:250 000 scale. Pretoria: Agricultural Research Council – Institute for Soil, Climate and Water.

Archie, G. E. 1942. The electrical resistivity log as an aid in determining some reservoir characteristics, *Transactions of the American Institute of Mining and Metallurgical Engineers*, 146, 54 – 61.

Arikunto, S. 2002. *Prosedur Penelitian*. 5th edn. Jakarta: PT Rineka Cipta.

Atanacković, N., Dragišić, V., Živanović, V., Štrbački, J. and Ninković1, S. 2016. Risk-based Regional Scale Screening of Groundwater Contamination from Abandoned Mining Sites in Serbia - Initial Results, in Carsten, D. and Michael, P. (eds) *Mining Meets Water – Conflicts and SolutionsI*. Freiberg, Germany: International Mine Water Association, 600–607.

Azar, A. T. 2010. Adaptive Neuro-Fuzzy Systems, in Azar, A. T. (ed.) *Fuzzy Systems*, 216.

Babiker, I. S., Mohamed, M. A. A., Hiyama, T. and Kato, K. 2005. A GIS-based DRASTIC model for assessing aquifer vulnerability in Kakamigahara Heights, Gifu Prefecture, Central Japan, *Science of the Total Environment*, 345(1–3), 127–140. doi: 10.1016/j.scitotenv.2004.11.005.

Baghapour, M., Talebbeydokhti, N., Bagherzadeh, S., Nadiri, A. A., Gharekhani, M. and Chitsazan, N. 2016. Optimization of DRASTIC method by artificial neural network, nitrate vulnerability index, and composite DRASTIC models to assess groundwater vulnerability for unconfined aquifer of Shiraz Plain, Iran, *Journal of Environmental Health Science and Engineering*, 14(1), 13. doi: 10.1186/s40201-016-0254-y.

Banks, V. J., Palumbo-Roe., Van Tonder, D. B., Davies, J., Fleming, C. and Chevrel, S. 2011. Conceptual models of the Witbank coalfield, South Africa. Earth observation for monitoring

and observing environmental and societal impacts of mineral resources exploration and exploitation. CEC FP7 Project EO-MINERS, Deliverable D3, 107.

Barnard, H. C. 2000. *An explanation of the 1:500 000 general hydrogeological map-Johannesburg 2526.*

Bartolino, J. R. and Cole, J. C. 2002. *Ground-water resources of the Middle Rio Grande Basin, New Mexico: U.S. Geological Survey Circular 1222.*

Bear, F. E. 1964. *Chemistry of the soil*. second. Reinhold.

Bell, F. G., Bullock, S. E. T., Hälbich, T. F. J. and Lindsay, P. 2001. Environmental impacts associated with an abandoned mine in the Witbank coalfield, South Africa, *International Journal of Coal Geology*, 45(2), 195–216. doi: 10.1016/S0166-5162(00)00033-1.

Bell, F. G., Hälbich, T. F. J. and Bullock, S. E. T. 2002. The effects of acid mine drainage from an old mine in the Witbank coalfield, South Africa, *Quarterly Journal of Engineering Geology and Hydrogeology*, 35(3), 265–278. doi: 10.1144/1470-9236/00121.

Berenji, R. H. 1992. A reinforcement learning-based architecture for fuzzy logic control, *International Journal of Approximate Reasoning*, 6(2), 267–292.

Bersini, H., Nordvik, J. P. and Bonarini, A. 1993. A simple direct adaptive fuzzy controller derived from its neutral equivalent, in *Second IEEE International Conference on Fuzzy Systems*, 345–350.

Bishop, C. M. 1995. *Neural Networks for Pattern Recognition*. London, United Kingdom: Oxford University Press.

Bonham-Carter, G. F. 1994. *Geographic information systems for Geoscientists modeling with GIS*. Edited by G. F. Bonham-Carter. Pergamon.

Bottrell, S., Tellam, J., Bartlett, R. and Hughes, A. 2008. Isotopic composition of sulfate as a tracer of natural and anthropogenic influences on groundwater geochemistry in an urban sandstone aquifer, Birmingham, UK, *Applied Geochemistry*, 23(8), 2382–2394. doi: 10.1016/j.apgeochem.2008.03.012.

Boufekane, A. and Saighi, O. 2013. Assessment of groundwater pollution by nitrates using intrinsic vulnerability methods : a case study of the Nil valley groundwater (Jijel, North-East Algeria), *African Journal of Environmental Science and Technology*, 7(10), 949–960. doi: 10.5897/AJEST2013.1428.

Brindha, K. and Elango, L. 2015. Cross comparison of five popular groundwater pollution vulnerability index approaches, *Journal of Hydrology*. Elsevier B.V, 524, 597–613. doi: 10.1016/j.jhydrol.2015.03.003.

Buchanan, P. C. and Reimold, W. U. 1998. Studies of the Rooiberg Group, Bushveld Complex, South Africa: no evidence for an impact origin, *Earth and Planetary Science Letters*, 155(3–4), 149–165. doi: http://dx.doi.org/10.1016/S0012-821X(97)00216-1.

Burger, M. 2012. *Geohydrological report for the proposed Usutu opencast colliery on the farms Jan Hendriksfontein 263 IT and Transutu 257 IT, Ermelo, Mpumalanga GPT ENV-11-359.*

Button, A. 1973. The stratigraphic history of the Malmani Dolomite in the eastern and northeastern Transvaal, *Transactions of the Geological Society of South Africa*, 76, 229–247.

Carpenter, G. A. and Grossberg, S. 1987. A massively parallel architecture for a self-organizing neural pattern recognition machine, *Computer Vision Graphics and Image Processing*, 37, 54–115.

Carranza, E. J. M. 2002. *Geologically-Constrained Mineral Potential Mapping (Examples from the Philippines)*. Delft University of Technology, Netherlands. unpublished PhD Thesis.

Chemicool. 2017. *Chemicool Periodic Table: Definition of Ligand*. Available at: https://www.chemicool.com/definition/ligand.html (Accessed: 23 September 2017).

Chudasama, B., Porwal, A., Kreuzer, O. P. and Butera, K. 2016. Geology, geodynamics and orogenic gold prospectivity modelling of the Paleoproterozoic Kumasi Basin, Ghana, West Africa, *Ore Geology Reviews*. Elsevier B.V., 78, 692–711. doi: 10.1016/j.oregeorev.2015.08.012.

Civita, M. V. 1994. *Le carte della vulnerabilità degli acquiferi all'inquinamento: teoria e pratica. Quaderni di Tecniche di Protezione Ambientale, Sezione "Protezione delle Acque Sotterranee". 31*. Bologna: Pitagora, Editrice.

Civita, M. V. 2010. The Combined Approach When Assessing and Mapping Groundwater Vulnerability to Contamination, *Journal of Water Resource and Protection*, 2(1), 14–28.

Clark, R. N., Swayze, G. A., Wise, R., Livo, E., Hoefen, T., Kokaly, R. and Sutley, S. J. 2007. *USGS digital spectral library splib06a: U.S. Geological Survey, Digital Data Series 231*, *U.S Geological Survey*. Available at: http://speclab.cr.usgs.gov/spectral.lib06 (Accessed: 22 September 2017).

Climate-data.org. 2017. *Climate data for cities worldwide*. Available at: https://en.climate-data.org/info/sources/ (Accessed: 29 December 2017).

Clubley-Armstrong, A. R. 1977. *The geology of the Selonsrivier area, north of Middelburg, Transvaal, with special reference to the structure of the regions southeast of the Dennilton dome*. University of Pretoria.

Cole, J., Cole, P., Yibas, B., Vadapalli, V., Novhe, O. and Netshitungulwana, R. 2015. *A holistic approach towards best management of mine pollution impacts on water resources of South Africa using river catchment strategy: Report on remote sensing*. Pretoria.

Crowley, J. K., Williams, D. E., Hammarstrom, J. M., Piatak, N. and Chou, I. 2003. Fe-hydroxide , and Fe-sulphate-hydrate minerals associated with sulphide-bearing mine wastes, *Geochemistry: Exploration, Environment, Analysis*, 3, 219–228. doi: 10.1144/1467-7873/03-001.

Daly, D. and Warren, W. P. 1998. Mapping groundwater vulnerability: the Irish perspective, in Robins, N. S. (ed.) *Groundwater Pollution, Aquifer Recharge and Vulnerability*. Special. London, United Kingdom: British Geological Society, 179–190.

Dan. 2017. *Artificial neural network architecture*. Available at: http://logicalgenetics.com/artificial-neural-network-architecture/ (Accessed: 29 September 2017).

Department of Energy. 2016. *Coal resources*. Available at: http://www.energy.gov.za/files/coal_frame.html (Accessed: 5 October 2016).

Department of Water and Sanitation (DWS). 2006. *Groundwater resource assessment II - task 3aE recharge*, *Department of Water and Sanitation*

Dixon, B. 2005a. Applicability of neuro-fuzzy techniques in predicting ground-water vulnerability: a GIS-based sensitivity analysis, *Journal of Hydrology*, 309(1–4), 17–38. doi: 10.1016/j.jhydrol.2004.11.010.

Dixon, B. 2005b. Groundwater vulnerability mapping: a GIS and fuzzy rule based integrated tool, *Applied Geography*, 25(4), 327–347. doi: 10.1016/j.apgeog.2005.07.002.

Djorovic, M. 1980. Slope effect on run-off and erosion, in De Boodt, M. and Gabriels, D. (eds) *Assessment of Erosion*. Chichester: Wiley-lnterscience, 215–225.

Domenico, P. A. and Schwartz, F. W. 1990. *Physical and Chemical Hydrogeology*. vol. 824. New York, USA: John Wiley and Sons, Ltd.

Dow, W. G. 1974. Application of oil correlation and source rock data to exploration in Williston Basin, *AAPG Bulletin*, 58, 1253–1262.

Draoui, M., Vias, J., Andreo, B., Targuisti, K. and Stitou El Messari, J. 2008. A comparative study of four vulnerability mapping methods in a detritic aquifer under mediterranean climatic conditions, *Environmental Geology*, 54(3), 455–463. doi: 10.1007/s00254-007-0850-3.

Eary, E. L. and Williamson, M. A. 2006. Simulations of the neutralising capacity of Silicate rocks in acid mine drainage environments, in *7th International Conference on Acid Rock Drainage (ICARD).*

El-Naqa, A. 2004. Aquifer vulnerability assessment using the DRASTIC model at Russeifa landfill, northeast Jordan, *Environmental Geology*, 47(1), 51–62. doi: 10.1007/s00254-004-1126-9.

Ellis, J., Clark, M., Rouse, H., Lamarche, G. and Britton, R. 2014. *Literature review of environmental management frameworks for offshore mining.*

Eriksson, P. G., Altermann, W. and Hartzer, F. J. 2006. The Transvaal Supergroup and its precursors, in Johnson, M. R., Anhaeusser, C. R., and Thomas, R. J. (eds) *Geology of South Africa*. Johannesburg/Council for Geoscience: Geological Society of South Africa, 237–257.

Eskom. 2016. *Coal Power*. Available at: http://www.eskom.co.za/AboutElectricity/ElectricityTechnologies/Pages/Coal_Power.aspx (Accessed: 3 October 2016).

ESRI. 2006. ArcGIS Help topic "Standard classification Schemes". ESRI Inc.

Everett, M. E. 2013. *Near-Surface Applied Geophysics*. 1st edn. Edited by M. . Everett. New York, USA: Cambridge University Press.

Ewusi, A., Ahenkorah, I. and Kuma, J. S. Y. 2017. Groundwater Vulnerability Assessment of the Tarkwa Mining Area Using SINTACS Approach and GIS, *Ghana Mining Journal*, 17(1), 18–30. doi: 10.4314/gm.v17i1.3.

Exxaro. 2006. *An independent competent persons' report on the mining assets of Exxaro Resources Limited*. Available at: http://www.exxaro.com/pdf/icpr/a/geology/coal.htm (Accessed: 4 October 2017).

Ferguson, K. D. and Erickson, P. M. 1988. Pre-mine prediction of acid mine drainage, in Salomons, W. and Forstner, U. (eds) *Environmental management of solid waste -dredged material and mine tailings*. Berlin: Springer-Verlag, 24–43.

Fijani, E., Nadiri, A. A., Asghari Moghaddam, A., Tsai, F. T. C. and Dixon, B. 2013. Optimization of drastic method by supervised committee machine artificial intelligence to assess groundwater vulnerability for maragheh-bonab plain aquifer, Iran, *Journal of Hydrology*, 503, 89–100. doi: 10.1016/j.jhydrol.2013.08.038.

Focazio, M., Reilly, T. E., Rupert, M. G. and Helsel, D. R. 2002. *Assessing ground-water vulnerability to contamination: Providing scientifically defensible information for decision makers.*

Foster, S. S. D. 1998. Groundwater recharge and pollution vulnerability of British aquifer: a critical overview, in Robins, N. (ed.) *Groundwater Pollution, Aquifer Recharge and Vulnerabilty Special Publication*, 7–22.

Fox, D. M., Bryan, R. B. and Price, A. G. 1997. The influence of slope gradient on infiltration rate for interrill conditions, *Geoderma*, 80, 181–194. doi: 10.1016/S0016-7061(97)00075-X.

Fraga, C. M., Fernandes, L. S., Pacheco, F. A. L., Reis, C. and Moura, J. P. 2013. Exploratory assessment of groundwater vulnerability to pollution in the Sordo River Basin, Northeast of Portugal, *Rem: Revista Escola de Minas*, 66(1), 49–58. doi: 10.1590/S0370-44672013000100007.

Freeze, R. A. and Cherry, J. A. 1979. *Groundwater*. Prentice-Hall Inc.

Frind, E. O., Molson, J. W. and Rudolph, D. L. 2006. Well vulnerability: a quantitative approach for source water protection, *Ground Water*, 44(5), 732–42.

Fuller, R. 2000. *Introduction to Neuro-Fuzzy Systems. Advances in Soft Computing Series*. Edited by R. Fuller. Berlin Heildelberg: Springer-Verlag.

Geiger, R. 1954. Classification of climates after W. Köppen, in *Landolt-Börnstein – Zahlenwerte und Funktionen aus Physik, Chemie, Astronomie, Geophysik und Technik*. 3rd edn. Berlin: Springer, 603–607.

Geosphere. 2007. *Seismic refraction*. Available at: http://www.geosphereinc.com/seis_ refraction.html.

Gheisari, N. 2017. *Modifed DRASTIC model in agricultural areas*. University of Ottawa, MSc Thesis.

Gholami, V., Chau, K. W., Fadaee, F., Torkaman, J. and Ghaffari, A. 2015. Modeling of groundwater level fluctuations using dendrochronology in alluvial aquifers, *Journal of Hydrology*. Elsevier B.V, 529, 1060–1069. doi: 10.1016/j.jhydrol.2015.09.028.

Goderniaux, P., Davy, P., Bresciani, E., De Dreuzy, J. R. and Le Borgne, T. 2013. Partitioning a regional groundwater flow system into shallow local and deep regional flow compartments, *Water Resources Research*, 49, 2274–2286. doi: 10.1002/wrcr.20186.

Gogu, R. C. and Dassargues, A. 2000. Current trends and future challenges groundwater vulnerability assessment using overlay and index methods, *Environmental Geology*, 39(6), 549–559. doi: 10.1007/s002540050466.

Gogu, R. C., Hallet, V. and Dassargues, A. 2003. Comparison of aquifer vulnerability assessment techniques. Application to the No'blon river basin (Belgium), *Environmental Geology*, 44(8), 881–892. doi: 10.1007/s00254-003-0842-x.

Gomo, M. and Masemola, E. 2016. Groundwater hydrogeochemical characteristics in rehabilitated coalmine spoils, *Journal of African Earth Sciences*. Elsevier Ltd, 116, 114–126. doi: 10.1016/j.jafrearsci.2015.12.015.

Gomo, M. and Van Tonder, G. 2013. Development of a Preliminary Hydrogeology Conceptual Model for a Heterogeneous Alluvial Aquifer using Geological Characterization, *Journal of Geology and Geosciences*, 2(3), 128. doi: 10.4172/2329-6755.1000128.

Greenshields, H. D. 1986. Eastern Transvaal coalfield, in Anhaeusse, C. R. and Maske, R. S. (eds) *Mineral Deposits of Southern Africa. Vol. II*. Johannesburg: Geological Society of South Africa, 1995–2010.

Griffiths, K. J., MacDonald, A. M., Robins, N. S., Merritt, J., Booth, S. J., Johnson, D. and McConvey, P. 2008. Improving the characterisation of Quaternary Deposits for groundwater vulnerability assessments, *ARPN Journal of Agricultural and Biological Science*, 3(4), 41–45.

Gunn, J. 1986. Modeling of conduit flow dominated karst aquifers, in Gunay, G. and Johnson, A. I. (eds). Wallingford, UK: karst water resources. IAHS, Publication 161, 587–596.

Gurdak, J. J., Geyer, G. E., Nanus, L., Taniguchi, M. and Corona, C. R. 2015. Scale dependence of controls on groundwater vulnerability in the water-energy-food nexus, California Coastal Basin aquifer system, *Journal of Hydrology: Regional Studies*. Elsevier B.V, 11(3), 126–138. doi: 10.1016/j.ejrh.2016.01.002.

Gurdak, J. J. and Qi, S. L. 2012. Vulnerability of recently recharged groundwater in principle aquifers of the United States to nitrate contamination, *Environmental Science and Technology*, 46(11), 6004–6012. doi: 10.1021/es300688b.

Hancox, P. J. and Götz, A. E. 2014. South Africa's coalfields - A 2014 perspective, *International Journal of Coal Geology*, 132, 170–254. doi: 10.1016/j.coal.2014.06.019.

Haque, E., Reza, S. and Ahmed, R. 2018. Assessing the vulnerability of groundwater due to open pit coal mining using DRASTIC model: a case study of Phulbari Coal Mine, Bangladesh, *Geosciences Journal*, 22(2), 359–371. doi: 10.1007/s12303-017-0054-0.

Harter, T. 2008. Assessing Vulnerability of Groundwater, *Watersheds, Groundwater and Drinking Water*, 274.

Heath, R. C. 1983. *Basic Ground-Water Hydrology*, *U.S. Geological Survey Water-Supply Paper 2220.*

Hebb, D. 1949. *The Organization of Behavior*. New York, USA: Wiley.

Hedrich, S. and Johnson, D. B. 2013. Acidithiobacillus ferridurans sp. nov., an acidophilic iron-, sulfur- and hydrogen-metabolizing chemolithotrophic gammaproteobacterium, *International Journal of Systematic and Evolutionary Microbiology*, 63, 4018–4025. doi: 10.1099/ijs.0.049759-0.

Hellendoorn, H. and Thomas, C. 1993. Defuzzification in fuzzy controllers, *Journal of Intelligent and Fuzzy Systems*, 1, 109–123.

Hellmann, M. 2002. *Fuzzy Logic lecture notes: Department of Informatics at the University of Fribourg. France*. Available at: http://diuf.unifr.ch/ds/courses/dss2002/pdf/FuzzyLogic.pdf.

Hobbs, P., Manders, P., Godfrey, L. and Hobbs, P. 2009. *Acid Mine Drainage in South Africa*, *CSIR.*

Hounslow, A. W. 1995. *Water Quality Data: Analysis and Interpretation*. Boca Raton, Florida: CRC Lewis Publishers.

Huan, H., Wang, J. and Teng, Y. 2012. Assessmen and validation of groundwater vulnerability to nitrate based on a modified DRASTIC model: a case study in Jilin City of northeast China, *Science of the Total Environment*, 440, 14–23.

Huddleston, J. H. 1994. *How soil properties affect groundwater vulnerability to pesticide contamination, EM 8559.*

Idowu, P. A., Osakwe, C., Kayode, A. A. and Adagunodo, E. R. 2012. Prediction of Stock Market in Nigeria Using Artificial Neural Network, I.J, *Intelligent Systems and Applications*, 11, 68–74.

Ignacio, R., Gonzalo, J. and Cabestany, J. 2013. Advances in Computational Intelligence, in *12th International Work-Conference on Artificial Neural Networks, Part 2*. Puerto de la Cruz, Tenerife, Spain.

Iqbal, M. and Rizwan, M. 2009. Application of 80/20 rule in software engineering Waterfall Model, *IEEE*, 223–228.

Jain, S. K., Singh, V. P. and Van Genuchten, M. T. 2004. Analysis of Soil Water Retention Data Using Artificial Neural Networks, *Journal of Hydrologic Engineering*, 9(5), 415–420. doi: 10.1061/(ASCE)1084-0699(2004)9:5(415).

Jang, C. S. and Chen, S. K. 2015. Integrating indicator-based geostatistical estimation and aquifer vulnerability of nitrate-N for establishing groundwater protection zones, *Journal of Hydrology*. Elsevier B.V., 523, 441–451. doi: 10.1016/j.jhydrol.2015.01.077.

Jang, J. S. R. 1993. ANFIS: adaptive-network-based fuzzy inference system, *IEEE Transactions on Systems, Man and Cybernetics*, 23(3), 665–685.

Jang, J. S. R. and Sun, C. T. 1995. Neuro-Fuzzy Modeling and Control, in *IEEE*, 378–406.

Jang, J. S. R. and Sun, C. T. 1997. *Neuro - fuzzy and soft computing: A computational approach to learning and machine intelligence*. NJ, USA: Prentice - Hall.

Jeffrey, L. S. 2005. Characterization of the coal resources of South Africa, *Journal of the South African Institute of Mining and Metallurgy*, 95–102.

Jeffrey, R., Falcon, R. and Kinghorn, A. 2014. The benefits and challenges associated with coal in South Africa, *Cornerstone*, 2(3), 66–70.

Jens, N., Diehl, R. and Busch, K. 2012. Efficient low - storage Runge – Kutta schemes with optimized stability regions, *Journal of Computational Physics*, 231(2), 364–372.

Johnson, M. R., Van Vauuren, C., Hegenberger, W. F., Key, R. and Shoko, U. 1996. Stratigraphy of the Karoo Supergroup in Southern Africa: an overview, *Journal of African Earth Sciences*, 23, 3–15.

Joly, A., Porwal, A. and McCuaig, T. C. 2012. Exploration targeting for orogenic gold deposits in the Granites-Tanami Orogen: mineral system analysis, targeting model and prospectivity analysis, *Ore Geology Reviews*. Elsevier B.V, 48, 349–383. doi: 10.1016/j.oregeorev.2012.05.004.

Kamiya, H., Ozaki, A. and Imahashi, M. 1974. Dissolution rate of powdered quartz in acid solution, *Geochemical Journal*, 8, 21–26.

Kanungo, D. P., Arora, M. K. and Gupta, R. P. 2009. Landslide Susceptibility Zonation (LSZ) Mapping–A Review, *Journal of South Asian Disaster Studies*, 2(1), 81–105.

Kaur, R. and Rosin, K. G. 2009. Ground Water Vulnerability Assessment: challenges and Opportunities, *Bhu-Jal news*. New Delhi, India, 24(4), 82–92. Available at: http://www.cgwb.gov.in/documents/papers/incidpapers/Paper 12- R. Kaur.pdf.

Kazakis, N. and Voudouris, K. S. 2015. Groundwater vulnerability and pollution risk assessment of porous aquifers to nitrate: modifying the DRASTIC method using quantitative parameters, *Journal of Hydrology*. Elsevier B.V, 525, 13–25. doi: 10.1016/j.jhydrol.2015.03.035.

Klopf, A. H. 1972. *Brain function and adaptive systems - a heterostatic theory Technical Report, AFCRL-72-0164.*

Knox-Robinson, C. M. and Wyborn, L. A. I. 1997. Towards a holistic exploration strategy: using Geographic Information Systems as a tool to enhance exploration, *Australian Journal of Earth Sciences*, 44(4), 453–463. doi: 10.1080/08120099708728326.

Kohavi, R. 1995. A Study of Cross-Validation and Bootstrap for Accuracy Estimation and Model Selection 2 Methods for Accuracy Estimation, in *International Joint Conference on Artificial Intelligence*, 1137–1145. doi: 10.1067/mod.2000.109031.

Krenker, A., Bešter, J. and Kos, A. 2011. *Introduction to the Artificial Neural Networks*, *Artificial Neural Networks - Methodological Advances and Biomedical Applications*. Edited by K. Suzuki. Available at: http://www.intechopen.com/books/numerical-analysis-theory-and-application/numerical-validation-methods.

Lambooy, A. M. 1984. Relationship between cation exchange capacity, clay content and water retention of Highveld soils, *South African Journal of Plant and Soil*, 1, 33–38.

Leyland, R. C., Witthüser, K. T. and Van Rooy, J. L. 2008. *Vulnerability Mapping in Karst Terrains, Exemplified in the Wider Cradle of Humankind World Heritage Site.*

Li, X., Masuda, H., Kusakabe, M., Yanagisawa, F. and Zeng, H. 2006. Degradation of groundwater quality due to anthropogenic sulfur and nitrogen contamination in the Sichuan Basin, China, *Geochemical Journal*, 40(4), 309–332. doi: 10.2343/geochemj.40.309.

Lin, C. T. and Lee, G. 1996. *Neural Fuzzy Systems: A Neuro-Fuzzy Synergism to Intelligent Systems*. Prentice Hall.

Lindeque, A., De Wit, M. J., Ryberg, T., Weber, M. and Chevallier, L. 2011. Deep crustal profile across the southern Karoo Basin and beattie magnetic anomaly, South Africa: An integrated interpretation with tectonic implications, *South African Journal of Geology*, 114, 265–292. doi: 10.2113/gssajg.114.3-4.265.

Loganathan, C. and Girija, K. V. 2014. Investigations on Hybrid Learning in ANFIS, *Journal of Engineering Research and Applications*, 4(10), 31–37.

Logica, N. 2015. *Artificial Intelligence in Law: The state of play 2016 part 1*. Available at: https://www.neotalogic.com/2016/02/28/artificial-intelligence-in-law-the-state-of-play-2016-part-1/ (Accessed: 10 November 2017).

Loke, D. M. 2000. *Electrical imaging surveys for environmental and engineering studies: A practical guide to 2-D and 3-D surveys.*

Luk, S. H., Cai, Q. and Wang, G. P. 1993. Effects of surface crusting and slope gradient on soil and water losses in the hilly loess region, North China, *Catena*, 24, 29–45.

Magoon, L. B. and Beaumont, E. A. 1999. *Treatise of Petroleum Geology / Handbook of Petroleum Geology: Exploring for Oil and Gas Traps*. The Ammerican Association of Petroleum Geologists.

Magoon, L. B. and Dow, W. G. 1994. The Petroleum System: from Source to Trap, *AAPG Memoir 60*, (2), 3–24.

Makarevich, S. 2015. *Validation*, *Slideshare*. Available at: https://www.slideshare.net/sermakarevich/validation-54360119.

Mani, P. K. 2014. *Lecture notes: Problem soils and soil acidity*. Available at: https://www.slideshare.net/pabitramani/problem-soils-and-soil-acidity (Accessed: 21 January 2018).

Manrique, L. A., Jones, C. A. and Dyke, P. T. 1991. Predicting cation-exchange capacity from soil physical and chemical properties, *Soil Science Society of America Journal*, 55, 787–794.

Martel, Y., Kimpe, C. R. D. and Laverdiere, M. R. 1978. Cation-exchange capacity of clay-rich soils in relation to organic matter, mineral composition and surface area, *Soil Science Society of America Journal*, 42, 764–767.

Martini, J. E. J. 1999. The Loskop Formation and its relationship to the Bushveld Complex, South Africa, *Journal of African Earth Sciences*, 27(2), 193–222. doi: 10.1016/S0899-5362(98)00057-8.

McCarthy, T. S. 2006. The Witwatersrand Supergroup, in Johnson, M. R., Anhaeusse, C. R., and Thomas, R. J. (eds) *The Geology of South Africa*. Pretoria: Geological Society of South Africa, 155–186.

McCarthy, T. S. 2011. The impact of acid mine drainage in South Africa, *South African Journal of Science*, 107(5/6), 1–7. doi: 10.4102/sajs.v107i5/6.712.

McCarthy, T. S. and Pretorius, K. 2009. Coal mining on the Highveld and its implications for future water quality in the Vaal River system, in *International Mine Water Conference*. Pretoria, South Africa, 56–65.

McCulloch, W. S. and Pitts, W. 1943. A logical calculus of the ideas immanent in nervous activity, *Bulletin of Mathematical Biophysics*, 5, 115–133.

Meggs, T. 2015. *ANFIS*. Available at: https://github.com/twmeggs/anfis (Accessed: 12 February 2015).

Menashe, E. 2004. Relationship between degrees , percent slope , and ratio to express slope gradient, in *Shoreline management and stabilisation using vegetation*. Washington DC.

Metni, M., El-Fadel, M., Sadej, S., Kayal, R. and el Khoury, D. L. 2004. Groundwater Resources in Lebanon: a vulnerability assessment, *Water Resources Development*, 20(4), 475–491.

Michel, M. D. and Elena, D. 2009. *Encyclopedia of Distances*. Springer.

Minsky, M. L. and Papert, S. 1969. *Perceptrons: An Introduction to Computational Geometry*. Cambridge: MIT Press.

Molson, J. and Aubertin, M. 2006. Simulating Transport and Geochemical Evolution of Acid Mine Drainage Through Discretely Fractured Porous Media, in *OttawaGeo2007*, 1236–1243.

Moncur, M. C., Jambor, J. L., Ptacek, C. J. and Blowes, D. 2009. Mine drainage from the weathering of sulphide minerals and magnetite, *Applied Geochemistry*, 24, 2362–2373.

Mongwe, H. G. and Fey, M. V 2004. The buffering capacity of soil materials for various contaminant types and the relationship between soil morphology, chemical properties and buffering capacity: a literature review. WRC TT 303/07. Pretoria.

Musekiwa, C. and Majola, K. 2013. Groundwater Vulnerability Map for South Africa, *South African Journal of Geomatics*, 2(2), 152–163.

Nadiri, A., Hassan, M. M. and Asadi, S. 2015. Supervised Intelligence Committee Machine to Evaluate Field Performance of Photocatalytic Asphalt Pavement for Ambient Air Purification, *Transportation Research Record: Journal of the Transportation Research Board*, 2528, 96–105. doi: 10.3141/2528-11.

Nassif, S. and Wilson, E. 1975. The influence of slope and rain intensity on overland flow and infiltration, *Hydrological Sciences Bulletin*, 20, 539–553.

National Research Council (NRC). 1993. *Groundwater vulnerability assessments: Contamination potential under conditions of uncertainty*. Washington, DC: National Academy Press.

Navarre-Sitchler, A., Brantley, S. L. and Rother, G. 2015. How Porosity Increases During Incipient Weathering of Crystalline Silicate Rocks, *Reviews in Mineralogy and Geochemistry*, 80(1), 331–354. doi: 10.2138/rmg.2015.80.10.

Negnevitsky, M. 2005. *Artificial Intelligence: A guide to Intelligent Systems*. 2nd edn, *Addison Wesley*. 2nd edn. England: Addison-Wesley.

Neshat, A., Pradhan, B., Pirasteh, S. and Shafri, H. Z. M. 2014. Estimating groundwater vulnerability to pollution using a modified DRASTIC model in the Kerman agricultural area, Iran, *Environmental Earth Sciences*, 71(7), 3119–3131. doi: 10.1007/s12665-013-2690-7.

Neukum, C. and Azzam, R. 2009. Quantitative assessment of intrinsic groundwater vulnerability to contamination using numerical simulations, *Science of The Total Environment*, 408(2), 245–254. doi: 10.1016/j.scitotenv.2009.09.046.

Nobre, R. C. M., Rotunno, F. O., Mansur, W. J., Nobre, M. M. M., Cosenza, C. A. N., Rotunno Filho, O. C., Mansur, W. J., Nobre, M. M. M. and Cosenza, C. A. N. 2007. Groundwater vulnerability and risk mapping using GIS, modeling and a fuzzy logic tool, *Journal of Contaminant Hydrology*, 94, 277–292. doi: 10.1016/j.jconhyd.2007.07.008.

Novhe, N. O., Maree, J. and Ogola, J. S. 2013. Characterization of potential acid leachate from raw coal, discard coal and slimes from a colliery in the Witbank coalfield, Mpumalanga Province, South Africa., in *International Mine Water Conference*. Golden CO, United States, 875–880.

Oelkers, E. H. and Schott, J. 1995. Experimental study of anorthite dissolution and the relative mechanism of feldspar hydrolysis, *Geochimica et Cosmochimica Acta*, 59(24), 5039–5053. doi: 10.1016/0016-7037(95)00326-6.

de Oliveira, R., Karatzoglou, A., Concejero, P., Armenta, A. and Oliver, N. 2011. Towards a psychographic user model from mobile phone usage Towards a Psychographic User Model From Mobile Phone Usage, in *CHI 2011*, 2191–2196. doi: 10.1145/1979742.1979920.

Oxford. 2017. Source, *English Dictionary*. Oxford University Press. Available at: https://en.oxforddictionaries.com/definition/source.

Pathak, D. R., Bhandary, N. P. and Yatabe, R. 2014. Hierarchical Fuzzy Rule based Model for Groundwater Vulnerability and Assessment of Nitrate Pollution Hazard in Kathmandu Basin, in *International Symposium Geohazards: Science, Engineering and Management*, 564–571.

Pathak, D. R. and Hiratsuka, A. 2011. An integrated GIS based fuzzy pattern recognition model to compute groundwater vulnerability index for decision making, *Journal of Hydro-Environment Research*, 5(1), 63–77. doi: 10.1016/j.jher.2009.10.015.

Pinetown, K. L. and Boer, R. H. 2006. *A quantitative evaluation of the modal distribution of minerals in coal deposits in the Highveld area and the associated impact on the generation of acid and neutral mine drainage 1264/06.*

Pinetown, K. L., Ward, C. R. and Van der Westhuizen, W. A. 2007. Quantitative evaluation of minerals in coal deposits in the Witbank and Highveld coalfields, and the potential impact on acid mine drainage, *International Journal of Coal Geology*, 70, 166–183. doi: 10.1016/j.coal.2006.02.013.

Pisciotta, A., Cusimano, G. and Favara, R. 2015. Groundwater nitrate risk assessment using intrinsic vulnerability methods: a comparative study of environmental impact by intensive farming in the Mediterranean region of Sicily, Italy, *Journal of Geochemical Exploration*. Elsevier B.V., 156, 89–100. doi: 10.1016/j.gexplo.2015.05.002.

Porwal, A., Carranza, E. J. and Hale, M. 2003. Knowledge-Driven and Data-Driven Fuzzy Models for Predictive Mineral Potential Mapping, *Natural Resources Research*, 12(1), 1–25. doi: 10.1023/A.

Porwal, A. and Carranza, E. J. M. 2015. Introduction to the Special Issue: GIS-based mineral potential modelling and geological data analyses for mineral exploration, *Ore Geology Reviews*. Elsevier B.V, 71, 477–483. doi: 10.1016/j.oregeorev.2015.04.017.

Porwal, A., Das, R. D., Chaudhary, B., Gonzalez-Alvarez, I. and Kreuzer, O. 2015. Fuzzy inference systems for prospectivity modeling of mineral systems and a case-study for prospectivity mapping of surficial Uranium in Yeelirrie Area, Western Australia, *Ore Geology Reviews*. Elsevier B.V, 71(August), 839–852. doi: 10.1016/j.oregeorev.2014.10.016.

Porwal, A. K. and Kreuzer, O. P. 2010. Introduction to the Special Issue: mineral prospectivity analysis and quantitative resource estimation, *Ore Geology Reviews*. Elsevier B.V, 38(3), 121–127. doi: 10.1016/j.oregeorev.2010.06.002.

PWC. 2017. *Artificial Intelligence and Robotics – 2017: Leveraging artificial intelligence and robotics for sustainable growth*. Available at: https://gita.org.in/Attachments/Reports/ artificial-intelligence-and-robotics-2017.pdf (Accessed: 4 October 2017).

Rahmati, O., Pourghasemi, H. R. and Melesse, A. M. 2016. Application of GIS-based data driven random forest and maximum entropy models for groundwater potential mapping: A case study at Mehran Region, Iran, *Catena*, 137, 360–372. doi: 10.1016/j.catena.2015.10.010.

Railsback, L. B. 2017. *Petroleum geoscience and subsurface geology: Lecture notes GEO 4320/6320.*

Remesan, R. and Mathew, J. 2014. *Hydrological Data Driven Modelling: a case study approach*. 1st edn. Springer.

Rich, E. and Knight, K. 1991. *Artificial Intelligence*. Vol. 2. New York: McGraw-Hill.

Roberts, F. and Roberts, D. 2000. *Correlation Coefficient*. Available at: https://mathbits.com/MathBits/TISection/Statistics2/correlation.htm (Accessed: 1 January 2018).

Robins, N. S. 1998. Recharge: the key to groundwater pollution and aquifer vulnerability, in Robins, N. S. (ed.) *Groundwater Pollution, Aquifer Recharge and Vulnerability*. London, UK: British Geological Society, 1–5.

Rojas, R. 2005. *Neural Networks:A Systematic Introduction*. Springer.

Rosenblatt, F. 1958. The perceptron: a probabilistic model for information storage and organization in the brain, *Psychological Review*, 65(6), 386–408.

Rumelhart, D. E., Hinton, G. E. and Williams, R. J. 1986. Learning internal representations by error propagation, in *Parallel Distributed Processing: Explorations in the Microstructure of Cognition*. Cambridge: MIT Press, 318–362.

Russell, S. J. and Norvig, P. 1995. *Artificial Intelligence: A Modern Approach*. New Jersey: Prentice-Hall.

SACS. 1980. *Lithostratigraphy of South Africa, South West Africa/Namibia and the Republics of Boputhatswana, Transkei and Venda*. 8th edn. Pretoria: Geological Survey of South Africa.

Saida, S., Tarik, H., Abdellah, A., Farid, H. and Hakim, B. 2017. Assessment of Groundwater Vulnerability to Nitrate Based on the Optimised DRASTIC Models in the GIS Environment (Case of Sidi Rached Basin, Algeria), *Geosciences*, 7(2), 20. doi: 10.3390/geosciences7020020.

Saidi, S., Bouri, S. and Ben Dhia, H. 2010. Groundwater vulnerability and risk mapping of the Hajeb-Jelma aquifer (Central Tunisia) using a GIS based DRASTIC model, *Environmental Earth Sciences*, 59, 1579–1588.

Sakala, E., Fourie, F., Gomo, M. and Coetzee, H. 2017a. Hydrogeological investigation of the Witbank , Ermelo and Highveld coalfields: implications for the subsurface transport and attenuation of acid mine drainage, in Wolkersdorfer, C., Sartz, L., Sillanpää, M., and Häkkinen, A. (eds) *13th International Mine Water Association Congress – Mine Water & Circular Economy*. Lappeenranta, Finland: IMWA, 564–571.

Sakala, E., Fourie, F., Gomo, M. and Coetzee, H. 2017b. Mapping surface sources of acid mine drainage using remote sensing: case study of the Witbank, Ermelo and Highveld coalfields, in Wolkersdorfer, C., Sartz, L., Sillanpää, M., and Häkkinen, A. (eds) *13th International Mine Water Association Congress – Mine Water & Circular Economy*. Lappeenranta, Finland: IMWA, 1246–1253.

Sakala, E., Fourie, F., Gomo, M. and Coetzee, H. 2018. GIS-based groundwater vulnerability modelling: a case study of the Witbank, Ermelo and Highveld coalfields in South Africa, *Journal of African Earth Sciences*, 137, 46–60. doi: 10.1016/j.jafrearsci.2017.09.012.

Sakala, E., Fourie, F., Gomo, M., Coetzee, H. and Magadaza, L. 2016. Specific groundwater vulnerability mapping: case study of acid mine drainage in the Witbank coalfield, South Africa, in *6th IASTED International Conference on Environment and Water Resource Management*, 93–100. doi: 10.2316/P.2016.836-010.

Salomons, W. 1995. Environmental impact of metals derived from mining activities: processes, predictions, prevention, *Journal of Geochemical Exploration*, 52, 5–23.

Satellite Imaging Corporation. 2017. *Sentinel-2A Satellite Sensor (10m)*. Available at: https://www.satimagingcorp.com/satellite-sensors/other-satellite-sensors/sentinel-2a/ (Accessed: 23 September 2017).

Schmidhuber, J. 2014. Deep learning in neural networks: an overview, *Neural Network*, 61, 85–117.

Schmidt, A. 2000. *Biological neural network*. Available at: https://www.teco.edu/~albrecht /neuro/html/node7.html (Accessed: 28 September 2017).

Secunda, S., Collin, M. L. and Melloul, A. J. 1998. Groundwater vulnerability assessment using a compsite model combining DRASTIC with extensive agricultural land use in Israel's Sharon region, *Journal of Environmental Management*, 54, 39–57.

Seyam, M. 2009. *Groundwater Salinity Modeling Using Artificial Neural Networks: Gaza Strip case study*. The Islamic University of Gaza.

Shapiro, S. C. 1995. Knowledge Representation and Reasoning Logics for Artificial Intelligence, 6–7.

Sharma, K., Singh, H. and Pareek, O. 1983. Rainwater infiltration into a bare loamy sand, *Hydrological Sciences Journal*, 28, 417–424.

Shigidi, A. and Garcia, L. A. 2005. Parameter estimation in groundwater hydrology using artificial neural networks, *Journal of computing in civil engineering*, 31, 281–289.

Snyder, D. T. 2008. *Estimated depth to ground water and configuration of the water table in the Portland, Oregon area. Report no. 2008–5059.*

Snyman, C. P. 1998. Coal, in Wilson, M. G. C. and Anhaeusser, C. R. (eds) *The Mineral Resources of South Africa. Handbook 16*. Pretoria.

Somaratne, N., Zulfic, H., Ashman, G., Vial, H., Swaffer, B. and Frizenschaf, J. 2013. Groundwater risk assessment model (GRAM): groundwater risk assessment model for wellfield protection, *Water (Switzerland)*, 5(3), 1419–1439. doi: 10.3390/w5031419.

Sorichetta, A., Masetti, M., Ballabio, C. and Sterlacchini, S. 2012. Aquifer nitrate vulnerability assessment using positive and negative weights of evidence methods, Milan, Italy, *Computers and Geosciences*, 48, 199–210. doi: 10.1016/j.cageo.2012.05.021.

South African National Standards (SANS). 2011. *Drinking Water Specifications. Drinking Water Management Guide for Water Service Aurhorities. Annexure 1*. Pretoria.

South African Weather Service (SAWS). 2016. *Historical Rain Maps*. Available at: http://www.weathersa.co.za/climate/historical-rain-maps (Accessed: 23 March 2016).

Statistics South Africa. 2016. *The importance of Coal*. Available at: http://www.statssa.gov.za/?p=4820 (Accessed: 5 October 2016).

Van Stempvoort, D., Ewert, L. and Wassenaar, L. 1993. Aquifer Vulnerability Index: a GIS - Compatible Method for Groundwater Vulnerability Mapping, *Canadian Water Resources Journal*, 18(1), 25–37. doi: 10.4296/cwrj1801025.

Stumm, W. and Morgan, J. J. 1996. *Aquatic Chemistry - Chemical Equilibria and Rates in Natural Waters*. 3nd edn. Wiley and Sons, New York.

Swayze, G., Smith, K. S., Clark, R. N., Sutley, S. J., Pearson, R. M., Vance, S., Hageman, P. L., … Roth, S. 2000. Using Imaging Spectroscopy To Map Acidic Mine Waste Using Imaging Spectroscopy To Map Acidic Mine Waste, *Environmental Science and Technology*, 34, 47–54. doi: 10.1021/es990046w.

Tabatabai, M. A. 1987. Physicochemical fate of sulfate in soils, *Journal of the Air Pollution Control Association*, 37(1), 34–38. doi: 10.1080/08940630.1987.10466194.

Takagi, H. and Hayashi, I. 1991. NN-driven fuzzy reasoning, *International Journal of Approximate Reasoning*, 5(3)

Telford, W. M., Geldart, L. P. and Sheriff, R. E. 1990. *Applied Geophysics*. 2nd edn. New York: Cambridge University Press

Thirumalaivasan, D., Karmegam, M. and Venugopal, K. 2003. AHP-DRASTIC: software for specific aquifer vulnerability assessment using DRASTIC model and GIS, *Environmental Modelling and Software*, 18(7), 645–656. doi: 10.1016/S1364-8152(03)00051-3.

du Toit, W. H. and Sonnekus, C. J. 2014. *An explanation of the 1:500 000 general hydrogeological map, Nelspruit 2530.* Pretoria: Department of Water and Sanitation.

Tuğrul, A. 2004. The effect of weathering on pore geometry and compressive strength of selected rock types from Turkey, *Engineering Geology*, 75(3–4), 215–227. doi: 10.1016/j.enggeo.2004.05.008.

U.S Environmental Protection Agency. 1977. *The report to Congress: Waste disposal practices and their effects on water*. Washington DC.

United State Geological Survey (USGS). 2016. *Earth Explorer–SRTM*, *United State Geological Survey*. Available at: www.earthexplorer.usgs.gov (Accessed: 30 March 2016).

United State Geological Survey (USGS). 2017. *Shuttle Radar Topography Mission (SRTM).* Available at: ftp://ftp.glcf.umd.edu/glcf/SRTM/Degree_Tiles/ (Accessed: 30 March 2017).

Vías, J. M., Andreo, B., Perles, M. J. and Carrasco, F. 2005. A Comparative Study of Four Schemes for Aquifer vulnerability Mapping in a Diffuse Flow Carbonate Aquifer under Mediterranean Climatic Conditions, *Environmental Geology*, 47, 586–595.

Voss, F. D. and Tesoriero, A. J. 1997. Predicting the Probability of Elevated Nitrate Concentrations in the Puget Sound Basin: implication for aquifer susceptibility and vulnerability, *Groundwater*, 35(6), 1029–1039.

Vrba, J. and Zoporozec, A. 1994. Guidebook on mapping groundwater vulnerability, in *International Contributions to Hydrogeology*. VerlagHeinzHeiseGmbHand Co. KG.

Weaver, J. M. C., Cave, L. and Talma, A. S. 2007. *Groundwater sampling: Comprehensive guide for sampling methods: TT 303/07*. Pretoria.

Werbos, P. J. 1990. Back propagation through time: what it does and how to do it, *Proceedings of the IEEE*, 78(10), 1550–1560.

Wild, A. 1996. *Soils and the environment*. Cambridge: Cambridge Univeristy Press.

Wolff, R. G. 1982. *U.S. Geological Survey Water-Resources Investgations Open-File Report 82–166. Reston, VA Physical Properties of Rocks–porosity, Permeability, Distribution Coefficients, and Dispersivity, vol. 118.*

Woodford, A. C. and Chevallier, L. 2002. *Hydrogeology of the Main Karoo Basin: Current Knowledge and Future Research Needs*. Pretoria: Water Research Commission. Available at: http://www.wrc.org.za/Knowledge Hub Documents/Research Reports/TT179-02.pdf.

World Coal Association. 2012. *Coal – Energy for Sustainable Development*. London, UK. Available at: www.worldcoal.org.

Wright, W. G., Simon, W., Bove, D. J., Mast, M. M. and Leib, K. J. 2001. Distribution of pH Values and Dissolved Trace-Metal Concentrations in Streams, in Church, S. E., von Guerard, P., and Finger, S. E. (eds) *Integrated Investigations of Environmental Effects of Historical Mining in the Animas River Watershed, San Juan County, Colorado*. U.S. Geological Survey, 501–539.

Wyborn, L. A. I., Heinrich, C. A. and Jaques, A. L. 1994. Australian Proterozoic mineral systems: essential ingredients and mappable criteria, in *Australian Institute of Mining and Metallurgy Annual Conference*, 109–115.

Wyman, D. A., Cassidy, K. F. and Hollings, P. 2016. Orogenic gold and the mineral systems approach: resolving fact, fiction and fantasy, *Ore Geology Reviews*. Elsevier B.V, 78, 322–335. doi: 10.1016/j.oregeorev.2016.04.006.

Xenonstack. 2017. *Overview of Artificial Neural Networks and its Applications*. Available at: https://www.xenonstack.com/blog/overview-of-artificial-neural-networks-and-its-applications (Accessed: 29 September 2017).

Yu, C., Yao, Y., Hayes, G., Zhang, B. and Zheng, C. 2010. Quantitative assessment of groundwater vulnerability using index system and transport simulation, Huangshuihe catchment, China, *Science of The Total Environment*, 408(24), 6108–6116. doi: 10.1016/j.scitotenv.2010.09.002.

Zadeh, L. A. 1965. Fuzzy sets, *Information and Control*, 8, 338–353.

Zaporozec, A. 1981. Groundwater Pollution and its sources, *GeoJournal*, 5, 457–471.

Zar, J. H. 1999. *Biostatistical Analysis. Upper Saddle River, NJ*. Prentice Hall.

Zhou, H., Wano, O. and Yang, Q. 1999. A multi-objective fuzzy pattern recognition model for assessing groundwater vulnerability based on the DRASTIC system, *Hydrological Sciences Journal*, 44, 611–618.

Zwahlen, F. 2003. *Vulnerability and risk mapping for the protection of carbonate (karst) aquifers, final report (COST action 620). European Commission, Directorate XII Science, Research and Development, Report EUR 20912*. Brussels.

APPENDICES

APPENDIX 1: SOIL BATCH LEACH EXPERIMENT

Appendix 1.1 Results of leachate analysis after the soil batch leach with AMD

Appendix 1.2 Results of leachate analysis after the soil batch leach with de-ionised water

Appendix 1.3 Results of major elements of soil samples analysed by XRF

APPENDIX 2: ROCK-AMD COLUMN LEACH EXPERIMENT

Appendix 2.1 Results of chemical analysis of leachate under saturated conditions

Appendix 2.2 Results of chemical analysis of leachate under unsaturated conditions

Appendix 2.3 Results of the mineralogical analysis of rock samples by XRD

Appendix 2.4 Results of the XRF analysis of the major elements of rock samples

APPENDIX 3: DETERMINATION OF OPTIMAL DATA-DRIVEN MODEL PARAMETERS

Appendix 3.1: Epoch determination algorithm for data-driven approaches

Binary map data are feed into a data-driven AI algorithm where training is carried out at various training iterations (epochs) and a fixed initial number of neurons in the hidden layer for ANN training. No number of neurons in the hidden layer is specified for the ANFIS system. The initial number of neurons in the hidden layer for ANN modelling may be determined by multiplying the number of inputs by two and adding one according to a simple rule formulated by Shigidi and Garcia (2005). Thus, in the case of ten input layers, the initial number of neurons in the hidden layer is 21 (from calculation: 10 x 2 + 1). This value is used for initialising the ANN but will be optimised by the hidden layer, determining the algorithm which will be executed once the optimum number of epochs has been determined.

For each training epoch, the data-driven AI is trained and used to determine the output values of each of the training points. The predicted value (f_{ei}) from the data-driven AI is compared with the actual values (y_{ei}) and the error returned is for each training point. The errors are then combined for each epoch and a mean square of errors (MSE) (MSE_{epoch}) for each training epoch recorded. The MSE_{epoch} value for each training epoch is calculated using Equation A1 (De Oliveira *et al.*, 2011):

$$MSE_{epoch} = \frac{1}{N}\sum_{i=1}^{N}(f_{ei} - y_{ei})^2 \qquad \text{A1}$$

Where N represents the number of data points, f_{ei} is the value predicted by the program and y_{ei} is the actual value for the data point i.

A graph of each epoch training value and the corresponding MSE_{epoch} values is produced (Figure A1). The epoch training value with the lowest MSE_{epoch} value is returned as the optimal number of epochs (M) such as M_2 in the example in Figure A1. The MSE_{epoch} is also called the "error rate".

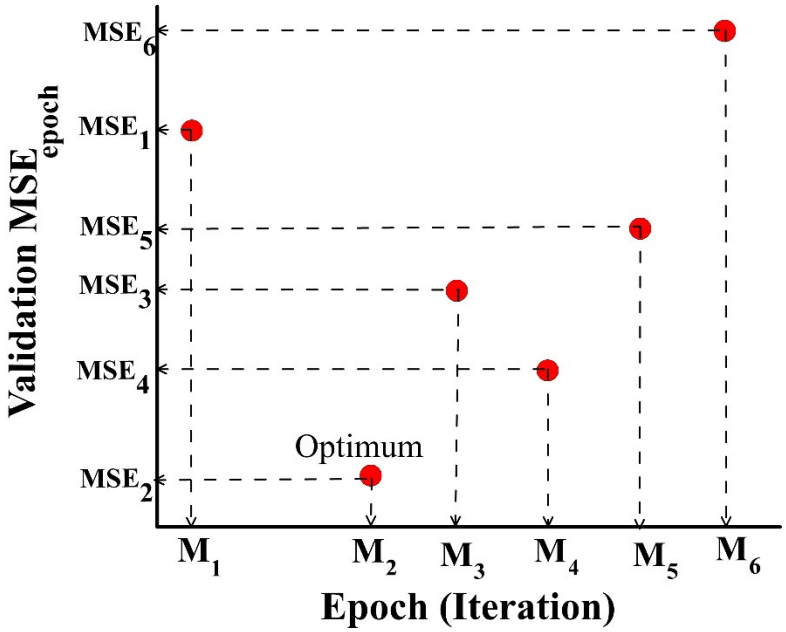

Figure A1: Determining the optimum number of epochs with minimum validation MSE

Appendix 3.2: Hidden layer neuron number determination algorithm for data-driven approaches

Using the optimum number of epochs (M) as fixed, the ANN algorithm is run with varying number of neurons in the hidden layer. For each neuron hidden layer training step, the ANN is used to determine the output values of each of the training points. The predicted value (f_{hi}) from the ANN network is compared with the actual values (y_{hi}) and the error ($f_{hi} - y_{hi}$) is returned for each training

point. The errors are then combined for each number of neurons in the hidden layer and an MSE (MSE_{hidden}) for each number of neurons in the hidden layer is recorded. The MSE_{hidden} is calculated using Equation A2 (De Oliveira *et al.*, 2011):

$$MSE_{hidden} = \frac{1}{N}\sum_{i=1}^{N}(f_{hi} - y_{hi})^2 \qquad \text{A2}$$

Where N the number of data points is, f_{hi} is the value predicted by the program and y_{hi} is the actual value for the data point i.

A graph of each number of neurons in the hidden layer and the corresponding MSE_{hidden} values is produced. The number of neurons in the hidden layer with the lowest MSE_{hidden} value is returned as the optimum number of neurons in the hidden layer (H), such as H_3 in the example in Figure A2.

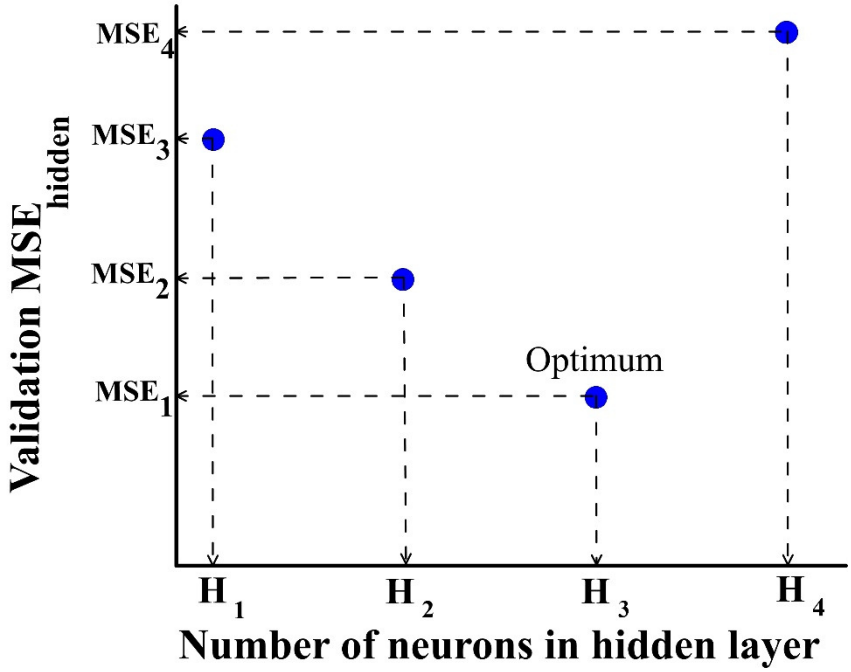

Figure A2: Determining the optimum number of neurons in the hidden layer with minimum validation MSE

Appendix 3.3: Data splitting algorithms

Using the optimum number of hidden layer neurons (H) and epochs (M), the data-driven (ANN or ANFIS) algorithm modelling can be done. First, an assessment of the method/technique for validation needs to establish if the resultant models are scientifically defensible.

With access to an unlimited number of examples (training points), models can be generated by simply choosing the model with the lowest error rate. However, in real applications, for example, using borehole data over a given area, only a finite set of points are available for training, and therefore

other approaches need to be devised (Makarevich, 2015). One approach is to use the entire dataset for training to generate the model and then to estimate the error in predicting the same points which were used for the training. However, this naive approach is likely to over-fit the training data in the final model. That is, the model will accommodate the training data but usually fail to predict/classify new data after the training process (Makarevich, 2015). The trained model is intended to be a generalised model so that it can accommodate irregularities and variations in future data that will be used for predications classification. In addition, the performance of the model is unknown as no known points were kept and used for validation. This problem can be solved by cross-validation, which is a process whereby the dataset is split into three distinct subsets for training, validation and testing (Makarevich, 2015) (Figure A3). The training dataset refers to a set of examples (points) used for learning to fit the parameters of the model. The validation dataset is a set of examples (point) used to fine-tune the model. The testing dataset comprises a set of examples (points) used only to assess the performance of a fully trained model. After assessing the final model with a test dataset, no further training is done. There are various ways to split datasets, with the most commonly used techniques being:

- holdout method;
- random subsampling;
- k-fold cross-validation; and
- leave-one-out cross-validation.

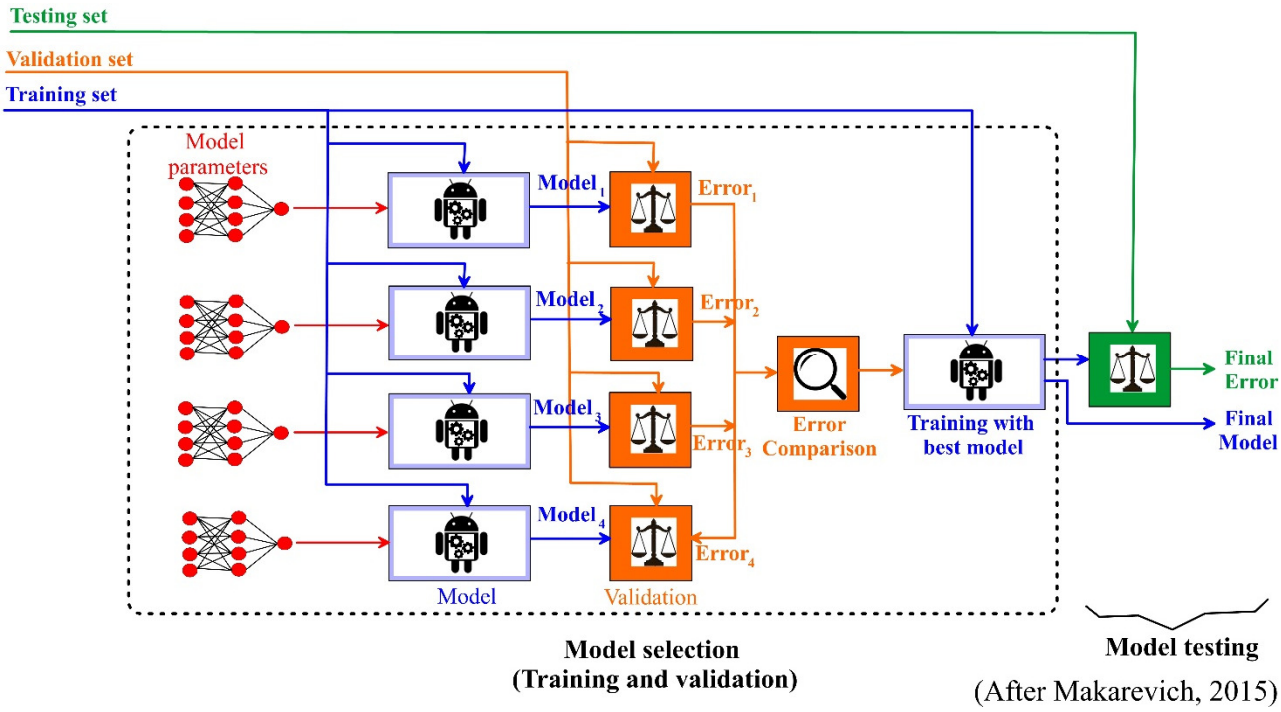

(After Makarevich, 2015)

Figure A3: Illustration of three way data splitting

Holdout method

In this technique, the dataset is split into training, testing and validation datasets, where a small portion of the data are selected for testing and the rest divided into a training-validating dataset (Figure A4). This approach is a once off train-validate experiment (Remesan and Mathew, 2014). The dataset is split into training/validation according to proportions decided by the expert, for example: 70/30, 75/25, 80/20 (Iqbal and Rizwan, 2009; Ignacio *et al.*, 2013; Gholami *et al.*, 2015).

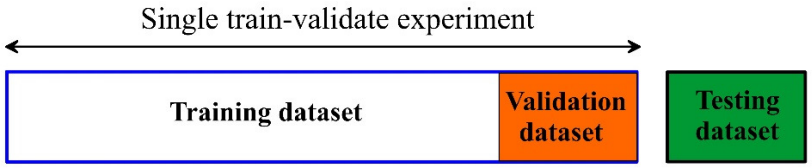

(After Remesan and Mathew, 2014)

Figure A4: Holdout method splitting the dataset into training, validation and testing sets

Training is then done and the trained model used to predict/classify values of the validating dataset to obtain the validation error. This model is then assessed by predicting/classifying values of the testing dataset to obtain the performance of the model.

Problems arise when the dataset is sparse and the researcher cannot afford to set aside a portion of the dataset for validation or testing. Another problem that can occur is when the split between training and validation is inappropriate or unfortunate. Despite these drawbacks, this method is used by several authors (Iqbal and Rizwan, 2009; Ignacio *et al.*, 2013; Gholami *et al.*, 2015) for its fast computation time as the training/validation process is a single operation.

This technique raises the question as to which splitting proportion is considered correct or best as the split is determined by the expert running the models and the accuracy of the resultant model is often questionable. Another consideration is which points to select as training points and which as validation datasets. These problems, related to the holdout method, can be solved by the random subsampling technique.

Random subsampling

In this approach, the data are split into two smaller groups, one for training-validation and the other for testing. The training-validation dataset is then randomly split further into a small portion for validation and the remainder for training. Training is done using the training dataset and the trained model used to predict the values of the validation dataset is termed experiment 1. The training-validation dataset is then split randomly again, but this time using a different random combination to that used in experiment 1, constituting experiment 2. This process of splitting the training-validation dataset continues until all the possible random combinations have been used, after which the

combination with the lowest validation error is selected as the best model (Figure A5). This best model will then be assessed for its performance by using it to predict/classify values of the test dataset. This technique produces better results than the holdout technique. The results from the approach where examples (points) are chosen randomly are also still debatable, as the random selection is not repeated in the event that one wants to run the model again. Thus, the model generated using randomly generated training/validation splitting is barely repeatable and may cause problems of model repeatability, one of the key fundamental requirements for the generation of a groundwater vulnerability model intended for critical policy and decision-making.

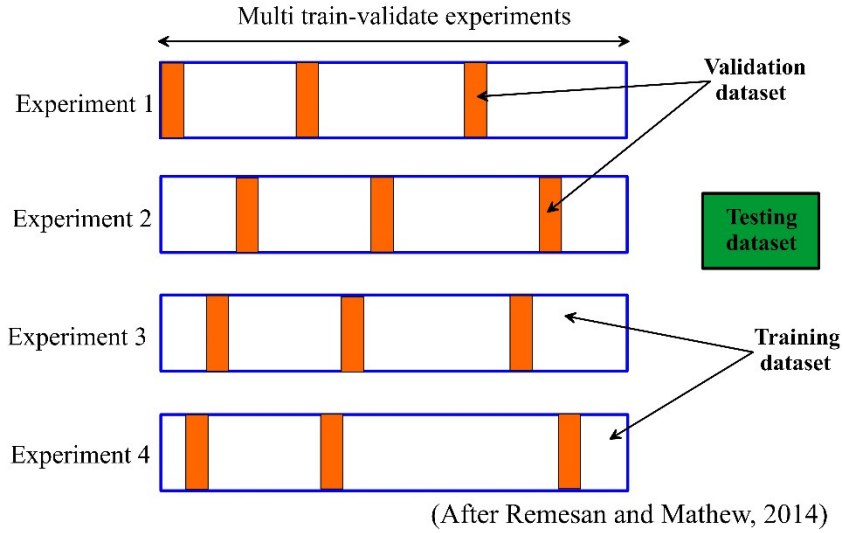

Figure A5: Random subsampling and splitting of the dataset into training, validation and testing sets

K-fold cross-validation

In this technique, the dataset is first split into training-validation and testing datasets. Then the training-validation dataset is further split into a K number of folds, where K is the number of splits. The technique is almost similar to the random subsampling technique, with the only difference being that instead of splitting the train-validate dataset randomly, the dataset is split in a sequential manner, as shown in Figure A6. The number of folds is selected where, for a large number of folds, the bias of the validation error will be small but the variance will be large because the size of the test set will have been greatly reduced. The computation time will be longer for many folds. If a smaller-sized fold is used, the computation time is greatly reduced and the variance will be small, but the bias larger. Thus, the number of folds depends on the size of dataset — for a larger dataset, even the threefold approach gives good results. For a smaller dataset, the leave-one-out method is preferable.

In machine learning, the tenfold method is the most common cross-validation method, as it offers a good compromise between processing time, bias and variance as the model is generated using over 90% of the dataset. This makes it more likely to be generalisable to the full data spectrum. This benefit

of the tenfold cross-validation method was illustrated by Kohavi (1995) after comparing several approaches, including the leave-one-out, bootstrap and stratified tenfold approaches.

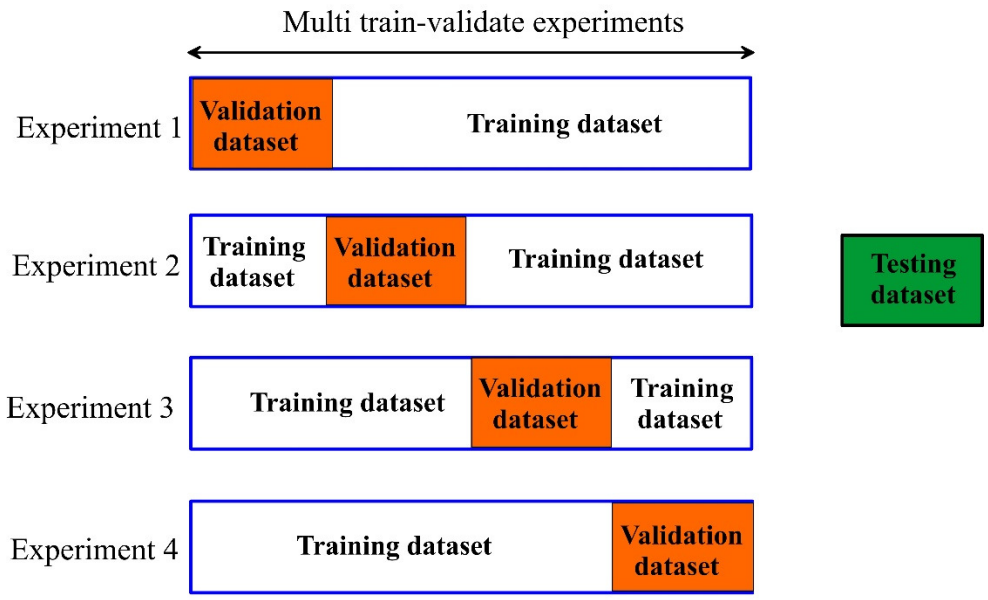

(After Remesan and Mathew, 2014)

Figure A6: K-fold cross-validation splitting of the dataset into training, validation and testing

To avoid the generation of folds which do not account for ones and zeros in each fold, stratified k-folding is used.

Leave-one-out cross-validation

In this technique, the dataset is first split into training-validation and testing datasets, after which the training-validation dataset is further split. The leave-one-out technique is a special case of the k-fold technique where the number of folds equals the number of instances in the datasets (Figure A7). Thus, for a dataset with N examples (points), N experiments are performed where, for each experiment, N-1 examples are used for training while the remaining examples (points) are used for validation.

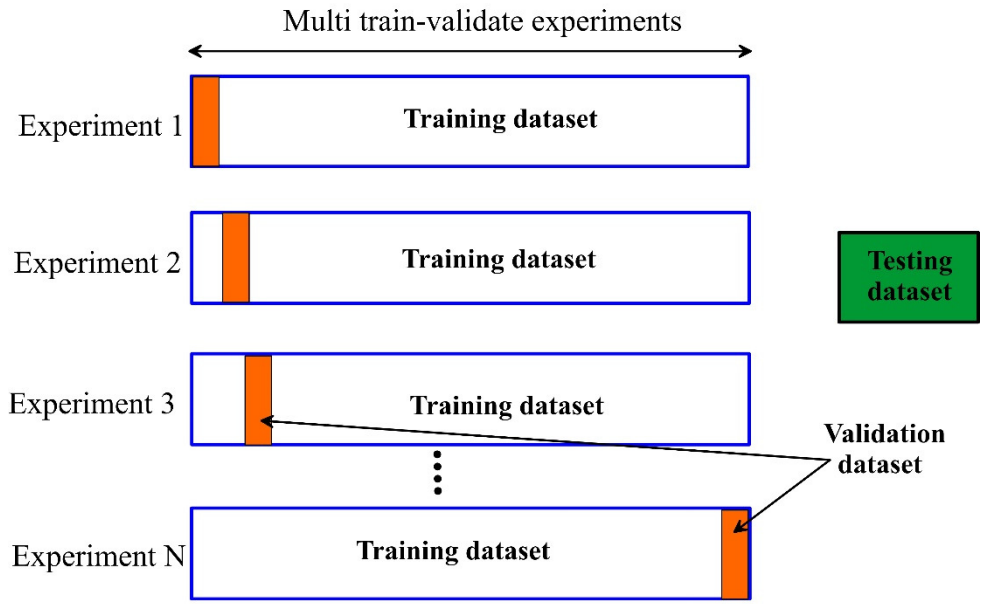

(After Remesan and Mathew, 2014)

Figure A7: Leave-one-out cross-validation splitting of the dataset into training, validation and testing

The leave-one-out technique of splitting the training-validation dataset involves the following simple steps:

11. For the given dataset, the first point (P_1) is extracted from the dataset as a validation dataset (V_1) and the remaining points as a training dataset (QX_1). The model is run and the trained model is used to predict the value of the first validation point denoted V_{p1}. This value is then compared with the actual output value (V_{out1}) and the difference between V_{p1} and V_{out1} is returned as the validation error (E_1).

12. The extracted point is returned into the original dataset and the first step repeated, but this time using the second point (P_2) and the error E_2 is generated as in the previous step. The process is repeated for all N training points and errors $E_1, E_2, \ldots\ldots, E_{n-1}$ returned. At the end of the splitting process, N errors are generated. A graph of $E_1, E_2, \ldots\ldots E_{n-1}$ against $P_1, P_2, \ldots\ldots, P_1$ is plotted and the best training split is the one with the fewest validation errors, as shown in Figure A8.

In order to understand how the training/validation algorithm works, consider an example where a given dataset has four training points, as shown in Table A2.

Table A2: Example of a dataset with four points for running the leave-one-out cross-validation technique

Training ID	Coordinates	Output data
P_1	X_1, Y_1	V_{out1}
P_2	X_2, Y_2	V_{out2}
P_3	X_3, Y_3	V_{out3}
P_4	X_4, Y_4	V_{out4}

The leave-one-out algorithm splits the dataset into training and validation datasets respectively, as shown in Table A3.

Table A3: Data splitting of a four points example using the leave-one-out algorithm

Training ID	Training dataset (QX)	Validation dataset (V)	Validation Error
P_1	QX_1 with (P_2, P_3, P_4) data values	V_1 with P_1 data value	E_1
P_2	QX_2 with (P_1, P_3, P_4) data values	V_2 with P_2 data value	E_2
P_3	QX_3 with (P_1, P_2, P_4) data values	V_3 with P_3 data value	E_3
P_4	QX_4 with (P_1, P_2, P_3) data values	V_4 with P_4 data value	E_4

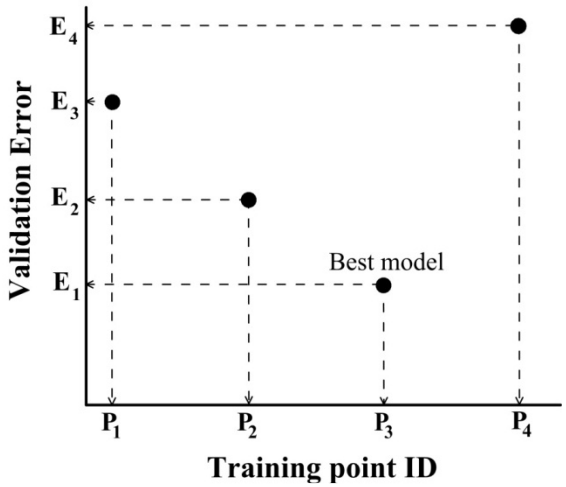

Figure A8: Leave-one-out cross-validation graph

To improve the repeatability of the model generation and to reduce the computational time in the design of data-driven models for groundwater vulnerability, the assessment tools to be developed would first verify the number of examples (points) and then decide between K-fold cross-validation for large datasets and leave-one-out cross-validation for small datasets.

APPENDIX 4: EXAMPLE OF HOW THE BACKPROPAGATION ALGORITHM WORKS

Consider a simple three-layer model with two inputs, a hidden layer with two neurons and one output, as shown in Figure A9:

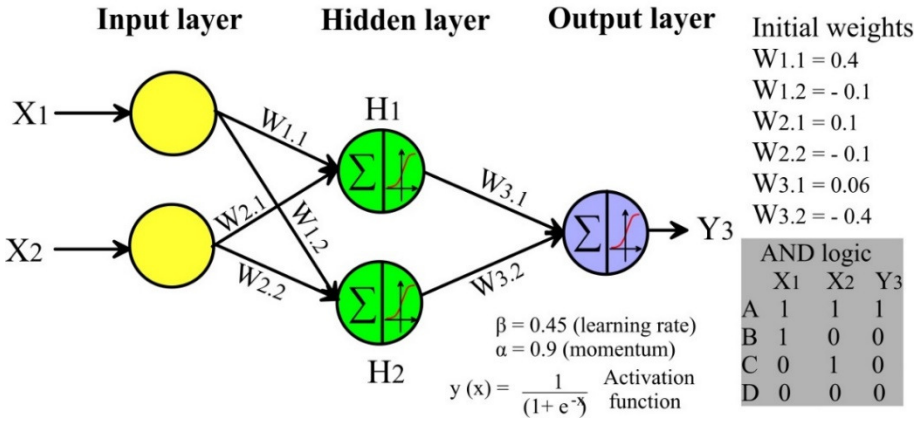

Figure A9: Example of how the back propagation algorithm works

As an illustration of how the back propagation algorithm works, training using dataset A of the AND logic was done, where inputs $X_1 = 1, X_2 = 1$ and the desired output $Y_3 = 1$. The bias was not used for simplicity. First, the feed-forward computations were done by calculating the output values ($Output_{H1}$ and $Output_{H2}$) for each hidden layer neuron by applying the activation function to the sum of the weighted inputs. These values were then used to calculate the network output ($Output_{y3}$).

$$Output_{H1} = f(X_1 * W_{1.1} + X_2 * W_{2.1}) = f(1 * 0.4 + 1 * 0.1) = f(0.5) = \frac{1}{(1 + e^{-0.5})} = 0.6225$$

$$Output_{H2} = f(X_1 * W_{1.2} + X_2 * W_{2.2}) = f(1 * -0.1 + 1 * -0.1) = f(-0.2) = \frac{1}{(1 + e^{0.2})} = 0.4502$$

$$Output_{y3} = f(H_1 * W_{3.1} + H_2 * W_{3.2}) = f(0.6225 * 0.06 + 0.4502 * -0.4) = f(-0.14271) = 0.4644$$

At this point, the feed forward computations were complete. The next step was to calculate the output error ($error_{y3}$) and to propagate it backwards to the hidden layer-output layer connections to calculate the new weights ($W_{3.1(new)}, W_{3.2(new)}$).

$$error_{y3} = O_{y3} * (1 - O_{y3}) * (O_{target} - O_{y3}) = 0.4643 * (1 - 0.4643) * (1 - 0.4643) = 0.13323$$

$$\Delta W_{3.1} = \beta * error_{y3} * H_1 = 0.45 * 0.13323 * 0.6225 = 0.03732$$

$$W_{3.1(new)} = W_{3.1(old)} + \Delta W_{3.1} + \alpha * \Delta(t-1) = 0.06 + 0.03732 + 0.9 * 0 = 0.09714$$

$$\Delta W_{3.2} = \beta * error_{y3} * H_2 = 0.45 * 0.13323 * 0.4502 = 0.02699$$

$$W_{3.2(new)} = W_{3.2(old)} + \Delta W_{3.2} + \alpha * \Delta(t-1) = -0.4 + 0.0699 + 0.9 * 0 = -0.3730$$

Where $\Delta(t-1)$ is zero for the first iteration.

After calculating the new weights for the hidden layer-output layer connections, the next step was to propagate the error back to the input layer-hidden layer connections. This was done by multiplying the new weights ($W_{3.1(new)}, W_{3.2(new)}$) by the output error ($error_{y3}$), after which the delta changed in the weights ($\Delta W_{1.1}$, $\Delta W_{2.1}$, $\Delta W_{1.2}$ and $\Delta W_{2.2}$). The input layer-hidden layer neurons were calculated and, ultimately, the new input layer-hidden layer weights ($W_{1.1(new)}, W_{2.1(new)}, W_{1.2(new)}$ and $W_{2.2(new)}$) were computed.

$$error_{H1} = error_{y3} * W_{3.1(new)} = 0.1332 * 0.09713 = 0.012965$$

$$error_{H2} = error_{y3} * W_{3.2(new)} = 0.1332 * -0.3730 = -0.04971$$

$$\Delta W_{1.1} = \beta * error_{H1} * X_1 = 0.45 * 0.01296 * 1 = 0.05834$$

$$\Delta W_{2.1} = \beta * error_{H1} * X_2 = 0.45 * 0.01296 * 1 = 0.05834$$

$$\Delta W_{1.2} = \beta * error_{H2} * X_1 = 0.45 * -0.04971 * 1 = -0.02237$$

$$\Delta W_{2.2} = \beta * error_{H2} * X_2 = 0.45 * -0.04971 * 1 = -0.02237$$

$$W_{1.1(new)} = W_{1.1(old)} + \Delta W_{1.1} + \big(\alpha * \Delta(t-1)\big) = 0.4 + 0.005834 + 0.9 * 0 = 0.4058$$

$$W_{2.1(new)} = W_{2.1(old)} + \Delta W_{2.1} + \big(\alpha * \Delta(t-1)\big) = 0.1 + 0.005834 + 0.9 * 0 = 0.1054$$

$$W_{1.2(new)} = W_{1.2(old)} + \Delta W_{1.2} + \big(\alpha * \Delta(t-1)\big) = -0.1 + (-0.02237) + 0.9 * 0 = -0.1224$$

$$W_{2.2(new)} = W_{2.2(old)} + \Delta W_{2.2} + \big(\alpha * \Delta(t-1)\big) = -0.1 + (-0.02237) + 0.9 * 0 = -01224$$

Once all the new weights had been calculated the same process was followed for training datasets B, C and D and the overall error for the first iteration could be calculated using the mean square error.

For the second iteration (2), the weights from the first iteration were used:

$$Output_{H1} = f\big(X_1 * W_{1.1(new)} + X_2 * W_{2.1(new)}\big) = f(0.406 + 0.1) = 0.6236$$

$$Output_{H2} = f\big(X_1 * W_{1.2(new)} + X_2 * W_{2.2(new)}\big) = f(-0.1224 - 0.122) = 0.4393$$

$$Output_{y3\,(2)} = f\big(H_1 * W_{3.1(new)} + H_2 * W_{3.2(new)}\big) = f(0.6225 * 0.097 + 0.4393 * -0373) = 0.4714$$

$$error_{y3(2)} = O_{y3(2)} * \big(1 - O_{y3(2)}\big) * \big(O_{target} - O_{y3(2)}\big) = 0.4714 * (1 - 0.4714) * (1 - 0.4714) = 0.131102$$

Thus, after the initial iteration, the calculated error was 0.133225 and the new calculated error was 0.131102. Therefore, the algorithm had been improved, albeit not by much. However, this example should illustrate how the back propagation algorithm works.

APPENDIX 5: EXAMPLE OF HYBRID LEARNING OF THE ANFIS SYSTEM

Let us consider an example with two inputs x, y, with fuzzy memberships A, B, respectively and output f. Two rules are defined, relating the inputs to the output given as:

Rule 1: IF x is small (A_1) AND y is small (B_1) THEN f_1 is small,

Rule 1: IF x is large (A_2) AND y is large (B_2) THEN f_1 is large.

The hybrid learning protocol is used with the following parameters to calculate the output of the trained network given the inputs $x = 3$ and $y = 4$.

- bell function with parameters $(a = 2, b = 1, c_{A1} = 1, c_{B1} = 2, c_{A2} = 9, c_{B2} = 14,)$ used to define the membership functions of the two inputs; and
- coefficients of the output membership function given by: $p_1 = 0.1,\ q_1 = 0.1,\ r_1 = 0.1,\ p_2 = 10,\ q_2 = 10, r_2 = 10.$

First, the calculations are calculated using Equation 7.9 to generate membership functions for each rule:

$$\mu_{A1}(x) = \frac{1}{1 + \left|\frac{x-1}{2}\right|^2}, \mu_{B1}(y) = \frac{1}{1 + \left|\frac{y-2}{2}\right|^2}$$

$$\mu_{A2}(x) = \frac{1}{1 + \left|\frac{x-9}{2}\right|^2}, \mu_{B2}(y) = \frac{1}{1 + \left|\frac{y-14}{2}\right|^2}$$

Data are fed into the first layer where corresponding fuzzy membership values for each input are extracted from the membership function, as shown in Figure A10. The outputs from layer 1 are fed into layer 2, where they are summed to produce a result for each rule (Figure A11). The output from layer 2 then enters layer 3 and the data are normalised against all the other inputs to layer 3. The resultants are normalised values which are fed into layer 4.

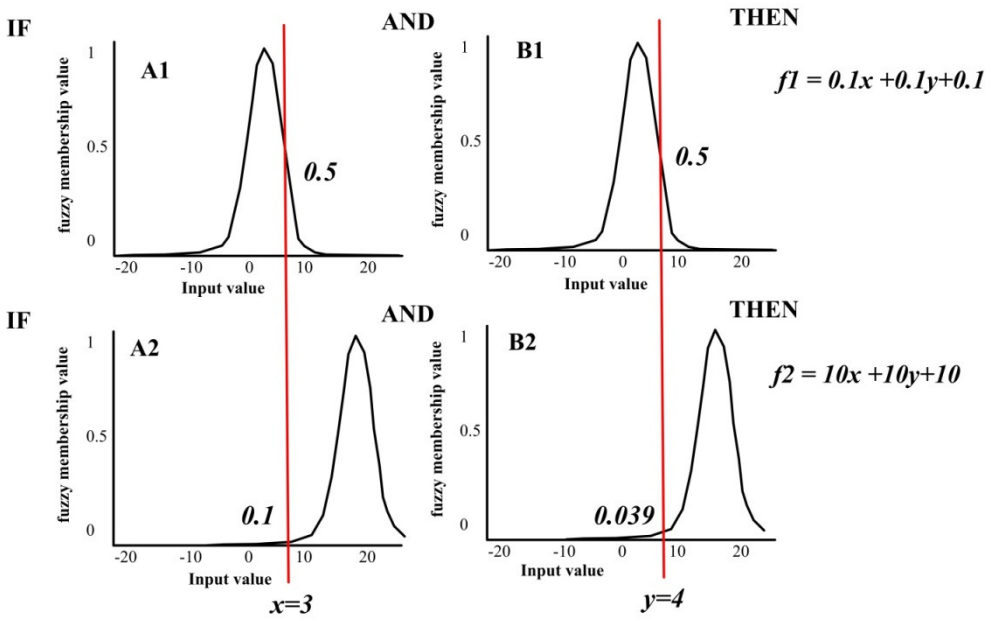

Figure A10: Plot of fuzzy membership function for each of the rules

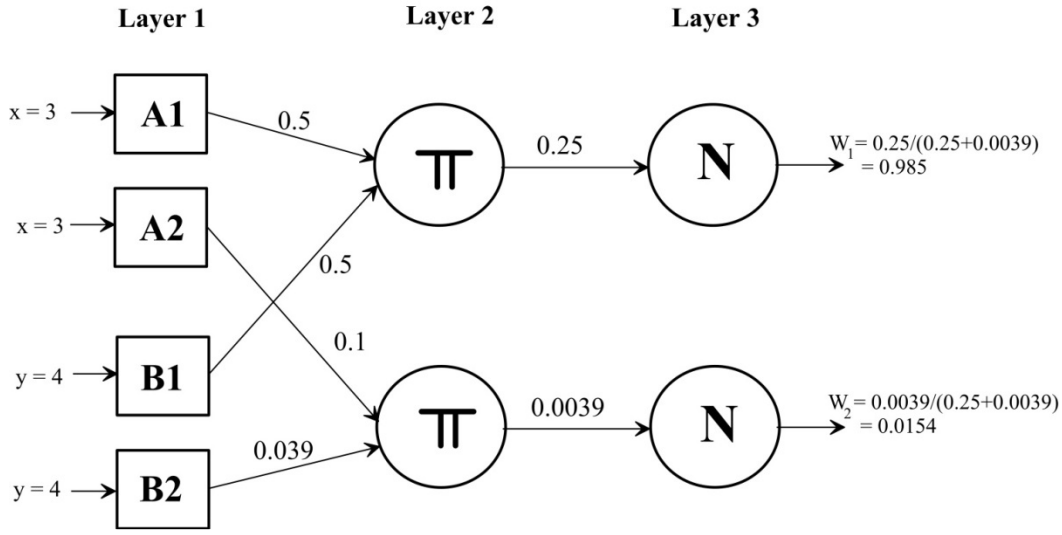

Figure A11: Example of calculations and layer connections for layers 1, 2 and 3

The normalised result from layer 3 enters layers 4 where it is combined with inputs using Equation 7.4. The output of layer 4 then enters layer 5 where all the outputs from layer 4 of all the rules are summed together to produce one output result, using Equation 7.5. The output value is then compared with the actual value and the error is calculated and propagated backwards. The parameters are adjusted and the process continues until the error has been sufficiently reduced for the training process to be terminated. At that time the network is termed "trained" and will be ready for use in solving the particular problem.

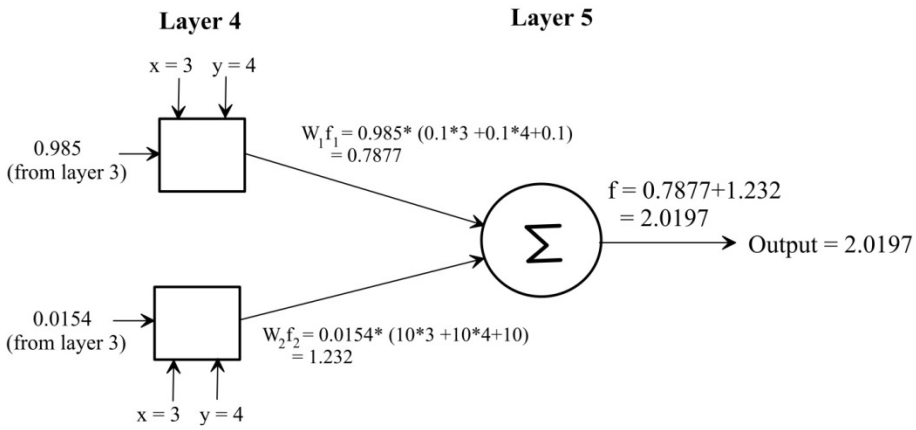

Figure A12: Example of calculations and layer connections for layers 4 and 5

APPENDIX 6: GVAI SOFTWARE OPERATING MANUAL

Program functionality

The Groundwater Vulnerability Artificial Intelligence (GVAI) software is a computer program used for the generation of groundwater vulnerability models using the three most common AI algorithms (Fuzzy Expert system, Artificial Neural Networks (ANN) and the Adaptive Neuro-Fuzzy Inference System (ANFIS).

The software also allows for automatic and semi-automatic processing and the generation of groundwater vulnerability models. The friendly interface of the software and many opportunities in the semi-automatic mode for AI modelling allows solving complex geological and hydrogeological conditions with great efficiency. The current version only runs on a IBM-PC compatible computers equipped with Windows.

System requirements

The GVAI software can be installed on a PC with OS Windows 98 and higher. The recommended system parameters are:

- processor > 2 GHz;
- memory at least 512 Mb; and
- screen resolution of 1 024 x 768 colour mode.

As the software actively uses the registry and writes in the C drive, it is recommended that the software be launched using administrator's read/write rights.

Program installations

To install the program, copy the files from the CD and create a directory in the computer. Updating simply entails overwriting the previous directory with the new directory files.

Program operation

Launch page

On the launch page the following can be done:

- to access the GVAI software modules, click the button "LAUNCH PROGRAM" and the software opens the data input module;

- to access to the manual, click the “HELP” button and the software will open the manual file in pdf format; and
- to access the software details and version, click the “ABOUT” button which will display a window.

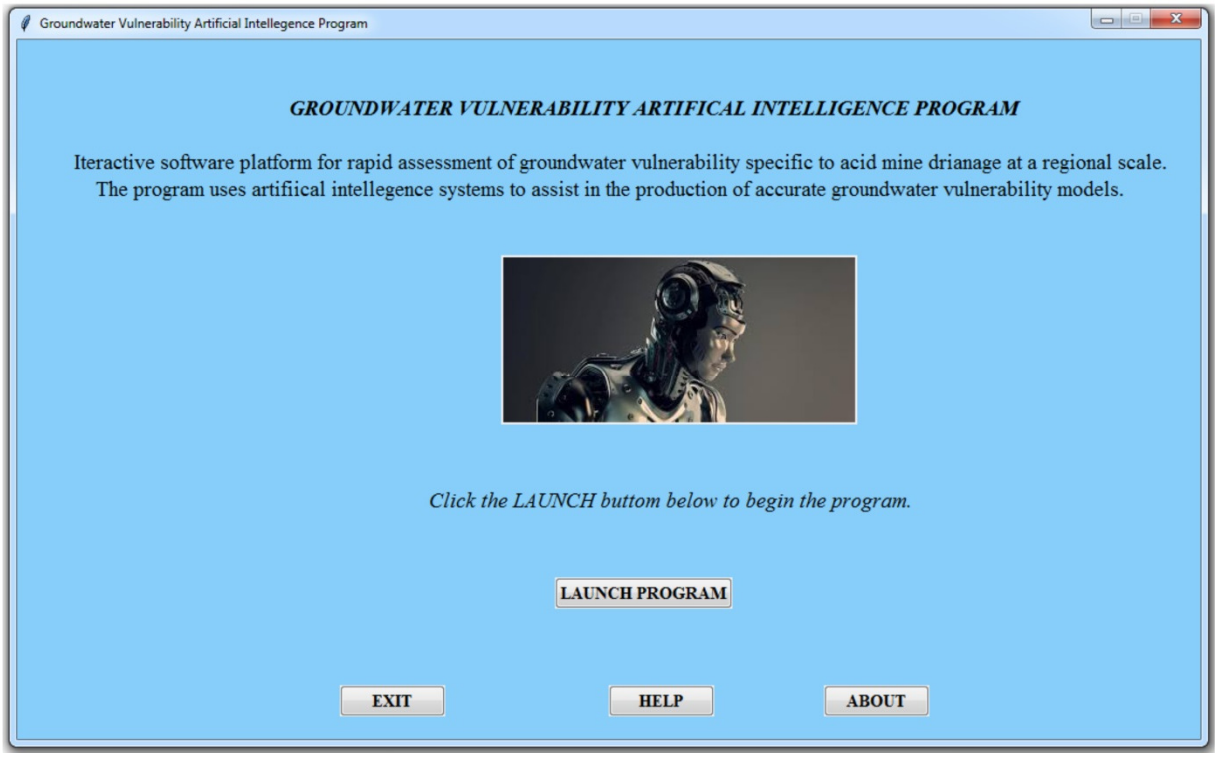

Figure A13: GVAI launch module

Data input module

The data input module facilitates loading all the relevant datasets and viewing them before proceeding to the other modules. This version of the software only works with (geotif) raster and (.csv) vector data types. The software only takes in the geotif which must comprise a similar number of rows, columns and grid cell sizes. Hence, it is strongly recommended that the user first prepare the input maps using GIS software such as ArcGIS, QGIS or MapINFO.

Figure 8.3 shows the GUI of the data input window. First, load each of the ten raster map layers using the corresponding “Browse” button next to the map name and view the map by clicking the corresponding “Plot” button. Once all ten maps have been added to the program, the program will pose question “*Are groundwater pollution data available*?”

If such data are indeed available, then click the “YES” button and the borehole point browse and plot buttons are enabled prompting the user to load this data file into the program. At the same time the previously disabled knowledge-driven approach (Fuzzy Expert system) and data-driven approaches (ANN and ANFIS) buttons are enabled. Thus, with the ten maps and pollution data loaded, the user

can execute both the knowledge and data-driven approaches. Alternatively, if the answer is "NO", then only the knowledge-driven approach (Fuzzy Expert system) button will be enabled.

Click the "*RETURN TO HOME PAGE*" button to return back to the launch page. This will refresh the entire program.

Click the "*HELP*" button to open the user manual which describes and gives a detailed step by step outline of the program functions.

Clicking the "*ABOUT*" leads the program to open a pop-up window which shows the software details including the version, copyright and disclaimer.

A description of each of the ten input maps is given below:

Rainfall - This map shows the rainfall distribution over a given area. The rainfall can be average long term, annual, monthly or a single rain event. The typical unit is millimetres (mm).

Slope – This map shows the topographic change in slope expressed in percentage (%). This can be generated from any topographic data, but SRTM data are free to download from the Internet.

Distance to surface sources – These map data refer to a distance map generated from mapped sources of surface sources. The sources can be mapped by physically recording GPS coordinates of potential sources and using this information to generate a distance map. Alternatively, the sources of AMD may be interpreted by using the mapping of the secondary iron-bearing minerals which are often indicators of AMD.

Distance to subsurface sources – This map is a distance map derived from the geology map showing the rocks where there are coal seams within the study area. The vector geology polygon of the host should be extracted from the geology vector map and changed to raster format to create a distance map from the information. ArcGIS, QGIS and any other GIS can be used for the creation of the distance to subsurface sources map.

Soil clay content – This map is a raster map showing the distribution of the soil clay over the study area. The clay content is expressed as a percentage values.

Relative hydraulic conductivity – This map shows the relative hydraulic conductivity of various aquifers within the area to be modelled. The values are ranked between 1 and 10, where 10 is the aquifer with the highest and 1 the lowest hydraulic conductivity values.

Distance to pathways – This map is a distance map derived from mapped lineaments from geophysical interpretation and/or geology maps. The vector lines of the lineaments are changed to raster format from which a "distance from pathway" map is created. ArcGIS, QGIS and any other GIS can be used to create the distance to subsurface maps.

Relative rock permeability – This map shows the relative permeability of various rocks within the area to be modelled. The values are ranked between 1 and 10, where a value of 10 is assigned to rocks with high permeability values and 1 is assigned to the rocks with the lowest permeability value. The values of permeability can be measured in the field or laboratory or extracted from publications.

Relative rock-AMD reactivity – This map shows the relative hydraulic conductivity of various aquifers within the area to be modelled. The values are ranked between 1 and 10, where 10 is the aquifer with the highest and 1 the lowest hydraulic conductivity values.

Depth to water table – This map shows the distance from the surface to the water table, as measured in boreholes within the area to be modelled. Data can be collected over the area to be modelled and interpolation methods used to create the map.

Borehole points – The data format should be an .csv file in the following format:

X	Y	SO4	Sulphate
784154	6958117	1	0.4
716826	7097336	0	256

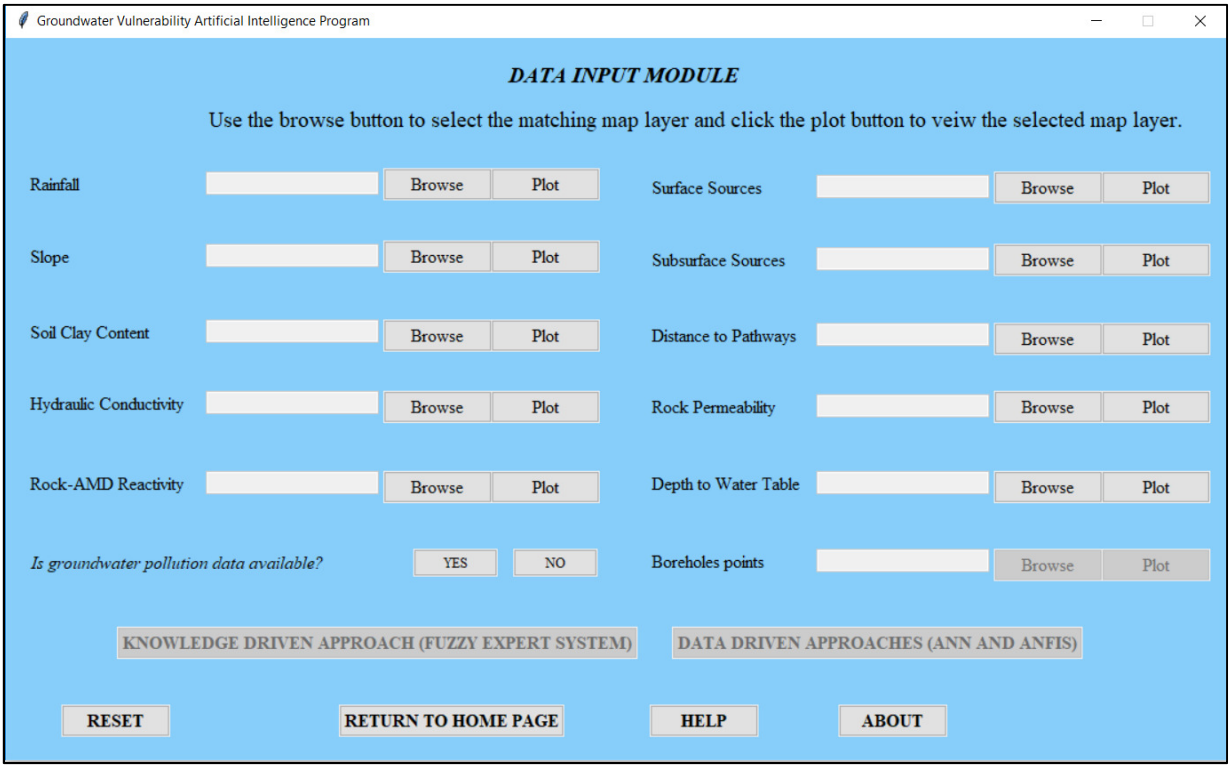

Figure A14: Input module window

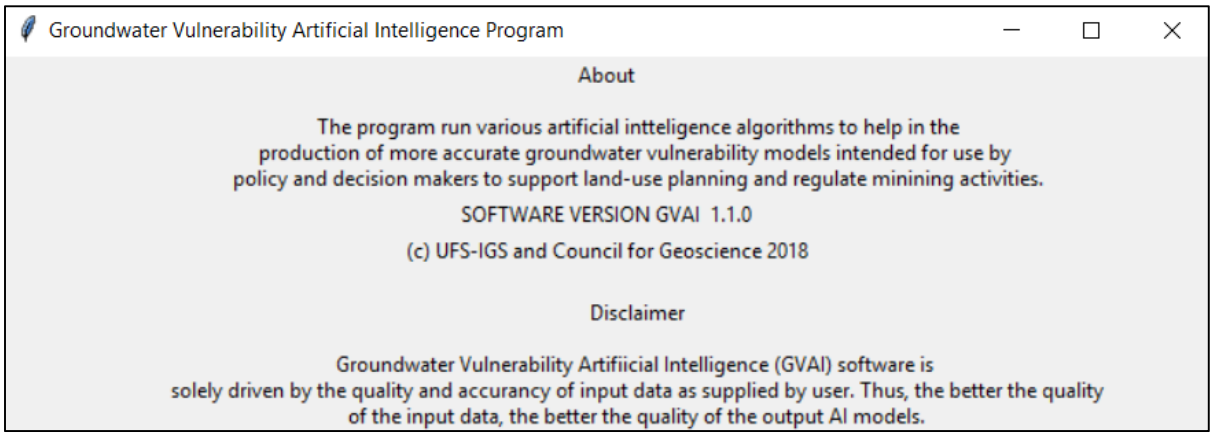

Figure A15: About window

As a demonstration of the functionality of the program, data for the Witbank, Ermelo and Highveld coalfield will be used. Using the steps for loading maps to the program, the following is an example of a view of the rainfall data in the program.

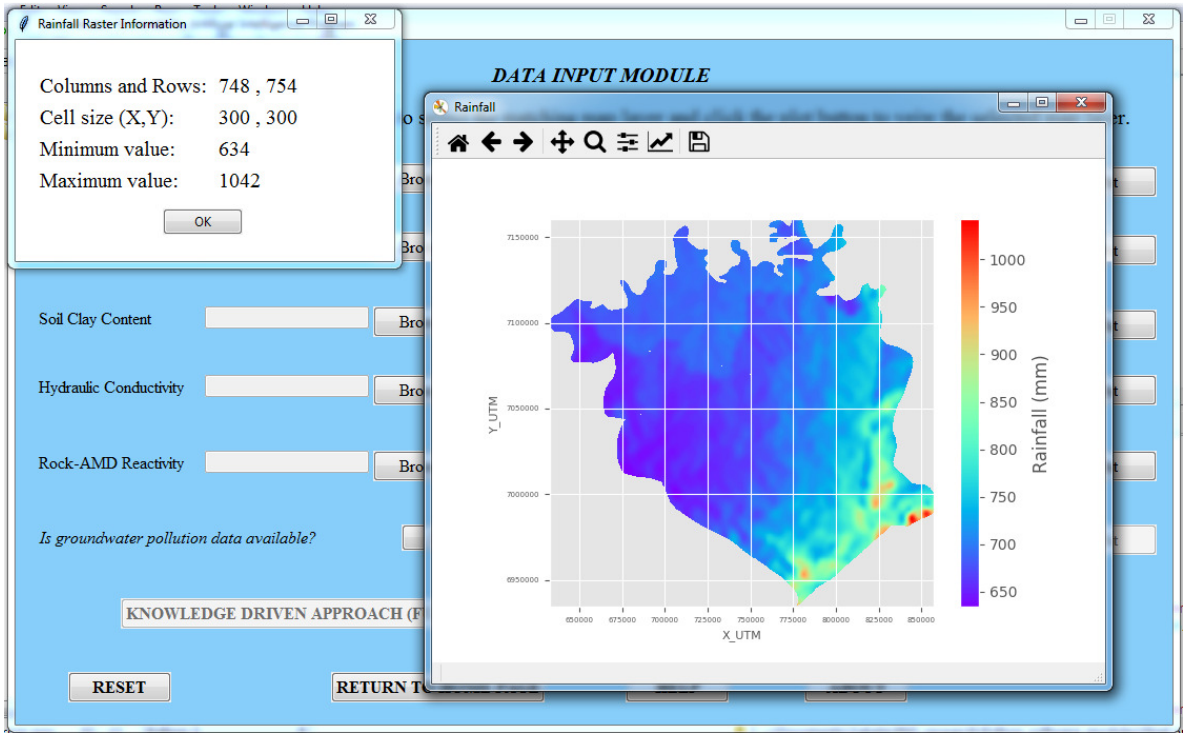

Figure A16: Input module window

Figure A16 presents a screen shot of the result when the plot button is pressed for a rainfall map layer. The window shows the spatial distribution of rainfall together with raster information (cell size, minimum, maximum and the number of rows and columns).

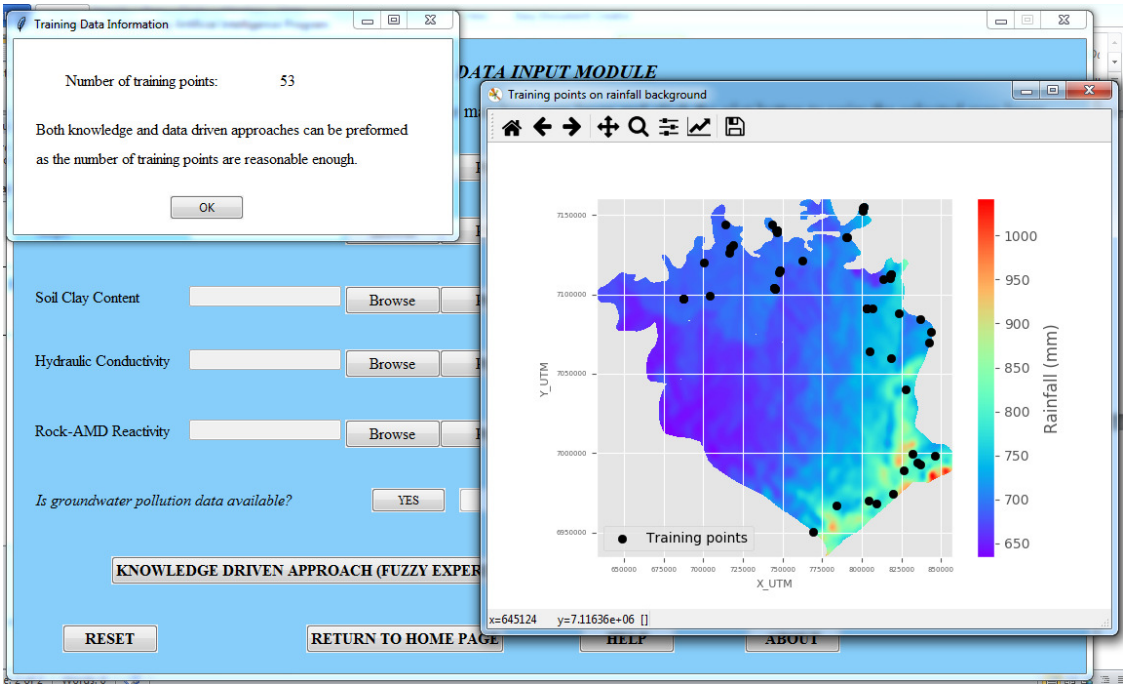

Figure A17: Input module window

Figure A17 presents a screen shot of the window that pops up after loading boreholes and clicking the plot button. This view displays the spatial distribution of the points on the rainfall map. In addition, a small window is displayed showing the number of points in the input data file.

Fuzzy Expert System Module

The fuzzy expert System module is used to generate a fuzzy groundwater vulnerability model using the ten map raster layers from the input data module. The module allows the user to design the fuzzy membership function for each map layer according to expert knowledge on AMD processes in the study area. In addition, the user is able to execute automatic processing which relies on parameters, as outlined in Sakala *et al.* (2018). When designing the fuzzy expert system, the drop-down buttons are used to select values for the map value (m_i) and confidence (cf_i), c_max and c_min for each of the corresponding map layers. The c_max value specifies the maximum values of w_i and the c_min value specifies the minimum value of w_i according to the equation below:

$$\mu_z = \frac{m_i * cf_i * w_i}{1000}$$

The steps for using the fuzzy module are as follows:

1. In the fuzzy module, adjust the design parameters (map value (m_i), confidence (cf_i), c_max and $\_min$).
2. Clicking on the corresponding "*PLOT*" button to view the fuzzy values for each map.

3. Once all the map layers have been converted to fuzzy values, specify the fuzzy operations (AND, OR, PRODUCT, GAMMA, SUM) reflecting the relationships between the map layers.

4. Click the "PLOT" button next to each operator to view the output for that stage. The colour of the button changes to red (Figure A19). Figure A20 presents an example of the combination of the input of all the sources into one fuzzy map for sources (Figure A20).

5. Select the map layer from folder C:\GVA_AI\Fuzzy for the sources, transport and traps and click the PLOT button on the far right to generate the combined output (Figure A21). The details of the map will also be displayed.

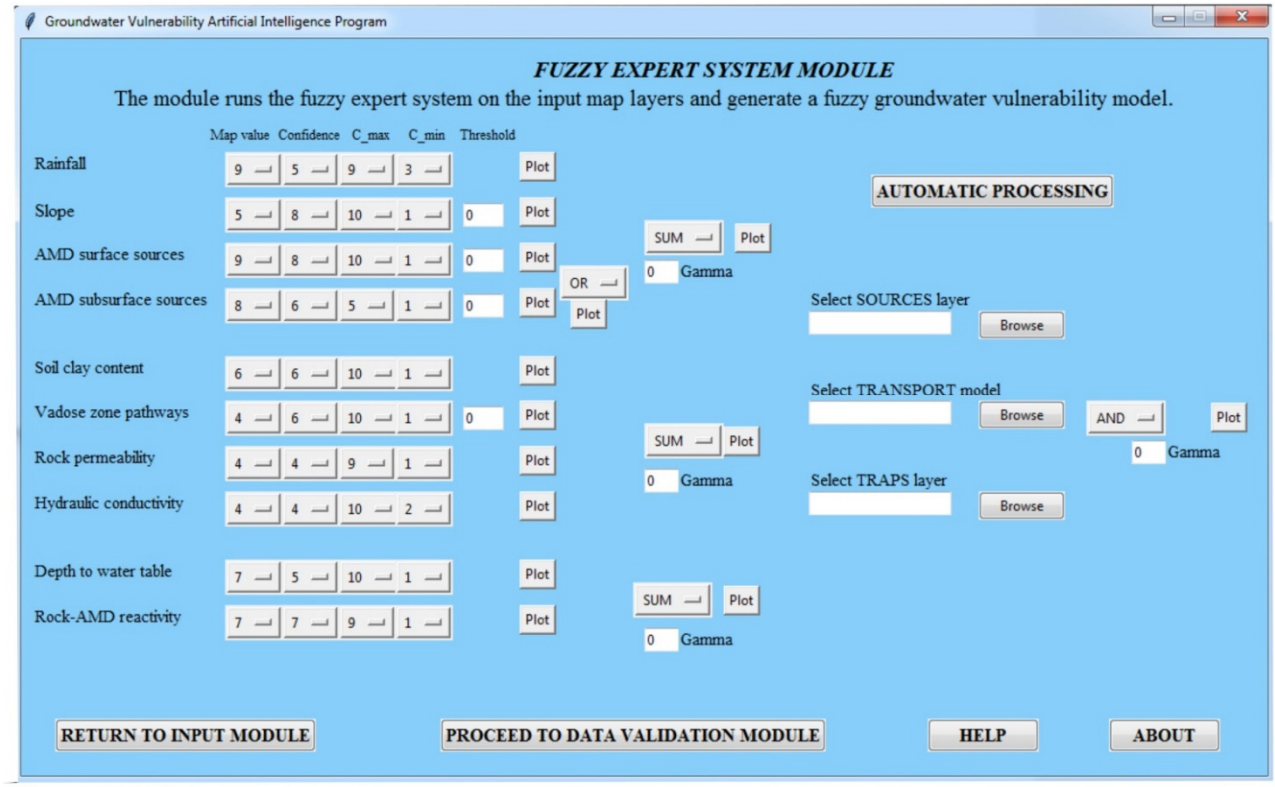

Figure A18: Fuzzy expert system module window

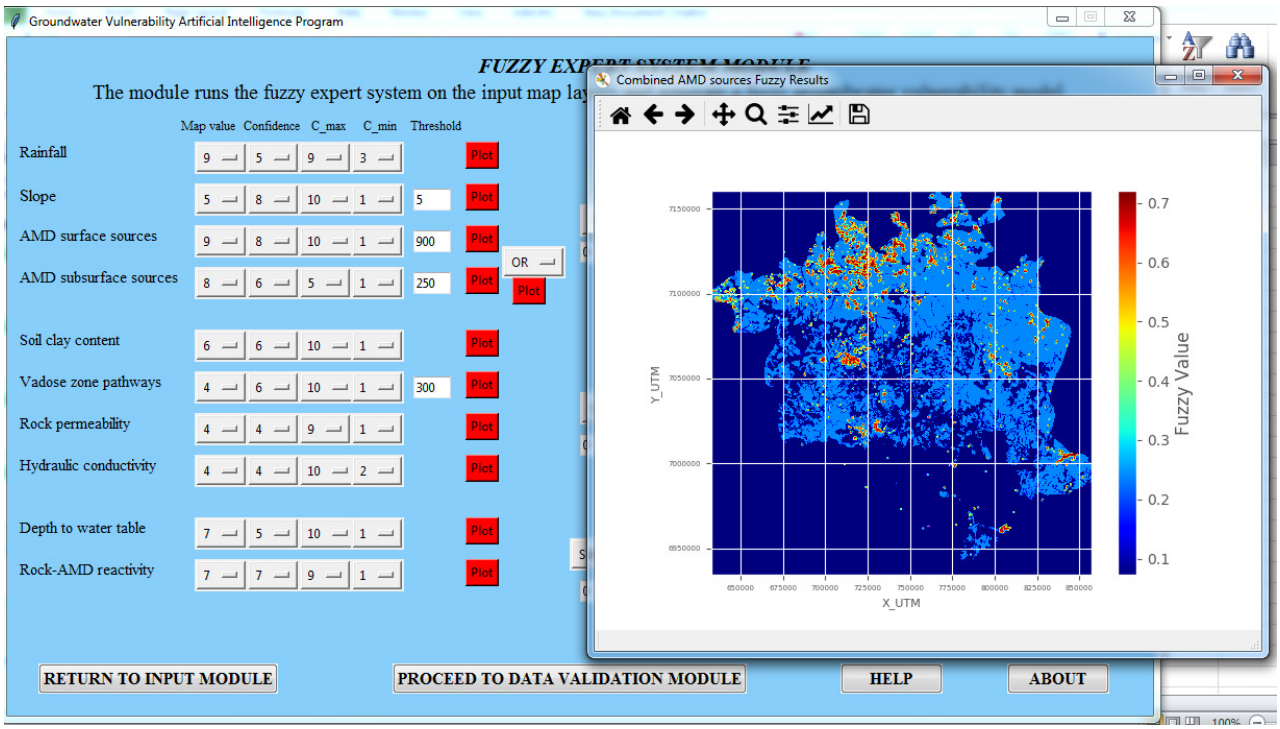

Figure A19: Source output in fuzzy values

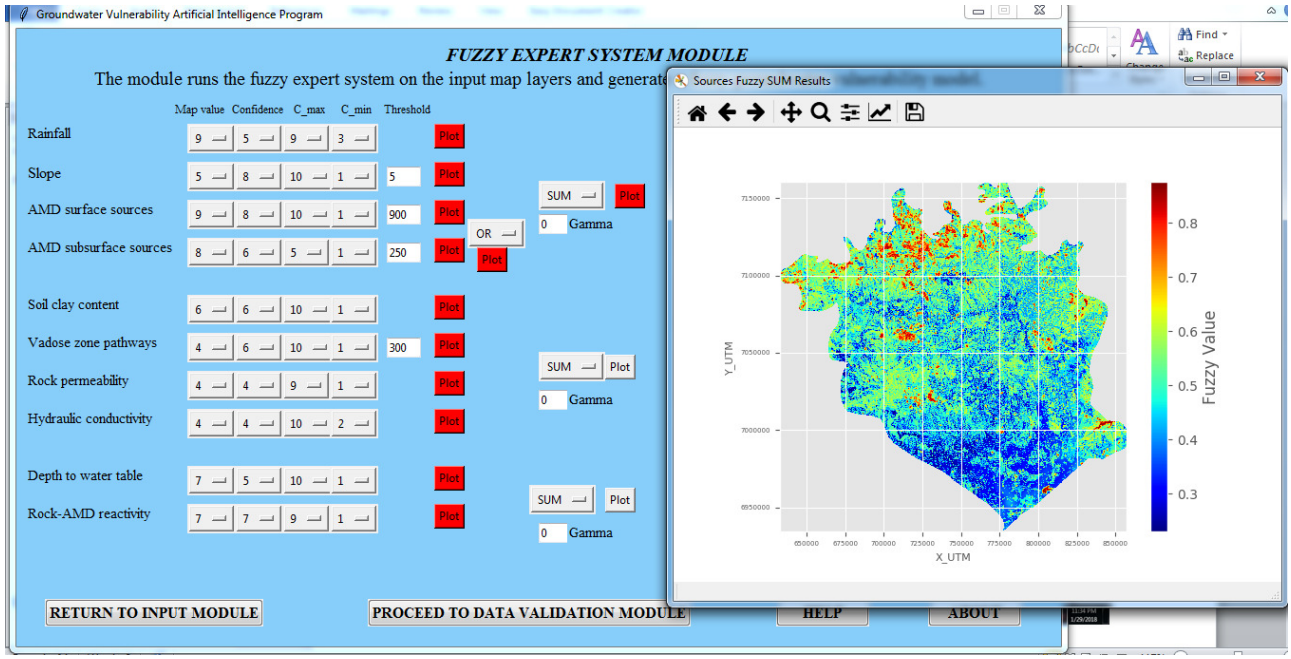

Figure A20: Map output after combining all the inputs from the sources

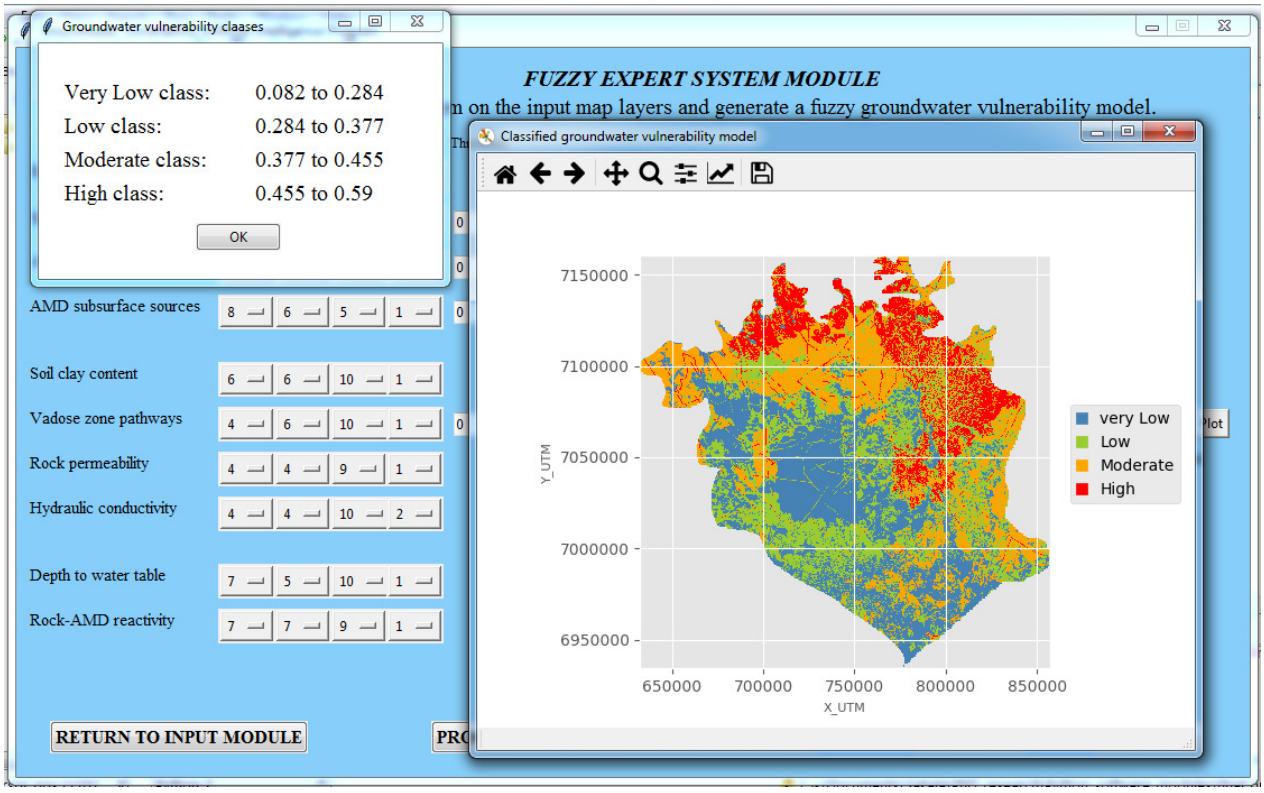

Figure A21: Fuzzy expert system output map

Data Pre-Processing Module for Data-Driven AI Systems

The purpose of the data pre-processing module (Figure A22) is to prepare the data in a format which is comprehensible to the data-driven system facilitating the production of a binary map. Figure 8.7 shows the GUI for the pre-processing module.

The step for the data pre-processing are:

1. Click on TEST button and a graph will appear, showing a cumulative graph (Figure A23). Use the cumulative graph to identify a range of values within which at least 50% of boreholes with a high sulphate concentration are found. If a test is complete, the test button turns red. Record the range of values for each map.

2. Enter the values on the set threshold values section for each map and click the corresponding PLOT button. After the map is displayed the colour of the button changes to red. Once all the maps have been plotted each of the buttons will have turned to red. Then, click on the "CREATE TRAINING DATASET" button. The previously disabled "GO TO ARTIFICIAL NEURAL NETWORK" and "GO TO ADAPTIVE NEURO-FUZZY INFERENCE SYSTEM" buttons will be enabled.

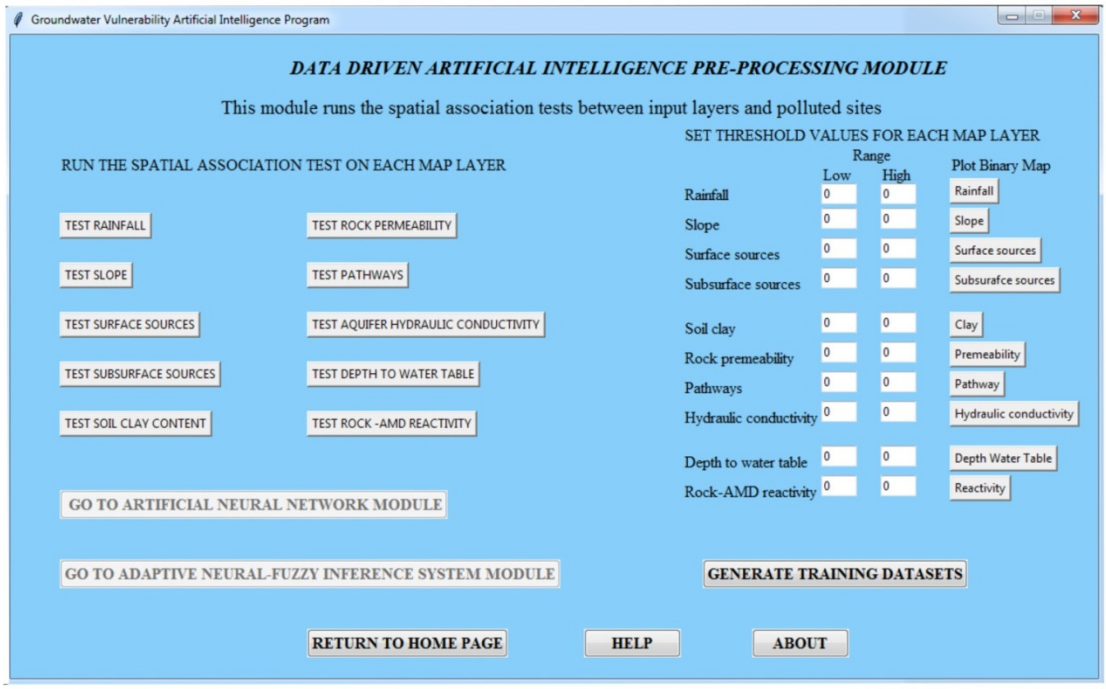

Figure A22: Data-driven artificial intelligence data pre-processing module window

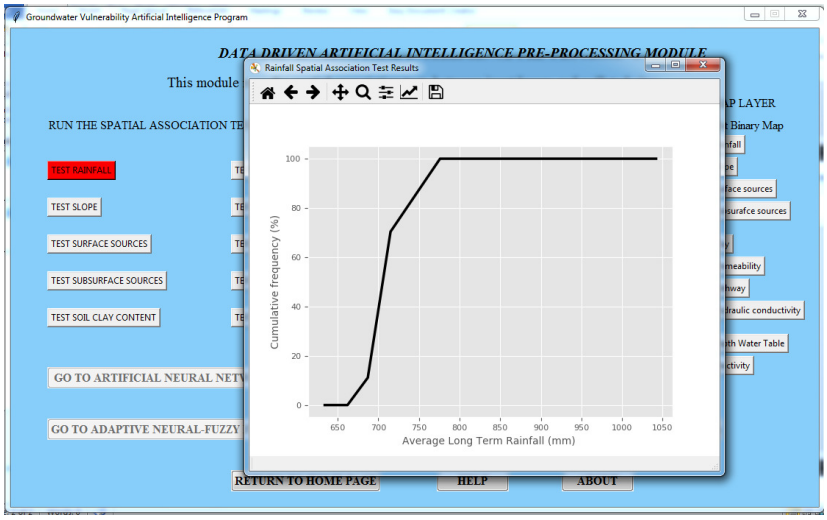

Figure A23: Spatial association test result

Artificial Neural Networks Module

The artificial neural network module receives data from the pre-processing module and computes the groundwater vulnerability model using the Artificial Neural Network (ANN) algorithm. Figure 10 shows the GUI for ANN module and the results are shown in Figure 11.

The steps for the production an ANN model are:

1. Enter the number of neurons in the hidden layer and the number of training epochs (iterations) and select the activation function,
2. Click the "RUN PROGRAM" button and graphs and the ANN model will also be displayed.

3. When clicking the “RUN AUTOMATIC TRAINING” button, the program will determine the number of hidden layers and epoch on its own.

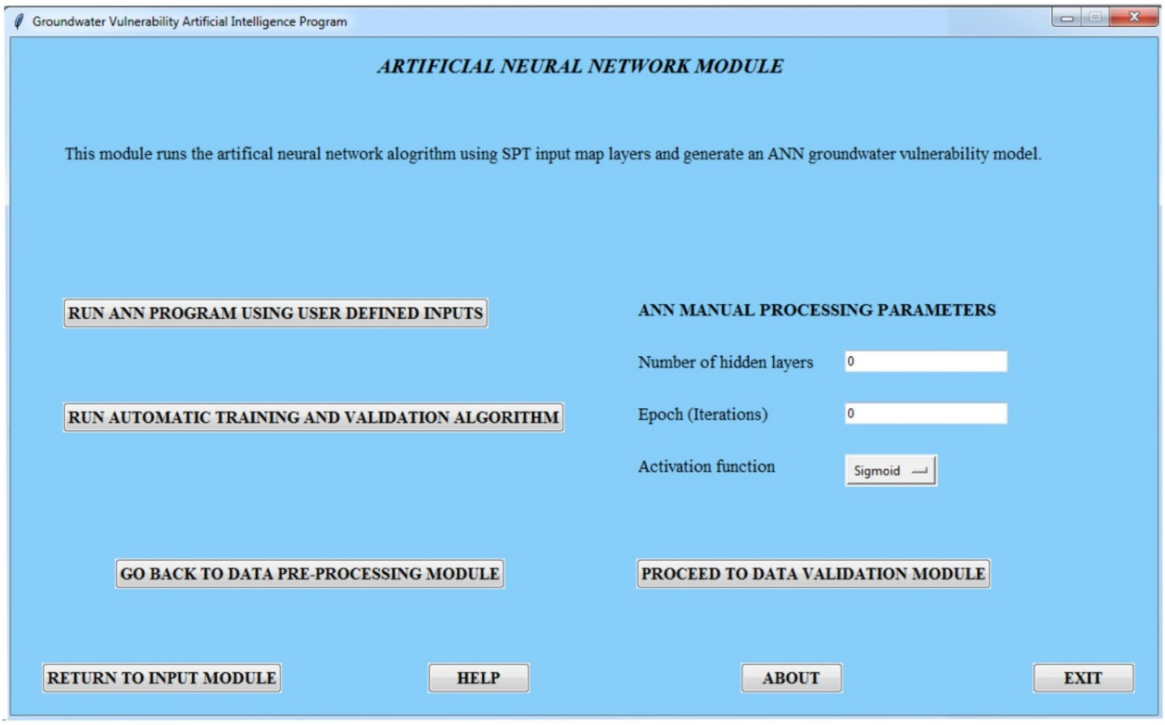

Figure A24: ANN module window

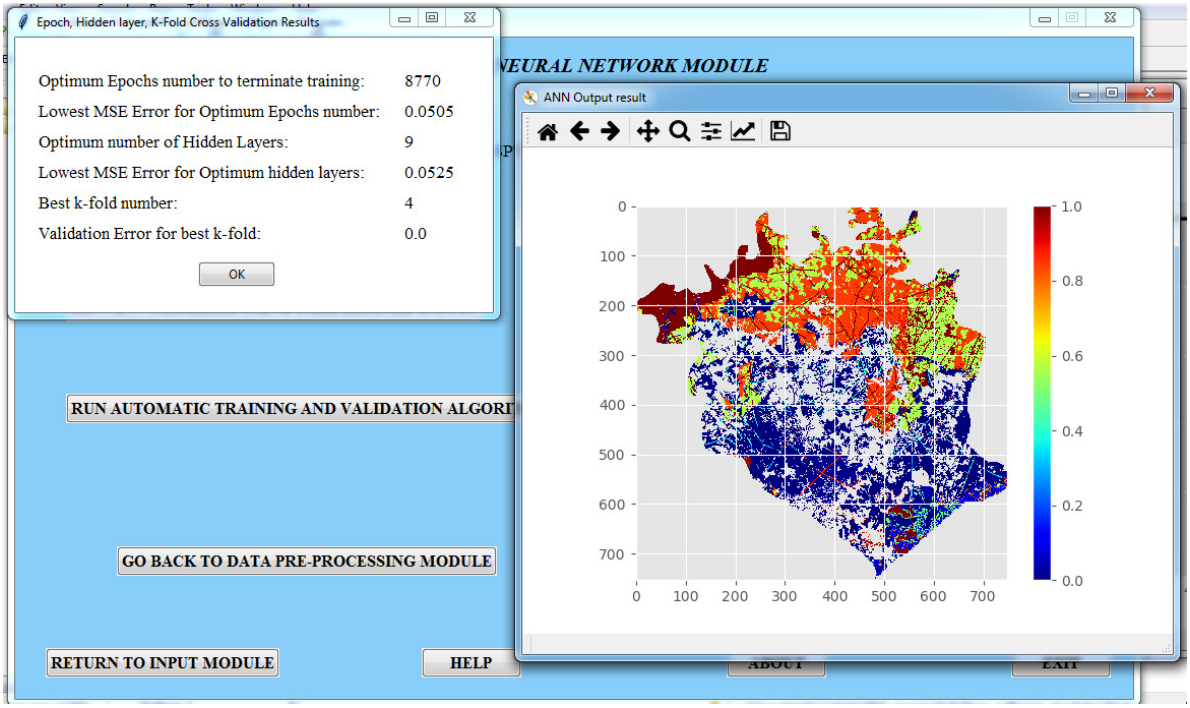

Figure A25: Display of ANN results

Adaptive Neural-Fuzzy Inference System (ANFIS) Module

This module runs the ANFIS hybrid algorithm to produce a groundwater vulnerability model. Figure 14 shows the GUI of the ANF module. The steps are:

1. Enter the number of training epochs (iterations) and values of mean and sigma and select the activation function,
2. Click the "RUN ANFIS" button and the output ANFIS model will be displayed (Figure 15),
3. Selecting the automatic processing program will run the ANFIS algorithm using pre-set parameters. Then click the "RUN AUTOMATIC ANFIS PROCESSING" button and the program will determine the number of training epochs and generate the ANFIS model.

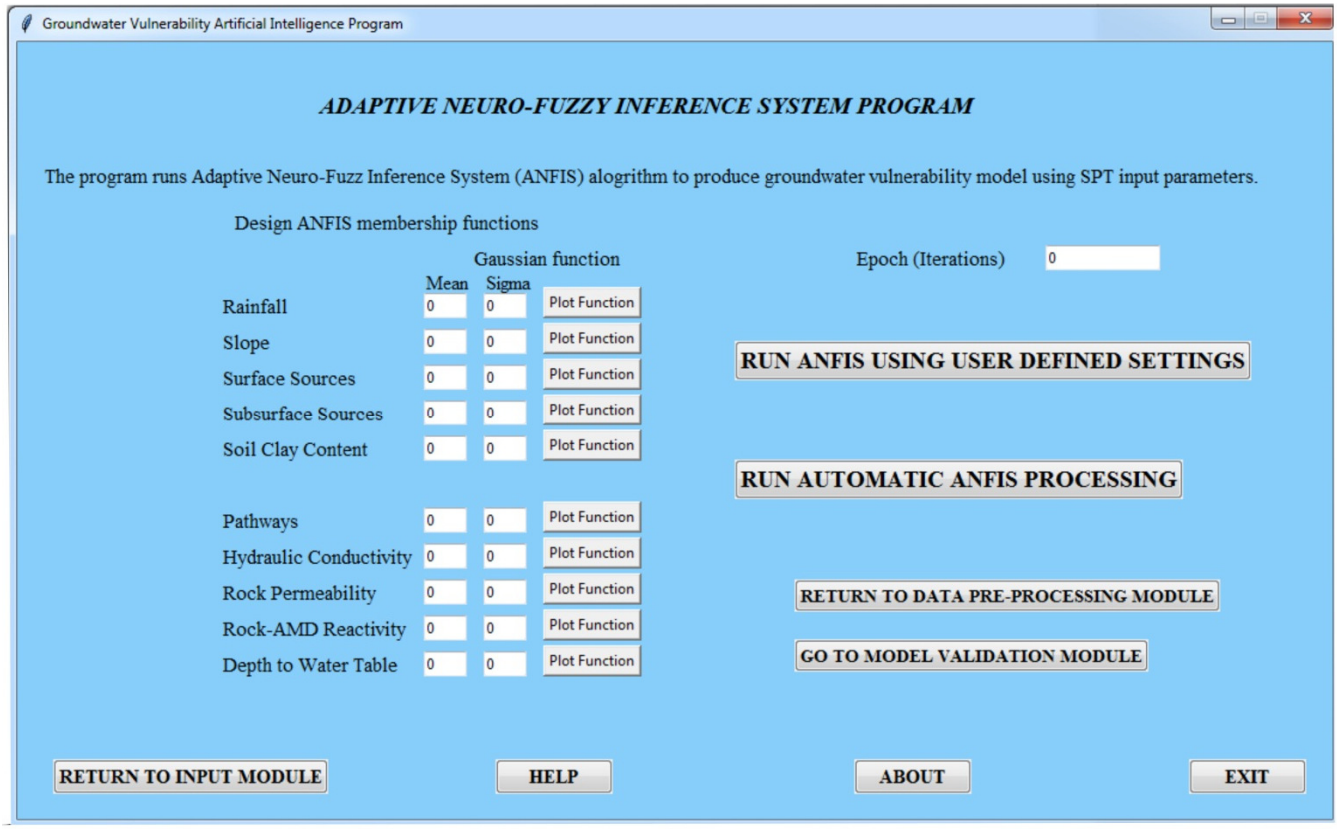

Figure A26: Adaptive Neural-Fuzzy Inference System module window

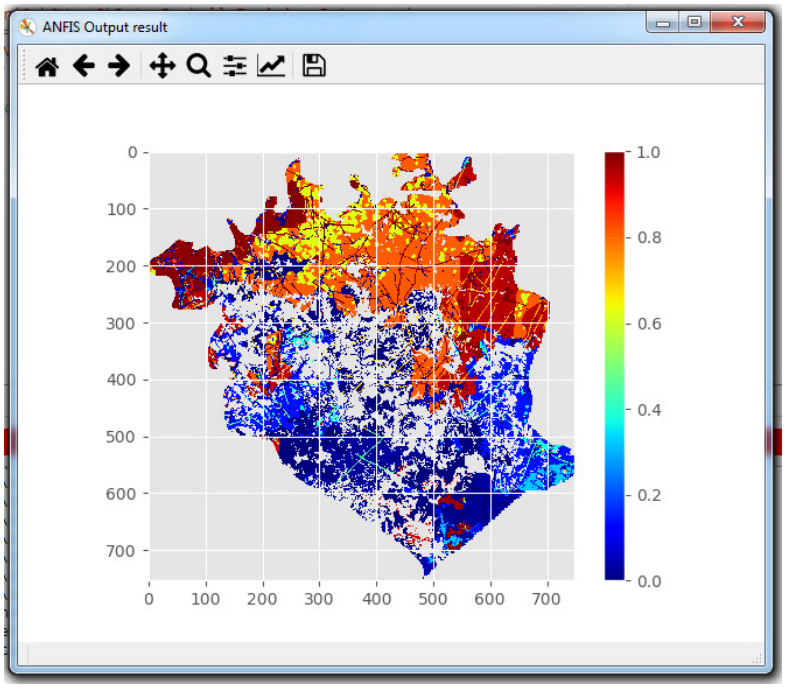

Figure A27: Adaptive Neural-Fuzzy Inference module

Model validation Module

The model validation module statistically validates the generated AI models using a separate validation vector dataset. Figure A28 shows the GUI for the module.

The steps for using the model validation module:

1. Browse the validation vector data from their stored location in the computer,
2. Search for the models produced: the data path is C:\GVAI\Fuzzy for the fuzzy module, C:\GVAI\ANN for the ANN model and C:\GVAI\ANFIS for the ANFIS model. The loaded models may be viewed by clicking of "PLOT" button of the corresponding model,
3. Click the "VALIDATE" button on each of the models to display a correlation coefficient value, as shown in Figure A29.

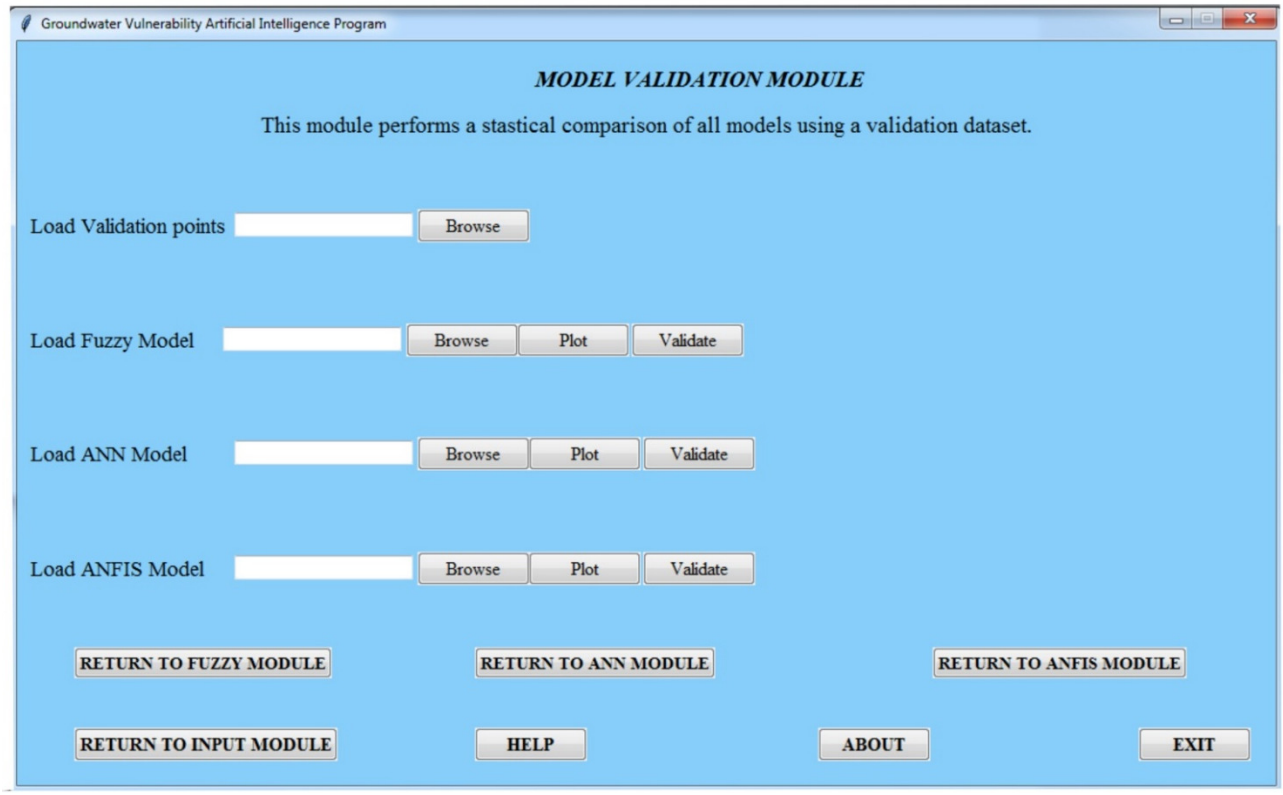

Figure A28: Model comparison module

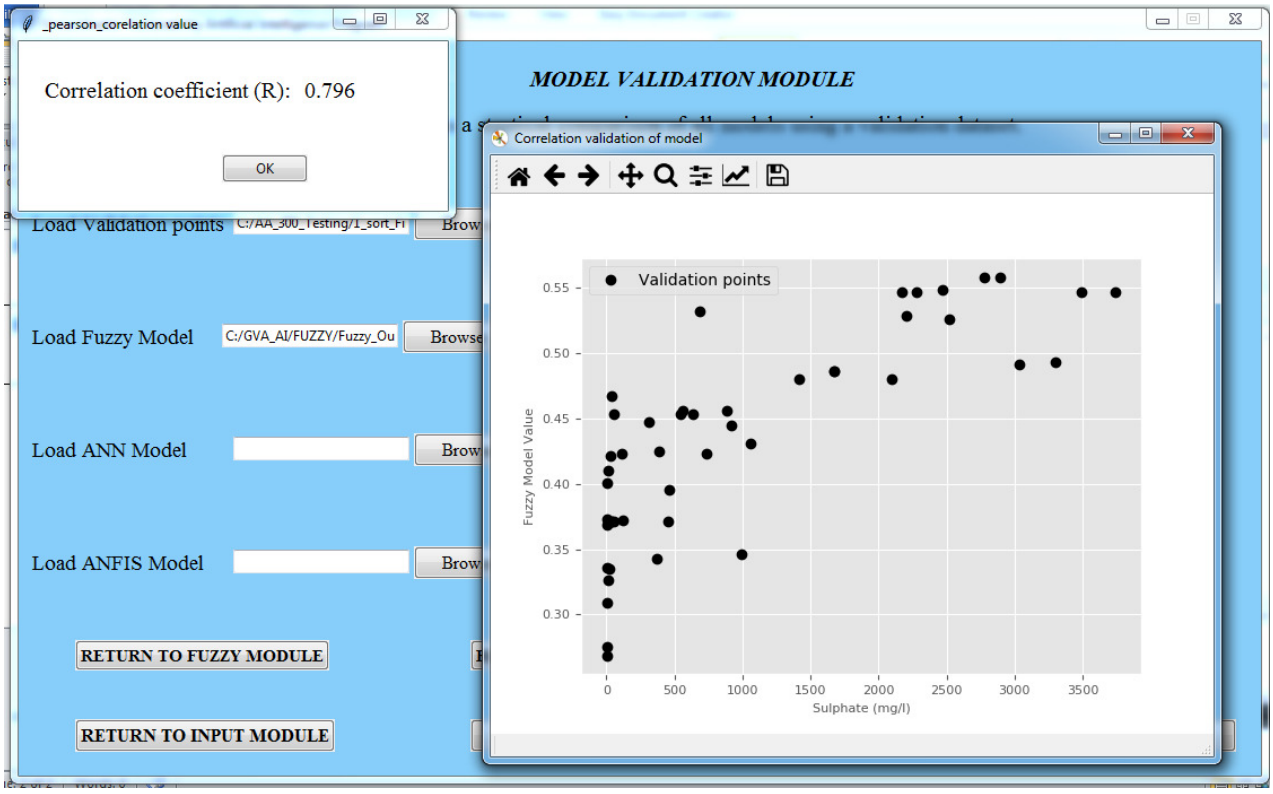

Figure A29: Validation graph of the fuzzy model

ABSTRACT

Despite groundwater being a very important and valuable source of water for humans it is under serious threat by human activities such as mining. Nevertheless, benefits of mining, in particular coal mining, have led to improvement in the social and economic development of many countries. However, despite the important benefits of coal to developing and developed countries, groundwater pollution caused by coal mining generated pollutants (acid mine drainage (AMD)) is a significant problem globally. Finding scientific solutions on how coal mining and coal waste disposal can be controlled and monitored from a policy and decision-making perspective in view of ultimately minimising the pollution of groundwater resources in coalfields is therefore an urgent imperative. This can be done by undertaking a coalfield-scale groundwater vulnerability assessment to rank areas in terms of the likelihood of pollutants reaching the groundwater.

The research discusses the development of a new approach for groundwater vulnerability assessment specific to AMD at a regional coalfield scale using artificial intelligence to automate some of the processes and to assist in the generation of rapid groundwater vulnerability assessment results for use by policy and decision-makers in controlling coal mining and coal waste disposal in a typical coalfield. The approach is a hybrid of the index and overlay, process-based simulation and statistical approaches generated by combining factors associated with pollutant sources, energy that drives the pollution migration and the ways AMD pollution interacts with the subsurface both physically and chemically. Laboratory analyses (rock-AMD reactivity, soil batch leach tests) and fieldwork (water sampling, ground geophysics) were done to generate the input map layers and to validate the produced results.

The modified approach is illustrated through a discussion of a case study of AMD pollution in the Witbank, Ermelo and Highveld coalfields of the Mpumalanga and KwaZulu-Natal Provinces in South Africa. Many AMD cases have been reported in these provinces in recent years and are a cause of concern for local municipalities, mining and environmental agencies. In the Witbank, Ermelo and Highveld coalfields, several areas have been mined out while mining has not yet started in others, hence the need to identify groundwater regions prone to AMD pollution in order to avoid further impacts on the groundwater resources.

A knowledge-based fuzzy expert system, an artificial neural network (ANN) system and an adaptive neuro-fuzzy inference system (ANFIS) were built using vulnerability factors (energy sources, ligands sources, pollutant sources, transportation pathways and traps) to generate groundwater vulnerability models of the coalfields. Highly vulnerable areas were identified in the Witbank coalfield and the eastern part of the Ermelo coalfield which are characterised by the presence of AMD sources and

good subsurface transport coupled with poor AMD pollution trapping properties. The results from all three AI systems show a strong positive correlation of over 0.8 with groundwater sulphate concentrations from two different datasets. In addition, relationships between geophysical responses (resistivity and seismic velocity) and model values were obtained and used to validate the models. The results show that the proposed approach can indeed be used for groundwater vulnerability assessment.

As a summary of the AI system, a toolbox containing all the tools needed for AI modelling of groundwater vulnerability was developed. The toolbox is flexible and works both for manual and semi-automatic processing allowing the user to contribute to the decisions taken in the modelling. The toolbox serves to automate many processes associated with this type of modelling, resulting in higher processing speed and improved accuracy in the generation of the model.

The methodology only considers the AMD pollution attenuation and migration at a regional scale and does not account for local-scale sources of pollution and attenuation. Further research to refine the approach may include the incorporation of groundwater flow direction and temporal datasets for the future prediction of groundwater vulnerability. The approach may also be applied to other coalfields to assess its robustness to changing hydrogeological conditions.

KEYWORDS: *Artificial Intelligence, Groundwater Vulnerability, Algorithm, Fuzzy Expert System, Artificial Neural Network, Adaptive Neuro-Fuzzy Inference System*